

Quantifying Earthquake Collapse Risk of Tall Steel Braced Frame Buildings Using Rupture-to-Rafters Simulations

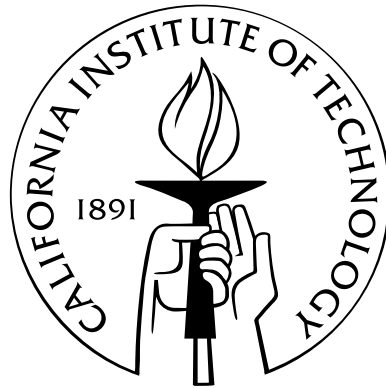
Thesis by

Ramses Mourhatch

In Partial Fulfillment of the Requirements

for the Degree of

Doctor of Philosophy



California Institute of Technology

Pasadena, California

2015

(Defended April 9, 2015)

© 2015
Ramses Mourhatch
All Rights Reserved

To
my mother, brothers, and the memory of my father

Acknowledgements

This thesis represents the result of my past six years at Caltech, years that forever changed my life in numerous ways. The pursuit of my Ph.D. degree was only possible because of the constant support from Caltech faculty members, friends, colleagues, and family. First and foremost, I would like to thank my advisors, Dr. Swaminathan Krishnan and Dr. Thomas Heaton. Dr. Krishnan has been extremely supportive from the day I started at Caltech, with his constant guidance and supervision. With great patience, hands-on approach, and a clear vision he helped me to grow as a researcher. Moreover, he continued his support without any disruption from India over the past two years; these assistances have been vital for me to finish my Ph.D. He provided me with opportunities to mentor undergraduate research students and also granted me the freedom to think and experiment with various ideas. In addition to the academic and research assistantship, Swami supported me during the emotionally tough times and gave me moral support. I would like to thank Dr. Thomas Heaton, who supported my research endeavors at the end of my time at Caltech. Discussions with him were always very interesting and thought provoking. Due to his great enthusiasm for science, and his love for teaching and mentorship, he will always remain a role model for me.

I would also like to thank Dr. Robert Graves, who patiently helped me on numerous occasions and generously provided me with the data needed at various points during my research. He guided me on a variety of topics, which made the first half of my research possible. I would like to thank the rest of my defense committee members, Dr. John Hall and Dr. James Beck, for their guidance and support during the course of my research. I would also like to thank the Civil Engineering department collectively for creating an unmatched environment with many unique and essential aspects necessary for a thriving research institute. An environment that encourages free thinking,

inspires collaborations, and cherishes a culture for openness, discussion, and sharing of knowledge. Additionally, I would like to thank the department for their support and understanding during the tough emotional period that I was going through over the last year with the loss of my beloved father. Also, my thanks to Carolina Oseguera, Cheryl Greer, Chris Silva, and Lynn Seymour at the MCE department for their help.

I would like to thank my fellow graduate students, Ahmed Elbanna, Daniel Stuyo, Inho Cho, Vanessa Heckman, Ming Hei Cheng, Shiyang Song, Pinaky Battacharya, Swetha Veeraraghavan, Abel Dizon, Arnar Bjornsson, Grant Hollis, and Stephen Wu. I should specially thank Anthony Massari, who shared his knowledge and experience regarding structural design. I would also like to thank my friend and colleague, Hemanth Siriki, who worked on a similar topic and shared an office for the past six years. His constant help, and numerous technical and non-technical discussions, directly impacted my work at Caltech. Also, I would like to thank my friends Hamed Bajgiran and Jasmin Javadi for their constant support, which was essential for me.

I would like to extend my gratitude towards my relatives, Fredrick Mirza, Emily Mourhatch, Hormoz Mourhatch, Henry Mourhatch, Mariet Mourhatch, Ramseen Bet-Niessan, Rameil Bet-Niessan, and Demeil Nissan. I would like to dedicate this thesis to my family: my sister in-law Shanit, my brothers Ryan and Ramoun, and my mother Frances, and the memory of my father Eddie (George). They have always been a constant source of motivation and encouragement and their unconditional support in all aspects of my life continuously provides me with the strength and courage to persevere.

Abstract

This thesis examines collapse risk of tall steel braced frame buildings using rupture-to-rafters simulations due to suite of San Andreas earthquakes. Two key advancements in this work are the development of (i) a rational methodology for assigning scenario earthquake probabilities and (ii) an artificial correction-free approach to broadband ground motion simulation. The work can be divided into the following sections: earthquake source modeling, earthquake probability calculations, ground motion simulations, building response, and performance analysis.

As a first step the kinematic source inversions of past earthquakes in the magnitude range of 6-8 are used to simulate 60 scenario earthquakes on the San Andreas fault. For each scenario earthquake a 30-year occurrence probability is calculated and we present a rational method to redistribute the forecast earthquake probabilities from UCERF to the simulated scenario earthquake. We illustrate the inner workings of the method through an example involving earthquakes on the San Andreas fault in southern California.

Next, three-component broadband ground motion histories are computed at 636 sites in the greater Los Angeles metropolitan area by superposing short-period (0.2 s-2.0 s) empirical Green's function synthetics on top of long-period (> 2.0 s) spectral element synthetics. We superimpose these seismograms on low-frequency seismograms, computed from kinematic source models using the spectral element method, to produce broadband seismograms.

Using the ground motions at 636 sites for the 60 scenario earthquakes, 3-D nonlinear analysis of several variants of an 18-story steel braced frame building, designed for three soil types using the 1994 and 1997 Uniform Building Code provisions and subjected to these ground motions,

are conducted. Model performance is classified into one of five performance levels: Immediate Occupancy, Life Safety, Collapse Prevention, Red-Tagged, and Model Collapse. The results are combined with the 30-year probability of occurrence of the San Andreas scenario earthquakes using the PEER performance based earthquake engineering framework to determine the probability of exceedance of these limit states over the next 30 years.

Contents

Acknowledgements	iv
Abstract	vi
1 Introduction	1
2 Risk Analysis Using Rupture-to-Rafters Simulations: Inferring Probabilities of Scenario Earthquakes from the Uniform California Earthquake Rupture Forecast	4
2.1 Introduction	4
2.2 Ground Motion Simulation	6
2.3 UCERF	7
2.4 Considerations for UCERF application to PSHA using rupture-to-rafters simulations	10
2.5 Scenario Earthquake Probabilities from Forecast Earthquake Probabilities	12
2.5.1 Southern San Andreas Fault Case Study	12
2.5.2 Methodology	13
2.6 Discussion	19
3 Simulation of Broadband Ground Motion by Superposing High-Frequency Empirical Green's Function Synthetics on Low-Frequency Spectral-Element Synthetics	21
3.1 Introduction	21
3.2 Source Model Selection	24

3.3	Low-Frequency Ground Motion Waveforms	25
3.4	High-Frequency Ground Motion Waveforms	26
3.4.1	EGF Event Selection	26
3.4.2	EGF Summation	28
3.5	Broadband Ground Motion Waveforms	30
3.6	Validation of Methodology	30
3.6.1	Validation 1: 1999 M_w 7.1 Hector Mine Earthquake	31
3.6.2	Validation 2 : 2004 M_w 6.0 Parkfield Earthquake	39
3.7	Discussion	46
4	Building Design: 18-Story Braced Frame (UBC 1994 and UBC 1997)	52
4.1	Introduction	52
4.1.1	Architectural and Structural Description	52
4.1.2	Damage Description	57
4.1.3	Past Studies	57
4.2	Building Codes Overview	61
4.3	UBC 1994 Design Guidelines	62
4.3.1	Load Combinations	62
4.3.2	Load Reductions	62
4.3.3	Gravity loading criteria for the design	63
4.3.4	Wind criteria for the deign	64
4.3.5	Seismic design criteria : Static force procedure	65
4.3.5.1	Estimating an initial fundamental period, T	65
4.3.5.2	Soil Type	66
4.3.5.3	Base shear calculations	68
4.3.5.4	Vertical distribution of lateral forces	69

4.3.5.5	Overturning and Horizontal Torsional Moments	70
4.3.6	Seismic design criteria : Dynamic force procedure	71
4.3.6.1	Ground Motion	71
4.3.6.2	Response Spectrum Analysis	71
4.3.7	Deflection and drift criteria	73
4.3.8	Special Requirements for Steel Structures	73
4.3.8.1	General Requirements for Columns	73
4.3.8.2	Requirements for Special Concentric Braced Frames (SCBF). . .	74
4.4	UBC 1994 SCBF Final Design	76
4.5	UBC 1997 Design Guidelines	80
4.5.1	Load Combinations	80
4.5.2	Load Reductions	81
4.5.3	Gravity loading criteria for the design	81
4.5.4	Wind criteria for the deign	81
4.5.5	Seismic design criteria : Static force procedure	81
4.5.5.1	Estimating an initial fundamental period, T	81
4.5.5.2	Soil Type	81
4.5.5.3	Base shear calculations	83
4.5.5.4	Vertical distribution of lateral forces	84
4.5.5.5	Overturning and Horizontal Torsional Moments	85
4.5.6	Seismic design criteria : Dynamic force procedure	85
4.5.6.1	Ground Motion	85
4.5.6.2	Response Spectrum Analysis	85
4.5.7	Deflection and drift criteria	86
4.5.8	Special Requirements for Steel Structures	87
4.5.8.1	General Requirements for Columns	87

4.5.8.2	Requirements for Special Concentrically Braced Frames	87
4.6	UBC 1997 SCBF Final Design	88
5	Quantification of Performance of 18-Story Steel Braced Frame Building Using Rupture-To-Rafters Simulations Under a Suite of Simulated San Andreas Earthquakes	91
5.1	Introduction	91
5.2	Methodology	93
5.3	Earthquake Source Models and Associated Probabilities	94
5.3.1	Source Models	94
5.3.2	Scenario Earthquake Probabilities	97
5.4	Ground Motion Simulation	99
5.5	Target Buildings	115
5.6	Pushover Analysis	119
5.7	Building Seismic Response Evaluation Criteria	123
5.8	Building Performance in Scenario Earthquakes	133
5.9	30-Year Exceedance Probabilities of Various Performance Levels Using the PEER PBEE Framework	145
6	Conclusions and Future Work	149
6.1	Conclusions	149
6.2	Future Work	151
A	Resampling Calculations	154
B	Bias in synthetics associated with S_a	157
C	List of stations	158
D	EGF methodology validation: 1999 Hector Mine earthquake	161

E	EGF methodology validation: 2004 Parkfield earthquake	196
F	Braced Frame Version of Canoga Park Building	
	Braced Frame - UBC 1994 Building Code	245
F.1	Braced Frame Version of Canoga Park Building	
	Braced Frame - UBC 1994 Building Code	
	S_3 Site Categories	
	Frame Elevations - Beam, Column, and Brace size	247
F.2	Braced Frame Version of Canoga Park Building	
	Braced Frame - UBC 1994 Building Code	
	S_3 Site Categories	
	Frame Elevations - Beam, Column, and Brace size	256
G	Braced Frame Version of Canoga Park Building	
	Braced Frame - UBC 1997 Building Code	266
G.1	Braced Frame Version of Canoga Park Building	
	Braced Frame - UBC 1997 Building Code	
	S_B Site Categories	
	Frame Elevations - Beam, Column, and Brace size	267
G.2	Braced Frame Version of Park Building	
	Braced Frame - UBC 1997 Building Code	
	S_C Site Categories	
	Frame Elevations - Beam, Column, and Brace size	277
G.3	Braced Frame Version of Canoga Park Building	
	Braced Frame - UBC 1997 Building Code	
	S_D Site Categories	
	Frame Elevations - Beam, Column, and Brace size	287

H Additional Fragility Curves	297
H.1 Fragility Curves for 94S2, 97SB, and 97SC	298

List of Figures

2.1	(a) The 1440 logic tree branches in UCERF-3 and their associated weights. (b) Fault segmentation used in UCERF-3. A “forecast earthquake” comprises two or more successive segments rupturing. Figure source: UCERF-3.	9
2.2	All plausible (or “forecast”) earthquakes that rupture at least one segment of the southern section of the San Andreas fault (from Parkfield in central California to Bombay Beach in southern California, shown in red). The X axis identifies the extent of rupture of a forecast earthquake and the Y axis identifies its magnitude. Line colors indicate forecast earthquake occurrence probabilities, with warmer colors (red, orange) indicative of higher probability of occurrence and colder colors (blue) indicative of lower probability of occurrence.	10
2.3	Slip distribution from a finite source inversion of the 2002 M_w 7.89 earthquake on the Denali fault mapped on to rupture locations 1, 3, and 5 of the southern San Andreas fault. (a)-(c) North-to-south rupture direction. (d)-(f) South-to-north rupture direction. The red star corresponds to the hypocenter location.	14
2.4	The 30 scenario earthquakes (shown in black) superposed on top of the forecast earthquakes from Fig. 2.2. Two rupture directions are considered for each, bringing the total number of scenario earthquakes to 60. Dashed black lines demarcate the magnitude bins adopted in the case study.	15

2.5	<p>Illustrative example of the method used to derive scenario earthquake probabilities from forecast earthquake probabilities. Horizontal blue line: target fault. Dotted black lines: fault segmentation. Red unfilled rectangles: forecast earthquakes (F.E.) with seismic moment rates indicated by rectangle heights [step (ii) of method]. Yellow shaded region: seismic moment rate contributions of several forecast earthquakes to a given segment [step (iii)]. Red shaded region: summation of yellow shaded regions [step (iv)]. Magenta colored region: seismic moment rate of a scenario earthquake (S.E.) by summing the moment rates of all the segments [step (v)]. Magenta lines: rupture extent of S.E.s.</p>	18
3.1	<p>Schematic representation of EGF event selection. Of all the historical records available in the vicinity of target site i from earthquakes on the target fault located in the vicinity of subfault j, the record g_{ij} best represents the path between target site i and subfault j (Irikura 1983).</p>	28
3.2	<p>Time shifts used in previous studies. (a) moment (or slip) vs. time and approximation using multiple EGFs (b) Moment-rate (or slip rate) vs. time and approximation using multiple EGFs (c) Subfault j time shifts $f_j(k)$ used in the EGF summation. . .</p>	30
3.3	<p>Time shifts used in this study. (a) moment (or slip) vs. time and approximation using multiple EGFs (b) Moment-rate (or slip rate) vs. time and approximation using multiple EGFs (c) Subfault j time shifts $f_j(k)$ used in the EGF summation. . .</p>	30
3.4	<p>Fault segments of source model for the 1999 M_w 7.1 Hector Mine earthquake, resampled to a subfault dimension of 0.5 km Color map: Slip distributions in centimeters Arrows: Slip direction Counters: Rupture times in seconds Star: Hypocenter of the event.</p>	32

3.5	(a) : Location of all stations used in the 1999 Hector Mine earthquake validation. Red line: San Andreas Fault Blue line: Surface projection of the Ji et al. source model Star: Epicenter Black triangles: Stations (b) Fault segments in the model Blue line: Surface projections Black line: Surface trace Star: Epicenter.	33
3.6	Comparison of simulated (red) and observed (black) ground velocity histories and spectra at station 9.	35
3.7	Comparison of simulated (red) and observed (black) ground velocity histories and spectra at station 15.	36
3.8	Comparison of simulated (red) and observed (black) ground velocity histories and spectra at station 30.	37
3.9	(a) Comparisons of peak ground velocity (PGV) of the simulated and the recorded broadband ground motions as a function of station distance to the hypocenter. (b) Natural log of the residual of simulated and recorded values.	38
3.10	(a) Comparisons of peak ground velocity (PGV) of the high-frequency content of the simulated and the recorded ground motions as a function of station distance to the hypocenter. (b) Natural log of the residual of simulated and recorded values.	38
3.11	Bias in the synthetic associated with 5%-damped acceleration response spectra at 32 stations relative to the corresponding spectra of recorded ground motion. Blue line: Bias. Red line: Standard error.	39
3.12	Resampled kinematic source model for the 2004 M_w 6.0 Parkfield earthquake by 21)	40
3.13	Location of all stations used in the 2004 Parkfield earthquake validation. Red line: San Andreas Fault Black line: Trace/surface projection of the 21)	40
3.14	Comparison of simulated (red) and observed (black) ground velocity histories and spectra at station 1.	42
3.15	Comparison of simulated (red) and observed (black) ground velocity histories and spectra at station 10.	43

3.16	Comparison of simulated (red) and observed (black) ground velocity histories and spectra at station 40.	44
3.17	(a) Comparisons of peak ground velocity (PGV) of the simulated and the recorded broadband ground motions as a function of station distance to the hypocenter. (b) Natural log of the residual of simulated and recorded values.	45
3.18	(a) Comparisons of peak ground velocity (PGV) of the high-frequency content of the simulated and the observed ground motions as a function of station distance. (b) Natural log of the residual of simulated and recorded values.	45
3.19	Bias in the synthetic 5%-damped acceleration response spectra at 46 stations relative to the corresponding spectra of recorded ground motion. Blue line: Bias. Red line: Standard error.	46
3.20	Comparison of the amplitude spectra of the transfer functions [p(t)] for the 2004 Parkfield earthquake. EGF magnitude: 2.5; Black line: Theoretical value; Red line: Uniform distribution; Blue line: Non-uniform distribution used in this study.	50
3.21	Comparison of the amplitude spectra of the transfer functions [p(t)] for the 1999 Hector Mine earthquake. EGF magnitude: 3.0; Black line: Theoretical value; Red line: Uniform distribution; Blue line: Non-uniform distribution used in this study.	50
3.22	Model bias in the 5%-damped acceleration spectra of the Hector Mine earthquake synthetics produced using (a) the traditional approach of uniformly spaced EGFs and (b) using the present approach of unevenly spaced EGFs. Red line: Standard error.	51
3.23	Model bias in the 5%-damped acceleration spectra of the Parkfield earthquake synthetics produced using (a) the traditional approach of uniformly spaced EGFs and (b) using the present approach of unevenly spaced EGFs. Red line: Standard error.	51
4.1	Existing building - Plan of ground level and second floor.	53
4.2	Existing building - Plan of third and fourth floors.	54

4.3	Existing building - Plan of floors 5 through 17.	54
4.4	Existing building - Penthouse floor plan.	55
4.5	Existing building - Roof floor plan.	55
4.6	Site categories assigned for the scope of this study. Light-blue triangles represent soil category S_2 and orange triangles represents soil category S_3	68
4.7	The UBC 1994 response spectrum used in the design.	72
4.8	Isometric view of the Canoga building designed based on UBC 1994 using braced frame lateral load resisting system.	77
4.9	Site categories assigned for the scope of this study at each of the 636 stations. Blue triangles represent soil category S_B , yellow triangles represent soil category S_C , and orange triangles represents soil category S_D	82
4.10	The UBC 1997 response spectrum used in the design.	86
5.1	Kinematic finite source model of the 2002 M_w 7.9 Denali earthquake mapped on the southern San Andreas fault at five locations. The left column illustrates the five north-to-south propagating scenario earthquakes whereas the right column illustrates the south-to-north propagating earthquakes. Note that in reversing the rupture direction, the slip distribution is flipped as well. The red stars correspond to the hypocenters.	96
5.2	Median peak geometric mean horizontal displacement (m), velocity (m/s), and 5%-damped spectral acceleration (g) at 1 s and 0.2 s periods plotted as a function of earthquake magnitude from scenario earthquake simulations (blue lines) and the Campbell-Bozorgnia NGA (red lines). The vertical bars correspond to the one standard deviation spread above and below the median values.	103
5.3	Median PGD [(a)-(b)] and PGV [(c)-(d)] values as a function of the Joyner-Boore source-to-site distance from scenario earthquake simulations [(a)-(c)] and the Campbell-Bozorgnia NGA [(b)-(d)].	104

5.5 Basin depth (km) map for southern California. Red triangles indicate the geographical distribution of the 636 southern California sites where ground motions from the scenario earthquakes are computed. The ellipses identify the basins in southern California: Simi valley, San Fernando valley, San Gabriel valley, and Los Angeles basin. 108

5.6 Predictions of spectral accelerations at 1 s and 3 s periods for the ten M_w 7.89 scenario earthquakes (five locations and two rupture directions) by simulations and the CB-08 NGA relations: (a) and (b). Median values as a function of the Joyner-Boore source-to-site distance: (c) and (d). Median S_a maps from simulations: (e) and (f). Median S_a maps from CB-08 NGA relations. 109

5.7 Directivity effect: Comparison of simulated peak horizontal velocity from north-to-south and south-to-north ruptures of the magnitude 7.89 scenario earthquake at locations 1 [(a)-(b)] and 5 [(c)-(d)]. 114

5.8 Geometric mean of peak horizontal ground velocities under the (a) simulated M_w 7.89 south-to-north propagating scenario earthquake at location 5, (b) the south-to-north propagating M_w 7.80 ShakeOut scenario earthquake rupturing the San Andreas fault from Bombay Beach in the south to Lake Hughes in the north, and (c) the predictions by the CB-08 NGA relations. 115

5.9 (a) Isometric view and (b) typical floor plan of the Canoga Park building. 117

5.10 Classification of the soils at the 636 target sites in southern California by the (a) 1994 and the (b) 1997 Uniform Building Codes. 118

5.11	Pushover curves for the 5 building models: Base shear normalized by the seismic weight as a function of the overall building drift in the (a) X (E-W) and (b) Y (N-S) directions; Evolution of the normalized base shear (solid lines) and the overall building drift (dashed lines) as a function of time in the (c) X (E-W) and (d) Y (N-S) directions.	123
5.12	97Sc model response under three-component ground motion at the city of Covina (station 580) from the north-to-south M_w 7.89 San Andreas fault scenario earthquake at location 3: (a) 3D snap shot of the deformed model at collapse initiation; (b) deformed shape of the north braced frame; (c) damage in members of the north frame (a segment damage index of 1.00 indicates a severed brace whereas a segment damage index of 0.00 indicates no damage whatsoever); circle size is proportional to the index. Red color indicates segment failure. (d) Idealization of the buckling/yielding-induced sidesway mechanism.	127
5.13	(a) Buckling/yielding-induced sidesway mechanism damage index (SMDI) as a function of the peak interstory drift ratio observed in the 1994 and 1997 UBC site-specific designs at the 636 analysis sites in southern California under the ten M_w 7.89 San Andreas fault earthquake scenarios. Blue circles correspond to cases where the computational model does not collapse, whereas red circles correspond to cases where model collapses. Blue line is the median SMDI as a function of the peak IDR. (b) Cumulative histogram and best-fitting log-normal CDF representing the frequentist probability of model collapse [red dots in (a)]. The red and magenta lines on both figures correspond to the 5 th and 10 th percentile of the CDF.	129

5.14	Story extent (vertical bars) of buckling/yielding-induced sidesway mechanisms in the 1994 and 1997 UBC site-specific designs at the 636 analysis sites in southern California under the ten M_w 7.89 San Andreas fault earthquake scenarios in increasing order of peak IDR. Bar color corresponds to the predominant period of ground motion whereas the central circle color corresponds to the PGV.	131
5.15	Frequentist probability of a given story being involved in a buckling/yielding-induced sidesway mechanism in each of the five building models.	132
5.16	Peak IDR response of the UBC94 [(a), (c), (e)] and UBC97 [(b), (d), (f)] designs of the 18-story steel braced frame building under north-to-south propagating ruptures at location 1 of the southern San Andreas fault: [(a)-(b)] M_w 7.89, [(c)-(d)] M_w 7.59, and [(e)-(f)] M_w 7.28.	134
5.17	Peak IDR response of the UBC94 [(a), (c), (e)] and UBC97 [(b), (d), (f)] designs of the 18-story steel braced frame building under north-to-south propagating ruptures at location 3 of the southern San Andreas fault: [(a)-(b)] M_w 7.89, [(c)-(d)] M_w 7.59, and [(e)-(f)] M_w 7.28.	135
5.18	Peak IDR in the five building models as a function of the peak ground velocity and displacement of all scenario earthquake records. The magenta, red, yellow, green, and blue colors correspond to collapse imminent (CO), red-tagged (RT), collapse prevention (CP), life safety (LS), and immediate occupancy (IO) performance categories, respectively.	138

5.19	Peak IDR as a function of directional PGV and predominant time period of ground motion from all scenario earthquake records: (a) E-W (X) direction of 94S2 design; (b) N-S (Y) direction of 94S2 design; (c) E-W (X) direction of 94S3 design; and (d) N-S (Y) direction of 94S3 design. The magenta, red, yellow, green, and blue colors correspond to collapse imminent (CO), red-tagged (RT), collapse prevention (CP), life safety (LS), and immediate occupancy (IO) performance categories, respectively. The black vertical lines correspond to the model fundamental period in the direction under consideration.	140
5.20	Peak IDR as a function of directional PGV and predominant time period of ground motion from all scenario earthquake records: (a) E-W (X) direction of 97Sb design; (b) N-S (Y) direction of 97Sb design; (c) E-W (X) direction of 97Sc design; (d) N-S (Y) direction of 97Sc design; (e) E-W (X) direction of 97Sc design; and (f) N-S (Y) direction of 97Sc design; The magenta, red, yellow, green, and blue colors correspond to collapse imminent (CO), red-tagged (RT), collapse prevention (CP), life safety (LS), and immediate occupancy (IO) performance categories, respectively. The black vertical lines correspond to the model fundamental period in the direction under consideration.	141
5.21	Fragility curves of the probability of the peak IDR in the 94S3 (solid) and the 97Sd (dashed) buildings exceeding the IO, LS, CP, RT, and CO performance levels as a function of the PGV in the (a) E-W and the (b) N-S directions. (c) The E-W and (d) the N-S PGV thresholds for 2%, 5%, 10%, and 50% exceedance probabilities of various performance levels in the 94S3 (circles) and the 97Sd (squares) designs. . . .	143

5.22	Fragility curves of the probability of the peak IDR in the 94S3 (solid) and the 97Sd (dashed) buildings exceeding the IO, LS, CP, RT, and CO performance levels as a function of the spectral acceleration at the building period in the (a) E-W and the (b) N-S directions. (c) The E-W and (d) the N-S S_a thresholds for 2%, 5%, 10%, and 50% exceedance probabilities of various performance levels in the 94S3 (circles) and the 97Sd (squares) designs.	144
5.23	Contribution of different magnitudes to total probability of exceedance of the IO, LS, CP, RT, and CO performance levels of the braced frame building at the 636 southern California sites from earthquakes on the San Andreas fault in the next 30 years for: (a) the older 1994 UBC designs and (b) the newer 1997 UBC designs. . .	148
A.1	Resampling Calculation	154
D.1	Location of all stations used in validation of the 1999 Hector Mine earthquake. Red line: San Andreas Fault; Black line: trace/surface projection of earthquake source model; Star: epicenter; Black triangles: stations	162
D.2	Comparison of simulated (red) and observed (black) ground motions at station 1. . .	164
D.3	Comparison of simulated (red) and observed (black) ground motions at station 2. . .	165
D.4	Comparison of simulated (red) and observed (black) ground motions at station 3. . .	166
D.5	Comparison of simulated (red) and observed (black) ground motions at station 4. . .	167
D.6	Comparison of simulated (red) and observed (black) ground motions at station 5. . .	168
D.7	Comparison of simulated (red) and observed (black) ground motions at station 6. . .	169
D.8	Comparison of simulated (red) and observed (black) ground motions at station 7. . .	170
D.9	Comparison of simulated (red) and observed (black) ground motions at station 8. . .	171
D.10	Comparison of simulated (red) and observed (black) ground motions at station 9. . .	172
D.11	Comparison of simulated (red) and observed (black) ground motions at station 10. . .	173
D.12	Comparison of simulated (red) and observed (black) ground motions at station 11. . .	174

D.13	Comparison of simulated (red) and observed (black) ground motions at station 12.	. 175
D.14	Comparison of simulated (red) and observed (black) ground motions at station 13.	. 176
D.15	Comparison of simulated (red) and observed (black) ground motions at station 14.	. 177
D.16	Comparison of simulated (red) and observed (black) ground motions at station 15.	. 178
D.17	Comparison of simulated (red) and observed (black) ground motions at station 16.	. 179
D.18	Comparison of simulated (red) and observed (black) ground motions at station 17.	. 180
D.19	Comparison of simulated (red) and observed (black) ground motions at station 18.	. 181
D.20	Comparison of simulated (red) and observed (black) ground motions at station 19.	. 182
D.21	Comparison of simulated (red) and observed (black) ground motions at station 20.	. 183
D.22	Comparison of simulated (red) and observed (black) ground motions at station 21.	. 184
D.23	Comparison of simulated (red) and observed (black) ground motions at station 22.	. 185
D.24	Comparison of simulated (red) and observed (black) ground motions at station 23.	. 186
D.25	Comparison of simulated (red) and observed (black) ground motions at station 24.	. 187
D.26	Comparison of simulated (red) and observed (black) ground motions at station 25.	. 188
D.27	Comparison of simulated (red) and observed (black) ground motions at station 26.	. 189
D.28	Comparison of simulated (red) and observed (black) ground motions at station 27.	. 190
D.29	Comparison of simulated (red) and observed (black) ground motions at station 28.	. 191
D.30	Comparison of simulated (red) and observed (black) ground motions at station 29.	. 192
D.31	Comparison of simulated (red) and observed (black) ground motions at station 30.	. 193
D.32	Comparison of simulated (red) and observed (black) ground motions at station 31.	. 194
D.33	Comparison of simulated (red) and observed (black) ground motions at station 32.	. 195
E.1	Location of all stations used in validation of the 2004 Parkfield earthquake. Red line: San Andreas Fault; Black line: trace/surface projection of earthquake source model; Star: epicenter; Black triangles: stations	197
E.2	Comparison of simulated (red) and observed (black) ground motions at station 1. . .	199

E.3	Comparison of simulated (red) and observed (black) ground motions at station 2.	200
E.4	Comparison of simulated (red) and observed (black) ground motions at station 3.	201
E.5	Comparison of simulated (red) and observed (black) ground motions at station 4.	202
E.6	Comparison of simulated (red) and observed (black) ground motions at station 5.	203
E.7	Comparison of simulated (red) and observed (black) ground motions at station 6.	204
E.8	Comparison of simulated (red) and observed (black) ground motions at station 7.	205
E.9	Comparison of simulated (red) and observed (black) ground motions at station 8.	206
E.10	Comparison of simulated (red) and observed (black) ground motions at station 9.	207
E.11	Comparison of simulated (red) and observed (black) ground motions at station 10.	208
E.12	Comparison of simulated (red) and observed (black) ground motions at station 11.	209
E.13	Comparison of simulated (red) and observed (black) ground motions at station 12.	210
E.14	Comparison of simulated (red) and observed (black) ground motions at station 13.	211
E.15	Comparison of simulated (red) and observed (black) ground motions at station 14.	212
E.16	Comparison of simulated (red) and observed (black) ground motions at station 15.	213
E.17	Comparison of simulated (red) and observed (black) ground motions at station 16.	214
E.18	Comparison of simulated (red) and observed (black) ground motions at station 17.	215
E.19	Comparison of simulated (red) and observed (black) ground motions at station 18.	216
E.20	Comparison of simulated (red) and observed (black) ground motions at station 19.	217
E.21	Comparison of simulated (red) and observed (black) ground motions at station 20.	218
E.22	Comparison of simulated (red) and observed (black) ground motions at station 21.	219
E.23	Comparison of simulated (red) and observed (black) ground motions at station 22.	220
E.24	Comparison of simulated (red) and observed (black) ground motions at station 23.	221
E.25	Comparison of simulated (red) and observed (black) ground motions at station 24.	222
E.26	Comparison of simulated (red) and observed (black) ground motions at station 25.	223
E.27	Comparison of simulated (red) and observed (black) ground motions at station 26.	224
E.28	Comparison of simulated (red) and observed (black) ground motions at station 27.	225

E.29	Comparison of simulated (red) and observed (black) ground motions at station 28.	. 226
E.30	Comparison of simulated (red) and observed (black) ground motions at station 29.	. 227
E.31	Comparison of simulated (red) and observed (black) ground motions at station 30.	. 228
E.32	Comparison of simulated (red) and observed (black) ground motions at station 31.	. 229
E.33	Comparison of simulated (red) and observed (black) ground motions at station 32.	. 230
E.34	Comparison of simulated (red) and observed (black) ground motions at station 33.	. 231
E.35	Comparison of simulated (red) and observed (black) ground motions at station 34.	. 232
E.36	Comparison of simulated (red) and observed (black) ground motions at station 35.	. 233
E.37	Comparison of simulated (red) and observed (black) ground motions at station 36.	. 234
E.38	Comparison of simulated (red) and observed (black) ground motions at station 37.	. 235
E.39	Comparison of simulated (red) and observed (black) ground motions at station 38.	. 236
E.40	Comparison of simulated (red) and observed (black) ground motions at station 39.	. 237
E.41	Comparison of simulated (red) and observed (black) ground motions at station 40.	. 238
E.42	Comparison of simulated (red) and observed (black) ground motions at station 41.	. 239
E.43	Comparison of simulated (red) and observed (black) ground motions at station 42.	. 240
E.44	Comparison of simulated (red) and observed (black) ground motions at station 43.	. 241
E.45	Comparison of simulated (red) and observed (black) ground motions at station 44.	. 242
E.46	Comparison of simulated (red) and observed (black) ground motions at station 45.	. 243
E.47	Comparison of simulated (red) and observed (black) ground motions at station 46.	. 244
F.1	East-west frame elevation along grid A (Braced frame - UBC 1994 - Site Category : S_2)	. 247
F.2	East-west frame elevation along grid B (Braced frame - UBC 1994 - Site Category : S_2)	. 248
F.3	East-west frame elevation along grid C (Braced frame - UBC 1994 - Site Category : S_2)	. 249

F.4	East-west frame elevation along grid D (Braced frame - UBC 1994 - Site Category : S_2)	250
F.5	East-west frame elevation along grid E (Braced frame - UBC 1994 - Site Category : S_2)	251
F.6	North-south frame elevation along grid 1 (Braced frame - UBC 1994 - Site Category : S_2)	252
F.7	North-south frame elevation along grid 2 (Braced frame - UBC 1994 - Site Category : S_2)	253
F.8	North-south frame elevation along grid 5 (Braced frame - UBC 1994 - Site Category : S_2)	254
F.9	North-south frame elevation along grid 6 (Braced frame - UBC 1994 - Site Category : S_2)	255
F.10	East-west frame elevation along grid A (Braced frame - UBC 1994 - Site Category : S_3)	257
F.11	East-west frame elevation along grid B (Braced frame - UBC 1994 - Site Category : S_3)	258
F.12	East-west frame elevation along grid C (Braced frame - UBC 1994 - Site Category : S_3)	259
F.13	East-west frame elevation along grid D (Braced frame - UBC 1994 - Site Category : S_3)	260
F.14	East-west frame elevation along grid E (Braced frame - UBC 1994 - Site Category : S_3)	261
F.15	North-south frame elevation along grid 1 (Braced frame - UBC 1994 - Site Category : S_3)	262
F.16	North-south frame elevation along grid 2 (Braced frame - UBC 1994 - Site Category : S_3)	263

F.17	North-south frame elevation along grid 5 (Braced frame - UBC 1994 - Site Category : S_3)	264
F.18	North-south frame elevation along grid 6 (Braced frame - UBC 1994 - Site Category : S_3)	265
G.1	East-west frame elevation along grid A (Braced frame - UBC 1997 - Site Category : S_B)	268
G.2	East-west frame elevation along grid B (Braced frame - UBC 1997 - Site Category : S_B)	269
G.3	East-west frame elevation along grid C (Braced frame - UBC 1997 - Site Category : S_B)	270
G.4	East-west frame elevation along grid D (Braced frame - UBC 1997 - Site Category : S_B)	271
G.5	East-west frame elevation along grid E (Braced frame - UBC 1997 - Site Category : S_B)	272
G.6	North-south frame elevation along grid 1 (Braced frame - UBC 1997 - Site Category : S_B)	273
G.7	North-south frame elevation along grid 2 (Braced frame - UBC 1997 - Site Category : S_B)	274
G.8	North-south frame elevation along grid 5 (Braced frame - UBC 1997 - Site Category : S_B)	275
G.9	North-south frame elevation along grid 6 (Braced frame - UBC 1997 - Site Category : S_B)	276
G.10	East-west frame elevation along grid A (Braced frame - UBC 1997 - Site Category : S_C)	278

G.11	East-west frame elevation along grid B (Braced frame - UBC 1997 - Site Category : <i>S_C</i>)	279
G.12	East-west frame elevation along grid C (Braced frame - UBC 1997 - Site Category : <i>S_C</i>)	280
G.13	East-west frame elevation along grid D (Braced frame - UBC 1997 - Site Category : <i>S_C</i>)	281
G.14	East-west frame elevation along grid E (Braced frame - UBC 1997 - Site Category : <i>S_C</i>)	282
G.15	North-south frame elevation along grid 1 (Braced frame - UBC 1997 - Site Category : <i>S_C</i>)	283
G.16	North-south frame elevation along grid 2 (Braced frame - UBC 1997 - Site Category : <i>S_C</i>)	284
G.17	North-south frame elevation along grid 5 (Braced frame - UBC 1997 - Site Category : <i>S_C</i>)	285
G.18	North-south frame elevation along grid 6 (Braced frame - UBC 1997 - Site Category : <i>S_C</i>)	286
G.19	East-west frame elevation along grid A (Braced frame - UBC 1997 - Site Category : <i>S_D</i>)	288
G.20	East-west frame elevation along grid B (Braced frame - UBC 1997 - Site Category : <i>S_D</i>)	289
G.21	East-west frame elevation along grid C (Braced frame - UBC 1997 - Site Category : <i>S_D</i>)	290
G.22	East-west frame elevation along grid D (Braced frame - UBC 1997 - Site Category : <i>S_D</i>)	291
G.23	East-west frame elevation along grid E (Braced frame - UBC 1997 - Site Category : <i>S_D</i>)	292

G.24	North-south frame elevation along grid 1 (Braced frame - UBC 1997 - Site Category : S_D)	293
G.25	North-south frame elevation along grid 2 (Braced frame - UBC 1997 - Site Category : S_D)	294
G.26	North-south frame elevation along grid 5 (Braced frame - UBC 1997 - Site Category : S_D)	295
G.27	North-south frame elevation along grid 6 (Braced frame - UBC 1997 - Site Category : S_D)	296
H.1	Fragility curves of the probability of the peak IDR in the 94S2 (solid), the 97Sb (dotted), and the 97Sc (dashed) buildings exceeding the IO, LS, and CP performance levels as a function of the PGV in the (a) E-W and the (b) N-S directions. (c) The E-W and (d) the N-S PGV thresholds for 2%, 5%, 10%, and 50% exceedance probabilities of various performance levels in the 94S2 (circles), the 97Sb (triangle), and 97Sc (squares) designs.	298
H.2	Fragility curves of the probability of the peak IDR in the 94S2 (solid), the 97Sb (dotted), and the 97Sc (dashed) buildings exceeding the IO, LS, and CP performance levels as a function of the spectral acceleration at the building period in the (a) E-W and the (b) N-S directions. (c) The E-W and (d) the N-S S_a thresholds for 2%, 5%, 10%, and 50% exceedance probabilities of various performance levels in the 94S2 (circles), the 97Sb (triangle), and 97Sc (squares) designs.	299

List of Tables

2.1	List of past earthquakes, fault parameters, and the finite source inversions used as kinematic source models for the southern San Andreas fault case study.	12
2.2	Time-independent 30-year occurrence probabilities of the scenario earthquakes in the southern San Andreas case study derived from UCERF forecast earthquake probabilities. Half of these probabilities may be assigned to north-to-south propagating ruptures and the other half to south-to-north propagating ruptures.	19
3.1	Source parameters for the the 1999 M_w 7.1 Hector Mine.	32
4.1	Member sizing, material specification and properties for the existing Canoga moment frame building.	56
4.2	Summary of the seismic weights used in past studies. All values are in kips.	59
	60table.caption.42	
4.4	Gravity loading criteria.	64
4.5	Values used for calculating wind forces.	65
4.6	UBC 1994 site categories and conditions.	67
4.7	Average shear wave velocities (top 30 meters of the soil profile) used in this study for categorizing the soil conditions for UBC 1994.	67
4.8	Summary of parameters used in seismic design and base shear calculation - UBC 1994.	69
4.9	Seismic design parameters for UBC 1994.	78

4.10	Building natural periods and modal directions for the first 3 modes of vibration for S_2 (UBC 1994) site condition.	78
4.11	Building natural periods and modal directions for the first 3 modes of vibration for S_3 (UBC 1994) site condition.	79
4.12	Member sizes, specifications, and properties for the new buildings (UBC 1994).	79
4.13	UBC 1997 site categories and conditions.	82
4.14	Summary of parameters used in seismic design and base shear calculation - UBC 1997.	84
4.15	Seismic design parameters for UBC 1997.	89
4.16	Building natural periods and modal directions for the first 3 modes of vibration for S_B (UBC 1997) site condition.	89
4.17	Building natural periods and modal directions for the first 3 modes of vibration for S_C (UBC 1997) site condition.	90
4.18	Building natural periods and modal directions for the first 3 modes of vibration for S_D (UBC 1997) site condition.	90
4.19	Member sizes, specifications, and properties for the new buildings (UBC 1997).	90
5.1	List of past earthquakes with fault geometry and rupture mechanisms closely matching earthquakes on the San Andreas fault whose kinematic finite source inversions are used in this study. The salient source parameters are listed as well.	95
5.2	UCERF3 time-independent 30-year occurrence probabilities for the 30 scenario earthquakes (six magnitudes and five rupture locations). Half of these probabilities are assigned to north-to-south propagating ruptures and the other half to south-to-north propagating ruptures.	98

5.3	Comparison of ground motion intensities from the ten (five locations and two rupture directions) simulated M_w 7.89 scenario earthquakes against CB-08 NGA predictions at fourteen locations in southern California, where a significant number of tall buildings exist.	110
5.4	Comparison of ground motion intensities from the ten (five locations and two rupture directions) simulated M_w 7.59 scenario earthquakes against CB-08 NGA predictions at fourteen locations in southern California where a significant number of tall buildings exist.	111
5.5	Comparison of ground motion intensities from the ten (five locations and two rupture directions) simulated M_w 7.28 scenario earthquakes against CB-08 NGA predictions at fourteen locations in southern California where a significant number of tall buildings exist.	112
5.6	Seismic design parameters and dynamic characteristics for the five building models.	120
5.7	Median and median + one standard deviation performance of the UBC 1994 and 1997 buildings under shaking from the ten (five locations and two rupture directions) M_w 7.89 San Andreas fault earthquakes at the 14 locations (Fig. 5.5) in southern California where a significant number of tall buildings exist.	136
5.8	Conditional probability of exceedance (as percentage) of the IO, LS, CP, RT, and CO performance levels in the older (1994 UBC designs) and the newer (1997 UBC designs) braced frame buildings at the 636 southern California sites given a particular earthquake magnitude.	147
5.9	Total probability of exceedance of the IO, LS, CP, RT, and CO performance levels in the older (1994 UBC designs) and the newer (1997 UBC designs) braced frame buildings at the 636 southern California sites from earthquakes on the San Andreas fault in the next 30 years.	148

5.10	Total probability of exceedance of the IO, LS, CP, RT, and CO performance levels in the older (1994 UBC designs) and the newer (1997 UBC designs) braced frame buildings at Downtown Los Angeles from earthquakes on the San Andreas fault in the next 30 years.	148
C.1	List of stations, latitude, longitude, name, and SCEC's abbreviation whose data is used for the 1999 Hector Mine earthquake simulation.	159
C.2	List of stations, latitude, longitude, name, and SCEC's abbreviation whose data is used for the 2004 Parkfield earthquake simulation.	160
D.1	List of stations (and their location) for the 1999 Hector Mine earthquake.	163
E.1	List of stations (and their location) for the 2004 Parkfield earthquake.	198

Chapter 1

Introduction

How would pre- and post-Northridge tall steel braced frame buildings in southern California behave under earthquakes on the San Andreas fault? What is the probability of collapse of these buildings under San Andreas earthquakes in the next 30 years? This thesis examines these and other such related questions using rupture-to-rafters simulations. Rupture-to-rafters simulations consist of the following stages: earthquake probability estimations, earthquake source modeling, ground motions predictions, building analysis, and performance analysis.

The first question that naturally arises before attempting to study the regional impacts of earthquakes, ground motion characteristics, and building responses is the question of the seismic capability of the region of study. The extent of the possibilities and the frequencies of the earthquakes in a seismically active region is one of the major areas of interest. This all depends on the amount and quality of the regional seismic data available. Southern California is located at the intersection of the north America and Pacific plates, and the interaction of these plates has created a network of faults that accommodate the movements between the two plates. Even though the region is very well studied and many of the major and minor regional faults are studied, mapped, and analyzed, there still might be many blind faults that have yet to be discovered.

Once the major source of seismic risk has been highlighted, the next step would be to select a sample of possible events that represents all the possible earthquakes on the selected seismic source. The selection should be such that it covers all spatial distributions of events as well as all possible damaging magnitudes that can occur on the seismic source. In this study, the seismic source is the southern portion of San Andreas fault from Parkfield in northern California to Bombay

Beach in the south. We select 60 scenario earthquakes as a subset that spans all locations and magnitudes (6-8) in the San Andreas fault. To each magnitude we assign a probability based on the Uniform California Earthquake Rupture Forecast (UCERF). Chapter 2 provides details about earthquake selection and the method of redistributing the forecast earthquake probabilities to the 60 scenario earthquakes.

The ground motion simulations are the second module in the rupture-to-rafter simulation framework and are covered in Chapter 3 and Chapter 4. Seismic wave propagation simulations are limited in their frequency content by two main factors: (1) the resolution of the seismic wave-speed structure of the region in which the seismic waves are propagated through and (2) the extent of our understanding about the rupture process, mainly on the short length scales. For this reason, high-frequency content in the ground motion must be simulated through other means. Toward this end, we adopt a variant of the classical empirical Green's function (EGF) approach of summing, with suitable time shift, recorded seismograms from small earthquakes in the past to generate high-frequency seismograms (0.5 Hz - 5.0 Hz) for engineering applications. We superimpose these seismograms on low-frequency seismograms, computed from kinematic source models using the spectral element method, to produce broadband seismograms. The non-uniform time shift scheme used in this work alleviates the over-estimation of high-frequency content of the ground motions observed. We validate the methodology by simulating broadband motions from the 1999 Hector Mine and the 2006 Parkfield earthquakes and comparing them against recorded seismograms.

Buildings considered in this study are based on an existing 18-story moment-frame building located in Woodland Hills, California; the full description of the existing building, redesigned buildings, design procedure, and building properties is covered in Chapter 4. The original building used in this study is located on Canoga Avenue in the Woodland Hills region of the city of Los Angeles, California, and hence it is referred to as the Canoga building. The building is located within the 5-mile radius of the epicenter of the 1994 Northridge earthquake and at the time of the earthquake the building was equipped with accelerometers. Thorough post earthquake investigation and availability of seismic records from the building's accelerometers have made this structure an excellent candidate for many scientific studies (e.g., [Paret and Sasaki 1995](#), [Filippou 1995](#), [Anderson and Filippou 1995](#), [Chi 1996](#), and [Krishnan et al. 2006b](#)). We altered the lateral

load resisting system of the existing structure from moment frame to braced frame using the 1994 Uniform Building Code (UBC) and the 1997 UBC as the design guidelines.

In Chapter 5 we combine the previous chapters to quantify earthquake risk of tall steel braced frame buildings. Kinematic source inversions of past earthquakes in the magnitude range of 6-8 are used to simulate 60 scenario earthquakes on the San Andreas fault. Using the method proposed in Chapter 3, three-component broadband ground motion histories are computed at 636 sites in the greater Los Angeles metropolitan area by superposing short-period (0.2 s-2.0 s) empirical Green's function synthetics on top of long-period (> 2.0 s) spectral element synthetics. 3-D nonlinear analysis of several variants of an 18-story steel braced frame building (Chapter 4), designed for three soil types using the 1994 and 1997 Uniform Building Code provisions, and subjected to these ground motions, are conducted. Model performance is classified into one of five performance levels: Immediate Occupancy, Life Safety, Collapse Prevention, Red-Tagged, and Model Collapse. The results are combined with the 30-year probability of occurrence of the scenario earthquakes using the PEER performance based earthquake engineering framework to determine the probability of exceedance of these limit states over the next 30 years.

Chapter 2

Risk Analysis Using Rupture-to-Rafters Simulations: Inferring Probabilities of Scenario Earthquakes from the Uniform California Earthquake Rupture Forecast

2.1 Introduction

Probabilistic seismic hazard analysis [PSHA, e.g., [Cornell \(1968\)](#); [Anderson and Trifunac \(1978\)](#); [McGuire \(1977\)](#); [McGuire \(1995\)](#)], typically used in risk assessment and hazard mitigation, has so far relied on ground motion prediction equations (GMPEs), also called attenuation relations [e.g., the next generation attenuation relations or NGA by [Campbell and Bozorgnia \(2008\)](#); [Chiou and Youngs \(2008\)](#); [Boore and Atkinson \(2008\)](#); [Abrahamson and Silva \(2008\)](#)] to arrive at the expected level of shaking at a site over a time horizon. GMPEs are regression relations on measurements of peak shaking intensities from globally recorded earthquakes. Unfortunately, the sparsity of records from large magnitude earthquakes at short distances or in deep sedimentary basins renders the predictions from these relations highly uncertain. Additionally, GMPEs do not consider source effects such as rupture directivity and slip distribution. The non-unique definition of source-to-site distance, especially for large magnitude earthquakes where the rupture may extend hundreds of kilometers and predominant energy release occurs in large slip asperities whose distance from a site may significantly differ from the shortest distance to the rupture, further adds to uncertainty

in predictions. Perhaps most importantly, the variance of the estimates of the nonlinear response of a structure (especially complex structures with multiple dominant modes) from a single ground motion intensity measure using fragility curves is generally quite high. Fragility curves represent the conditional probability of failure of a structure or component given a ground motion intensity measure. They are typically developed through repeated nonlinear time history analysis of the structure (or component) using available earthquake records, scaled to various levels of shaking intensity. Complex structures such as tall buildings are sensitive to the duration, amplitude, and frequency characteristics of the entire three component ground motion history, and reducing this dependence down to a single ground motion intensity measure generally results in great spread in the structural response estimates. Furthermore, the ground motion characteristics (especially with regard to frequency content and duration) of the expected ground motion at the site from regional faults may have little resemblance to the scaled ground motions used in developing the fragility curves. As a result, the implied failure probability at a given ground shaking intensity from the fragility curve may not be close to the actual failure probability under the expected event.

The shortcomings of traditional PSHA may be overcome by undertaking region-, fault-, and structure-specific rupture-to-rafter simulations (at least on known and well-mapped faults). These simulations consist of the generation of an earthquake on a fault, the computational propagation of the radiated seismic energy in the form of waves through a regional model of the earth, the computation of three-component ground shaking histories at regional sites of interest, and the simulation of the response of engineered structures at these sites. Suppose the risk from a particular fault over a given time horizon is to be quantified. A suite of potentially damaging scenario earthquakes is conceived at several locations that are uniformly spaced along the fault. Unilateral or bilateral ruptures may be included. A kinematic representation or a dynamically evolving source may be used to generate ground motions from each scenario earthquake. Using recently developed computational tools, damage and losses to computational models of the engineered structures may be determined for each event. Uncertainties in material properties, workmanship, unit costs, etc. may be accounted for. However, damage and losses thus computed would be conditional upon the occurrence of the scenario earthquakes. To quantify risk to the target structures over a particular time horizon, this conditioning must be eliminated. This can be done if the probability of occur-

rence of all plausible events on the target fault can be rationally distributed among the smaller set of considered scenario earthquakes. It is here that rupture forecasts have an important role to play.

Rupture forecasts such as the Uniform California Earthquake Rupture Forecast [UCERF, (Field et al. 2009) and (Field et al. 2013)] combine data from several sources, including local and global earthquake catalogs, magnitude frequency distributions, paleoseismic observations, and GPS measurements of the tectonic movements of plates, to predict probabilities of all plausible earthquakes on known faults during a specified time interval. UCERF bases these probabilities on four layers of modeling: (i) a fault model with a mapping of the physical geometry of known California faults; (ii) a deformation model of slip rates and related factors for each fault section; (iii) an earthquake rate model of the region; and (iv) a probability model. It hypothesizes hundreds of thousands of ruptures (referred to as “forecast earthquakes” in this article) on specific seismogenic locations of faults and provides yearly occurrence rates that are most consistent with observations. These rates are transformed to probabilities of occurrence assuming an underlying probability distribution such as the Poisson distribution.

Here, we present a rational method to redistribute the forecast earthquake probabilities to the scenario earthquakes simulated for PSHA studies using rupture-to-rafters simulations. We illustrate the inner workings of the method through an example involving earthquakes on the San Andreas fault in southern California. We start with a brief background on ground motion simulation and UCERF, set up a case study of scenario earthquakes on the San Andreas fault, and illustrate the methodology through application to this case study.

2.2 Ground Motion Simulation

Numerical seismic wave propagation simulations of ground motion require a description of the earthquake source (kinematic or dynamic), a regional seismic wave-speed model that resolves seismic wave speeds in the earth medium through spatial distributions of density and elasticity of the medium, and a numerical wave propagation algorithm that is based on the finite-difference or the finite-element or the spectral-element method.

Seismic source models describe the earthquake rupture process by either kinematic prescription or dynamic evolution of the source parameters of slip, slip velocity (or rise-time) and rupture speed on a uniform or non-uniform grid spanning the full extent of fault rupture. Whereas, in theory, dynamic models are more natural and perhaps physically more accurate in characterizing earthquake sources, the lack of data constraining the driving normal stress and the friction on the fault has meant that these methods are still a work in progress. Knowledge of kinematic description of the source, on the other hand, has matured considerably through finite-source inversions of recorded earthquakes around the globe.

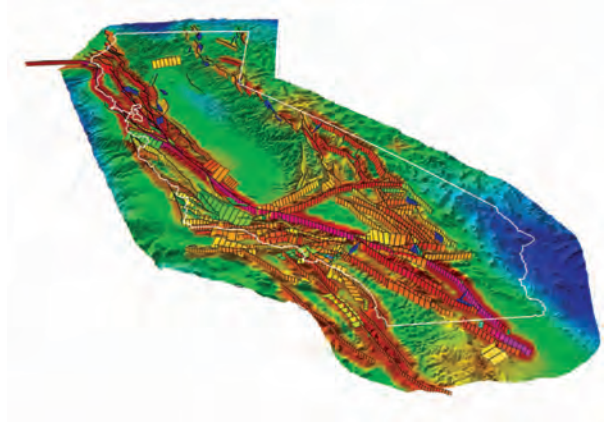
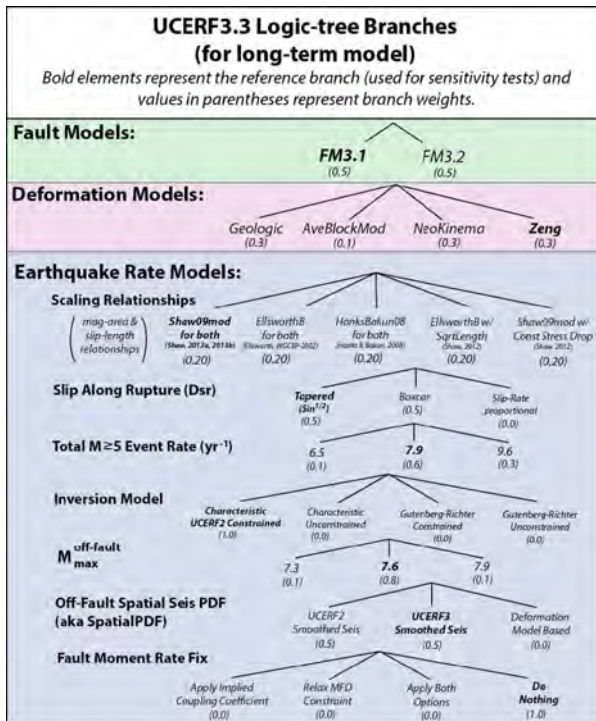
Each subfault in the kinematic source model slips in sequence radiating energy, and this disturbance is propagated through a meshed earth's wavespeed model using numerical methods such as finite-difference, finite-element, or spectral-element. Several software packages have been developed for this. One example is SPECFEM3D (V2.0 SESAME, [Kellogg 2011](#)), an open-source software that uses the spectral element method. It accounts for 3-D variations of seismic wave speeds and density, topography and bathymetry, and attenuation as dictated by the SCEC Community Velocity Model (CVM-H 11.9). This regional earth model incorporates tens of thousands of direct velocity measurements that describe the Los Angeles basin and other structures in southern California ([Suss and Shaw 2003](#), [Plesch et al. 2011](#)). It includes background crustal tomography ([Lin et al. 2007](#) and [Hauksson 2000](#)) enhanced by 3-D adjoint waveform methods ([Tape et al. 2009](#)), the Moho surface ([Plesch et al. 2011](#)), and a teleseismic upper mantle wave-speed description ([Prindle and Tanimoto 2006](#)).

2.3 UCERF

The Working Group on California Earthquake Probabilities (WGCEP) is a joint effort by the U.S. Geological Survey (USGS), the California Geological Survey (CGS), and the Southern California Earthquake Center (SCEC) with the goal of producing credible estimations for earthquake hazard in California in the form of a Uniform California Earthquake Rupture Forecast [UCERF, [Field et al. \(2013\)](#)] to feed into the National Seismic Hazard Mapping (NSHM) project.

The UCERF framework for calculating earthquake probabilities is composed of a logic tree structure where epistemic (or modeling) uncertainty is accounted for by allocating likelihood-dependent weights to all branches. The logic tree is composed of four modeling layers: fault models, deformation models, earthquake rate models, and probability models. There exist 1440 logic tree branches in UCERF-3 [Figure 2.1(a)]. These models are based on the best available geologic, geodetic (e.g., GPS), seismic (earthquake catalogs), and paleoseismic data. At the base of the logic tree are the fault models that outline the spatial geometry of active faults and fault systems. They offer alternate representations of fault geometry, all of which satisfy available data constraining fault geometry in equally good measure. These alternatives introduce the first level of branching into the UCERF logic tree. Next up on the tree are the deformation models that provide slip rates and/or creeps on the faults listed in the fault models. This is followed by earthquake rate models that provide long-term rates of occurrence of a vast set of plausible earthquakes on these well-defined faults. The long term rates of these earthquakes are converted to time independent probabilities of occurrence using a Poisson probability model. Other probability models such as the Brownian passage time renewal model based on last event may be used for evaluating time-dependent probabilities (Field et al. 2009). Presently, UCERF-3 provides time-independent probabilities alone.

In version 3 of UCERF, major faults in California are divided into a total number of 2,606 \sim 2 km-13 km long segments [Figure 2.1(b)]. A plausible earthquake may comprise two or more successive fault segments fully rupturing. UCERF-3 postulates 10,445 plausible earthquakes (referred to as “forecast earthquakes” here) on the southern portion of the San Andreas fault starting from Parkfield in central California to Bombay Beach in southern California (Figure 2.2). For each one of the 1440 logic tree branches, the long term yearly rate of occurrence of these forecast earthquakes is calculated simultaneously by a “grand inversion” of a system of equations formulated to satisfy the slip rates along the faults predicated by the deformation models.



(a)

(b)

Figure 2.1: (a) The 1440 logic tree branches in UCERF-3 and their associated weights. (b) Fault segmentation used in UCERF-3. A “forecast earthquake” comprises two or more successive segments rupturing. Figure source: UCERF-3.

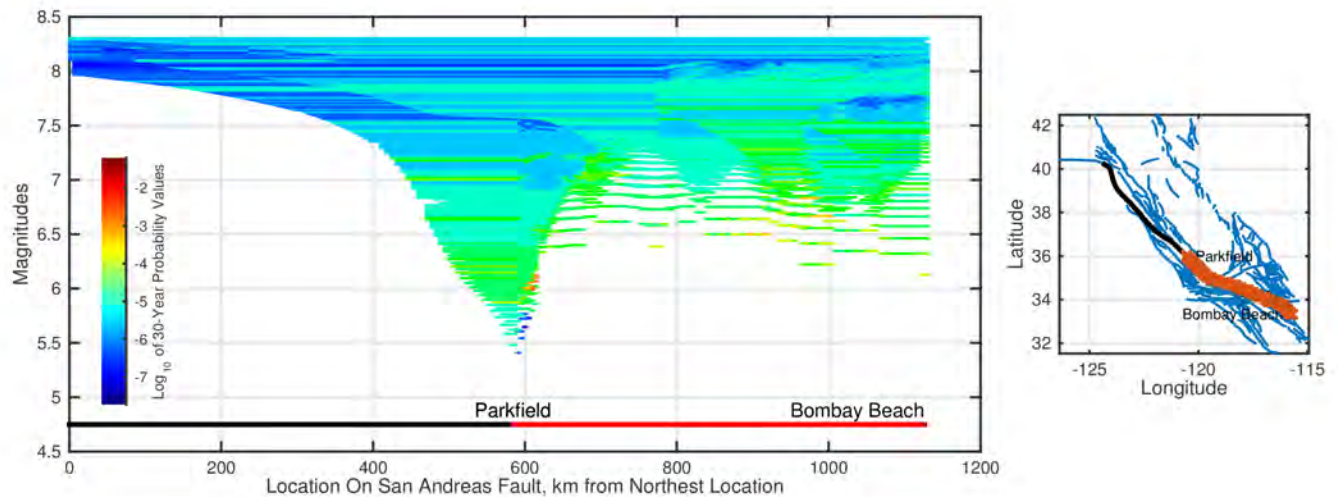


Figure 2.2: All plausible (or “forecast”) earthquakes that rupture at least one segment of the southern section of the San Andreas fault (from Parkfield in central California to Bombay Beach in southern California, shown in red). The X axis identifies the extent of rupture of a forecast earthquake and the Y axis identifies its magnitude. Line colors indicate forecast earthquake occurrence probabilities, with warmer colors (red, orange) indicative of higher probability of occurrence and colder colors (blue) indicative of lower probability of occurrence.

2.4 Considerations for UCERF application to PSHA using rupture-to-rafters simulations

Because rupture-to-rafters simulations require significant computational resources, it would not be practical to simulate each of the forecast earthquakes and its effects. For example, a single SPECFEM3D simulation using 144 Intel 2.33 GHz processors with 8 GB RAM of a magnitude 7.89 earthquake may take about 1 hour. The 3D nonlinear analysis of a 20-story building under the simulated 3-component ground motion at one of the sites may take anywhere from 4 hours to 48 hours on a single processor (it is most efficient to perform building analysis in an embarrassingly parallel fashion, unless super-tall buildings above say 60 stories are being simulated). It would not be possible to perform such analyses for over 10,000 forecast earthquakes and analyze the data in a reasonable amount of time. A logical alternative would be to simulate a subset of forecast earthquakes that are likely to cause damage/losses in the target structures. For instance, to

evaluate the seismic risk to a 20-story steel building in Los Angeles from earthquakes on the San Andreas fault, it may be sufficient to simulate earthquakes with magnitudes 6-8 on the southern portion of the fault, from Parkfield in central California to Bombay Beach in southern California. Unfortunately, this subset would still amount to 4,950 earthquakes, far too many to perform rupture-to-rafter simulations. It is apparent that it would not be feasible to consider the UCERF forecast earthquakes when planning the simulations to be conducted. It would be best to independently select a few uniformly spaced rupture locations along the southern section of the fault and simulate earthquakes with as many magnitudes in the 6-8 range as feasible. Henceforth, we will refer to these simulated earthquakes as “scenario” earthquakes. The primary task then would be to partition and redistribute the probabilities of forecast earthquakes to these scenario earthquakes. In other words, the probability space of forecast earthquakes is to be mapped onto a new probability space for scenario earthquakes. This mapping should be such that the total probability of the forecast earthquakes in the magnitude range of 6-8 should be conserved. Two important questions arise: (i) The rupture extents and locations of forecast earthquakes will in general not match those of the scenario earthquakes. What fraction of the probability of a given forecast earthquake must then be assigned to a given scenario earthquake, and what rationale should be used for this determination? (ii) To which scenario earthquakes must the probability of forecast earthquakes with magnitudes not equal to that of any of the scenario earthquakes be assigned? And in what proportion? Or alternately, what are the adjustments that must be made to account for the differences in the energy (or seismic moment) release of forecast and scenario earthquakes? Again, what rationale should be used for this determination?

In the next section, we set up a case study on the southern San Andreas fault and present our method and its rationale by direct application to this case study.

2.5 Scenario Earthquake Probabilities from Forecast Earthquake Probabilities

2.5.1 Southern San Andreas Fault Case Study

Suppose we wish to use rupture-to-rafters simulations to estimate the expected losses to a 20-story building in Los Angeles from earthquakes on the San Andreas fault in the next 30 years. Based on prior knowledge, we hypothesize that only magnitude 6-8 earthquakes on the southern section of the San Andreas fault (extending from Parkfield in central California to Bombay Beach in southern California) produce ground motions that could result in measurable losses in this building. For this case study, sixty earthquakes with magnitudes M_w 6.00, 6.56, 6.92, 7.28, 7.59, and 7.89, two rupture directivities (north-to-south and south-to-north), and five rupture locations are selected as scenario earthquakes. The two unilateral rupture directions may represent the two ends of the spectrum in terms of the effects of rupture directivity on ground motions. Kinematic finite source inversions of past earthquakes on geometrically similar faults (right lateral strike-slip, i.e., rake angle of 180° , dip angle of 90° and a depth of 20 km) as the San Andreas are used as source models for ground motion simulations (Table 5.1). Fig. 2.3 illustrates the sources for the M_w 7.89 scenario earthquakes at rupture locations 1, 3, and 5.

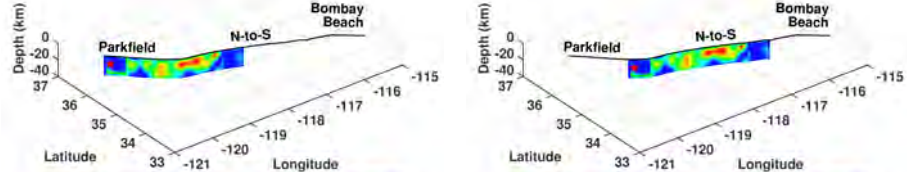
	Name	Date	Location	M_w	Length (km)	Depth (km)	Dip ($^\circ$)	Rake ($^\circ$)	Reference
1	Denali	2002	AK, USA	7.89	290.0	20.0	90.0	180.0	Krishnan et al. (2006a)
2	Izmit	1999	Turkey	7.59	155.0	18.0	90.0	180.0	Bouchon et al. (2002)
3	Landers	1992	CA, USA	7.28	78.0	15.0	89.0	180.0	Wald and Heaton (1994)
4	Kobe	1995	Japan	6.92	60.0	20.0	85.0	180.0	Wald (1996)
5	Imperial Valley	1979	CA, USA	6.58	42.0	10.4	90.0	180.0	Hartzell and Heaton (1983)
6	Parkfield	2004	CA, USA	6.00	40.0	14.5	83.0	180.9	Custódio et al. (2005)

Table 2.1: List of past earthquakes, fault parameters, and the finite source inversions used as kinematic source models for the southern San Andreas fault case study.

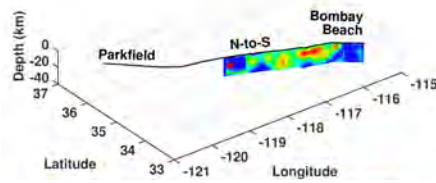
Fig. 2.4 shows the locations of the 30 scenario earthquakes (without consideration to rupture direction) on the southern San Andreas fault along with the subset of forecast earthquakes from UCERF-3 in the magnitude range of 6-8 and rupturing at least one of the UCERF-3 segments on the southern San Andreas fault. The method to reassign the probabilities of occurrence of these forecast earthquakes (indicated by line color) to the scenario earthquakes is outlined next.

2.5.2 Methodology

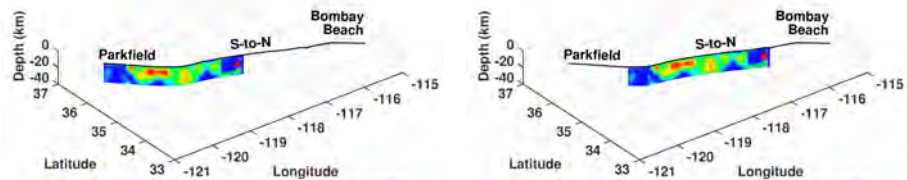
1. We start with “magnitude binning” of forecast earthquakes. We define as many bins as the number of distinct magnitude scenario earthquakes. The lower and upper magnitude limits of a bin are the magnitudes derived from the averages of the seismic moments of the corresponding scenario earthquake and the scenario earthquakes tied to the previous and next bins, respectively. Corresponding to the six scenario earthquake magnitudes of 6.00, 6.56, 6.92, 7.28, 7.59, and 7.89, the following six magnitude bins are defined: [5.90 - 6.42], (6.42 - 6.80], (6.80 - 7.15], (7.15 - 7.45], (7.47 - 7.78], and (7.78 - 8.34]. The seismic moments of the M_w 6.00, 6.56, 6.92, 7.28, 7.59, and 7.89 scenario earthquakes correspond to the average of the seismic moments of the upper and lower magnitude limits of the first five bins, respectively. The upper limit of the last bin is assumed higher to include all forecast earthquakes with magnitude greater than 7.89. Each of the forecast earthquakes will be assigned to one of these magnitude bins. For instance, a forecast earthquake with magnitude, say, between 6.42 and 6.80 will be assigned to the magnitude bin tied to the scenario earthquake with magnitude M_w 6.56. Its probability of occurrence will be redistributed among the ten M_w 6.56 scenario earthquakes (five rupture locations and two rupture directions). The dashed black lines in Fig. 2.4 demarcate the magnitude bins.
2. The seismic moment of forecast earthquake i , M_o^i , is multiplied by the UCERF yearly occurrence rate r_i to arrive at a term with a unit of seismic moment times yearly rate (seismic moment/year). These values are determined for all forecast earthquakes in this manner.
3. Within each magnitude bin, the $M_o^i \times r_i$ value of a forecast earthquake is distributed among



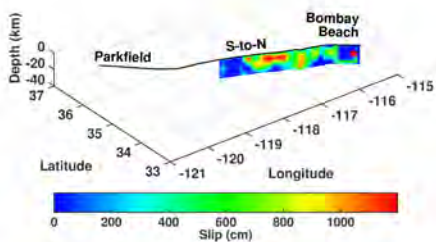
(a) Rupture Location - 1 - North to South (b) Rupture Location - 3 - North to South



(c) Rupture Location - 5 - North to South



(d) Rupture Location - 1 - South to North (e) Rupture Location - 3 - South to North



(f) Rupture Location - 5 - South to North

Figure 2.3: Slip distribution from a finite source inversion of the 2002 M_w 7.89 earthquake on the Denali fault mapped on to rupture locations 1, 3, and 5 of the southern San Andreas fault. (a)-(c) North-to-south rupture direction. (d)-(f) South-to-north rupture direction. The red star corresponds to the hypocenter location.

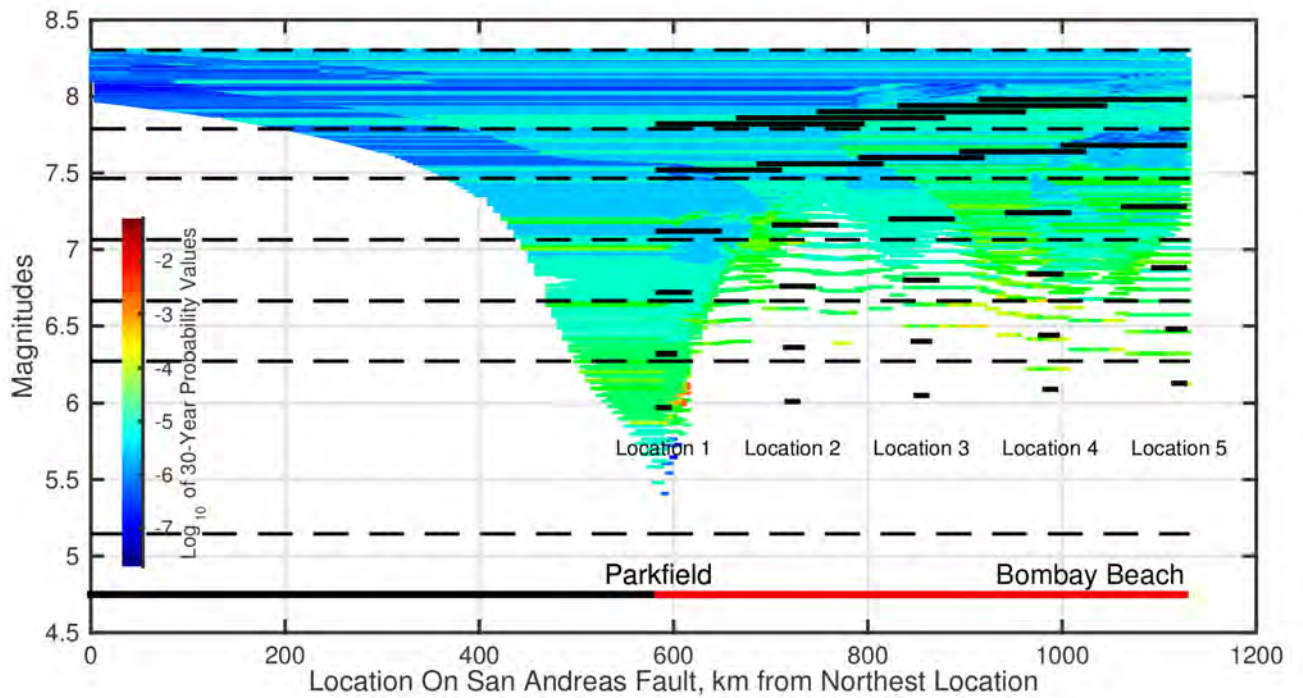


Figure 2.4: The 30 scenario earthquakes (shown in black) superposed on top of the forecast earthquakes from Fig. 2.2. Two rupture directions are considered for each, bringing the total number of scenario earthquakes to 60. Dashed black lines demarcate the magnitude bins adopted in the case study.

the UCERF segments being ruptured by that forecast earthquake in proportion to their areas. Thus the $M_o^i \times r_i$ contribution of the i^{th} forecast earthquake to the j^{th} UCERF segment equals $r_i M_o^i \frac{A_j}{A_i}$, where A_i is the area of forecast earthquake i and A_j is the area of the UCERF segment j .

4. Within each magnitude bin, the contributions to fault segment j of all N forecast earthquakes in that bin are summed: $\sum_{i=1}^N r_i M_o^i \frac{A_j}{A_i}$. This represents the yearly seismic moment buildup in segment j that is expected to be released periodically by earthquakes with magnitudes lying within the magnitude limits of that bin. It may be term with a unit of seismic moment per year for segment j in earthquakes from that magnitude bin.
5. Within each magnitude bin, the cumulative seismic moment times rate values of segment j , determined in the previous step, is assigned to the scenario earthquake tied to that bin and whose rupture location is closest to segment j . Then the sum of all seismic moments times rates of that scenario earthquake is given by $\sum_{j=1}^M \sum_{i=1}^N r_i M_o^i \frac{A_j}{A_i}$, where M is the number of UCERF segments occurring within the rupture extent of that scenario earthquake. It is possible that the rupture extents of two or more scenario earthquakes may extend over the same fault segment(s). The moment release rates on such segments are evenly distributed among the overlapping scenario earthquakes.
6. For value obtained from previous step for scenario earthquake k is divided by its seismic moment $M_o^{SE_k}$ to obtain its yearly occurrence rate $q_k = \sum_{j=1}^M \sum_{i=1}^N r_i M_o^i \frac{A_j}{A_i} / M_o^{SE_k}$.
7. The probability of occurrence of scenario earthquake k over a period of ΔT years is then given by the Poisson distribution as: $P(SE_k) = 1 - e^{-q_k \Delta T}$.
8. Steps (iii)-(vii) are repeated for all magnitude bins and the scenario earthquakes associated with them.

Fig. 2.5 graphically illustrates the results the various steps of the method applied to a hypothetical fault. The horizontal blue line represents the section of the target fault of interest. For the case study this line would represent the southern portion of the San Andreas fault. The dotted black lines show

the segmentation (labeled “Seg.”) of the target fault, say from UCERF. The red unfilled rectangles represent forecast earthquakes (labeled “F.E.”). The heights of the rectangles are proportional to the seismic moment times yearly rates of forecast earthquakes [computed in step (ii)]. The yellow shaded regions represent the seismic moment times rate contributions of several forecast earthquakes to a given UCERF segment [computed in step (iii)]. The red shaded region represents their summation [step (iv)]. The magenta colored region represents the sum of all seismic moment times rate for a scenario earthquake determined by summing the moment times yearly rates of all the UCERF segments within the extent of the scenario earthquake rupture [step (v)]. Magenta lines at the very bottom of the figure show scenario earthquake (labeled “S.E.”) rupture extent.

Shown in Tab. 2.2 are the 30-year occurrence probabilities of the case study M_w 6-8 scenario earthquakes on the southern San Andreas fault determined using this approach. Half of these probabilities will be assigned to the north-to-south propagating ruptures and the other half to the south-to-north propagating ruptures. It should be noted that these probabilities are time-independent and should be treated as probabilities of occurrence in any given 30-year period, not just the next 30 years. Furthermore, based on stress renewal models and elastic rebound theory, the occurrence of any of these events will significantly alter the probabilities in this table. This table is valid only up until the next big event occurs. Joint probabilities of events cannot be inferred from this table. To ensure that the probabilities determined using this method are reasonable, we compare these values against probabilities derived from event return rates found in literature. The return period for a large magnitude 1857 Fort Tejon-like earthquake (M_w 7.89) is around 150-300 years (Sieh 1978). Taking the yearly rate (1/225) implied by an average return period of 225 years, its 30-year probability of occurrence may be computed as $1 - e^{-(1/225) \times 30} = 0.125$, which is close to the total probability value of 0.123 for the (7.78 - 8.34] magnitude bin in our case study. The return period for the magnitude 6 Parkfield earthquake is about 22 years (Bakun and Lindh 1985). The 30-year probability of occurrence (independent of the 2004 event) may be evaluated to be $1 - e^{-(1/22) \times 30} = 0.74$, which is reasonably close to the total probability value of 0.81 for the [5.90 - 6.42] magnitude bin in our case study.

Siriki et al. (2015) have successfully used this method within a broader study characterizing the risk to tall steel moment frame buildings in southern California from earthquakes on the San

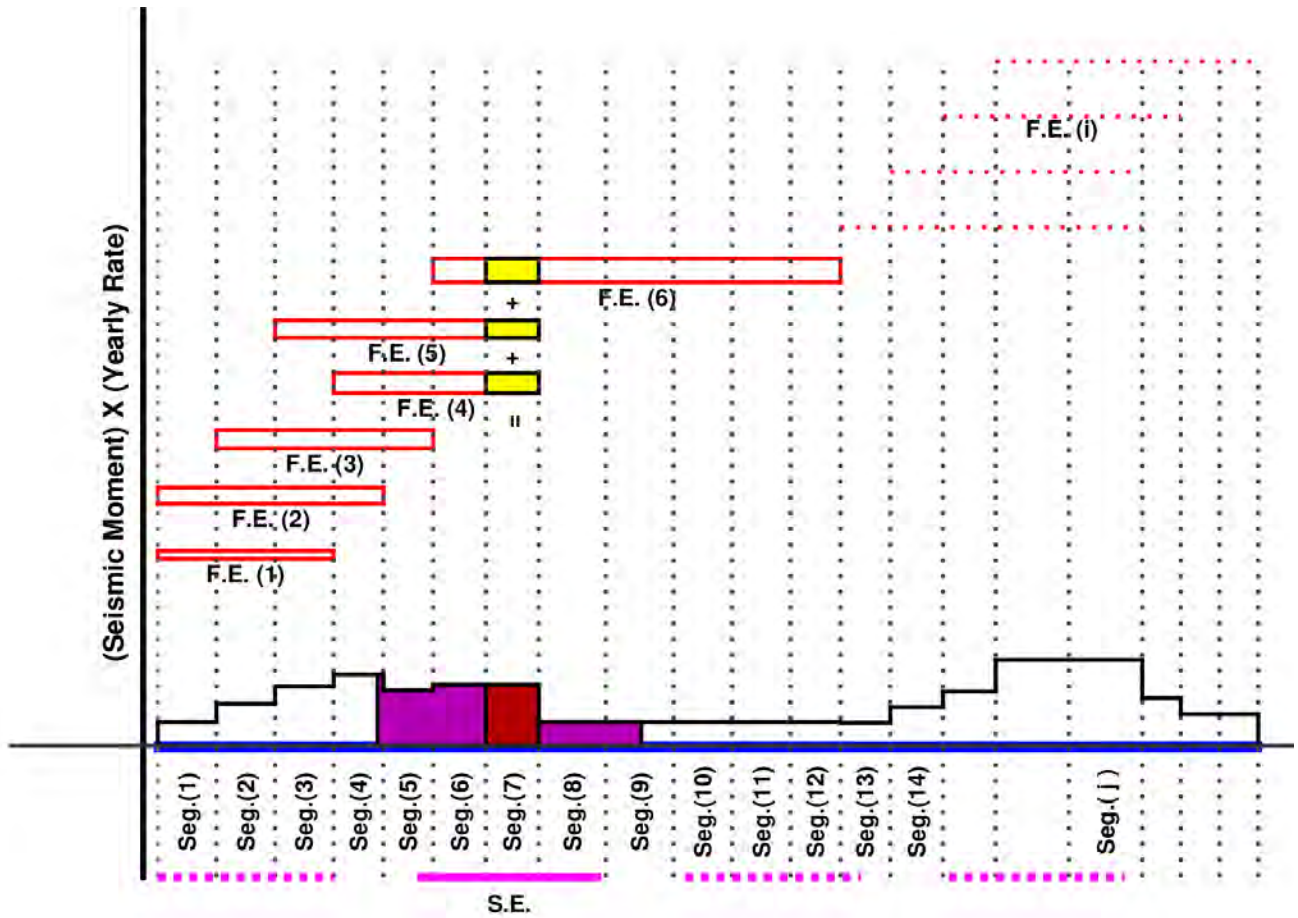


Figure 2.5: Illustrative example of the method used to derive scenario earthquake probabilities from forecast earthquake probabilities. Horizontal blue line: target fault. Dotted black lines: fault segmentation. Red unfilled rectangles: forecast earthquakes (F.E.) with seismic moment rates indicated by rectangle heights [step (ii) of method]. Yellow shaded region: seismic moment rate contributions of several forecast earthquakes to a given segment [step (iii)]. Red shaded region: summation of yellow shaded regions [step (iv)]. Magenta colored region: seismic moment rate of a scenario earthquake (S.E.) by summing the moment rates of all the segments [step (v)]. Magenta lines: rupture extent of S.E.s.

Andreas fault using rupture-to-rafters simulations.

M_w [Bin]	Location 1 (Parkfield)	Location 2	Location 3	Location 4	Location 5 (Bombay Beach)	Total Probability (All Locations)
6.00 [5.90 - 6.42]	0.6449	0.0459	0.1910	0.2485	0.0685	0.8081
6.58 (6.42 - 6.80]	0.0051	0.0100	0.0854	0.1280	0.0183	0.2288
6.92 (6.80 - 7.15]	0.0180	0.0171	0.0060	0.0764	0.0271	0.1380
7.28 (7.15 - 7.45]	0.0211	0.0182	0.0059	0.0153	0.0365	0.0935
7.59 (7.47 - 7.78]	0.0124	0.0121	0.0061	0.0082	0.0192	0.0568
7.89 (7.78 - 8.34]	0.0339	0.0281	0.0236	0.0225	0.0215	0.1231
Total Probability M_w [5.90 - 8.34]	0.6760	0.1249	0.2904	0.4221	0.1773	0.8553

Table 2.2: Time-independent 30-year occurrence probabilities of the scenario earthquakes in the southern San Andreas case study derived from UCERF forecast earthquake probabilities. Half of these probabilities may be assigned to north-to-south propagating ruptures and the other half to south-to-north propagating ruptures.

2.6 Discussion

Using a single scenario earthquake to represent all forecast earthquakes within a magnitude bin is error-prone by construction. For instance, in the southern San Andreas case study, a magnitude 7.28 scenario earthquake is used to represent seismic risk from all earthquakes with magnitudes 7.15-7.45. To eliminate bias in the results, we have selected the scenario earthquake magnitude to be at the bin center based on seismic moment. However, if an alternate method is adopted to choose the magnitude of the scenario earthquake to be simulated such that the scenario earthquake happens to have a magnitude closer to the upper (or lower) limit of the bin, the lower (or higher) occurrence probability for the scenario earthquake assigned by our seismic moment rate-based method automatically compensates for the introduced bias. For example, let there be just two forecast earthquakes, one with magnitude 7.15 and a yearly rate of 0.0010, and the other with magnitude 7.45 and a yearly rate of 0.0005. If we use an M_w 7.28 scenario earthquake to represent this bin in our rupture-to-rafters simulations-based PSHA, our method would result in a scenario earthquake probability of occurrence of 0.045 over the next 30 years. If, on the other hand, an M_w 7.40 scenario earthquake is used to represent this bin, the probability of occurrence drops to

0.030. Obviously, our rupture-to-rafters simulations would predict higher ground motions, heavier building damage, and losses when the 7.40 magnitude scenario earthquake is used. Fortunately, the lower probability of occurrence estimated for the M_w 7.40 earthquake would at least partially offset these increases, perhaps resulting in comparable 30-year losses. Likewise, if we use a M_w 7.18 scenario earthquake to represent this bin, the 30-year probability of occurrence increases to 0.063. This time the lower ground motions and economic losses predicted by the simulations would be at least partially offset by the higher occurrence probability.

The deaggregation of forecast earthquake rates into seismic moment release rates of the segments comprising the rupture solves another commonly encountered problem in PSHA. No matter what domain is chosen for the earthquakes to be considered in the PSHA, at least one or more of the forecast earthquakes will straddle the domain boundary, i.e., only portions of these ruptures will lie within the domain. The question then arises of what fraction of the probability of occurrence of these earthquakes should be assigned to our closest-occurring scenario earthquake? The deaggregation in our method breaks these ruptures down to the participating segments, and within a small margin of error these segments will lie wholly either inside or outside the domain, thus automatically resolving this problem.

Chapter 3

Simulation of Broadband Ground Motion by Superposing High-Frequency Empirical Green's Function Synthetics on Low-Frequency Spectral-Element Synthetics

3.1 Introduction

The broader purpose of this work is to produce site-specific broadband ground motions (< 5 Hz) in southern California from a suite of large earthquakes on the San Andreas fault. A major challenge in seismology is predicting the expected ground motions from large earthquakes for future events. These predictions are essential for engineering design, hazard estimation, and risk analysis. Theoretically, to produce site-specific ground motions deterministically, one needs a detailed description of (1) the earthquake rupture process and (2) the three-dimensional regional wave-speed structure of the earth. The frequency content of the ground motions generated using finite element, spectral element, or finite difference approaches is limited by our knowledge and resolution of these aspects. While the lack of data related to the state of stress in the earth and the laws of friction governing fault rupture nucleation and propagation has hampered our understanding of the dynamics of the rupture process, methods to develop kinematic representation of earthquake sources have matured significantly. Kinematic source models from past earthquakes at one location hold the

greatest promise for predicting ground motions from future events at other locations where fault geometry and focal mechanisms are similar. The resolution of the seismic wave-speed structure is another governing factor in determining the limits of the frequency content of the propagating waves (the higher the resolution of the wave-speed structure the higher the frequency content that can be reliably propagated). This resolution is limited by the spatial density of seismic observations. Even in well-studied regions such as southern California the wave-speed models [SCEC Community Velocity Model - Harvard (CVM-H) 11.9.0] are capable of propagating waves with frequencies of only up to 0.5 Hz (Komatitsch et al. 2004; Liu et al. 2004), well below that required for many engineering applications. To overcome this limitation, several hybrid approaches that combine the low-frequency shaking histories from a deterministic simulation and the high-frequency shaking histories from a stochastic approach have been proposed (e.g., Mai et al. 2010, Frankel 2009, and Graves and Pitarka 2010). Here, we present a deterministic hybrid approach for generating ground motions from large earthquakes. The low-frequency content (< 0.5 Hz) of the ground motion is generated from a kinematic source model using a spectral element based program called SPECFEM3D (Komatitsch et al. 2004), which incorporates the regional 3-D wave-speed structure of the earth. Low-frequency synthetic seismograms from this method are combined with high-frequency seismograms generated using a variant of the classical EGF approach, which will be the main focus of this article.

Hartzell (1978) was the first to outline the framework for the empirical Green's function (EGF) method. He proposed using aftershock records of an event as the Green's functions (EGFs) to capture the travel paths of the seismic waves. Since then, several variants of the method have been proposed (e.g., Irikura 1983, Irikura 1986, Joyner and Boore 1986, Heaton and Hartzell 1989, Somerville et al. 1991, Tumarkin and Archuleta 1994, and Frankel 1995). In these methods, the rupture plane of the target event is subdivided into a grid of subfaults (uniform or non-uniform) and the seismic waves radiated from each subfault is time shifted and summed carefully to yield the shaking at any given site under the target event. However, there is an inherent problem with the EGF method. Brune (1970) showed that for a given source dimension, the displacement spectrum at low-frequencies is controlled by the effective seismic moment but not at high-frequencies. Using earthquake scaling laws, on the one hand, if we add the events such that the moment of the

target event equals the total moment of all added events (in the simplest case of using one EGF this can be viewed as scaling based on the seismic moment of the EGF to that of the target event), the low-frequency content (below the corner frequency of the large event) would be correctly reproduced, but the high-frequency content (above the corner frequency of the target event) would be overestimated. On the other hand, if we fill the rupture area with non-overlapping EGF events (scaling based on area or equivalently scaling based on moment ratio to the power of $2/3$) the high-frequency content (above the corner frequency of the small event) would be accurately represented, but the low-frequency content (below the corner frequency of the small event) would be underestimated. [Joyner and Boore \(1986\)](#), who were one of the earliest to recognize this problem, suggested that if $N^{4/3}$ events are randomly added in time over the total rise-time of the event and the final result is multiplied by $N^{-1/3}$ (N being the ratio of the seismic moment of the main event to the seismic moment of the EGF), then the resulting spectrum would be consistent with Brune's spectrum. [Heaton and Hartzell \(1989\)](#) also presented a quantitative discussion on the source of inconsistency in the use of EGFs. [Somerville et al. \(1991\)](#) illustrated that a low bias between the simulated and observed ground motions can also be obtained by stochastically perturbing the time shifts at which the EGFs are supposed to be added. Moreover, a desirable scaling of the displacement spectrum in the high- and low- frequency bands that matches the Brune's spectrum can be achieved by scaling, filtering, or convolving the EGFs with appropriate functions. For example, [Frankel \(1995\)](#) suggested populating the rupture area with non-overlapping events and then applying appropriate filter (or a frequency domain operator designed based on relative magnitudes of the slip velocity of the target event and that of the EGF event) to increase the low-frequency content without modulating the high-frequency content. However, all these methods have been shown to work well only when the magnitudes of the target event and the EGF event do not differ by more than 2.

Here, we use EGF events with three or four magnitudes smaller than the target event to produce only the high-frequency (0.5 – 5 Hz) part of the ground motions to be combined with the low-frequency part from wave propagation simulations. We start with kinematic source models from past earthquakes, resampled to a finer resolution (typically down to 0.5 km). The choice of this resolution is dictated by the highest frequency wave that can be reliably propagated through the

spectral element mesh using the wave-speed model at hand. We then select EGFs from previously recorded events on the target fault in the 2.5-4.5 magnitude range, located within in the rupture extent of the target event or as close to it as possible. The main assumption here is that the source mechanism of the small event is the same as that of the target event. Similar to previous studies (e.g., [Irikura 1983](#), [Heaton and Hartzell 1989](#), and [Somerville et al. 1991](#)), the formulation consists of two summations, one over all the subfaults and one within each subfault. In both summations proper time shifts are applied to account for rupture front propagation. Additionally, in the second summation, the EGFs are further shifted in time to ensure that the impulse source-time functions of the EGFs collectively span the duration of slip of the target subfault. An additional correction is applied to the records to account for geometric spreading. The key advances in this work are (i) expanding and exploring the limits of applicability of the EGF method by utilizing the large quantity of seismic data available in the low magnitude range of 2.5 – 4.5, and (ii) achieving good agreement in the synthetics with [Brune \(1970\)](#) spectrum without artificial filtering or convolution in the frequency band of interest by introducing a new method of selecting time shifts. This method is based on the assumption that seismic moment in each subfault is released in equal-moment steps by EGFs assigned to that subfault. We validate our approach by simulating the 2004 Parkfield (M_w 6.0) and the 1999 Hector Mine (M_w 7.1) earthquakes at various stations across southern California.

3.2 Source Model Selection

Source models for earthquake simulations are selected from kinematic finite source inversions of past earthquakes on faults that are geometrically similar to that of the target event, with a rupture mechanism similar to that of the target event. For example, the source model for a target event on the San Andreas fault will be a kinematic finite source inversion of an earthquake that has occurred on a right-lateral strike-slip fault with a dip angle of approximately $90^\circ (\pm 5^\circ)$ and a depth of 20 km (± 5 km). Source spectrum is closely related to fault geometry and rupture mechanism; conforming the scenario earthquake source characteristics to the physically observed characteristics on the target fault may help produce realistic energy release on the fault. The selected source model, if

coarsely sampled, is resampled to a finer resolution of about 0.5 km (see Appendix A for calculations), in order to be able to generate waves of periods 2~s and longer [consistent with the highest frequency (0.5 Hz) that can be propagated with the wave-speed model used in this study (CVM-H 11.9.0)] .

3.3 Low-Frequency Ground Motion Waveforms

The simulation of low-frequency ground motion using SPECFEM3D has been described in great detail in other works (e.g., Komatitsch and Tromp 1999, Komatitsch et al. 2004, and Tape et al. 2010). Here, we give only a brief overview.

The low-frequency ground motion waveforms are generated using numerical methods incorporating the 3-D seismic wave-speed structure of the earth. Seismologists have created 3-D earth models (Magistrale et al. 1996, Magistrale et al. 2000, Kohler et al. 2003, Süss and Shaw 2003, Prindle and Tanimoto 2006, Tape et al. 2009, Tape et al. 2010, Ely et al. 2010, and Plesch et al. 2011) of seismic wave speeds and density, and now have the ability to study 3-D global and regional seismic wave propagation using approaches based, for instance, on the finite element and the finite difference methods (for e.g., Heaton et al. 1995, Olsen et al. 1995, Bao et al. 1998, Graves 1998, Akcelik et al. 2003, Komatitsch et al. 2004, Liu et al. 2004, Komatitsch et al. 2010, Komatitsch 2011, etc.).

Here, to numerically propagate seismic waves, we use the open source package SPECFEM3D (V2.0 SESAME, Kellogg 2011) that is based on the spectral element method (Komatitsch and Tromp 1999 and Tromp et al. 2008). SPECFEM3D accounts for 3-D variations of seismic wave speeds and density, topography and bathymetry, and attenuation as dictated by the SCEC Community Velocity Model (CVM-H 11.9). This model is based on current research, and incorporates tens of thousands of direct velocity measurements that describe the Los Angeles basin and other structures in southern California (Plesch et al. 2011 and Süss and Shaw 2003). The model includes background crustal tomography (Hauksson 2000 and Lin et al. 2007) enhanced using 3-D adjoint waveform methods (Tape et al. 2009), the Moho surface (Plesch et al. 2011), and a teleseismic

upper mantle wave-speed description (Prindle and Tanimoto 2006). Earlier versions of this wave-speed model have been used to reliably model the basin response accurately down to a shortest period of approximately 2~s (Komatitsch et al. 2004 and Liu et al. 2004). Casarotti et al. (2008) have created a spectral element mesh of the Southern California region, compatible with the wave-speed model, using an advanced unstructured mesher, CUBIT, developed by the Sandia National Laboratory, USA (Sandia National Laboratory 2011), and adapted as GeoCUBIT for large-scale geological applications. Additionally, to generate the shortest wave in this range, a burst of at least five impulses must occur within the temporal extent of one wave-period (or the spatial extent of one wave-length). Based on rupture propagation speeds and the regional wave-speed model of the earth in southern California, the kinematic source models need to be resampled to a maximum subfault dimension of about 0.5 km to be capable of generating waves in this frequency band.

3.4 High-Frequency Ground Motion Waveforms

The algorithm for producing the high-frequency ground motion waveforms consists of two major steps: (i) EGF event selection and quality check and (ii) EGF summation. Additionally, to eliminate low-frequency motion, the synthetic seismograms generated, using Green's functions, are filtered using a second order high-pass Butterworth filter with a corner frequency of 0.5 Hz.

3.4.1 EGF Event Selection

The elastodynamic Green's function is the displacement field resulting from a unidirectional unit impulse. If Green's functions of all subfaults of a rupture event are known, the seismic representation theorem (Burridge and Knopoff 1964) can be used to synthesize the displacement field in both space and time due to a realistic earthquake source model describing that event.

In the EGF approach, seismograms from small earthquakes are used as surrogates for Green's functions emanating from a unit impulse. Spatial coverage and resolution of the displacement field are directly dependent upon seismic station distribution and density. It is unlikely that the location

of the seismic station, at which the recording from a small earthquake is available, will exactly match the location of the target site where ground motions are to be computed. Furthermore, it is quite likely that no small earthquakes, centered exactly at the centroid of each subfault of our rupture event, have occurred or been recorded. Thus, the task of EGF event selection for a target subfault - target site pair consists of finding a record of a small earthquake whose source-to-station path closely tracks the path between the target subfault and target site. Here, “closeness” (E in Equation 3.1) is measured by the weighted average of two distances: (i) distance d_1 between the hypocenter of the actual event and the target subfault of the target event and (ii) distance d_2 between the seismic station where ground motion from the actual event is recorded and the target site where ground motion is to be synthesized. For each target subfault - target site pair, we search the existing catalog of historical earthquakes ($M_w > 2.5$) on the fault under consideration to determine the record that is “closest” by this measure (without any consideration to the magnitude). The selected record is assigned as the EGF for that target subfault-site pair if its signal-to-noise ratio and overall quality are at acceptable levels. If these aspects are not satisfactory, the next best candidate is evaluated. For far-field stations, the distance d_2 is given greater weightage because local site effects are likely to dominate over source effects (see Equation 3.1 and Figure 3.1). Both distances (d_1 and d_2) are given equal weightage for near-field stations.

$$E = \begin{cases} \frac{d_1+d_2}{2}, & \text{Near-field stations } \frac{2L}{R_{ij}} \geq 1 \\ \frac{\frac{2L}{R_{ij}}d_1+d_2}{2}, & \text{Far-field stations } \frac{2L}{R_{ij}} < 1 \end{cases} \quad (3.1)$$

E : Closeness measure

R_{ij} : Distance between the target site i and the centroid of the subfault j

L : Length of the fault in the strike direction

d_1 : Distance between the EGF hypocenter and the centroid of the subfault j (in 3-D space)

d_2 : Distance between the seismic station and the target site i (in 3-D space)

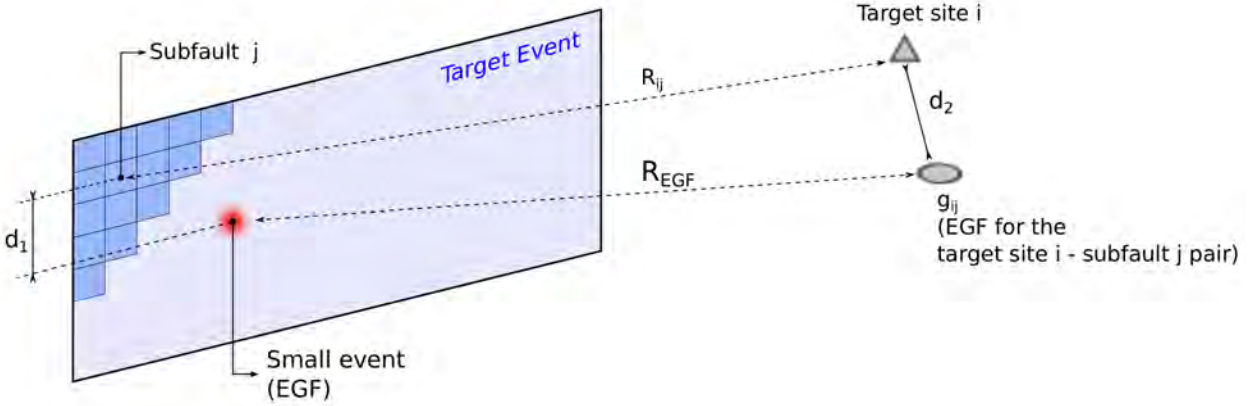


Figure 3.1: Schematic representation of EGF event selection. Of all the historical records available in the vicinity of target site i from earthquakes on the target fault located in the vicinity of subfault j , the record g_{ij} best represents the path between target site i and subfault j (Irikura 1983).

3.4.2 EGF Summation

Ground motion synthesis at analysis site i involves a double summation of the selected EGFs of all the subfaults. The first sum corresponds to the number of times a given subfault EGF must be superposed in order to release seismic moment equivalent to the seismic moment release of the subfault as prescribed by the kinematic source model. This number, K_j , is estimated by the ratio of the seismic moments rounded down to the nearest integer. A correction involving moments, $M_o^{(j)} / K_j M_o^{EGF}$, is needed to account for this round-off. Here, $M_o^{(j)}$ is the seismic moment of the j^{th} subfault prescribed by the kinematic source model and M_o^{EGF} is the seismic moment released by EGF. There is one other complication. The rise-time of the EGF will typically be much smaller than the rise-time assigned to the subfault in the kinematic source model because of differences in the moment/energy release. To ensure that the energy release by the EGF summed K_j times occurs over the same duration as the rise-time of the subfault prescribed by the kinematic source model, the EGF must be shifted slightly in time at each instance it is added. In previous studies

(e.g., [Irikura 1983](#), [Irikura 1986](#)), this time shift, termed the source sampling function $f_j(k)$, has been determined by dividing the subfault rise-time $T_r^{(j)}$ by K_j equally spaced times (Figure 3.2). In order to remove any artificial periodicity and to reduce the high frequency content [Somerville et al. 1991](#) added stochastic perturbation to each of the time shifts illustrated in Figure 3.2. Here, we compute the time shifts by assuming that subfault seismic moment is released in K_j equal moment steps (red lines in Figure 3.3a). In other words, given $M_o^{(j)}(t)$, the seismic moment release in subfault j as a function of time, we compute the times corresponding to $M_o^{(j)}/K_j$, $2M_o^{(j)}/K_j$, $3M_o^{(j)}/K_j$, ..., and so on. The source-time function is then sampled by an uneven distribution of Dirac delta functions centered at each of these times (Figures 3.3b-c). The time spacing between delta functions decreases as $1/\sqrt{t}$ up to half the rise-time $t = T_r^{(j)}/2$ and then increases symmetrically with respect to $t = T_r^{(j)}/2$ up to $T = T_r^{(j)}$ (see Figure 3.3c). This results in a lower density of delta functions at the start and the end of the subfault rupture and a higher density in the middle; it translates into higher contribution to high-frequency motions from the start and the end of the rupture process, with a smoother rupture in the middle or less intense high-frequency radiation during the mid-portion of subfault rupture. The time shifts $f_j(k)$ are given by:

$$f_j(k) = \begin{cases} \frac{T_r^{(j)}}{2} \sqrt{2\left(\frac{k}{K_j}\right)} & k \in 0, 1, \dots, \leq \frac{K_j}{2} \\ T_r^{(j)} - \frac{T_r^{(j)}}{2} \sqrt{2\left(1 - \frac{2k}{K_j}\right)} & k \in \frac{K_j}{2} + 1, \dots, K_j - 1 \\ T_r^{(j)} = \text{Rise-time} & \end{cases} \quad (3.2)$$

The ground displacement at target site i is given by:

$$u_i(t) = \sum_{j=1}^N \sum_{k=1}^{K_j} \left(\frac{R_{EGF}}{R_{ij}} \right) \left(\frac{M_o^{(j)}}{K_j M_o^{EGF}} \right) g_{ij}[t - t_{rup}^{(j)} - f_j(k)], \quad (3.3)$$

where $t_{rup}^{(j)}$ is the time shift that accounts for rupture front propagation. It is inferred from the prescribed subfault rupture velocities of the kinematic source model.

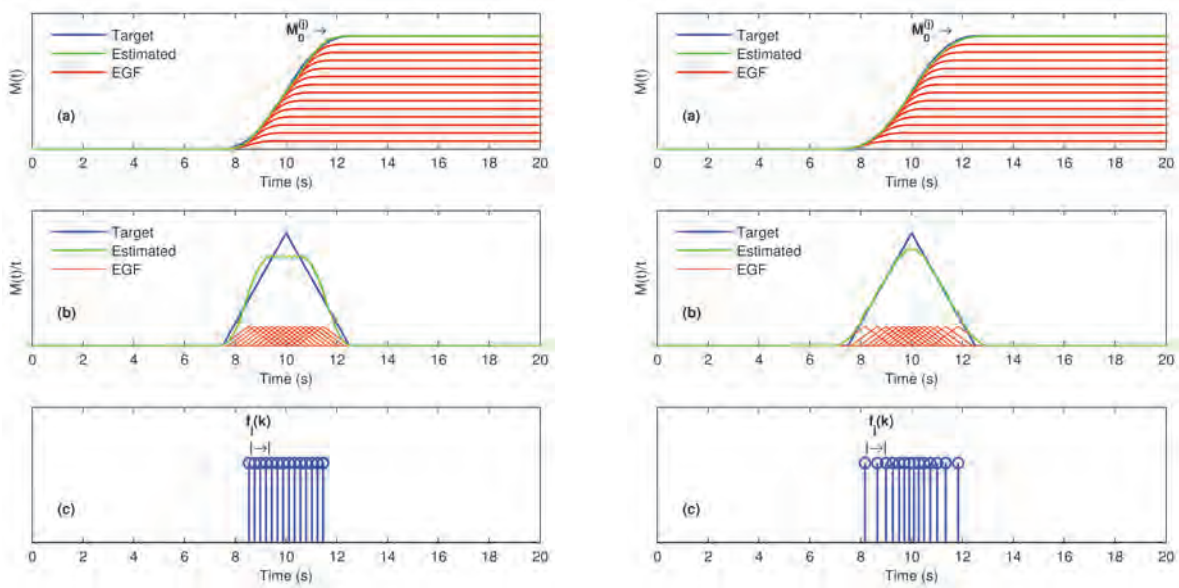


Figure 3.2: Time shifts used in previous studies. **Figure 3.3:** Time shifts used in this study. (a) moment (or slip) vs. time and approximation using multiple EGFs | (b) Moment-rate (or slip rate) vs. time and approximation using multiple EGFs | (c) Subfault j time shifts $f_j(k)$ used in the EGF summation.

3.5 Broadband Ground Motion Waveforms

High-frequency synthetic seismograms from the EGF approach are superposed on the corresponding low-frequency spectral element synthetic waveforms to produce broadband ground motion histories.

3.6 Validation of Methodology

We simulate broadband ground motion for two earthquakes to validate our approach: (a) the 2004 M_w 6.0 Parkfield earthquake and (b) the 1999 M_w 7.1 Hector Mine earthquake. For the high-frequency component of the ground motion we use records from M_w 2.5-4.0 earthquakes,

obtained from the Southern California Earthquake Data Center’s (SCEDC - www.data.sceec.org) Seismogram Transfer Program (STP), as EGFs. We limit our EGFs to high-gain broadband stations (BH) with sampling rates of 0.025 *s* or 0.050 *s*. For each earthquake we calculate (i) the velocity time series at various broadband stations located within a 250 *km* radius of the earthquake hypocenter (see Appendix C for the list of stations), (ii) velocity spectra, (iii) peak ground velocities (PGV), and (iv) the 5%-damped acceleration response spectra. We compare the synthetic time histories, their spectra, and peak values against that of recorded ground motions in the low, the high, and the broadband frequency regimes. Additionally, the velocity spectra, peak ground velocities (PGV), and the 5%-damped response spectra of the synthetic seismograms are compared statistically against that of recorded ground motion at all stations. Mean residuals, standard deviation, and model bias (Appendix B) are computed. It should be noted that in here we are not using and of the near-field stations for our comparisons because: (1) this method will be applied for simulation of high-frequency ground motions for San Andreas earthquake at relatively high distances and (2) high frequency ground motions tend to saturate at very close distances to the fault requiring further investigation of the method for near-filed ground motion simulations. While, the complete synthetics dataset and figures are included in appendices (For Hector Mine: Appendix D and for Parkfield Appendix E), we present results for only a small subset of stations here.

3.6.1 Validation 1: 1999 M_w 7.1 Hector Mine Earthquake

The magnitude 7.1 Hector Mine earthquake of 16th October 1999 occurred on several faults in the eastern California shear zone. The hypocenter of this earthquake was located at 34.60° N - 116.27° W, approximately, at a depth of 15 *km*. The kinematic source model, from an inversion of geodetic and seismic data by Ji et al. (2002a, 2002b), contains three fault segments with a total seismic moment of 3.33×10^{26} dyne-cm. Strike and dip angles for the three segments are:

- (i) 322° and 75°, respectively, for the northern segment,
- (ii) 346° and 85°, respectively, for the central segment, and
- (iii) 322° and 75°, respectively, for the southern segment.

The maximum depth of the source model in all three segments is approximately 16 *km*. The

average rupture velocity is about 1.9 km/s , the average rise-time is approximately 3.5 sec , and the average rake angle is around 175° . The original subfault dimensions for this source model are 3 km along strike and 2.7 km along dip. Subfault source time functions are assumed triangular with variable rise-times. A complete description of the source model is available in the finite-source rupture model database at www.seismo.ethz.ch. Source parameters are given in Table 3.1 and the source model, resampled to a 0.5 km grid, is shown in Figures 3.4(a), 3.4(b), and 3.4(c). Figure 3.5(a) illustrates the location of all stations where synthetics are computed and validated. The near field station are not considered for this study because of high-frequency saturated at near-field distances. Detailed station information is provided in Appendix C.

Segment	Length(km)	Width(km)	Dip($^\circ$)	Strike($^\circ$)	Avg. Rake($^\circ$)
1	33	16	322	75	175
2	21	16	346	85	175
3	50	16	322	75	175

Table 3.1: Source parameters for the the 1999 M_w 7.1 Hector Mine.

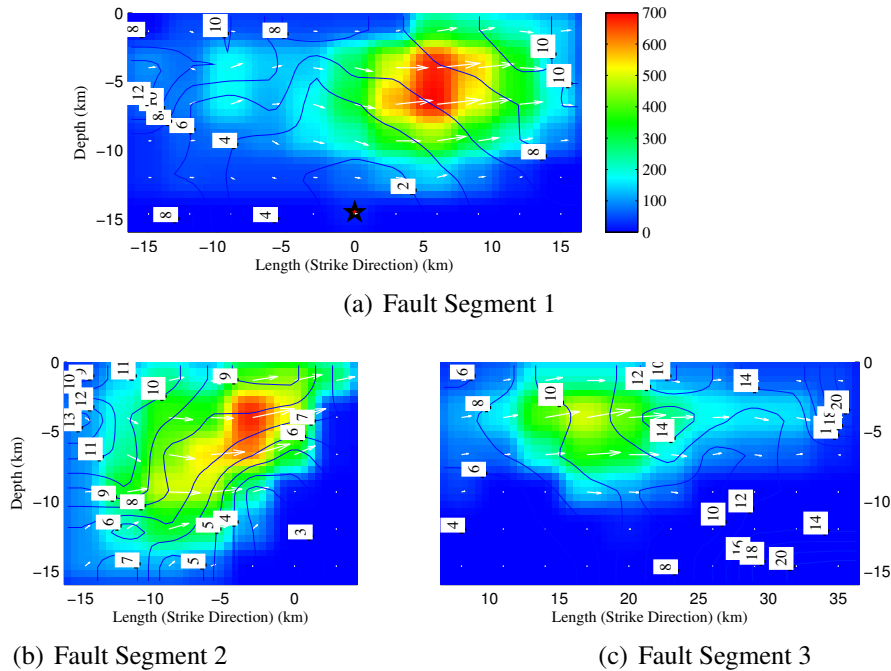


Figure 3.4: Fault segments of source model for the 1999 M_w 7.1 Hector Mine earthquake, resampled to a subfault dimension of 0.5 km | Color map: Slip distributions in centimeters | Arrows: Slip direction | Counters: Rupture times in seconds | Star: Hypocenter of the event.

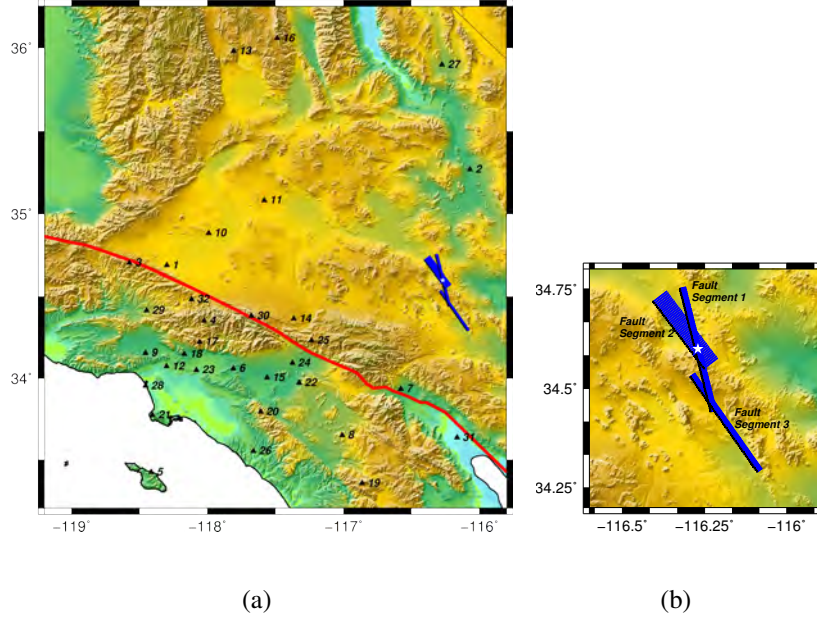


Figure 3.5: (a) : Location of all stations used in the 1999 Hector Mine earthquake validation. Red line: San Andreas Fault | Blue line: Surface projection of the Ji et al. source model | Star: Epicenter | Black triangles: Stations
 (b) Fault segments in the model | Blue line: Surface projections | Black line: Surface trace | Star: Epicenter.

Figures 3.6(a), 3.6(c), and 3.6(e) illustrate the north-south, east-west and vertical components of ground velocities at station 9 [see Figure 3.5(a) for station location]. The first column (on the left) of each of the figures corresponds to low-frequency (< 0.5 Hz) velocity waveforms generated using the spectral element approach, the second column (middle) corresponds to high-frequency (0.5–5 Hz) velocity waveforms from the EGF approach, and the third column illustrates the broadband ground motion waveforms (< 5 Hz), synthesized by superimposing the two. Figures 3.6(b), 3.6(d), and 3.6(f) compare the corresponding velocity spectra of these components of simulated and recorded ground motion. Figures 3.8(a)-3.8(f) and 3.7(a)-3.7(f) show similar comparisons for stations 15 and 30, respectively.

Additionally, we compare horizontal peak ground velocities obtained from our simulations against that recorded at the 32 stations of interest in broadband and high-frequency regimes. Figures 3.9(a) and 3.10(a) show this comparison as a function of distance to the hypocenter location. Figures 3.9(b) and 3.10(b) illustrate the ratio of observed to simulated PGVs plotted on a natural

log scale as a function of station distance to the hypocenter location. The PGVs in the long-period regime of the synthesized broadband ground motion histories are systematically higher than that of recorded motions [Figure 3.9(b)]. Possible sources for this mismatch can be attributed to either the source model or the differences between the wave speed models used for the source inversion and forward wave propagation (CVM-H 11.9.0). On the other hand, there is no systematic bias in the PGV estimates in the high-frequency band of 0.5 Hz to 5.0 Hz. Additionally, Figures 3.11(a), 3.11(b), and 3.11(c) illustrate the bias in the synthetics associated with 5%-damped acceleration response spectra for the north component, the east component and the geometric mean of the horizontal ground motion, respectively, at the 32 stations. The procedure for computing this bias is outlined in Appendix B. The model bias is relatively low and very close to zero for the individual and the average horizontal components across all frequencies, considering the distances at which the stations are located at.

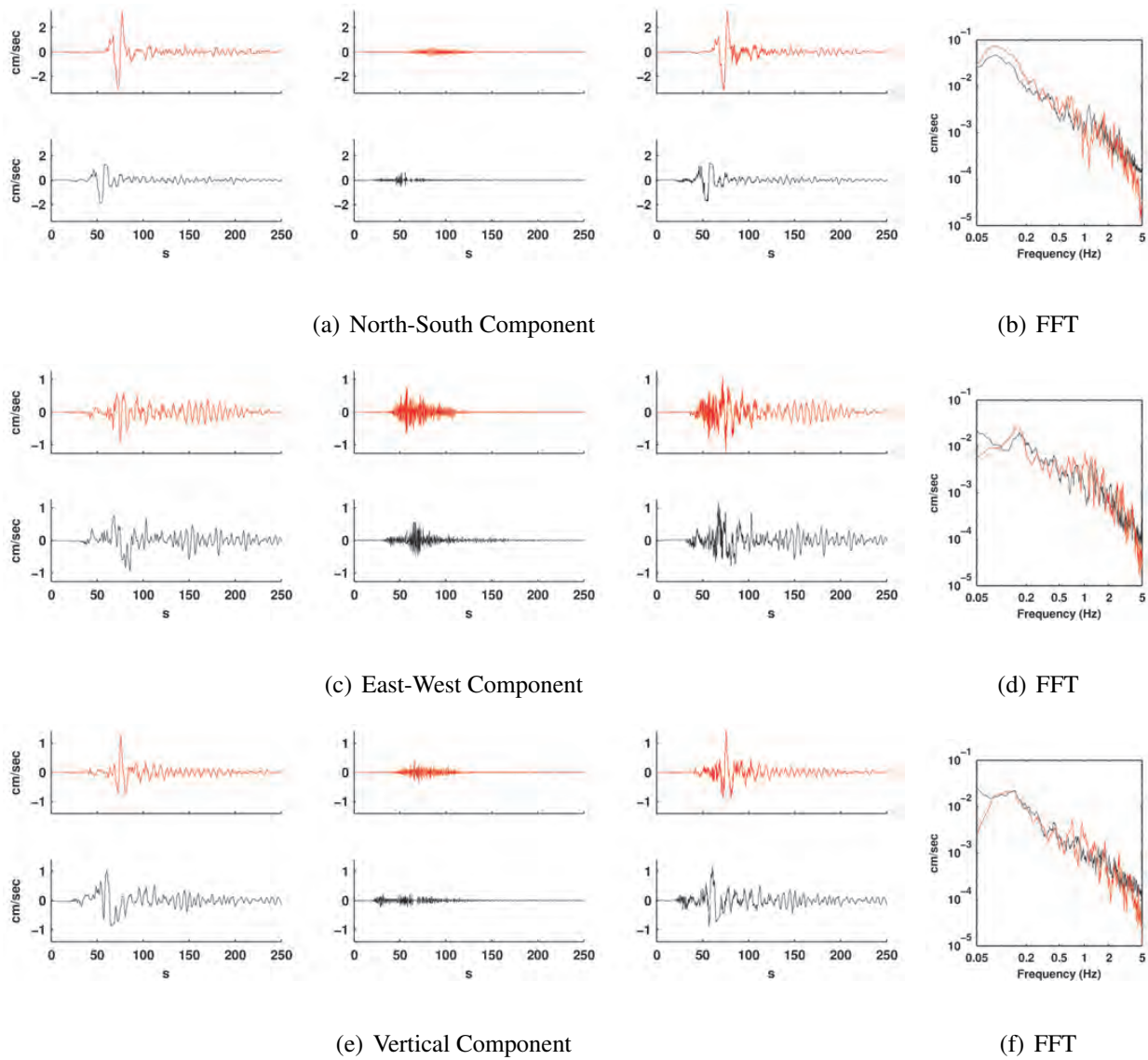


Figure 3.6: Comparison of simulated (red) and observed (black) ground velocity histories and spectra at station 9.

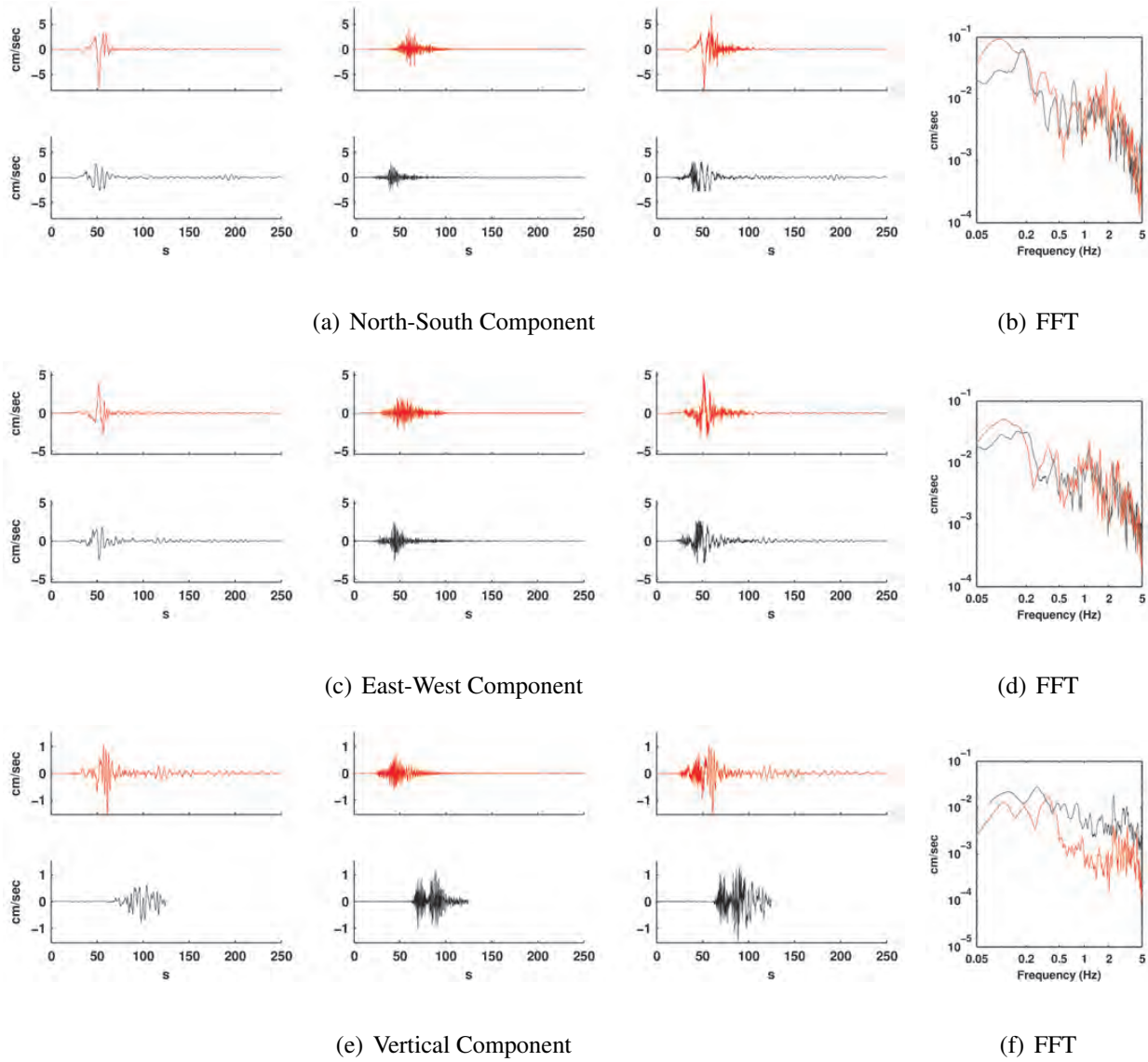
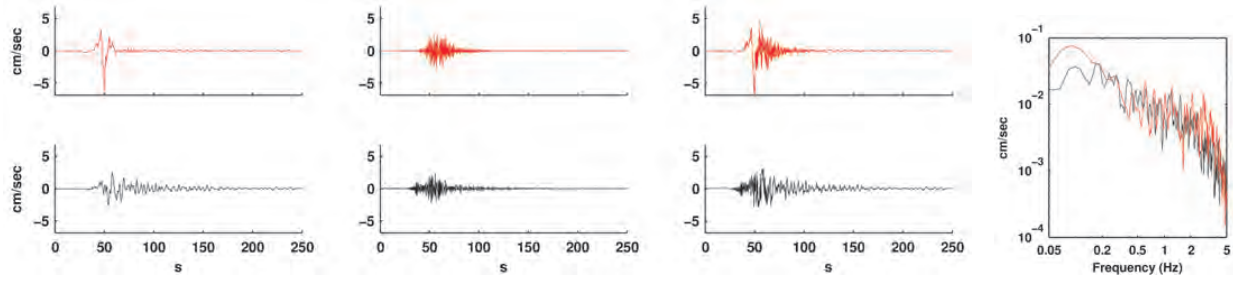
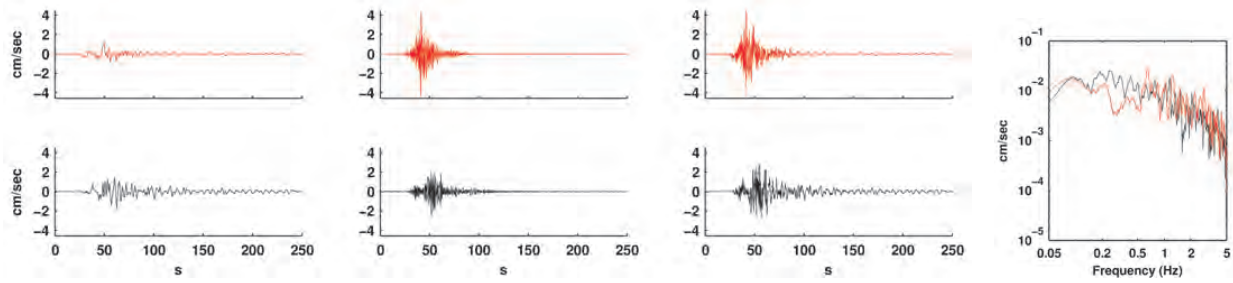


Figure 3.7: Comparison of simulated (red) and observed (black) ground velocity histories and spectra at station 15.



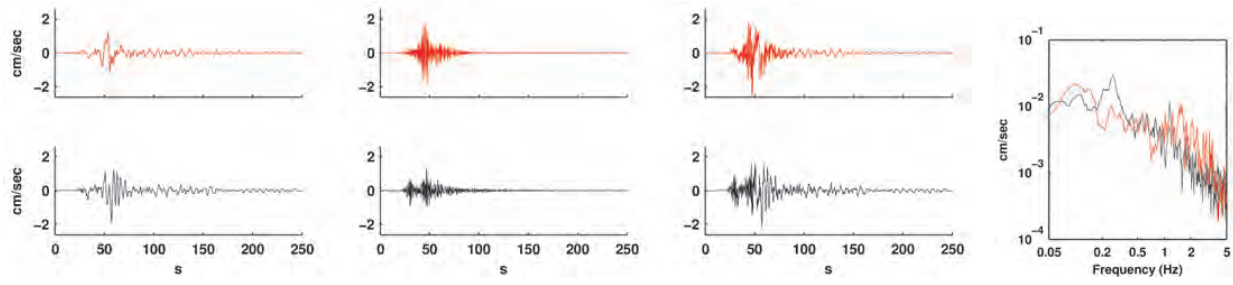
(a) North-South Component

(b) FFT



(c) East-West Component

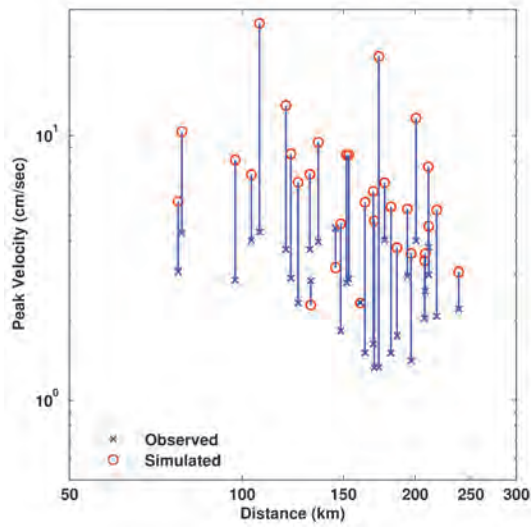
(d) FFT



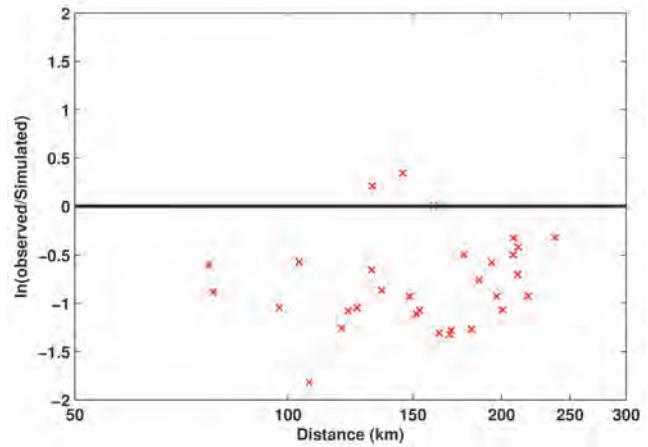
(e) Vertical Component

(f) FFT

Figure 3.8: Comparison of simulated (red) and observed (black) ground velocity histories and spectra at station 30.

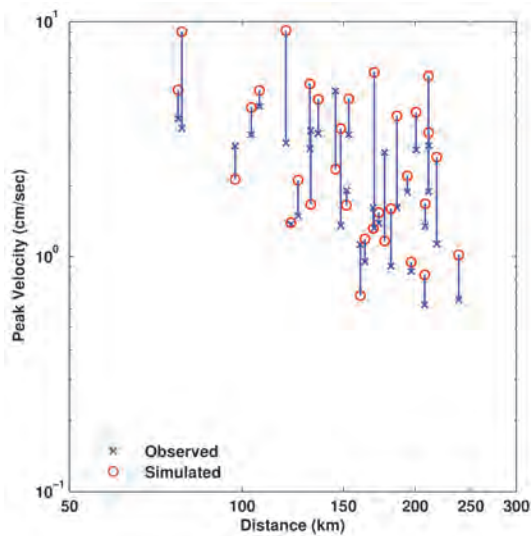


(a) PGV

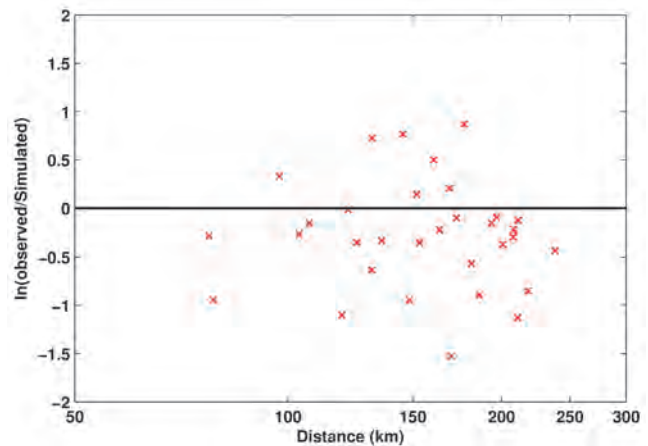


(b) Residuals

Figure 3.9: (a) Comparisons of peak ground velocity (PGV) of the simulated and the recorded broadband ground motions as a function of station distance to the hypocenter. (b) Natural log of the residual of simulated and recorded values.



(a) PGV



(b) Residuals

Figure 3.10: (a) Comparisons of peak ground velocity (PGV) of the high-frequency content of the simulated and the recorded ground motions as a function of station distance to the hypocenter. (b) Natural log of the residual of simulated and recorded values.

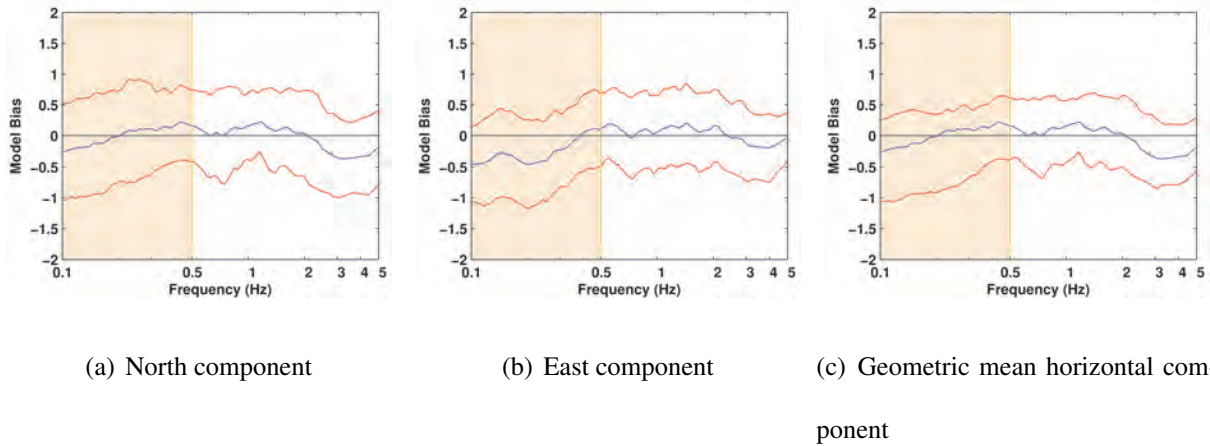


Figure 3.11: Bias in the synthetic associated with 5%-damped acceleration response spectra at 32 stations relative to the corresponding spectra of recorded ground motion. Blue line: Bias. Red line: Standard error.

3.6.2 Validation 2 : 2004 M_w 6.0 Parkfield Earthquake

The M_w 6.0 Parkfield earthquake of 24th of September 2004 occurred on the San Andreas fault with its epicenter at approximately 11 km south-southeast of the city of Parkfield, California. The hypocenter was located at 35.815° N, 120.374° W, and a depth of 7.9 km. The kinematic source model from a finite fault inversion of strong-motion data by Custódio et al. (2005) shows a total seismic moment of 1.36×10^{25} dyne-cm being released on a single fault segment with a rupture extent of 40 km along strike and 15 km along dip with a 140° strike angle from the geographic north and an 87° dip angle from the surface of the earth. Rupture starts at the southern section of the rupture plane and propagates north (south-to-north directivity) for 10~s approximately. The peak slip on the fault is about 50 cm and is located close to the hypocenter of the fault. The subfault dimensions in the model are 1.9 km along strike and 1.67 km along dip and are resampled to 0.5 km in either direction (Figure 3.12). Source time functions for individual subfaults are assumed triangular with variable rise-times (see finite-source rupture model database at www.seismo.ethz.ch for details). Figure E.1 illustrates the location of all the stations used in this validation. Detailed station information is provided in C.

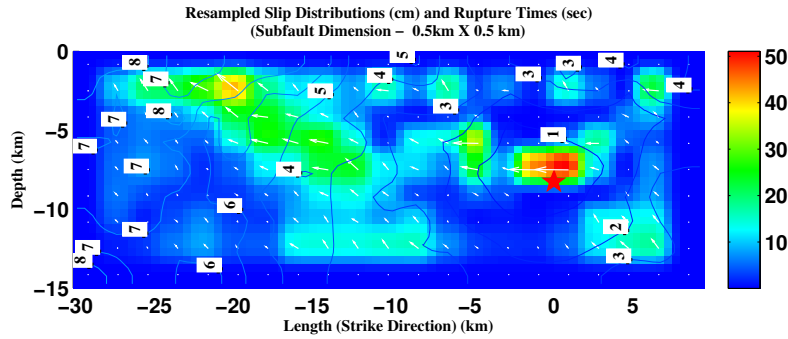


Figure 3.12: Resampled kinematic source model for the 2004 M_w 6.0 Parkfield earthquake by Custódio et al. (2005) | Subfault dimension $0.5\text{ km} \times 0.5\text{ km}$ | Color map: Slip distribution in centimeters | Arrows: Slip direction | Counters: Rupture times in seconds | Star: Hypocenter of the event.

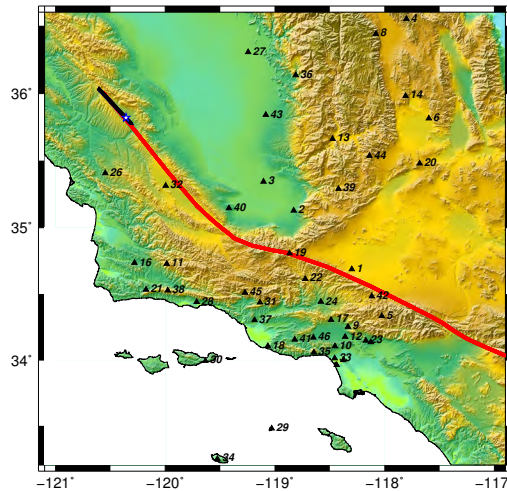


Figure 3.13: Location of all stations used in the 2004 Parkfield earthquake validation. Red line: San Andreas Fault | Black line: Trace/surface projection of the Custódio et al. (2005) earthquake source model | Star: Epicenter | Black triangles: Stations.

Figures 3.14(a), 3.14(c), and 3.14(e) illustrate the north-south, east-west, and vertical components of the synthesized and the recorded ground velocities at station 1 (see Figure 3.12 for station location). The first column (on the left) of each of the figures corresponds to low-frequency ($< 0.5\text{ Hz}$) velocity waveforms generated using the spectral element approach, the second column (middle) corresponds to high-frequency ($0.5 - 5\text{ Hz}$) velocity waveform the EGF approach, and the third column illustrates the broadband ground motion waveforms ($< 5\text{ Hz}$), synthesized by

superimposing the two. Figures 3.14(b), 3.14(d), and 3.14(f) compare the corresponding velocity spectra of these components of simulated and recorded ground motion. Figures 3.15(a)-3.15(f) and 3.16(a)-3.16(f) show similar comparisons for stations 10 and 40, respectively.

Figures 3.17(a) and 3.18(a) compare the peak horizontal ground velocities for broadband and high-frequency ground motions as a function of station distance to the hypocenter location. Figures 3.17(b) and 3.18(b) illustrate the residuals of observed and simulated peak ground velocities as a function of station distance [the residuals (y axis) are plotted on natural log scale]. The PGVs from the synthesized broadband ground motions appear to be slightly higher than that from the recorded ground motion [Figure 3.17(b)] at distances of 250~km or higher. This may possibly be attributed to the quality of the available wave-speed model. However, yet again, there is no particular bias in the simulation results in the high-frequency band and the attenuation of PGVs with distance is quite similar to the observations. Additionally, Figures 3.19(a), 3.19(b), and 3.19(c) illustrate the bias in the synthetics associated with 5%-damped acceleration response spectra for the north component, the east component, and the geometric mean of the horizontal ground motion, respectively, at the 46 stations. The model bias is relatively low and very close to zero for the individual and the average horizontal components, specifically at high-frequencies.

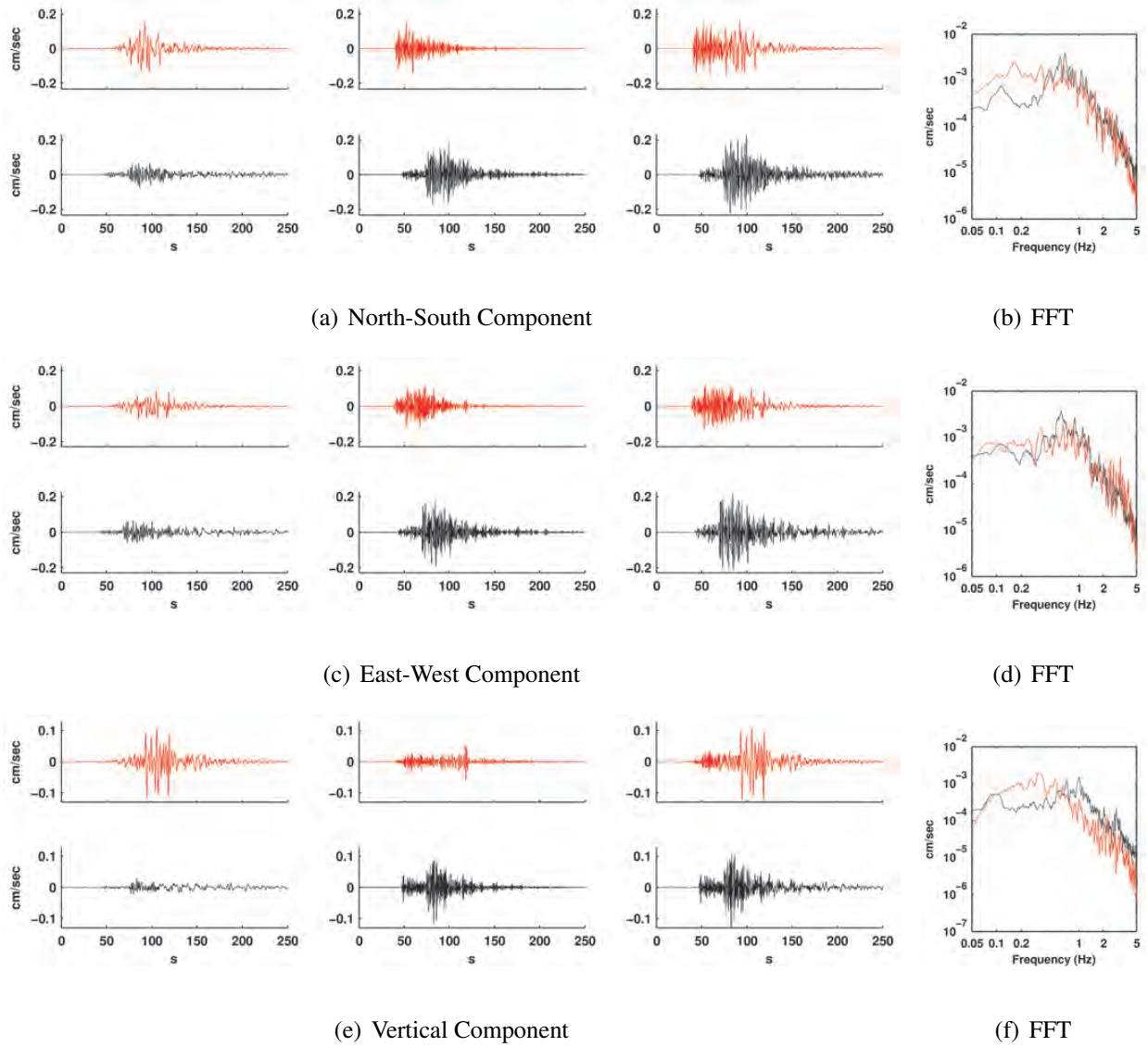
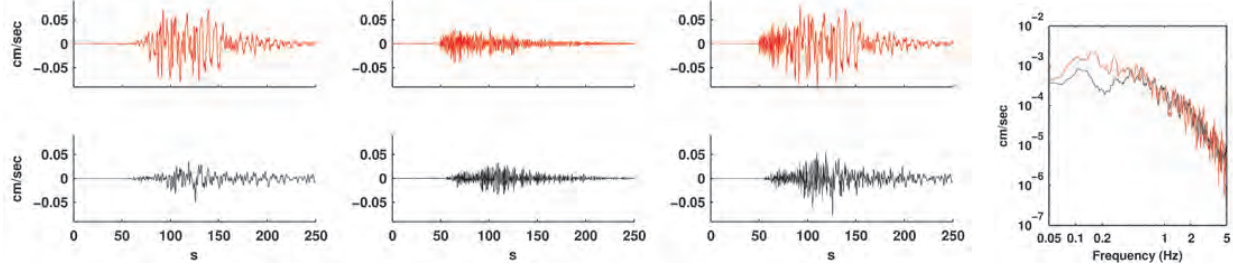
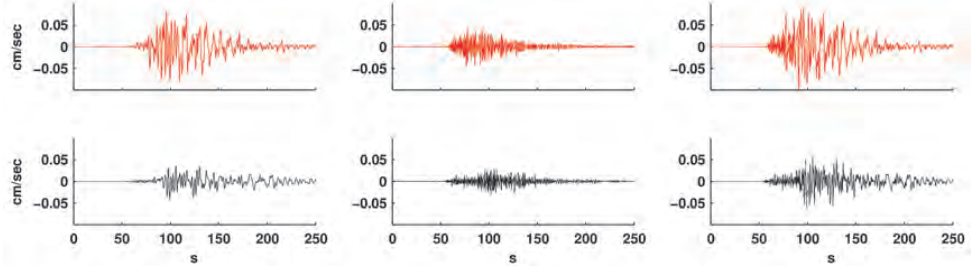


Figure 3.14: Comparison of simulated (red) and observed (black) ground velocity histories and spectra at station 1.



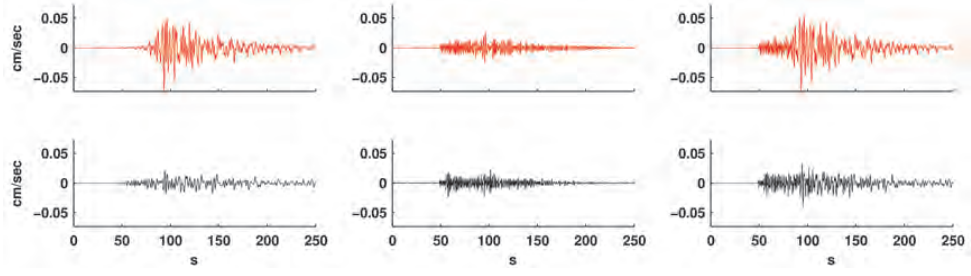
(a) North-South Component

(b) FFT



(c) East-West Component

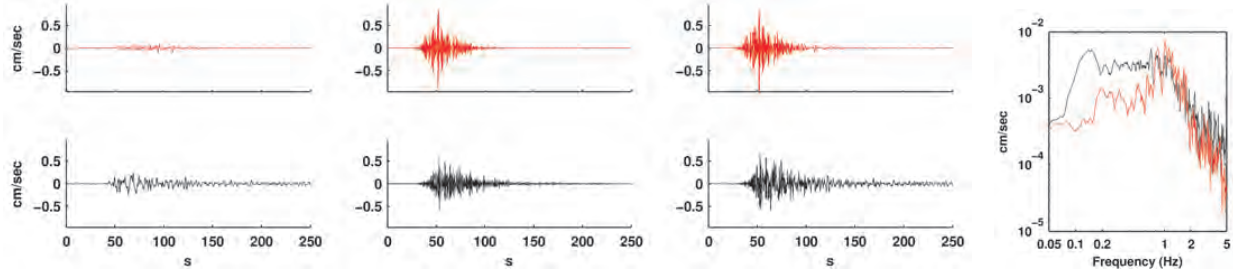
(d) FFT



(e) Vertical Component

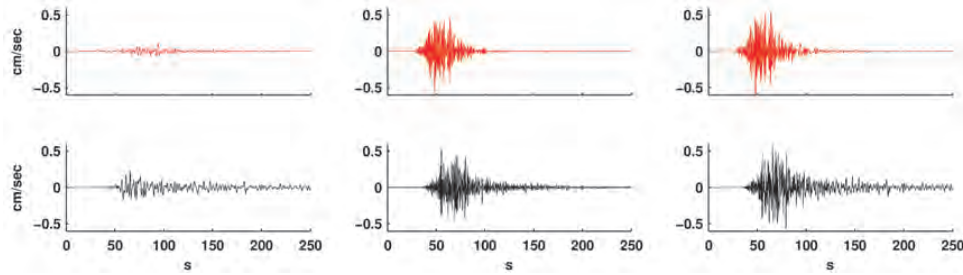
(f) FFT

Figure 3.15: Comparison of simulated (red) and observed (black) ground velocity histories and spectra at station 10.



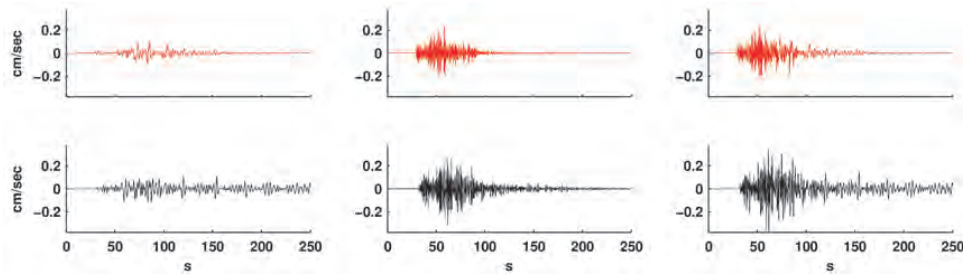
(a) North-South Component

(b) FFT



(c) East-West Component

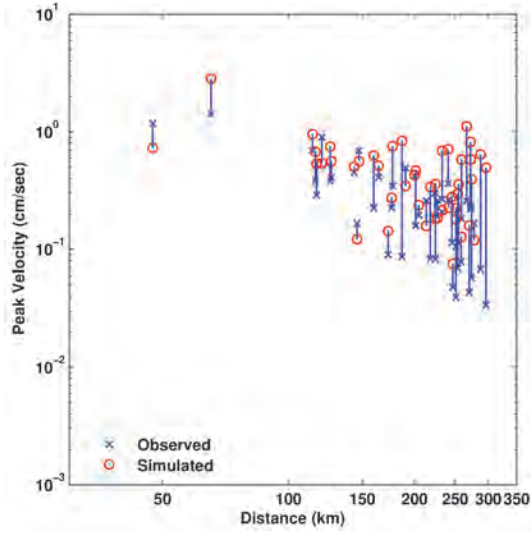
(d) FFT



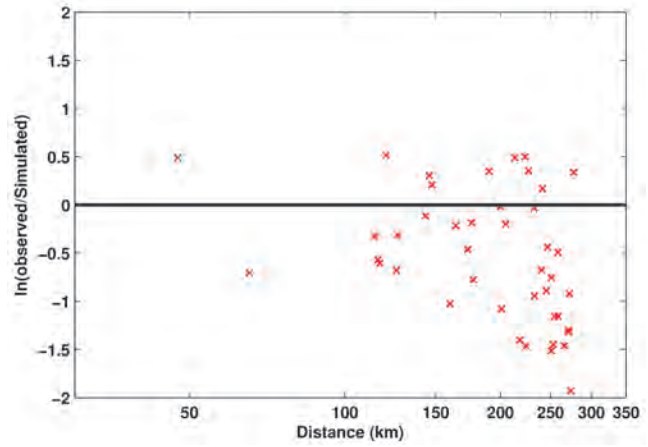
(e) Vertical Component

(f) FFT

Figure 3.16: Comparison of simulated (red) and observed (black) ground velocity histories and spectra at station 40.

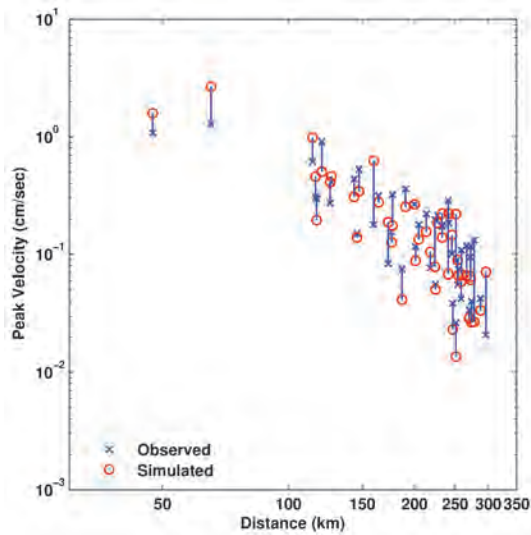


(a) PGV

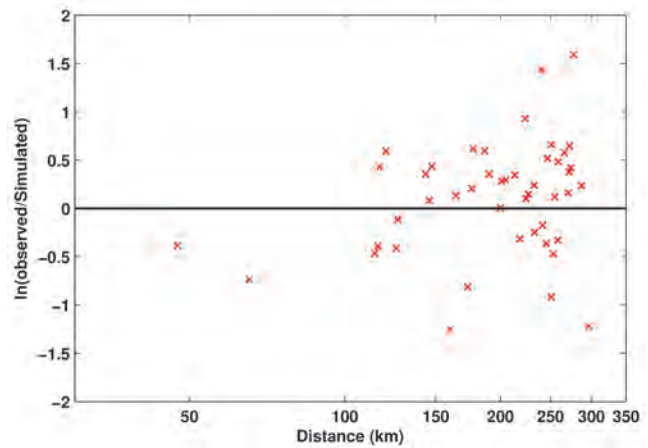


(b) Residuals

Figure 3.17: (a) Comparisons of peak ground velocity (PGV) of the simulated and the recorded broadband ground motions as a function of station distance to the hypocenter. (b) Natural log of the residual of simulated and recorded values.



(a) PGV



(b) Residuals

Figure 3.18: (a) Comparisons of peak ground velocity (PGV) of the high-frequency content of the simulated and the observed ground motions as a function of station distance. (b) Natural log of the residual of simulated and recorded values.

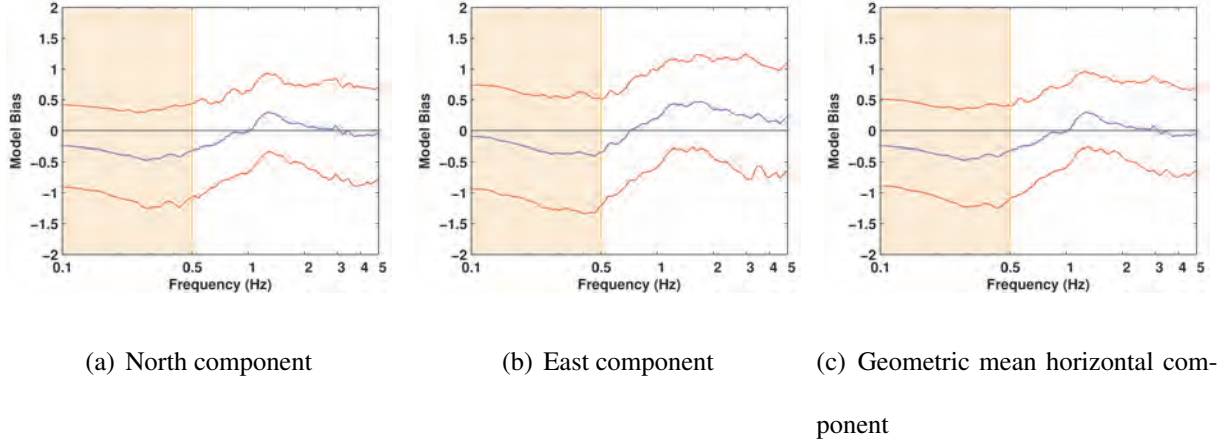


Figure 3.19: Bias in the synthetic 5%-damped acceleration response spectra at 46 stations relative to the corresponding spectra of recorded ground motion. Blue line: Bias. Red line: Standard error.

3.7 Discussion

As we stated previously, the choice of $f_j(k)$ alleviates the overestimation of the high-frequency content typically encountered in EGF-based ground motion simulation methods. We illustrate this point by expanding the double summation for the synthetic ground displacement $u_i(t)$ at target site i (Equation 3.3) and comparing it to theory. Additionally, we illustrate the improvements and reductions in bias in 5%-damped acceleration response spectra. Without loss of generality, a single EGF can be used for all subfaults by substituting $g_{ij} = g_i$ in Equation 3.3:

$$u_i(t) = \sum_{j=1}^N \sum_{k=1}^{K_j} \left(\frac{R_{EGF}}{R_{ij}} \right) \left(\frac{M_o^{(j)}}{K_j M_o^{EGF}} \right) g_i[t - t_{rup}^{(j)} - f_j(k)]. \quad (3.4)$$

The Green's function g_i evaluated at time $t - t_{rup}^{(j)} - f_j(k)$ can be replaced with a convolution of g_i evaluated at time t and a Dirac delta function located at $t = t_{rup}^{(j)} + f_j(k)$ leading to:

$$u_i(t) = \sum_{j=1}^N \sum_{k=1}^{K_j} \left(\frac{R_{EGF}}{R_{ij}} \right) \left(\frac{M_o^{(j)}}{K_j M_o^{EGF}} \right) g_i(t) * \delta[t - t_{rup}^{(j)} - f_j(k)]. \quad (3.5)$$

Rearranging Equation 3.5:

$$u_i(t) = g_i(t) * \sum_{j=1}^N \sum_{k=1}^{K_j} \left(\frac{R_{EGF}}{R_{ij}} \right) \left(\frac{M_o^{(j)}}{K_j M_o^{EGF}} \right) \delta[t - t_{rup}^{(j)} - f_j(k)]. \quad (3.6)$$

All terms, except $g_i(t)$ on the right hand side of Equation 3.6 can be consolidated into a single time function $p(t)$. This represents a mapping (or transfer function) of $g_i(t)$ on to u_i :

$$u_i(t) = g_i(t) * \underbrace{\sum_{j=1}^N \sum_{k=1}^{K_j} \left(\frac{R_{EGF}}{R_{ij}} \right) \left(\frac{M_o^{(j)}}{K_j M_o^{EGF}} \right) \delta[t - t_{rup}^{(j)} - f_j(k)]}_{p(t)} \quad (3.7)$$

$$u_i(t) = g_i(t) * p(t) \quad (3.8)$$

and in frequency domain:

$$U_i(\omega) = G_i(\omega).P(\omega) \rightarrow P(\omega) = \frac{U_i(\omega)}{G_i(\omega)}, \quad (3.9)$$

where $P(\omega)$ is:

$$\begin{aligned} P(\omega) &= \mathcal{F}[p(t)] = \int_{-\infty}^{\infty} \sum_{j=1}^N \sum_{k=1}^{K_j} \frac{R_{EGF}}{R_{ij}} \frac{M_o^{(j)}}{K_j M_o^{EGF}} \delta(t - t_{rup}^{(j)} - f_j(k)) e^{i\omega t} dt \\ &= \sum_{j=1}^N \sum_{k=1}^{K_j} \int_{-\infty}^{\infty} \frac{R_{EGF}}{R_{ij}} \frac{M_o^{(j)}}{K_j M_o^{EGF}} \delta(t - t_{rup}^{(j)} - f_j(k)) e^{i\omega t} dt \\ &= \sum_{j=1}^N \sum_{k=1}^{K_j} \frac{R_{EGF}}{R_{ij}} \frac{M_o^{(j)}}{K_j M_o^{EGF}} e^{i\omega t_{rup}^{(j)}} e^{i\omega f_j(k)}. \end{aligned} \quad (3.10)$$

If EGF records are available for each subfault-target site combination, R_{EGF} and R_{ij} would be equal. Additionally, if the number of EGFs needed to match the seismic moment of the target sub-

written as¹:

$$P(\omega) = \frac{M_o}{M_o^{EGF}} \frac{1 + \left(\frac{\omega}{\omega_c^{EGF}}\right)^2}{1 + \left(\frac{\omega}{\omega_c}\right)^2}. \quad (3.14)$$

Now, the theoretical transfer function of Equation 3.14 can be compared to the empirical transfer function of Equation 3.12. The empirical transfer function is evaluated for two different choices of $f_j(k)$: (1) assuming a non-uniform distribution (equal moments) of events within the subfault's rise-time as in this study (Equation 3.2), and (2) assuming a uniform distribution of events within the subfault's rise-time (Figure 3.2), with an added randomness².

These two empirical transfer functions can be compared against the theoretical transfer function of Equation 3.14 following Brune (1970). Figures 3.20 and 3.21 illustrate this comparison for the Parkfield and the Hector Mine earthquakes, respectively. Single magnitude 2.5 and 3.0 earthquakes are used as the EGFs for the ground motion synthesis of the two earthquakes, respectively. The black line is the amplitude of the theoretical transfer function, the red line is that of the traditional evenly distributed EGFs and the blue is that of the unevenly distributed EGFs adopted in this study. In the 2 Hz - 10 Hz band, the traditional approach clearly overestimates the ground motion intensities whereas our approach agrees better with the theoretical spectrum. This is the case for both earthquakes.

¹Note: This equation is equivalent to Equation 5 in Frankel 1995. However, Frankel 1995 used this equation as frequency domain operator in order to increase the low frequency without changing the high frequency contents of the ground motion.

²The randomness in the second choice is implemented using a gaussian distribution for each f_j using a mean at $f_j(k)$ and standard deviation equal to $\frac{T_r^{(j)}}{2.575 \times K_j}$ (99% confidence interval).

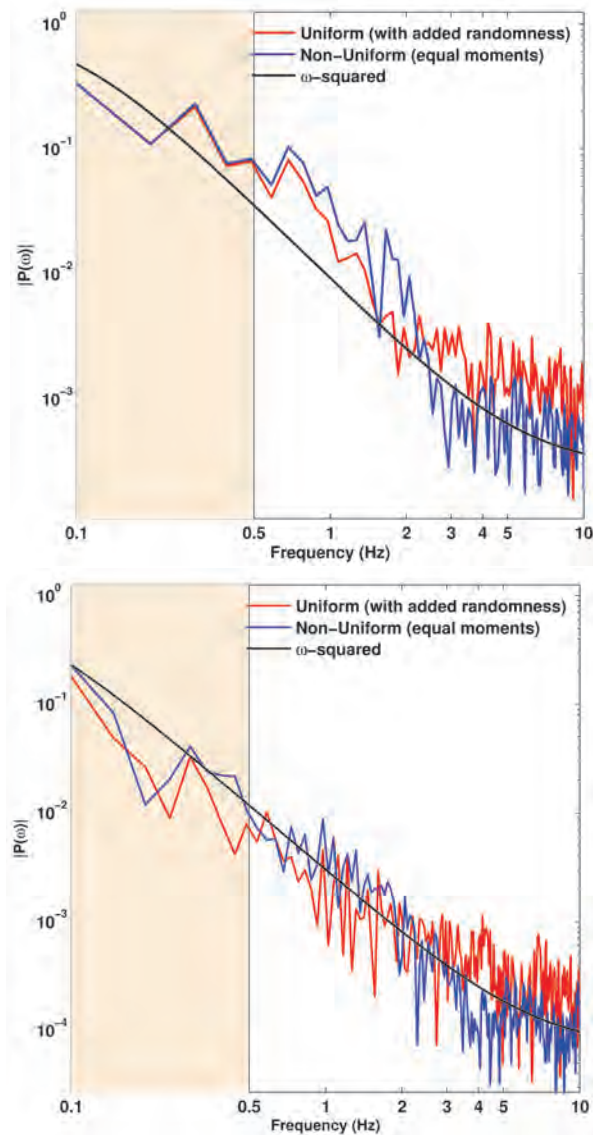
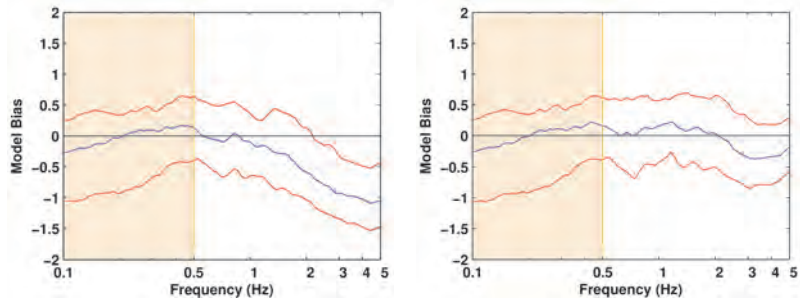


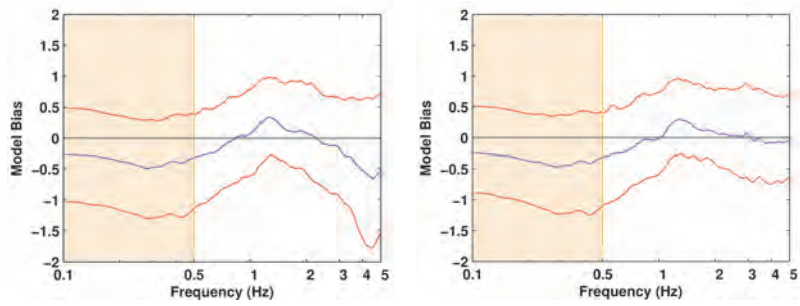
Figure 3.21: Comparison of the amplitude spectra of the transfer functions $[p(t)]$ for the 1999 Hector Mine earthquake. EGF magnitude: 3.0; Black line: Theoretical value; Red line: Uniform distribution; Blue line: Non-uniform distribution used in this study.

Additionally, we compare the bias in the 5%-damped acceleration response spectra of the synthetics produced by the uniformly spaced EGFs [Figures 3.22(a) and 3.23(a)] and that produced using our approach of non-uniformly spaced EGFs [Figures 3.22(b) and 3.23(b)]. The improvement in high-frequency ground motion prediction is clear.



(a) Even distribution of time shifts (b) Time shifts used in this study

Figure 3.22: Model bias in the 5%-damped acceleration spectra of the Hector Mine earthquake synthetics produced using (a) the traditional approach of uniformly spaced EGFs and (b) using the present approach of unevenly spaced EGFs. Red line: Standard error.



(a) Even distribution of time shifts (b) Time shifts used in this study

Figure 3.23: Model bias in the 5%-damped acceleration spectra of the Parkfield earthquake synthetics produced using (a) the traditional approach of uniformly spaced EGFs and (b) using the present approach of unevenly spaced EGFs. Red line: Standard error.

Chapter 4

Building Design: 18-Story Braced Frame (UBC 1994 and UBC 1997)

4.1 Introduction

The original building used in this study is located on Canoga Avenue in Woodland Hills region of the city of Los Angeles, California and hence it is referred to as the Canoga building. Thorough post earthquake investigation and availability of seismic records from the building's accelerometers have made this structure an excellent candidate for many scientific studies. Studies by [Paret and Sasaki \(1995\)](#), [Filippou \(1995\)](#), [Anderson and Filippou \(1995\)](#), [Chi \(1996\)](#), and [Krishnan et al. \(2006b\)](#) are used as architectural and structural blueprints for redesigning this structure. Buildings are designed using the ETABS commercial software, and are analyzed using the FRAME3D program.

4.1.1 Architectural and Structural Description

The Canoga Park building is an 18-story welded steel moment frame building designed based on 1982 UBC guidelines. The building has 17 stories of office space and a mechanical penthouse above that. The building height is 75.7 m with a typical story height of 3.96 m except at the ground level (6.20 m), the 17th level (4.77 m), and the penthouse level (5.28 m). The floor plan throughout the height is relatively uniform with a rectangular footprint of 35.56 m (north-south direction) by

47.04 m (east-west direction) and minor setbacks at the 4th, the penthouse, and the roof levels. Figures 4.1 – 4.5 illustrate the floor plans of the building, the moment frames are boxed and their beam-column connections are shown using small triangles at the location of the connections. The lateral load resisting system of the building consists of two 2-bay long welded moment frames in each direction. These 2-bay long moment frames are located on the west, south, and east perimeter of the building and one bay inside the perimeter of the building on the north side (see Figures 4.1 – 4.4). The asymmetric location of the moment frames causes torsional effects which requires larger member sizing for the north bay moment frame relative to the south bay moment frame.

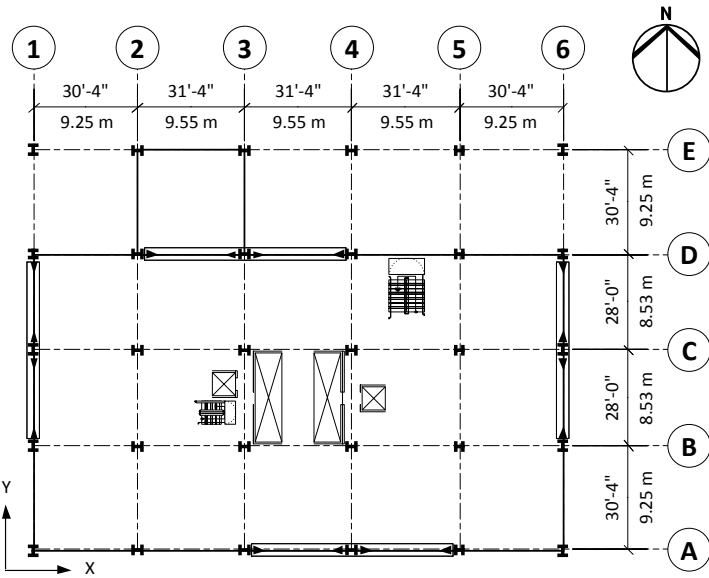


Figure 4.1: Existing building - Plan of ground level and second floor.

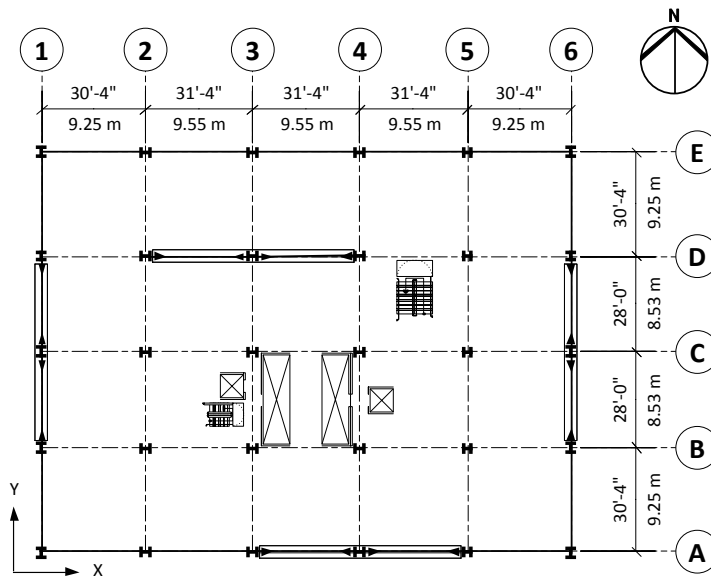


Figure 4.2: Existing building - Plan of third and fourth floors.

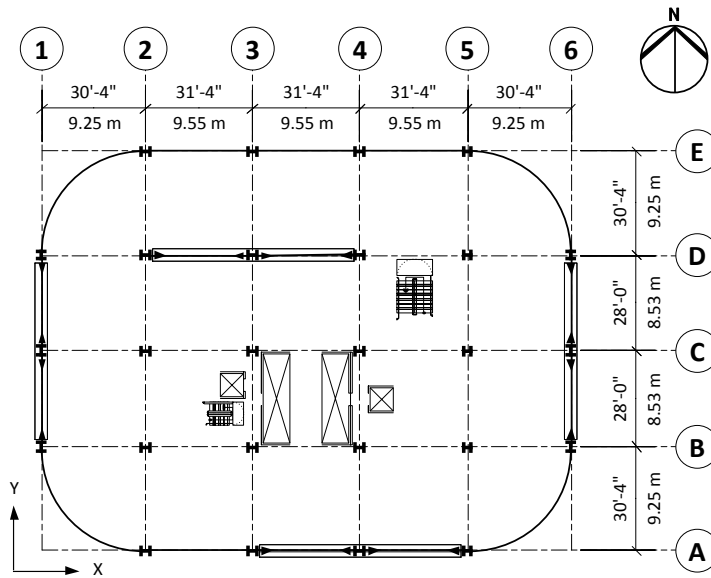


Figure 4.3: Existing building - Plan of floors 5 through 17.

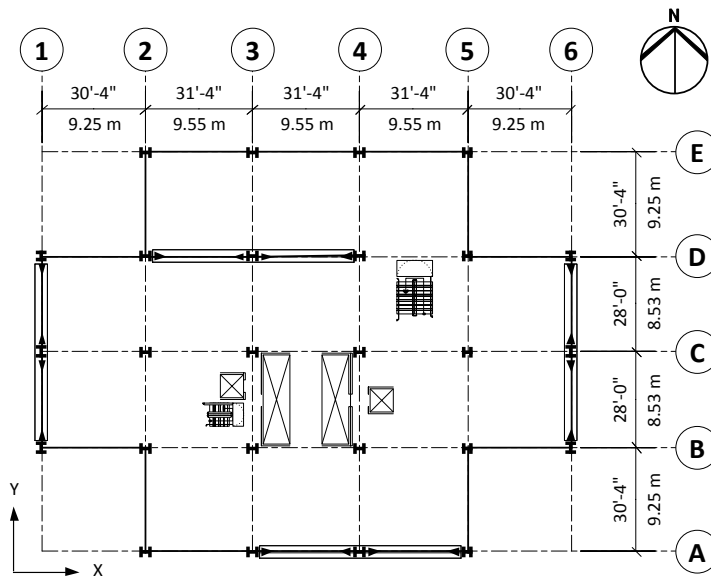


Figure 4.4: Existing building - Penthouse floor plan.

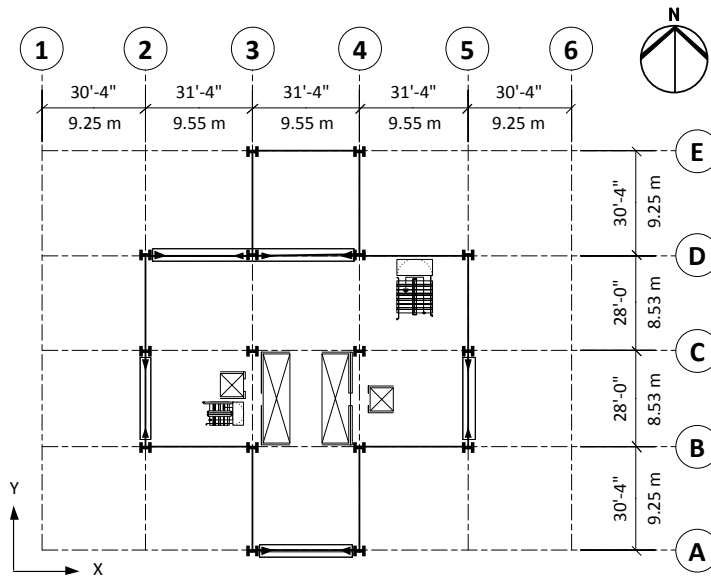


Figure 4.5: Existing building - Roof floor plan.

The columns used in the moment frames vary in section size from W14×311 to W14×730 and the moment frame beams range from W30×90 to W36×300. Column sections used in moment frames are specified as A572 grade 50 steel and the beams are specified as A36 steel. A typical moment connection consists of a full penetration weld (between the beam and the column flanges) with a shear tab (welded to the column flange and bolted to the beam web). W14×90 to W14×283 are used as gravity columns throughout the building. Typical primary beams (girders) are W24×68 and secondary beams are W16×36. Table 4.1 lists all the member sizes and properties for various structural components. The frame sections for the moment frames on the west and east side are identical and very similar to the frame section specification of the south moment frame; however, the north moment frames consists of slightly larger member sizes [a more detailed structural description of the existing building can be found in [Krishnan et al. \(2006b\)](#)].

Structural Component	Member Size	Structural Steel Type	F_y (ksi) Yield Stress	F_u (ksi) Ultimate Stress
Moment Frame - Beams	W30×90 - W36×300	A36	36	58
Moment Frame - Columns	W14×311 - W14×730	A572-G50	50	65
Gravity Frame - Primary Beams	W24×68	A36	36	58
Gravity Frame - Secondary Beams	W16×35	A36	36	58
Gravity Frame - Columns	W14×90 - W14×283	A36	36	58
Connection bolts - moment frame	—	A325F	—	—

Table 4.1: Member sizing, material specification and properties for the existing Canoga moment frame building.

Floor slabs are designed to act as horizontal diaphragms constraining the horizontal degrees of freedom of the joints of the 2-D moment frame to enforce three-dimensional action, and to allow the discretely placed 2-D moment frames in a given direction to share the lateral loads in proportion to their stiffnesses. They consist of 5.5 in concrete slab on metal deck. Load transfer between diaphragms and moment frame beams occurs through 3/4 in diameter studs fuse welded through the metal deck onto the beam top flange.

4.1.2 Damage Description

Initial visual inspections after the Northridge earthquake determined that the building was safe and ready for immediate occupancy. However, problems experienced with elevators in the weeks following the earthquake prompted a more thorough investigation of the building. This investigation revealed that the building was out of plumb by about 15 cm (six inches) towards north ([Anderson and Filippou 1995](#)). The investigation of the moment frames included visual inspection of all welds connecting bottom flanges to columns, ultrasonic testing of 39 weldings along the top flange and columns, and a couple of ultrasonic testings of welds along the bottom flange and columns. This investigation revealed 29 fractures along the bottom flange-to-column welds and no fracture on top flange-to-column welds. Out of 29 fractures, 23 of them were on the west moment frames and 6 on the east moment frames, leaving the north and south moment frames intact and undamaged. The majority of fractures, 20 out of 23 on the west moment frame and 4 out of the 6 on the east moment frame, were above the 10th floor ([Paret and Sasaki 1995](#)).

4.1.3 Past Studies

[Paret and Sasaki \(1995\)](#) focused on the damaged moment frames on the east and the west side of the building, and hence did not consider the torsional effects due to asymmetric arrangement of the moment frames. The 2-D models were analyzed using SAP90 and Drain2D commercial software packages. The seismic weight (total dead load) of 31,400 kips used in the models was estimated using a uniform 94 psf dead load [for summary see [Table 4.2](#)]. The estimated period for the first 3 modes of vibration in the north-south direction for the initial building model were 4.92, 1.68, and 0.97 seconds. However, through visual inspection of the seismic records available on the top of the building, the period of the damaged building was estimated to be around 4.7 seconds, a lower value than the fundamental period of the base building model. Thus, an additional improved model was generated by stiffening the base line model through increasing the rigid end offsets of the beam and column elements. The resulting period for the first 3 modes vibration for the improved building model were estimated to be 4.20, 1.42, and 0.81 seconds [see [Table 4.3](#)]. For analysis purposes,

[Paret and Sasaki \(1995\)](#) used the 5% damped response spectra for five different records in addition to the equal hazard spectrum (code base). The five records were as following: three records from the Northridge earthquake (Canoga Park, Oxnard boulevard, and Sylmar records), one record from the El Centro earthquake (1940), and one record from the 1978 Tabas (Iran) earthquake. The response spectra results were used to determine various engineering parameters such as demand to capacity ratios for individual members, max displacements, drift ratios, and base shear values. The maximum base shear values calculated using the aforementioned response spectra analyses were 3823 kips (24% of the seismic weight), 1903 kips (12 %), and 2258 kips (14%) for the three Northridge records, 1348 kips (9%) for El Centro, 8938 kips (57%) for Tabas, and 3489 kips (22 %) for the equal hazard response spectrum (code based).

[Anderson and Filippou \(1995\)](#) used both 2-D and 3-D models to investigate the seismic behavior of this building, and the models had approximately 28,000 kips seismic weight (10% less than the seismic weight used in [Paret and Sasaki \(1995\)](#)) [Table 4.2]. These models were used in a set of elastic (modal, response spectrum, and time history analysis) and inelastic (nonlinear static, nonlinear dynamic) analyses. Building periods were estimated using the 5% linear elastic response spectra and Fourier amplitude spectra of the recorded time histories. Moreover, moving window Fourier analyses were performed to evaluate the changes in the building behavior and fundamental periods during the course of the earthquake. The fundamental period of the models are summarized in Table 4.3.

Study by [Carlson \(1999\)](#) further examined the building using 3D nonlinear analysis that incorporated connection fracture into the model. The goal was to regenerate the fracture pattern observed during the 1994 Northridge earthquake. [Carlson \(1999\)](#) used two ground motions which were recorded close to the building during the Northridge earthquake to represent the ground shaking at the base of the building. Additionally, several other records were used (such as records from Kobe, Takatori, and Tabas earthquakes) to study the torsional response of unsymmetrical structure and the effect of larger ground motions on the building response.

[Krishnan et al. \(2006b\)](#) examined the performance of the existing building and also the same building redesigned based on 1997 building codes. End-to-end simulations were performed to determine the extent of the damage to the existing and redesigned building. 3-D models were

used for non-linear time-history analysis using the FRAME3D finite element program ¹. The estimated periods for the first 3 modes of vibration were 4.43, 4.22, and 2.47 for the existing building model and 3.72, 3.51, and 2.24 for the redesigned model [see Table 4.3]. Krishnan et al. (2006b) considered 100% dead load alone in calculating the periods, whereas Krishnan and Muto (2012) considered 100% dead load plus 30% live load in calculating the periods. The estimated periods for the original 1982 building were 4.52, 4.26, and 2.69 and for the redesigned building were 4.06, 3.85, and 2.60.

Paret and Sasaki (1995)			Anderson and Filippou (1995)			Krishnan et al. (2006b)	
Base line model	Damaged building	Improved model	Damaged		ETABS	Building model	Redesigned model (UBC97)
			LERS	FAS	models		
A	B	C	D	E	F	G	H
Dead Load 31,400			Dead Load 28,000			Dead Load	
						27,974	28,297
						Dead + 30 % Live Load	
						~31,330	~32,540

Table 4.2: Summary of the seismic weights used in past studies. All values are in kips.

¹<http://www.frame3d.caltech.edu>

	Paret and Sasaki (1995)			Anderson and Filippou (1995)			Krishnan et al. (2006b)	Krishnan and Muto (2012)*		
	Base line model	Damaged building	Improved model	Damaged		ETABS models	Original UBC82	Redesigned UBC97	Original UBC82	Redesigned UBC97
				LERS	FAS					
	A	B	C	D	E	F	G	H	I	J
1	4.92 NS	4.7 NS	4.20 NS	4.3 NS	4.6 NS	4.0-4.8 EW	4.43 NS	3.72 NS	4.52 NS	4.06 NS
2	N/A	N/A	N/A	4.0 EW	4.0 EW	3.8-4.5 NS	4.22 EW	3.51 EW	4.26 EW	3.85 EW
3	N/A	N/A	N/A	N/A	N/A	2.2-2.5 RO	2.47 RO	2.24 RO	2.69 RO	2.60 RO
4	1.68 NS	N/A	1.42 NS	2.40 EW	2.50 EW	1.4-1.8 EW	N/A	N/A	N/A	N/A
5	N/A	N/A	N/A	2.3 NS	2.4 NS	1.2-1.6 NS	N/A	N/A	N/A	N/A
6	0.97 NS	N/A	0.81 NS	1.7 EW	1.7 NS	1.0-1.2 EW	N/A	N/A	N/A	N/A

Table 4.3: Summary of the modal periods from past studies. All values are in seconds. Columns A, C, F, G, and I represent the values of the modal periods estimated for the existing undamaged building using a model representation of the building. Columns B, D, and E represent the estimate for modal period of the building after the earthquake (damaged building), 5% linear elastic response spectra (LERS) analysis, and Fourier Amplitude Spectra (FAS), respectively. [Krishnan et al. \(2006b\)](#) considered 100% dead load alone in calculating the periods, whereas [Krishnan and Muto \(2012\)](#) considered 100% dead load plus 30% live load in calculating the periods.

4.2 Building Codes Overview

The Canoga Park building is redesigned using braced frame lateral load resisting system. The building is redesigned once based on the UBC 1994 and once based on the UBC 1997. The goal here is to quantify collapse risk in tall steel braced framed buildings from a suite of possible San Andreas earthquakes in the next 30 years. Therefore, having representative buildings will be key in achieving this goal.

By choosing the 1994 and 1997 building codes, the majority of tall steel buildings in Southern California are covered and represented (buildings that are built using either a pre- or a post-Northridge building codes). The significant changes implemented in the building that incorporate the lessons learned from the 1994 Northridge earthquake are accounted for by choosing these building codes. Additionally, we can examine the adequacy of the building codes in providing sufficient resistance for future earthquakes.

The 1997 UBC incorporates a number of important lessons learned from the 1994 Northridge and the 1995 Kobe earthquakes. Time histories recorded in these events revealed that the ground motions can be significantly higher near the source of earthquakes. These earthquakes had near source ground motions that greatly exceeded the effective peak acceleration (EPA) given for seismic zone 4 in UBC 1994. It was also observed that amplification of the long-period ground motions was greater for less ideal site soil conditions. As a result, two parameters N_a and N_v were introduced in UBC 1997 to account for the near-source effects and soil amplifications at distances close to the fault ([Naeim 2001](#) and [Taranath 2004](#)).

The overall seismic design concept generally involves the following steps: (1) selecting an overall structural layout, (2) determining code-prescribed forces, ground motions, and deformations, (3) determining the proper analysis procedures, and (4) analysis of the building for combined effects of gravity and seismic loads to verify adequacy of vertical and lateral load carrying capacities. For most buildings, inelastic response can be expected to occur during a major earthquake, implying that an inelastic analysis is more proper for design. However, in spite of the availability of nonlinear inelastic programs, they are not used in typical design practices because (1) their proper use requires knowledge and deep understanding of their working, (2) results produced are

very hard to interpret, and (3) the necessary computations are expensive. Therefore, engineers in practice typically use linear elastic procedures based on the response spectrum method. Next, we will provide a brief description of the steps taken for calculating loads, member sizings, and final designs using UBC 1994 and UBC 1997 ([UBC 1994](#) and [UBC 1997](#)).

4.3 UBC 1994 Design Guidelines

The following sections describe the design guidelines for calculating design loads for the building based on the UBC 1994 (all equations and descriptions are inferred from [UBC 1994](#)).

4.3.1 Load Combinations

The code requires all components of the structure to resist the most critical effects (stress²) resulting from the following combinations of structural loads:

1. Dead + Floor Live + Roof Live (or Snow)
2. Dead + Floor Live + Wind (or Seismic)
3. Dead + Floor Live + Wind + Snow/2
4. Dead + Floor Live + Snow +Wind/2
5. Dead + Floor Live + Snow +Seismic

4.3.2 Load Reductions

The code allows for reduction of live, roof live, and snow loads (not applicable to this study). Uniform roof live loads and live loads for floors may be reduced on members supporting more than 150 square feet except for live loads greater than 100 pounds per square foot or places of

²The code allows for a one-third increase for working stress design when considering wind or earthquake forces either acting alone or when combined with vertical loads.

public assembly using Equation 4.1. The reduction for members receiving load from only one story is limited to 40 percent, and for other members is limited to 60 percent or R , calculated using Equation 4.2.

$$R = r(A - 150) \quad (4.1)$$

$$R = 23.1(1 + D/L), \quad (4.2)$$

where

- R is reduction factor in percentage
- r is rate reduction (0.08 for floors and flat roofs)
- A is area of floor supported by the member in square feet
- D is dead load per square foot
- L is live load per square foot

Additionally, the code prohibits any reduction of storage live loads exceeding 100 pounds per square foot, except for the design live load on columns, which can be reduced by 20.

4.3.3 Gravity loading criteria for the design

The gravity loads used in the design are obtained from [Krishnan et al. \(2006b\)](#) and summarized in Table 4.4. The loads are based on three occupancy categories: (1) office loading category (used for all floors except at the penthouse and roof), (2) roof loading category (used for the roof), and (3) mechanical loading category (used for the penthouse level). Other loads, such as floor fills, partitions, slabs, and cladding, are estimated based on typical values used in engineering practices.

Occupancy	Item	Load	
		psf	$\sim \frac{kg}{m^2}$
Office	Concrete slab on metal deck	50	255
	Floor fill (carpet)	2	10
	Partitions (metal stud and dry wall)	20	100
	Mechanical	10	50
	Floor framing	4.1	20
	Live load	50	250
Mechanical	Concrete slab on metal deck	50	255
	Floor fill	25	120
	Mechanical	7	35
	Floor framing	9.1	44.5
	Live load	250	1200
Roof	Concrete slab on metal deck	50	250
	Waterproofing	2	10
	Mechanical	7	35
	Floor framing	4.1	20
	Live load	50	250
Cladding	Glass cladding	8	40

Table 4.4: Gravity loading criteria.

4.3.4 Wind criteria for the design

The design wind loads are calculated using Equation 4.3, which accounts for basic wind speed, exposure category of the building site, the height of the building, and the importance of the building. Basic wind speed is the fastest wind speed in miles per hour measured at 33 feet above the ground with an annual probability of 0.02 in a flat open terrain extending one-half mile from the building site in any full quadrant (exposure category C). The exposure category takes into account the terrain and the coverage (building, forests, etc.) of the surrounding areas. A basic wind speed of 70 mph and an exposure B category is assumed for all building sites located within the scope of this study. The “exposure B” is defined as a “terrain which has buildings, forest or surface irregularities 20 feet or more in height covering at least 20 percent of the area extending one mile or more from the site”. Table 4.5 provides values for coefficients used in calculating wind pressures at various building heights. The calculated pressures are then multiplied by the tributary cladding

area to obtain the total wind load acting on a particular story.

$$p = C_e C_q q_s I_w, \quad (4.3)$$

where

- p is design wind pressure
- C_e is combined height, exposure, and gust factor coefficient which varies with height.
- C_q is pressure coefficient for the structure.
- q_s is wind stagnation pressure at the standard height of 33 feet.
- I_w is building importance factor.

	Variable	Symbol	Value	Reference (within UBC 94)/Remarks
1	Height, exposure and gust factor	C_e	0.62–1.52	Table 16-G / 1.52 at 248.33 feet
2(a)	Pressure coefficient (Windward)	C_q	0.8	Table 16-H
2(b)	Pressure coefficient (Leeward)	C_q	0.5	Table 16-H
3	Wind stagnation pressure (psf)	q_s	12.6	Table 16-F / for 70 <i>mph</i>
4	Importance factor	I	1.00	Table 16-K

Table 4.5: Values used for calculating wind forces.

4.3.5 Seismic design criteria : Static force procedure

4.3.5.1 Estimating an initial fundamental period, T

The code provides the following methods for determining the fundamental period of the building T :

- Method 1 : T can be approximated using Equation 4.4:

$$T = C_t (h_n)^{3/4}, \quad (4.4)$$

where h_n is the height of the building feet above the base and C_t is a numerical coefficient accounting for lateral load resisting system used in the building, for braced frame buildings; this value is 0.020.³

- Method 2 : T can be calculated using Equation 4.5:

$$T = 2\pi \sqrt{\left(\sum_{i=1}^n w_i \delta_i^2 \right) \div \left(g \sum_{i=1}^n f_i \delta_i \right)}, \quad (4.5)$$

where w_i , δ_i , f_i , and g respectively represent the weight of the structure at the i^{th} level, the deflection of the i^{th} level, applied lateral force on the i^{th} level, and acceleration due to gravity.

Additionally, the code requires the value of the T calculated using Equation 4.5 not to be 30 percent greater than the estimated value using method 1 (Equation 4.4).

Using Equation 4.4, the initial estimate for the fundamental period of the building is 1.25 and the maximum value that T can have is 1.63. This limitation was implemented in the code to prevent designing structures using very low seismic forces and base shear values, and justifying the design by softening the lateral load resisting system. The 30 percent limitation is only used for selecting member sizes and is not applicable when checking for deflections and story drifts.

$$T = 0.020 \times (248.333)^{3/4} = 1.25$$

$$T_{max} = 1.25 + 30\% \times 1.25 = 1.63$$

4.3.5.2 Soil Type

UBC 1994 incorporates the soil conditions using S factor, which varies from 1.0 for a rock-like soil to 2.0 for a soft clay soil conditions. The code divides the soil conditions into four different

³ C_t is 0.0488 if h_n is given in meters (SI)

categories of S_1 , S_2 , S_3 , and S_4 . Table 4.6 provides descriptions and S values for each of the soil categories.

Category	Description	S factor
S_1	A rock-like material - shear wave velocity greater than 2,500 ft/s or 762 m/s. or Medium-dense to dense or medium stiff to stiff soil conditions, where soil depth is less than 200 ft or 60.96 m	1.0
S_2	Predominantly medium-dense to dense or medium stiff to stiff conditions, where soil depth exceeds 200 ft or 60.96 m	1.2
S_3	Soil profile containing more than 20 ft or 6.096 m of soft to medium-stiff clay but not more than 40 ft or 12.192 m of soft clay.	1.5
S_4	Soil profile containing more than 40 ft or 12.192 m of soft clay characterized by a shear wave velocity less than 500 ft/s or 152.4 m/s	2.0

Table 4.6: UBC 1994 site categories and conditions.

We used shear wave velocity in the upper 30 meters of soil profile (V_s^{30} map) to determine the soil conditions. For S_1 and S_4 soil categories, the code provides cutoff values for shear wave velocities (see Table 4.6); however, it does not provide a shear wave velocity division for S_2 and S_3 soil conditions. For classification of these 2 soil categories we matched the descriptions given in UBC 1994 to those provided in UBC 1997 (see Table 4.13) and used the average shear wave velocities given in UBC 1997 (see Table 4.13) to classify the soil conditions. Using this logic, we divided the local soil conditions for UBC 1994 using the shear wave velocities provided in Table 4.7. Figure 4.6 illustrates the soil categories for the 636 stations used in this study.

Category	Average Shear Wave Velocity feet/second (m/s)
S_1	>2500 (762)
S_2	1200-2500 (360-762)
S_3	500-1200 (152.4-360)
S_4	<500 (152.4)

Table 4.7: Average shear wave velocities (top 30 meters of the soil profile) used in this study for categorizing the soil conditions for UBC 1994.

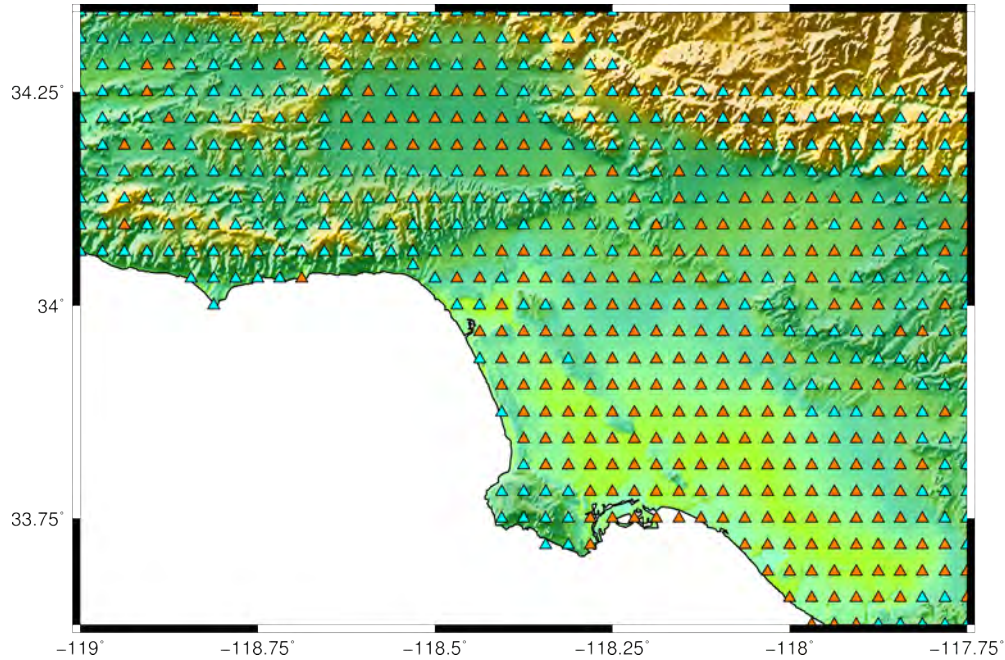


Figure 4.6: Site categories assigned for the scope of this study. Light-blue triangles represent soil category S_2 and orange triangles represents soil category S_3 .

4.3.5.3 Base shear calculations

Based on the UBC 1994 the structures shall be designed to resist stresses produced by the total lateral forces assumed to act non-concurrently in the direction of each axis of the structure. Equation 4.6 is used for calculating base shear, which is ZIC/R_w percentage of the seismic weight of the structure:

$$V = \frac{ZIC}{R_w} W, \quad (4.6)$$

where Z , I , C , R_w , and W are (values provided in Table 4.8):

- Z is the seismic zone factor coefficient. Southern California is considered as seismic zone 4 (UBC 1994 Figure 16.1 - Page 2-40). The Z value associated with this seismic zone is 0.4.
- I is the occupancy importance factor which incorporates the importance of the building, safety, and usability for emergency purposes after and earthquake.

- C is the numerical value incorporating the fundamental period of the building and soil characteristics of the building:

$$C = \frac{1.25 \times S}{T^{\frac{2}{3}}}, \quad (4.7)$$

where T is the fundamental period of the building in the direction considered for design and S is the site coefficient for soil characteristics (see Table 4.6 and Figure 4.6). The code specifies that the value of C shall need not exceed 2.75 and may be used for any structure without regard to soil type or structure period. Additionally, the code requires a minimum value of C/R_w of 0.075.

- R_w is the coefficient depending on the structural system used as the lateral load resisting system. For special concentrically braced frames (SCBF) this value is 9.0.
- W is the total dead load of the structure (seismic weight).

	Variable	Symbol	Value	Remarks
1	Seismic Zone Coefficient	Z	0.4	Zone 4, Figure 16-2
2	Seismic Weight	W	29655 (kips)	Total Dead Load - Table 4.4
3	Fundamental Periods	T	1.25-1.63 sec	Equations 4.4 and 4.5
4	Seismic Importance Factor	I	1.00	UBC 1994, Table 16-K
5	Site Coefficients (S-factor)	S	1.2-1.5	Tables 4.6 and 4.7 - Figure 4.6
6	Structural System Coefficient	R_w	9	UBC 1994, Table 16-N
7	Site-Structure Coefficient	C	$\sim 1.08-1.62$	Equation 4.7

Table 4.8: Summary of parameters used in seismic design and base shear calculation - UBC 1994.

4.3.5.4 Vertical distribution of lateral forces

The base shear calculated in previous section is distributed over the height of the structure in accordance with the following 3 equations:

$$V = F_t + \sum_{i=1}^n F_i, \quad (4.8)$$

$$F_t = 0.07TV \leq 0.25V, \quad (4.9)$$

$$F_x = \frac{(V - F_t)w_x h_x}{\sum_{i=1}^n w_i h_i}, \quad (4.10)$$

where w_x and w_i are the portion of total seismic weight (dead load W) assigned to the i^{th} or x^{th} floors, h_x and h_i are the heights in feet above the base to the i^{th} or x^{th} floors, and F_t is the portion of the total base shear (V) considered be concentrated at the top of the structure.

4.3.5.5 Overturning and Horizontal Torsional Moments

The code requires the structure to be designed such that it can resist the overturning effects caused by the seismic forces. The overturning moment at each level is calculated using the earthquake forces acting on the floors above (F_x and F_t - Equations 4.9 and 4.10), and are distributed proportionally among the lateral load resisting members based on their rigidity.

In structures where diaphragms are not flexible, the code requires provisions to include the additional shear that results from horizontal torsional moment at any story. The horizontal torsional moment is the result of eccentricity between the applied forces at levels above the story of interest and the vertical resisting elements in that story plus an accidental torsion to account for uncertainties in mass and rigidity of the building. The accidental torsion is accounted for by addition of a moment that equals the applied forces times 5% of the building dimension perpendicular to the direction of the force under consideration.

Torsional irregularities exist in a building when the maximum story drift (computed using accidental torsion) at one end of the structure transverse to an axis is more than 1.2 times the average story drift of the two ends of the structure. In buildings with torsional irregularities, the code requires the accidental torsion to be amplified by A_x , given in Equation 4.11. In cases where accidental torsion exist in the structure, the code implements additional requirements for structural

members.

$$A_x = \min\left\{3, \left[\frac{\delta_{max}}{1.2 \delta_{avg}}\right]^2\right\} \quad (4.11)$$

4.3.6 Seismic design criteria : Dynamic force procedure

Buildings with symmetric mass and stiffness properties behave in a predictable manner; therefore, static load procedure can be deemed sufficient for most of these buildings. However, any vertical and/or plan irregularities in stiffness, mass, and geometry can alter the dynamic behavior of the building, and hence, the static load procedures are considered insufficient. For such buildings, dynamic analysis is required to capture the behavior of the building under earthquake motions. UBC 1994 allows the use of two procedures for dynamic analysis: (1) response spectrum analysis and (2) time-history analysis. The response spectrum analysis is easier to implement and therefore it is the preferred method of dynamic analysis.

4.3.6.1 Ground Motion

Ground motions used for dynamic analysis should have a 10 percent probability of being exceeded in the next 50 years. The code provides the following options for ground motion representations: (1) normalized response spectrum shapes given by the code for various soil types ⁴, (2) a site-specific response spectrum, and (3) site-specific ground motion time histories.

Normalized spectral shapes are used for this study. The normalized shapes are multiplied by Z , seismic zone factor (effective peak acceleration), to obtain the design spectra. Figure 4.7 illustrates normalized spectral shapes for the 3 soil conditions (S_2 and S_3 are used in this study).

4.3.6.2 Response Spectrum Analysis

There are number of requirements that the UBC 1994 code prescribes for response spectrum analysis:

⁴Additional requirements are to be fulfilled for site category S_4 , which is out of the scope of this study

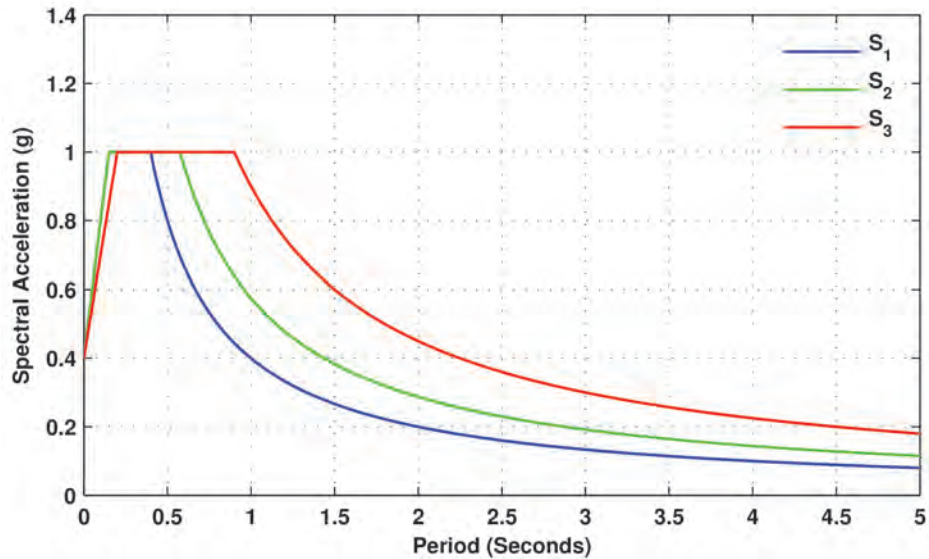


Figure 4.7: The UBC 1994 response spectrum used in the design.

1. Maximum number of modes should be included in an statistical manner to obtain a response close to the total response of the structure. This can be satisfied by showing that 90 % of the participating mass of the structure is included in the calculation for each principal direction.
2. The values for peak member forces, displacements, story forces, shear forces, and base reactions for each mode should be combined. When three-dimensional models are used for analysis, modal interaction effects shall be considered when combining modal maxima.
3. In cases where the base shears calculated using response spectrum analysis is less than the base shear calculated using static force procedure (Equation 4.6), the base shear shall be scaled as following:
 - (a) For irregular buildings⁵ : base shear shall be scaled up to 100 % of the base shear calculated using the static force procedure
 - (b) For regular buildings : base shear shall be scaled up to 90 % of the base shear calculated using the static force procedure. Additionally, base shear cannot be less than 80 % of

⁵For definitions of irregular and regular buildings refer to UBC 1994 building code.

the base shear calculated using T from Equation 4.4 in Equation 4.6.

4. The base shear for a given direction determined using response spectrum analysis need not exceed that required by Item 3.

4.3.7 Deflection and drift criteria

Deflection of all structural members when loaded by the total live load is limited by $L/360$ for roof and flooring members in steel structures. The inter story drift ratios under seismic loads shall not exceed $0.04/R_w$ or 0.005 for structures with fundamental period of less than 0.7 and $0.03/R_w$ or 0.004 for structures with fundamental period of 0.7 second or greater (drift ratio limit for concentric braced frame steel building in seismic zone 4 is 0.0033) .

To ensure the overall frame stability, the code requires that the P- Δ effects be considered when calculating the story drift ratios and the resulting forces in members. In seismic zones 3 and 4, where the story drift ratios does not exceed $0.04/R_w$, P- Δ effects are not to be considered. Additionally, in cases where the ratio of the secondary moment to the primary moment does not exceed 0.1, the P- Δ effects are not to be considered.

4.3.8 Special Requirements for Steel Structures

The code provides additional constrains on the design of structural members for buildings located in seismic zone 4.

4.3.8.1 General Requirements for Columns

In seismic zones 3 and 4 the code specifies additional load combinations that the columns should be able to resist. Columns in compression should have the strength to resist the load combination

4.12 and columns in tension should have the strength to resist the load combination 4.13.

$$1.0P_{DL} + 0.7P_{LL} + 3(R_w/8)P_E \quad (4.12)$$

$$0.85P_{DL} \pm 3(R_w/8)P_E, \quad (4.13)$$

where

- P_{DL} is the axial dead load
- P_{LL} is the axial live load
- P_E is the axial load on member due to earthquake
- R_w is structural system coefficient (Table 4.8)

4.3.8.2 Requirements for Special Concentric Braced Frames (SCBF).

- *Slenderness*: kl/r ⁶ for bracing members shall not exceed $1000/\sqrt{F_y}$ ⁷; this detail is added to the code to ensure that the braces can properly dissipate energy in the cyclic loading during earthquake motion.
- *Width-To-Thickness ratio*: Plastic hinges created during an earthquake loading can rapidly develop local buckling in the brace elements, which results in low energy dissipation in the system. To avoid this, the code restricts the width-to-thickness ratio in braces. The code requires all compression members to meet the compact section requirements provided in the code. Additionally, the code requires width⁸-to-thickness ratio in rectangular tubes to be less than $110/\sqrt{F_y}$ ⁹.

⁶ l : length of segment, k : effective length factor, and r : radius of gyration.

⁷All equations in Section 4.3.8.2 are in English Units.

⁸Outside walls.

⁹Due to this constrain many of the HSS section are not permitted, members such as HSS 12×12×0.5 (and smaller wall thickness), HSS 10×10×0.5 (and smaller wall thickness), HSS 8×8×0.375 (and smaller wall thickness), and HSS 7×7×0.3125 (and smaller wall thickness).

- *Beams in Chevron bracings:*
 - Beams intersected by the bracing elements are required to be continuous.
 - Beams used in the Chevron bracing, where they are intersected from below, need to resist the total gravity load from the tributary area, presuming there are no bracing. In other words, the beams shall not rely on the bracing as a midspan support.
 - The intersected beam in Chevron bracing shall be capable of resisting the following gravity loads and unbalanced brace force combinations¹⁰
 - * $1.2D + 0.5L + P_b$ ¹¹
 - * $0.9D - P_b$
 - Flanges of beams at the point of interception with the bracing elements shall have a direct or indirect lateral support
- *Lateral force distribution:* In order to increase the redundancy in the system and a balance between members in tension and compression in a bracing system, the code requires that seismic lateral load to be distributed such that the sum of compression or tension components of the forces be less than 70% of the total force.

¹⁰This constrain highly effects the beam member sizes and is the reason that some of the beams in the bracing systems are larger than the required ones for moment frames (see Figures F.1-F.18).

¹¹where D is tributary dead load, L is tributary live load, and P_b maximum unbalanced post buckling force that can be applied to the beam by the brace. P_b is calculated using the strength of member in axial tension and 0.3 of axial compression.

4.4 UBC 1994 SCBF Final Design

The building was modeled using the commercial ETABS software. Figure 4.8 illustrates the isometric view of the braced frame building. Table 5.6 summarizes the seismic parameters related to the final building model. The base shear values are based on the static load procedure and using ASD. It should be noted that dynamic procedure was used for building analysis, frame sizes for the lateral load resisting frame members. The periods and modal direction for the final building model are given in Tables 4.10 and 4.11. The existing building was used as the starting point for the design of beams, columns, and bracings. The size of members was reduced gradually to obtain a high demand over capacity ratio. A summary of the member sizes and properties are tabulated in Table 4.12. The bracing columns are relatively smaller than the ones used in the moment frames (see Table 4.1 for comparisons). However, the beams used on the braced frame bays are slightly larger than the ones in moment frames; this is due to the design being governed by the post brace buckling unbalanced forces that can exert additional force onto to beam almost equaling the tension capacity of the beam. HSS sections, ranging from HSS 10×10×0.625 at the base of the building to HSS7×7×0.375 on the roof level, were used for braces. The brace sizes in the upper levels are governed by the deflection criteria imposed by the code hence the upper story brace sizes are deflection controlled. On the other hand, the lower story brace sizes are governed by the required lateral load (strength design). The gravity columns remained the same, and the columns used in braced frames were smaller than the ones used in the original moment frames.

Appendices F.1 and F.2 provide elevation views and member sizes for the new building for site categories S_2 and S_3 , respectively.

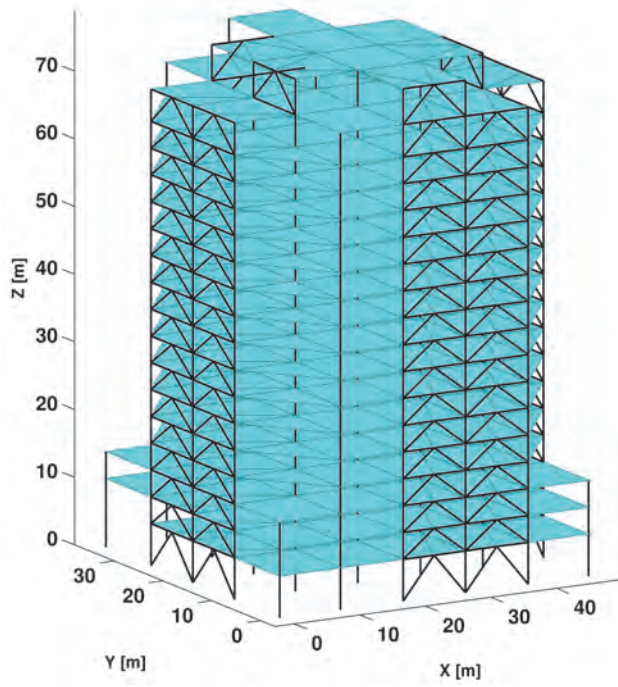


Figure 4.8: Isometric view of the Canoga building designed based on UBC 1994 using braced frame lateral load resisting system.

	Units	S_2 Soil	S_3 Soil
Dead Load (Seismic weight)	kips	27920	28025
Dead Load + 30 % Live Load	kips	33070	33175
Average Steel Weight	psf ($\frac{kg}{m^2}$)	12.08 (59.0)	12.45 (60.8)
Strength Design Base shear E-W % of seismic weight (using $T = 1.63$)	kips	1,346 4.82 %	1,689 6.03 %
Drift Design Base shear E-W % of seismic weight (using actual building periods)	kips	1,089 3.90 %	1,366 4.87 %
Strength Design Base shear N-S % of seismic weight (using $T = 1.63$)	kips	1,346 4.82 %	1,689 6.03 %
Drift Design Base shear N-S % of seismic weight (using actual building periods)	kips	1,013 3.63 %	1,271 4.54 %
Periods Calculated Using Dead + 30 % Live Loads			
Period - Mode 1 (N-S)	sec	2.79	2.75
Period - Mode 2 (E-W)		2.49	2.42
Period - Mode 3 (Rot.)		1.60	1.58
Periods Calculated Using Dead Load			
Period - Mode 1 (N-S)	sec	2.49	2.46
Period - Mode 2 (E-W)		2.34	2.17
Period - Mode 3 (Rot.)		1.44	1.42
Drift Ratio Limit		0.0033	0.0033

Table 4.9: Seismic design parameters for UBC 1994.

Building	Mode Number	Period (<i>sec</i>)	Modal Direction Factors		
			X-Trans	Y-Trans	Z-Rotn
Brace	1	2.79	0.0	100.0	0.0
Frame	2	2.49	97.5	0.0	2.5
1994 - S_2	3	1.60	2.6	0.0	97.4

Table 4.10: Building natural periods and modal directions for the first 3 modes of vibration for S_2 (UBC 1994) site condition.

Building	Mode Number	Period (<i>sec</i>)	Modal Direction Factors		
			X-Trans	Y-Trans	Z-Rotn
Brace	1	2.75	0.0	100.0	0.0
Frame	2	2.42	97.5	0.0	2.5
1994 - S_3	3	1.58	2.5	0.0	97.5

Table 4.11: Building natural periods and modal directions for the first 3 modes of vibration for S_3 (UBC 1994) site condition.

Structural Component	Member Size	Structural Steel	F_y (ksi) Yield Stress	F_u (ksi) Ultimate Stress
Beam (brace)	W30×90 - W36×300	A36	36	58
Column (brace)	W14×51- W14×455	A572-G50	50	65
Bracing (brace)	HSS10×10×0.625 - 7×7×0.375	A500-GrB	46	58
Primary Beam (gravity)	W24×68	A36	36	58
Secondary Beam (gravity)	W16×35	A36	36	58
Columns (gravity)	W14×90 - W14×311	A36	36	58

Table 4.12: Member sizes, specifications, and properties for the new buildings (UBC 1994).

4.5 UBC 1997 Design Guidelines

Major changes were implemented in UBC 1997 that accounted for the lessons learnt during the 1994 Northridge and 1995 Kobe earthquakes. The most significant changes are adoption of strength based Load and Resistance Factor Design (LRFD), inclusion of the near source factors to account for near source effects during earthquakes, and revision of the soil profiles along with the implementation of soil profiles in base shear and design response spectrum. The following sections describe the UBC 1997 design guidelines and a description of changes in design codes relative to UBC 1994 ([UBC 1994](#)).

4.5.1 Load Combinations

The code requires all components of the structure to resist the most critical effects (stress¹²) resulting from the provided load combinations. UBC 1997 adopts the strength-based design methodology as opposed to the previous codes, where allowable stress designed (ASD) was used. However, the code allows the use of ASD as an alternative to the LRFD load combinations. We are using the following LRFD load combinations provided by the code:

1. $1.4D$
2. $1.2D + 1.6L + 0.5(L_r \text{ or } S)$
3. $1.2D + 1.6(L_r \text{ or } S) + (f_1L \text{ or } 0.8W)$
4. $1.2D + 1.3W + f_1L + 0.5(L_r \text{ or } S)$
5. $1.2D + 1.0E + (f_1L + f_2S)$
6. $0.9D \pm (1.0E \text{ or } 1.3W),$

¹²The code allows for a one-third increase for working stress design when considering wind or earthquake forces either acting alone or when combined with vertical loads.

where D stands for the dead load, L stands for the live load, L_r stands for roof live load, W stands for wind load, E stands for seismic load, and S stands for snow load. f_1 is 0.5 for live loads except for live loads greater than 100 psf which is 1.0.

4.5.2 Load Reductions

The load reduction for UBC 1997 is identical to UBC 1994 (see Section 4.3.2).

4.5.3 Gravity loading criteria for the design

The gravity loads used in the design are the same as UBC 1994 and are summarized in Table 4.4 in Section 4.3.3.

4.5.4 Wind criteria for the design

The calculations and coefficients for wind load calculations will remain the same as UBC 1994 (Section 4.3.4).

4.5.5 Seismic design criteria : Static force procedure

4.5.5.1 Estimating an initial fundamental period, T

The methods which the code requires for estimation of the fundamental period of the building T remains the same as UBC 1994 (Section 4.3.5.1)¹³.

4.5.5.2 Soil Type

UBC 1997 divides the local soil conditions into six different categories of S_A , S_B , S_C , S_D , S_E , and S_F . Table 4.13 describes the soil conditions and the average soil properties for the top 100 ft

¹³The 30 % limitation mentioned in Section 4.3.5.1 remains the same as UBC 1994.

or approximately 30 m of soil profiles. Using the shear wave velocity in the upper 30 meters of soil profile (V_s^{30} map) we determine the soil category for each of the 636 stations as illustrated in Figure 4.9.

Category	Description	Average Shear Wave Velocity feet/second (m/s)
S_A	Hard Rock	>5000 (1500)
S_B	Rock	2500-5000 (760-1500)
S_C	Very Dense Soil/Soft Rock	1200-2500 (760-1500)
S_D	Stiff Soil	600-1200 (180-360)
S_E	Soft Soil	<600 (180)
S_F	-	Site Specific Evaluation Required

Table 4.13: UBC 1997 site categories and conditions.

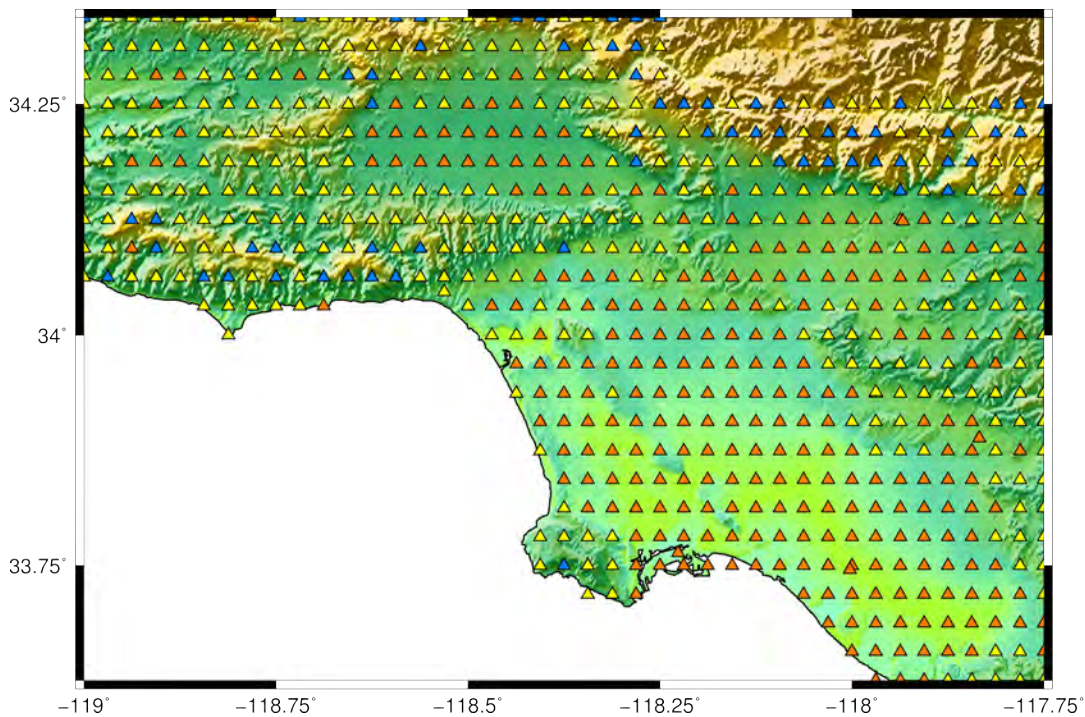


Figure 4.9: Site categories assigned for the scope of this study at each of the 636 stations. Blue triangles represent soil category S_B , yellow triangles represent soil category S_C , and orange triangles represents soil category S_D .

4.5.5.3 Base shear calculations

The design base shear in UBC 1997 is determined from the following equation:

$$V = \frac{C_v I}{R T} W \quad (4.14)$$

and need not exceed the following:

$$V = \frac{2.5 C_a I}{R} W \quad (4.15)$$

and shall not be less than the following:

$$V = 0.11 C_a I W. \quad (4.16)$$

Additionally, in seismic zone 4 it shall not be less than the following:

$$V = \frac{0.8 Z N_v I}{R} W, \quad (4.17)$$

where Z , I , N_a , N_v , C_a , C_v , R , and W are (values provided in Table 4.14):

- Z : Seismic zone factor coefficient. Southern California is considered a seismic zone 4 (UBC 1997 Figure 16.2). The Z value associated with this seismic zone is 0.4.
- I : Occupancy importance factor, which incorporates the importance of the building, safety, and usability for emergency purposes after and earthquake.
- N_a : Near-source factor used in the determination of C_a
- N_v : Near-source factor used in the determination of C_v
- C_a : Seismic coefficient used in base shear calculation, which incorporates the soil condition, seismic zone, and proximity of the building site to the seismic source. For seismic zone 4 C_a equals to $0.32 N_a$, $0.4 N_a$, $0.4 N_a$, $0.44 N_a$, and $0.36 N_a$ for soil profile types S_A , S_B , S_C , S_D , and S_E , respectively.

- C_v : Seismic coefficient used in base shear calculation, which incorporates the soil condition, seismic zone, and proximity of the building site to the seismic source. For seismic zone 4 C_a equals to $0.32N_v$, $0.4N_v$, $0.56N_v$, $0.64N_v$, and $0.96N_v$ for soil profile types S_A , S_B , S_C , S_D , and S_E , respectively.
- R : Numerical value representing the inherent over strength and global ductility capacity of the lateral force resisting system. This value for special concentrically braced frames (SCBF) is 6.4.
- W : The total dead load of the structure (seismic weight).

	Variable	Symbol	Value	Remarks
1	Seismic Zone Coefficient	Z	0.4	Zone 4 - UBC 1997, Figure 16-2
2	Seismic Weight	W	~ 28000 (kips)	Total Dead Load - Table 4.4
3	Fundamental Periods	T	1.25-1.63 sec	Equations 4.4 and 4.5
4	Seismic Importance Factor	I	1.00	UBC 1994, Table 16-K
5	Near Source Factor	N_a	1.20	UBC 1997, Table 16-S
6	Near Source Factor	N_v	1.60	UBC 1997, Table 16-T
7	Seismic Coefficient	C_a	$0.32N_a=0.384$ $0.40N_a=0.480$ $0.40N_a=0.480$	S_A Soil Profile S_B Soil Profile S_C Soil Profile
8	Seismic Coefficient	C_v	$0.32N_v=0.512$ $0.40N_v=0.640$ $0.56N_v=0.896$	S_A Soil Profile S_B Soil Profile S_C Soil Profile
9	Structural Systems Factor	R	6.4	UBC 1997, Table 16-N

Table 4.14: Summary of parameters used in seismic design and base shear calculation - UBC 1997.

4.5.5.4 Vertical distribution of lateral forces

The guidelines for vertical distribution of the lateral forces will remain the same as UBC 1994 (Section 4.3.5.4).

4.5.5.5 Overturning and Horizontal Torsional Moments

The guidelines for overturning and horizontal torsional moments of the lateral forces will remain the same as UBC 1994 (Section 4.3.5.5).

4.5.6 Seismic design criteria : Dynamic force procedure

Similar to UBC 1994, the 1997 code requires dynamic analysis for buildings with vertical and plan irregularities in stiffness, mass, and geometry or all buildings with heights exceeding 240 feet in seismic zones 3 and 4. The dynamic procedures for dynamic analysis also remains the same as the UBC 1994, which allows the use of two procedures for dynamic analysis: (1) response spectrum analysis and (2) time-history analysis. The response spectrum analysis is easier to implement and therefore is the preferred method of dynamic analysis.

4.5.6.1 Ground Motion

Ground motions used for dynamic analysis should have a 10 percent probability of being exceeded in the next 50 years. Code provides the following options for ground motion representations: (1) elastic design response spectrum shapes given by the code for various soil types, (2) a site-specific elastic response spectrum, and (3) site-specific ground motion time histories.

The code-prescribed spectral shapes are used for this study, and which are based on the C_a and C_v values for the specific site. Figure 4.10 illustrates spectral shapes for the S_A , S_B , and S_C soil conditions.

4.5.6.2 Response Spectrum Analysis

The requirements that UBC 1997 code prescribes for response spectrum analysis as far as limits on the resultant base shear, maximum number of modes used in analysis, and the modal combinations remains the same as UBC 1994 (See section 4.3.6.2).

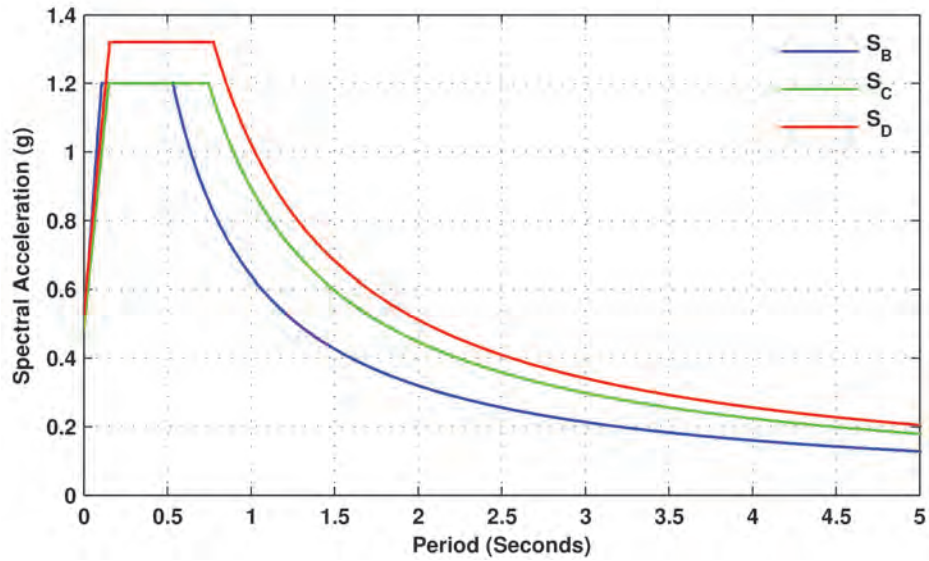


Figure 4.10: The UBC 1997 response spectrum used in the design.

4.5.7 Deflection and drift criteria

Deflection of all structural members remains the same as prescribed in UBC 1994, when loaded by the total live load, is limited by $L/360$ for roof and flooring members in steel structures; however, the drift ratio limits are modified in the UBC 1997. The code requires that static drift ratios Δ_S be determined using static, elastic analysis, or (if required) dynamic analysis. Based on the static drift ratio the maximum inelastic drift ratio is calculated using the following equation:

$$\Delta_M = 0.7R\Delta_S \quad (4.18)$$

The calculated Δ_M shall not exceed 0.025 for buildings with periods less than 0.7 second and 0.020 for buildings with periods exceeding 0.7 second. This means that the static drift ratio, Δ_S , of the building used in this study shall not exceed 0.00446.

4.5.8 Special Requirements for Steel Structures

The code provides additional constraints on the design of structural members for buildings located in seismic zone 4.

4.5.8.1 General Requirements for Columns

In seismic zones 3 and 4 the code specifies additional load combinations that the columns should be able to resist. Columns in compression should have the strength to resist the load combination 4.19 and columns in tension should have the strength to resist the load combination 4.20.

$$1.0P_{DL} + 0.7P_{LL} + \Omega_o P_E, \quad (4.19)$$

$$0.85P_{DL} \pm \Omega_o P_E, \quad (4.20)$$

where

- P_{DL} is the axial dead load
- P_{LL} is the axial live load
- P_E is the axial load on member due to earthquake
- Ω is the seismic force amplification factor - for SCBF $\Omega = 2.2$

4.5.8.2 Requirements for Special Concentrically Braced Frames

The additional requirements for special concentrically braced frames remain the same as the requirements for UBC 1994 (see Section 4.3.8.2).

4.6 UBC 1997 SCBF Final Design

Table 4.15 summarizes the seismic parameters related to the final building model. The base shear values are based on the static load procedure and using LRFD [base shear values using LRFD should be divided by 1.4 when comparing against base shear values calculated using ASD in the UBC 1994 design (Table 5.6)]. It should be noted that dynamic procedure was used for building analysis, frame sizes for the lateral load resisting frame members. The periods and modal direction for the final building models for the three site conditions are given in Tables 4.16, 4.17, and 4.18. A summary of the member sizes and properties is tabulated in Table 4.19. The bracing columns are relatively smaller than the ones used in the moment frames (see 4.1 for comparisons). However, the beams used on the braced frame bays are slightly larger than the ones in moment frames because the design is governed by the post brace buckling unbalanced forces that can exert additional force onto the beam, almost equaling the tension capacity of the beam. HSS sections, ranging from HSS 10×10×0.625 at the base of the building to HSS7×7×0.375 on the roof level, were used for braces. Similar to the UBC 1994 design, the brace sizes in the upper levels are governed by the deflection criteria imposed by the code hence the upper story brace sizes are deflection controlled. On the other hand, the lower story brace sizes are governed by the required lateral load (strength design). The gravity columns remained the same, and the columns used in braced frames were smaller than the ones used in the original moment frames. Appendices G.1, G.2, and G.3 provide elevation views and member sizes for the new building for site categories S_B , S_C , and S_D , respectively.

	Units	S_B Soil	S_C Soil	S_D Soil
Dead Load (Seismic weight)	kips	28,125	28,200	28,310
Dead Load + 30 % Live Load	kips	33,275	33,350	33,460
Average Steel Weight	psf ($\frac{kg}{m^2}$)	12.82 (62.55)	13.08 (63.85)	13.47 (65.78)
Strength Design Base shear E-W % of seismic weight (using $T = 1.63$)	kips	2,250 8.00 %	2,422 8.59 %	2,780 9.82 %
Drift Design Base shear E-W % of seismic weight (using actual building periods)	kips	1,322 4.70 %	1,870 6.63 %	2,214 7.82 %
Strength Design Base shear N-S % of seismic weight (using $T = 1.63$)	kips	2,250 8.00 %	2,422 8.59 %	2,780 9.82 %
Drift Design Base shear N-S % of seismic weight (using actual building periods)	kips	1,181 4.20 %	1,678 5.95 %	2,078 7.34 %
Periods Calculated Using Dead + 30 % Live Loads				
Period - Mode 1 (N-S)		2.665	2.630	2.445
Period - Mode 2 (E-W)	sec	2.376	2.356	2.284
Period - Mode 3 (Rot.)		1.535	1.518	1.44
Periods Calculated Using Dead Load				
Period - Mode 1 (N-S)		2.381	2.351	2.180
Period - Mode 2 (E-W)	sec	2.129	2.111	2.045
Period - Mode 3 (Rot.)		1.379	1.365	1.292
Drift Ratio Limit		0.0045	0.0045	0.0045

Table 4.15: Seismic design parameters for UBC 1997.

Building	Mode Number	Period (sec)	Modal Direction Factors		
			X-Trans	Y-Trans	Z-Rotn
Brace	1	2.665	0.0	100.0	0.0
Frame	2	2.376	97.6	0.0	2.4
1997 - S_B	3	1.535	2.4	0.0	97.6

Table 4.16: Building natural periods and modal directions for the first 3 modes of vibration for S_B (UBC 1997) site condition.

Building	Mode Number	Period (sec)	Modal Direction Factors		
			X-Trans	Y-Trans	Z-Rotn
Brace Frame 1997 - S_C	1	2.630	0.0	100.0	0.0
	2	2.356	97.7	0.0	2.3
	3	1.518	2.4	0.0	97.6

Table 4.17: Building natural periods and modal directions for the first 3 modes of vibration for S_C (UBC 1997) site condition.

Building	Mode Number	Period (sec)	Modal Direction Factors		
			X-Trans	Y-Trans	Z-Rotn
Brace Frame 1997 - S_D	1	2.445	0.0	100.0	0.0
	2	2.284	98.4	0.0	1.6
	3	1.518	1.7	0.0	98.3

Table 4.18: Building natural periods and modal directions for the first 3 modes of vibration for S_D (UBC 1997) site condition.

Structural Component	Member Size	Structural Steel	F_y (ksi) Yield Stress	F_u (ksi) Ultimate Stress
Beam (brace)	W30×90 - W40×327	A36	36	58
Column (brace)	W14×51- W14×605	A572-G50	50	65
Bracing (brace)	HSS12×12×0.625-7×7×0.375	A500-GrB	46	58
Primary Beam (gravity)	W24×68	A36	36	58
Secondary Beam (gravity)	W16×35	A36	36	58
Columns (gravity)	W14×90 - W14×311	A36	36	58

Table 4.19: Member sizes, specifications, and properties for the new buildings (UBC 1997).

Chapter 5

Quantification of Performance of 18-Story Steel Braced Frame Building Using Rupture-To-Rafters Simulations Under a Suite of Simulated San Andreas Earthquakes

5.1 Introduction

The interactions of the north American and the Pacific tectonic plates across much of California have created a network of major and minor active faults in the proximity of major cities such as Los Angeles and San Francisco that are capable of generating earthquakes as large as M_w 8.3. Major north-south trending faults in the vicinity of Los Angeles include the San Andreas fault, the San Jacinto fault, the Elsinore fault, and the Newport-Inglewood fault. East-west trending faults include the Santa Monica-Hollywood-Raymond fault, the Sierra Madre fault, and the Puente Hills blind-thrust fault. Other yet-to-be discovered blind-thrust faults may be present as well. The proximity of these faults to the Los Angeles metropolitan area and the existence of a large number of tall steel structures have prompted several investigations into the performance of these types of buildings (mainly of the steel moment frame variety) under hypothetical earthquake scenarios.

[Heaton et al. \(1995\)](#), [Hall et al. \(1995\)](#), and [Hall \(1998\)](#) simulated the near-source ground motions of a magnitude 7.0 thrust earthquake on a spatial grid of 60 km by 60 km using a vertically

stratified crustal model that approximates the rock properties in the Los Angeles basin, and then modeled the response of a 20-story steel-frame building and a three-story base-isolated building. The 20-story building was later used by [Bjornsson \(2014\)](#) for development of twelve retrofitting schemes by either upgrading the beam-column connections or implementing brace elements into the existing moment frames. [Krishnan et al. \(2006a\)](#) and [Krishnan et al. \(2006b\)](#) computationally re-created an 1857 Fort Tejon-like magnitude 7.0 earthquake on the southern San Andreas fault and simulated the damage to existing and redesigned 18-story steel moment frame buildings at 636 sites in the greater Los Angeles region. The existing building was designed according to the 1982 Uniform Building Code (UBC) provisions and built in 1984-1986 on Canoga Avenue in Woodland Hills (in the San Fernando valley of southern California). It experienced fracture at several beam-to-column connections during the 1994 Northridge earthquake. The building has been investigated using 2D and 3D elastic and inelastic analysis by [Paret and Sasaki \(1995\)](#), [Filippou \(1995\)](#), [Anderson and Filippou \(1995\)](#), and [Chi \(1996\)](#). Study by [Carlson \(1999\)](#) further examined the building using 3D nonlinear analysis and incorporated connection fracture into the moment frame model of the building. The “redesigned” building had the same architecture as the existing building, but was designed according to the 1997 UBC provisions. [Muto et al. \(2008\)](#) used the Matlab Damage and Loss Analysis toolbox ([Mitrani-Reiser 2007](#)), developed to implement the Pacific Earthquake Engineering Research (PEER) center’s loss-estimation methodology, to estimate seismic losses in the two buildings under the 1857-like earthquake. [Muto and Krishnan \(2011\)](#) used region-wide simulations to help inform the first southern California ShakeOut exercise of the number of tall steel moment frame building collapses that may occur under the ShakeOut scenario earthquake ([Hudnut et al. 2008](#)). [Siriki et al. \(2015\)](#) extended the [Krishnan et al. \(2006a\)](#) prototype study to quantitatively assess the collapse probability of 18-story steel moment frame buildings in southern California under San Andreas fault earthquakes in the next 30 years. They based their study on simulations of 60 earthquakes using stochastically generated earthquake sources. Here, we quantify the risk to 18-story steel braced frame buildings from San Andreas fault earthquakes in the next 30 years, based on earthquake simulations generated using kinematic finite source inversions of past earthquakes. The architectural configuration of the buildings is identical to the existing moment frame building of [Krishnan et al. \(2006a\)](#). The moment frames have been replaced by

concentric chevron braced frames.

The 1994 M_w 6.7 Northridge and the 1995 M_w 6.8 Kobe earthquakes are among only a few earthquakes that have struck densely populated urban regions. The damage observed in these earthquakes has led to important changes to building codes, including the inclusion of near-source factors in defining the design base shear. It is thus of interest to compare pre-Northridge and post-Northridge building designs in terms of earthquake response and risk. With this goal in mind, we develop five designs, two using the 1994 UBC and three using the 1997 UBC. Prior to 1994, the soils in the greater Los Angeles region were classified as one of two types, S2 or S3. Post-1997, three soil types, SB, SC, and SD, were used to classify the same. The five designs correspond to these five soil types.

5.2 Methodology

The steps involved in the risk quantification are as follows:

1. Kinematic finite source inversions of past earthquakes on geometrically similar faults are selected, modified, mapped onto multiple locations on the southern San Andreas fault, and allowed to propagate in two alternate directions, north-to-south and south-to-north. We refer to these simulated earthquakes as “scenario earthquakes”. For this study, we simulate a total of 60 scenario earthquakes spread over a magnitude range of 6-8, as described in Chapter 3.
2. The 30-year time-independent probability of occurrence of each scenario earthquake is calculated using the Uniform California Earthquake Rupture Forecast (UCERF).
3. For each scenario earthquake, 3-component ground motion histories are computed at 636 “analysis” or “target” sites on a 3.5 km grid in southern California using the spectral element method for the low frequencies ($< 0.5 Hz$) and empirical Green’s functions for the high frequencies (0.5-5.0 Hz).
4. Following UBC94 and UBC97 design guidelines, the existing 18-story steel moment frame building is redesigned for each target site using a lateral load resisting system comprised

of braced frames, taking into account the type of soil at the site. 3-D nonlinear response analyses of the UBC94 and UBC97 variants of the building are performed at each site under the three-component ground motion from each scenario earthquake using FRAME3D.

5. Applying the PEER performance based earthquake engineering (PBEE) framework on the simulated data set, the 30-year probabilities of the buildings exceeding various performance levels under earthquakes on the San Andreas fault are calculated.

5.3 Earthquake Source Models and Associated Probabilities

5.3.1 Source Models

The San Andreas fault is an almost vertically dipping (dip angle of approximately 90°) right-lateral strike slip fault (rake angle of 180° approximately) with an average seismogenic depth of approximately 20 km. The six earthquakes listed in Tab. 5.1, with magnitudes M_w 6.0 (2004 Parkfield), 6.58 (1979 Imperial Valley), 6.92 (1995 Kobe), 7.28 (1992 Landers), 7.59 (1999 Izmit), and 7.89 (2002 Denali), occurred on faults that are geometrically similar to the San Andreas fault. Kinematic finite source inversions of these events, developed by various research groups, are archived in the finite source rupture model database, [SRCMOD \(Finite-Source Rupture Model Database\)](#). As evident from Tab. 5.1, their source mechanisms are similar to that of a typical earthquake on the San Andreas fault. Seismic source spectrum is closely related to fault geometry and rupture mechanism; conforming the scenario earthquake source characteristics to physically observed characteristics on the target fault may help produce realistic energy release on the fault. So, we select the source models of these earthquakes as seeds for the scenario earthquakes on the San Andreas fault.

The selected source models are used for both low- and high-frequency contents of the time-histories. The source modelers have made sure that the discretization in these models (Tab. 5.1) is sufficiently small enough to radiate seismic energy at 2 s and longer periods. However, we still have to ensure that these frequencies are coherently propagated to the target sites through the

	Name	Date	Location	M_w	Length (km)	Depth (km)	Dip ($^\circ$)	Rake ($^\circ$)	Reference
1	Denali	2002	AK, USA	7.89	290.0	20.0	90.0	180.0	Ji et al. (2002)
2	Izmit	1999	Turkey	7.59	155.0	18.0	90.0	180.0	Bouchon et al. (2002)
3	Landers	1992	CA, USA	7.28	78.0	15.0	89.0	180.0	Wald and Heaton (1994)
4	Kobe	1995	Japan	6.92	60.0	20.0	85.0	180.0	Wald (1996)
5	Imperial Valley	1979	CA, USA	6.58	42.0	10.4	90.0	180.0	Hartzell and Heaton (1983)
6	Parkfield	2004	CA, USA	6.00	40.0	14.5	83.0	180.9	Custódio et al. (2005)

Table 5.1: List of past earthquakes with fault geometry and rupture mechanisms closely matching earthquakes on the San Andreas fault whose kinematic finite source inversions are used in this study. The salient source parameters are listed as well.

wave-speed model used for the ground motion simulation. Based on the average wave-speed of 3 km/s in the SCEC CVM-H 11.9.0 southern California model and an average rupture speed of 2.5 km/s in all of the source models, we estimate that resampling the source to a finer resolution of 0.5 km would ensure that a 2 s wave (and longer period waves) is reliably propagated to the target sites. This calculation is based on a 1-D source idealization (see Appendix A). The fact that our sources are two-dimensional makes this estimate conservative. So, we resample each of the source models to a 0.5 km resolution, allocating to the daughter sub-faults the same slips as the parent sub-faults (from the original model), and applying a Gaussian filter to marginally smoothen the slip distribution, with 98% of the slip in the parent sub-fault being preserved within the daughter sub-faults.

Each of the resampled source models is mapped onto the San Andreas fault at 5 separate locations distributed along the southern section of the fault, starting at Parkfield in central California and ending at Bombay Beach in southern California. Two alternate rupture propagation directions are considered at each location, north-to-south and south to north rupture. Figs. 5.1(a)-5.1(j) illustrate these mappings for the M_w 7.9 scenario earthquake. A total of 60 scenario earthquakes (six magnitudes \times five rupture locations \times two rupture propagation directions) are simulated here to cover the broad range of potential San Andreas fault earthquakes that could be damaging to tall buildings in the greater Los Angeles region.

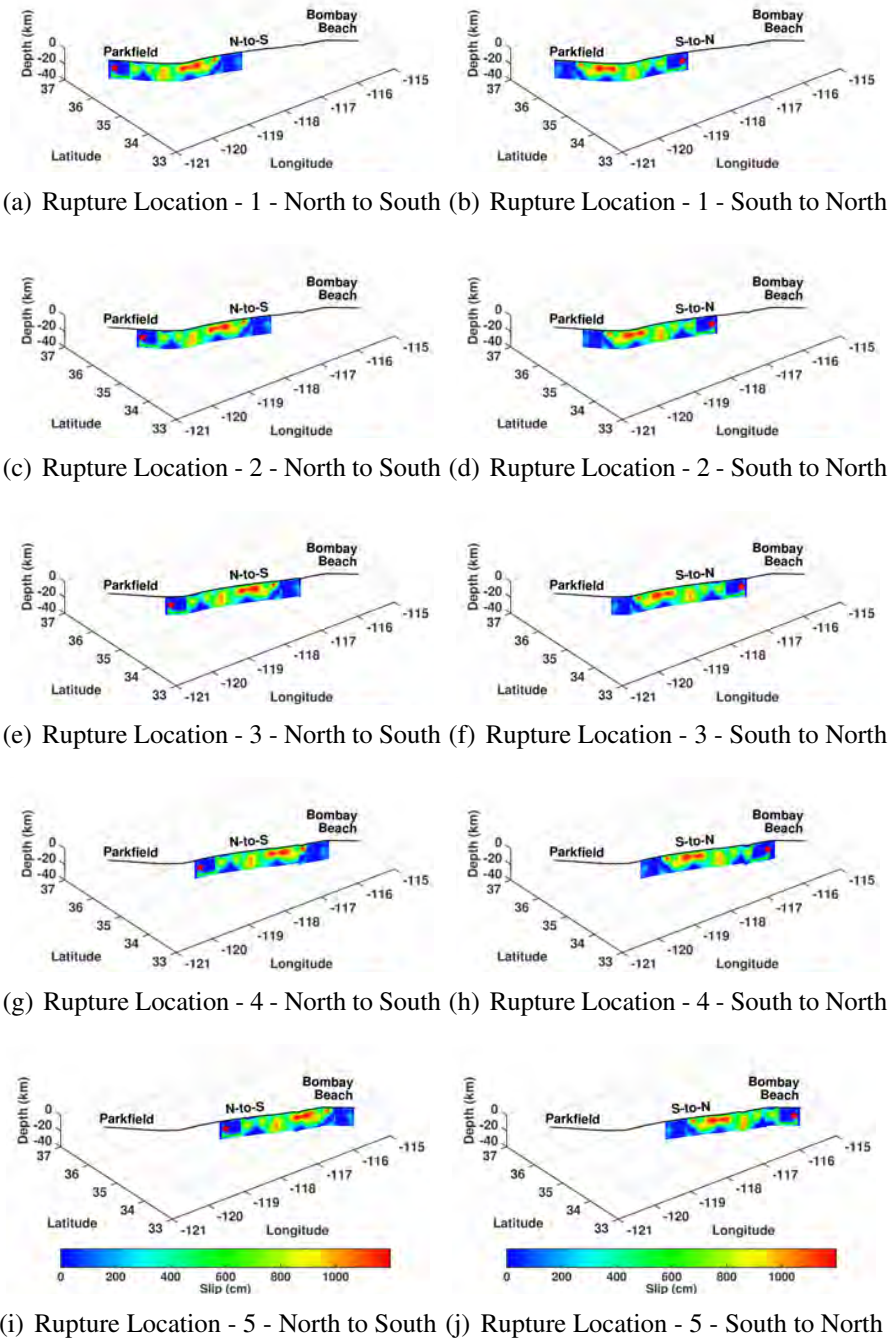


Figure 5.1: Kinematic finite source model of the 2002 M_w 7.9 Denali earthquake mapped on the southern San Andreas fault at five locations. The left column illustrates the five north-to-south propagating scenario earthquakes whereas the right column illustrates the south-to-north propagating earthquakes. Note that in reversing the rupture direction, the slip distribution is flipped as well. The red stars correspond to the hypocenters.

5.3.2 Scenario Earthquake Probabilities

The probability of occurrence of each scenario earthquake over the target time horizon of 30 years is calculated using the methodology proposed by [Mourhatch and Krishnan \(2015a\)](#) and successfully applied to a similar rupture-to-rafters study on moment frame buildings by [Siriki et al. \(2015\)](#). Here we only provide an overview of the procedure along with the calculated values.

The Uniform California Earthquake Rupture Forecast (UCERF, [Field et al. 2009](#); [Field et al. 2013](#)) by the Working Group on California Earthquake Probabilities (WGCEP), a joint effort of the U.S. Geological Survey (USGS), the California Geological Survey (CGS), and the Southern California Earthquake Center (SCEC) postulates a large set of plausible earthquakes on Californian faults and estimates their annual rates of occurrence on the basis of geologic, geodetic, seismic, and paleoseismic data. All the mapped-out faults in California are discretized into segments of 2 km to 13 km length. A plausible event, hereafter referred to as a “forecast earthquake”, is a hypothetical earthquake that ruptures two or more of these segments. Annual rates of occurrence of all forecast earthquakes are estimated from a grand inversion of diverse datasets of measured fault slip-rates, creep rates, historical earthquake timelines from paleoseismic investigations, etc. The model and data uncertainties are accounted for by the use of a logic tree. The weighted average of the forecast earthquake rates from all branches of this logic tree are converted to time-independent probabilities of occurrence over the target time horizon by assuming a Poisson distribution [Note: in this study we use the latest version of UCERF (Version 3), which provides only the long-term time-independent earthquake rates at the present time].

To estimate scenario probabilities, all forecast earthquakes with magnitudes between 5.90 and 8.34 whose rupture extent occurs wholly or partially within the southern San Andreas fault are allocated to one of the following magnitude bins: [5.90 - 6.42], (6.42 - 6.80] , (6.80 - 7.15] , (7.15 - 7.45], (7.47 - 7.78], and (7.78 - 8.34]. Note that the scenario earthquake magnitudes of 6.0, 6.58, 6.92, 7.28, and 7.59 correspond to centers of the first five magnitude bins based on seismic moment. The last bin is extended to a magnitude of 8.34 to include the probability of the largest plausible forecast earthquake. In the current risk framework, the forecast earthquakes in each magnitude bin will be represented by the ten scenario earthquakes (five rupture locations

and two rupture directions) matches the bin’s central magnitude. Accordingly, the UCERF yearly rates of the forecast earthquakes in a given magnitude bin are redistributed among the ten scenario earthquakes representing that bin. This involves converting the forecast earthquake yearly rates to seismic moment rates (multiplying by the seismic moment corresponding to forecast earthquake magnitude), deaggregating the moment rates to the segments being ruptured, summing the moment rate contributions of all forecast earthquakes to each segment, assigning the total moment rate of each segment to the closest scenario earthquake, aggregating the moment rate contributions to each scenario earthquake, and converting the scenario earthquake moment rate to a yearly rate (dividing by the seismic moment corresponding to scenario earthquake magnitude). The scenario earthquake yearly rates are converted to 30-year occurrence probabilities using a Poisson distribution [$P(M_w/loc) = 1 - e^{-r\Delta T}$, where r is the yearly rate and $\Delta T = 30$]. Shown in Tab. 5.2 are the 30-year occurrence probabilities of the 30 scenario earthquakes (six earthquake magnitudes and five rupture locations) determined using this approach. Half of these probabilities are assigned to north-to-south propagating ruptures and the other half to south-to-north propagating ruptures.

M_w [Bin]	Location 1 (Parkfield)	Location 2	Location 3	Location 4	Location 5 (Bombay Beach)	Total Probability (All Locations)
6.00 [5.90 - 6.42]	0.6449	0.0459	0.1910	0.2485	0.0685	0.8081
6.58 (6.42 - 6.80)	0.0051	0.0100	0.0854	0.1280	0.0183	0.2288
6.92 (6.80 - 7.15)	0.0180	0.0171	0.0060	0.0764	0.0271	0.1380
7.28 (7.15 - 7.45)	0.0211	0.0182	0.0059	0.0153	0.0365	0.0935
7.59 (7.47 - 7.78)	0.0124	0.0121	0.0061	0.0082	0.0192	0.0568
7.89 (7.78 - 8.34)	0.0339	0.0281	0.0236	0.0225	0.0215	0.1231
Total Probability M_w [5.90 - 8.34]	0.6760	0.1249	0.2904	0.4221	0.1773	0.8553

Table 5.2: UCERF3 time-independent 30-year occurrence probabilities for the 30 scenario earthquakes (six magnitudes and five rupture locations). Half of these probabilities are assigned to north-to-south propagating ruptures and the other half to south-to-north propagating ruptures.

5.4 Ground Motion Simulation

In addition to a mathematical description of the earthquake source, a detailed mapping of the earth's density and elasticity structure is needed to characterize the seismic wave speeds in the region, allowing for the deterministic simulation of site-specific ground motions. The spatial resolution of this mapping dictates the limiting wavelength (and frequency) of the seismic waves that can be reliably propagated through a finite-element/finite-difference/spectral-element model of the earth; the higher the resolution, the shorter the limiting wavelength and the higher the limiting frequency. Two regional wave-speed models of southern California exist, both developed and maintained by the Southern California Earthquake Center (SCEC): (i) the SCEC Community Velocity Model (CVM, [Magistrale et al. 1996](#), [Magistrale 2000](#), [Kohler 2003](#)), and (ii) the SCEC-CVM-Harvard or SCEC-CVMH ([Süss and Shaw 2003](#); [Prindle and Tanimoto 2006](#); [Tape et al. 2009](#); [Tape et al. 2010](#); [Ely et al. 2010](#); [Plesch et al. 2011](#)). Both models are capable of propagating seismic waves with frequencies at least up to 0.5 Hz and have been used in long-period ground motion simulations in the Los Angeles and surrounding basins (e.g., [Heaton et al. 1995](#), [Olsen et al. 1995](#), [Bao et al. 1998](#), [Graves 1998](#), [Akcelik et al. 2003](#), [Komatitsch et al. 2004](#), [Liu et al. 2004](#), [Komatitsch et al. 2010](#), [Komatitsch 2011](#), etc.). To synthesize the higher frequencies (above 0.5 Hz) in the ground motion, stochastic (e.g., [Mai et al. 2010](#); [Graves and Pitarka 2010](#)) and empirical (e.g., [Mourhatch and Krishnan 2015b](#)) methods have been developed. Broadband ground motion is produced by combining these with the deterministic low-frequency ground motion from finite-element, finite-difference, or spectral-element simulations.

Here, we follow the [Mourhatch and Krishnan \(2015b\)](#) methodology to produce broadband

ground motions with frequencies up to 5 Hz. High-frequency seismograms generated using a variant of the classical empirical Green's function (EGF) approach of summing recorded seismograms from small historical earthquakes (with suitable time shifts) are combined with low-frequency seismograms produced using the open-source seismic wave propagation package SPECFEM3D (V2.0 SESAME, Kellogg 2011; Komatitsch and Tromp 1999; Komatitsch et al. 2004; Tape et al. 2010) that implements the spectral-element method. SESAME uses Version 11.9 of the SCEC-CVMH seismic wave-speed model, accounting for 3-D variations of seismic wave speeds, densities, topography, bathymetry, and attenuation. The SCEC-CVMH model incorporates tens of thousands of direct velocity measurements that describe the Los Angeles basin and other structures in southern California (Süss and Shaw 2003; Plesch et al. 2011). It includes background crustal tomography down to a depth of 35 km (Hauksson 2000; Lin et al. 2007) enhanced using 3-D adjoint waveform methods (Tape et al. 2009), the Moho surface (Plesch et al. 2011), and upper mantle teleseismic and surface wave-speed models extending down to a depth of 300 km (Prindle and Tanimoto 2006). The wave-speed model-compatible spectral element mesh of the Southern California region was developed by Casarotti et al. (2008), who adapted the unstructured mesher CUBIT (Sandia National Laboratory 2011) into GeoCUBIT for large-scale geological applications such as this.

The classical empirical Green's function (EGF) approach involves the use of aftershock earthquake records as the Green's functions sampling the travel paths from the source to those stations (Hartzell 1978; Irikura 1983; Irikura 1986; Joyner and Boore 1986; Heaton and Hartzell 1989; Somerville et al. 1991; Tumarkin and Archuleta 1994; Frankel 1995). The rupture plane of an event is divided into (uniform or non-uniform) sub-faults. A pre-selected Green's function (selected on the basis of the closest match to the subfault-to-target site path) is used to represent

the seismic wave radiated from a given sub-fault. The Green's functions from all sub-faults are time-shifted and summed to yield the ground shaking at a target site. The key challenge in this approach is that it is difficult to replicate the globally observed Brune's spectral scaling law in both the high- and low-frequency regimes simultaneously. Scaling based on seismic moments, where the total seismic moment of the EGFs matches that of the simulated event, will correctly reproduce the low-frequency content of the ground motion. On the other hand, scaling based on areas, where the total area of the EGFs matches that of the simulated event, will correctly reproduce the high-frequency content (Joyner and Boore 1986; Heaton and Hartzell 1989). To achieve full agreement with Brune's spectrum, some form of filtering or convolving or other refinement must be introduced into the EGF summation. Mourhatch and Krishnan (2015b) were recently successful in developing a variant of the EGF summation that allows for the simulation of high-frequency ground motion (0.5 Hz-5.0 Hz) without the use of any artificial filters to achieve agreement with Brune's spectrum. They used low-magnitude (M_w 2.5-4.5) earthquakes as EGFs and combined the high-frequency waveforms generated using this approach with low-frequency waveforms from the deterministic spectral element approach (lowpass-filtered using a second order Butterworth filter with corner at 0.5 Hz) to reproduce ground motions at large distances under the M_w 6.0 Parkfield and the M_w 7.1 Hector Mine earthquakes. We use this hybrid approach to simulate ground motions at the 636 greater Los Angeles sites from the 60 scenario earthquakes on the San Andreas fault.

Fig. 5.2 shows the median values of three commonly used ground shaking intensities, peak horizontal displacement, peak horizontal velocity, and 5%-damped spectral acceleration S_a at 1 s and 0.2 s periods, for the ten ruptures corresponding to each magnitude level of the scenario earthquakes (see the blue lines). The vertical bars show the one standard deviation spread of the data on

either side of the median correspond to median. Also shown for comparison are the corresponding values determined using the Campbell-Bozorgnia (CB-08) Next Generation Attenuation (NGA) relation (Campbell and Bozorgnia 2008). The soil properties for the 636 sites, as characterized by the V_S^{30} values from Wald and Allen (2007), the basin depths from the SCEC-CVMH model (Plesch et al. 2011), and the Joyner-Boore distance, defined as the shortest distance from a site to the surface projection of the rupture plane, are used as inputs for the NGA computation.

There is good agreement between simulations and CB-08 in the peak velocity and displacement intensity measures for the lower magnitude earthquakes (up to 6.92). For the larger earthquakes, the simulations predict larger peak horizontal velocities (and much larger variances as well), whereas CB-08 predicts higher peak ground displacements (with comparable variances). CB-08 relies on observed near-field permanent displacements to constrain the PGD attenuation relation. The large permanent ground displacements (up to 9 m) observed during the magnitude 7.6 Chi-Chi earthquake of 1999, one of the few large magnitude earthquakes for which seismic, geologic, and geodetic near-source data is available, may have a strong influence on the PGD attenuation relation. On the other hand, CB-08 relies on seismic data alone for the PGV relation. Unfortunately, there is a sparsity of records from large magnitude earthquakes, especially in deep sedimentary basins such as the Los Angeles basin. This may, in part, explain the differences between the predictions by the simulations and the attenuation relations. Fig. 5.3 shows the median value of PGD and PGV as a function of Joyner and Boore distance corresponding to each earthquake magnitude obtained from simulated ground motions and CB-08. The figure illustrates the prediction of higher PGV and under prediction of PGD in simulations compare to those observed by NGA.

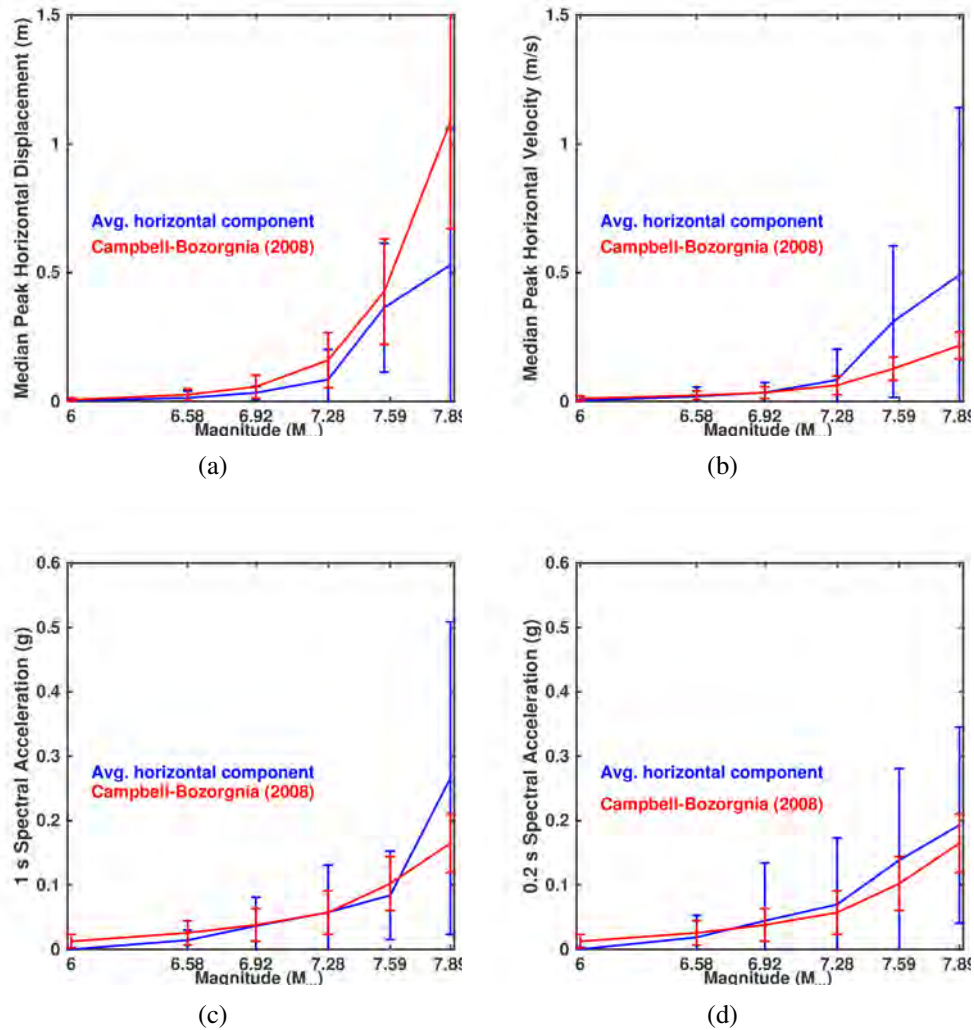


Figure 5.2: Median peak geometric mean horizontal displacement (m), velocity (m/s), and 5%-damped spectral acceleration (g) at 1 s and 0.2 s periods plotted as a function of earthquake magnitude from scenario earthquake simulations (blue lines) and the Campbell-Bozorgnia NGA (red lines). The vertical bars correspond to the one standard deviation spread above and below the median values.

The median values of 1 s S_a predicted by CB-08 are higher for the magnitude 6.00 and 6.58 earthquakes, about the same for the magnitude 6.92, 7.28, and 7.59 earthquakes, and significantly lower for the magnitude 7.89 earthquakes, when compared against those predicted by the simulations. CB-08 predictions for 0.2 s S_a are higher for the lower magnitude 6.00 and 6.58 earthquakes,

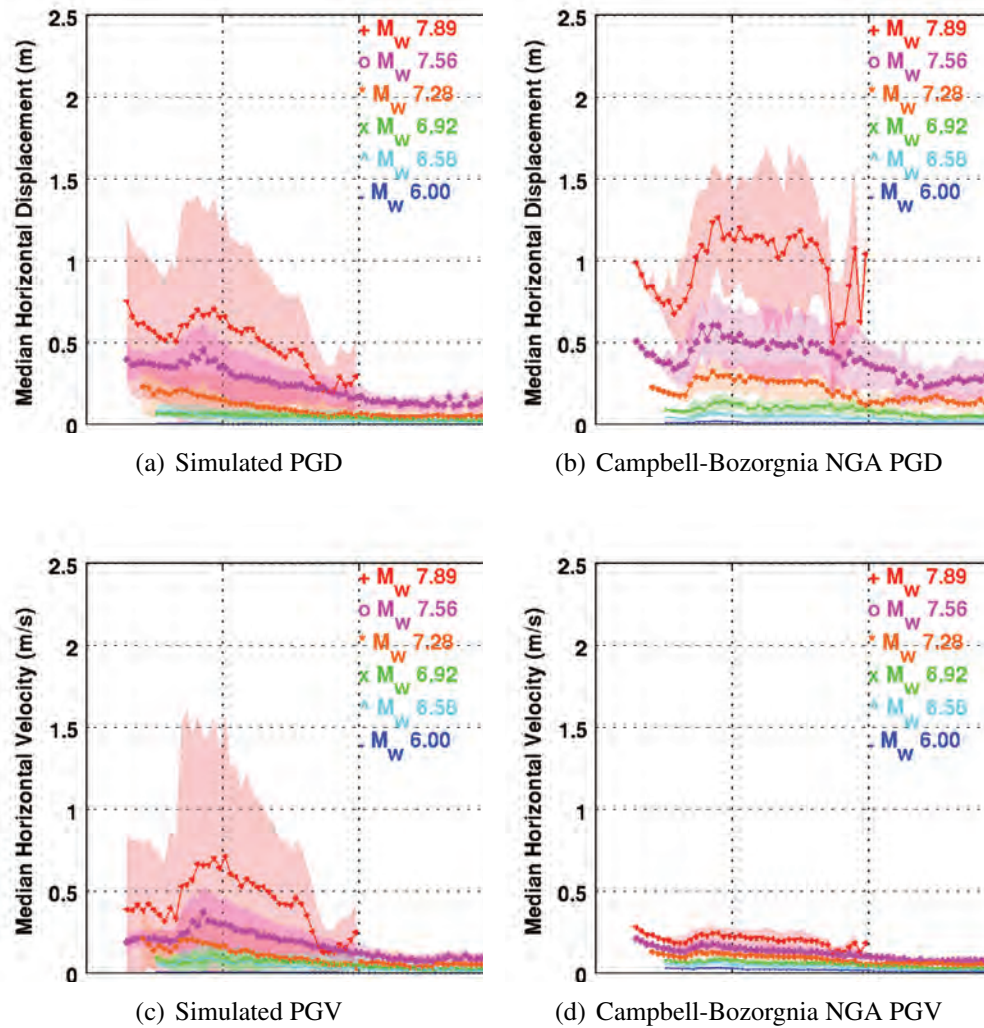


Figure 5.3: Median PGD [(a)-(b)] and PGV [(c)-(d)] values as a function of the Joyner-Boore source-to-site distance from scenario earthquake simulations [(a)-(c)] and the Campbell-Bozorgnia NGA [(b)-(d)].

but lower for the higher magnitude 6.92, 7.28, 7.59, and 7.89 earthquakes. We should note that the lower limit of the range of validity of the simulated ground motions is 0.2 s. The two-pass Butterworth filter used in filtering out the higher frequency ground motions has a corner at 0.2 s or 5 Hz. Ground motion intensities fall off smoothly with increasing frequency beyond this filter corner frequency and the values for 0.2 s S_a are probably under-estimated.

Figs. 5.4(a), 5.4(c), and 5.4(e) show maps of the median values of the geometric mean of the horizontal ground velocity under the ten ruptures of the magnitude 7.28, 7.56, and 7.89 scenario earthquakes, respectively. The maps cover the 636 analysis sites in southern California at which ground motions are computed. The corresponding maps, generated using the CB-08 attenuation relations with the site-specific soil and basin depth (Fig. 5.5) information for the 636 analysis sites, are shown in Figs. 5.4(b), 5.4(d), and 5.4(f). The strong influence of the basins is clearly seen. Ground motions are significantly amplified in each of the three basins, San Fernando, Los Angeles (LA), and San Gabriel (SG). The San Fernando valley's proximity to the San Andreas fault (and perhaps seismic wave-speed structure) results in far more intense shaking there as compared to the LA and SG basins. The simulated ground motions are significantly more intense than the intensities predicted by CB-08, with this difference growing with earthquake magnitude.

Spectral accelerations at 1 s and 3 s periods from the scenario earthquake simulations are compared against those generated using the CB-08 NGA relations in Fig. 5.6. Mean S_a and the one standard deviation spread on either side of the mean are shown plotted as a function of source-to-site distance in Figs. 5.6(a) and 5.6(b). The fact that the peaks occur not at shorter distances, but at 35-65 km distances is due to the combined effect of basins (the closest distance to which is about 40 km from the fault) and the Joyner-Boore definition of distance that does not take into account the location of slip asperity on the fault or rupture directivity, being based upon fault proximity alone instead. It is interesting to note that the simulated ground motions carry comparable power at 1 s and 3 s periods. If anything, the peaks in the 3 s S_a are higher than those in the 1 s S_a plots. This is not the case with the NGA predictions with the 3 s period spectral accelerations being significantly diminished when compared to the 1 s period spectral accelerations.

Muto and Krishnan (2011) identified fourteen locations in the greater Los Angeles region where a significant number of tall buildings exist. These include Irvine, downtown Los Angeles, Anaheim, Long Beach, Hollywood, El Segundo, Santa Monica, Century City, Universal City, and Park La Brea in the Los Angeles basin, Encino, Canoga Park in the San Fernando basin, and Glendale and Pasadena in the San Gabriel basin (see Fig. 5.5 for locations). Tab. 5.3 shows the median and standard deviation of the PGV, PGD, S_a^{1s} , and S_a^{3s} at these fourteen locations from the ten (five locations and two rupture directions) simulated M_w 7.89 scenario earthquakes on the San Andreas fault. Ground motion is particularly strong at downtown LA, Canoga Park, Anaheim, El Segundo, Santa Monica, and Century City. The corresponding tables for the M_w 7.59 and 7.28 earthquakes can be found in Tables 5.4 and 5.5.

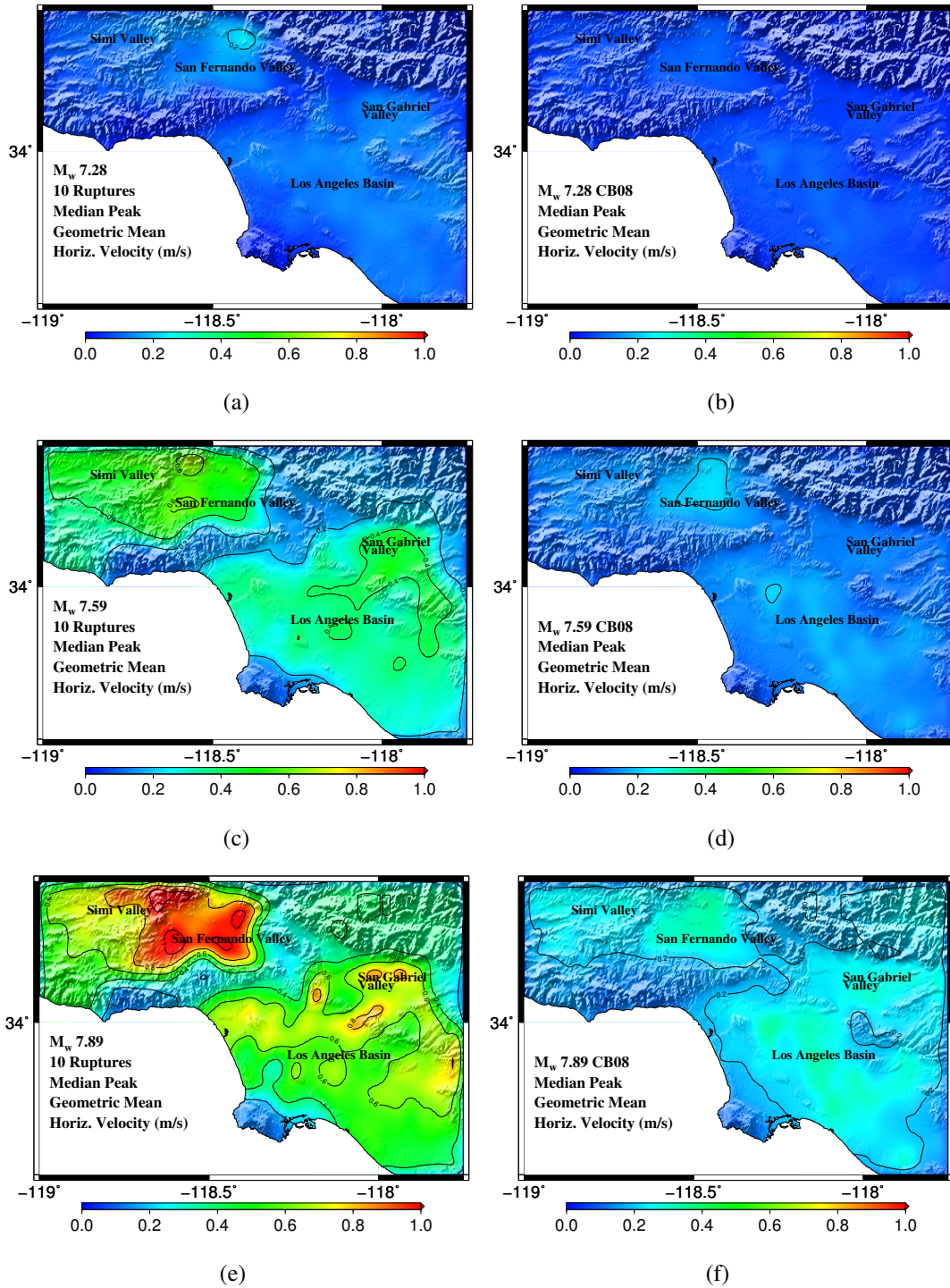


Figure 5.4: Map of median peak geometric mean horizontal velocities (m/s) for ten scenario earthquakes compared to CB-08 for M_w 7.28, M_w 7.59, and M_w 7.89 scenario earthquake. (a), (c), and (e): Simulated scenario earthquakes. (b), (d), and (e): Campbell and Bozorgnia (2008) NGA relation.

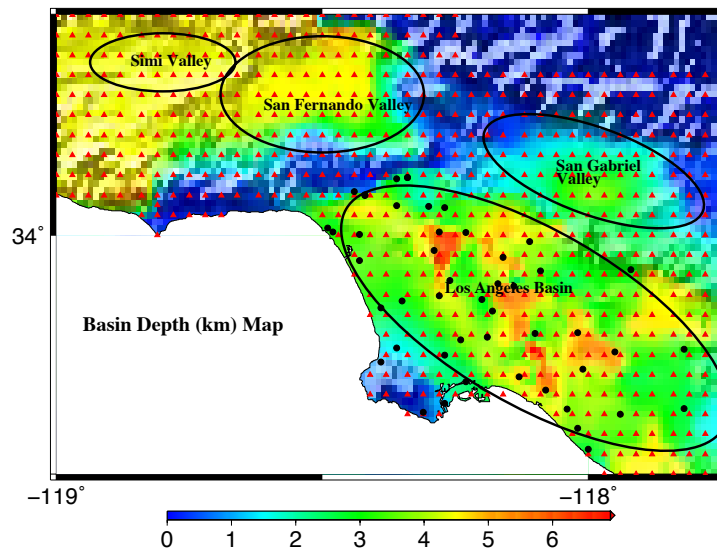


Figure 5.5: Basin depth (km) map for southern California. Red triangles indicate the geographical distribution of the 636 southern California sites where ground motions from the scenario earthquakes are computed. The ellipses identify the basins in southern California: Simi valley, San Fernando valley, San Gabriel valley, and Los Angeles basin.

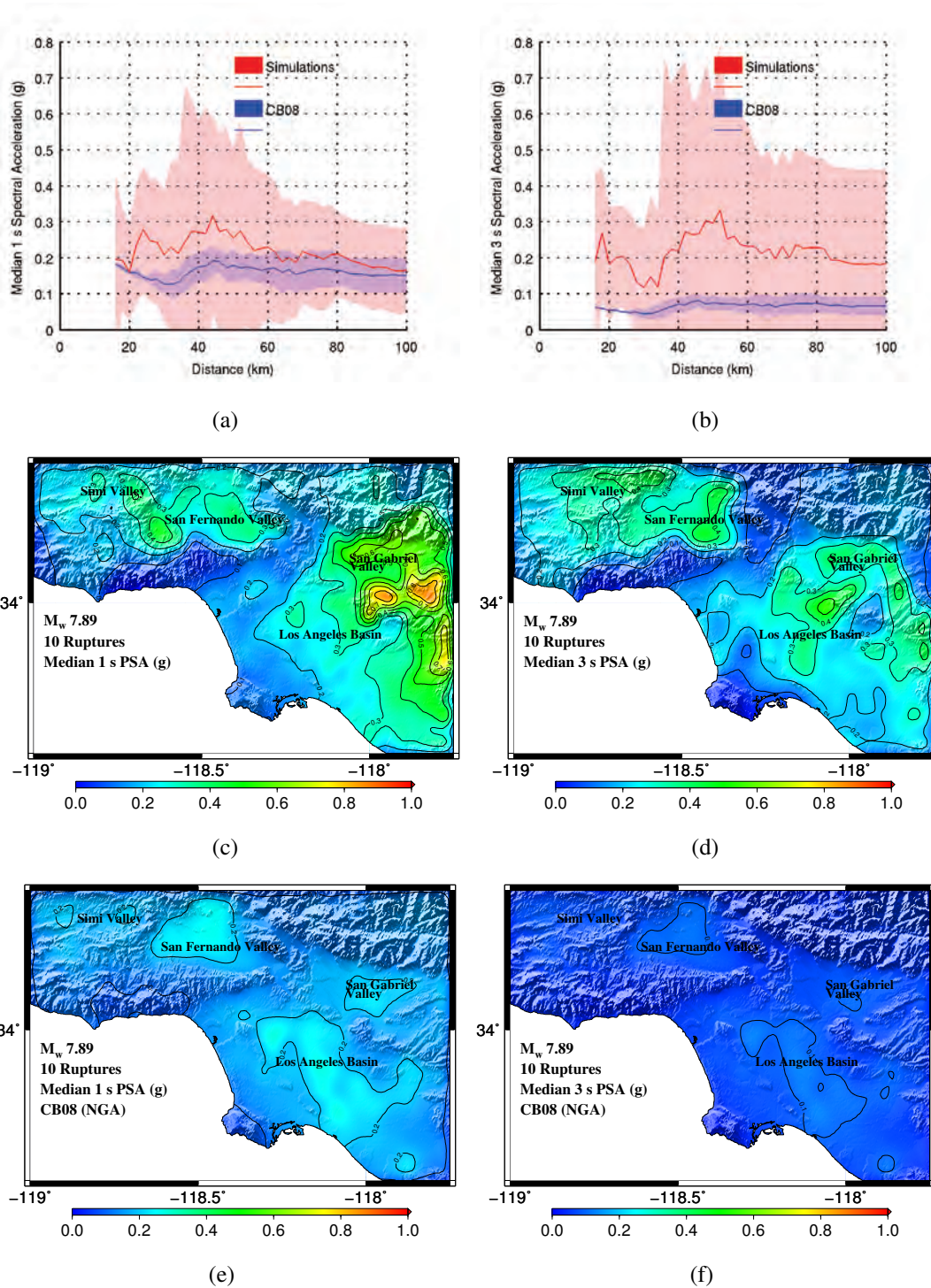


Figure 5.6: Predictions of spectral accelerations at 1 s and 3 s periods for the ten M_w 7.89 scenario earthquakes (five locations and two rupture directions) by simulations and the CB-08 NGA relations: (a) and (b). Median values as a function of the Joyner-Boore source-to-site distance: (c) and (d). Median S_a maps from simulations: (e) and (f). Median S_a maps from CB-08 NGA relations.

Site Location	Latitude	Longitude	Simulated								CB-08				Soil Type	
			PGV (m/s)		PGD (m)		S_a^{1s} (g)		S_a^{3s} (g)		PGV (m/s)	PGD (m)	S_a^{1s} (g)	S_a^{3s} (g)	UBC 94	UBC 97
			Md	σ	Md	σ	Md	σ	Md	σ	Md	Md	Md	Md		
Irvine	33.67	117.80	0.46	0.35	0.56	0.29	0.21	0.17	0.15	0.18	0.21	1.18	0.17	0.08	S_3	S_d
Encino	34.16	118.50	0.30	0.46	0.43	0.24	0.12	0.19	0.13	0.27	0.19	0.89	0.14	0.06	S_2	S_c
Downtown LA	34.05	118.25	0.79	0.75	0.79	0.60	0.26	0.15	0.38	0.43	0.28	1.70	0.23	0.10	S_3	S_d
Canoga Park	34.20	118.60	0.94	0.53	0.70	0.41	0.38	0.24	0.30	0.37	0.18	0.87	0.14	0.06	S_2	S_c
Pasadena	34.16	118.13	0.13	0.09	0.20	0.13	0.04	0.10	0.01	0.03	0.15	0.77	0.12	0.05	S_3	S_d
Anaheim	33.84	117.89	0.73	0.61	0.70	0.48	0.26	0.18	0.42	0.41	0.22	1.16	0.17	0.07	S_2	S_c
Long Beach	33.77	118.19	0.26	0.21	0.33	0.27	0.14	0.10	0.08	0.09	0.23	1.38	0.19	0.09	S_3	S_d
Glendale	34.17	118.25	0.26	0.33	0.40	0.30	0.15	0.09	0.08	0.15	0.20	0.93	0.15	0.06	S_2	S_c
Hollywood	34.10	119.33	0.31	0.41	0.49	0.27	0.16	0.12	0.19	0.29	0.18	0.85	0.14	0.06	S_2	S_c
El Segundo	33.92	118.41	0.63	0.39	0.60	0.29	0.18	0.13	0.22	0.19	0.20	1.09	0.16	0.07	S_3	S_d
Santa Monica	34.02	118.48	0.66	0.32	0.68	0.30	0.17	0.10	0.16	0.12	0.19	0.94	0.14	0.06	S_2	S_c
Century City	34.08	118.42	0.66	0.41	0.68	0.45	0.16	0.10	0.21	0.16	0.20	0.99	0.15	0.06	S_2	S_c
Universal City	34.14	118.35	0.27	0.13	0.38	0.19	0.06	0.05	0.06	0.06	0.14	0.54	0.10	0.04	S_2	S_c
Park La Brea	34.06	118.35	0.30	0.46	0.43	0.24	0.12	0.19	0.13	0.27	0.19	0.89	0.14	0.06	S_2	S_c

Table 5.3: Comparison of ground motion intensities from the ten (five locations and two rupture directions) simulated M_w 7.89 scenario earthquakes against CB-08 NGA predictions at fourteen locations in southern California, where a significant number of tall buildings exist.

Site Location	Latitude	Longitude	Simulated								CB-08				Soil Type	
			PGV (m/s)		PGD (m)		S_a^{1s} (g)		S_a^{3s} (g)		PGV (m/s)	PGD (m)	S_a^{1s} (g)	S_a^{3s} (g)	UBC 94	UBC 97
			Md	σ	Md	σ	Md	σ	Md	σ	Md	Md	Md	Md		
Irvine	33.67	117.80	0.31	0.17	0.31	0.10	0.08	0.08	0.11	0.08	0.14	0.53	0.12	0.05	S_3	S_d
Encino	34.16	118.50	0.19	0.08	0.26	0.09	0.03	0.02	0.05	0.05	0.13	0.42	0.11	0.04	S_2	S_c
Downtown LA	34.05	118.25	0.42	0.29	0.50	0.28	0.11	0.06	0.16	0.19	0.18	0.73	0.15	0.06	S_3	S_d
Canoga Park	34.20	118.60	0.48	0.28	0.52	0.25	0.10	0.03	0.14	0.11	0.12	0.40	0.10	0.04	S_2	S_c
Pasadena	34.16	118.13	0.10	0.03	0.16	0.06	0.02	0.02	0.01	0.01	0.10	0.33	0.08	0.03	S_3	S_d
Anaheim	33.84	117.89	0.45	0.27	0.39	0.15	0.07	0.05	0.13	0.14	0.14	0.49	0.11	0.04	S_2	S_c
Long Beach	33.77	118.19	0.20	0.07	0.24	0.08	0.04	0.04	0.04	0.03	0.14	0.58	0.12	0.05	S_3	S_d
Glendale	34.17	118.25	0.15	0.10	0.25	0.07	0.03	0.06	0.04	0.05	0.13	0.40	0.10	0.04	S_2	S_c
Hollywood	34.10	119.33	0.21	0.16	0.24	0.11	0.04	0.09	0.04	0.08	0.12	0.39	0.10	0.04	S_2	S_c
El Segundo	33.92	118.41	0.34	0.21	0.40	0.15	0.07	0.03	0.10	0.06	0.14	0.50	0.12	0.05	S_3	S_d
Santa Monica	34.02	118.48	0.36	0.20	0.45	0.16	0.07	0.04	0.11	0.10	0.13	0.44	0.11	0.04	S_2	S_c
Century City	34.08	118.42	0.35	0.25	0.49	0.26	0.08	0.04	0.11	0.07	0.13	0.45	0.10	0.04	S_2	S_c
Universal City	34.14	118.35	0.15	0.06	0.22	0.07	0.03	0.02	0.03	0.02	0.10	0.25	0.07	0.02	S_2	S_c
Park La Brea	34.06	118.35	0.19	0.08	0.26	0.09	0.03	0.02	0.05	0.05	0.13	0.42	0.11	0.04	S_2	S_c

Table 5.4: Comparison of ground motion intensities from the ten (five locations and two rupture directions) simulated M_w 7.59 scenario earthquakes against CB-08 NGA predictions at fourteen locations in southern California where a significant number of tall buildings exist.

Site Location	Latitude	Longitude	Simulated								CB-08				Soil Type	
			PGV (m/s)		PGD (m)		S_a^{1s} (g)		S_a^{3s} (g)		PGV (m/s)	PGD (m)	S_a^{1s} (g)	S_a^{3s} (g)	UBC 94	UBC 97
			Md	σ	Md	σ	Md	σ	Md	σ	Md	Md	Md	Md		
Irvine	33.67	117.80	0.12	0.08	0.10	0.07	0.05	0.04	0.04	0.04	0.06	0.17	0.06	0.02	S_3	S_d
Encino	34.16	118.50	0.06	0.05	0.06	0.07	0.02	0.08	0.03	0.02	0.06	0.15	0.06	0.02	S_2	S_c
Downtown LA	34.05	118.25	0.13	0.10	0.12	0.11	0.04	0.05	0.04	0.05	0.09	0.26	0.08	0.03	S_3	S_d
Canoga Park	34.20	118.60	0.11	0.12	0.11	0.11	0.06	0.06	0.05	0.04	0.06	0.14	0.05	0.02	S_2	S_c
Pasadena	34.16	118.13	0.03	0.02	0.03	0.05	0.01	0.01	0.00	0.01	0.05	0.13	0.05	0.02	S_3	S_d
Anaheim	33.84	117.89	0.15	0.18	0.16	0.14	0.07	0.06	0.06	0.06	0.06	0.15	0.05	0.02	S_2	S_c
Long Beach	33.77	118.19	0.05	0.04	0.05	0.06	0.02	0.02	0.01	0.02	0.08	0.22	0.07	0.03	S_3	S_d
Glendale	34.17	118.25	0.06	0.05	0.06	0.06	0.02	0.06	0.01	0.02	0.06	0.13	0.05	0.02	S_2	S_c
Hollywood	34.10	119.33	0.06	0.05	0.06	0.06	0.03	0.05	0.02	0.02	0.06	0.13	0.05	0.02	S_2	S_c
El Segundo	33.92	118.41	0.11	0.10	0.11	0.10	0.05	0.05	0.03	0.06	0.07	0.20	0.07	0.02	S_3	S_d
Santa Monica	34.02	118.48	0.11	0.10	0.10	0.09	0.04	0.05	0.02	0.05	0.07	0.17	0.06	0.02	S_2	S_c
Century City	34.08	118.42	0.13	0.08	0.12	0.10	0.04	0.04	0.03	0.05	0.07	0.17	0.06	0.02	S_2	S_c
Universal City	34.14	118.35	0.05	0.04	0.05	0.05	0.01	0.04	0.00	0.01	0.05	0.09	0.04	0.01	S_2	S_c
Park La Brea	34.06	118.35	0.06	0.05	0.06	0.07	0.02	0.08	0.03	0.02	0.06	0.15	0.06	0.02	S_2	S_c

Table 5.5: Comparison of ground motion intensities from the ten (five locations and two rupture directions) simulated M_w 7.28 scenario earthquakes against CB-08 NGA predictions at fourteen locations in southern California where a significant number of tall buildings exist.

Fig. 5.7 illustrates the effect of source directivity on ground motions. The north-to-south rupture at location 1 (see Fig. 5.1) directs a great amount of energy into the region of forward directivity, which is the San Fernando Valley and Los Angeles beyond. The south-to-north rupture, on the other hand, directs the energy away from the LA basin into the central valley to the north. The focusing effect is enhanced by the added proximity of the target region to the primary slip asperity in the source in the case of the north-to-south rupture scenario, while the opposite is true for the south-to-north rupture scenario. Note that in reversing the rupture direction, the slip distribution is reversed as well, such that an asperity on the south side of the north-to-south rupture is located on the north side of the south-to-north rupture. Peak horizontal velocity in the target region under the north-to-south rupture scenario is two to four times that under the south-to-north rupture scenario. For scenario earthquakes at rupture location 5, it is the south-to-north rupture that produces the stronger ground motions in the target region and the contrast is comparable to that in the location 1 scenario.

The simulated ShakeOut scenario earthquake, used in the Great California ShakeOut Exercise and Drill (Jones, Lucile M and Benthien, Mark 2011), is a M_w 7.80 rupture, initiating at Bombay Beach and propagating northwest through the San Gorgonio Pass, terminating 304 km away at Lake Hughes in the north. Using a source developed by Hudnut et al. (2008) and the SCEC-CVM wave-speed model (Magistrale et al. 1996; Magistrale et al. 2000; Kohler et al. 2003), Graves et al. (2011) simulated 3-component long-period ground motion waveforms in the greater Los Angeles region. The south-to-north propagating M_w 7.89 scenario earthquake at location 5 [Figure 5.1(j)] closely resembles this earthquake in as far as location, rupture directivity, and magnitude (with scenario earthquake having a slightly higher moment magnitude) are concerned.

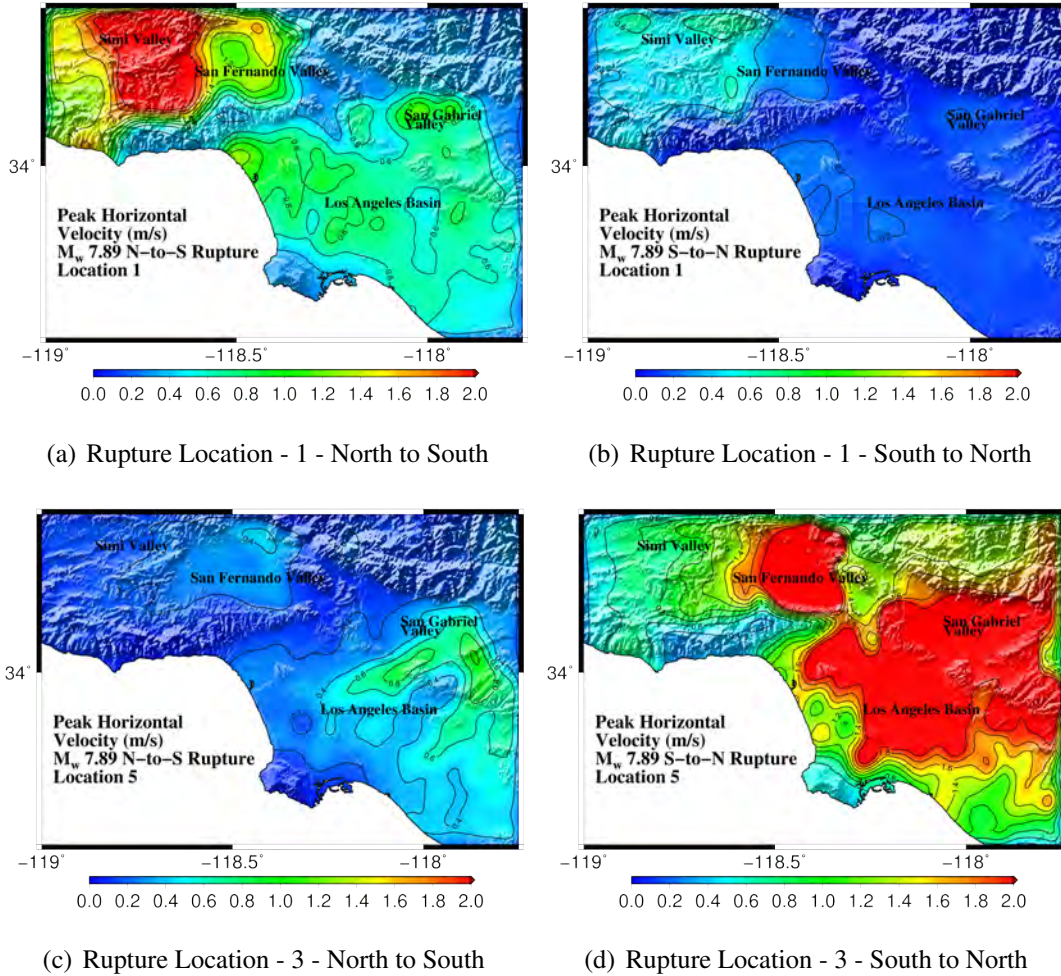


Figure 5.7: Directivity effect: Comparison of simulated peak horizontal velocity from north-to-south and south-to-north ruptures of the magnitude 7.89 scenario earthquake at locations 1 [(a)-(b)] and 5 [(c)-(d)].

The ShakeOut scenario has served as a benchmark for ground motion simulation methodologies (Bielak et al. 2010) and we compare the results of the simulations here against this established benchmark in Fig. 5.8. The ground motions simulated in this study are more intense than those predicted for the ShakeOut scenario, but the overall pattern of basin amplification is quite similar. The differences may be attributed to the slightly lower magnitude of the ShakeOut earthquake (with 30% smaller energy release) as well as the differences in the source (e.g., peak slip of 16

m in the ShakeOut source versus 12 m in the Denali earthquake source used for the earthquake simulated here) and wave-speed (SCEC-CVM versus SCEC-CVMH) models. The predictions by the NGA relations are far lower. The large red blob in the ShakeOut motions, attributed to a wave-guide through Whittier-Narrows by Olsen et al. (2009), cannot be found in the NGA predictions. Rupture directivity and wave-guide focusing, that clearly may have a strong influence on ground motions, are not explicitly accounted for in the NGA relations. In our simulation, a larger feature encompassing the wave-guide-related feature of the ShakeOut earthquake can be seen.

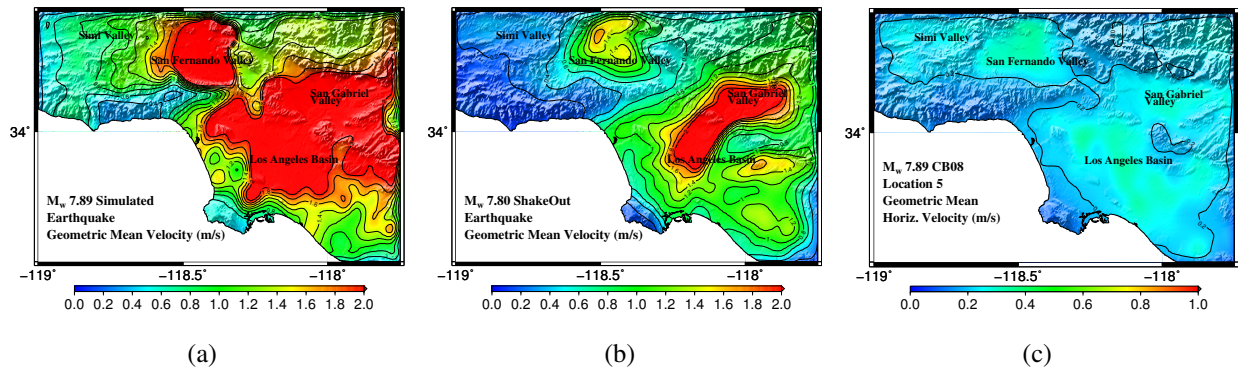


Figure 5.8: Geometric mean of peak horizontal ground velocities under the (a) simulated M_w 7.89 south-to-north propagating scenario earthquake at location 5, (b) the south-to-north propagating M_w 7.80 ShakeOut scenario earthquake rupturing the San Andreas fault from Bombay Beach in the south to Lake Hughes in the north, and (c) the predictions by the CB-08 NGA relations.

5.5 Target Buildings

We use the simulated ground motions from the scenario earthquakes to characterize the performance of tall braced frame buildings through 3-D nonlinear analysis. Building models are based on an existing 18-story steel moment frame building located in Canoga Avenue in Woodland Hills, California, commonly referred to as the “Canoga Park” building. This building is redesigned, with

the moment frames replaced by braced frames, according to the 1994 and 1997 Uniform Building Codes (UBC), taking into account various site conditions at the 636 target sites in southern California.

This building has been the subject of several studies (Paret and Sasaki 1995; Filippou 1995; Anderson and Filippou 1995; Chi 1996; Krishnan et al. 2006a; Krishnan et al. 2006b) because of several attractive features: (1) the presence of an owner-operated accelerometer on the roof of this building at the time of the 1994 M_w 6.7 Northridge earthquake, which fractured several beam-to-column welded moment connections, causing the building to tilt six inches; (2) the building's proximity to the earthquake epicenter (within five miles); and (3) the thorough field investigations (including visual and ultrasonic testing of moment connections) that followed the earthquake. Such fractures were observed in several moment frame buildings and this phenomenon has resulted in a vast body of work on this lateral force-resisting system type. Probabilistic seismic hazard analysis of braced frame buildings have not received as much attention and it is for this reason that the present study is focused on this lateral force-resisting system type.

The Canoga Park building is an 18-story welded steel moment frame building designed according to the 1982 UBC. The building has 17 stories of office space and a mechanical penthouse above that. Its height is 75.69 m with a typical story height of 3.96 m, except at the first (6.20 m), the seventeenth (4.77 m), and the penthouse (5.28 m) stories. The floor plan is relatively uniform over the building height with a rounded-rectangular footprint of 35.4 m (north-south direction) by 47.0 m (east-west direction) and minor setbacks at the fourth, the penthouse, and roof levels. Figs. 5.9(a) and 5.9(b) illustrate the isometric view and the typical floor plan of the building, respectively. The lateral load-resisting system consists of two 2-bay long welded moment frames in

either principal direction. These frames are located on the west, south, and east faces the building, and one bay inside the north face of the building. The asymmetric location of the moment frames makes this building torsionally sensitive and results in larger sizes for the members in the north frame compared to the south frame.

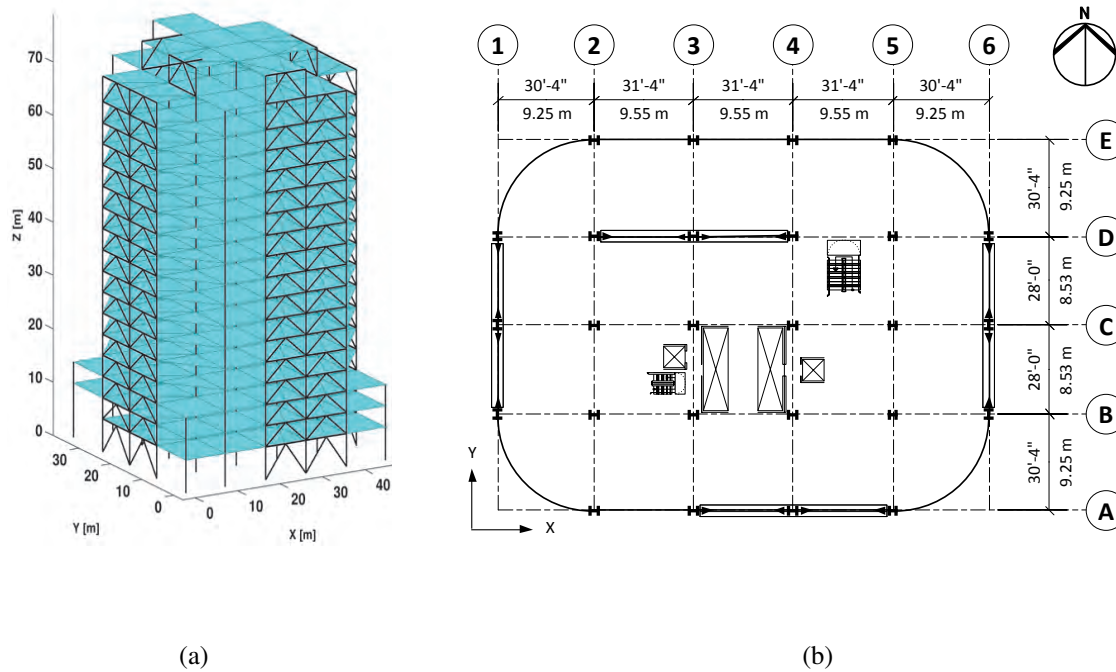


Figure 5.9: (a) Isometric view and (b) typical floor plan of the Canoga Park building.

The choice of the 1994 and 1997 building codes allows us to study pre-Northridge and post-Northridge designs and assess the impact of the changes that were introduced into the code based upon the lessons learned from building performance under the 1994 Northridge and the 1995 Kobe earthquakes. Ground motion histories recorded in these events revealed that the intensity of shaking may be significantly higher near the source of earthquakes with the effective peak acceleration (EPA) far exceeding the values prescribed by the 1994 code for seismic zone 4. It was also observed that long-period ground motions were more strongly amplified than previously acknowledged at

sites with relatively softer soils. To account for near-source effects and soil amplifications at distances close to the fault, two “near-source” parameters N_A and N_V were introduced into the 1997 UBC, which generally realized greater design base shears for sites located at distances closer than 5 km from an active fault.

The classification of soils at the 636 target sites by the 1994 and the 1997 UBC is shown in Figs. 5.10(a) and 5.10(b), respectively. We used shear wave velocity in the upper 30 meters of soil profile (V_s^{30} map) to determine the soil condition at each site. Soils at basin sites in southern California are typically classified as type S_3 by the 1994 UBC and as type S_d by the 1997 UBC. The corresponding soil types for mountainous sites with rocky soils (e.g., San Gabriel mountains, Hollywood hills, etc.) are S_2 and S_b , respectively. The 1997 UBC introduces an intermediate soil type, S_c , to achieve a smooth transition between the rocky mountainous sites and the softer soil sites in the deepest parts of the basins. Here, we designate the buildings designs corresponding to these five soil types as 94S2, 94S3, 97Sb, 97Sc, and 97Sd.

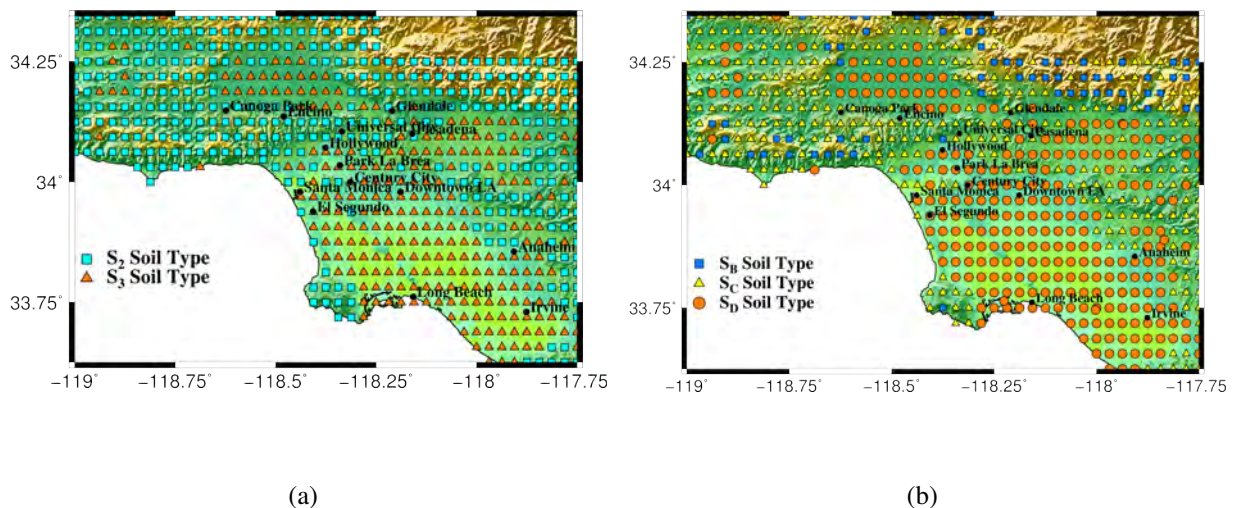


Figure 5.10: Classification of the soils at the 636 target sites in southern California by the (a) 1994 and the (b) 1997 Uniform Building Codes.

Commercial software ETABS is used for the linear elastic analysis and design of the five building models. The seismic weights, design base shears, total dead load plus 30% live load (used in the FRAME3D model employed for the nonlinear time history analysis under earthquake excitation), and the amount of steel per unit area (includes gravity columns, brace frame columns, brace frame beams, and braces; excludes floor framing beams) and the fundamental periods of the final designs (with and without 30% live load) are tabulated in Tab. 5.6. As required by both building codes, dynamic design procedure was used for the design process. The UBC 1994 designs are based on Allowable Stress Design (ASD) and the UBC 1997 designs are based on Load and Resistance Factor Design (LRFD). The strength design base shears are based on a period that is 1.3 times the code Method A period of 1.25 s, whereas the code allows this clause to be omitted in the drift check, thus resulting in lower drift design base shears. It should be noted that the base shear values for the UBC 1994 designs are based on ASD, whereas for UBC 1997 these values are based on LRFD. For any comparison, the LRFD values should be divided by 1.4 when comparing against the ASD (for example, a strength design base shear of 2,422 for $97S_c$ is equivalent to 1,730 is ASD). The architectural details, design loads, design methodology, member sizes, and material properties can be found in Chapter 4.

5.6 Pushover Analysis

Nonlinear pushover analysis is performed on each of the 5 building models using FRAME3D (Krishnan 2003; Krishnan and Hall 2006b; Krishnan and Hall 2006a; Krishnan 2009; Krishnan 2010). FRAME3D is a specialized program for the three-dimensional nonlinear failure analysis

Design Parameter	unit	Building Design				
		94S2	94S3	97Sb	97Sc	97Sd
Dead Load (Seismic weight)	kips	27920	28025	28,125	28,200	28,310
Dead Load + 30 % Live Load	kips	33070	33175	33,275	33,350	33,460
Average Steel Weight	psf	12.1	12.4	12.8	13.1	13.5
Strength Design Base shear N-S % of seismic weight (using $T = 1.63 s$)	kips %	1,346 4.82 %	1,689 6.03 %	2,250 8.00 %	2,422 8.59 %	2,780 9.82 %
Drift Design Base shear N-S % of seismic weight (using actual building periods)	kips %	1,013 3.63 %	1,271 4.54 %	1,181 4.20 %	1,678 5.95 %	2,078 7.34 %
Strength Design Base shear E-W % of seismic weight (using $T = 1.63 s$)	kips %	1,346 4.82 %	1,689 6.03 %	2,250 8.00 %	2,422 8.59 %	2,780 9.82 %
Drift Design Base shear E-W % of seismic weight (using actual building periods)	kips %	1,089 3.90 %	1,366 4.87 %	1,322 4.70 %	1,870 6.63 %	2,214 7.82 %
Periods Using Dead Load Only						
N-S Mode Period	sec	2.49	2.46	2.38	2.35	2.18
E-W Mode Period		2.34	2.17	2.13	2.11	2.04
Torsional Mode Period		1.44	1.42	1.38	1.36	1.29
Periods Using Dead + 30 % Live Loads						
N-S Mode Period	sec	2.79	2.75	2.66	2.63	2.44
E-W Mode Period		2.49	2.42	2.38	2.36	2.28
Torsional Mode Period		1.60	1.58	1.53	1.52	1.44

Table 5.6: Seismic design parameters and dynamic characteristics for the five building models.

of steel buildings, capable of modeling plasticity, fracture, and buckling of steel members, and the overall stability of the building (by properly accounting for member local $P - \delta$ and global structural $P - \Delta$ effects). It has been extensively validated against known solutions to analytical

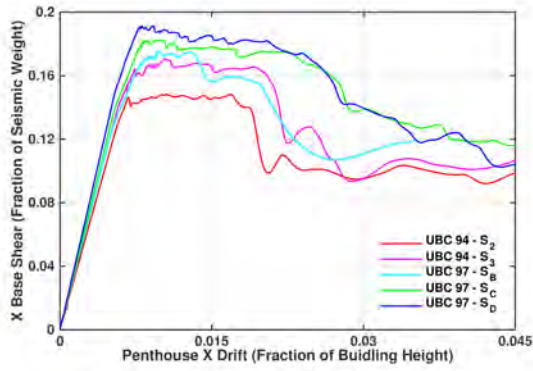
problems and data from full-scale tests on component assemblies and full building models. It has also been verified against the commercial program PERFORM3D (Björnsson and Krishnan 2014).

Here, nonlinear pushover analyses are performed dynamically by applying monotonically increasing horizontal acceleration at a very slow rate of 0.3 g/min in the pushover direction, thus pushing the building in an almost static manner. For these analyses, the masses of the horizontal degrees of freedom of the building (associated with the dead weight of the building) are redistributed according to the code static lateral force distribution, effectively performing the pushover using this load pattern. The deformation potential and the lateral pushover strengths of the five models are compared in the pushover curves of Fig. 5.11. These curves Figs. 5.11(a) and 5.11(b) illustrate the base shear normalized by the building seismic weight as a function of the penthouse displacement normalized by the penthouse height (70.41 m) in the X (E-W) and Y (N-S) directions, respectively. Figs. 5.11(c) and 5.11(d) show the same base shear fractions and the overall drift ratios as a function of time.

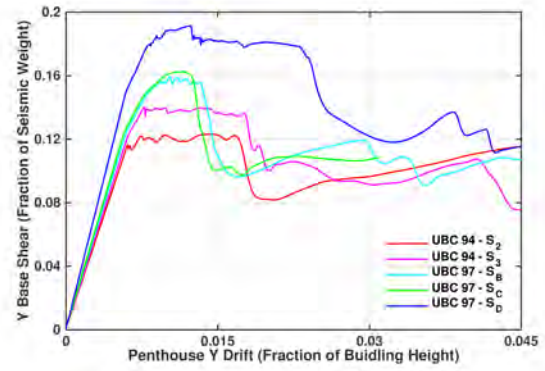
For all five models, the X-direction pushover strength is higher than that in the Y direction. It appears that “stiffer” implies “stronger” as well for these buildings. The asymmetric placement of the north frame results in the center of stiffness shifting to the south, leading to torsional eccentricity in the building as mentioned previously. Controlling X drift on the north face of the building requires relatively larger sizing for the north frame (note that the north face is farther from the center of stiffness than the south face because greater drifts tend to occur on that face). The longer spans of the braced frames in the X direction (9.55 m) compared to those in the Y direction (8.53 m) further necessitate greater sizes for the X direction frames in order to control drift. It is for these reasons that the X direction pushover strengths for the five models [0.148 (94S2),

0.170 (94S3), 0.176 (97Sb), 0.182 (97Sc), and 0.191 (97Sd)] are greater than the corresponding strengths in the Y direction [0.121 (94S2), 0.140 (94S3), 0.160 (97Sb), 0.163 (97Sc), and 0.190 (97Sd)]. The strength design seismic base shears are 0.048 (94S2), 0.060 (94S3), 0.080 (97Sb), 0.086 (97Sc), and 0.098 (97Sd) in either direction. This yields over strength factors of 3.08, 2.83, 2.20, 2.12, and 1.95 in the X direction, and 2.52, 2.33, 2.00, 1.90, and 1.94 in the Y direction.

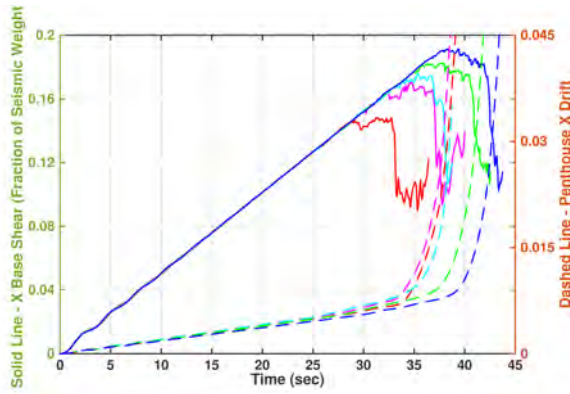
The overall drifts at the yield points of the five models are 0.0067 (94S2), 0.0074 (94S3), 0.0079 (97Sb), 0.0081 (97Sc), and 0.0083 (97Sd) in the X direction and 0.0060 (94S2), 0.0060 (94S3), 0.0061 (97Sb), 0.0075 (97Sc), and 0.0089 (97Sd) in the Y direction. The corresponding drifts at the points on the pushover curves where there is a sudden drop in strength are 0.0186 (94S2), 0.0192 (94S3), 0.0198 (97Sb), 0.0225 (97Sc), and 0.0238 (97Sd) in the X direction, and 0.0166 (94S2), 0.0170 (94S3), 0.0134 (97Sb), 0.0131 (97Sc), and 0.0216 (97Sd) in the Y direction. This implies effective ductilities of 1.78 (94S2), 1.59 (94S3), 1.51 (97Sb), 1.78 (97Sc), and 1.87 (97Sd) in the X direction, and 1.77 (94S2), 1.68 (94S3), 1.22 (97Sb), 1.18 (97Sc), and 1.88 (97Sd) in the Y direction, for the five models.



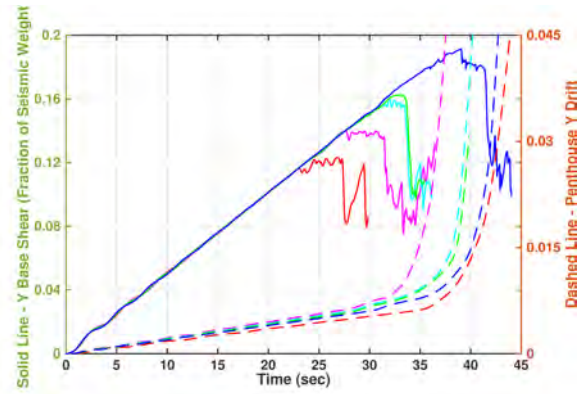
(a)



(b)



(c)



(d)

Figure 5.11: Pushover curves for the 5 building models: Base shear normalized by the seismic weight as a function of the overall building drift in the (a) X (E-W) and (b) Y (N-S) directions; Evolution of the normalized base shear (solid lines) and the overall building drift (dashed lines) as a function of time in the (c) X (E-W) and (d) Y (N-S) directions.

5.7 Building Seismic Response Evaluation Criteria

In performance based earthquake engineering (PBEE), three structural performance levels are used to characterize structural response to earthquake excitation (FEMA 2000): Immediate Occupancy

(IO), Life Safety (LS), and Collapse Prevention (CP). For braced frames, the IO performance limit signifies minor yielding or buckling of braces; the LS performance limit signifies yielding or buckling of braces at multiple locations, but no total failure, while several connection failures may fail; and the CP performance limit signifies extensive yielding and buckling of braces which may fail along with their connections. The limits on the transient interstory drift ratios (IDR) for the IO, LS, and CP performance levels are 0.005, 0.015, and 0.020, respectively.

Another limit state of interest is that of the global collapse of the computational model. Unfortunately, model collapse cannot be tied precisely to a specific IDR limit. In fact, the farther the analysis program is able to follow the structure into collapse, the greater the IDR will be. It is possible, however, to identify an IDR limit at which model collapse is initiated in a certain percentage of analysis cases, say 10%. Here, we adopt an alternate approach to set the IDR limit for model collapse. As in the case of moment frame buildings (Krishnan and Muto 2012), model damage under earthquake excitation localizes in a few stories in braced frame buildings as well. For example, Fig. 5.12 illustrates the response of the 97Sc model to the simulated ground motion at a site in Covina under the north-to-south propagating M_w 7.89 scenario earthquake rupture at location 3. Localization of damage at the bottom five stories has initiated a sidesway mechanism of collapse in this case. The buckling/yielding-induced sidesway mechanism forms due to yielding at the top of all columns in an upper-story, the yielding at the bottom of all columns in a lower-story, and buckling of all braces in those upper and lower stories as well as all intermediate stories [Fig. 5.12(d)]. This is the typical mode of collapse observed in our models, through the formation of one of the $N_s(N_s + 1)/2$ possible buckling/yielding-induced sidesway mechanisms, where N_s is the number of stories in the building. Note that N_s 1-story mechanisms, $N_s - 1$ 2-story mechanisms, and so

on, are possible.

It should be noted that only a 5% fixity is assumed at the beam-to-column connections in our models. This, added to the fact that the proportioning of beams according to the UBC precludes their buckling, means that beams do not dictate the formation of the mechanism. We quantify the severity of damage and the closeness to collapse through a mechanism damage index, which is the arithmetic average of the damage indices of the stories constituting the mechanism. Where damage localizes in multiple regions over the building height, the mechanism with the largest damage index is identified as the governing mechanism. The mechanism top-story damage index is the arithmetic average of the column and brace damage indices (defined below), likewise with the bottom story of the mechanism. The intermediate-story damage index is the arithmetic average of the damage indices of the braces in that story.

FRAME3D quantifies damage in the model through nonlinear-segment damage indices in each element. Braces and columns are modeled using modified elastofiber elements that have three nonlinear segments (two at the ends and one in the middle) sandwiching two elastic segments (Krishnan 2010). The nonlinear segments are discretized into 20 fibers in the cross-section. The modeling is based on the observation made by Gan (1996) and Gan and Hall (1998) that depending on the end fixity conditions, the strains in the braces is concentrated in mid and/or two ends of the brace element, hence an accurate representation of the brace can be made by incorporating nonlinearly at the very ends and the mid span of the brace elements. The uniaxial tension-compression behavior of each fiber is modeled using a nonlinear stress-strain law with hysteresis rules based on an extended Masing's hypothesis (Hall and Challa 1995). Fibers may yield, fracture, or rupture. Buckling is modeled through continuous coordinate updating of all element interior and exterior

nodes and ensuring dynamic equilibrium in the updated configuration. FRAME3D computes a segment damage index as the average of the damage indices of all the fibers constituting the segment. Here, we express it as a percentage. The fiber damage index is the peak plastic strain normalized by the plastic strain to fracture or rupture, whichever is smaller ([Krishnan and Muto 2012](#)).

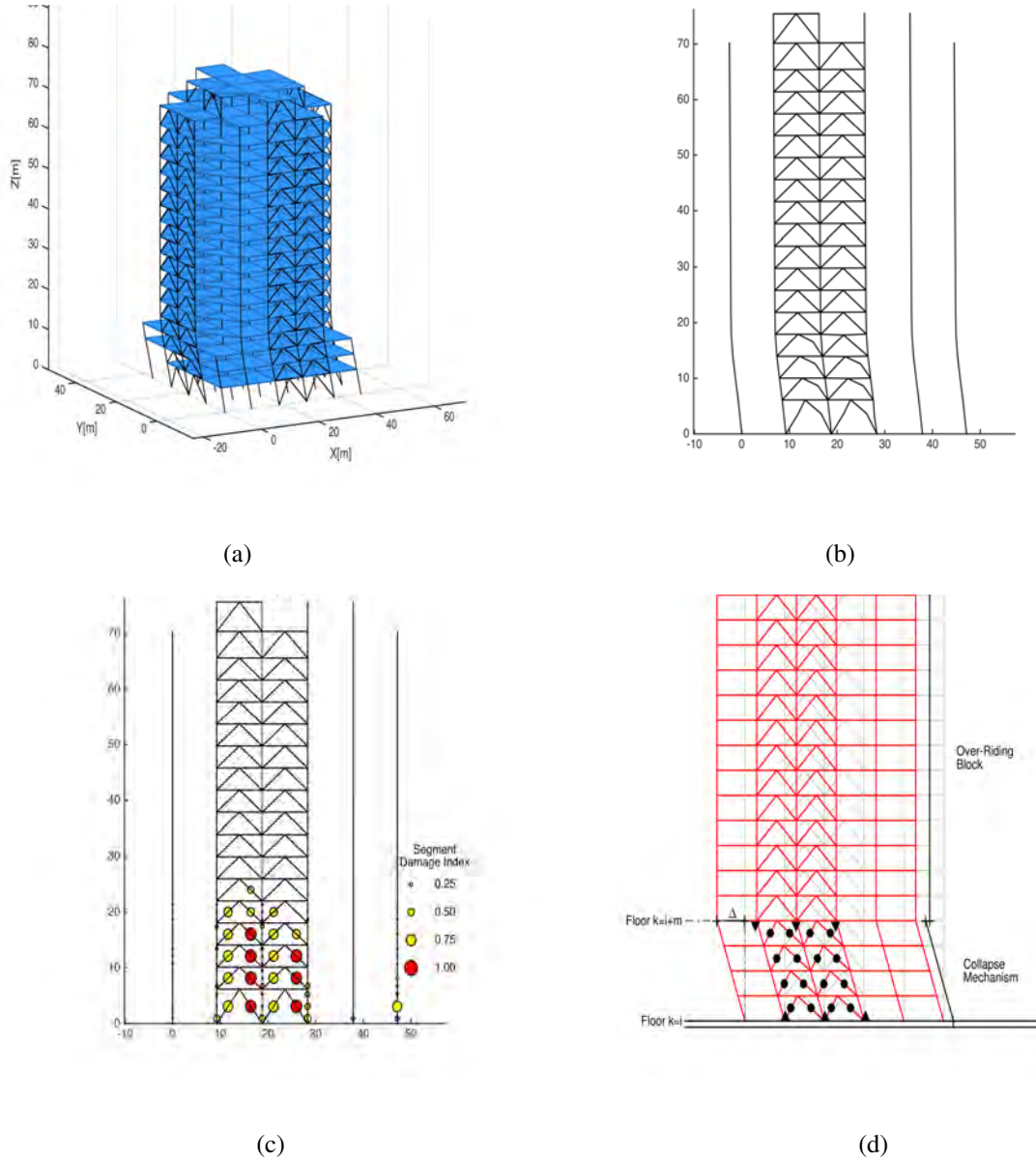


Figure 5.12: 97Sc model response under three-component ground motion at the city of Covina (station 580) from the north-to-south M_w 7.89 San Andreas fault scenario earthquake at location 3: (a) 3D snap shot of the deformed model at collapse initiation; (b) deformed shape of the north braced frame; (c) damage in members of the north frame (a segment damage index of 1.00 indicates a severed brace whereas a segment damage index of 0.00 indicates no damage whatsoever); circle size is proportional to the index. Red color indicates segment failure. (d) Idealization of the buckling/yielding-induced sideways mechanism.

To set the IDR limit for model collapse, we determine the governing buckling/yielding-induced

sidesway mechanism and the corresponding damage index (SMDI) for the applicable UBC94 and UBC97 building models subjected to the 3-component ground motion histories at the 636 analysis sites in southern California from the ten (five rupture locations and two rupture directions) M_w 7.9 scenario earthquakes. The SMDI for the 12,720 analysis cases is shown plotted as a function of the peak IDR in Fig. 5.13(a). The peak IDR for collapsing models is artificially set at 0.10 for better visualization. These are indicated by the red circles stacked up at the IDR value of 0.10 in the figure. The dark blue line represents the median SMDI as a function of peak IDR. Shown in Fig. 5.13(b) is the cumulative histogram of model collapse as a function of the damage index, SMDI. The shape of the histogram closely resembles that of a log-normal cumulative distribution function (CDF). Indeed, the best-fitting log-normal CDF closely follows the profile of the histogram and may be considered to be a frequentist representation of the probability of collapse. The 10th percentile of the CDF corresponds to an SMDI of 42, whereas the 5th percentile corresponds to an SMDI of 37. In other words, there is a 10% probability of model collapse if the SMDI reaches a value of 42 and a 5% probability of model collapse if the SMDI reaches a value of 37. The median peak IDRs corresponding to these values of SMDI are 0.057 and 0.043, respectively. Rounding these peak IDRs, we set the model collapse CO and red-tagged RT performance limits to 0.06 and 0.04, respectively. Analysis instances of a model with a peak IDR above the CP performance limit of 0.02 and below the RT performance limit would be indicative of incipient partial collapse and a candidate for model red-tagging. A peak IDR between the RT and CO performance limits would be indicative of partial collapse and/or incipient total collapse. Such a building would likely have to be torn down.

Shown in Fig. 5.14 are the identified buckling/yielding-induced sidesway mechanisms for the

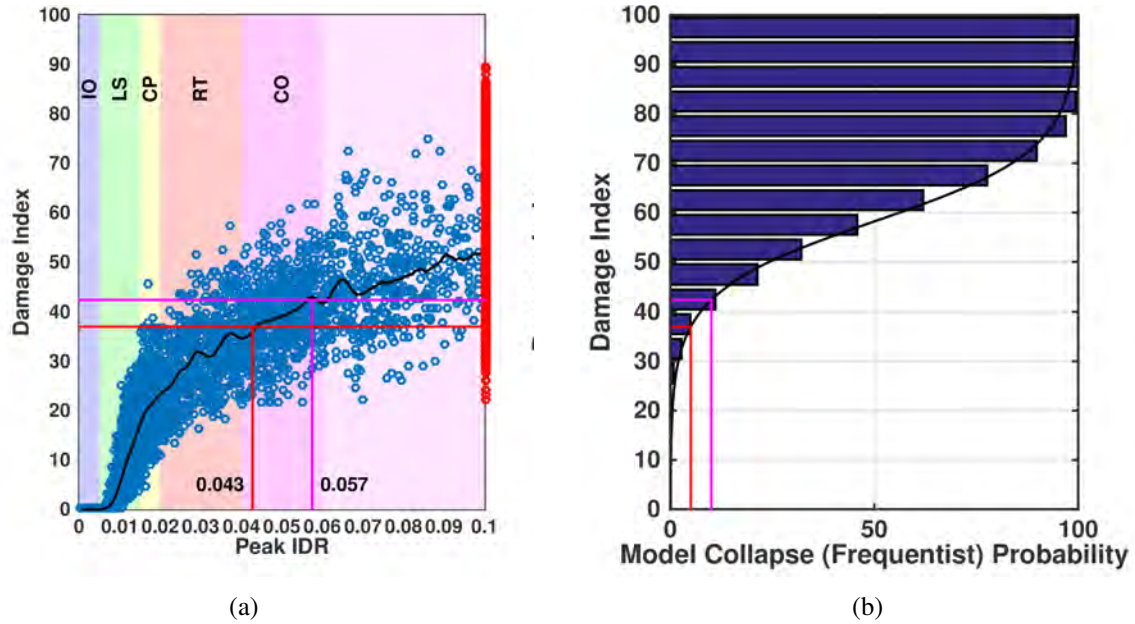
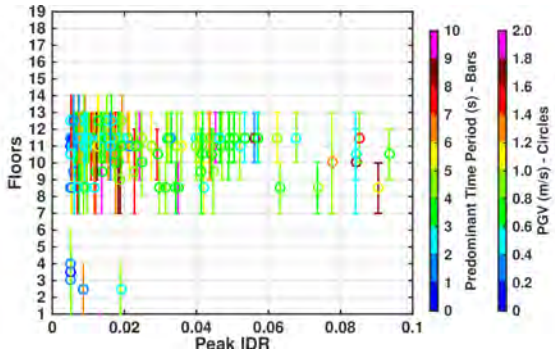


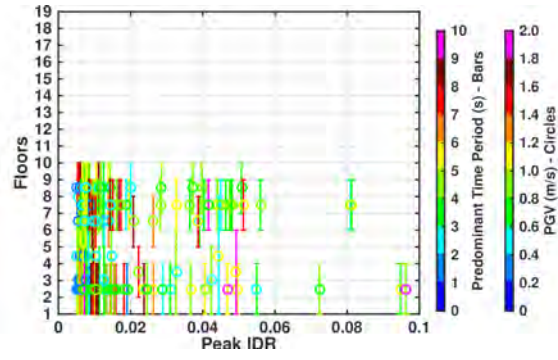
Figure 5.13: (a) Buckling/yielding-induced sidesway mechanism damage index (SMDI) as a function of the peak interstory drift ratio observed in the 1994 and 1997 UBC site-specific designs at the 636 analysis sites in southern California under the ten M_w 7.89 San Andreas fault earthquake scenarios. Blue circles correspond to cases where the computational model does not collapse, whereas red circles correspond to cases where model collapses. Blue line is the median SMDI as a function of the peak IDR. (b) Cumulative histogram and best-fitting log-normal CDF representing the frequentist probability of model collapse [red dots in (a)]. The red and magenta lines on both figures correspond to the 5th and 10th percentile of the CDF.

five building models under three-component simulated ground motion from the ten M_w 7.89 scenario earthquakes. Both upper story and lower story mechanisms are observed. Of particular interest are the locations of mechanisms at large peak IDR levels (say above 0.04) as they may provide insights into the likely mechanisms of collapse of this class of buildings. The mechanisms in the 94S2 design form primarily in the upper stories, between floors 9 and 13, whereas those in the 94S3 design form at one of two locations, in upper stories between floors 6 and 9, and in a lower set of stories between floors 1 and 4. The 97Sc design has the greatest variety of mechanisms, with mechanisms occurring between floors 1 and 4, floors 3 and 6, and floors 7 and 10.

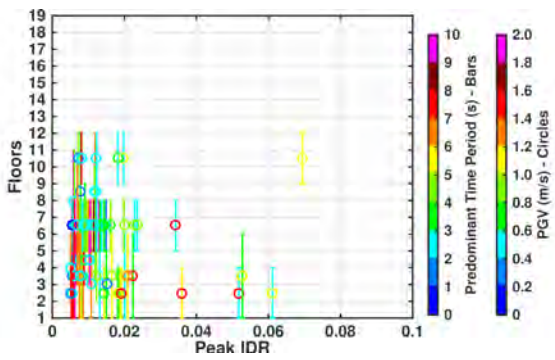
The mechanisms in the 97Sd model predominantly form in the lower stories, between floors 1 and 4. The ground motions at the S_b soil sites are generally not strong enough to cause peak IDRs greater than 0.04 in the 97Sb model. Not much can be inferred about the collapse mechanisms in this case. With few exceptions, the sidesway mechanisms form only under long period ground excitation with predominant ground motion period exceeding 2 s.



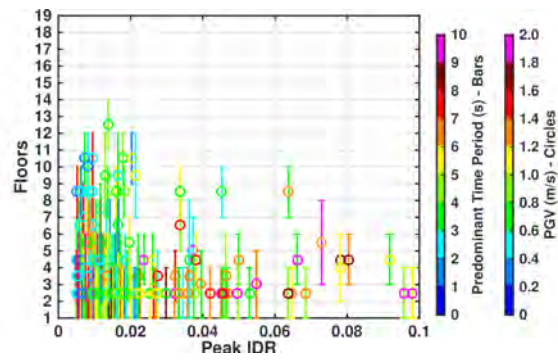
(a) 94S2



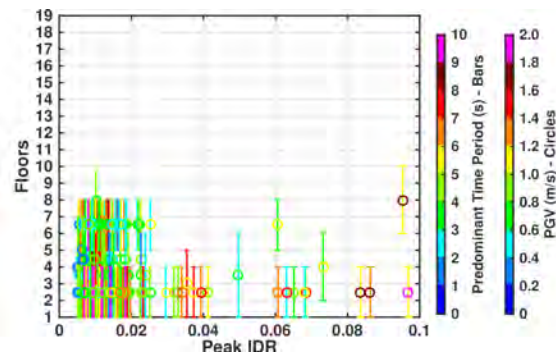
(b) 94S3



(c) 97Sb



(d) 97Sc



(e) 97Sd

Figure 5.14: Story extent (vertical bars) of buckling/yielding-induced sideways mechanisms in the 1994 and 1997 UBC site-specific designs at the 636 analysis sites in southern California under the ten M_w 7.89 San Andreas fault earthquake scenarios in increasing order of peak IDR. Bar color corresponds to the predominant period of ground motion whereas the central circle color corresponds to the PGV.

Figure 5.15 illustrates the frequentist probability of each story being part of a buckling/yielding-induced sidesway mechanism (determined from the fraction of cases where a mechanism encompasses a given story). Two observations may be made: (i) the probability of an upper story being part of a mechanism is more common in the 1994 UBC designs as compared to the 1997 UBC designs; (ii) the stiffer a building is (or the lower the fundamental natural period of the building), the greater is the probability of a lower story participating in a mechanism. The converse is true for an upper story. In other words, the mechanisms seem to migrate the lower stories with increasing stiffness (or decreasing fundamental period).

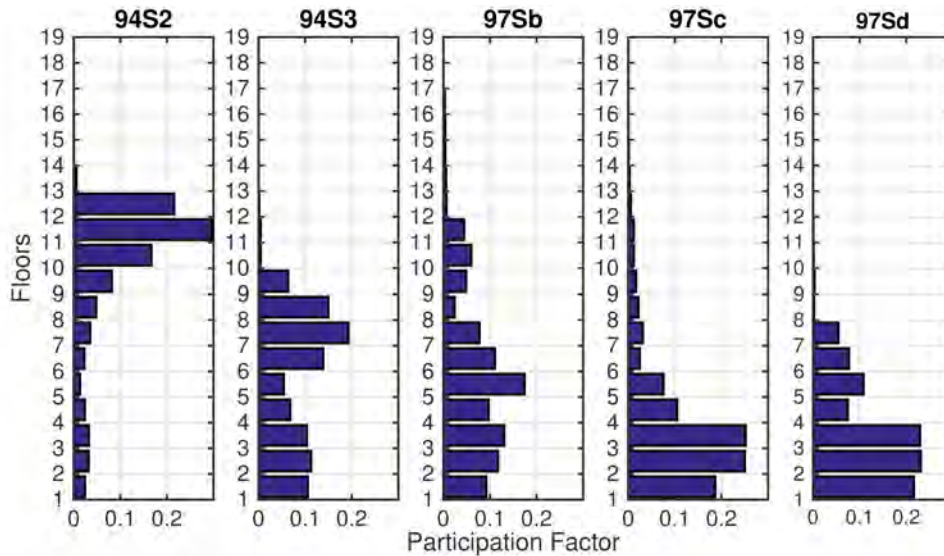


Figure 5.15: Frequentist probability of a given story being involved in a buckling/yielding-induced sidesway mechanism in each of the five building models.

5.8 Building Performance in Scenario Earthquakes

Fig. 5.16 shows maps of peak IDR in the UBC 1994 and UBC 1997 designs at the 636 sites in southern California under 3-component ground motion from north-to-south propagating M_w 7.89, 7.59, and 7.28 scenario earthquakes at location 1. Fig. 5.17 shows the corresponding maps for the same magnitude earthquakes at location 3. It is clear that earthquakes at location 3 are far more detrimental to buildings located in the Los Angeles (LA) and San Gabriel (SG) basins, whereas earthquakes at location 1 are more detrimental to those located in the San Fernando (SF) and Simi Valley (SV) basins. Building performances in the SF basin range from CO in the M_w 7.89 earthquakes, RT-LS in the M_w 7.59 earthquakes, and RT-IO in the M_w 7.28 earthquakes, whereas those in the LA basin range from CO-LS in the M_w 7.89 and 7.59 earthquakes, and RT-IO in the M_w 7.28 earthquakes. What is interesting is that many of these sites are at about the same distance from the rupture, yet the structural responses are quite different. It demonstrates the strong dependence of structural performance on the full waveform of ground motion, and not just on the gross features of the earthquake source and building site conditions.

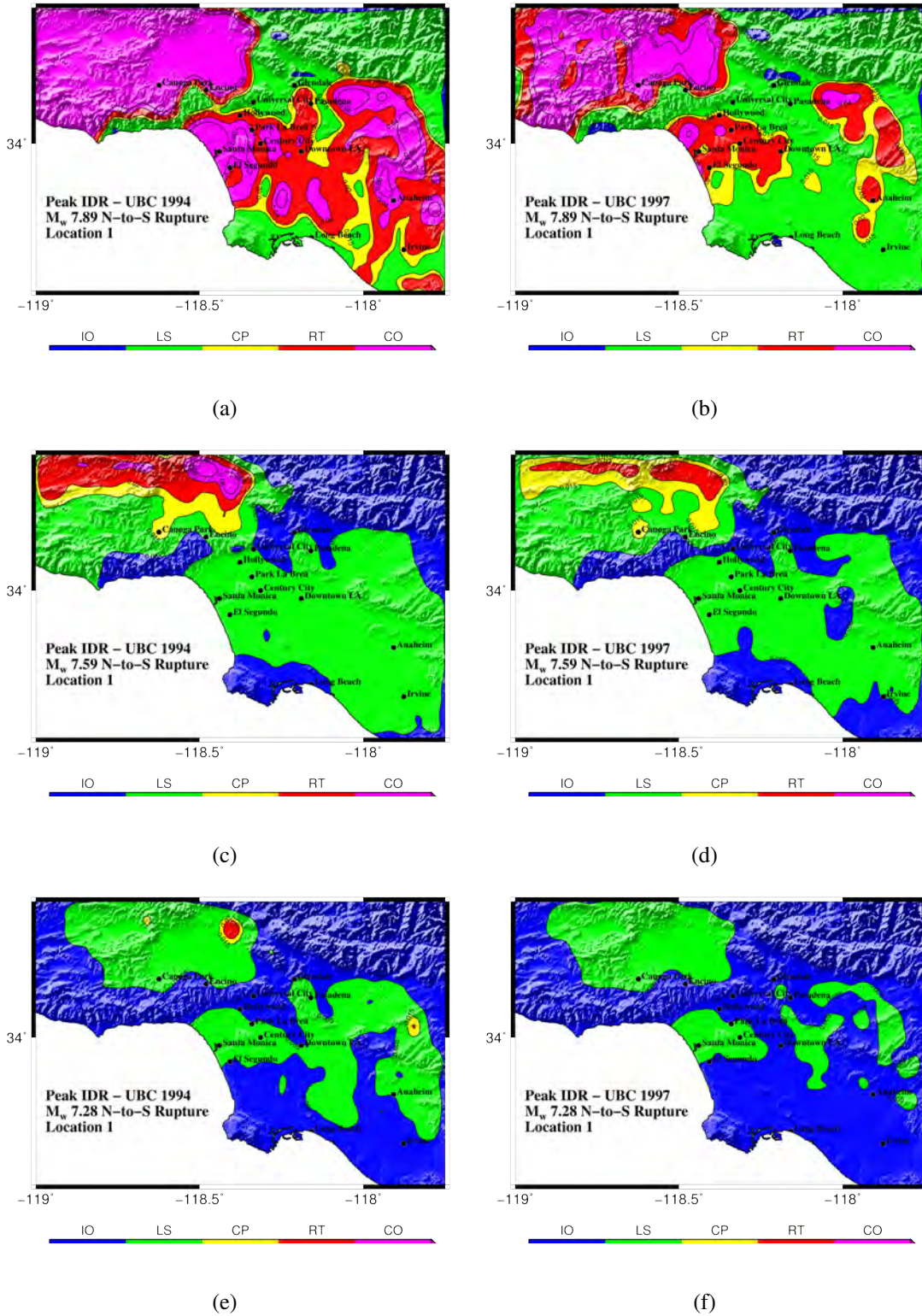


Figure 5.16: Peak IDR response of the UBC94 [(a), (c), (e)] and UBC97 [(b), (d), (f)] designs of the 18-story steel braced frame building under north-to-south propagating ruptures at location 1 of the southern San Andreas fault: [(a)-(b)] M_w 7.89, [(c)-(d)] M_w 7.59, and [(e)-(f)] M_w 7.28.

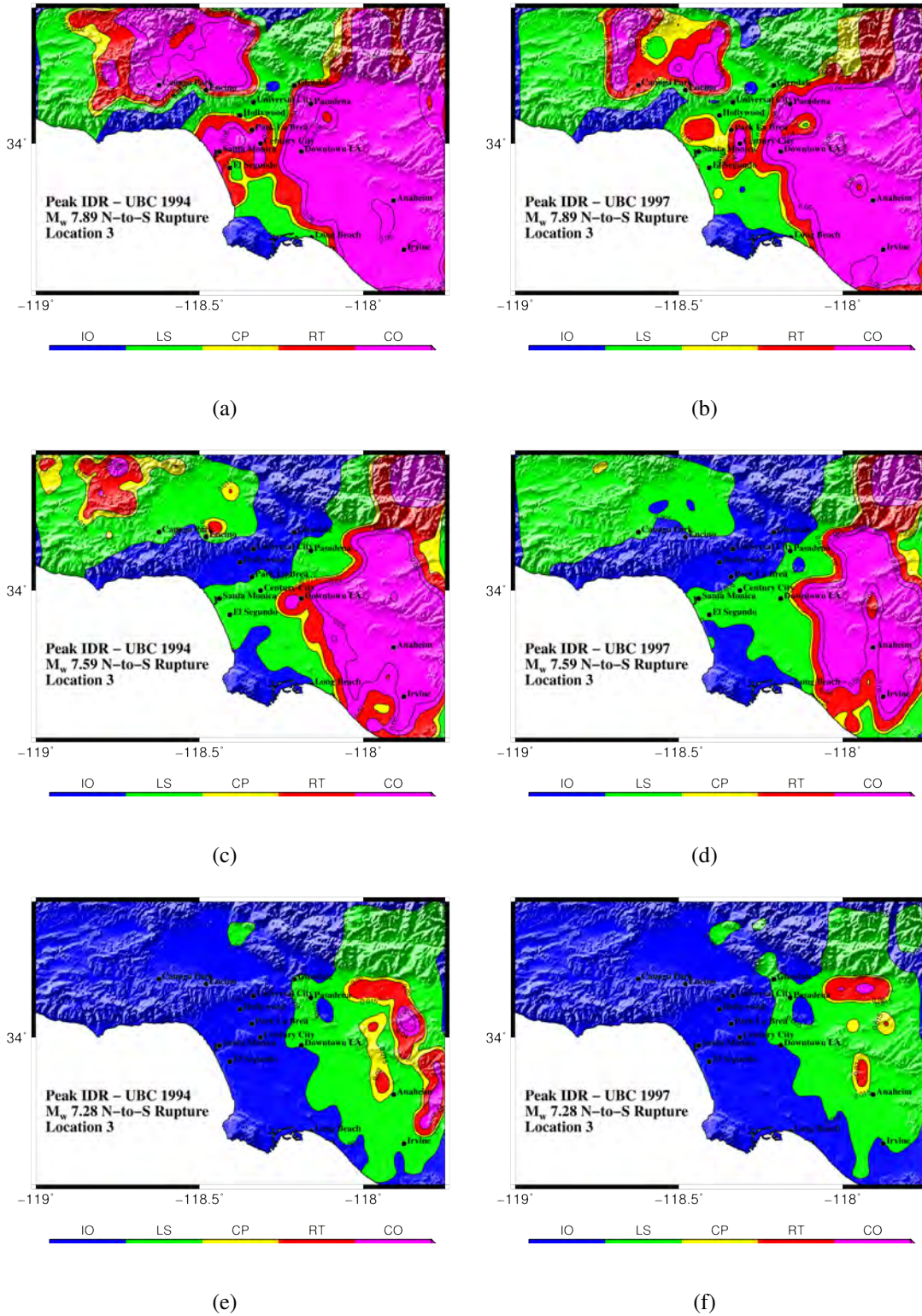


Figure 5.17: Peak IDR response of the UBC94 [(a), (c), (e)] and UBC97 [(b), (d), (f)] designs of the 18-story steel braced frame building under north-to-south propagating ruptures at location 3 of the southern San Andreas fault: [(a)-(b)] M_w 7.89, [(c)-(d)] M_w 7.59, and [(e)-(f)] M_w 7.28.

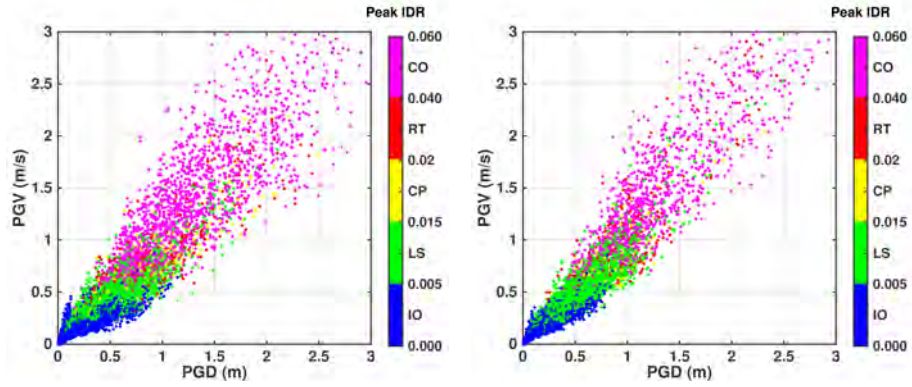
Shown in Tab. 5.7 are the performance levels, based on the median peak IDR and the median plus one standard deviation peak IDR, of the UBC 1994 and the UBC 1997 site-specific building designs at the fourteen locations (Fig. 5.5) in southern California where a significant number of tall buildings exist. The peak ground motions at these locations were summarized earlier in Tab. 5.3. The results look ominous indeed with median performance of RT at downtown LA, Santa Monica, and Century City, and CO at Canoga Park and Anaheim for the UBC94 building. The UBC97 are significantly better than median performance in most locations is LS with the exception of Anaheim (CP). Moreover, the median plus one standard deviation performance improved in most locations as many of the CO performances are changed to RT.

Site	UBC 1994					UBC 1997				
	Soil	Md		$Md+\sigma$		Soil	Md		$Md+\sigma$	
Irvine	S_3	0.0100	LS	0.0339	RT	S_d	0.0095	LS	0.0344	RT
Encino	S_2	0.0126	LS	0.0378	RT	S_c	0.0098	LS	0.0277	RT
Downtown LA	S_3	0.0353	RT	0.0578	CO	S_d	0.0143	LS	0.0340	RT
Canoga Park	S_2	0.0423	CO	0.0600	CO	S_c	0.0184	LS	0.0384	RT
Pasadena	S_3	0.0110	LS	0.0420	RT	S_d	0.0010	LS	0.0299	CP
Anaheim	S_2	0.0461	CO	0.0600	CO	S_c	0.0192	CP	0.0399	RT
Long Beach	S_3	0.0045	IO	0.0180	CP	S_d	0.0036	IO	0.0168	CP
Glendale	S_2	0.0080	LS	0.0252	RT	S_c	0.0055	LS	0.0170	CP
Hollywood	S_2	0.0105	LS	0.0391	RT	S_c	0.0071	LS	0.0211	RT
El Segundo	S_3	0.0181	LS	0.0443	CO	S_d	0.0123	LS	0.0368	RT
Santa Monica	S_2	0.0322	RT	0.0589	CO	S_c	0.0106	LS	0.0249	RT
Century City	S_2	0.0335	RT	0.0589	CO	S_c	0.0124	LS	0.0299	RT
Universal City	S_2	0.0050	LS	0.0191	CP	S_c	0.0039	IO	0.0169	CP
Park La Brea	S_2	0.0126	LS	0.0378	RT	S_c	0.0098	LS	0.0277	RT

Table 5.7: Median and median + one standard deviation performance of the UBC 1994 and 1997 buildings under shaking from the ten (five locations and two rupture directions) M_w 7.89 San Andreas fault earthquakes at the 14 locations (Fig. 5.5) in southern California where a significant number of tall buildings exist.

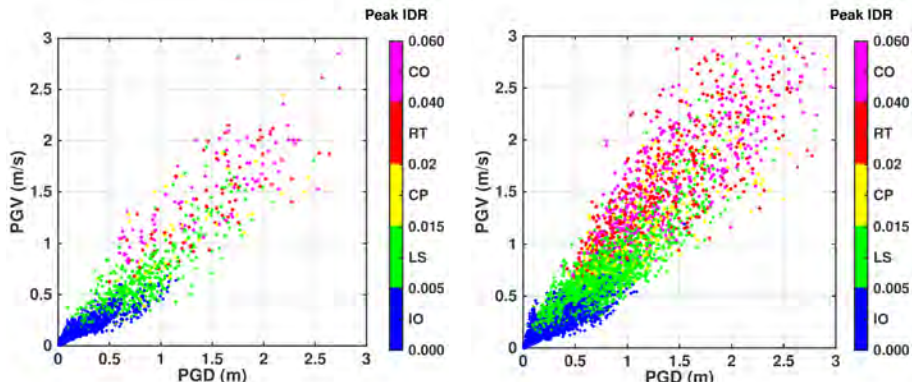
Figs. 5.18(a)-5.18(e) show the peak IDR in each of the 5 building models as a function of PGV and PGD from all earthquake scenarios. The approximate PGV and PGD thresholds for the

collapse of the 94S2 model are 0.6 m/s and 0.4 m, respectively. The corresponding thresholds for the 94S3 model are 0.75 m/s and 0.5 m, respectively; 0.8 m/s and 0.6 m, respectively, for the 97Sb model; 1.0 m/s and 0.6 m, respectively, for the 97Sc model; and 1.1 m/s and 0.75 m, respectively for the 97Sd model. A similar study by [Siriki et al. \(2015\)](#) found that the PGV and PGD threshold limits for collapse of the moment frame version of the 97Sb building model are 0.5 m/s and 0.5 m, respectively, suggesting that braced frame buildings may be better able to resist shaking from large San Andreas fault earthquakes.



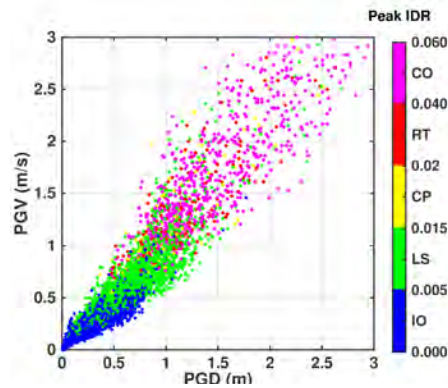
(a) 94S2 Model

(b) 94S3 Model



(c) 97Sb Model

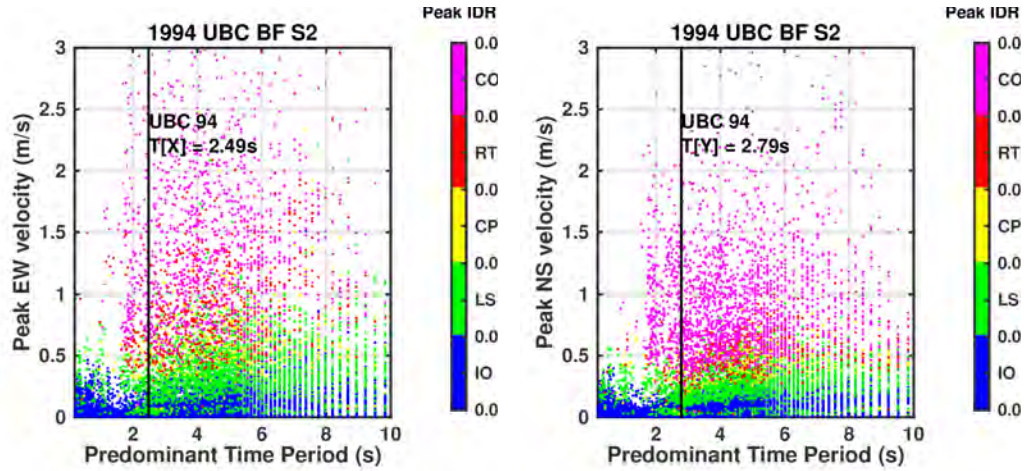
(d) 97Sc Model



(e) 97Sd Model

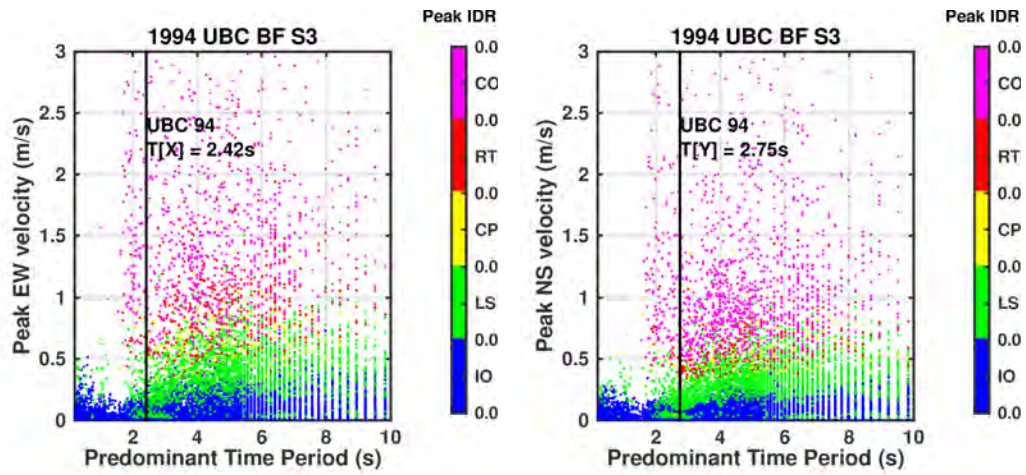
Figure 5.18: Peak IDR in the five building models as a function of the peak ground velocity and displacement of all scenario earthquake records. The magenta, red, yellow, green, and blue colors correspond to collapse imminent (CO), red-tagged (RT), collapse prevention (CP), life safety (LS), and immediate occupancy (IO) performance categories, respectively.

Figs 5.19(a)-5.19(d) and 5.20(a)-5.20(f) show the peak IDR as a function of directional predominant time period and directional peak ground velocities. The predominant time period of ground motion in a given direction is the period at which pseudovelocity (PSV) spectrum for that ground motion component peaks. It is quite clear from these figures that there is no risk for collapse to any of the five building models if PGV remains below 0.5 m/s in either principal direction of the building (note that in general buildings are provided with separate lateral-force resisting systems in the two orthogonal directions and the ground motion components should be strong enough to fail at least one of these two systems to induce building collapse). Another observation from the figures is that the predominant time period of ground motion must be close to or greater than the fundamental period of the building to induce collapse. This observation is similar to what was found to hold true for moment frame buildings by [Siriki et al. \(2015\)](#), the theoretical basis for which has been discussed by [Uang and Bertero \(1988\)](#) and [Krishnan and Muto \(2012\)](#).



(a) 94S2 Model - EW

(b) 94S2 Model - NS



(c) 94S3 Model - EW

(d) 94S3 Model - NS

Figure 5.19: Peak IDR as a function of directional PGV and predominant time period of ground motion from all scenario earthquake records: (a) E-W (X) direction of 94S2 design; (b) N-S (Y) direction of 94S2 design; (c) E-W (X) direction of 94S3 design; and (d) N-S (Y) direction of 94S3 design. The magenta, red, yellow, green, and blue colors correspond to collapse imminent (CO), red-tagged (RT), collapse prevention (CP), life safety (LS), and immediate occupancy (IO) performance categories, respectively. The black vertical lines correspond to the model fundamental period in the direction under consideration.

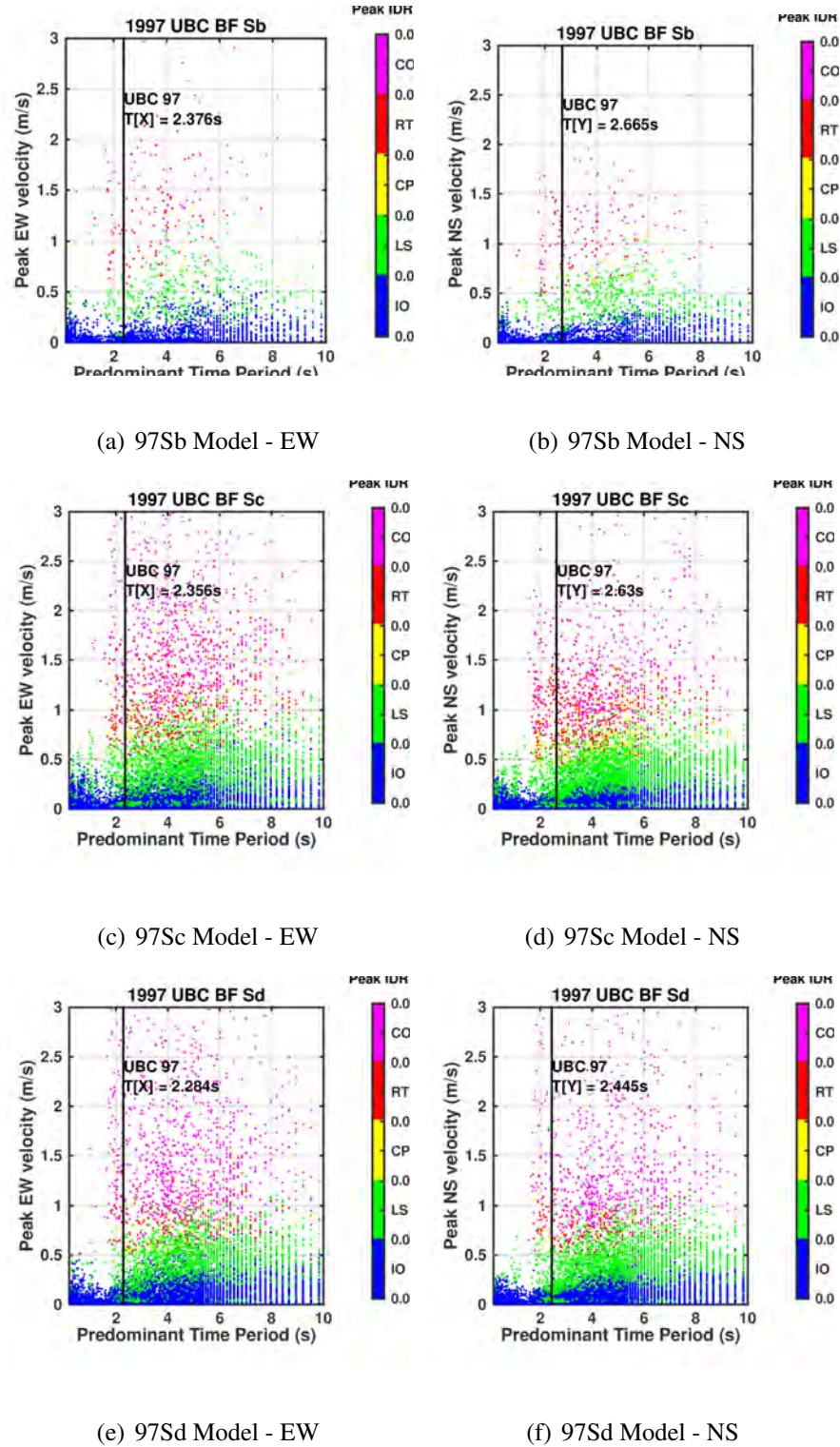
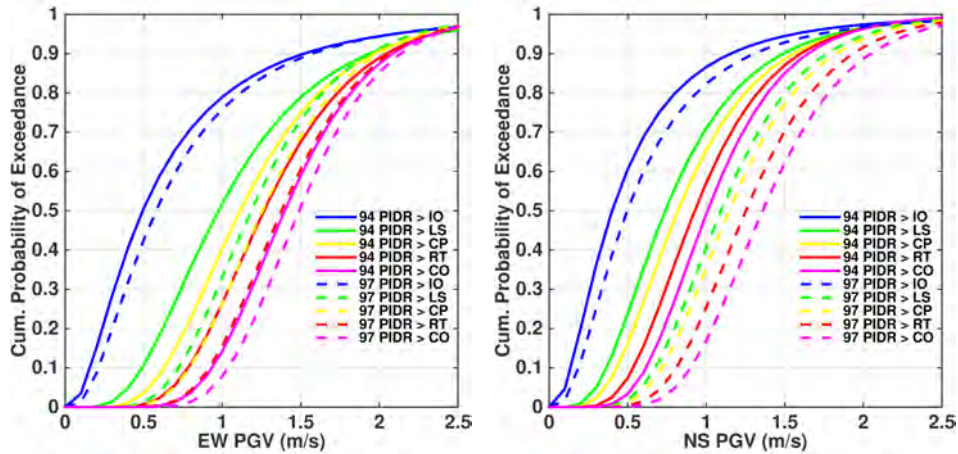


Figure 5.20: Peak IDR as a function of directional PGV and predominant time period of ground motion from all scenario earthquake records: (a) E-W (X) direction of 97Sb design; (b) N-S (Y) direction of 97Sb design; (c) E-W (X) direction of 97Sc design; (d) N-S (Y) direction of 97Sc design; (e) E-W (X) direction of 97Sd design; and (f) N-S (Y) direction of 97Sd design; The magenta, red, yellow, green, and blue colors correspond to collapse imminent (CO), red-tagged (RT), collapse prevention (CP), life safety (LS), and immediate occupancy (IO) performance categories, respectively. The black vertical lines correspond to the model fundamental period in the direction under consideration.

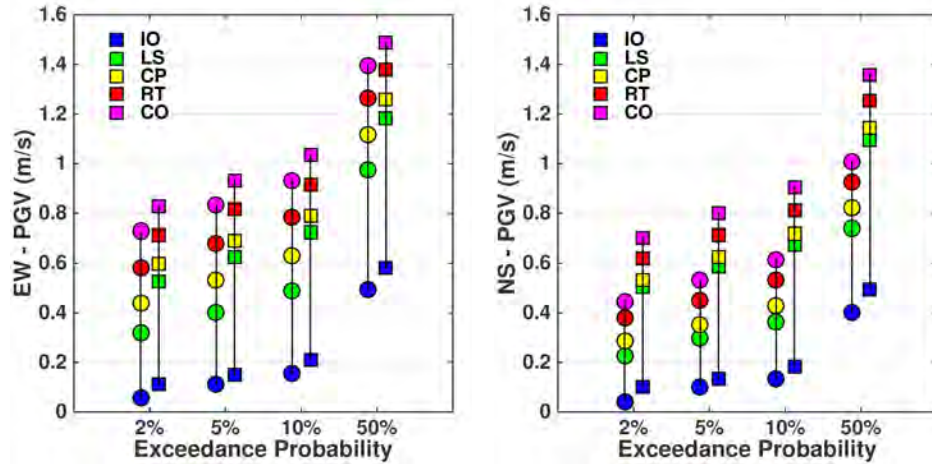
Figs. 5.21(a) and 5.21(b) show the fragility curves for the 94S3 and the 97Sd building models (these designs are applicable to a majority of the basin sites) as a function of the peak ground velocity in the EW and NS directions, respectively (for additional fragility curves see Appendix H). The curves represent the probability of exceeding the IO, LS, CP, RT, and CO performance levels at various levels of PGV. Figs. 5.21(c) and 5.21(d) are obtained by slicing Figs. 5.21(a) and 5.21(b), respectively, at 2%, 5%, 10%, and 50% probabilities to highlight the improvement in performance of the building code from 1994 to 1997. For example, the PGV threshold in north-south direction for a 50% probability of collapse is 1.0 m/s for the 1994 design, and 1.4 m/s for the 1997 design. Similar observations can be made for all exceedance probabilities and for all performance levels except for the IO which remains unchanged going for UBC 1994 to UBC 1997.

Both the 1994 and the 1997 UBC designs are more vulnerable in the NS direction as compared to the EW direction. Both designs are more flexible (longer periods) in the NS direction (Tab. 5.6) and the ground motion is rich in long-period (3 s to 6 s) content (Figs. 5.19(d) and 5.20(f)). The difference in the vulnerability of the two buildings in the NS direction is greater than that in the EW direction. Again, this is related to the fact that the difference in the periods of the two buildings in the NS direction (94S3: 2.75 s; 97Sd: 2.44 s) is greater than that in the EW direction (94S3: 2.42 s; 97Sd: 2.28 s). Recall that the differences in the periods in the two directions arise out of larger frame sizes in the EW direction necessitated by the torsional eccentricity due to asymmetric placement of the north frame and the need to control the IDR on the north face of the building.



(a)

(b)



(c)

(d)

Figure 5.21: Fragility curves of the probability of the peak IDR in the 94S3 (solid) and the 97Sd (dashed) buildings exceeding the IO, LS, CP, RT, and CO performance levels as a function of the PGV in the (a) E-W and the (b) N-S directions. (c) The E-W and (d) the N-S PGV thresholds for 2%, 5%, 10%, and 50% exceedance probabilities of various performance levels in the 94S3 (circles) and the 97Sd (squares) designs.

Figs. 5.22(a) and 5.22(b) show the building fragility curves as a function of spectral acceleration at the building fundamental period in EW and NS directions, respectively. The observations made

from the PGV-based fragilities hold true for the spectral acceleration-based fragilities as well. For example, at S_a of 0.5 g in the NS direction, the collapse probability drop from 52% for the 1994 UBC design to 29% for the 1997 UBC design (i.e., by a factor of 1.8).

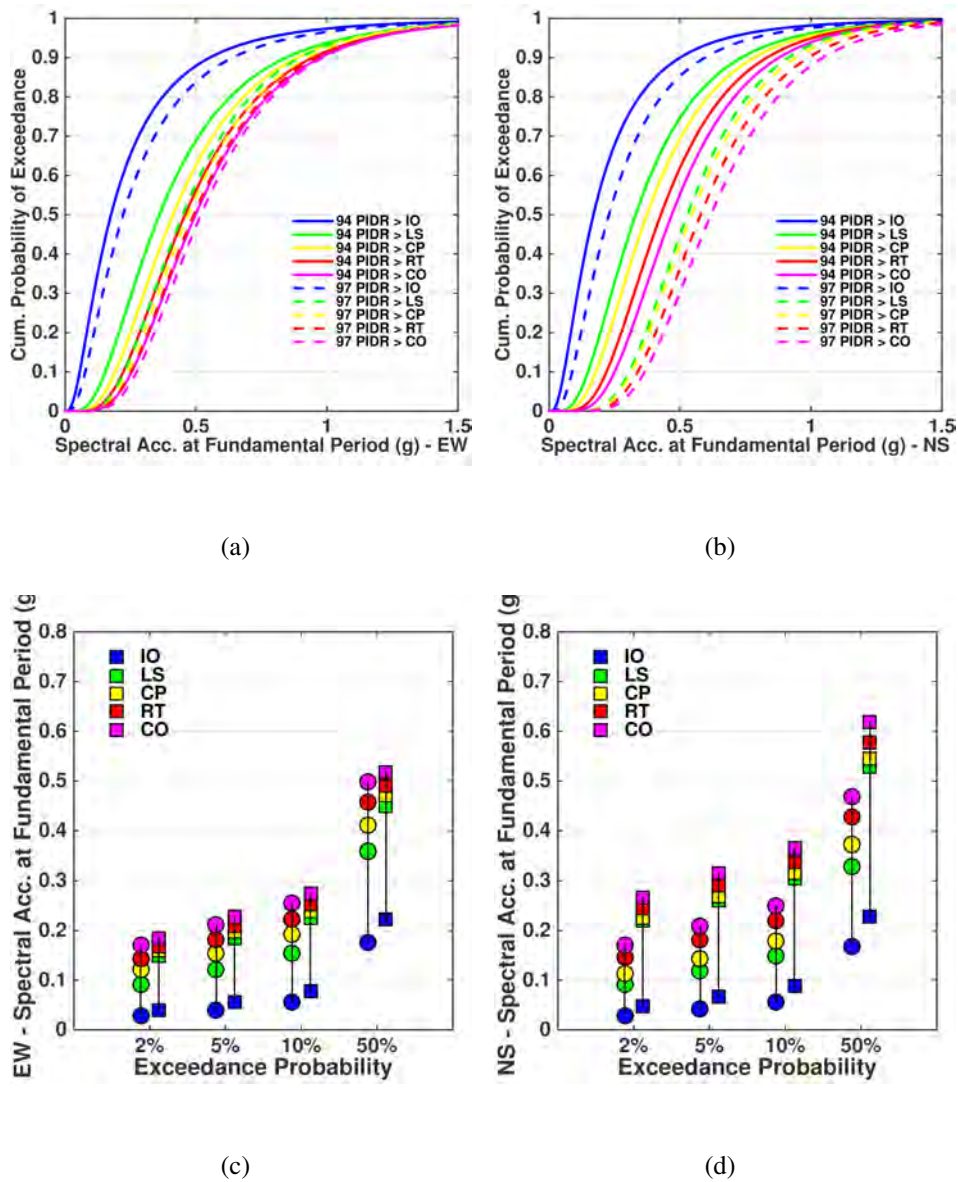


Figure 5.22: Fragility curves of the probability of the peak IDR in the 94S3 (solid) and the 97Sd (dashed) buildings exceeding the IO, LS, CP, RT, and CO performance levels as a function of the spectral acceleration at the building period in the (a) E-W and the (b) N-S directions. (c) The E-W and (d) the N-S S_a thresholds for 2%, 5%, 10%, and 50% exceedance probabilities of various performance levels in the 94S3 (circles) and the 97Sd (squares) designs.

5.9 30-Year Exceedance Probabilities of Various Performance Levels Using the PEER PBEE Framework

Hazard analysis, structural analysis, damage analysis, and loss analysis are the four steps in the performance based earthquake engineering (PBEE) framework (Porter 2003) developed by the Pacific earthquake Engineering Research (PEER) center. The rupture-to-rafters simulations of the scenario earthquakes along with the scenario earthquake probabilities determined earlier may be considered to constitute the hazard and structural analysis components. The engineering demand parameters, including peak IDR, from the rupture-to-rafters simulations, may be used for damage and loss analyses. However, we leave this for a follow-up study, and focus here instead on estimating the probability of exceedance of the IO, LS, CP, RT, and CO performance limit states in the 1994 and 1997 UBC designs under San Andreas fault earthquakes over the next 30 years.

The detailed procedure for this is documented in Siriki et al. (2015). The basic idea is to (i) extract from the rupture-to-rafters simulations, the probability density function $p(PGV|M_w, loc)$ of the peak ground velocity conditioned upon earthquake magnitude (M_w) and location (loc) and the probability of the peak IDR response of a given building exceeding a given limit state $P(IDR > Limit State|PGV)$, conditioned upon PGV [the PDFs corresponding to the CDFs in Figs. 5.21(a) and 5.21(b)]; (ii) multiply it by the probability of a given magnitude earthquake in the next 30 years $P(M_w/loc)$, conditioned upon location (from Tab. 5.2); (iii) integrate it over the entire range of PGVs; and (iv) sum over all earthquake magnitudes and all locations to arrive at the probability of the response of that building exceeding that performance limit state over the next 30

years $P(IDR > Limit State)$. Mathematically, this may be represented by Eq. 5.1.

$$P(IDR > Limit State) = \sum_{M_w} \sum_{loc} \int_{PGV} P(IDR > Limit State|PGV) p(PGV|M_w, loc) dPGV P(M_w, loc) \quad (5.1)$$

We use the ground motion intensity measure of peak ground velocity (PGV) in this formulation as [Uang and Bertero \(1988\)](#) have shown the input energy of seismic excitation into buildings to be proportional to the square of PGV and [Krishnan and Muto \(2012\)](#) have shown PGV to be reasonably well correlated with tall moment frame building response. The latter observation appears to hold true for the target braced frame buildings as well (Figs. 5.18, 5.19, and 5.20).

Tab. 5.8 lists the probability of exceedance of the performance limit states conditioned upon magnitude, obtained from Eq. 5.1 sans the first summation, that is, conditional on each discrete M_w value. It is clear that collapse probability (CO) for UBC94, as well as UBC97 designs, is insignificant for San Andreas fault earthquakes with magnitude less than about 7.3. Beyond this magnitude, the collapse probability of the 1997 UBC designs is about half of that of the 1994 designs. Although recent studies have pointed to the possibility of wall-to-wall ruptures on the southern San Andreas fault with magnitudes as high as 8.1 ([Akçiz et al. 2010](#)), seismologists would find it reasonable if an engineer uses a magnitude 7.89 to characterize the code maximum considered earthquake (MCE with a 2475-year return period) for the design of buildings in southern California. Under the scenario earthquakes of this magnitude, the probability of collapse for UBC94 designs is over 17%, more than the code intended limit of 10% probability of collapse ([ATC-63 2013](#)). The UBC97 designs, with a lower probability of collapse of about 7%, appear to better achieve the intent of the building code.

Tab. 5.9 lists the probability of exceedance of the performance limit states in the 1994 and 1997 UBC

M_w	IO		LS		CP		RT		CO	
	UBC94	UBC97								
7.89	51.82	49.69	32.21	20.85	27.67	16.90	21.88	11.63	17.23	7.21
7.59	19.27	18.01	10.14	5.22	8.49	4.17	6.09	3.12	4.64	2.34
7.28	2.88	2.24	0.46	0.16	0.34	0.09	0.21	0.05	0.10	0.04
6.92	0.67	0.52	0.04	0.00	0.01	-	-	-	-	-
6.58	0.51	0.41	0.08	0.02	0.04	-	-	-	-	-
6.00	-	-	-	-	-	-	-	-	-	-

Table 5.8: Conditional probability of exceedance (as percentage) of the IO, LS, CP, RT, and CO performance levels in the older (1994 UBC designs) and the newer (1997 UBC designs) braced frame buildings at the 636 southern California sites given a particular earthquake magnitude.

braced frame building designs under magnitude 6-8 earthquakes on the southern San Andreas fault over the next 30 years, determined using Eq. 5.1 in its full form. The probability of exceeding the CO performance limit in the 1994 UBC design in the next 30 years is about 3.34% whereas that in the 1997 design is about 1.71%. Both probabilities are significantly higher than the code intent of limiting the probability of collapse in the next 50 years to 2%. The exceedance probabilities for the FEMA CP level are about 5.0% and 3.2%, respectively, in the 1994 and 1997 UBC designs. It is clear that the 1997 UBC has been quite effective in lowering the collapse risk to the braced frame buildings. Moreover, we calculated the 30-year exceedance probabilities for Downtown Los Angeles, the region which is home to the largest cluster of the tall steel structures in southern California. The probability of exceeding CO limit state in the next 30 years in Downtown Los Angeles is 3.5 for the UBC 1994 and is 2.3 for the UBC 1997; even higher than the regional values listed in Tab. 5.9. An interesting point of comparison is that Siriki et al. (2015) found a probability of exceedance of the CP limit in the moment frame version of the 1997 UBC design to be 5.3%. Fig. 5.23 illustrates the contribution from each individual magnitude to the 30 year probability of exceedance of the performance limit states listed in Tab. 5.9. Majority of the probability of exceeding the LS, CP, RT, and CO levels solely comes from M_w 7.89 and M_w 7.59 earthquakes for both set of buildings and the lower and mid range earthquakes only contribute to the probability of exceedance of the IO limit states. This shows the

importance of the larger magnitude earthquakes on the overall regional seismic hazard.

	IO	LS	CP	RT	CO
UBC 1994	13.29	5.82	5.03	4.08	3.34
UBC 1997	11.86	3.76	3.22	2.36	1.71

Table 5.9: Total probability of exceedance of the IO, LS, CP, RT, and CO performance levels in the older (1994 UBC designs) and the newer (1997 UBC designs) braced frame buildings at the 636 southern California sites from earthquakes on the San Andreas fault in the next 30 years.

	IO	LS	CP	RT	CO
UBC 1994	13.71	6.11	5.46	4.34	3.48
UBC 1997	12.39	4.94	4.54	3.27	2.30

Table 5.10: Total probability of exceedance of the IO, LS, CP, RT, and CO performance levels in the older (1994 UBC designs) and the newer (1997 UBC designs) braced frame buildings at Downtown Los Angeles from earthquakes on the San Andreas fault in the next 30 years.

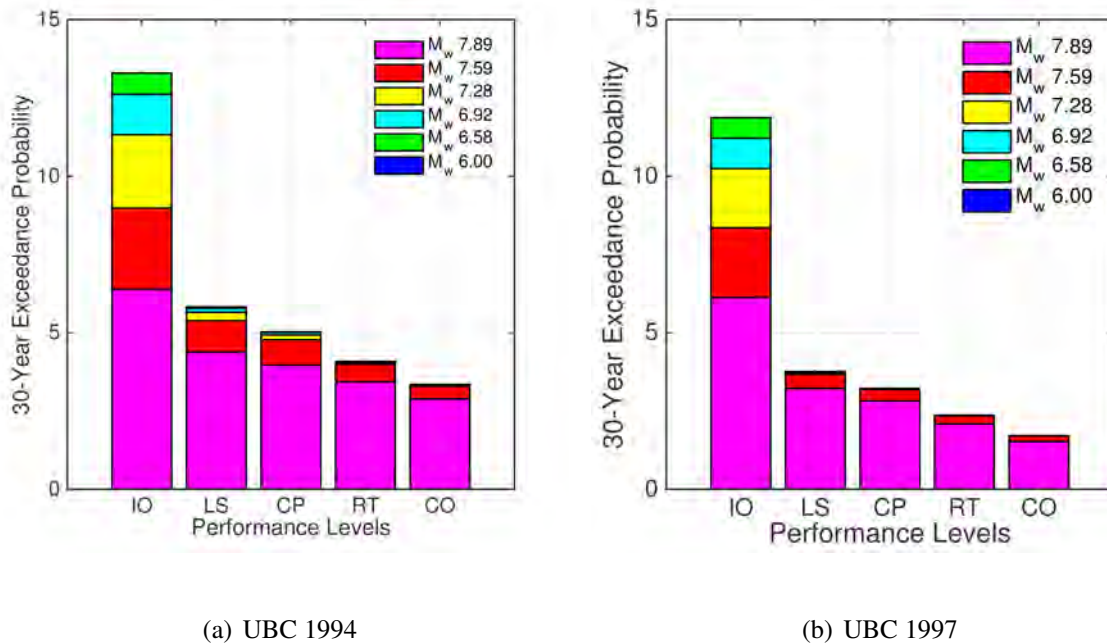


Figure 5.23: Contribution of different magnitudes to total probability of exceedance of the IO, LS, CP, RT, and CO performance levels of the braced frame building at the 636 southern California sites from earthquakes on the San Andreas fault in the next 30 years for: (a) the older 1994 UBC designs and (b) the newer 1997 UBC designs.

Chapter 6

Conclusions and Future Work

6.1 Conclusions

Rupture-to-rafters simulations of a carefully selected set of scenario earthquakes are used for quantitative probabilistic seismic risk analysis in a region. Presented in this work were the methodology and the results of ruptures-to-rafters simulations of 18-story tall steel braced frame buildings in southern California, subjected to sixty M_w 6-8 scenario earthquakes on the San Andreas fault. The buildings are designed according to the 1994 and 1997 Uniform Building Codes, based upon site-specific soil types at 636 sites in southern California.

First, we presented a method to derive scenario earthquake probabilities from Uniform California Earthquake Rupture Forecast (UCERF) model. The approach involved binning the forecast earthquakes based on magnitude and redistributing the probabilities of the forecast earthquakes in each bin to the scenario earthquake(s) of that bin. For this, the yearly rates of occurrence of the forecast earthquakes were converted to seismic moment release rates that were then deaggregated to the segments comprising these ruptures. The seismic moment rate contributions to each segment from all forecast earthquakes in a given magnitude bin were summed and assigned to the nearest scenario earthquake rupture. The total seismic moment rate assigned to a scenario earthquake was then converted back into a yearly rate based on the scenario earthquake

magnitude and substituted into a Poisson probability model to arrive at its occurrence probability over a specific period (30 years). The method, by construction, resolves a couple of commonly-encountered problems in scenario-earthquake based PSHA discussed in Chapter 2.

The broadband ground motions were then generated using a hybrid method, simulating low frequency synthetics using the spectral element approach and high frequency synthetics using a new empirical Green's function (EGF) approach.

We successfully presented a simple, intuitive, and effective method for generating broadband ground motions for engineering applications by superimposing long-period (> 2 s) waveforms from spectral element simulations with high-frequency waveforms from an empirical Green's function approach.

The key advancement here, pertaining to the EGF approach, were a modified summing strategy, that alleviates the over-estimation of high-frequency ground motions in current EGF-based ground motion simulation methods. We successfully used relatively lower magnitude EGFs recorded at larger distances for generating high-frequency ground motions compared to previous methods.

However, we should point out that results remain sensitive to many contributing factors, including rupture velocities in kinematic source models from inversions, the resolution of these source models, as well as the number and nature of the selected EGFs. EGF features affecting the synthetics include absolute magnitude, magnitude relative to the target event, local site characteristics, signal quality, etc. Further studies are needed to quantify the effects of these factors and establish the limits and applicability of the EGF approach to ground motion prediction. Additionally, it should be noted that the nonlinear soil behaviors were beyond the scope of this study and were not taken into consideration in these simulations. Nonlinear behavior of the soil can have significant effects on ground motions, specially on high intensity ground motions observed during large earthquakes.

The ground motions from 60 scenario earthquakes were then used for the 3-D nonlinear analysis of

the target buildings. The results were incorporated into the PEER performance earthquake engineering framework to estimate the probability of exceedance of various performance limit states in the designs due to San Andreas fault earthquakes in the next 30 years. The following observations were made:

- PGVs, S_a^{1s} , and S_a^{3s} from the simulated ground motions are significantly greater than those predicted by the Campbell-Bozorgnia NGA relations. The reverse is true for PGD.
- Performance of the buildings is classified using the FEMA performance levels of IO, LS, and CP, and two additional categories for red-tagging (RT) and partial/complete collapse (CO). It is found that the 1997 UBC designs consistently out-perform the 1994 designs and are better capable of handling the MCE level ground motions.
- The probabilities of exceedance of both CO (1994 UBC: 3.34%, 1997 UBC: 1.71%) and CP (1994 UBC: 5.03%, 1997 UBC: 3.22%) limit states over the next 30 years due to San Andreas earthquakes are significantly higher for both 1994 and 1997 UBC designs when compared against the code intent of limiting the probability of collapse over the next 50 years to under 2%. The braced frame buildings appear to out-perform the corresponding moment frame versions. [Siriki et al. \(2015\)](#) found a probability of exceedance of CP limit in the moment frame version of the 1997 UBC to be 5.3%. It should also be noted that these probabilities will only increase as more faults are considered in the analysis.

6.2 Future Work

1. In this study a single source model was used for a given earthquake magnitude. [Siriki et al. \(2015\)](#) used five stochastically generated source models for a given earthquake magnitude. An interesting question to investigate would be, "what is the number of source models needed to realistically capture the variability of sources and the resulting variability in the ground motions?" The variation in

source models may have to do with location and size of slip asperities, rupture propagation direction (including bilateral propagation), rupture speeds, source time functions, subfault discretization, etc.

2. Another interesting question that may be investigated is "what are the features in the source that lead to the generation of high and low frequency ground motions?"
3. The empirical Green's function approach proposed here was validated for far-field ground motions. Further investigations are needed to evaluate the proposed methodology and possibly modify this methodology to be applicable to near-field simulations.
4. This study is limited to earthquakes on the San Andreas fault. When assessing the performance of structures, seismic risk from all regional faults must of course be considered. Future work may involve broadening the scope of this study by considering earthquakes on the north-south trending San Jacinto, the Elsinore, and the Newport Inglewood faults, and the east-west trending Santa Monica-Hollywood-Raymond, the Sierra Madre, and the Puente Hills faults.
5. The probabilities for the scenario earthquakes in this study are time-independent, i.e., the assigned 30-year probability of a given magnitude event is applicable to any period of 30 years without consideration to the time elapsed from the last seismic event of comparable magnitude on the fault. It would be interesting, and perhaps, important to consider time-dependent probabilities, especially for faults such as the San Andreas where the return period of large earthquakes is of the order of only 150-300 years.
6. The building sample size in this study is quite small, just five designs all with the same geometry and function. Future studies may involve conducting such simulations on a larger number and types of existing buildings to characterize region-wide risk.

7. Perfect member connections were assumed in the nonlinear response analysis of the building models.
As observed during the Northridge earthquake, connection fractures can have significant effect on the building response. Future investigations may take into account the fracture of brace connections and their effects on the overall response of the structure.
8. Inclusion of foundation models and soil-structure interactions were beyond the cope of this study.
It would be important to include a model for the building foundation and to study the soil-structure interaction.
9. The study here was limited to building performance characterization. An important undertaking would be to conduct damage analysis and loss analysis (including repair/replacement costs and business interruption costs associated with the down-time for repairs).

Appendix A

Resampling Calculations

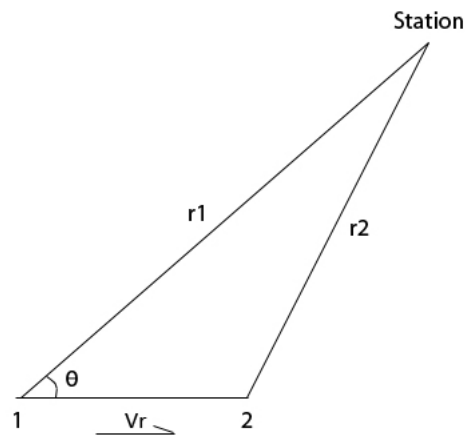


Figure A.1: Resampling Calculation

Calculation for resampled sub-fault dimension (Ref. (Stein and Wysession 2003)).

1. ΔX : Length of the sub-fault, or the distance between two sub-faults
2. ΔT : Difference between the arrival times of the impulses from 2 sub-faults to our station
3. r_1 : Distance from sub-fault 1 to station A (Figure A.1)
4. t_1 : Arrival of the wave from sub-fault 1 to station A
5. r_2 : Distance from sub-fault 2 to station B (Figure A.1)

6. t_2 : Arrival of the wave from sub-fault 2 to station A

7. V_R : Rupture velocity (Figure A.1)

8. V : Seismic wave velocity

9. Rupture Directivity: from station 1 to 2

10. θ : angle of between the station 1 and station

The ΔT can be calculated from the difference between the arrival times.

$$t_1 = \frac{r_1}{V} \quad (\text{A.1})$$

$$t_2 = \frac{r_2}{V} + \frac{L}{V_R} \quad (\text{A.2})$$

$$\Delta T = t_2 - t_1 = \frac{r_2}{V} + \frac{L}{V_R} - \frac{r_1}{V} \quad (\text{A.3})$$

$$r_2^2 = r_1^2 + L^2 - 2r_1 \cos \theta \rightarrow r \gg L \Rightarrow r_2 \approx r_1 - L \cos \theta \quad (\text{A.4})$$

$$\Delta T = t_2 - t_1 = \frac{L}{V} \left(\frac{V}{V_R} - \cos \theta \right) \quad (\text{A.5})$$

The worst case can be for $\theta = 180$ (station located upstream from the directivity), and will result to the

smallest sub-fault dimensions. Re-arranging for $\theta = 180$ and L we will have:

$$L = \frac{VV_R\Delta T}{V + V_r} \quad (\text{A.6})$$

Assuming that for a 2 sec waves 5 samples are needed per wave length or in other words one sample every 0.4 sec which means $\Delta T = 0.4$. For a typical lower range for rupture velocity of 2.5 km per second and shear wave velocity of about 3 km/sec the resulting resolution is 0.54 km:

$$L = \frac{VV_R\Delta T}{V + V_r} = \frac{(2.5)(3)(0.4)}{2.5 + 3} = 0.54km \quad (\text{A.7})$$

Appendix B

Bias in synthetics associated with S_a

The error $e_i(T)$ in the station i 5%-damped response spectral acceleration S_a at a period T is computed as [\(Graves and Pitarka 2010\)](#):

$$e_i(T) = \ln[S_a^{(obs-i)}(T)] - \ln[S_a^{(sim-i)}(T)] \quad (\text{B.1})$$

Bias in the synthetics at a given T is the average of the prediction errors at N stations for that time period:

$$b_i(T) = \frac{1}{N} \sum_{i=1}^N e_i(T) \quad (\text{B.2})$$

Standard deviation of the bias is:

$$\sigma_{bias}(T) = \left\{ \frac{1}{N} \sum_{i=1}^N [e_i(T) - b_i(T)]^2 \right\}^{\frac{1}{2}}$$

Appendix C

List of stations

Station Number	Latitude	Longitude	Station Name	Abbreviation
1	34.68708	-118.29946	Antelope	ALP
2	35.26930	-116.07030	Baker	BKR
3	34.68224	-118.57398	Burnt Peak	BTP
4	34.33341	-118.02585	Chilao Flat Rngr. Sta.	CHF
5	33.40190	-118.41502	Catalina Island Airport	CIA
6	34.06020	-117.80900	Cal Poly Pomona	CPP
7	33.93597	-116.57794	Devers	DEV
8	33.65001	-117.00947	Domenigoni Reservoir	DGR
9	34.10618	-118.45505	Donna Jones Jenkins	DJJ
10	34.88303	-117.99106	Edwards Air Force Base	EDW
11	35.08200	-117.58267	Federal Prison Camp	FPC
12	34.11816	-118.30024	Griffith Observatory	GR2
13	35.98230	-117.80760	Joshua Ridge	JRC
14	34.36560	-117.36683	Lugo	LUG
15	34.00460	-117.56162	Mira Loma Substation	MLS
16	36.05799	-117.48901	Manuel Prospect Mine	MPM
17	34.22362	-118.05832	Mount Wilson Obsv.	MWC
18	34.14844	-118.17117	White Mtn. Res. Sta. - Crooked Creek	S08C
19	33.35361	-116.86265	Palomar	PLM
20	33.79530	-117.60906	Pleasants Peak	PLS
21	33.74346	-118.40412	Rancho Palos Verdes	RPV
22	33.97327	-117.32674	Riverside Surface	RSS
23	34.05073	-118.08085	Rush	RUS
24	33.99351	-117.37545	Riverside	RVR
25	34.23240	-117.23484	Strawberry Peak	BPX
26	33.55259	-117.66171	Saddleback	SDD
27	35.89953	-116.27530	Shoshone	SHO
28	34.01438	-118.45617	Santa Monica Fire Station	SMS
29	34.41600	-118.44900	Solamint	SOT
30	34.38203	-117.67822	Table Mountain	TA2
31	33.63495	-116.16402	Thermal Airport	THX
32	34.48364	-118.11783	Vincent Substation	VCS

Table C.1: List of stations, latitude, longitude, name, and SCEC's abbreviation whose data is used for the 1999 Hector Mine earthquake simulation.

Station Number	Latitude	Longitude	Station Name	Abbreviation
1	34.687080	-118.29946	Antelope	ALP
2	35.126900	-118.83009	Arvin	ARV
3	35.344440	-119.10445	Calstate Bakersfield	BAK
4	36.550400	-117.80295	Cerro Gordo	CGO
5	34.333410	-118.02585	Chilao Flat Rangr. Station	CHF
6	35.815740	-117.59751	China Lake	CLC
7	34.136240	-118.12705	Caltech Robinson Pit	CRP
8	36.439880	-118.08016	Cottonwood Creek	CWC
9	34.253530	-118.33383	Green Verdugo Microwave Site	DEC
10	34.106180	-118.45505	Donna Jones Jenkins	DJJ
11	34.728320	-119.98803	Figueroa Mountain	FIG
12	34.176430	-118.35967	North Hollywood	HLL
13	35.662780	-118.47403	Isabella	ISA
14	35.982490	-117.80885	Joshua Ridge: China Lake	JRC2
15	34.000330	-118.37794	La Cienega	LCG
16	34.735510	-120.27996	Los Alamos County Park	LCP
17	34.305290	-118.48805	Los Angeles Filtration Plant	LFP
18	34.108190	-119.06587	Laguna Peak	LGU
19	34.807620	-118.86775	Lone Juniper Ranch	LJR
20	35.479540	-117.68212	Laurel Mtn Radio Fac	LRL
21	34.534120	-120.17737	Nojoqui County Park	NJQ
22	34.614500	-118.72350	Osito Audit: Castaic Lake Dam	OSI
23	34.148440	-118.17117	White Mtn. Res. Sta. - Crooked Creek	S08C
24	34.441990	-118.58215	Pardee	PDE
25	33.962730	-118.43702	Playa Del Rey	PDR
26	35.407730	-120.54556	Park Hill	PHL
27	36.305230	-119.24384	Rector	RCT
28	34.440760	-119.71492	Santa Barbara	SBC
29	33.480460	-119.02986	Santa Barbara Island	SBI
30	33.995430	-119.63510	Santa Cruz Island 2	SCZ2
31	34.436920	-119.13750	Summit Elementary School	SES
32	35.314200	-119.99581	Simmler	SMM
33	34.014380	-118.45617	Santa Monica Fire St	SMS
34	33.247870	-119.52437	San Nicolas Island	SNCC
35	34.059330	-118.64614	Saddle Peak Fire Camp 8	SPF
36	36.135500	-118.81099	Springville	SPG
37	34.303020	-119.18676	Santa Clara	STC
38	34.527750	-119.97834	Santa Ynez Peak	SYP
39	35.291300	-118.42079	Cattani Ranch	TEH
40	35.145920	-119.41946	Taft Base	TFT
41	34.156070	-118.82039	Thousand Oaks Ventura	TOV
42	34.483640	-118.11783	Vincent Substation	VCS
43	35.840890	-119.08469	Vestal	VES
44	35.536640	-118.14035	Bird Spring	WBS
45	34.510850	-119.27407	Wheeler Gorge Ranger Station	WGR
46	34.171700	-118.64971	West Side Station	WSS

Table C.2: List of stations, latitude, longitude, name, and SCEC's abbreviation whose data is used for the 2004 Parkfield earthquake simulation.

Appendix D

EGF methodology validation: 1999 Hector Mine earthquake

Figure [D.1](#) illustrates the location of each station, epicenter location of the 1999 Hector Mine earthquake, surface projection of the fault rupture extend, and the surface projection of the San Andreas fault. Figures [E.2](#) - [E.33](#) compare the low-frequency, high-frequency, and broadband synthetic seismograms (red) at 32 stations against observations (black) from the 1999 Hector Mine earthquake. Also, compared are the corresponding Fourier spectra in the 0.1 – 5.0 Hz frequency band. Station ID and location are listed in Table [D.1](#).

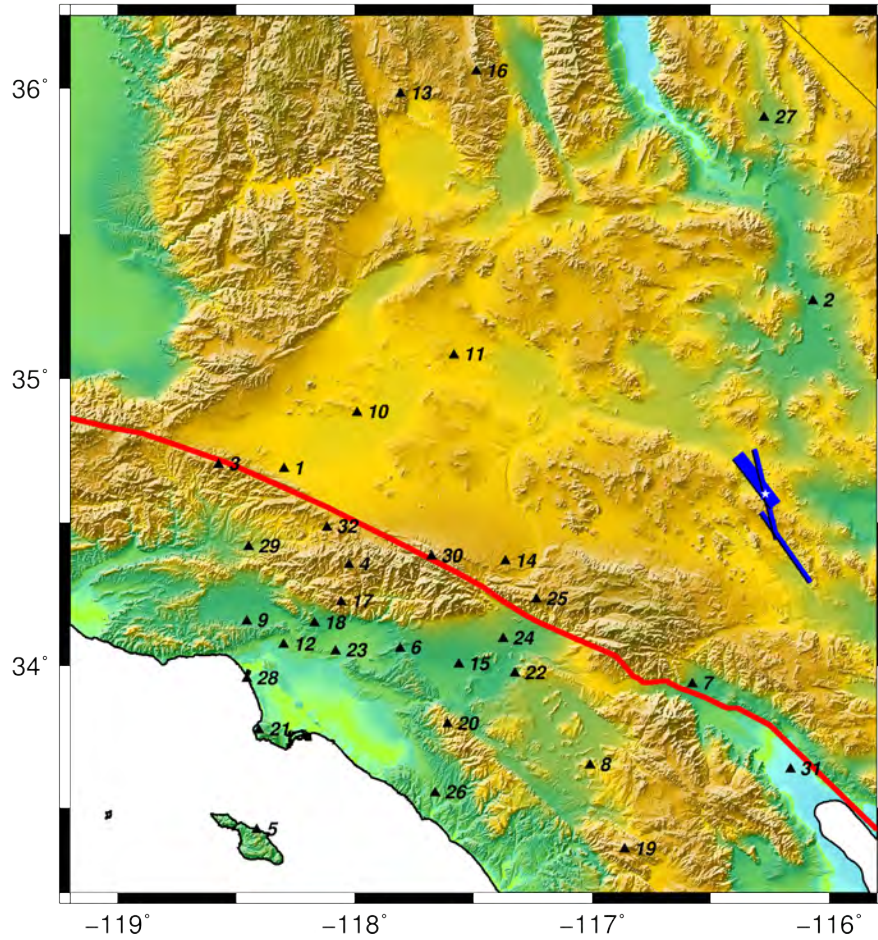


Figure D.1: Location of all stations used in validation of the 1999 Hector Mine earthquake. Red line: San Andreas Fault; Black line: trace/surface projection of earthquake source model; Star: epicenter; Black triangles: stations

Station Number	Latitude	Longitude	Station Name	Abbreviation
1	34.68708	-118.29946	Antelope	ALP
2	35.26930	-116.07030	Baker	BKR
3	34.68224	-118.57398	Burnt Peak	BTP
4	34.33341	-118.02585	Chilao Flat Rngr. Sta.	CHF
5	33.40190	-118.41502	Catalina Island Airport	CIA
6	34.06020	-117.80900	Cal Poly Pomona	CPP
7	33.93597	-116.57794	Devers	DEV
8	33.65001	-117.00947	Domenigoni Reservoir	DGR
9	34.10618	-118.45505	Donna Jones Jenkins	DJJ
10	34.88303	-117.99106	Edwards Air Force Base	EDW
11	35.08200	-117.58267	Federal Prison Camp	FPC
12	34.11816	-118.30024	Griffith Observatory	GR2
13	35.98230	-117.80760	Joshua Ridge	JRC
14	34.36560	-117.36683	Lugo	LUG
15	34.00460	-117.56162	Mira Loma Substation	MLS
16	36.05799	-117.48901	Manuel Prospect Mine	MPM
17	34.22362	-118.05832	Mount Wilson Obsv.	MWC
18	34.14844	-118.17117	White Mtn. Res. Sta. - Crooked Creek	S08C
19	33.35361	-116.86265	Palomar	PLM
20	33.79530	-117.60906	Pleasants Peak	PLS
21	33.74346	-118.40412	Rancho Palos Verdes	RPV
22	33.97327	-117.32674	Riverside Surface	RSS
23	34.05073	-118.08085	Rush	RUS
24	33.99351	-117.37545	Riverside	RVR
25	34.23240	-117.23484	Strawberry Peak	BPX
26	33.55259	-117.66171	Saddleback	SDD
27	35.89953	-116.27530	Shoshone	SHO
28	34.01438	-118.45617	Santa Monica Fire Station	SMS
29	34.41600	-118.44900	Solamint	SOT
30	34.38203	-117.67822	Table Mountain	TA2
31	33.63495	-116.16402	Thermal Airport	THX
32	34.48364	-118.11783	Vincent Substation	VCS

Table D.1: List of stations (and their location) for the 1999 Hector Mine earthquake.

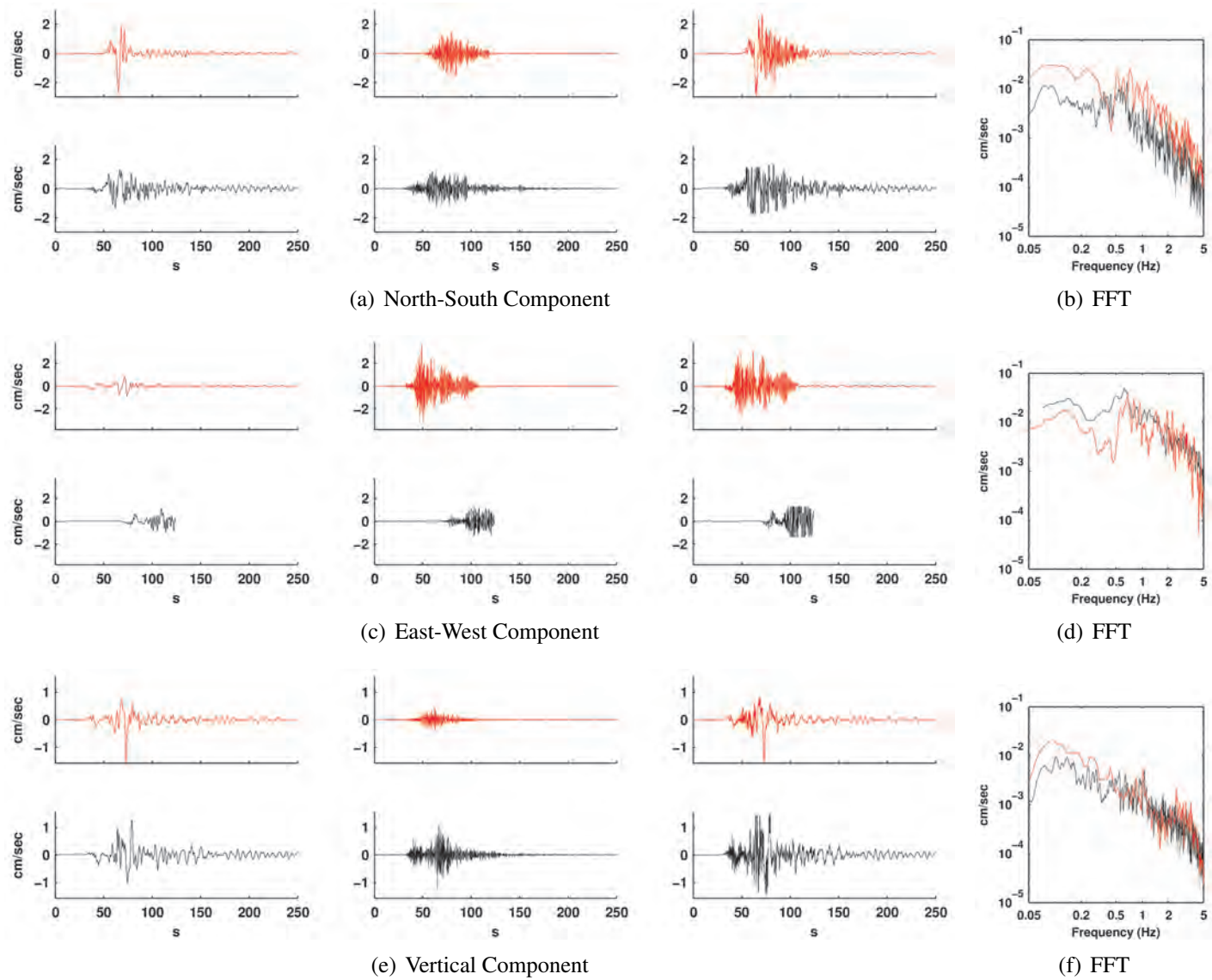


Figure D.2: Comparison of simulated (red) and observed (black) ground motions at station 1.

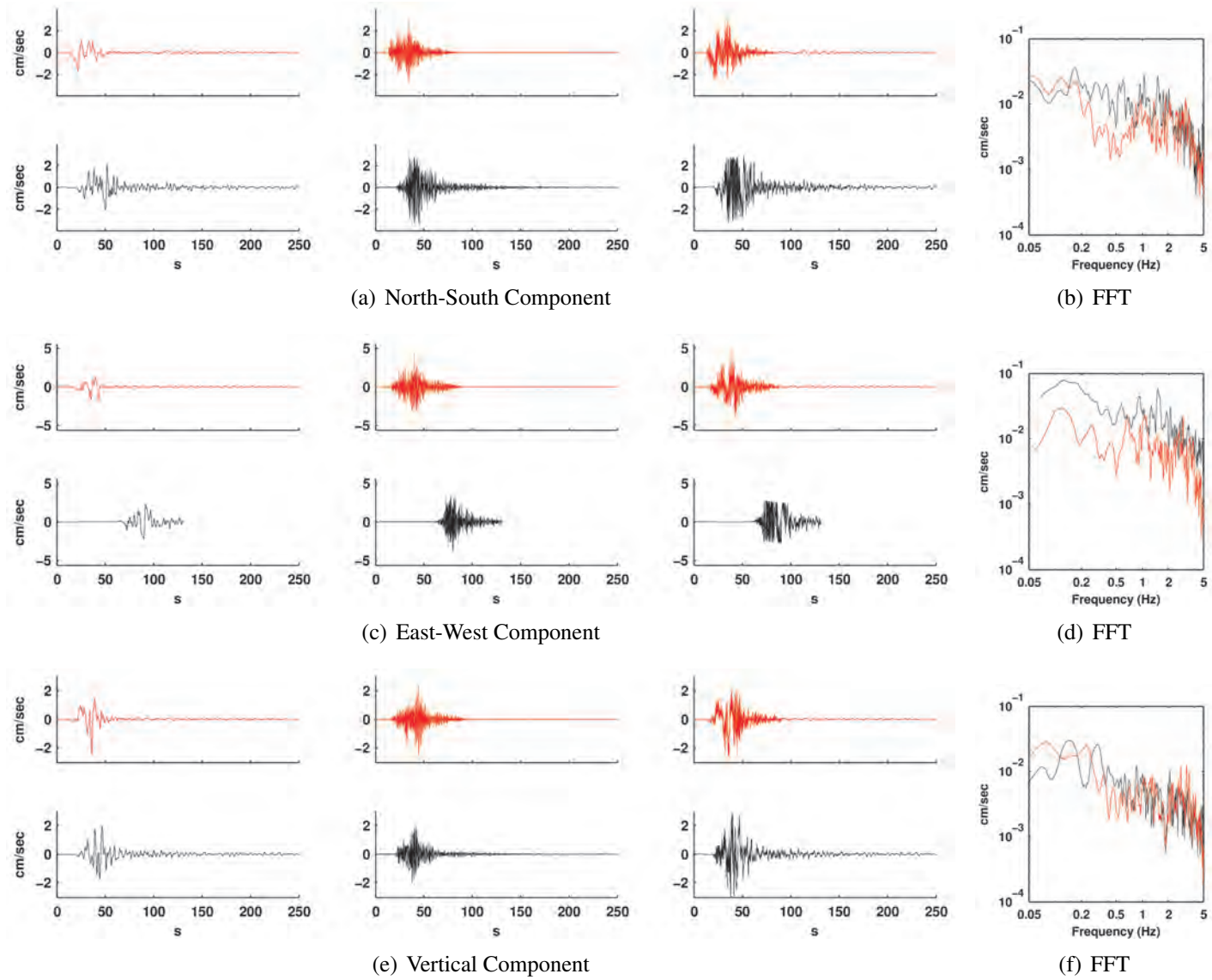


Figure D.3: Comparison of simulated (red) and observed (black) ground motions at station 2.

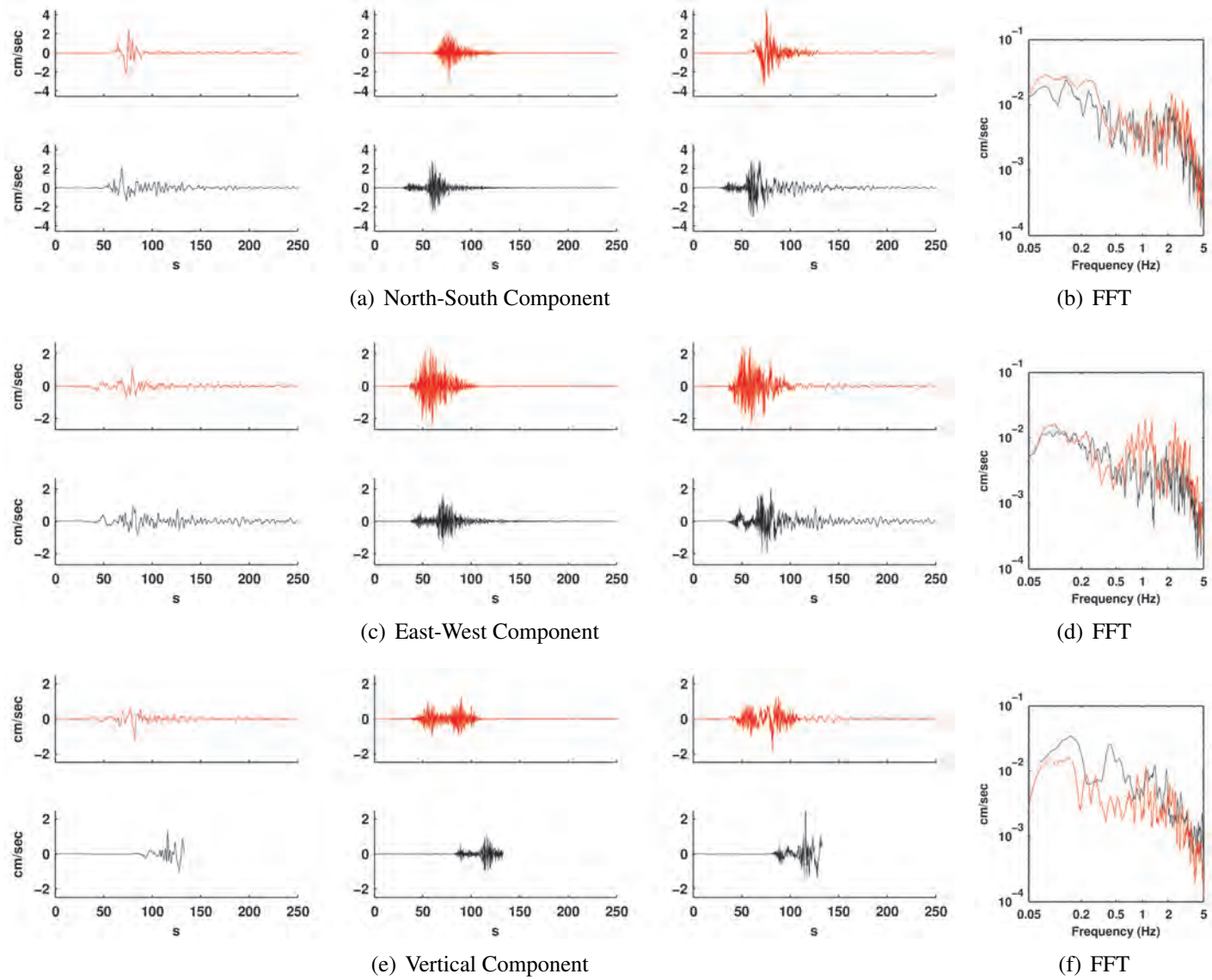


Figure D.4: Comparison of simulated (red) and observed (black) ground motions at station 3.

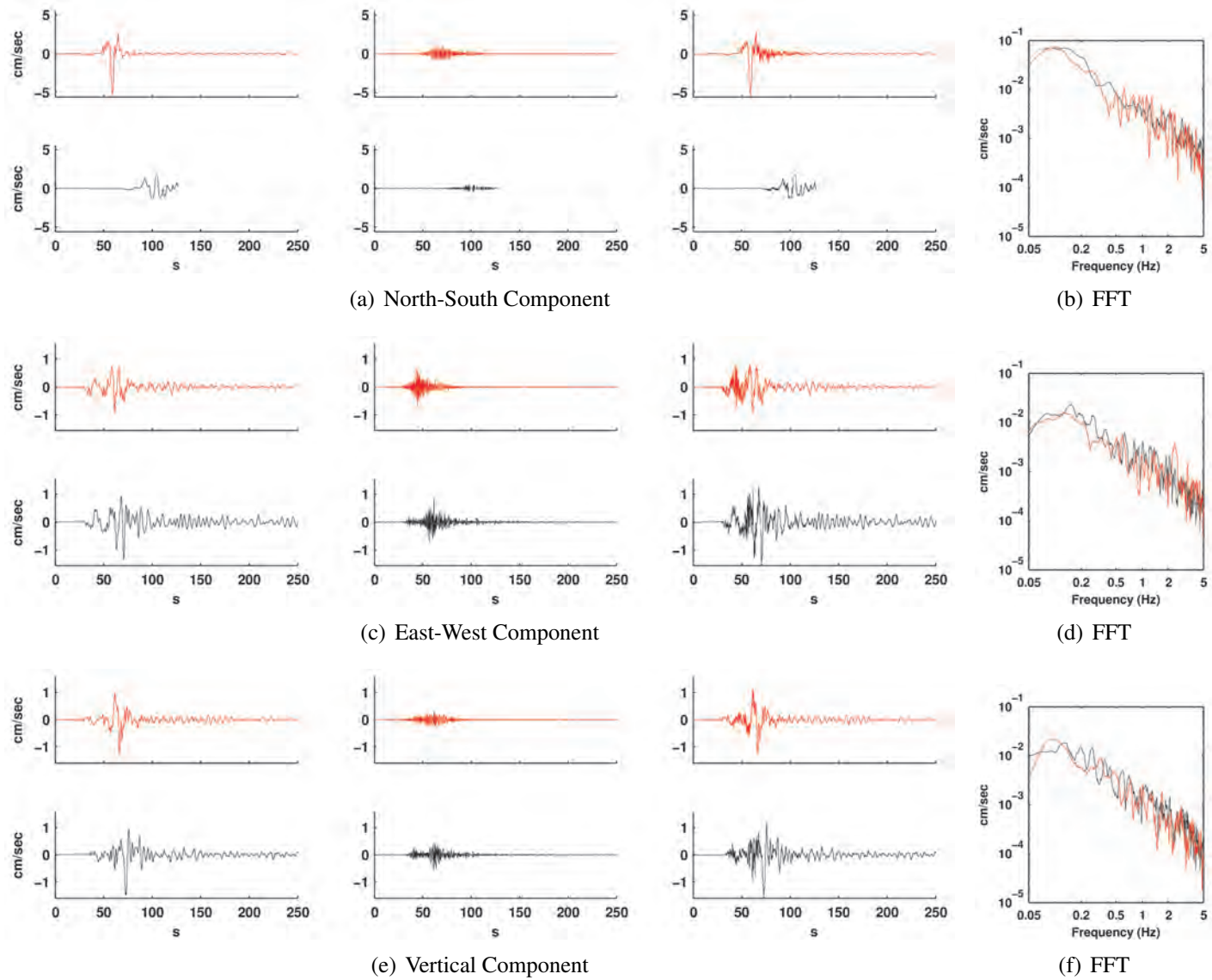


Figure D.5: Comparison of simulated (red) and observed (black) ground motions at station 4.

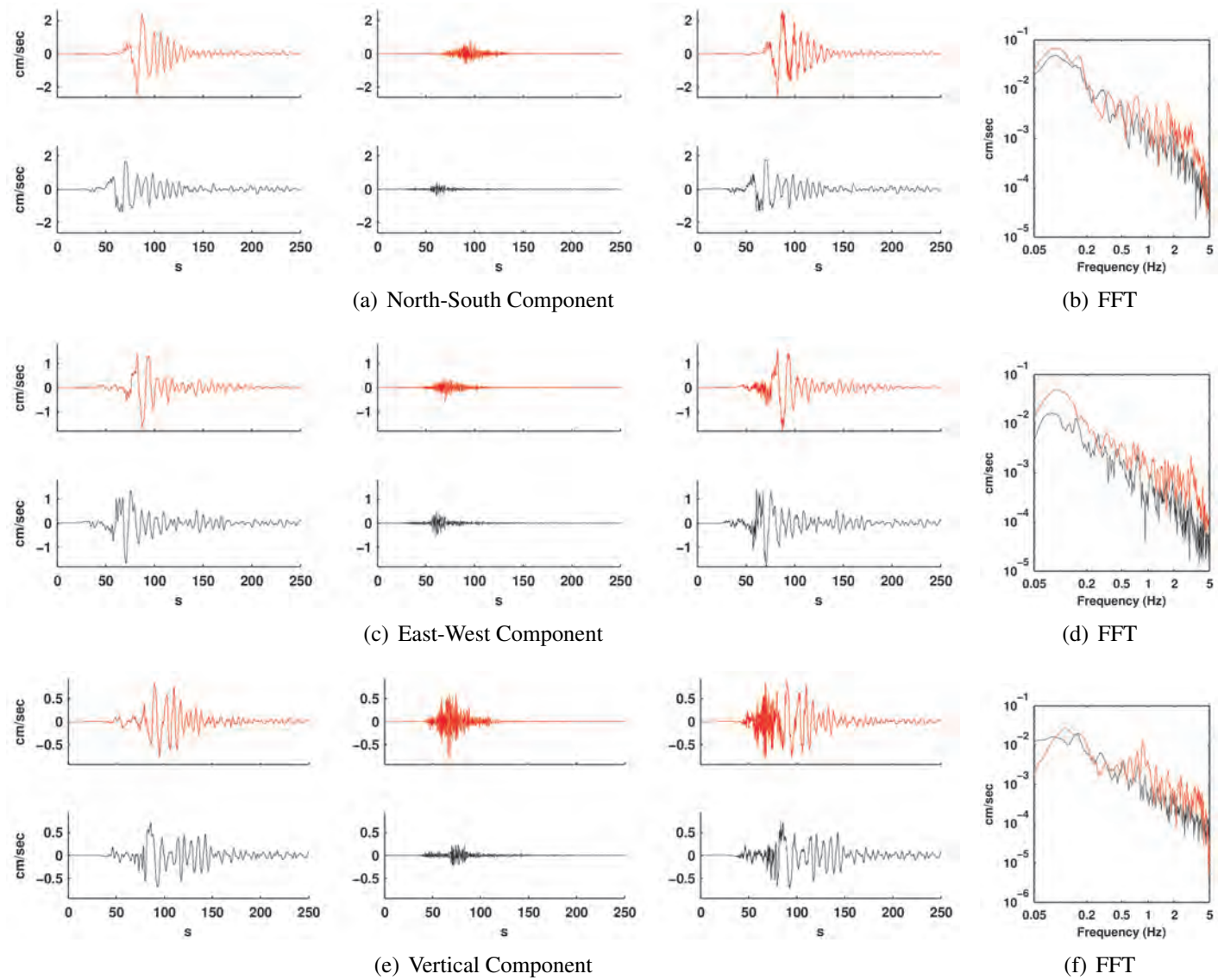


Figure D.6: Comparison of simulated (red) and observed (black) ground motions at station 5.

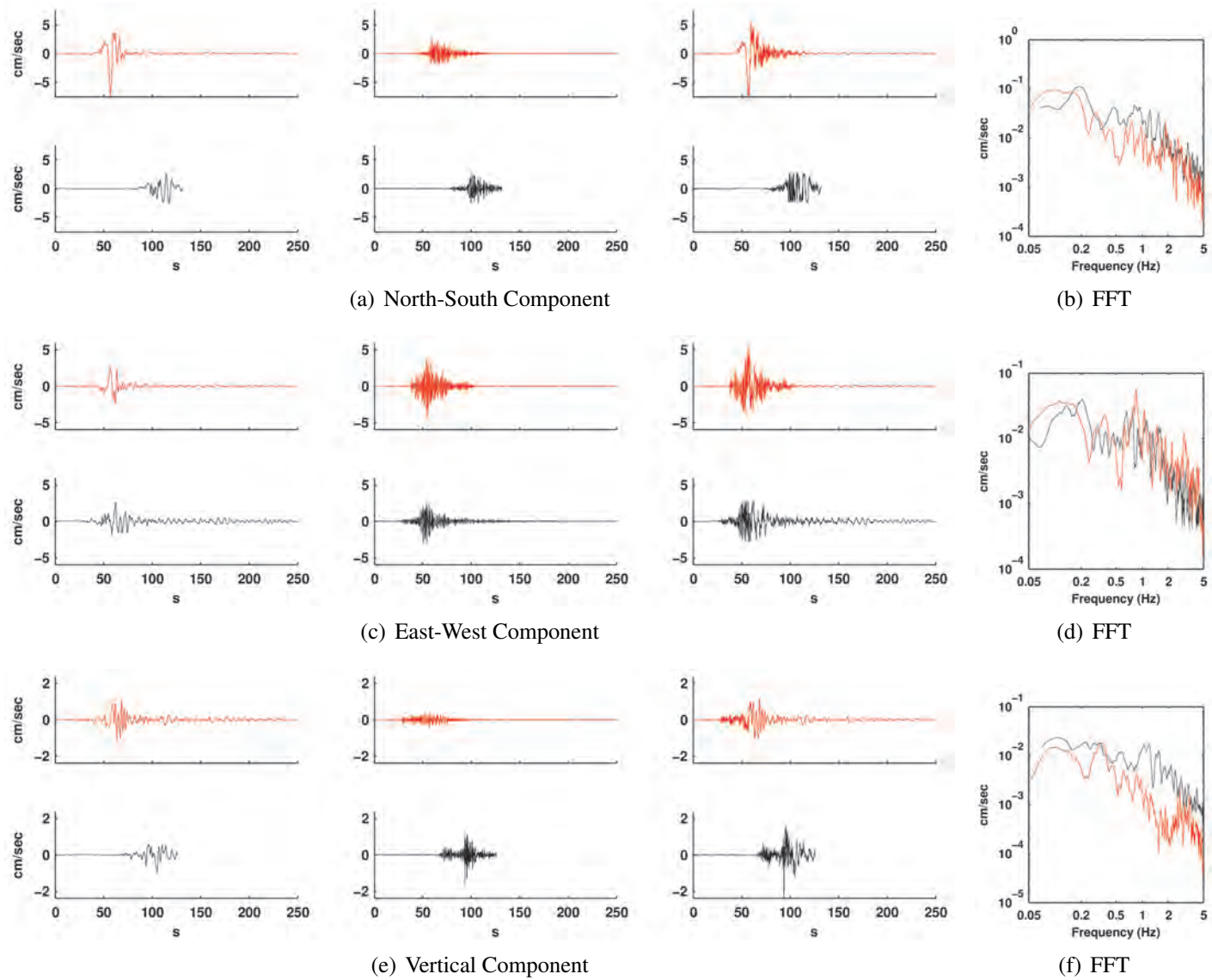


Figure D.7: Comparison of simulated (red) and observed (black) ground motions at station 6.

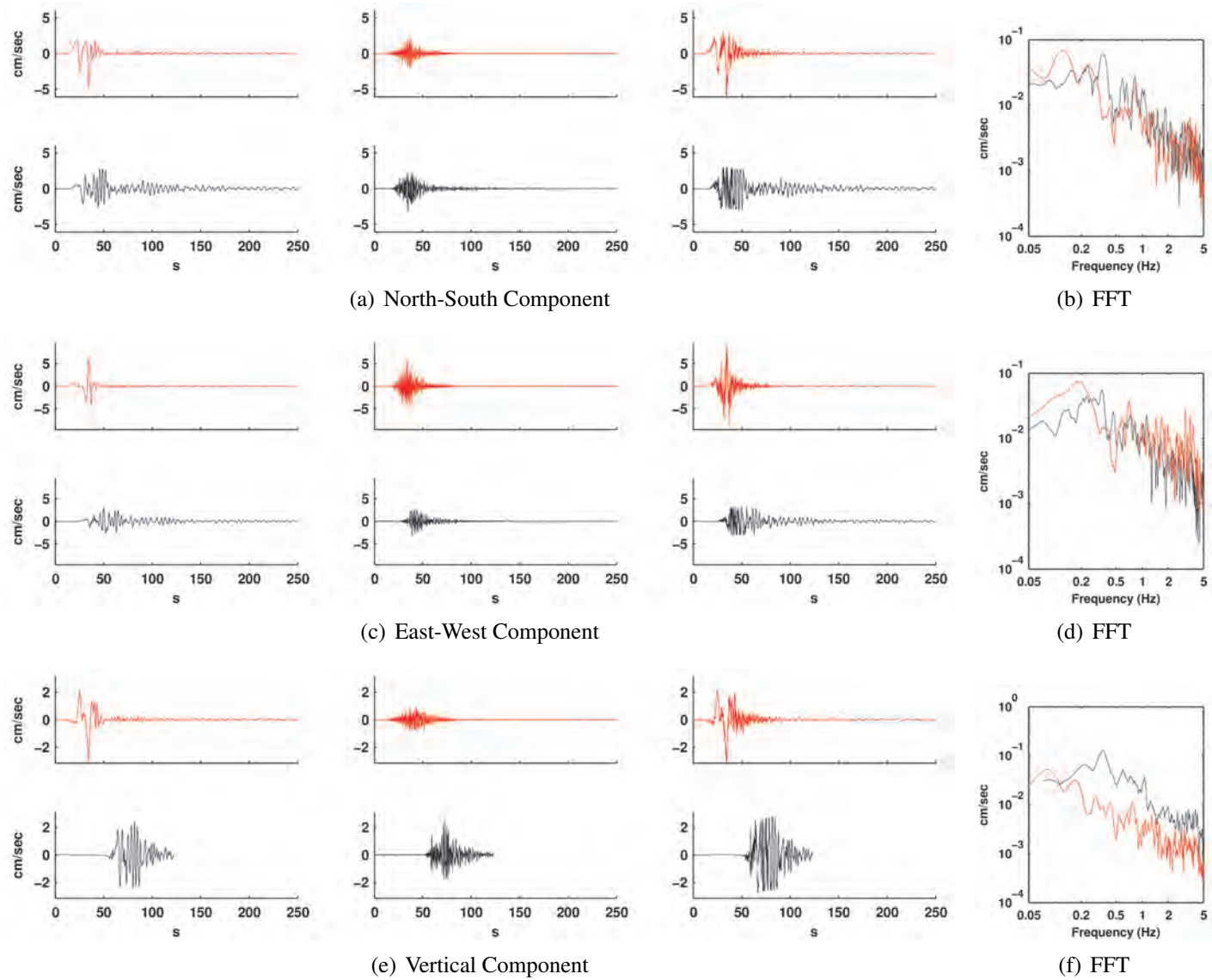


Figure D.8: Comparison of simulated (red) and observed (black) ground motions at station 7.

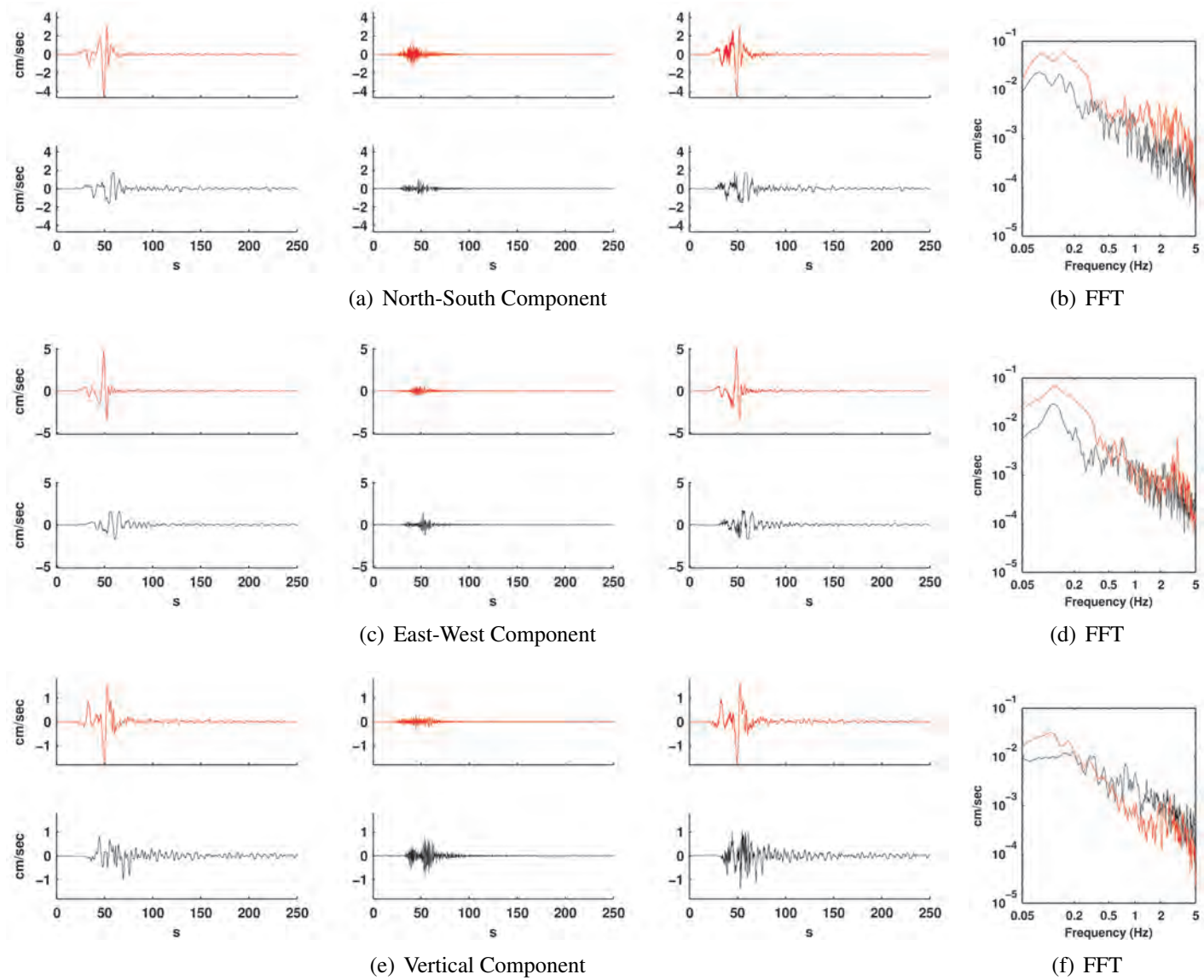


Figure D.9: Comparison of simulated (red) and observed (black) ground motions at station 8.

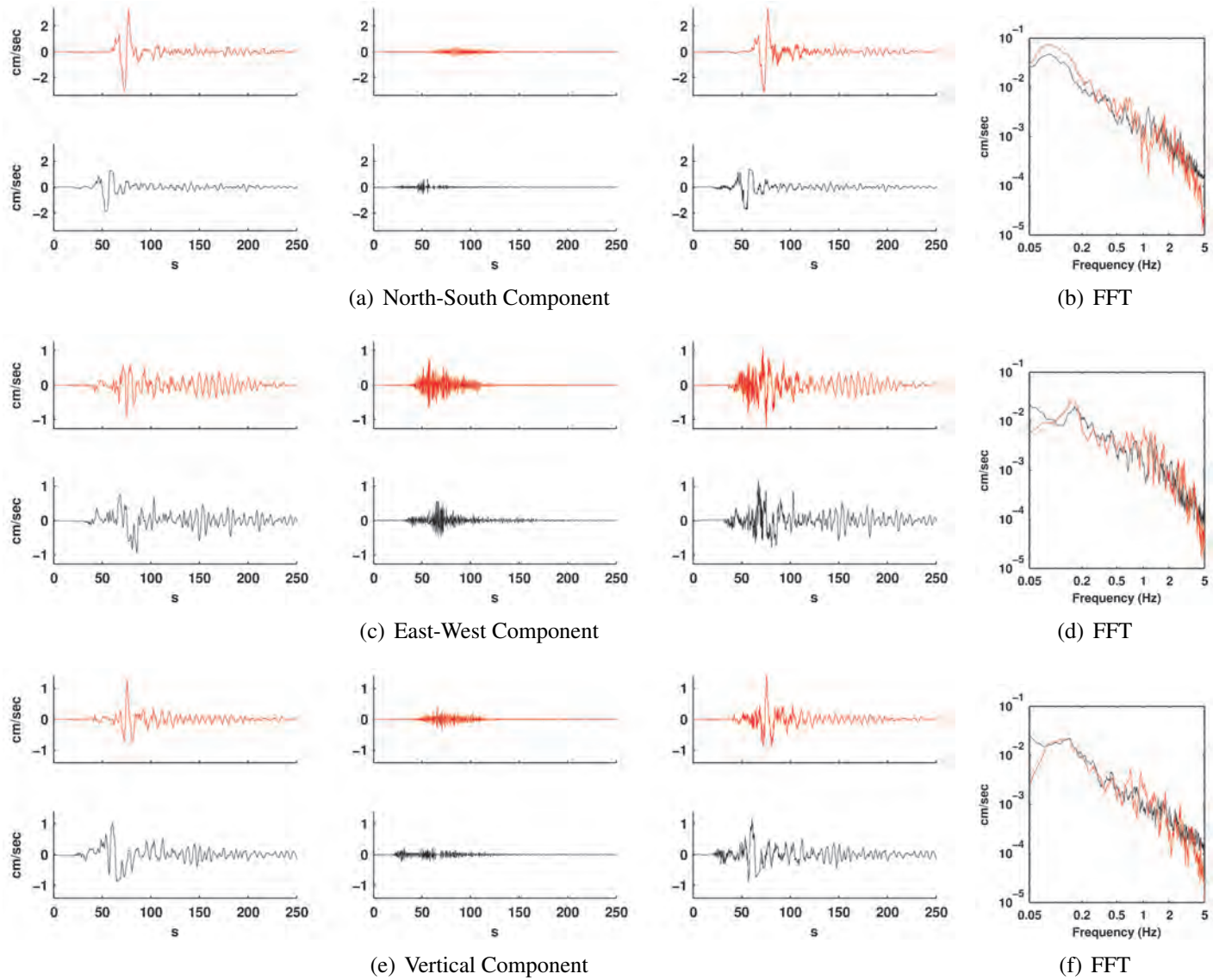


Figure D.10: Comparison of simulated (red) and observed (black) ground motions at station 9.

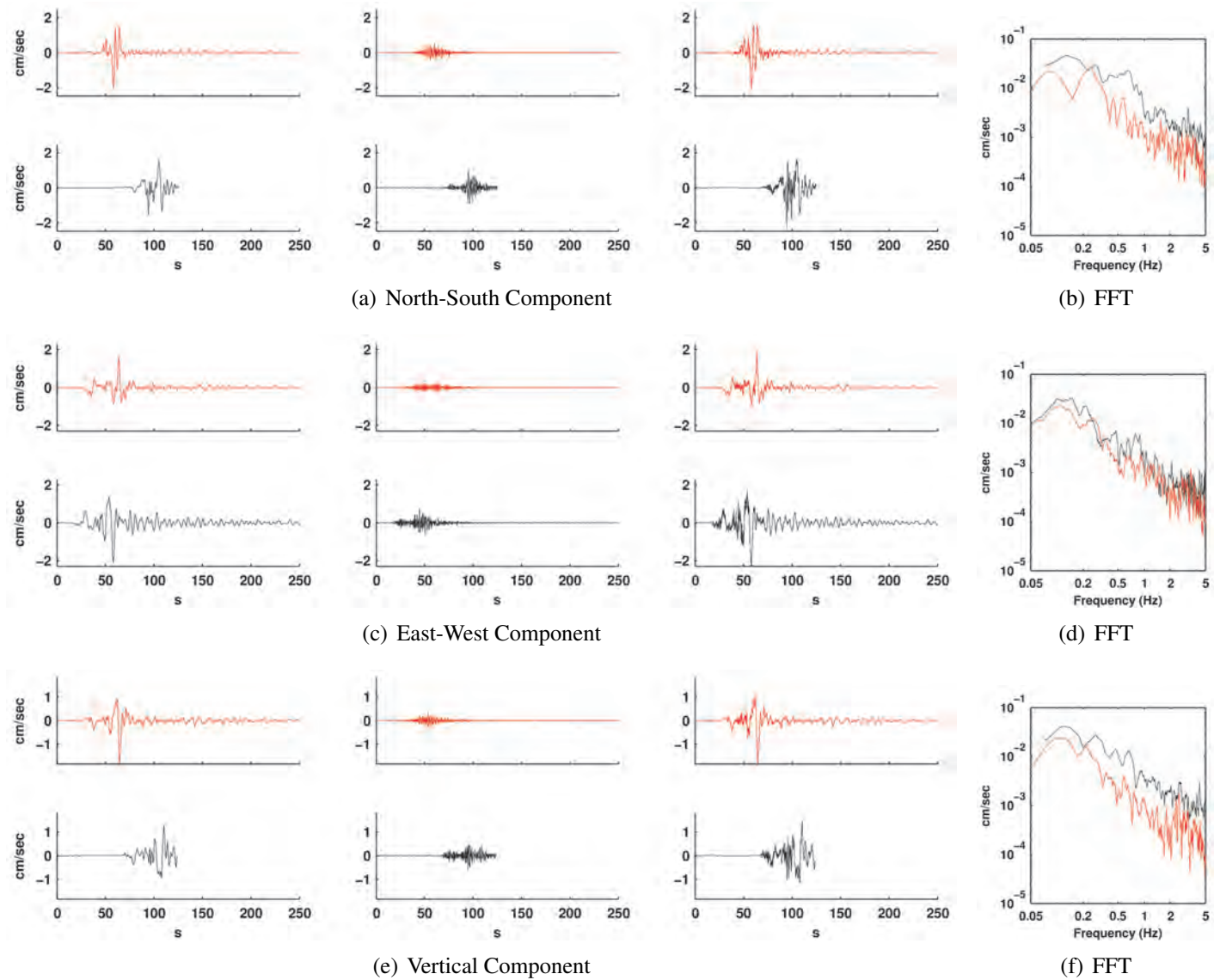


Figure D.11: Comparison of simulated (red) and observed (black) ground motions at station 10.

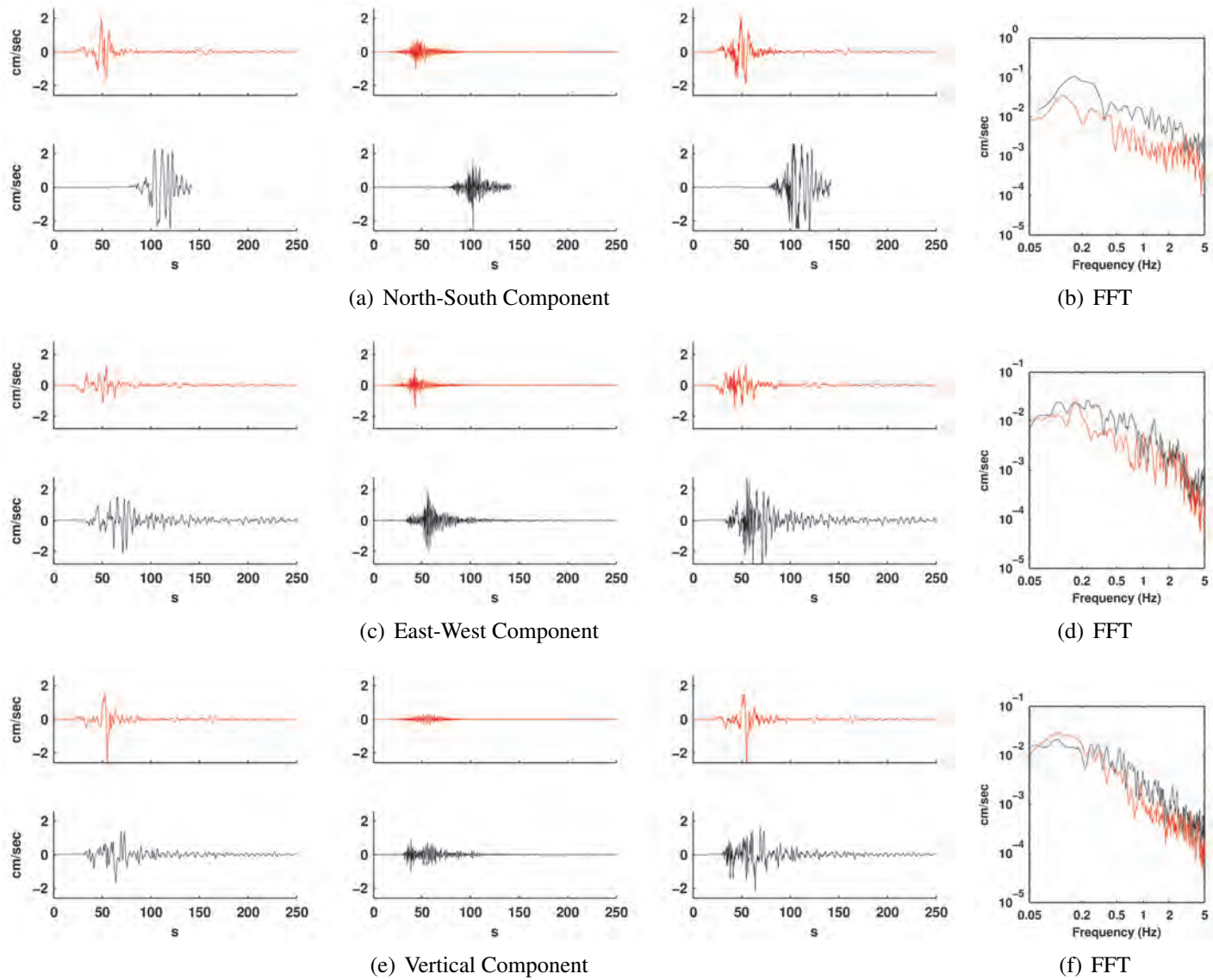


Figure D.12: Comparison of simulated (red) and observed (black) ground motions at station 11.

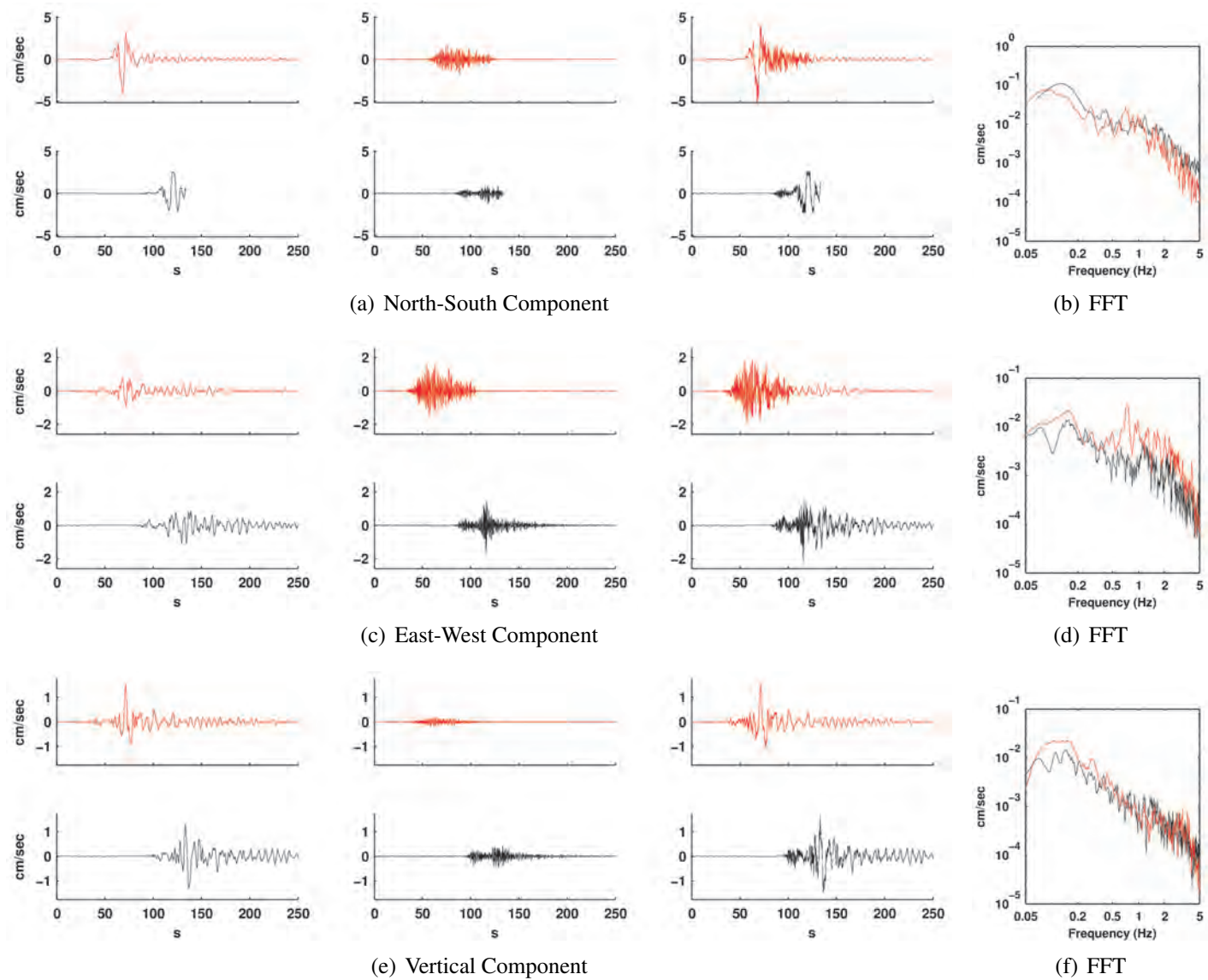


Figure D.13: Comparison of simulated (red) and observed (black) ground motions at station 12.

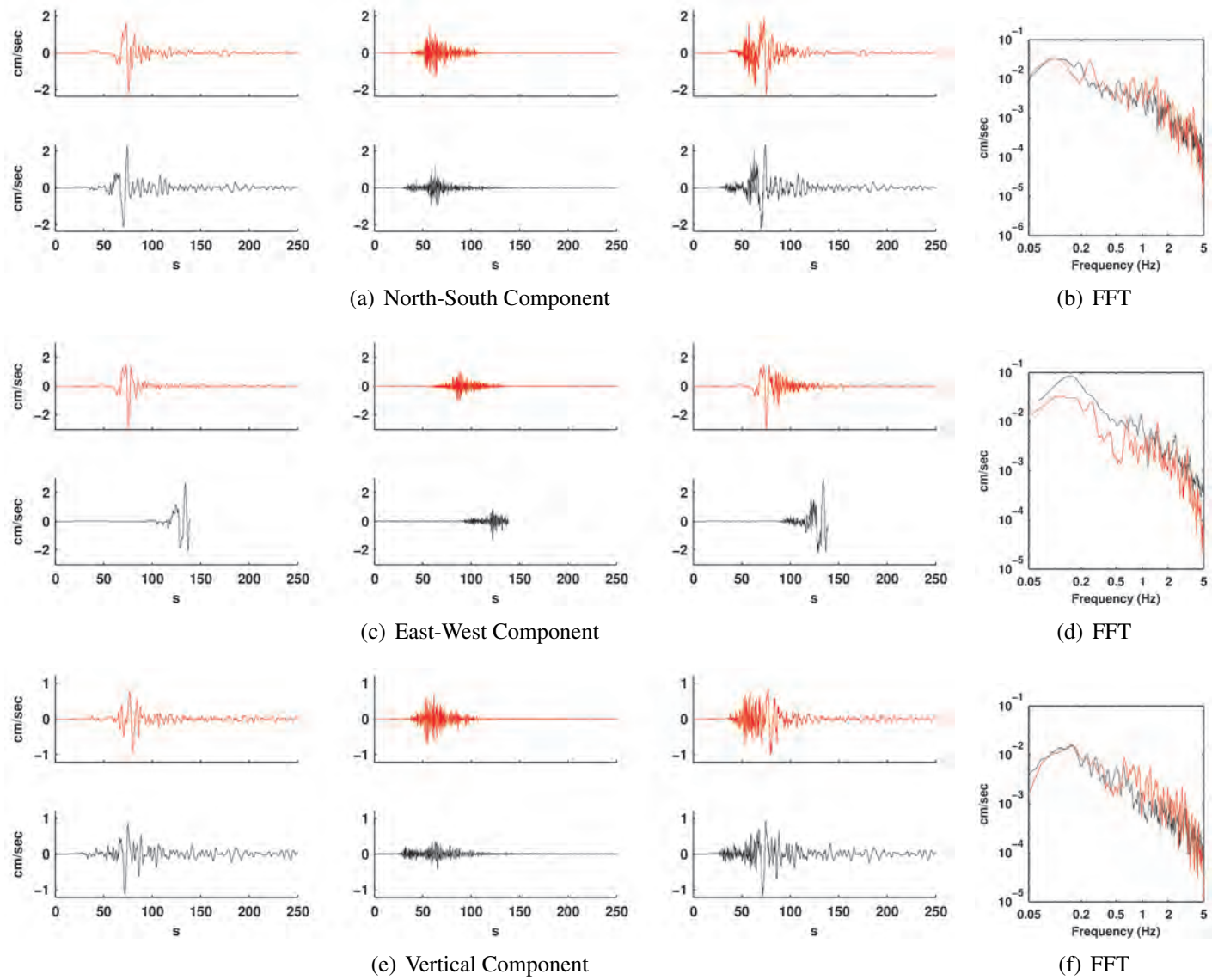


Figure D.14: Comparison of simulated (red) and observed (black) ground motions at station 13.

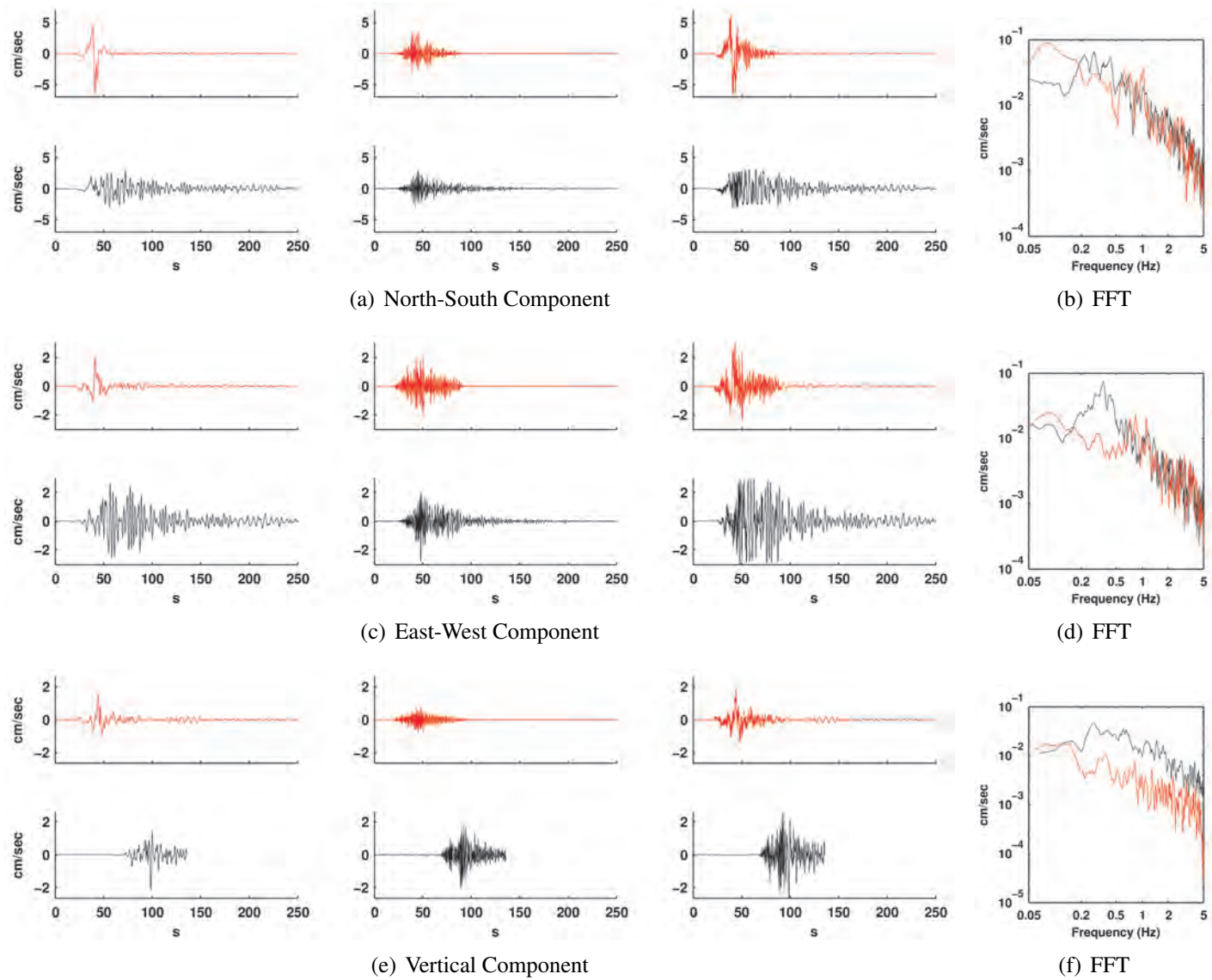


Figure D.15: Comparison of simulated (red) and observed (black) ground motions at station 14.

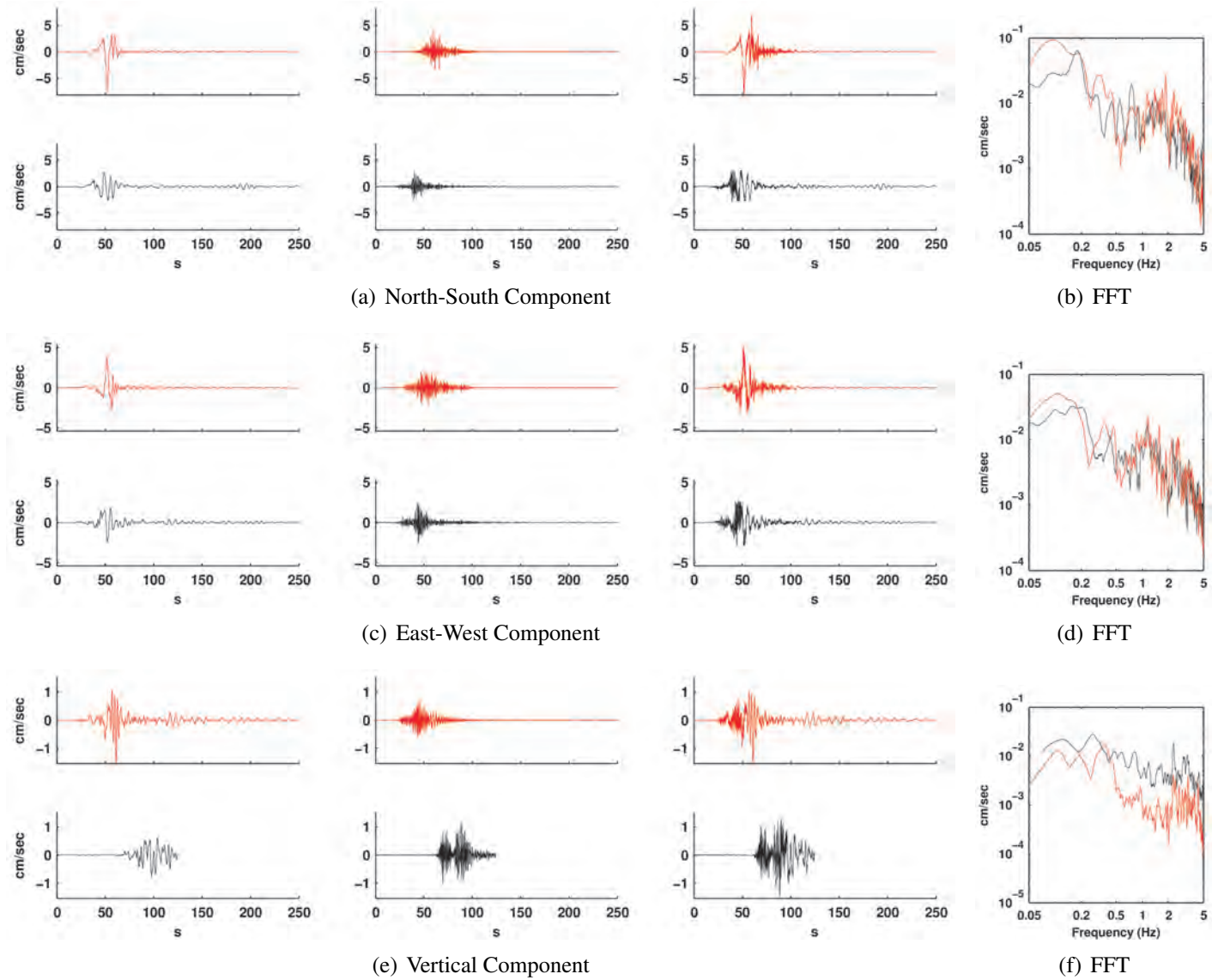


Figure D.16: Comparison of simulated (red) and observed (black) ground motions at station 15.

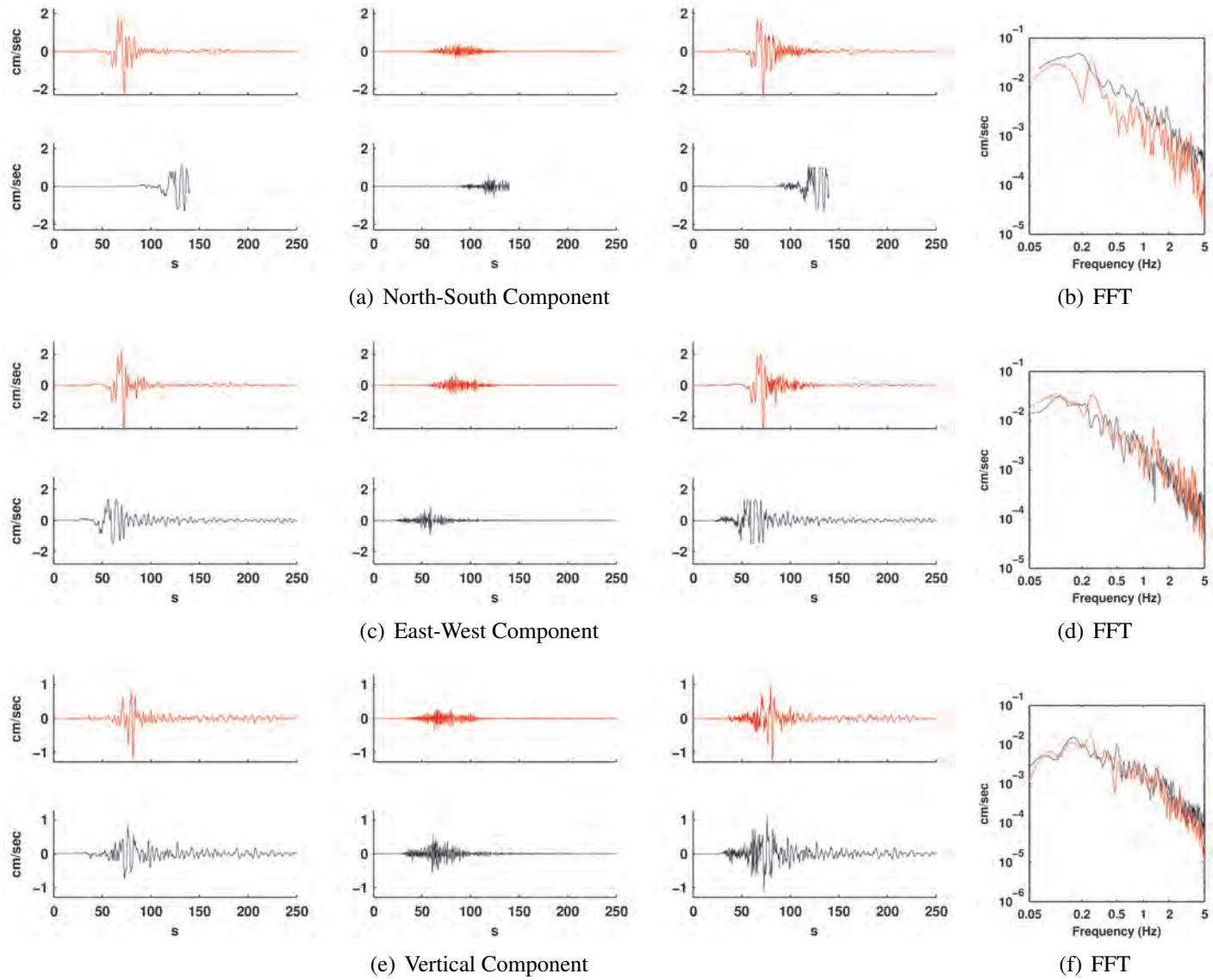


Figure D.17: Comparison of simulated (red) and observed (black) ground motions at station 16.

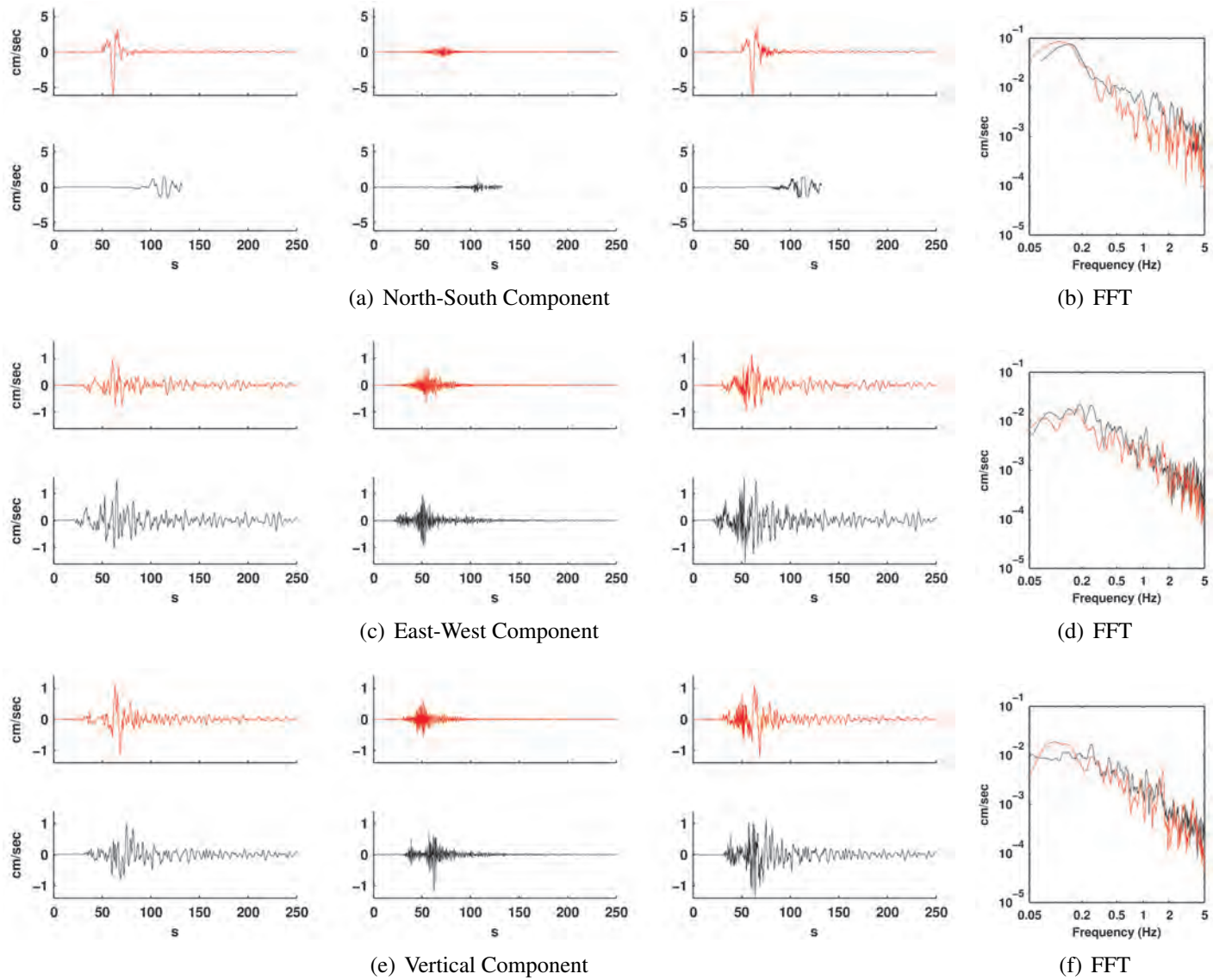


Figure D.18: Comparison of simulated (red) and observed (black) ground motions at station 17.

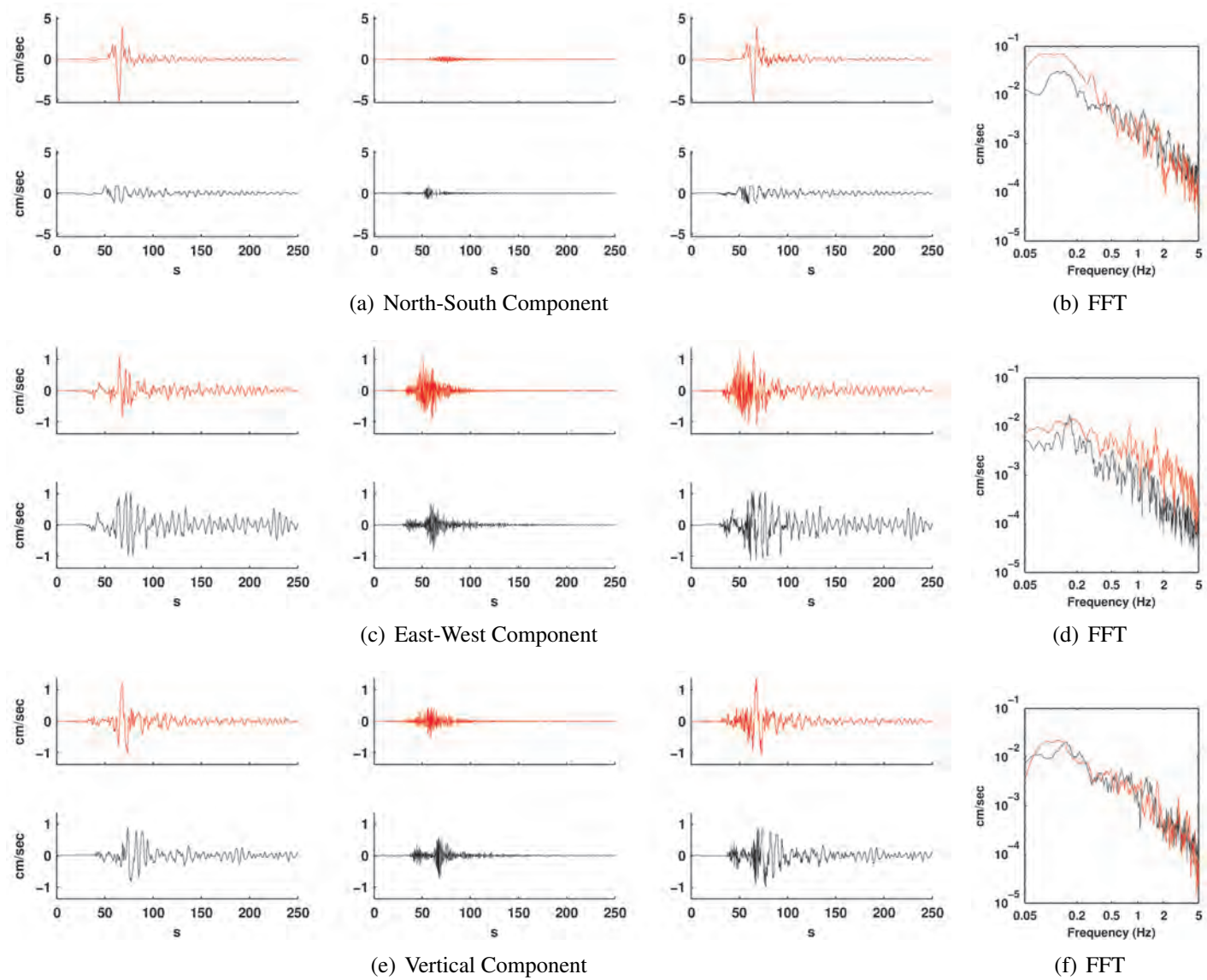


Figure D.19: Comparison of simulated (red) and observed (black) ground motions at station 18.

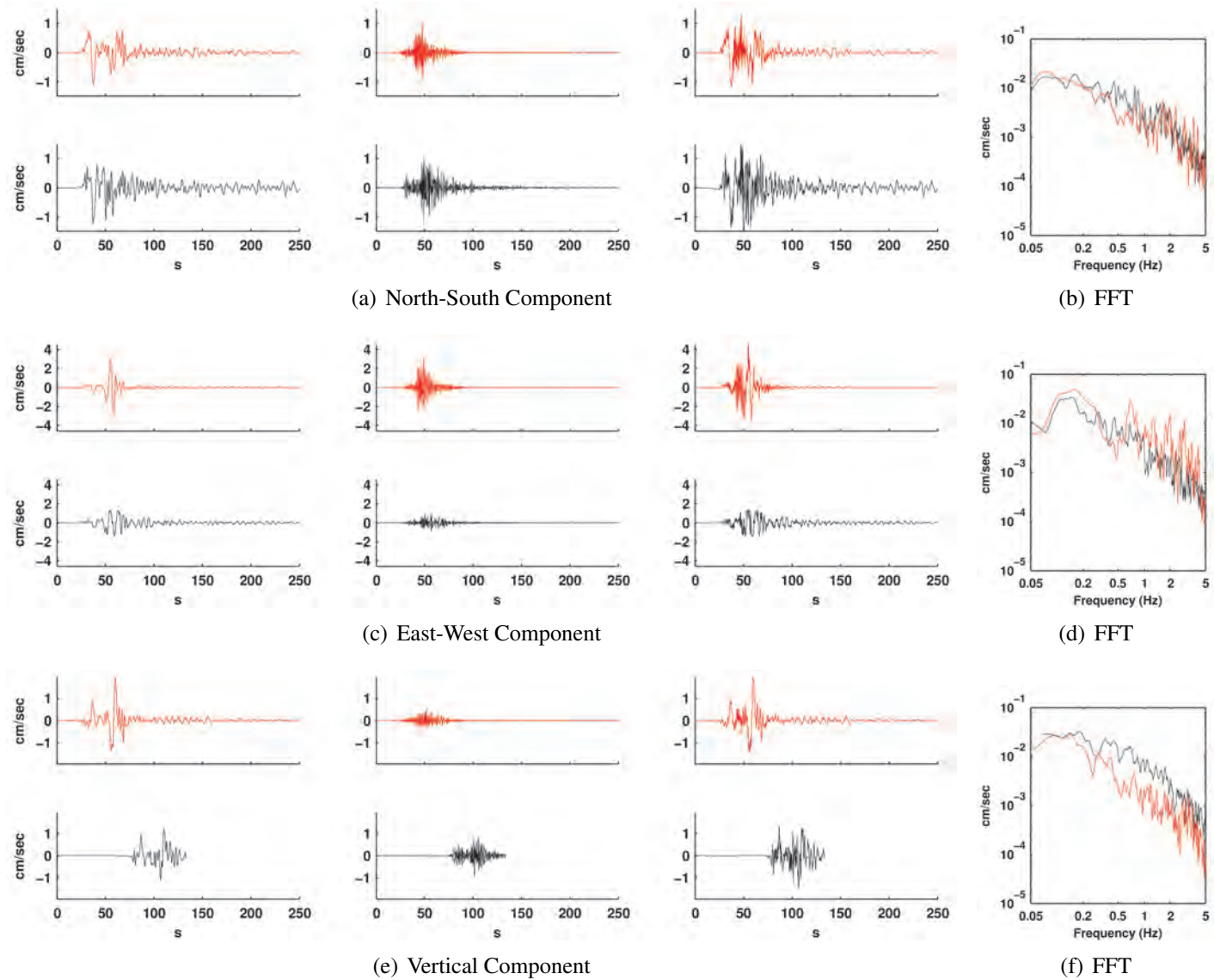


Figure D.20: Comparison of simulated (red) and observed (black) ground motions at station 19.

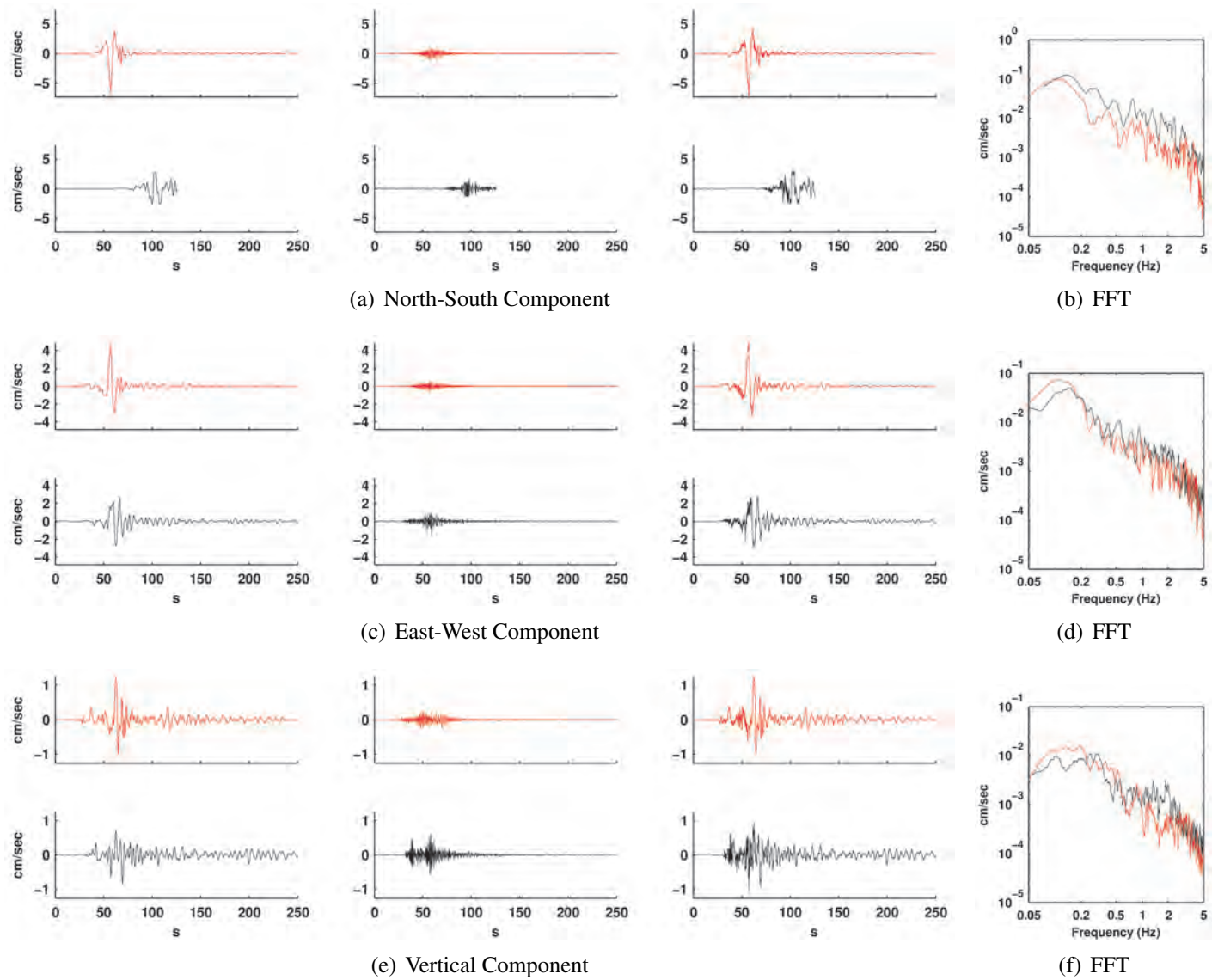


Figure D.21: Comparison of simulated (red) and observed (black) ground motions at station 20.

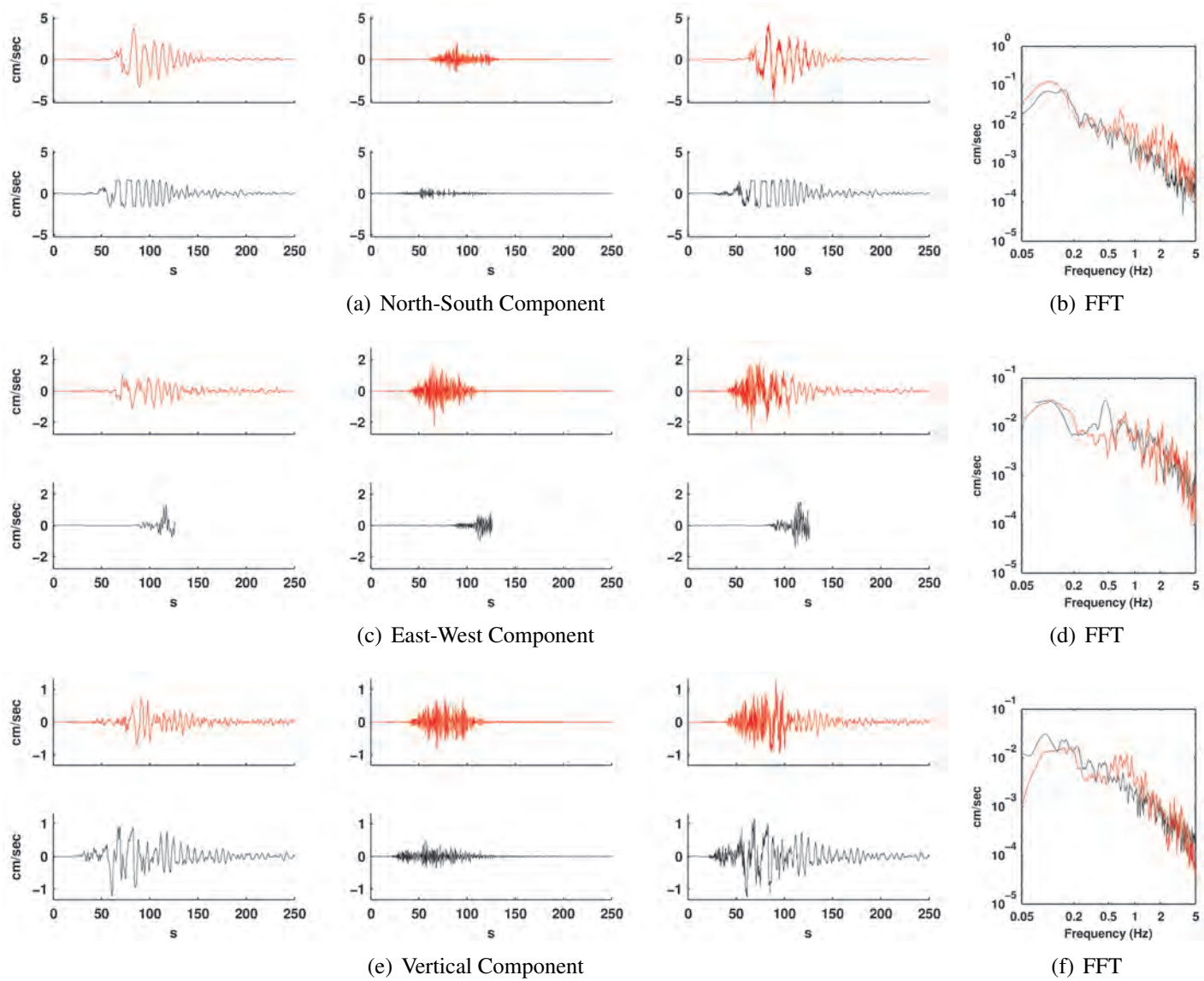


Figure D.22: Comparison of simulated (red) and observed (black) ground motions at station 21.

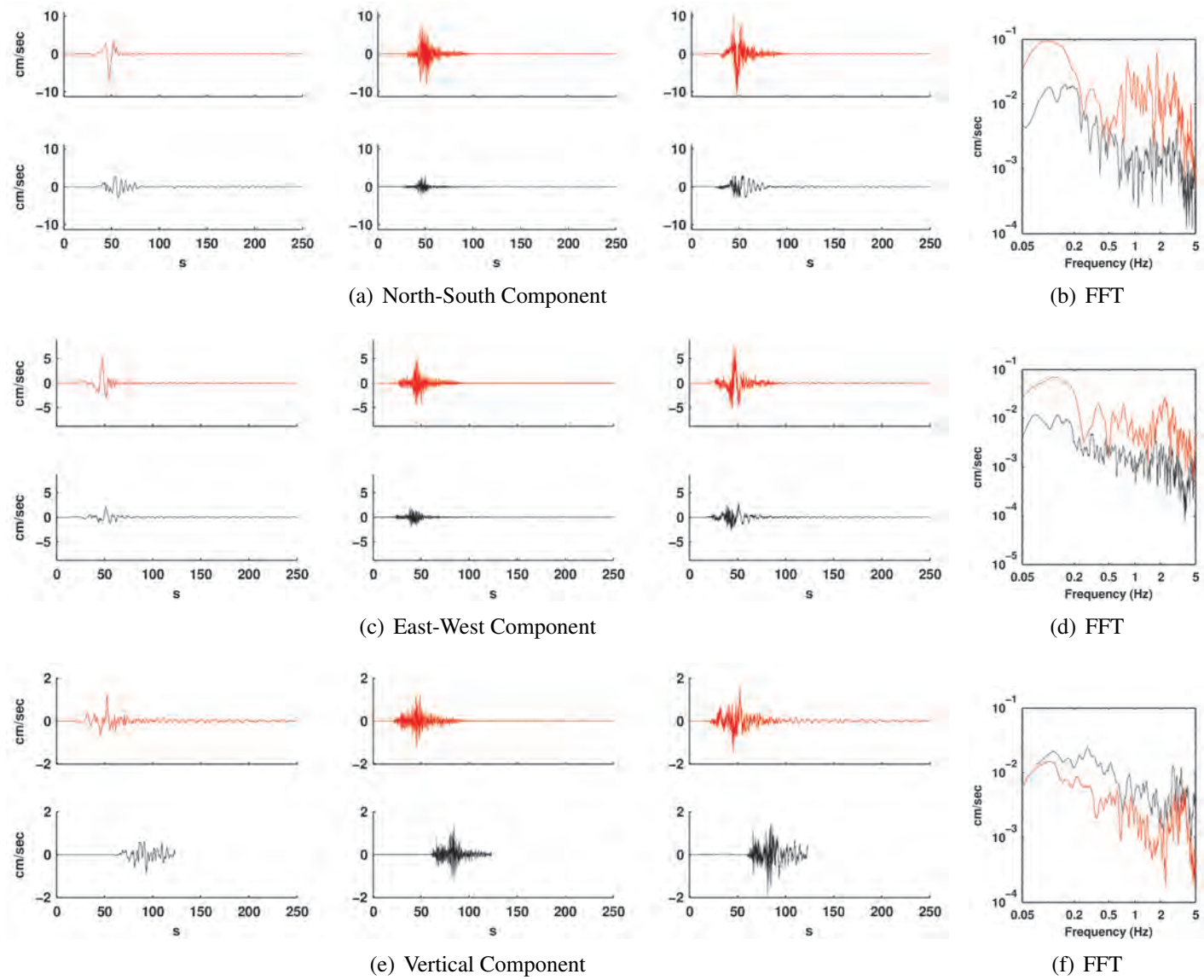


Figure D.23: Comparison of simulated (red) and observed (black) ground motions at station 22.

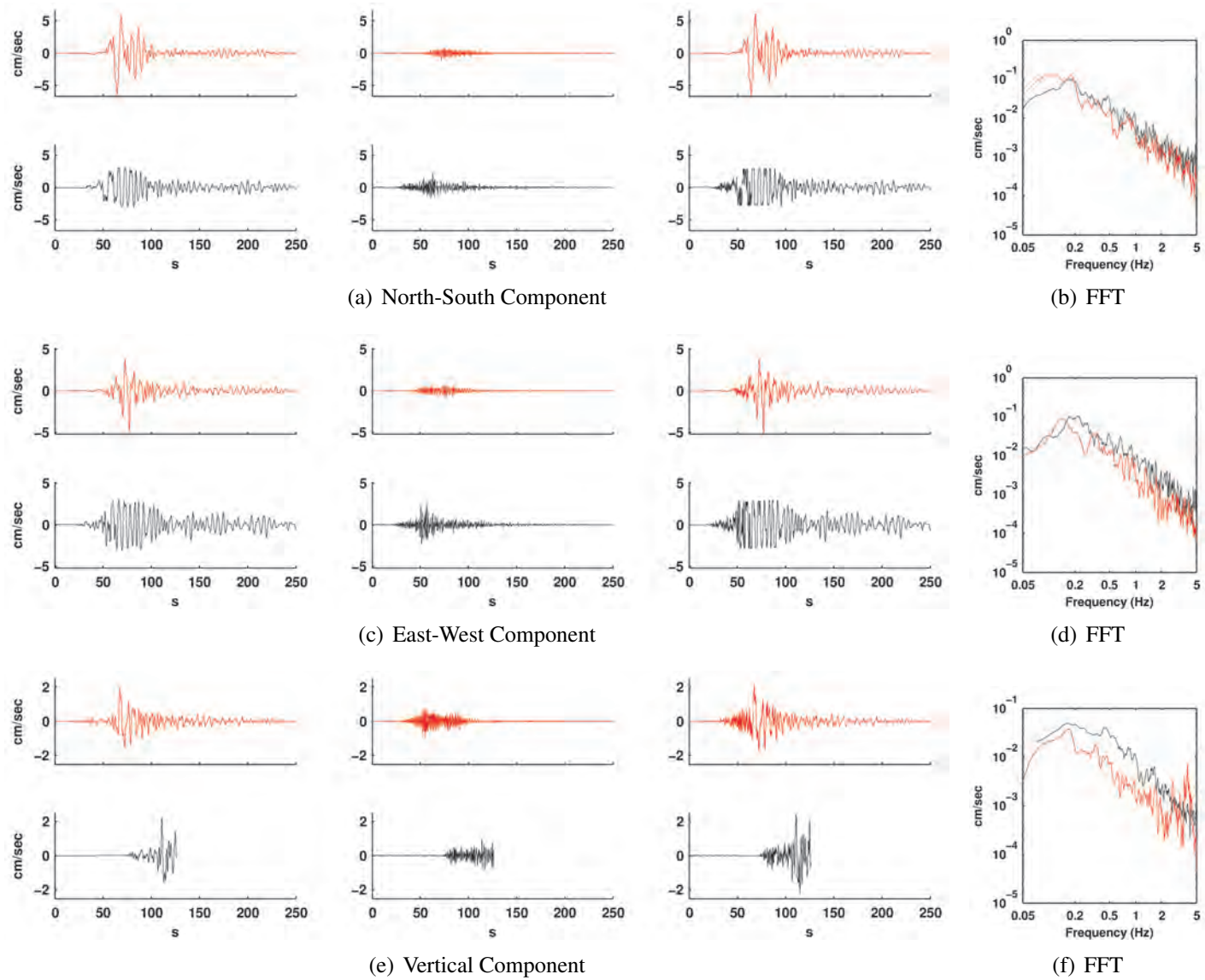


Figure D.24: Comparison of simulated (red) and observed (black) ground motions at station 23.

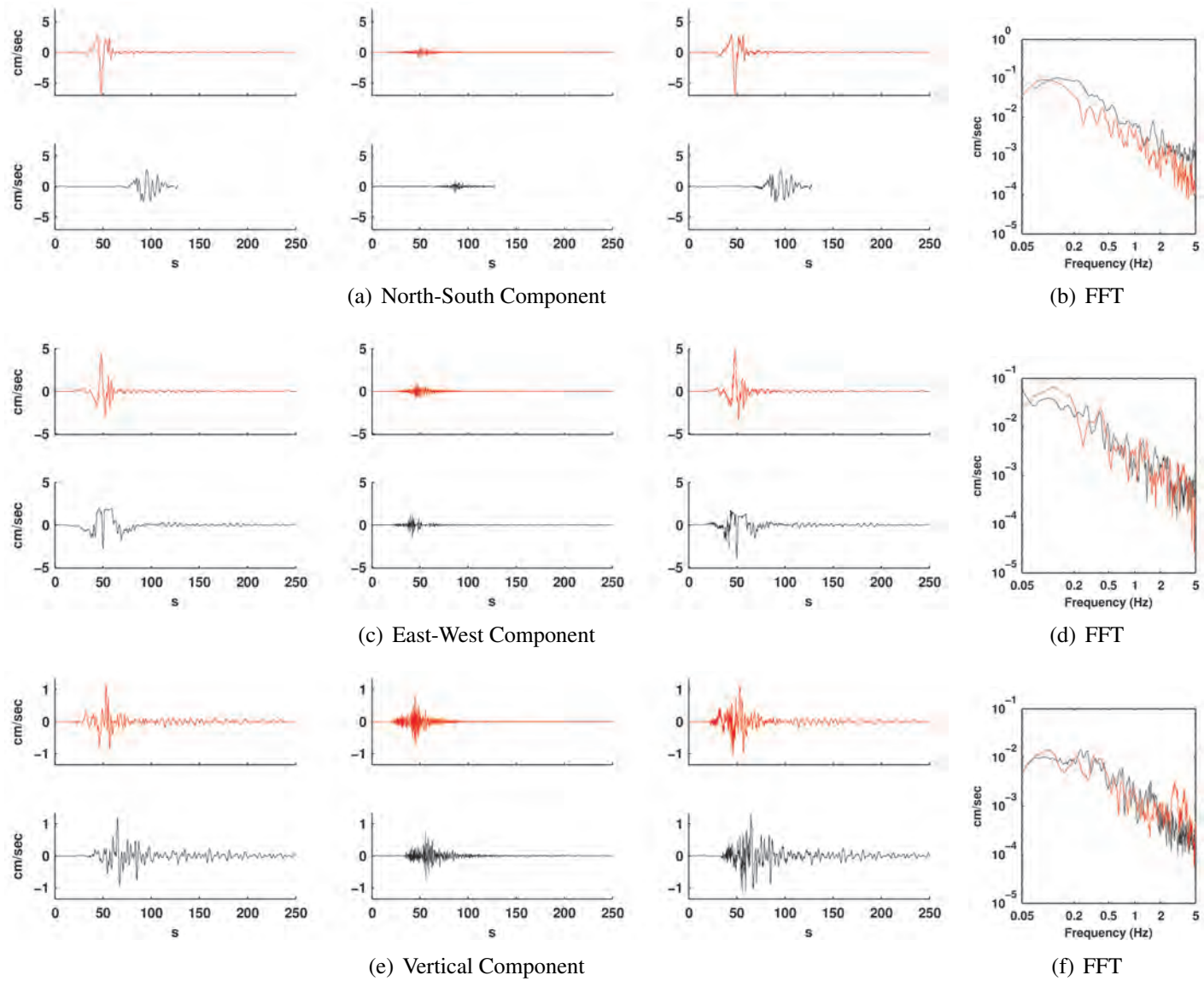


Figure D.25: Comparison of simulated (red) and observed (black) ground motions at station 24.

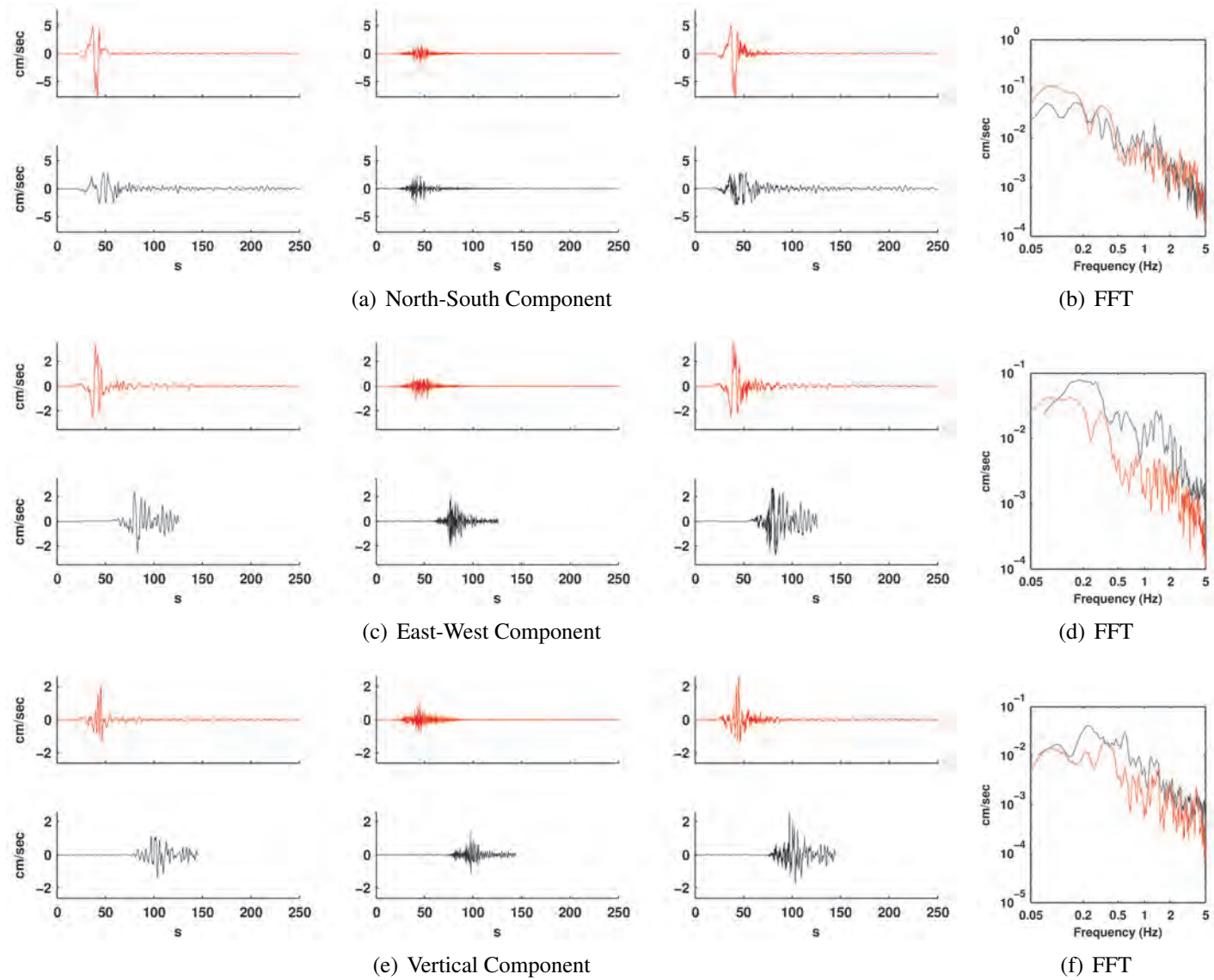


Figure D.26: Comparison of simulated (red) and observed (black) ground motions at station 25.

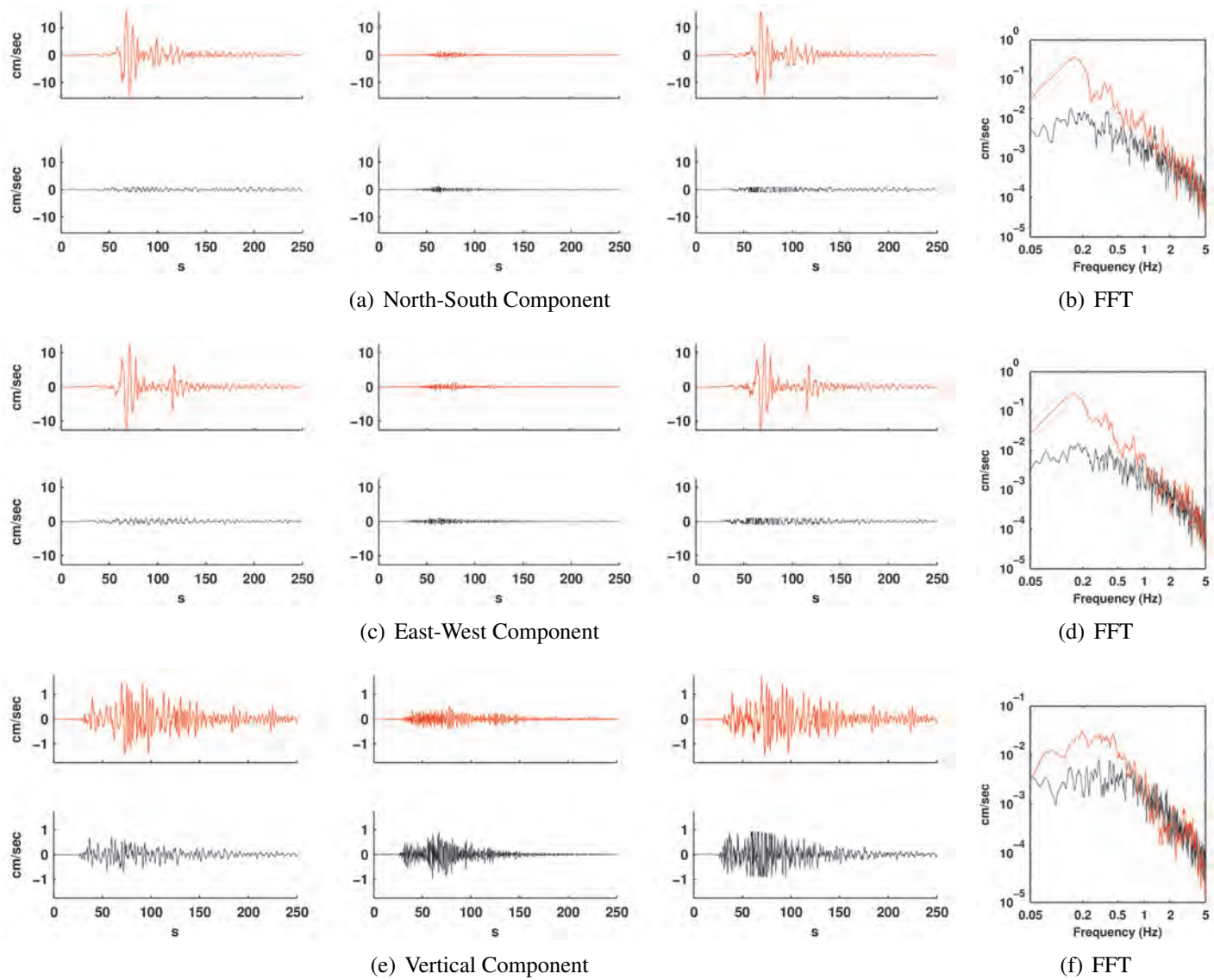


Figure D.27: Comparison of simulated (red) and observed (black) ground motions at station 26.

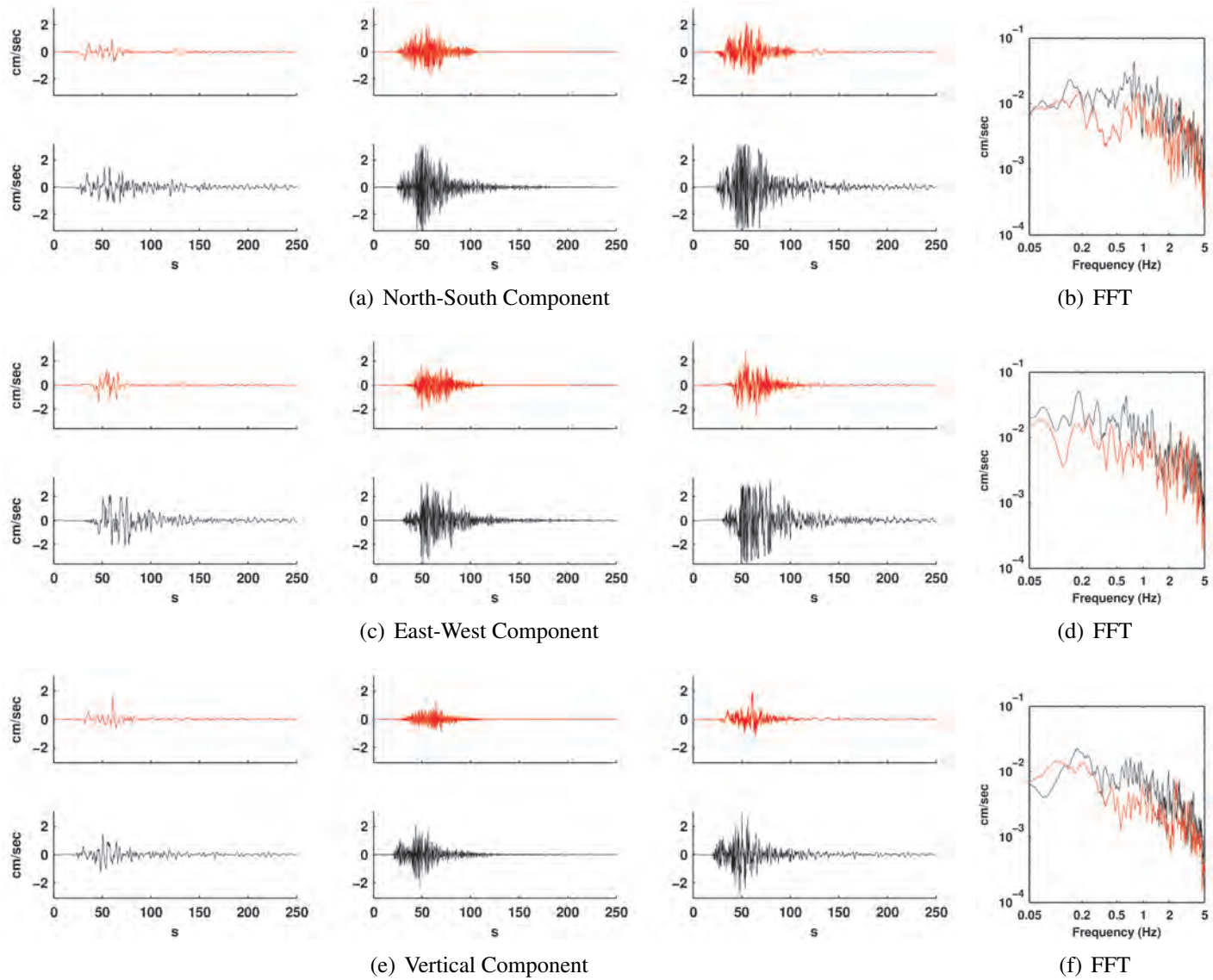


Figure D.28: Comparison of simulated (red) and observed (black) ground motions at station 27.

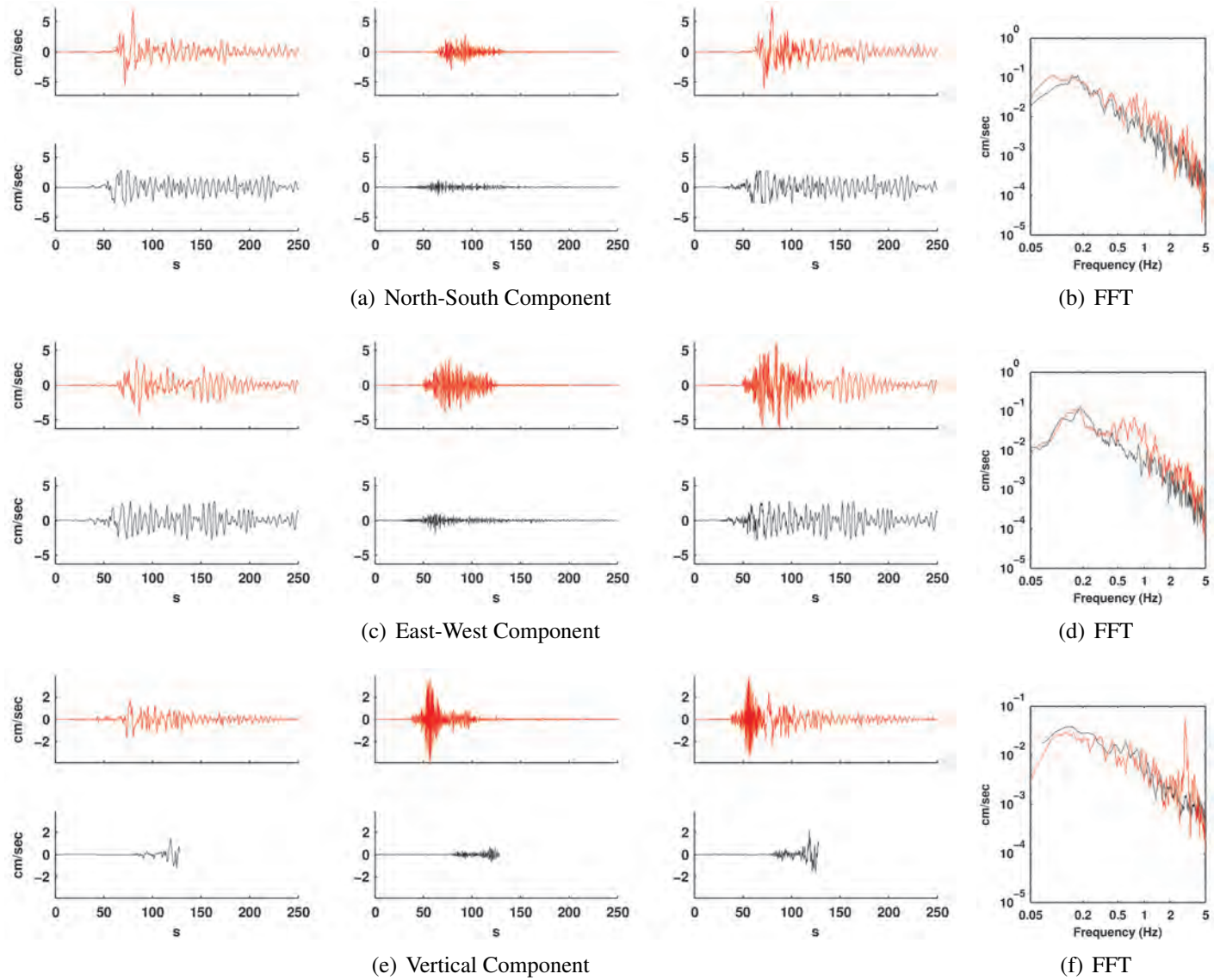


Figure D.29: Comparison of simulated (red) and observed (black) ground motions at station 28.

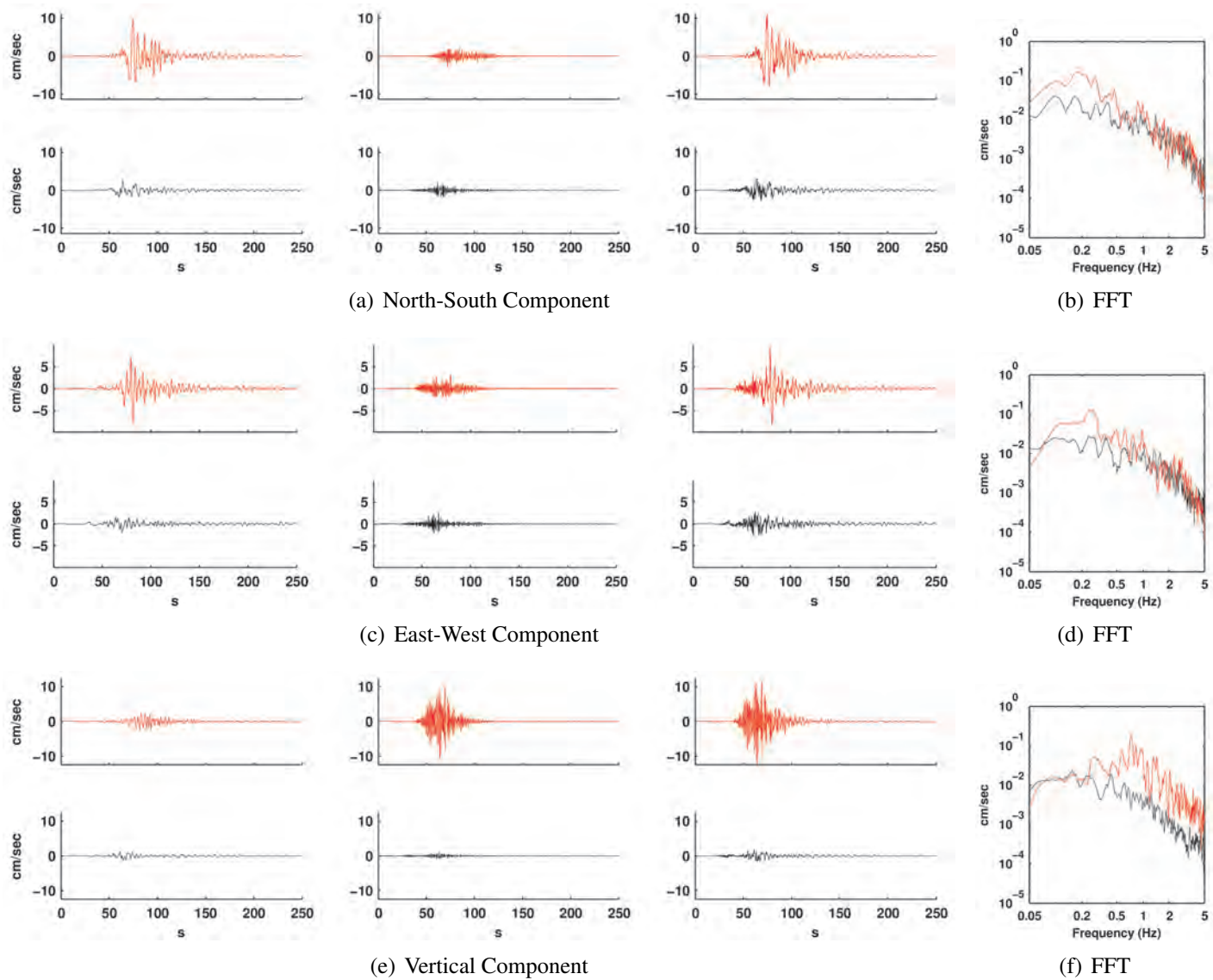


Figure D.30: Comparison of simulated (red) and observed (black) ground motions at station 29.

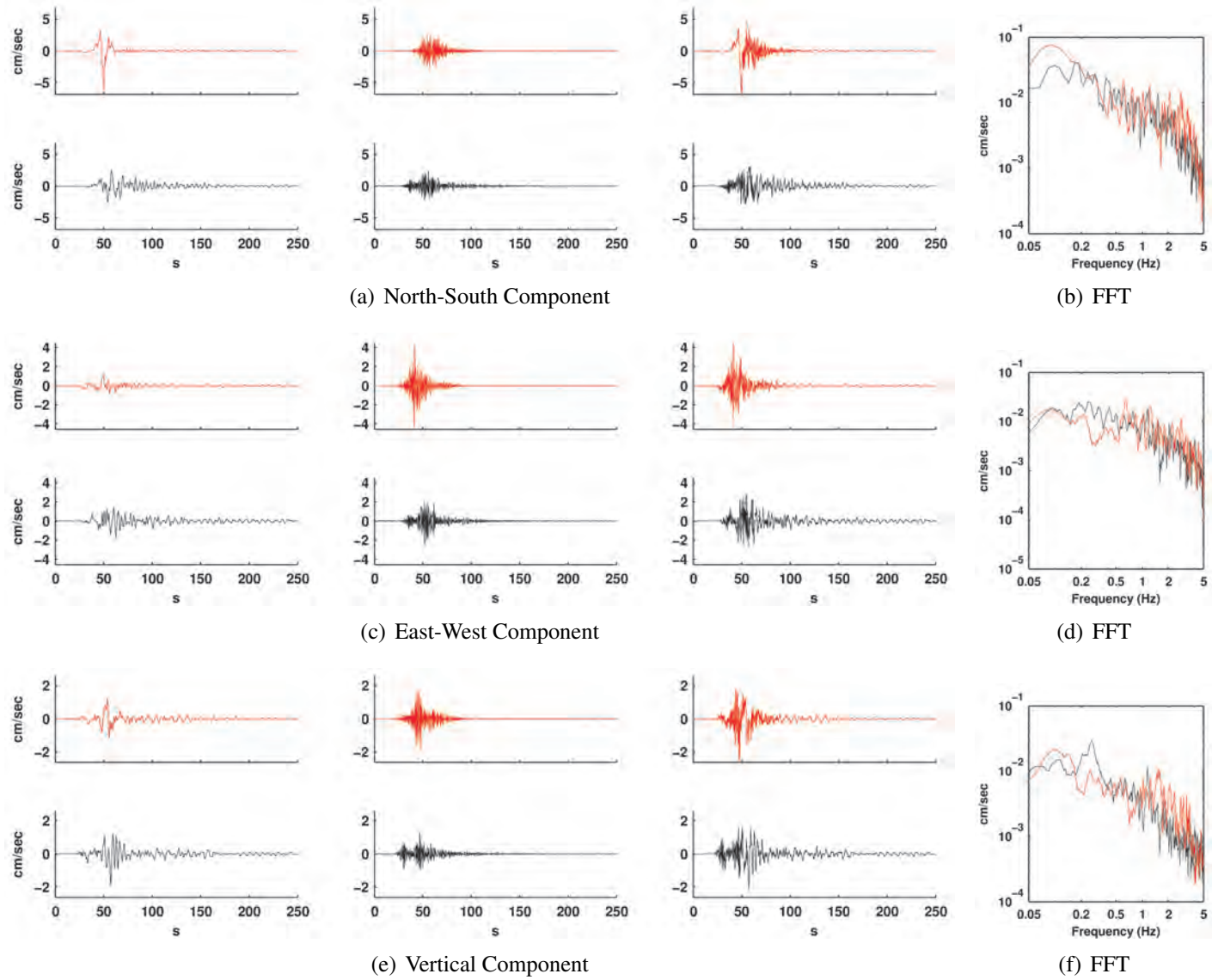


Figure D.31: Comparison of simulated (red) and observed (black) ground motions at station 30.

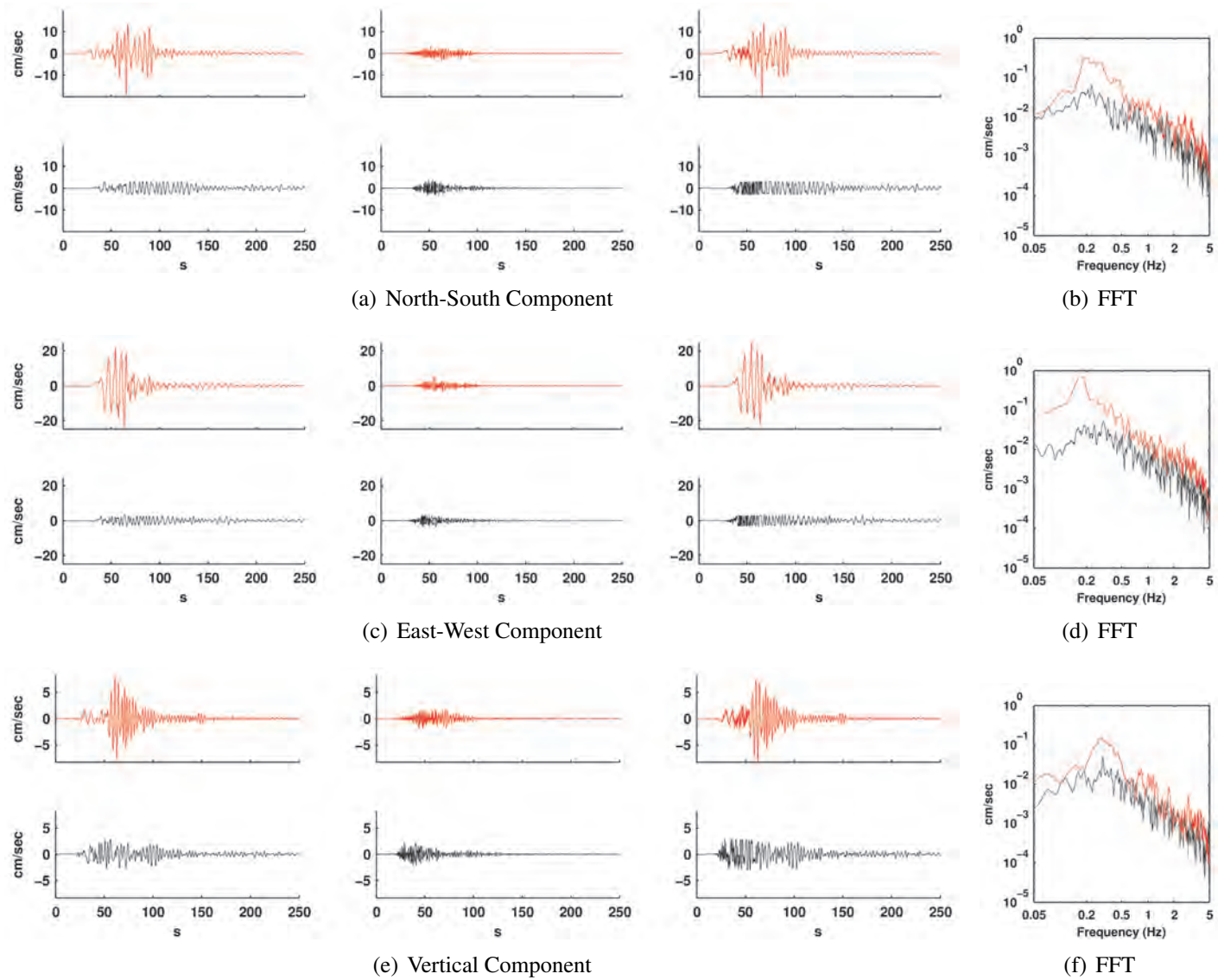


Figure D.32: Comparison of simulated (red) and observed (black) ground motions at station 31.

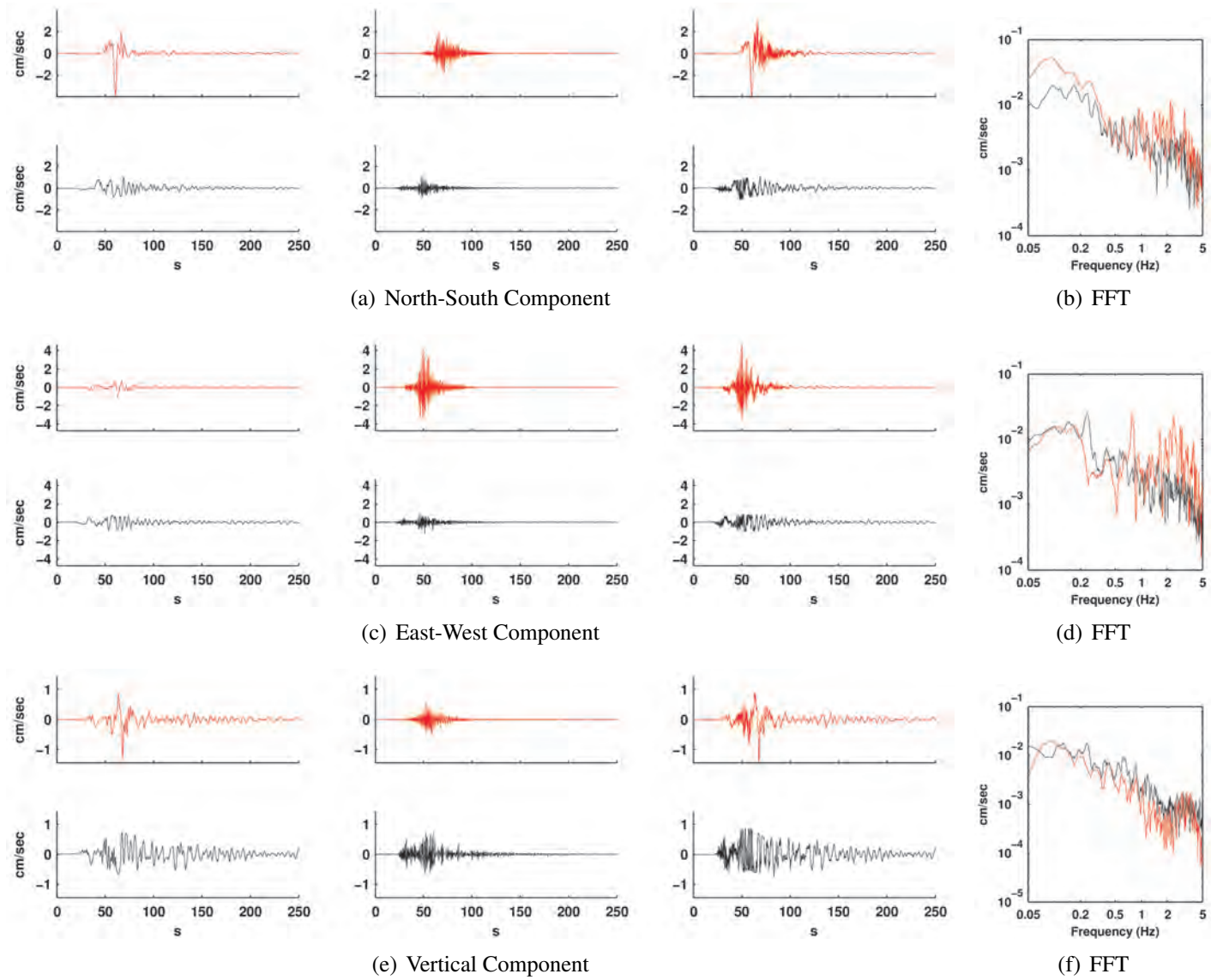


Figure D.33: Comparison of simulated (red) and observed (black) ground motions at station 32.

Appendix E

EGF methodology validation: 2004 Parkfield earthquake

Figure [E.1](#) illustrates the location of each station, epicenter location of the 2004 Parkfield earthquake, surface projection of the fault rupture extend, and the surface projection of the San Andreas fault. Figures [E.2](#) - [E.47](#) compare the low-frequency, high-frequency, and broadband synthetic seismograms (red) at 46 stations against observations (black) from the 2004 Parkfield earthquake. Also, compared are the corresponding Fourier spectra in the 0.1 – 5.0 Hz frequency band. Station ID and location are listed in Table [E.1](#).

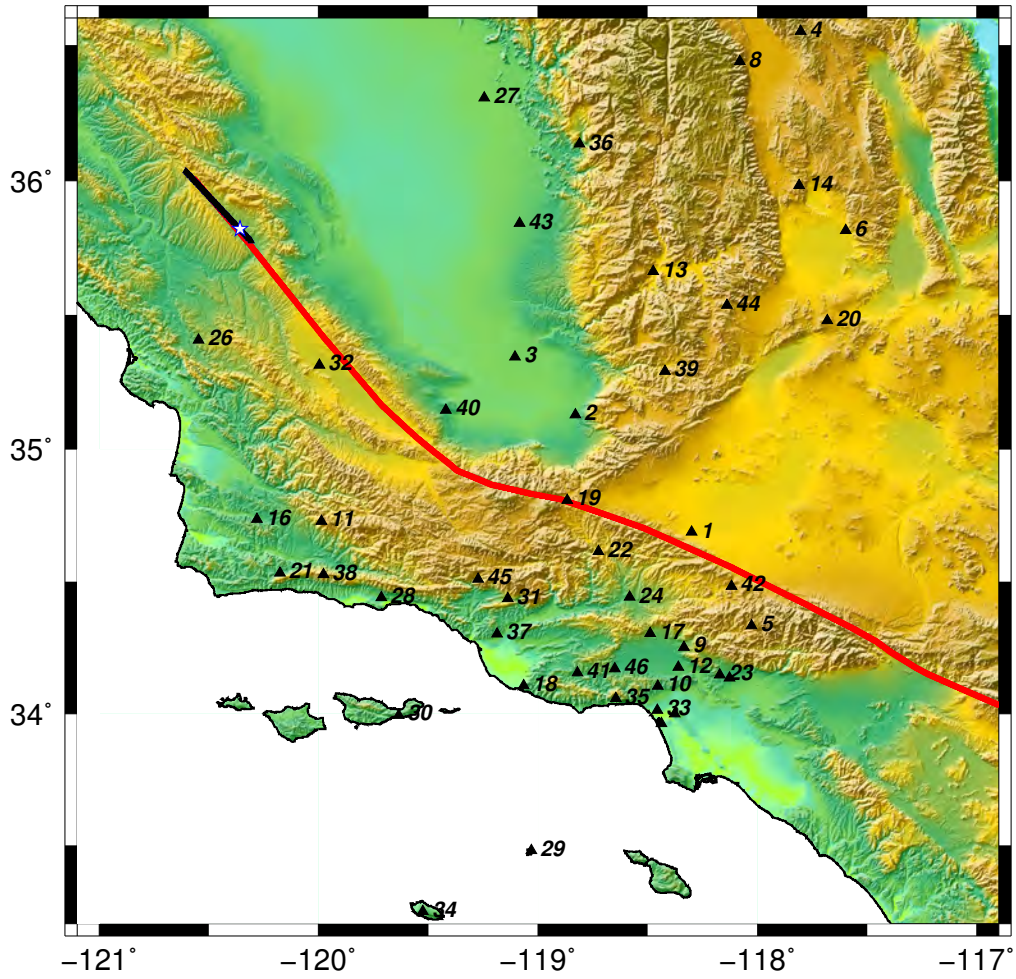


Figure E.1: Location of all stations used in validation of the 2004 Parkfield earthquake. Red line: San Andreas Fault; Black line: trace/surface projection of earthquake source model; Star: epicenter; Black triangles: stations

Station Number	Latitude	Longitude	Station Name	Abbreviation
1	34.687080	-118.29946	Antelope	ALP
2	35.126900	-118.83009	Arvin	ARV
3	35.344440	-119.10445	Calstate Bakersfield	BAK
4	36.550400	-117.80295	Cerro Gordo	CGO
5	34.333410	-118.02585	Chilao Flat Rangr. Station	CHF
6	35.815740	-117.59751	China Lake	CLC
7	34.136240	-118.12705	Caltech Robinson Pit	CRP
8	36.439880	-118.08016	Cottonwood Creek	CWC
9	34.253530	-118.33383	Green Verdugo Microwave Site	DEC
10	34.106180	-118.45505	Donna Jones Jenkins	DJJ
11	34.728320	-119.98803	Figueroa Mountain	FIG
12	34.176430	-118.35967	North Hollywood	HLL
13	35.662780	-118.47403	Isabella	ISA
14	35.982490	-117.80885	Joshua Ridge: China Lake	JRC2
15	34.000330	-118.37794	La Cienega	LCG
16	34.735510	-120.27996	Los Alamos County Park	LCP
17	34.305290	-118.48805	Los Angeles Filtration Plant	LFP
18	34.108190	-119.06587	Laguna Peak	LGU
19	34.807620	-118.86775	Lone Juniper Ranch	LJR
20	35.479540	-117.68212	Laurel Mtn Radio Fac	LRL
21	34.534120	-120.17737	Nojoqui County Park	NJQ
22	34.614500	-118.72350	Osito Audit: Castaic Lake Dam	OSI
23	34.148440	-118.17117	White Mtn Res Sta-Crooked Creek	S08C
24	34.441990	-118.58215	Pardee	PDE
25	33.962730	-118.43702	Playa Del Rey	PDR
26	35.407730	-120.54556	Park Hill	PHL
27	36.305230	-119.24384	Rector	RCT
28	34.440760	-119.71492	Santa Barbara	SBC
29	33.480460	-119.02986	Santa Barbara Island	SBI
30	33.995430	-119.63510	Santa Cruz Island 2	SCZ2
31	34.436920	-119.13750	Summit Elementary School	SES
32	35.314200	-119.99581	Simmler	SMM
33	34.014380	-118.45617	Santa Monica Fire St	SMS
34	33.247870	-119.52437	San Nicolas Island	SNCC
35	34.059330	-118.64614	Saddle Peak Fire Camp 8	SPF
36	36.135500	-118.81099	Springville	SPG
37	34.303020	-119.18676	Santa Clara	STC
38	34.527750	-119.97834	Santa Ynez Peak	SYP
39	35.291300	-118.42079	Cattani Ranch	TEH
40	35.145920	-119.41946	Taft Base	TFT
41	34.156070	-118.82039	Thousand Oaks Ventura	TOV
42	34.483640	-118.11783	Vincent Substation	VCS
43	35.840890	-119.08469	Vestal	VES
44	35.536640	-118.14035	Bird Spring	WBS
45	34.510850	-119.27407	Wheeler Gorge Ranger Station	WGR
46	34.171700	-118.64971	West Side Station	WSS

Table E.1: List of stations (and their location) for the 2004 Parkfield earthquake.

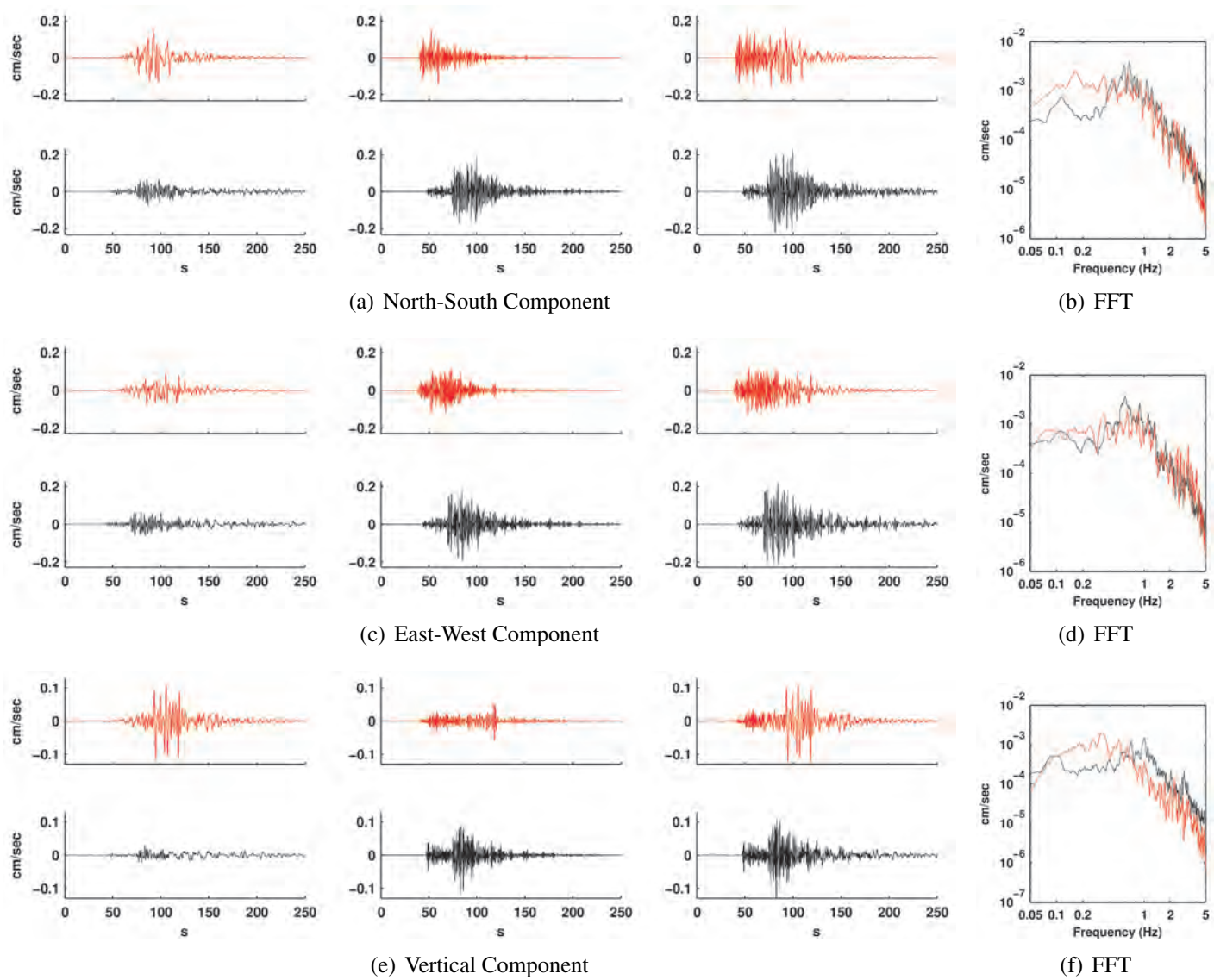


Figure E.2: Comparison of simulated (red) and observed (black) ground motions at station 1.

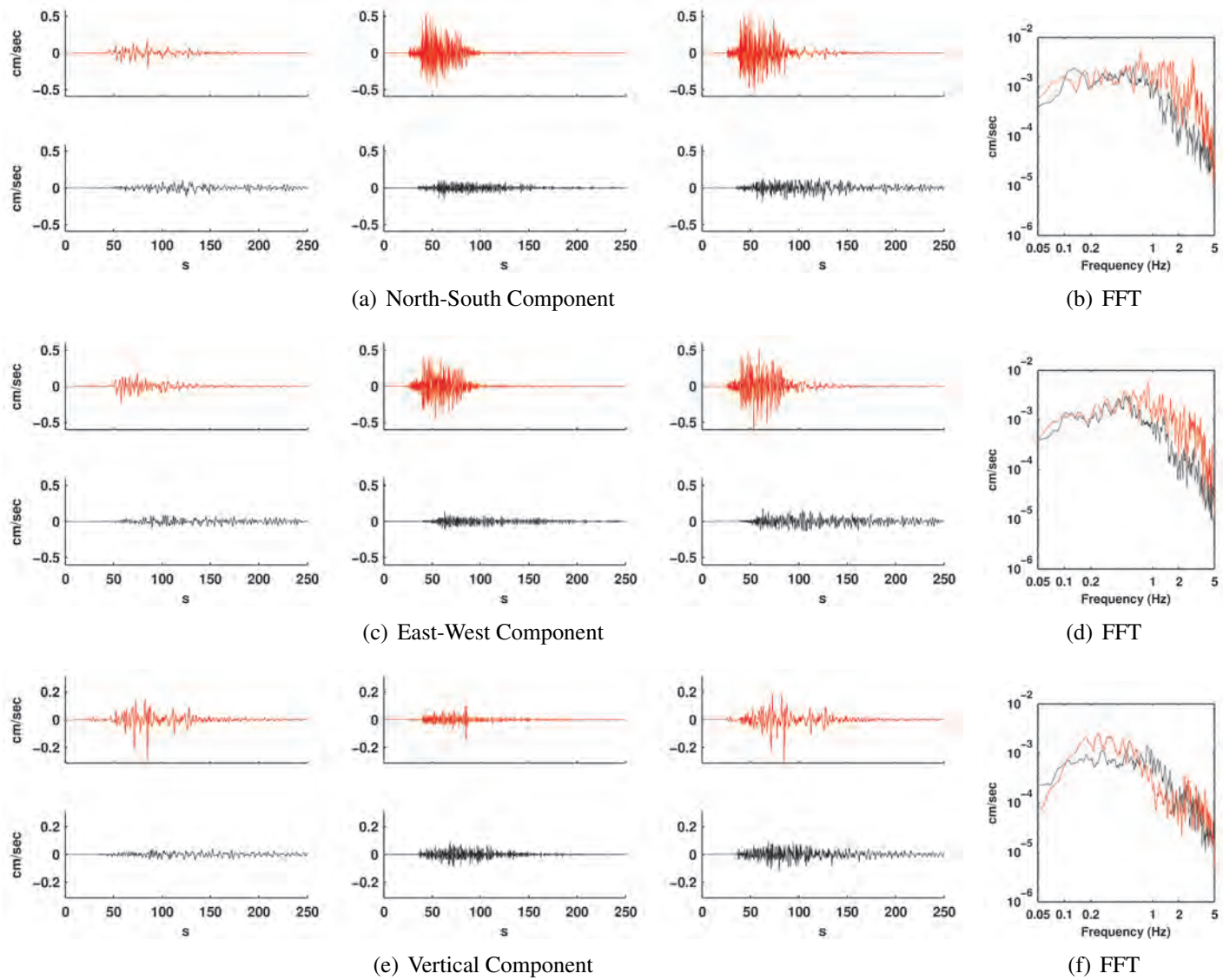


Figure E.3: Comparison of simulated (red) and observed (black) ground motions at station 2.

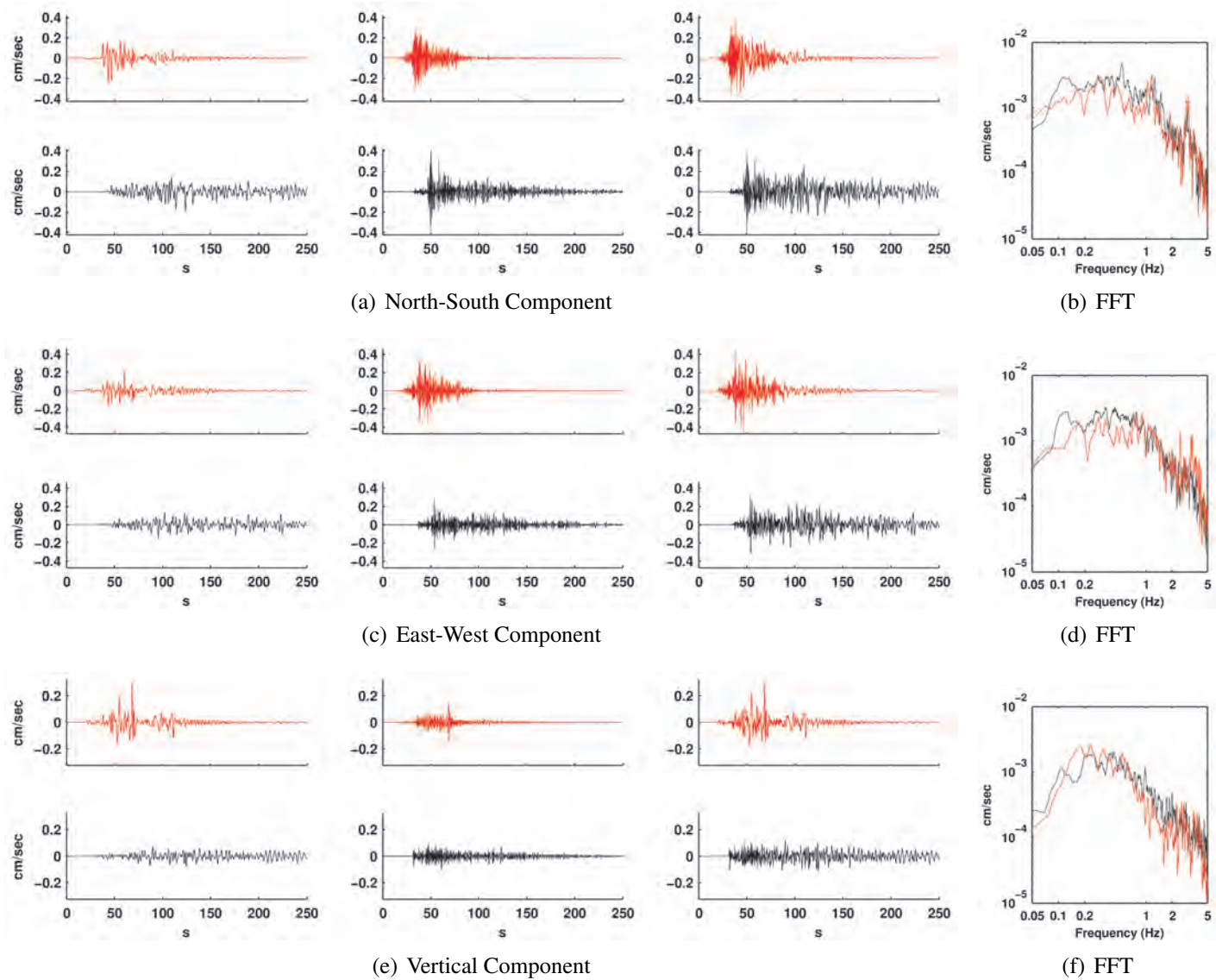


Figure E.4: Comparison of simulated (red) and observed (black) ground motions at station 3.

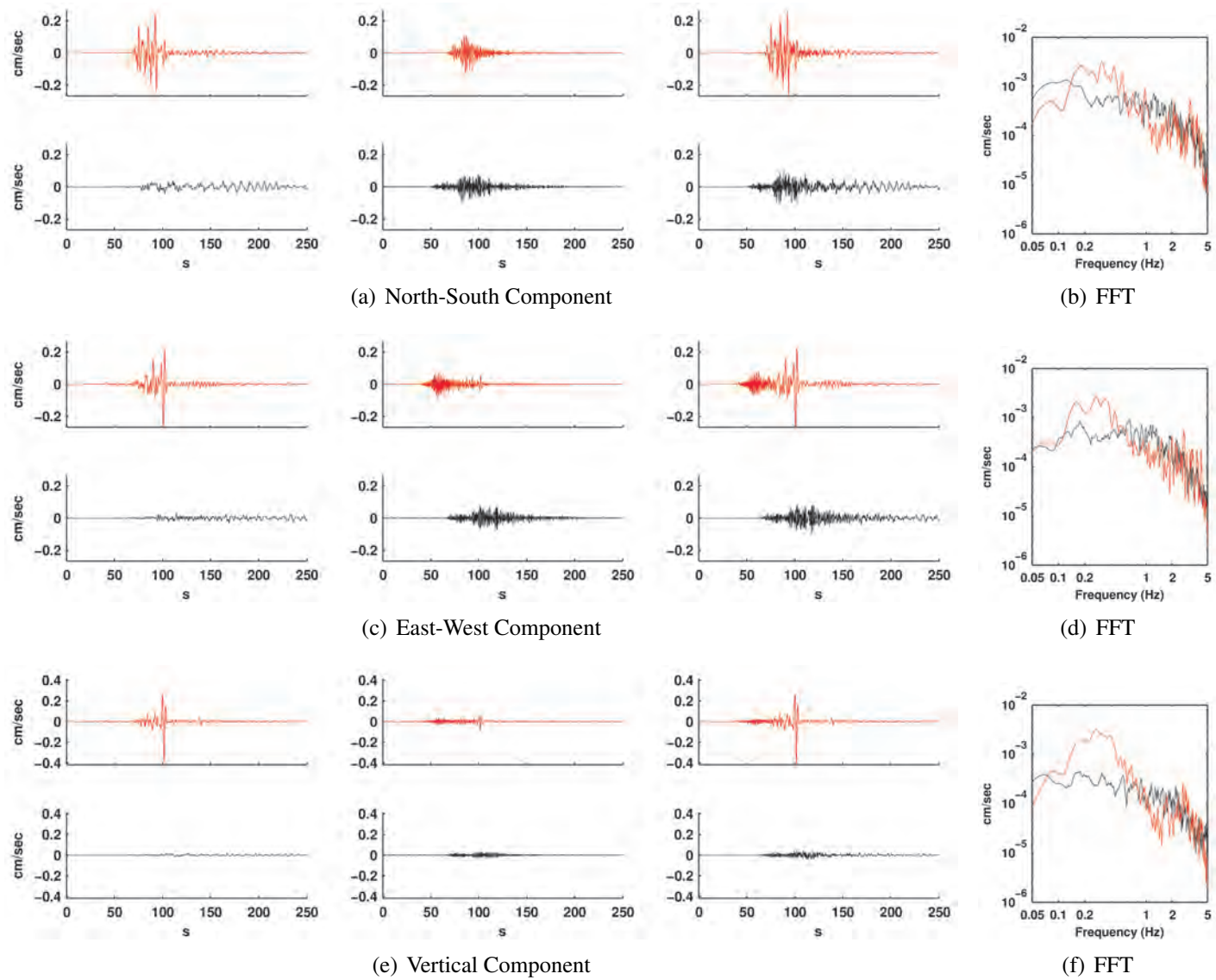


Figure E.5: Comparison of simulated (red) and observed (black) ground motions at station 4.

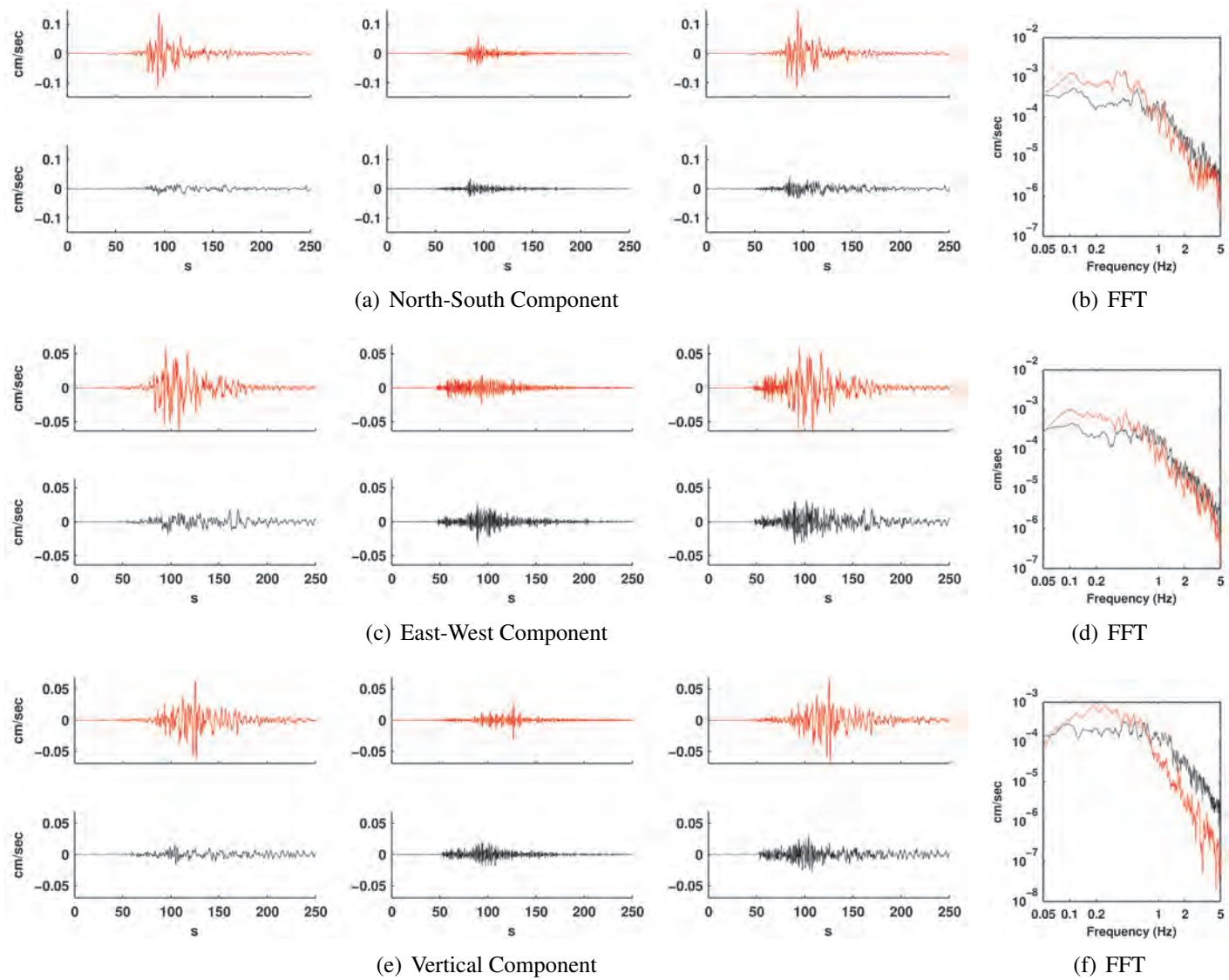


Figure E.6: Comparison of simulated (red) and observed (black) ground motions at station 5.

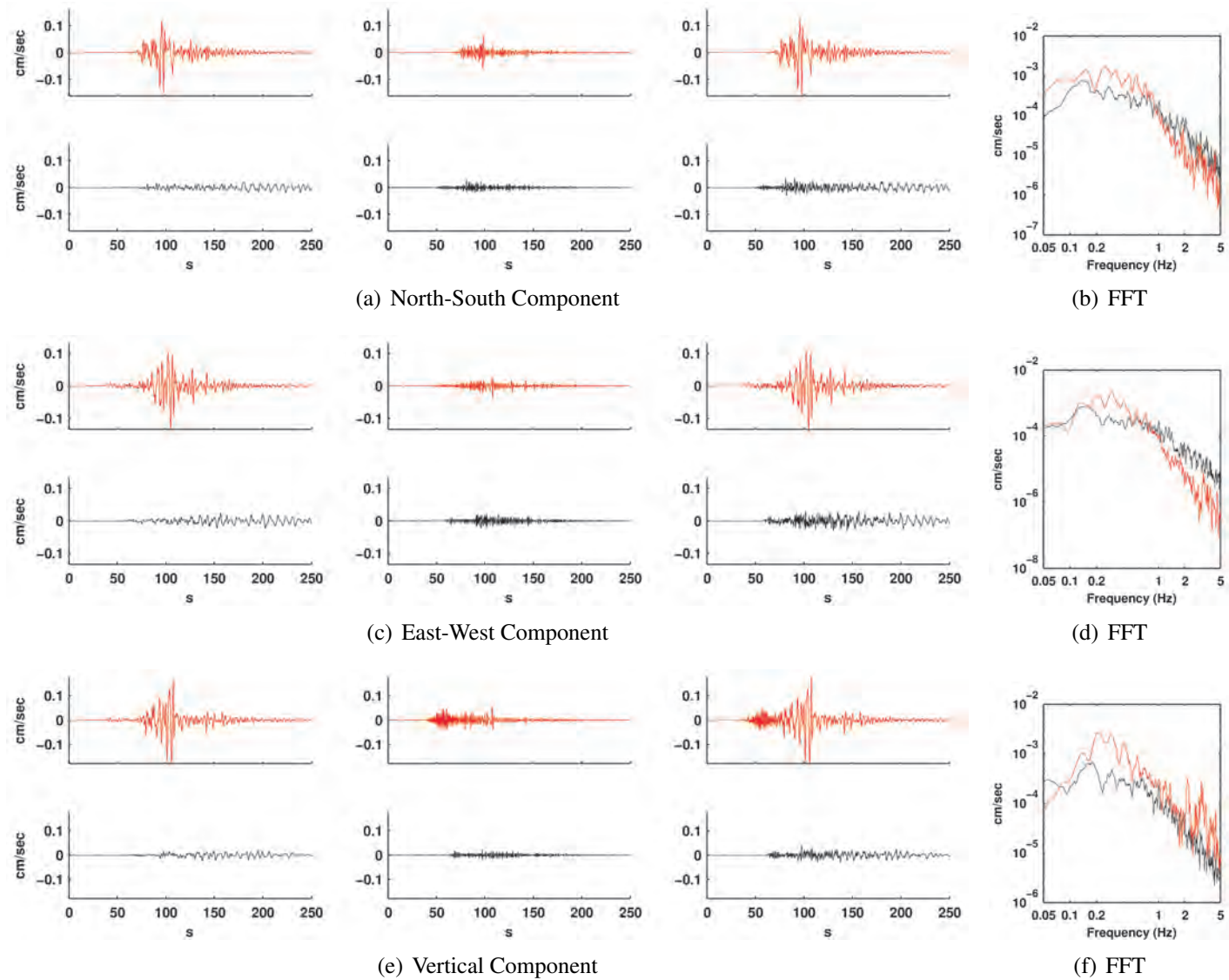


Figure E.7: Comparison of simulated (red) and observed (black) ground motions at station 6.

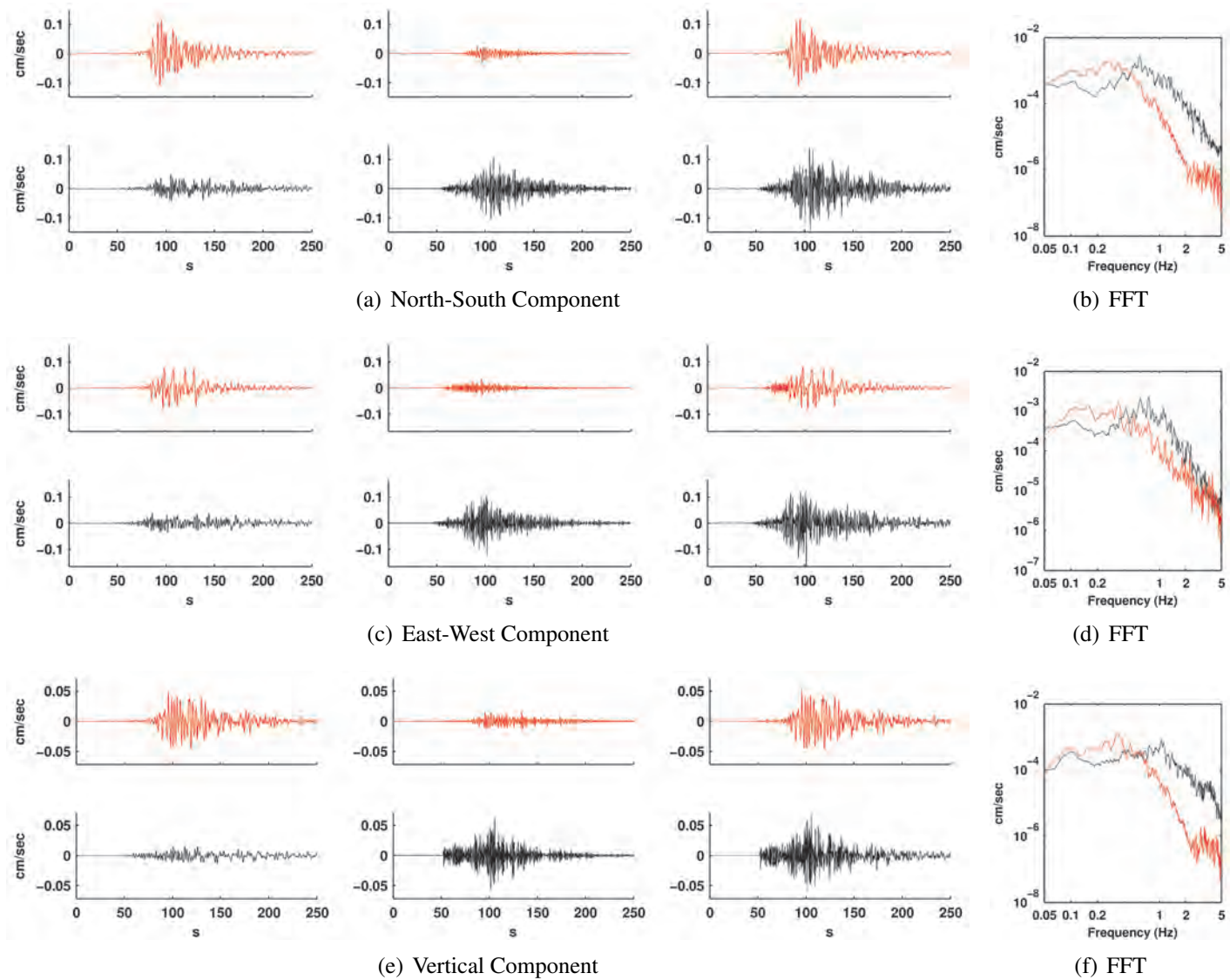


Figure E.8: Comparison of simulated (red) and observed (black) ground motions at station 7.

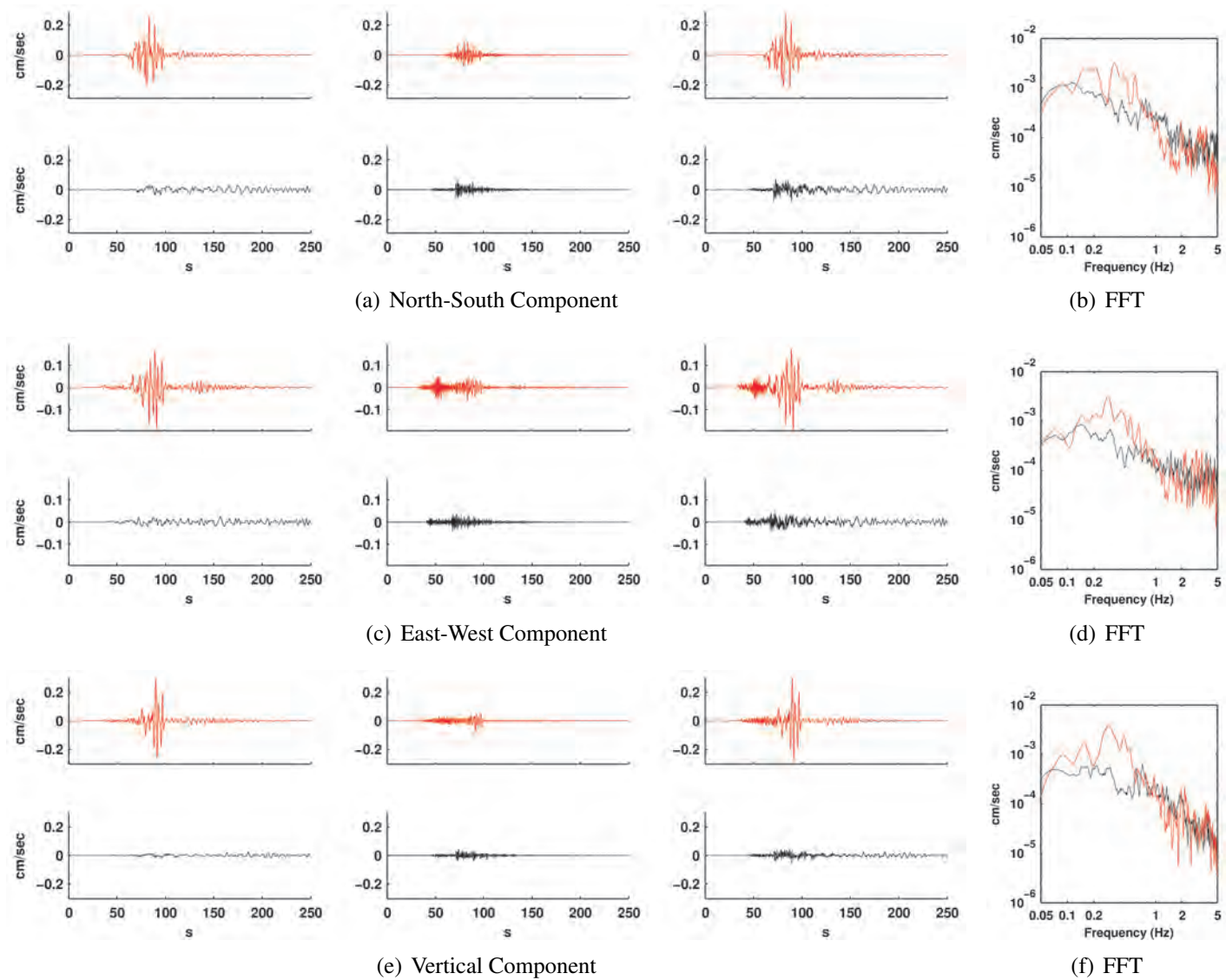


Figure E.9: Comparison of simulated (red) and observed (black) ground motions at station 8.

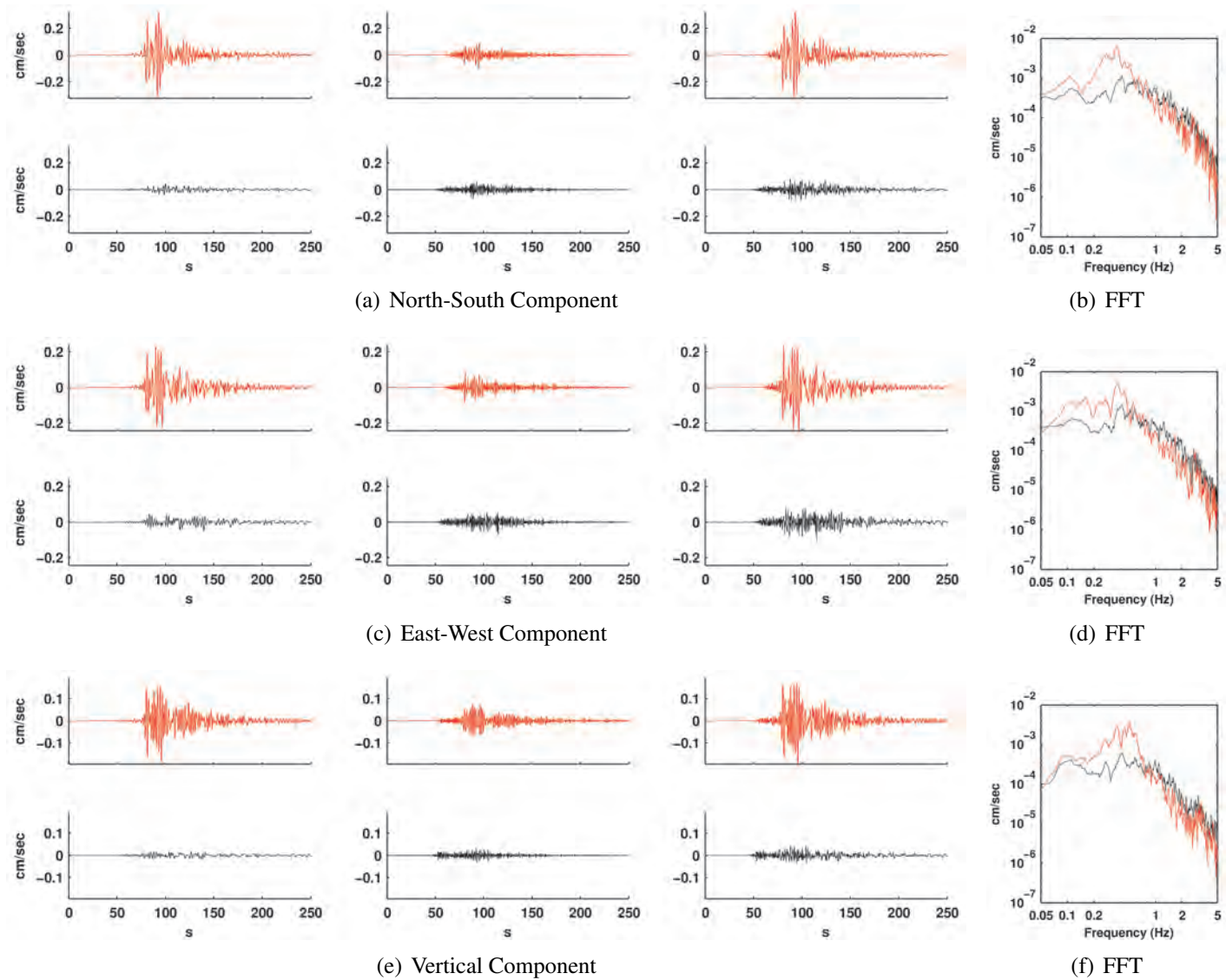


Figure E.10: Comparison of simulated (red) and observed (black) ground motions at station 9.

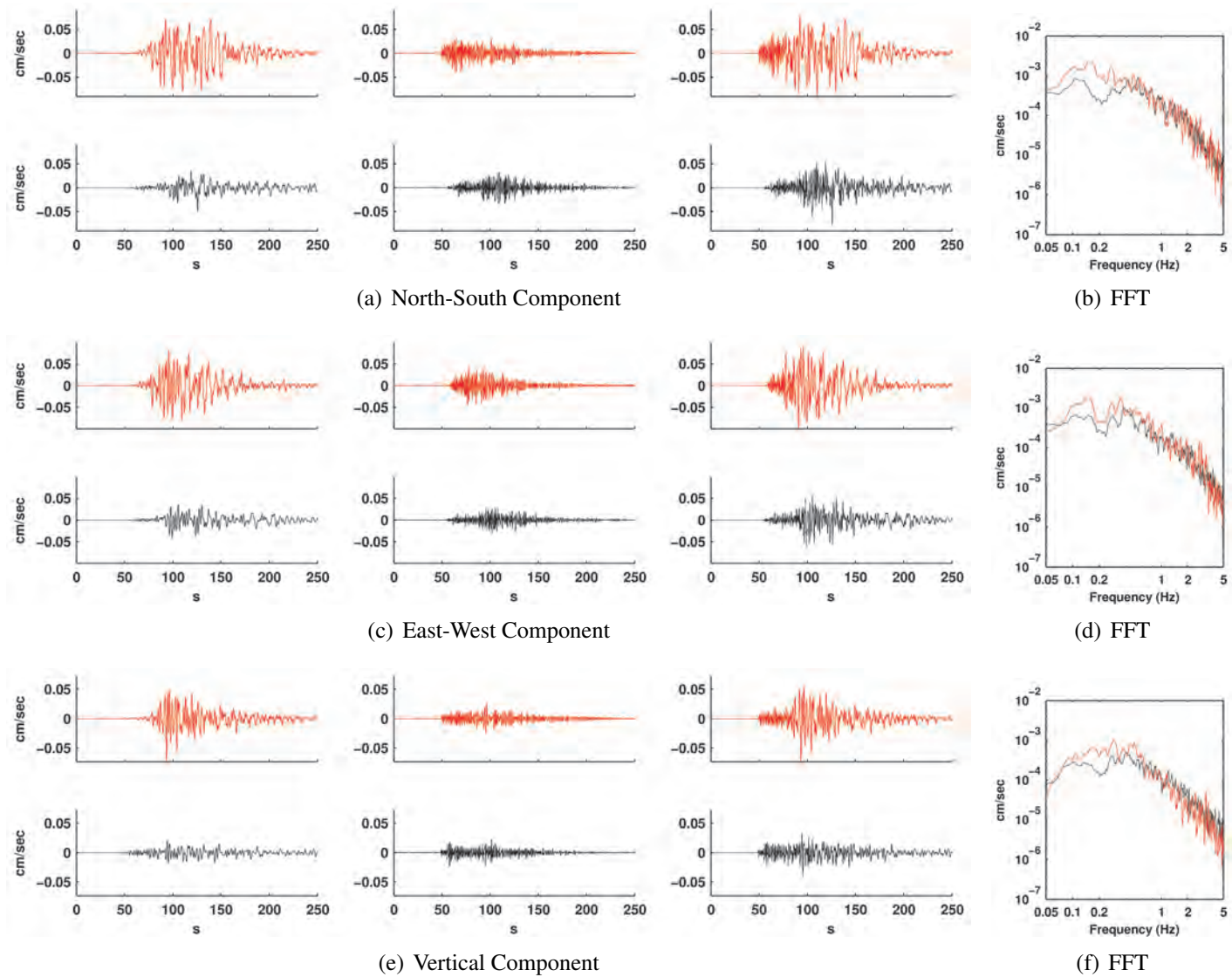


Figure E.11: Comparison of simulated (red) and observed (black) ground motions at station 10.

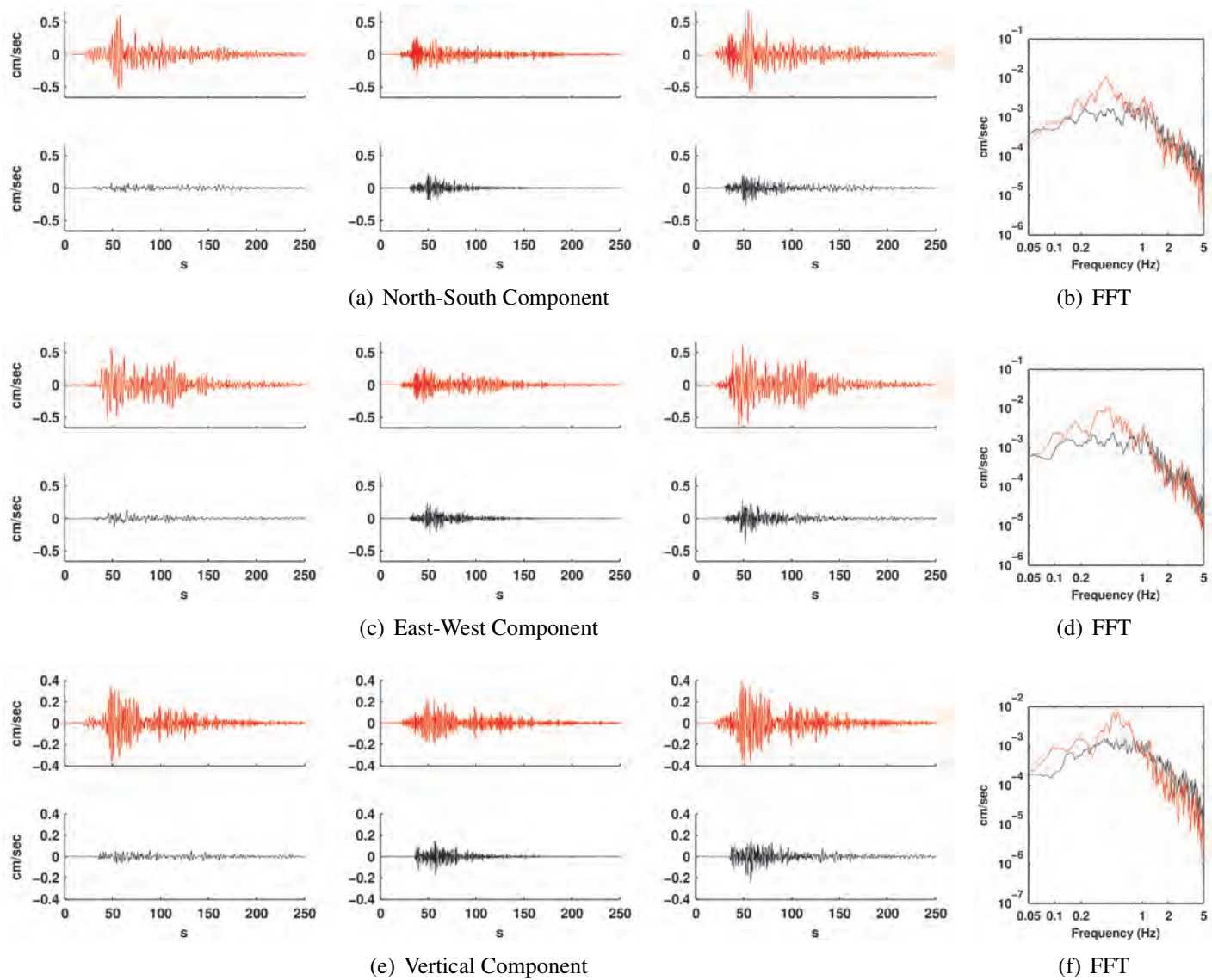


Figure E.12: Comparison of simulated (red) and observed (black) ground motions at station 11.

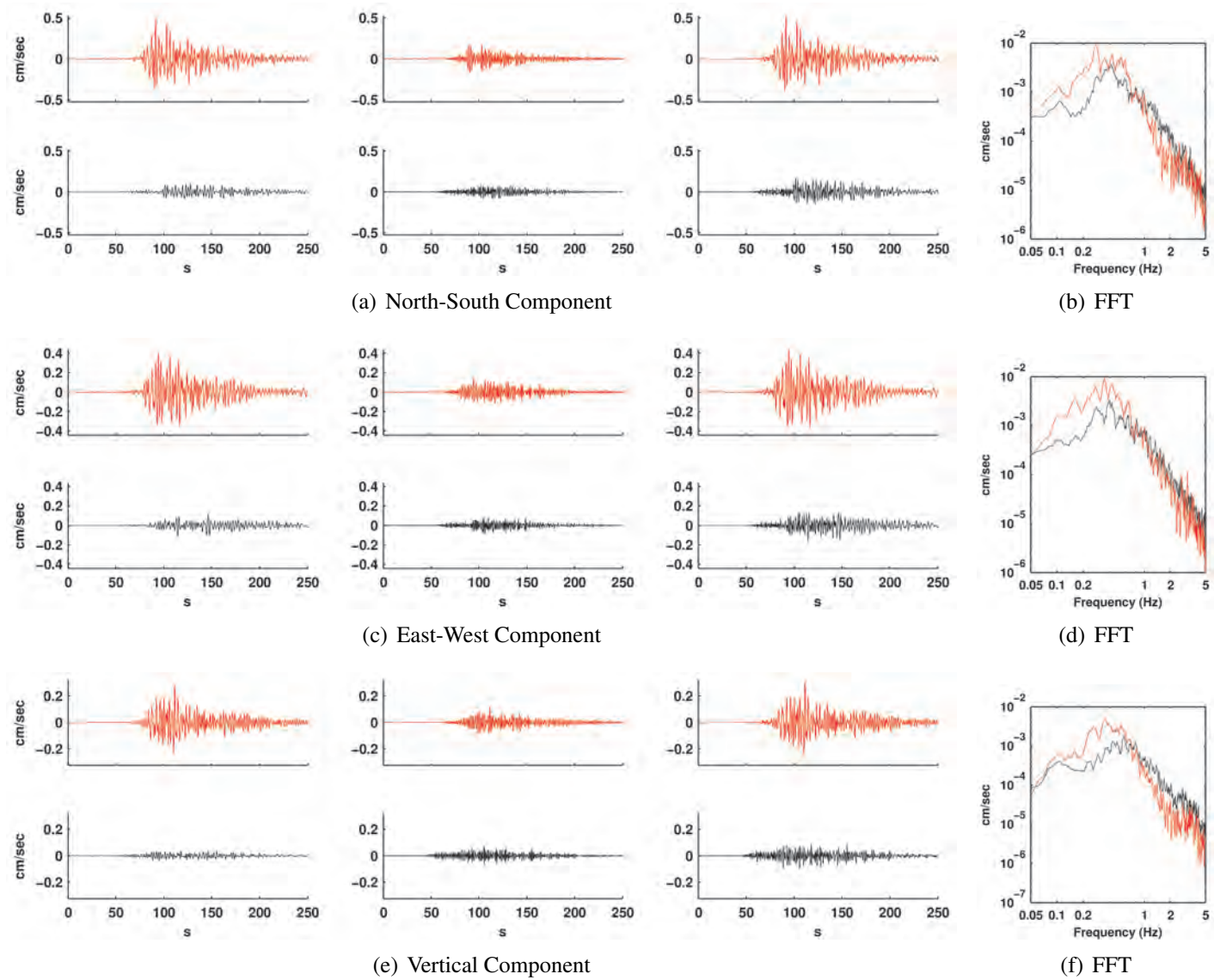


Figure E.13: Comparison of simulated (red) and observed (black) ground motions at station 12.

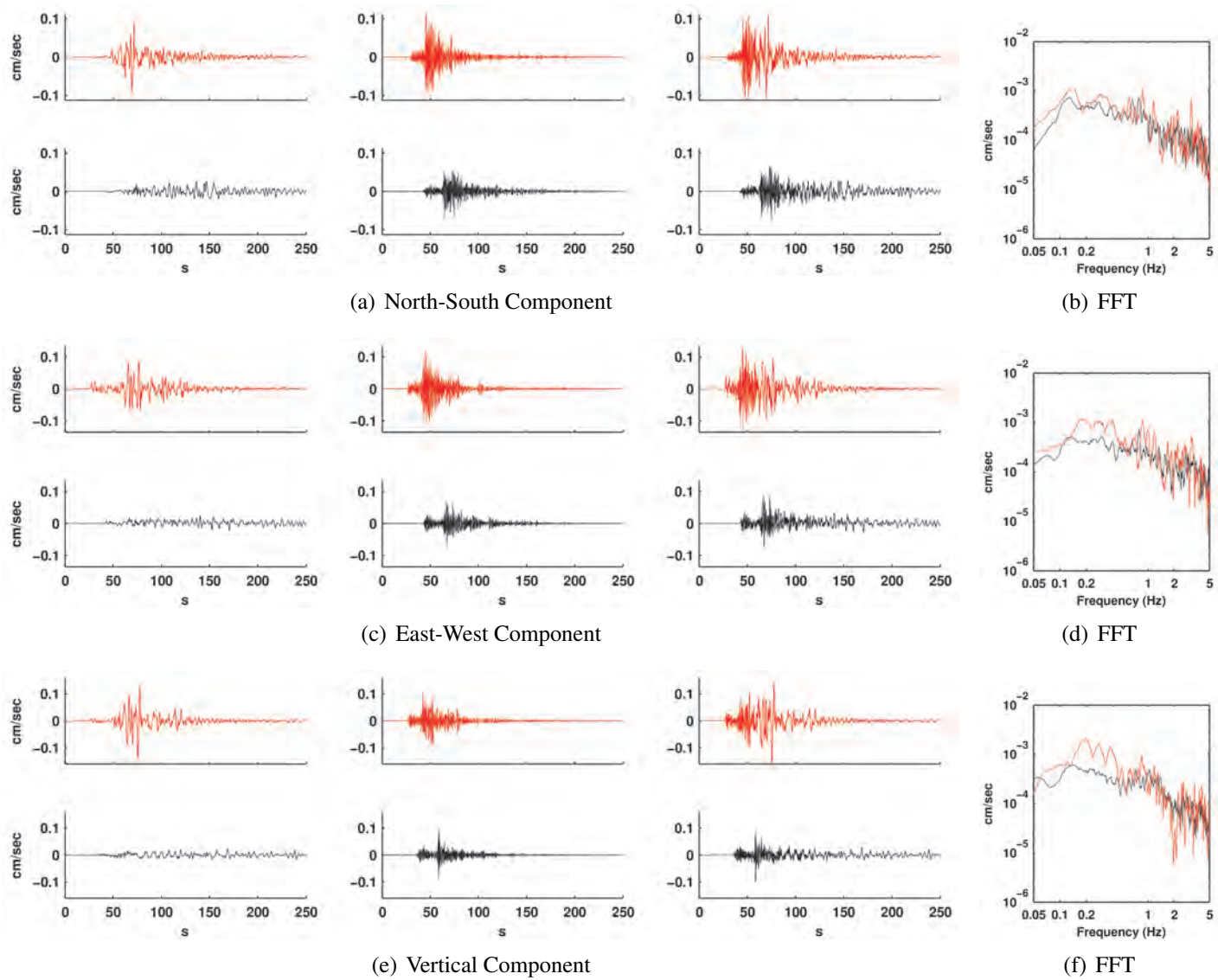


Figure E.14: Comparison of simulated (red) and observed (black) ground motions at station 13.

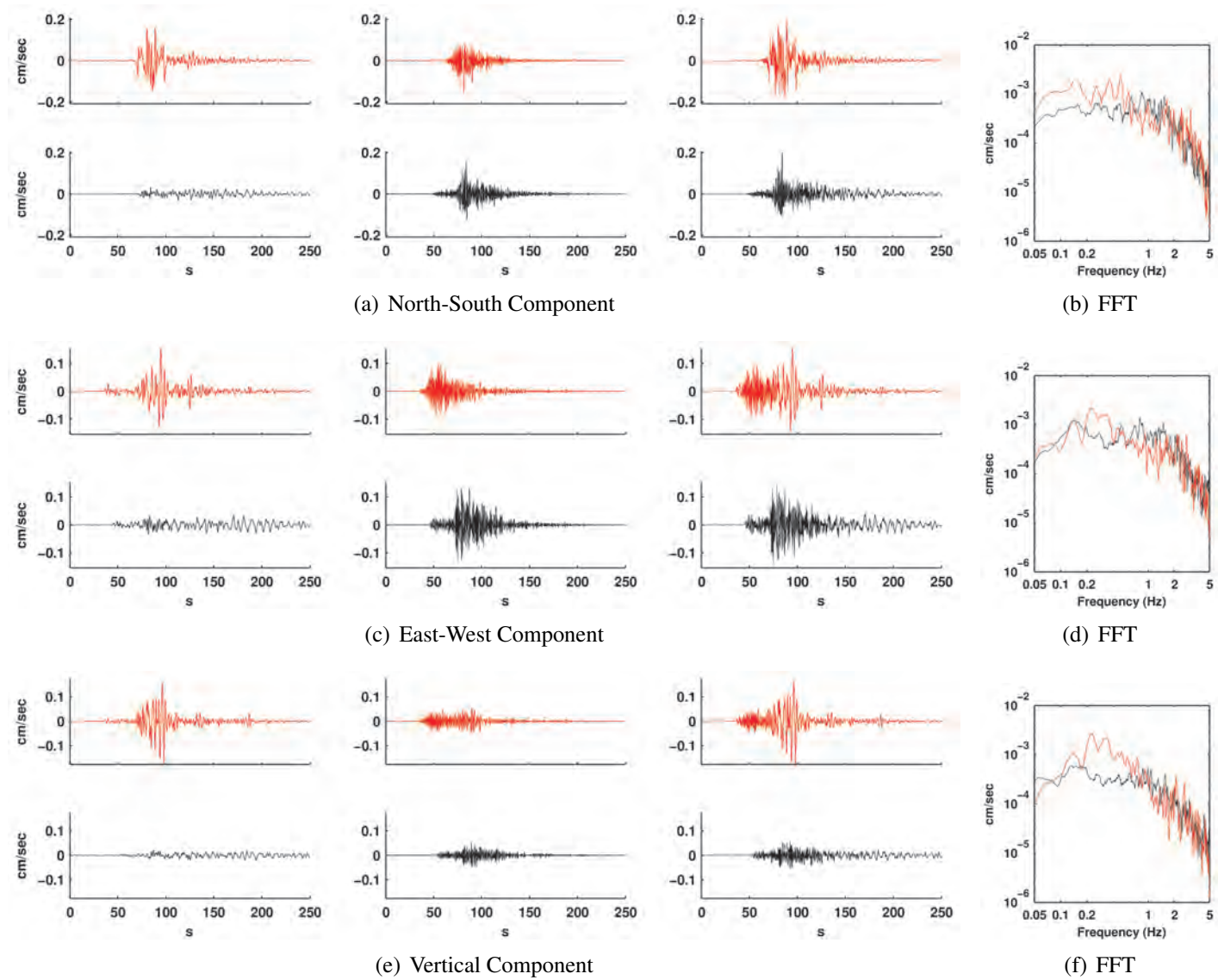


Figure E.15: Comparison of simulated (red) and observed (black) ground motions at station 14.

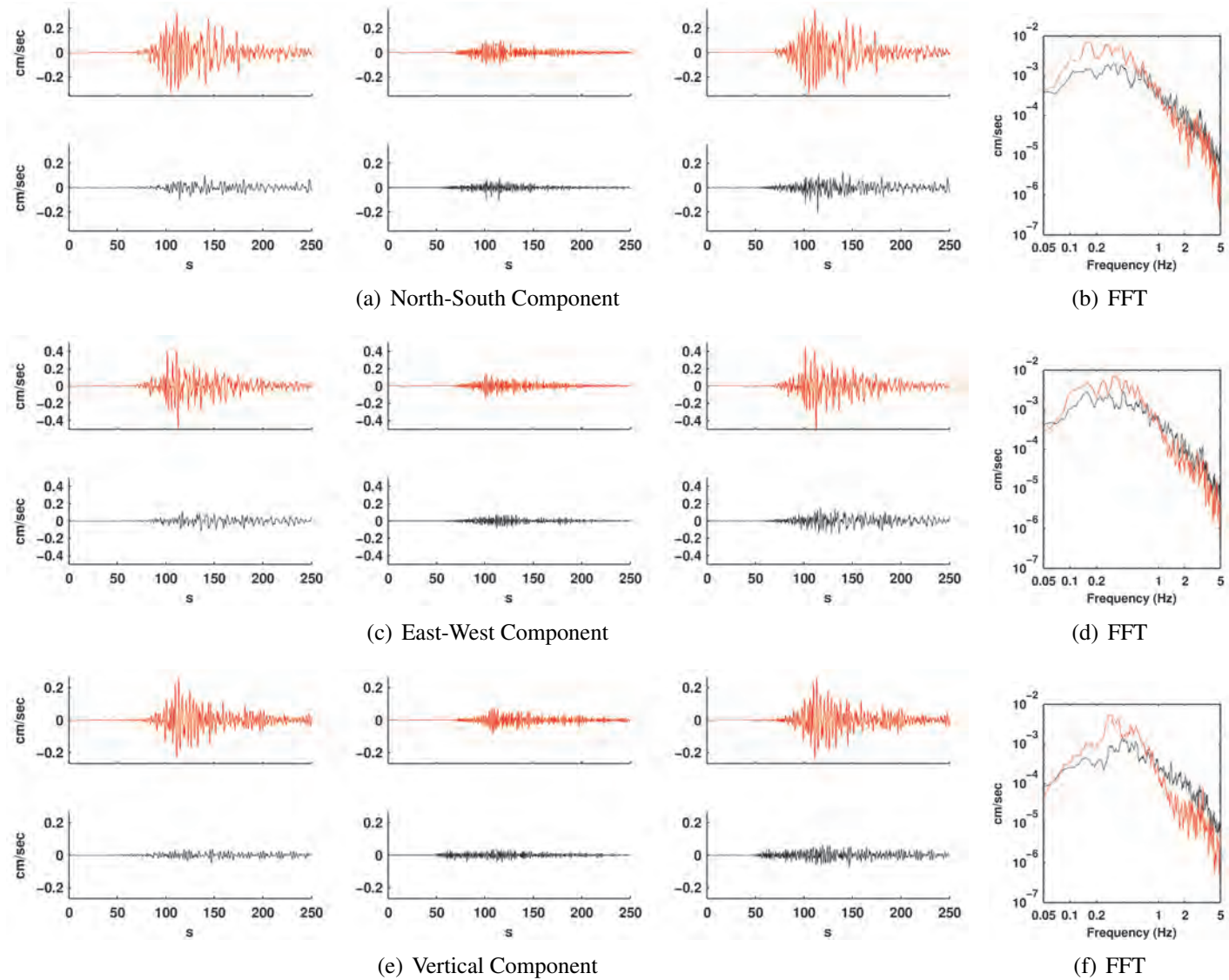


Figure E.16: Comparison of simulated (red) and observed (black) ground motions at station 15.

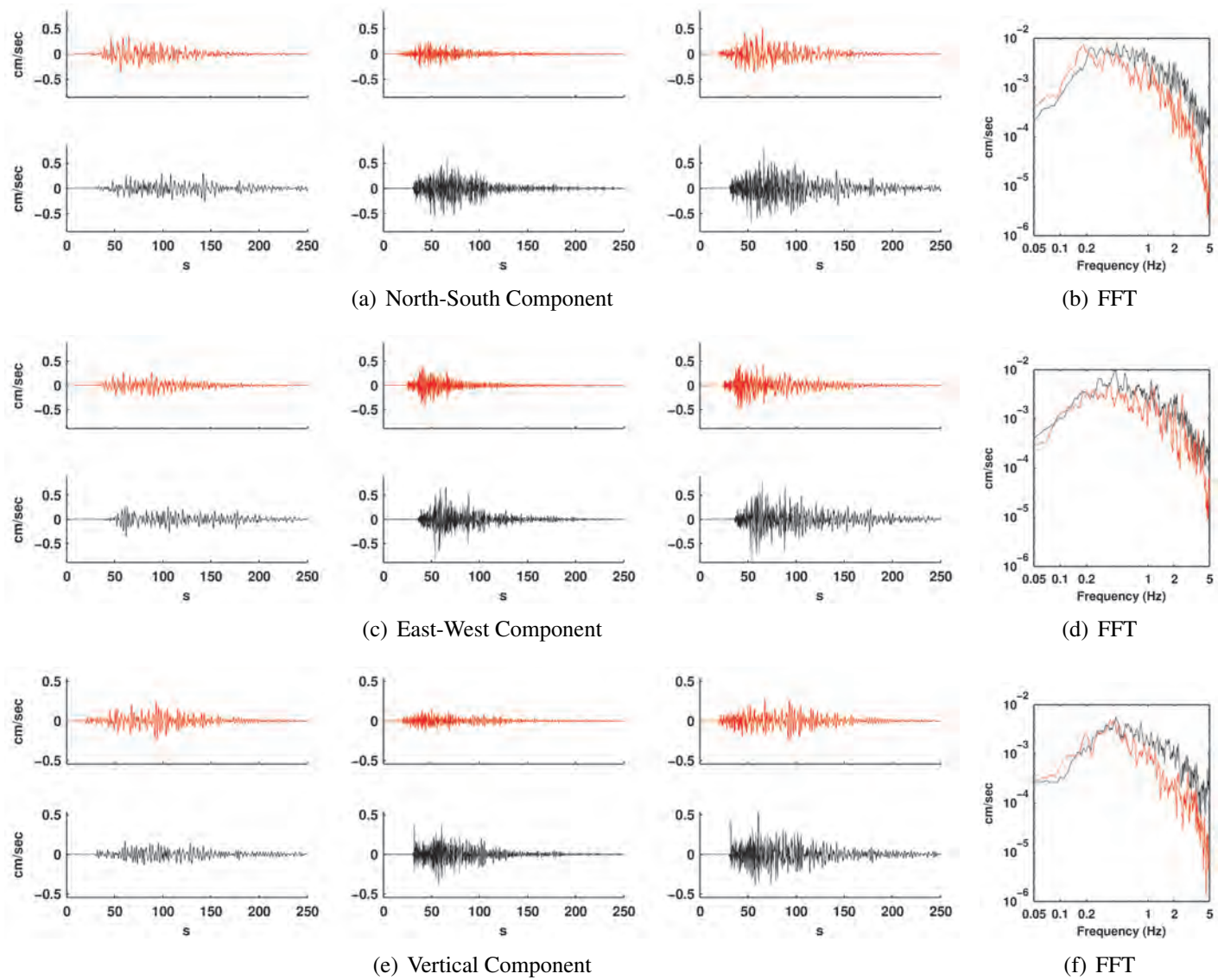


Figure E.17: Comparison of simulated (red) and observed (black) ground motions at station 16.

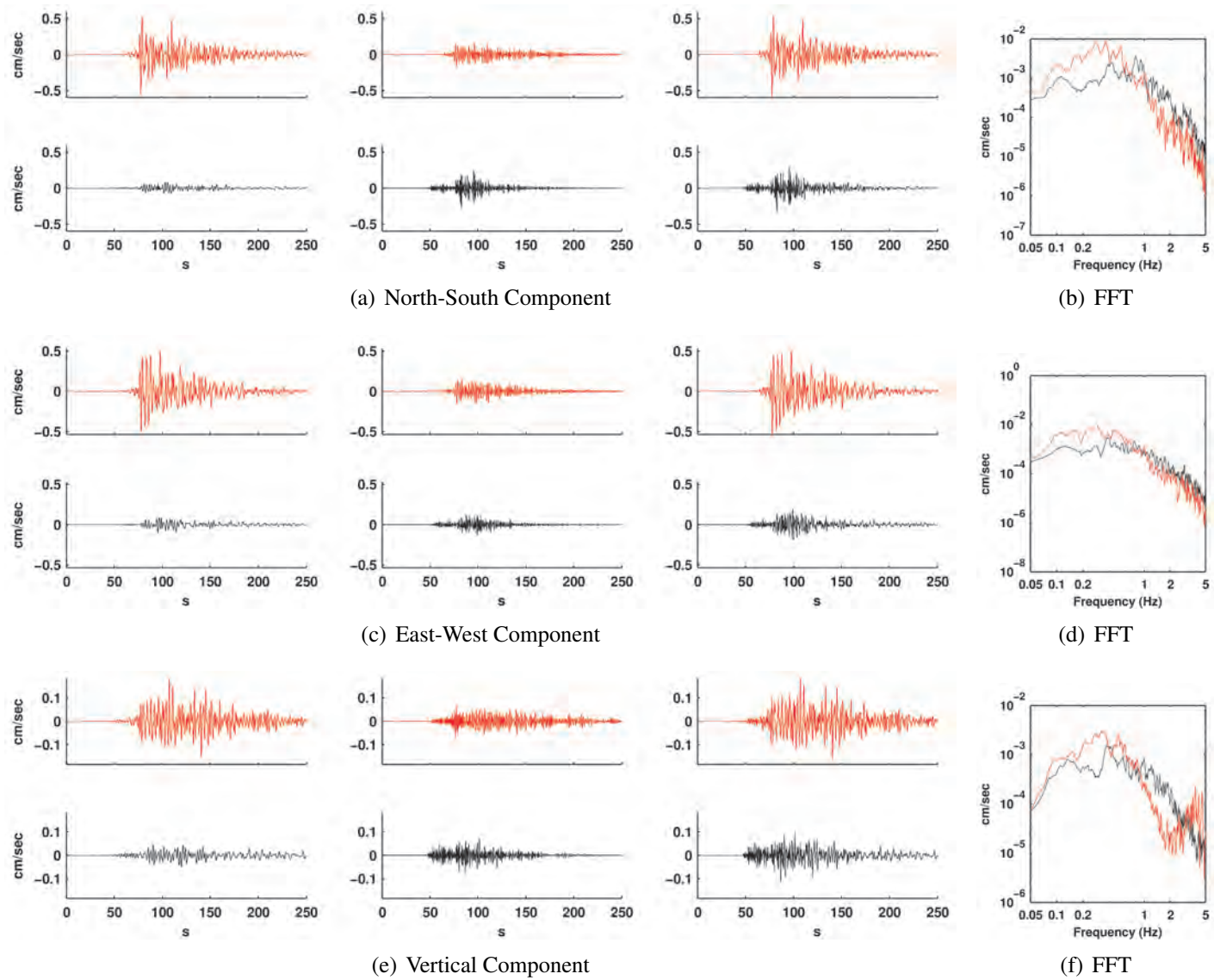


Figure E.18: Comparison of simulated (red) and observed (black) ground motions at station 17.

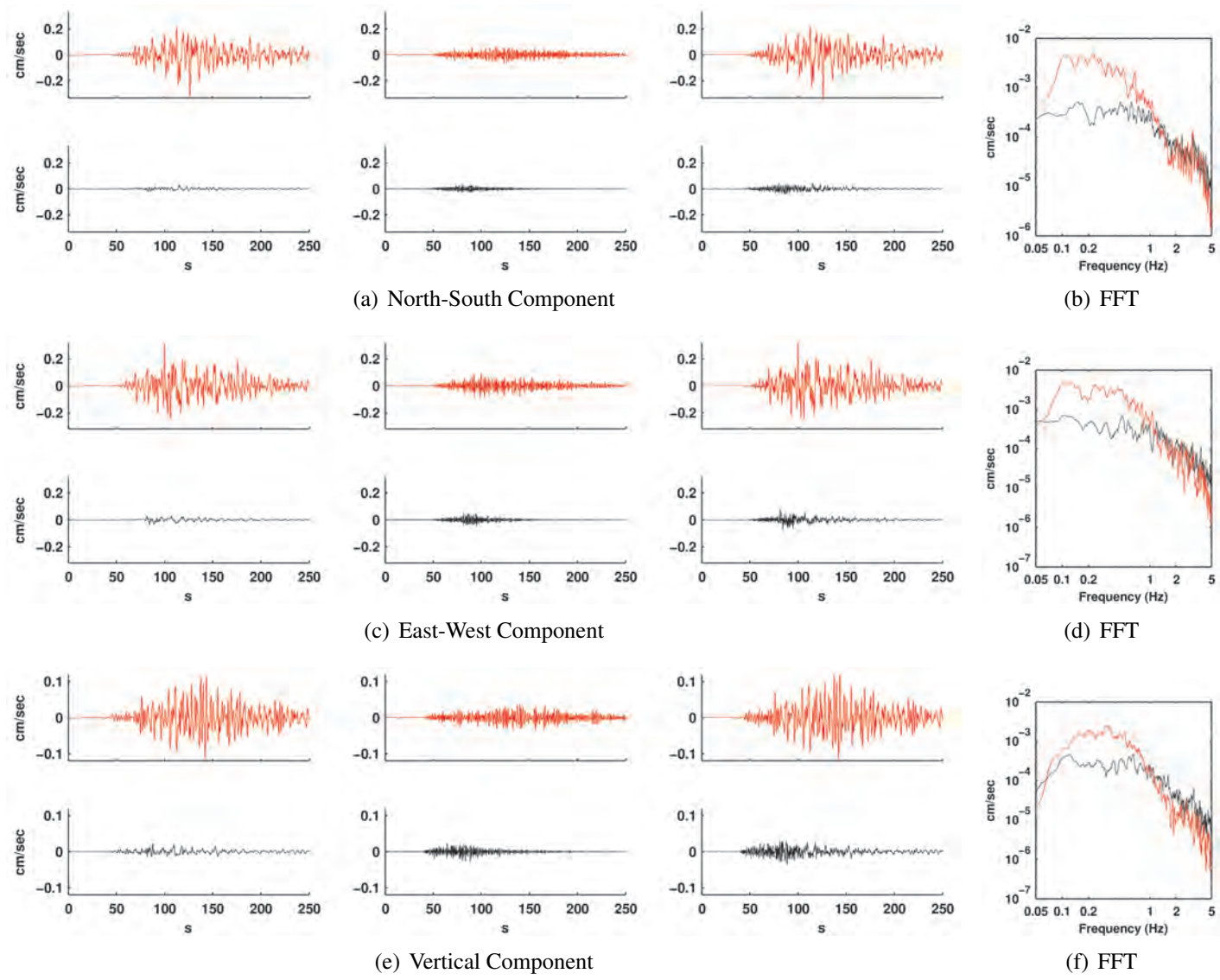


Figure E.19: Comparison of simulated (red) and observed (black) ground motions at station 18.

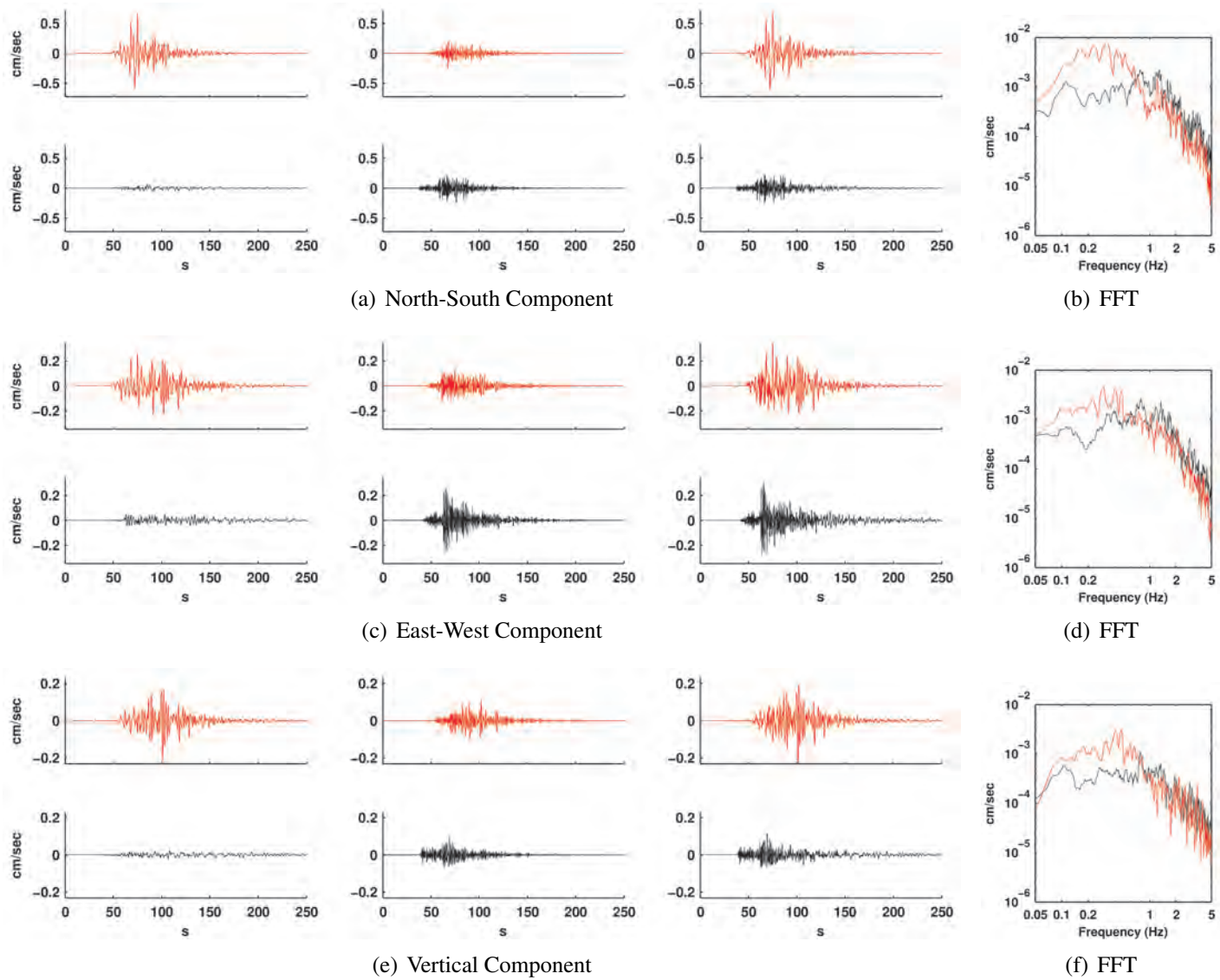


Figure E.20: Comparison of simulated (red) and observed (black) ground motions at station 19.

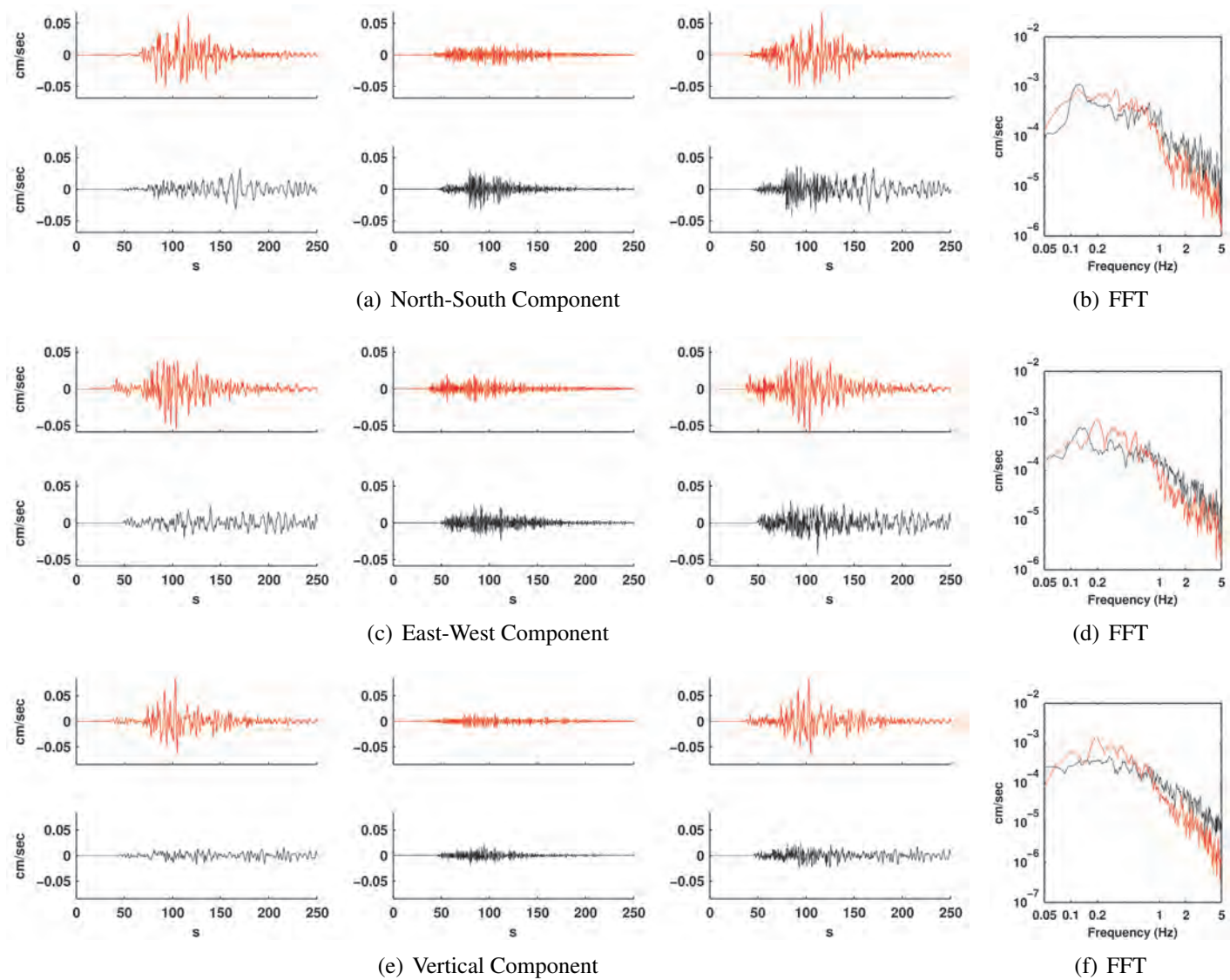


Figure E.21: Comparison of simulated (red) and observed (black) ground motions at station 20.

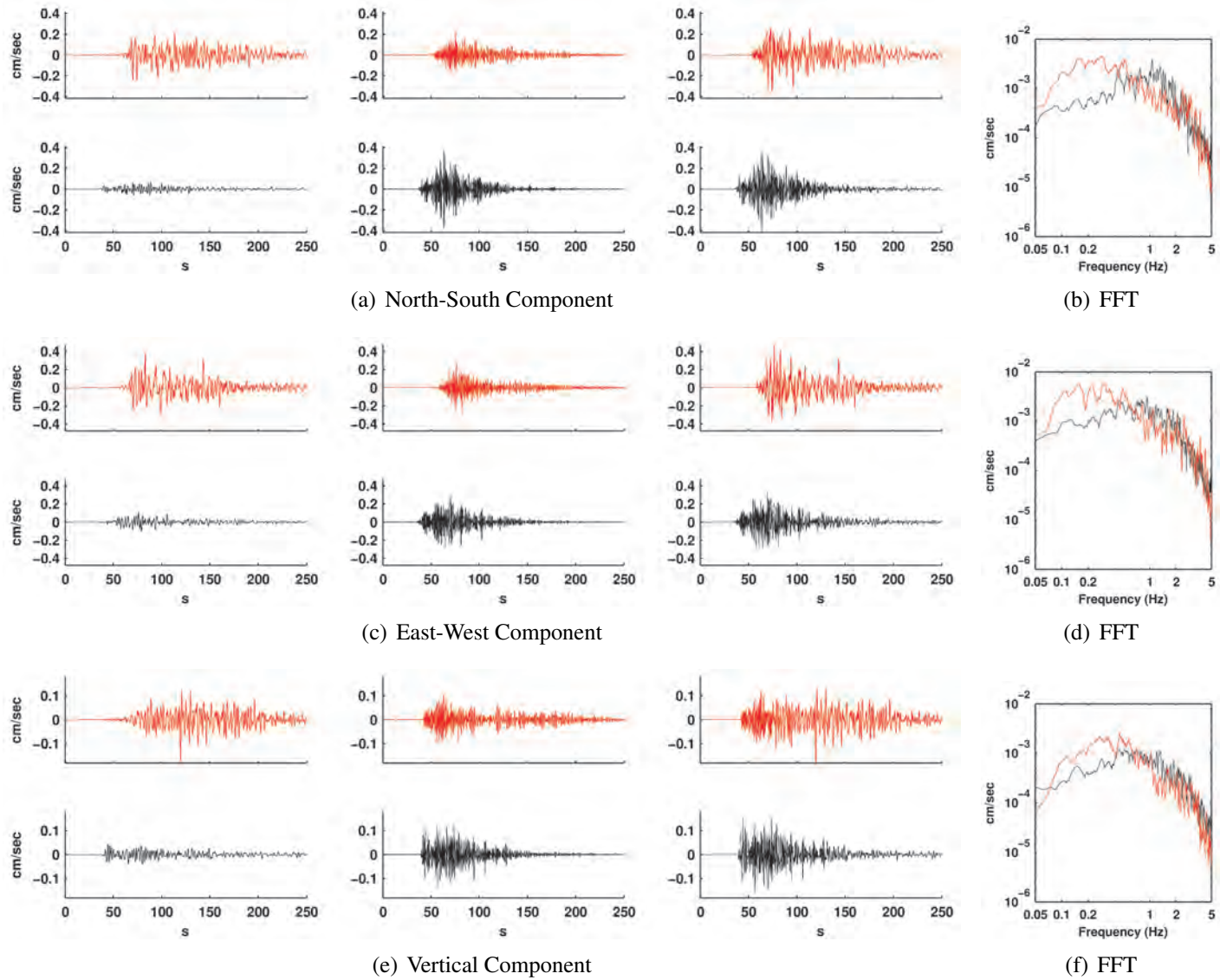


Figure E.22: Comparison of simulated (red) and observed (black) ground motions at station 21.

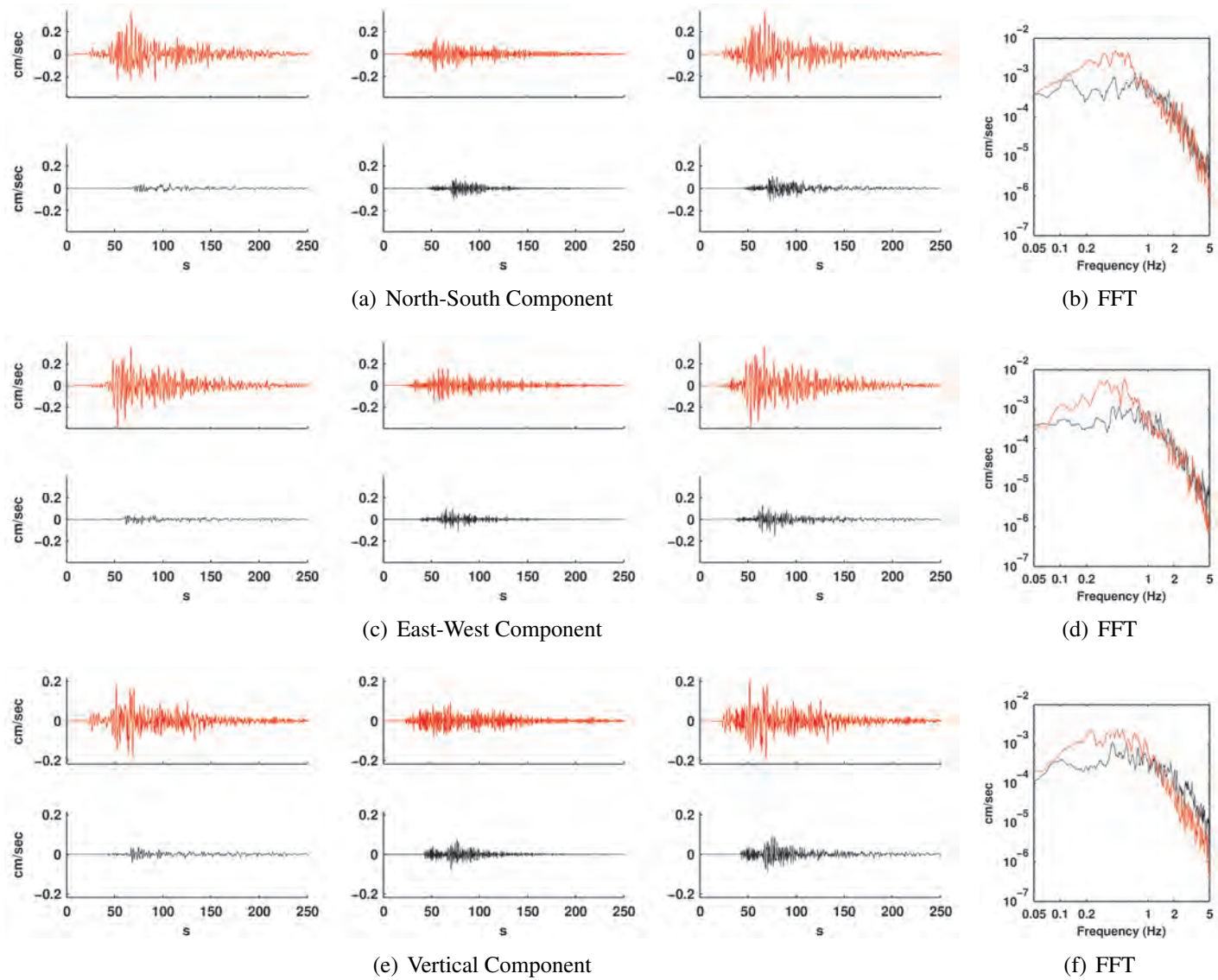


Figure E.23: Comparison of simulated (red) and observed (black) ground motions at station 22.

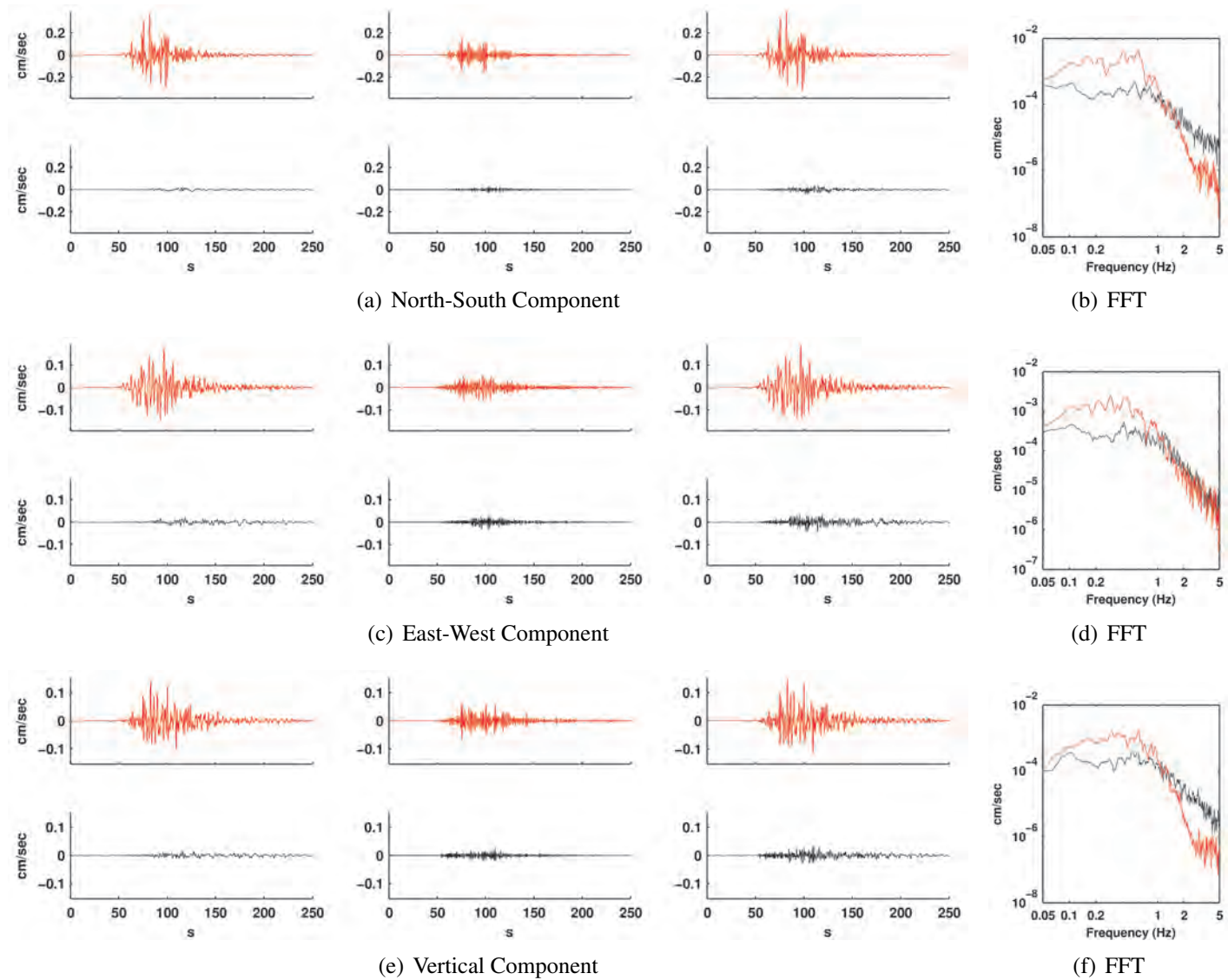


Figure E.24: Comparison of simulated (red) and observed (black) ground motions at station 23.

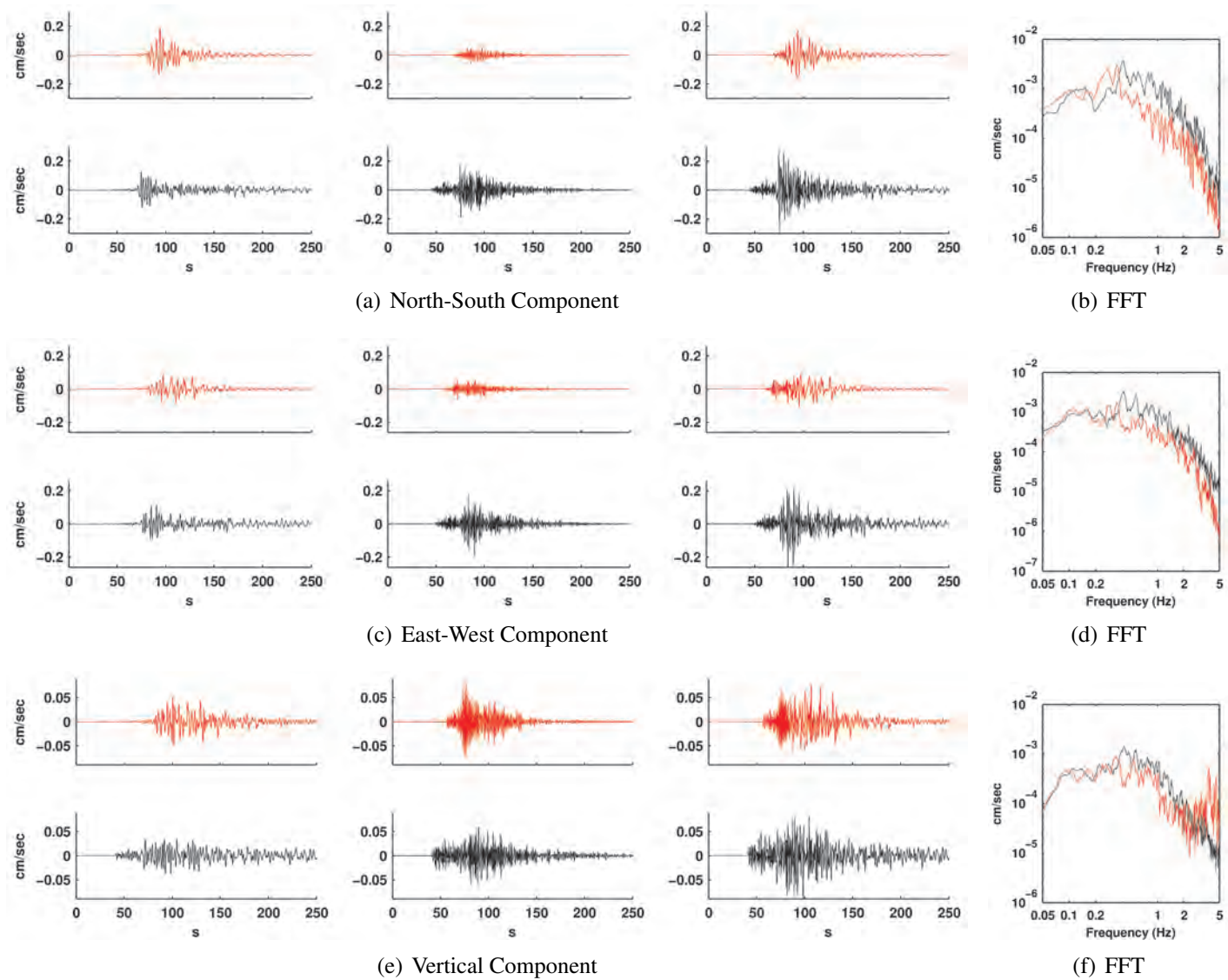


Figure E.25: Comparison of simulated (red) and observed (black) ground motions at station 24.

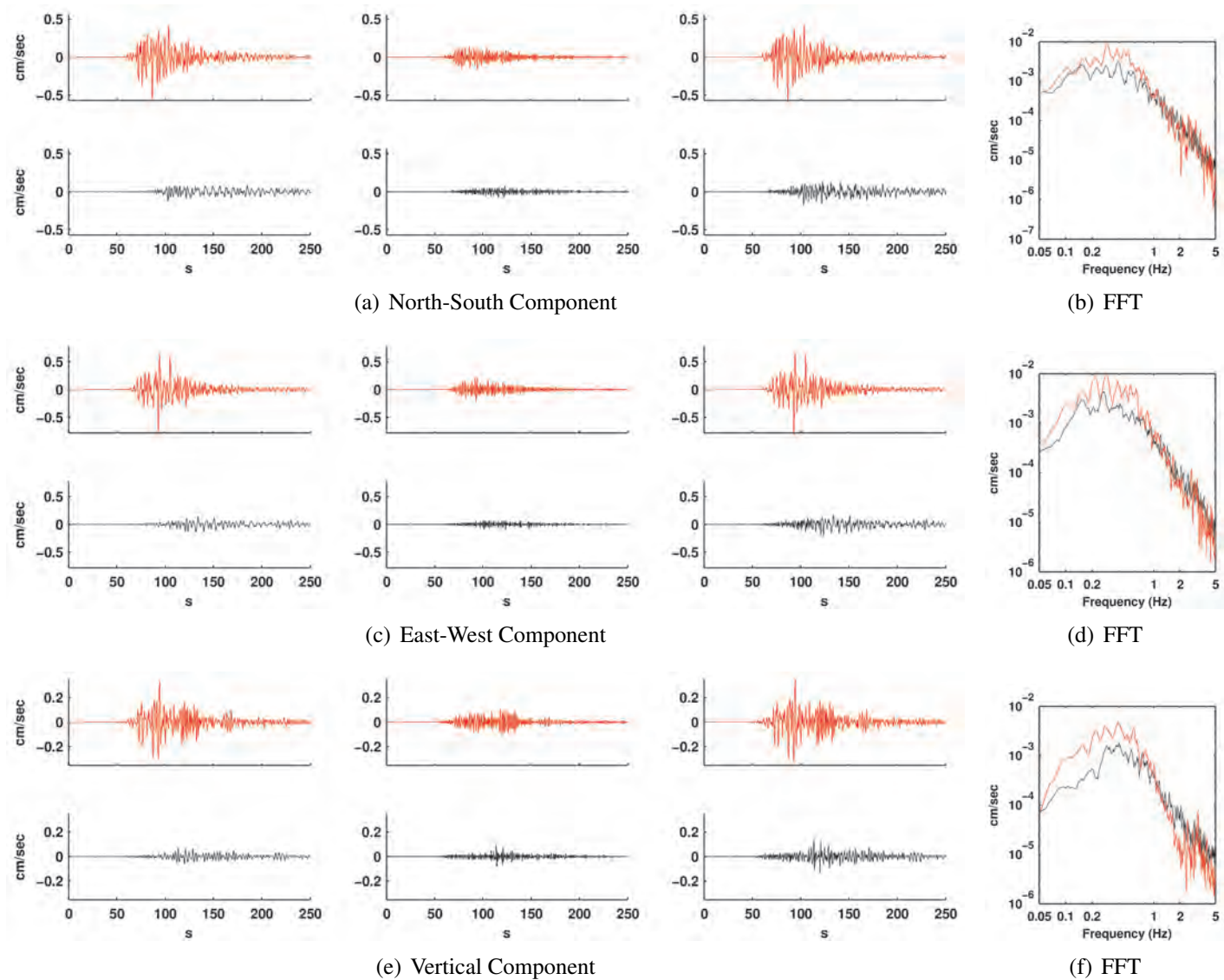


Figure E.26: Comparison of simulated (red) and observed (black) ground motions at station 25.

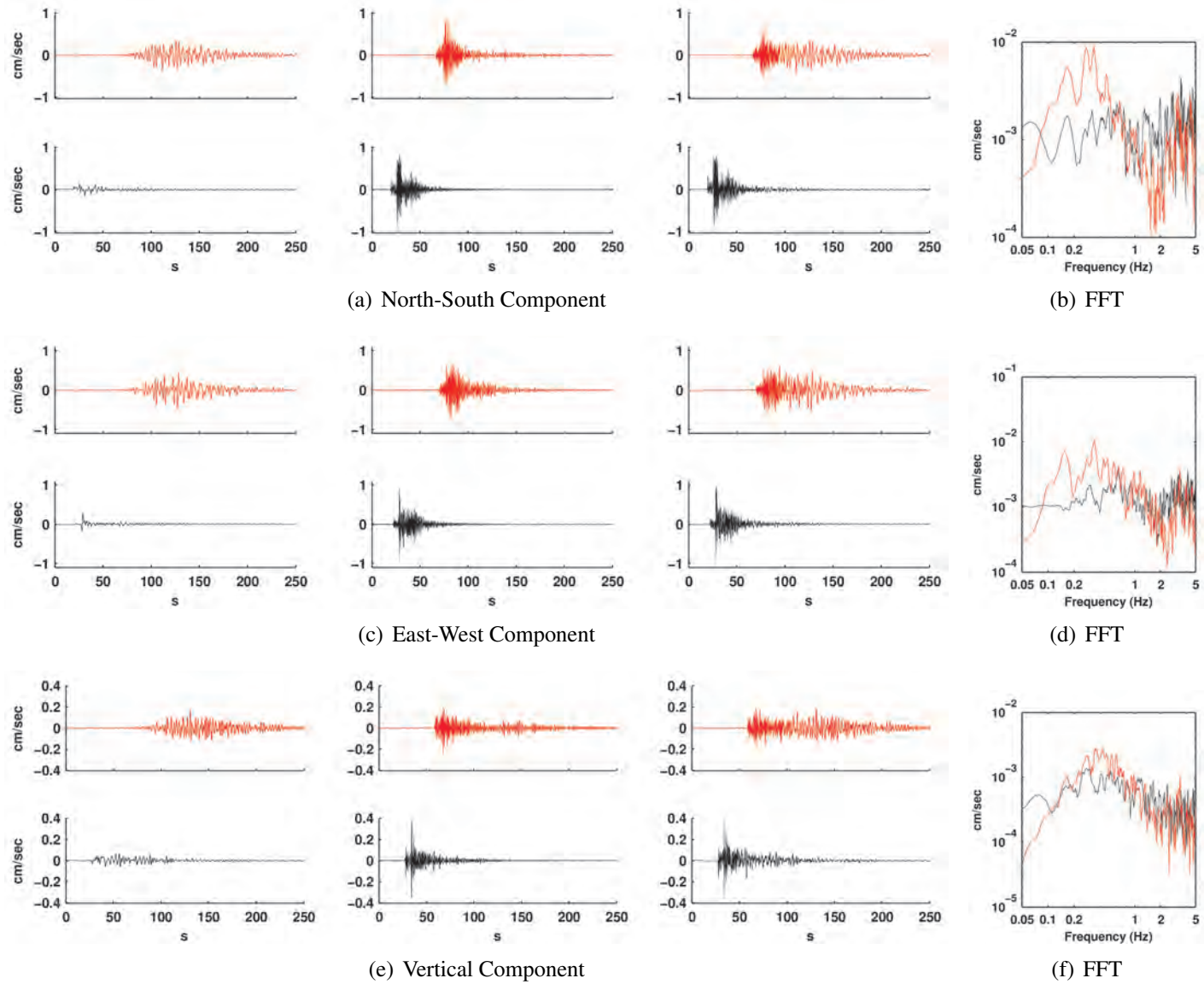


Figure E.27: Comparison of simulated (red) and observed (black) ground motions at station 26.

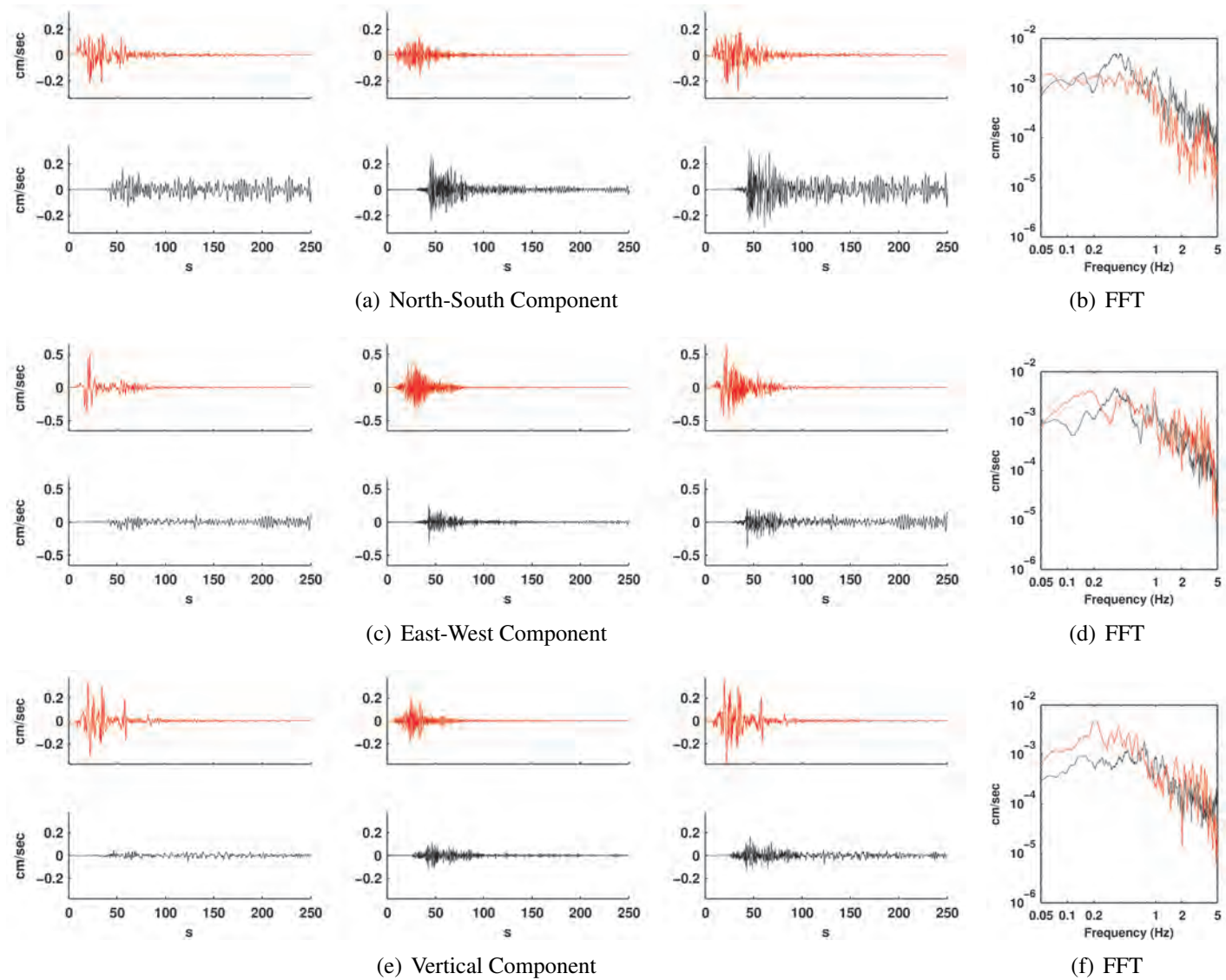


Figure E.28: Comparison of simulated (red) and observed (black) ground motions at station 27.

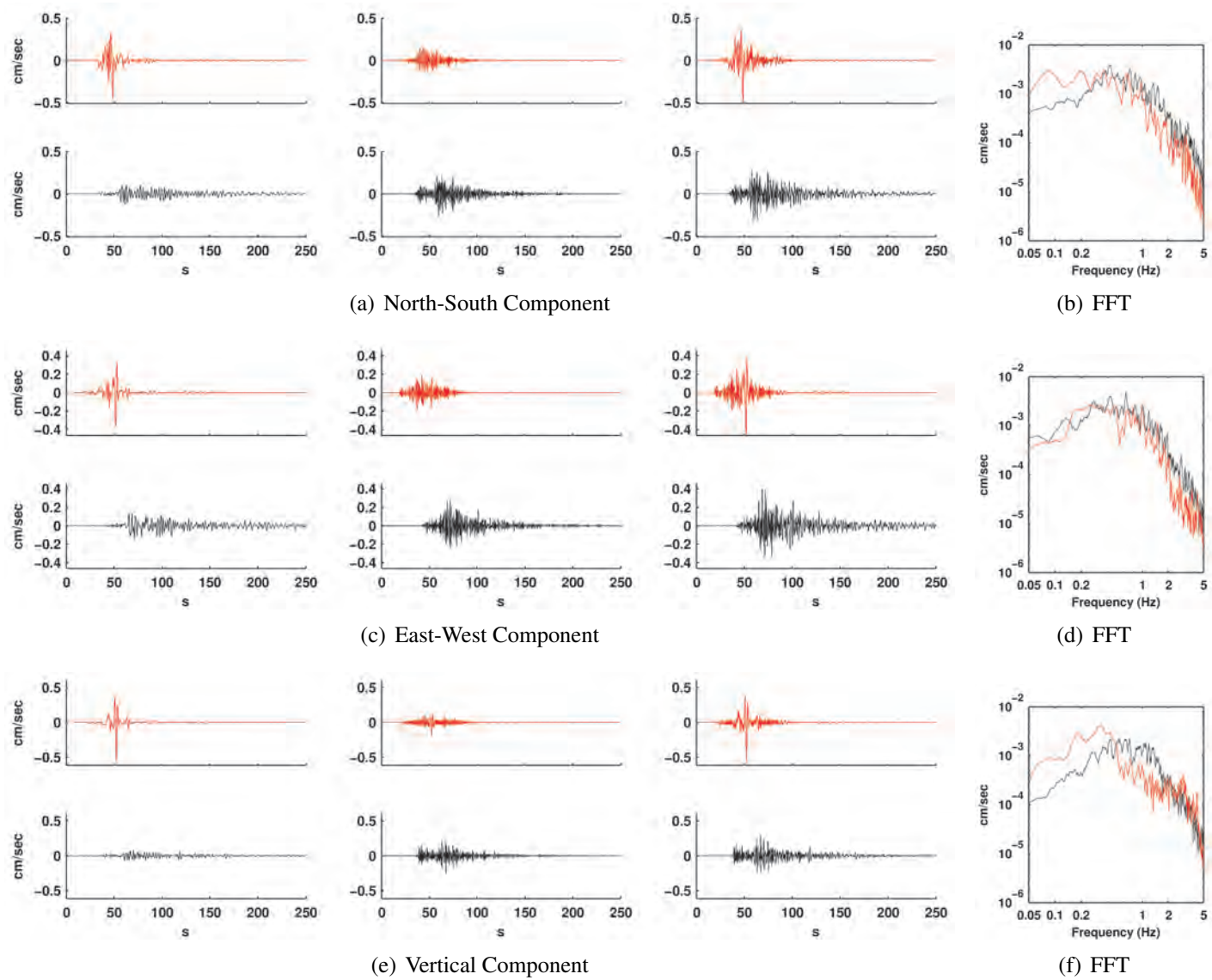


Figure E.29: Comparison of simulated (red) and observed (black) ground motions at station 28.

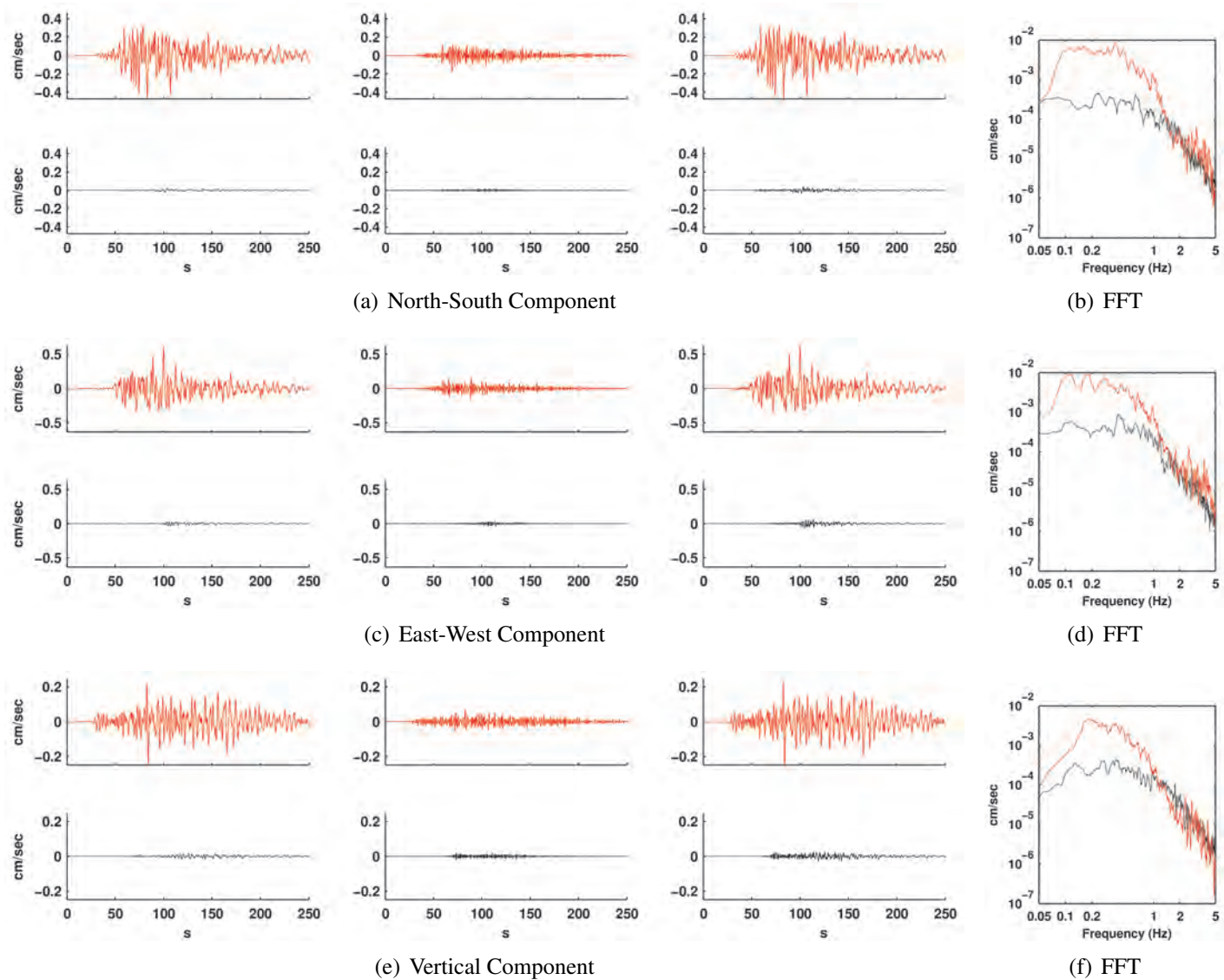


Figure E.30: Comparison of simulated (red) and observed (black) ground motions at station 29.

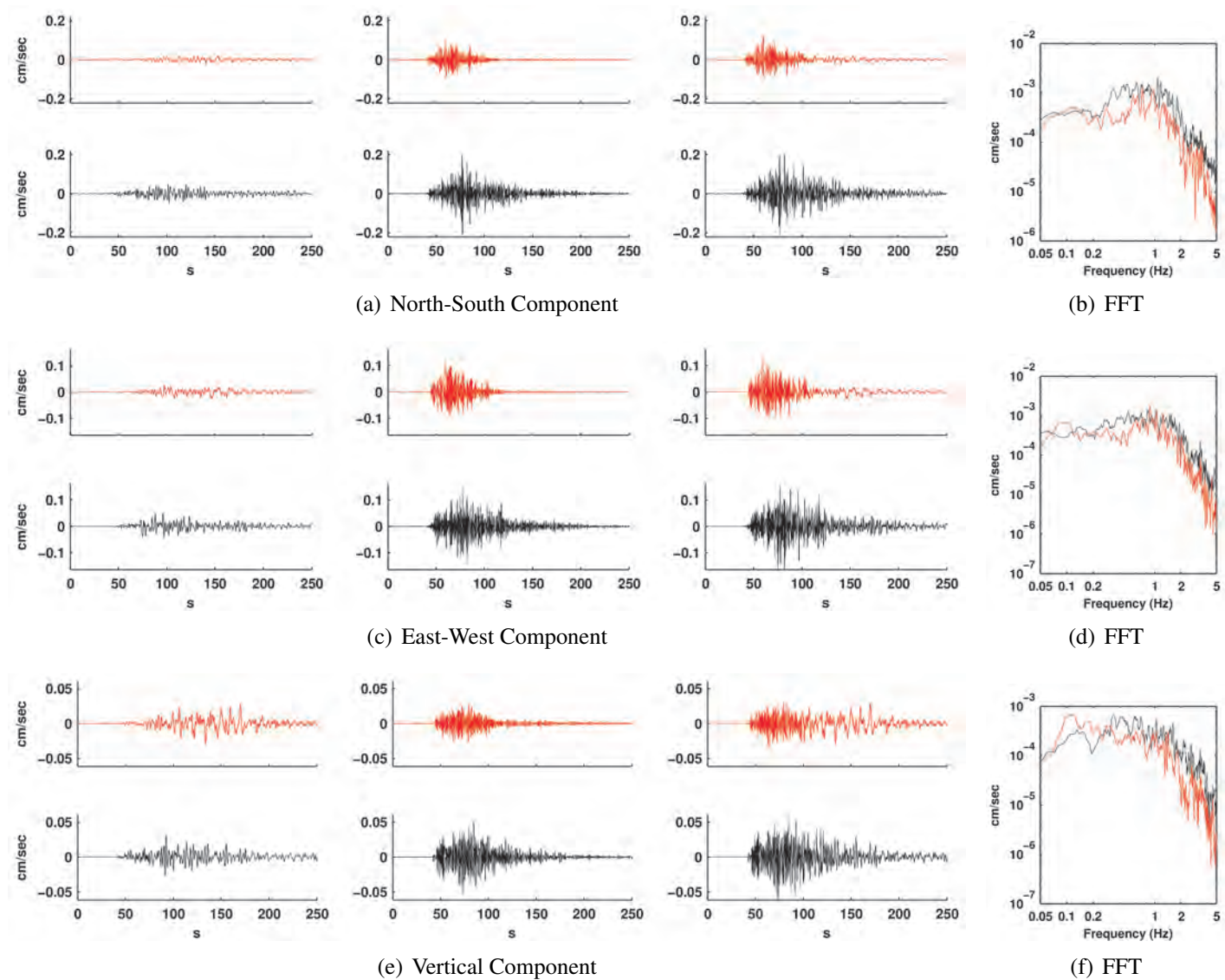


Figure E.31: Comparison of simulated (red) and observed (black) ground motions at station 30.

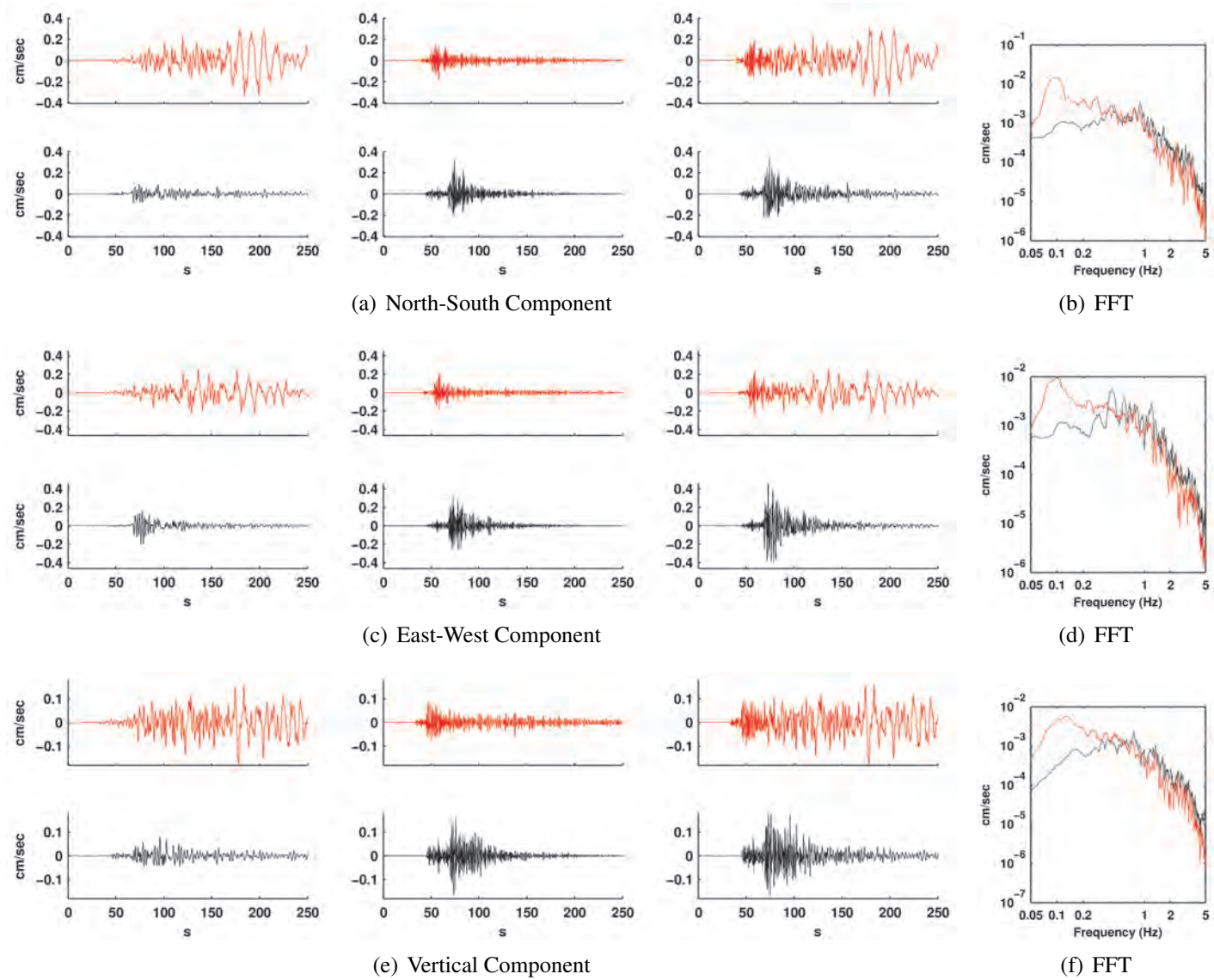


Figure E.32: Comparison of simulated (red) and observed (black) ground motions at station 31.

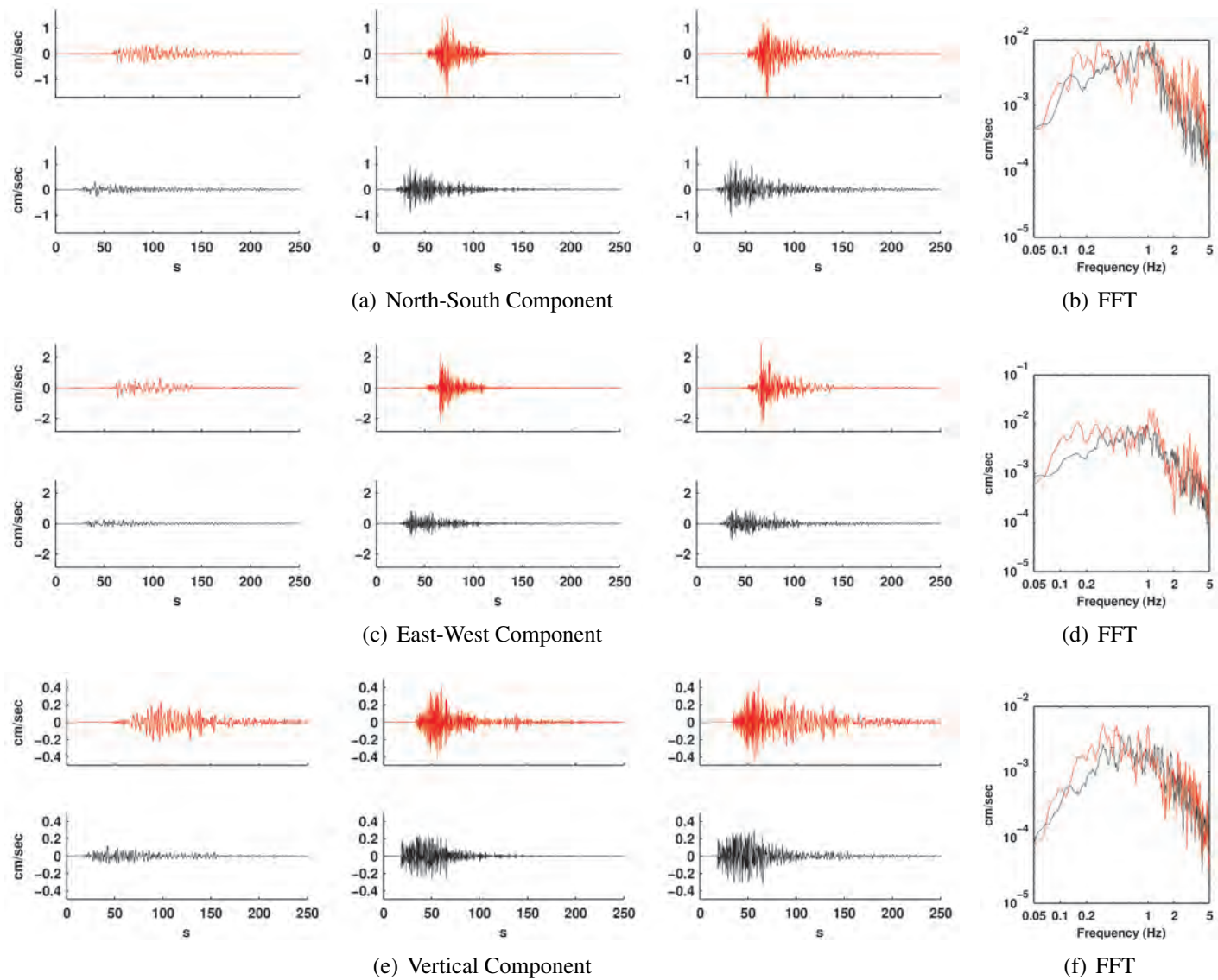


Figure E.33: Comparison of simulated (red) and observed (black) ground motions at station 32.

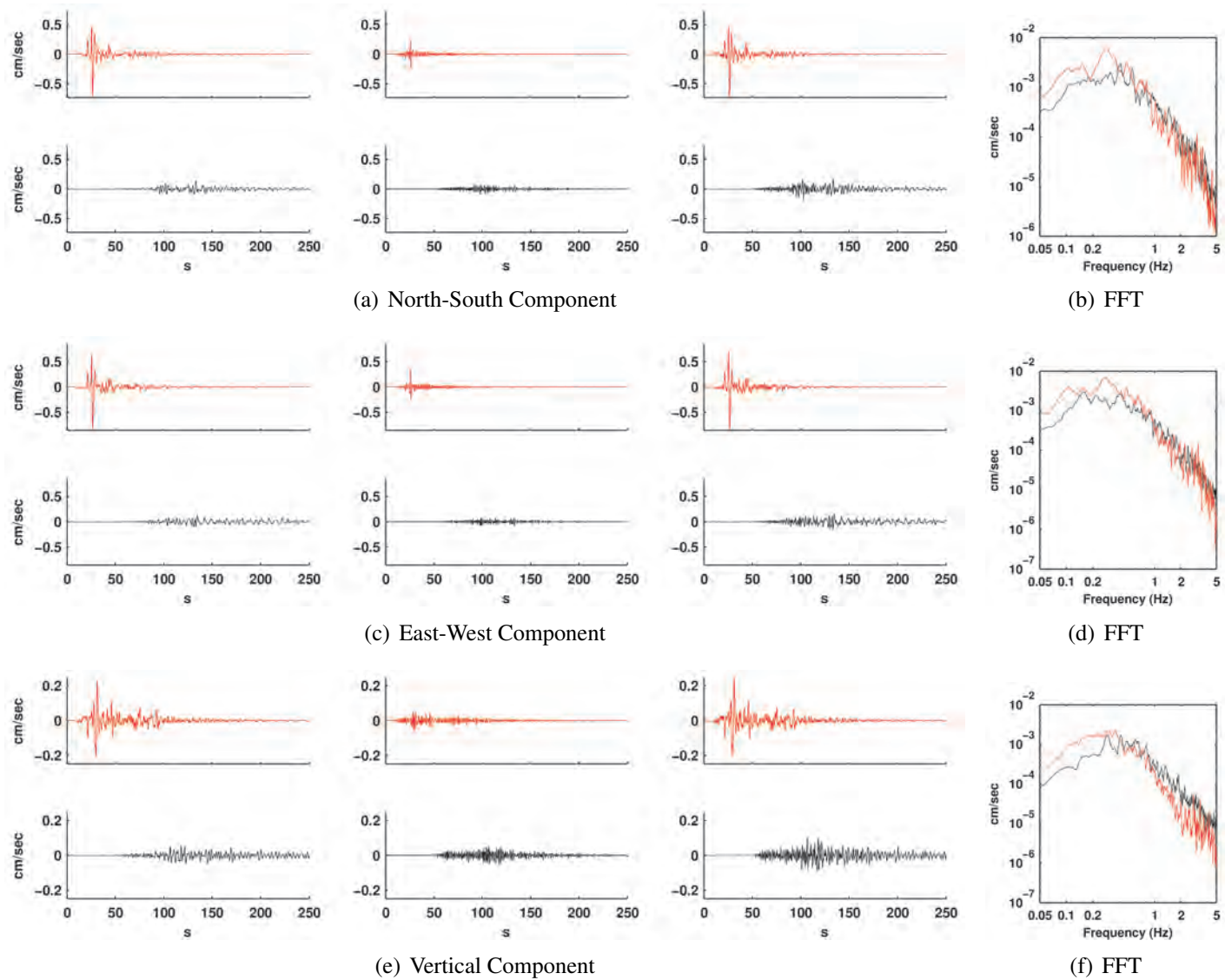


Figure E.34: Comparison of simulated (red) and observed (black) ground motions at station 33.

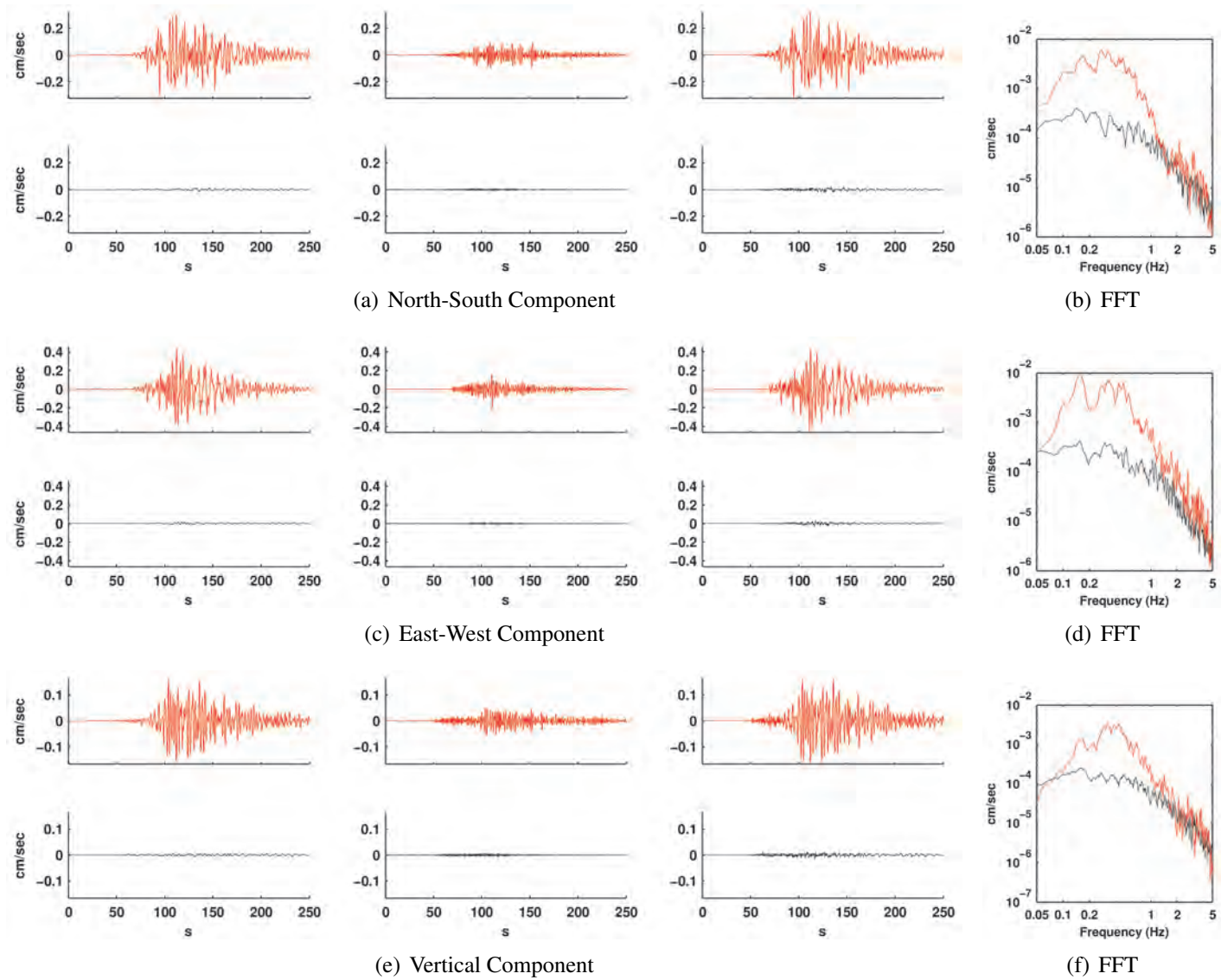


Figure E.35: Comparison of simulated (red) and observed (black) ground motions at station 34.

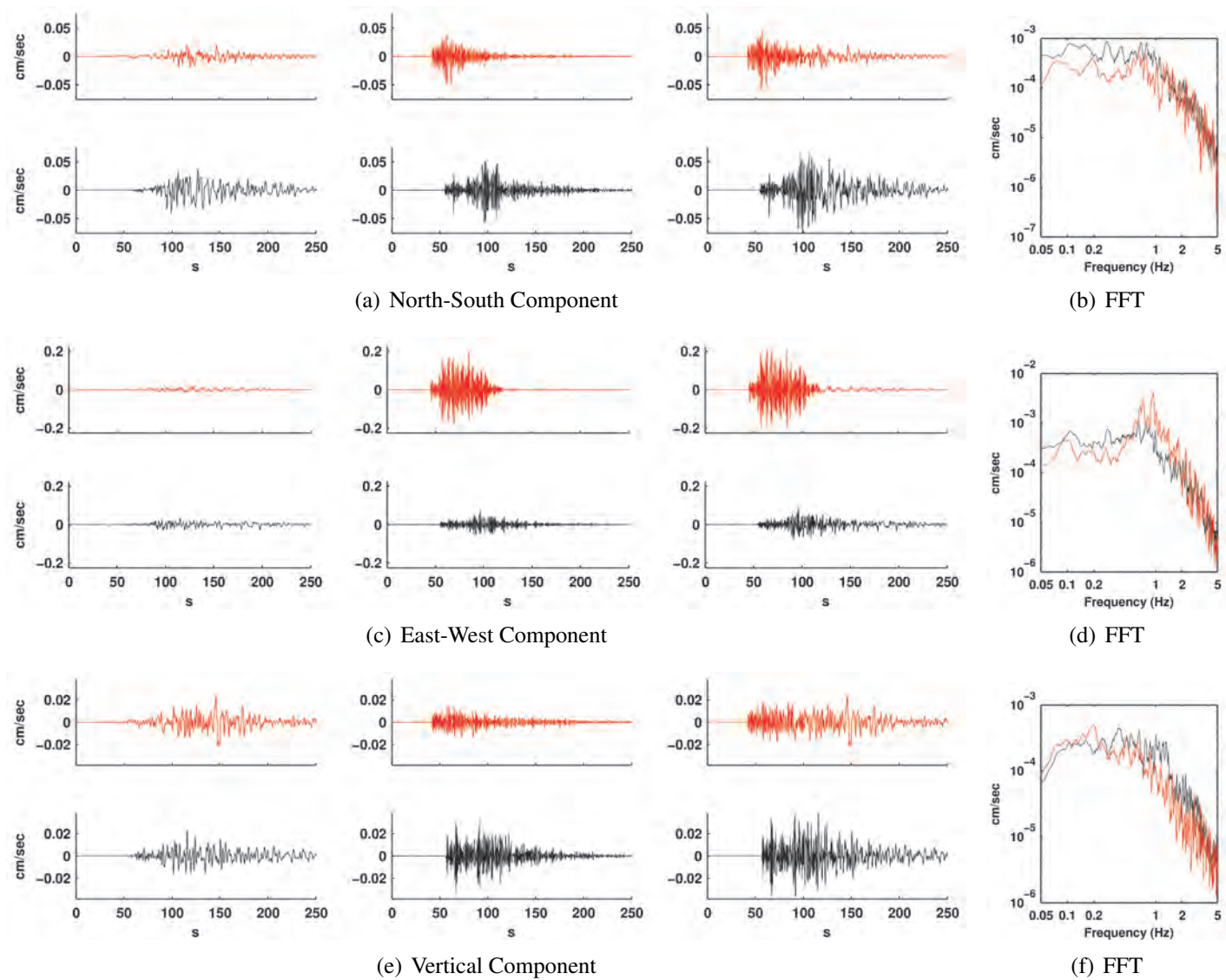


Figure E.36: Comparison of simulated (red) and observed (black) ground motions at station 35.

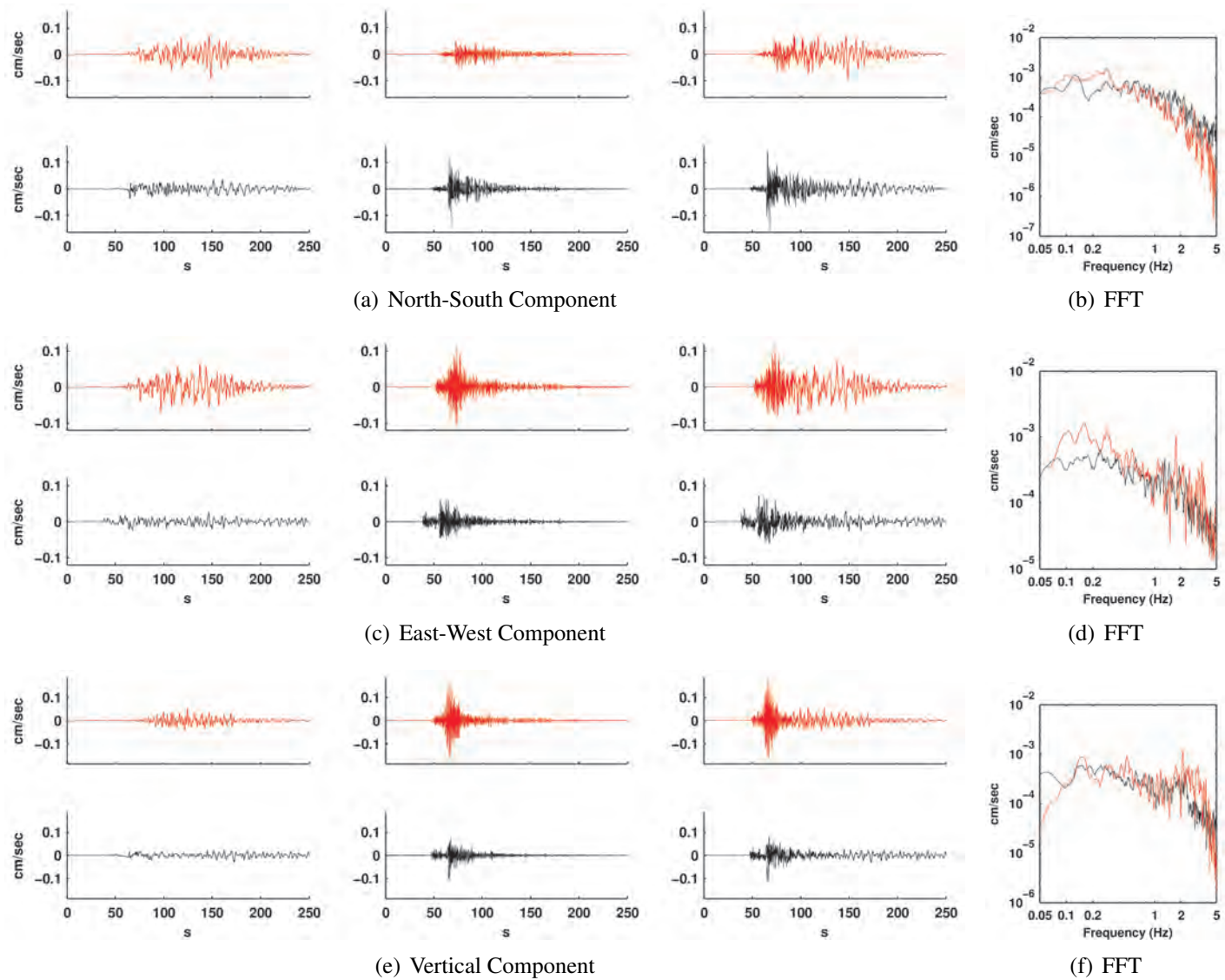


Figure E.37: Comparison of simulated (red) and observed (black) ground motions at station 36.

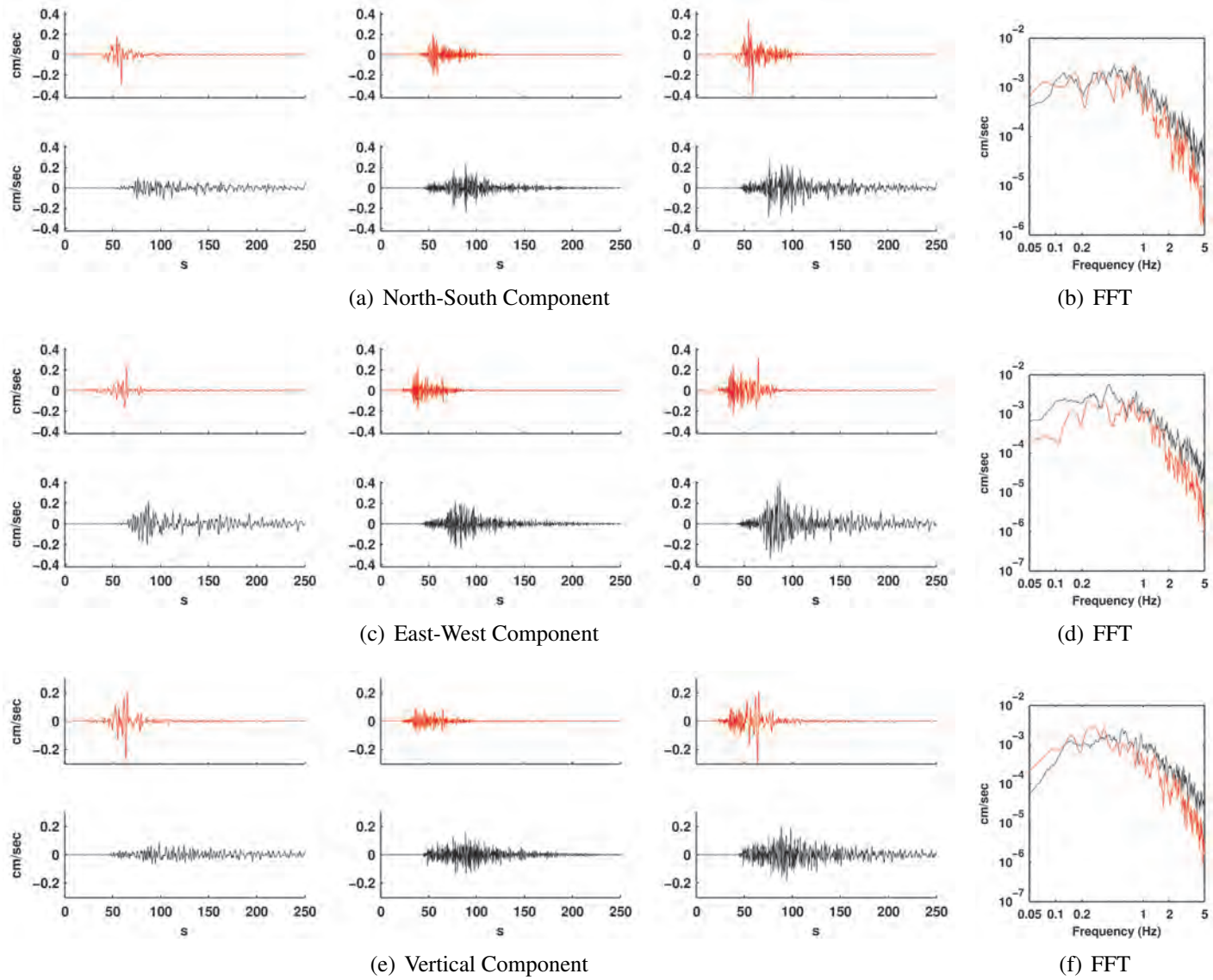


Figure E.38: Comparison of simulated (red) and observed (black) ground motions at station 37.

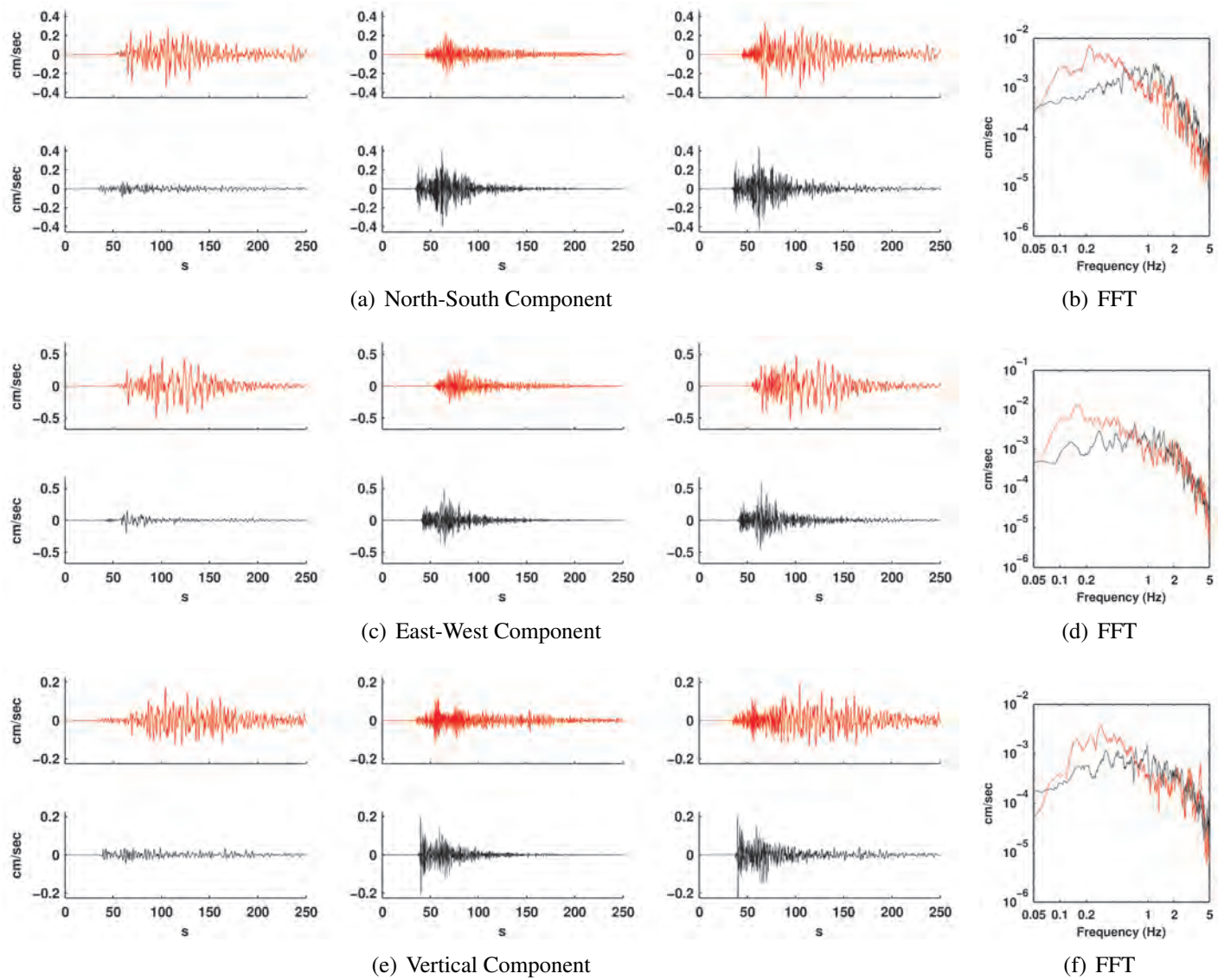


Figure E.39: Comparison of simulated (red) and observed (black) ground motions at station 38.

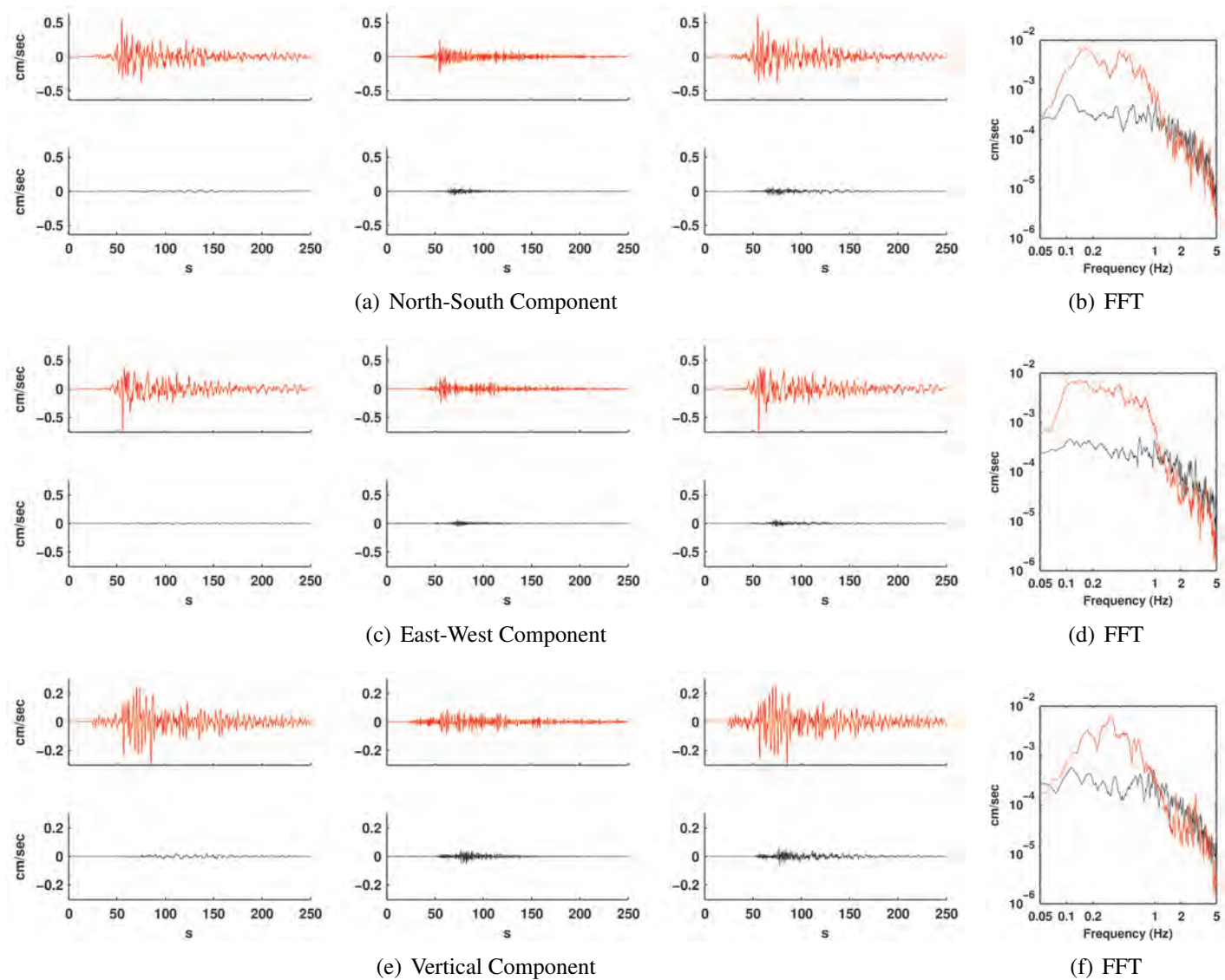


Figure E.40: Comparison of simulated (red) and observed (black) ground motions at station 39.

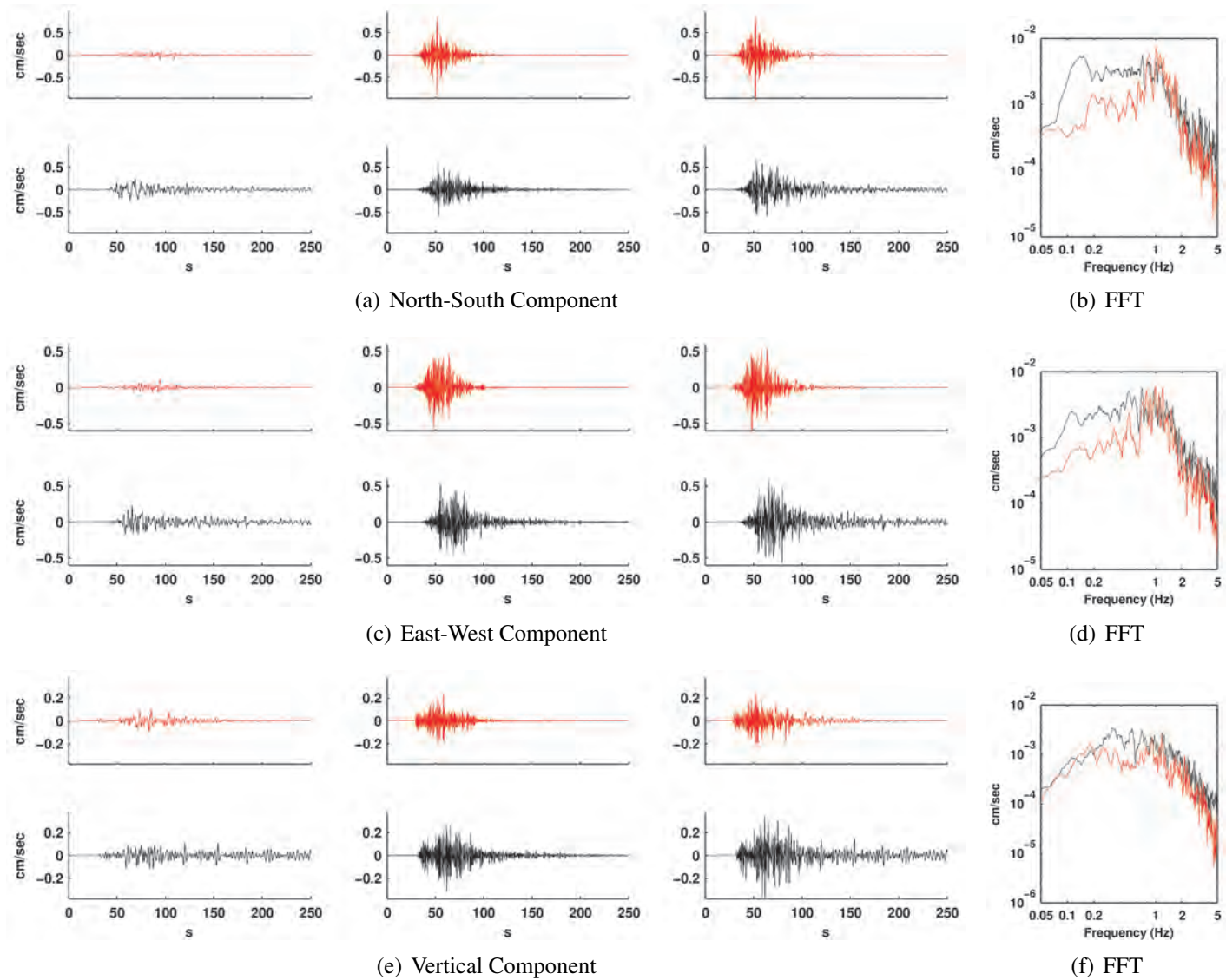


Figure E.41: Comparison of simulated (red) and observed (black) ground motions at station 40.

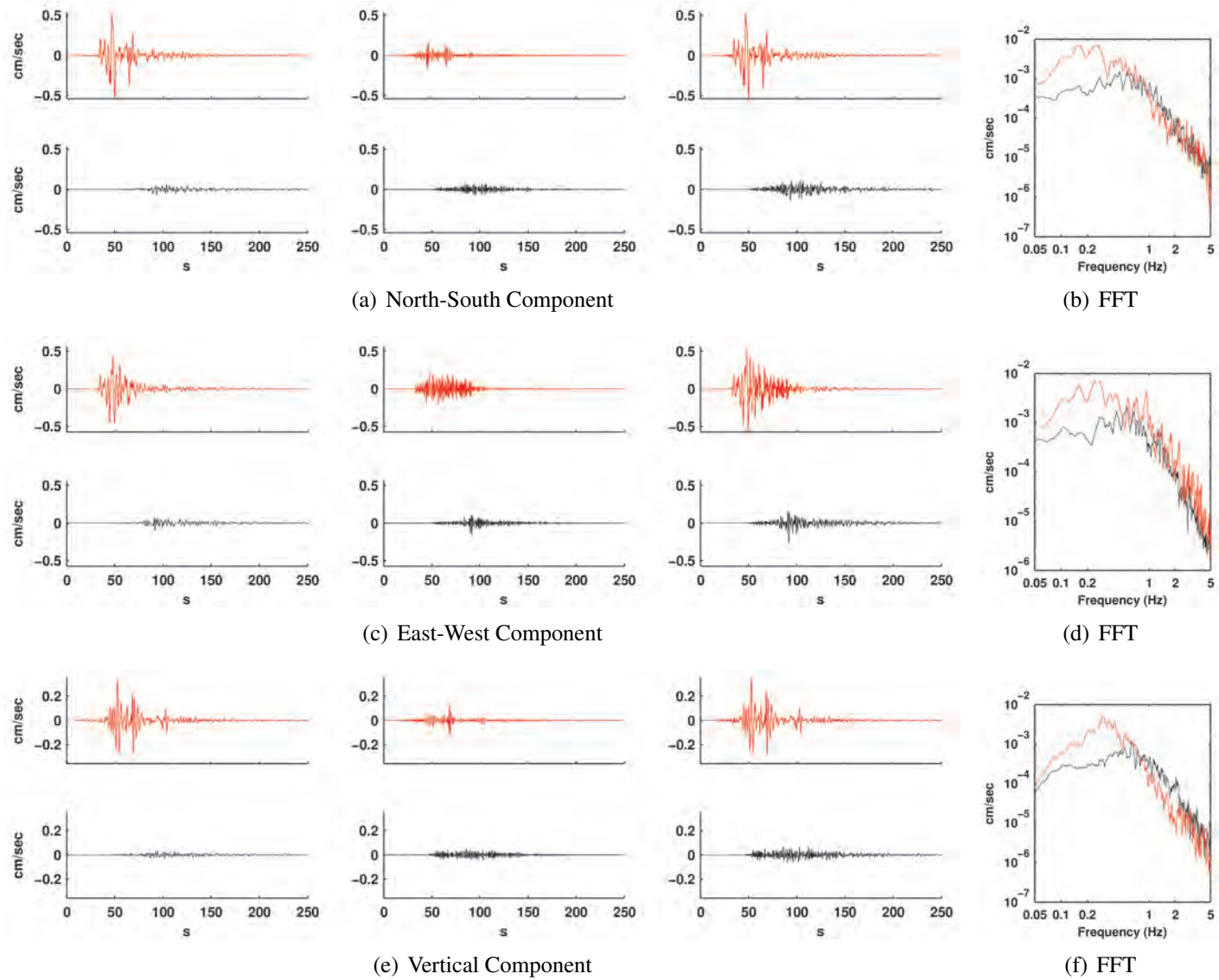


Figure E.42: Comparison of simulated (red) and observed (black) ground motions at station 41.

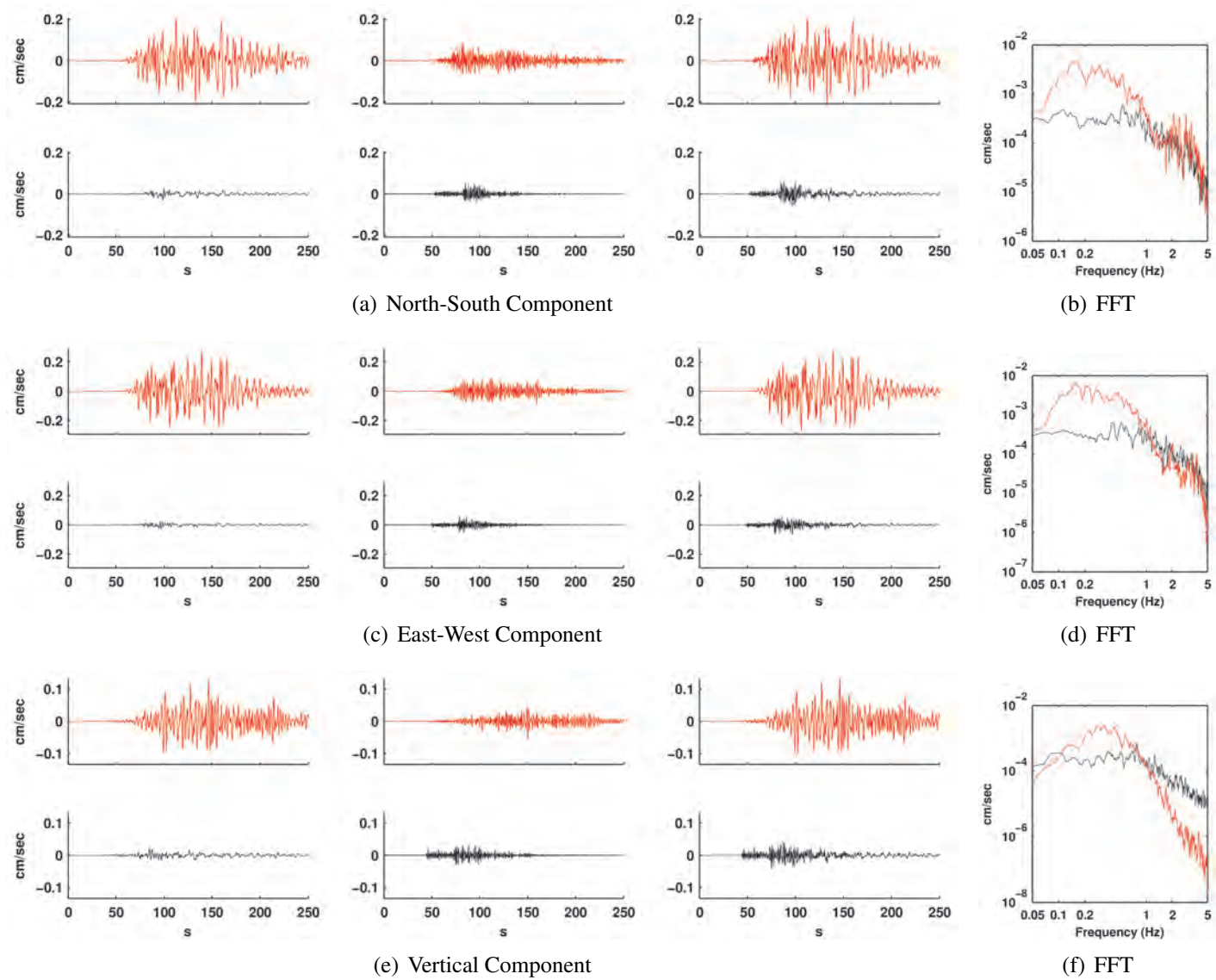


Figure E.43: Comparison of simulated (red) and observed (black) ground motions at station 42.

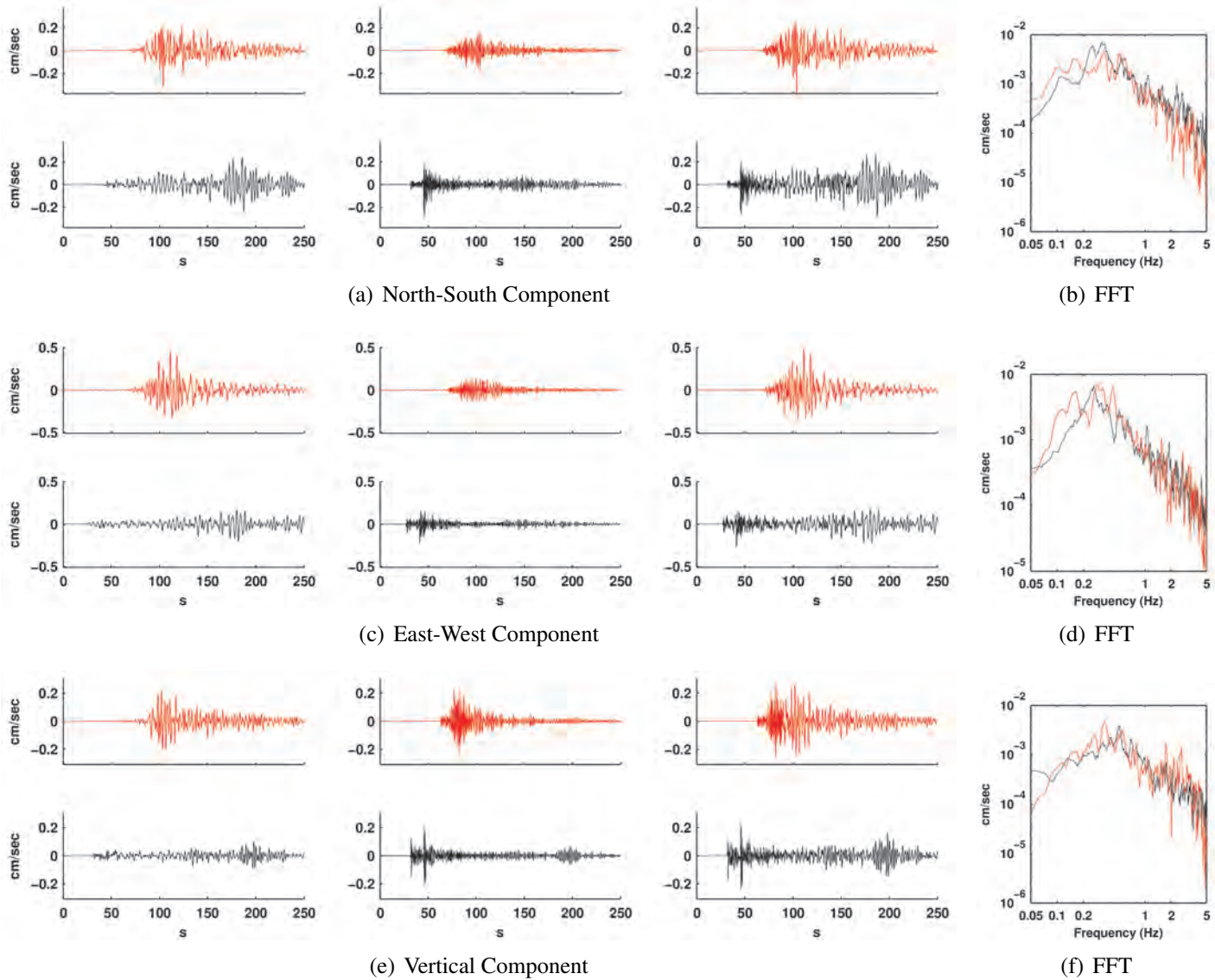


Figure E.44: Comparison of simulated (red) and observed (black) ground motions at station 43.

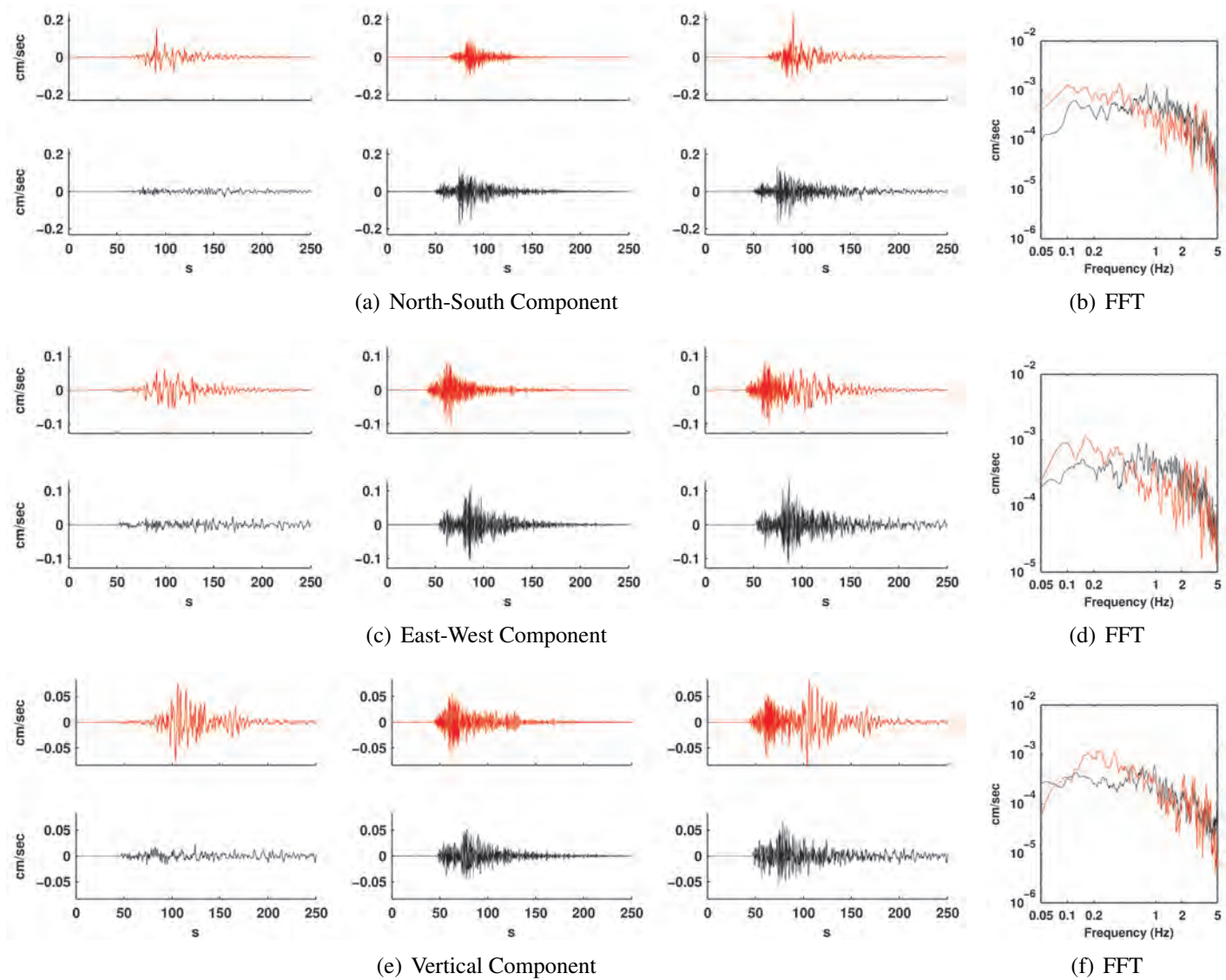


Figure E.45: Comparison of simulated (red) and observed (black) ground motions at station 44.

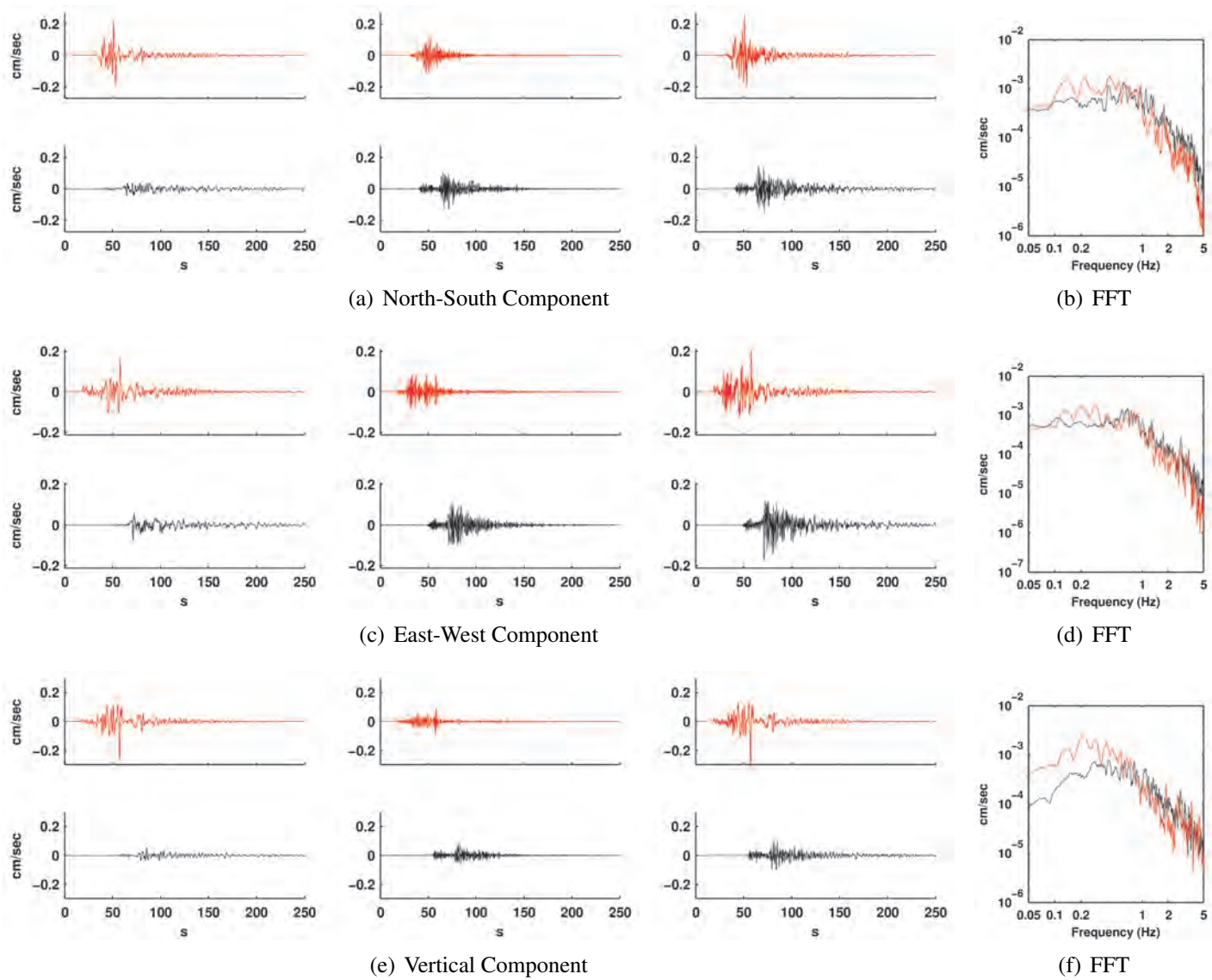


Figure E.46: Comparison of simulated (red) and observed (black) ground motions at station 45.

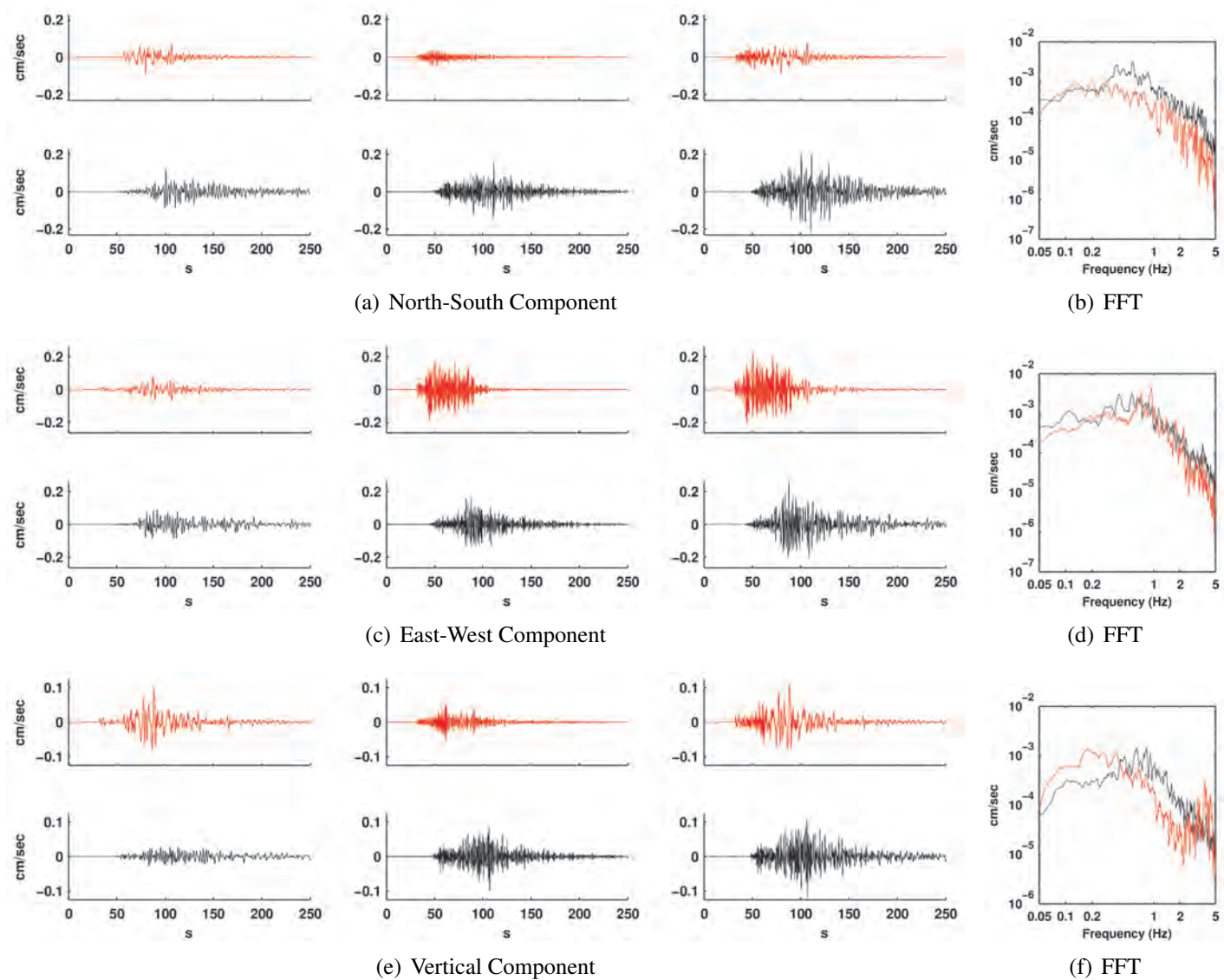


Figure E.47: Comparison of simulated (red) and observed (black) ground motions at station 46.

Appendix F

Braced Frame Version of Canoga Park Building

Braced Frame - UBC 1994 Building Code

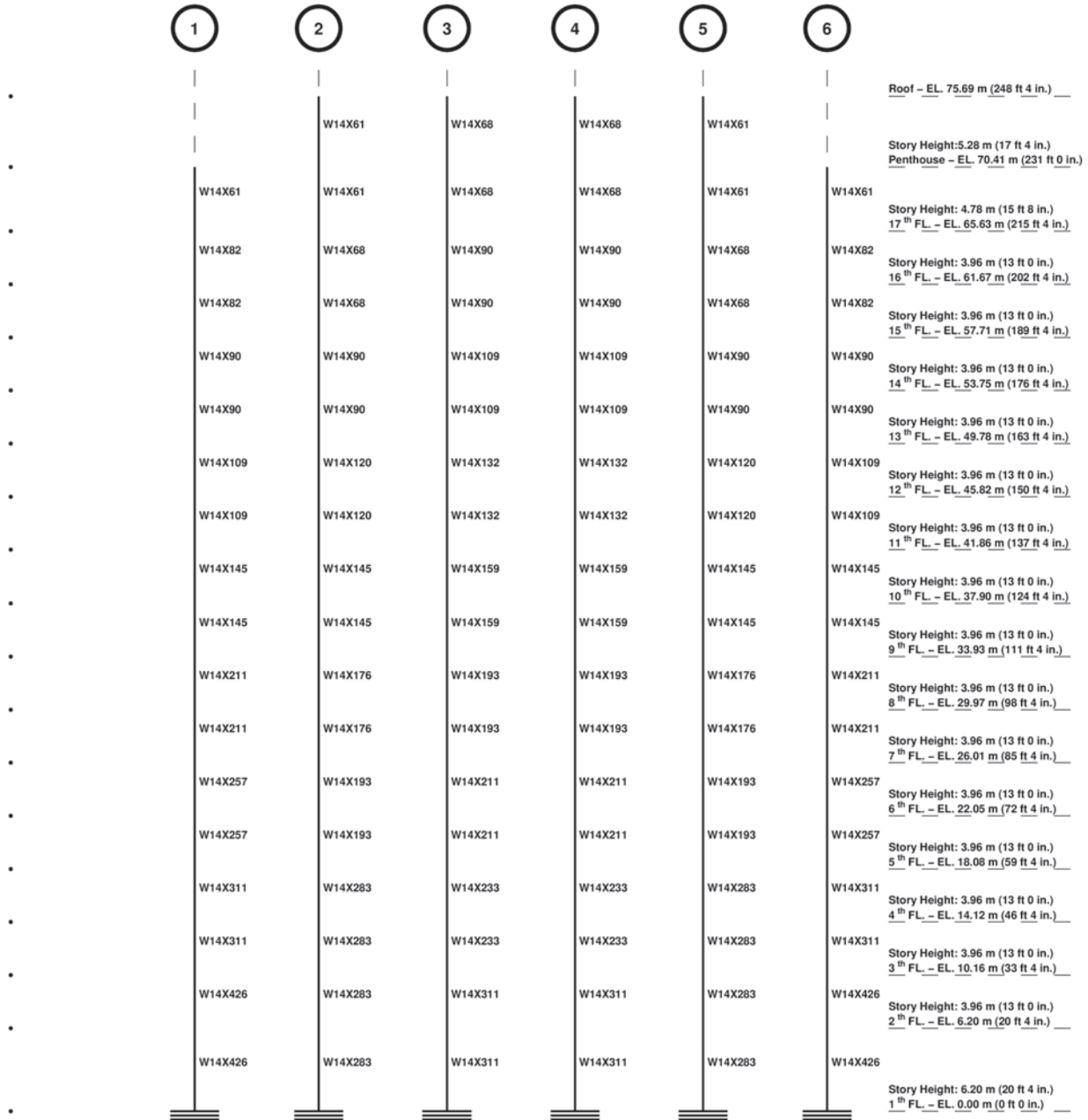


Figure F.2: East-west frame elevation along grid B (Braced frame - UBC 1994 - Site Category : S_2)

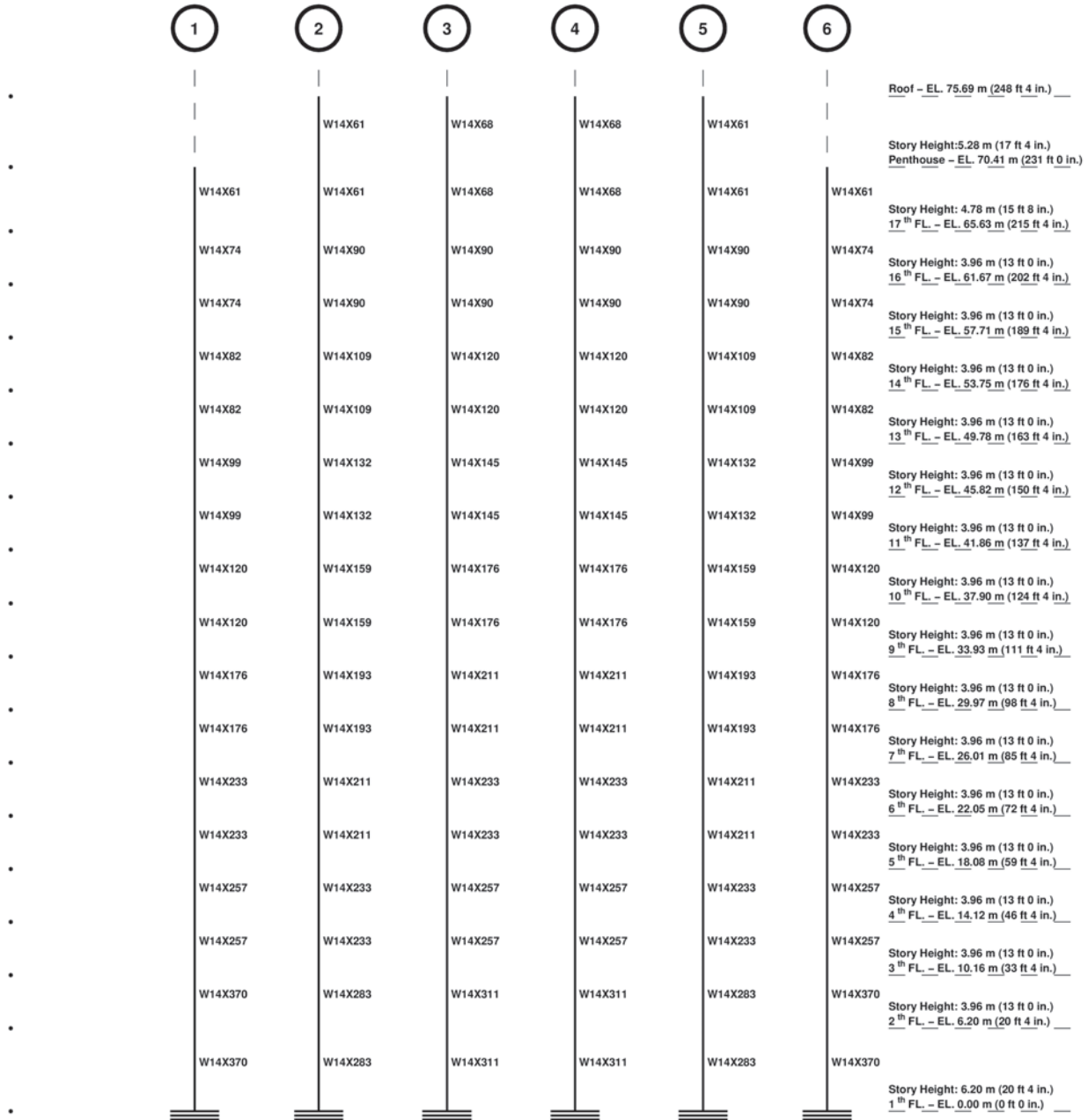


Figure F.3: East-west frame elevation along grid C (Braced frame - UBC 1994 - Site Category : S_2)

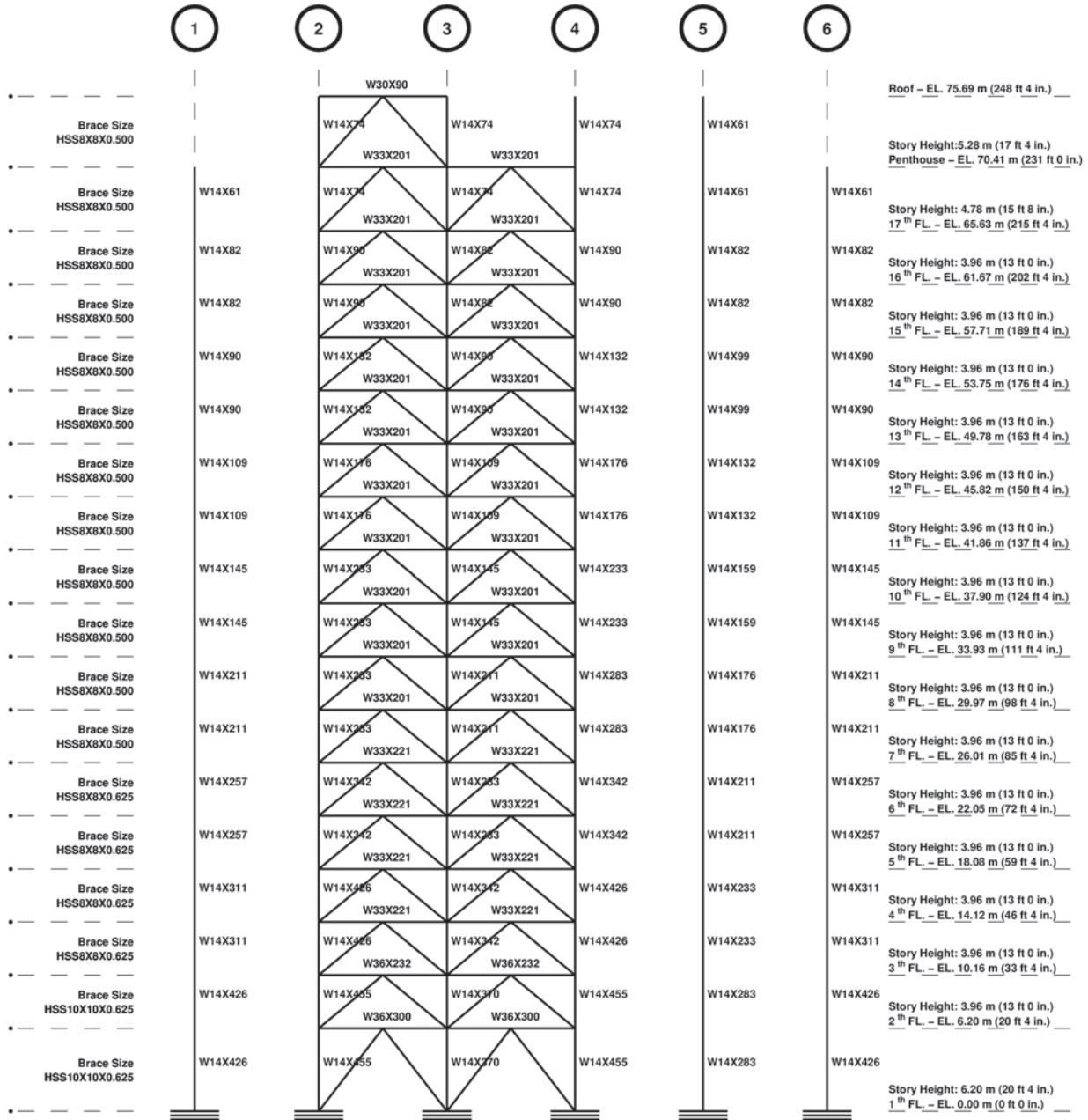


Figure F.4: East-west frame elevation along grid D (Braced frame - UBC 1994 - Site Category : S_2)

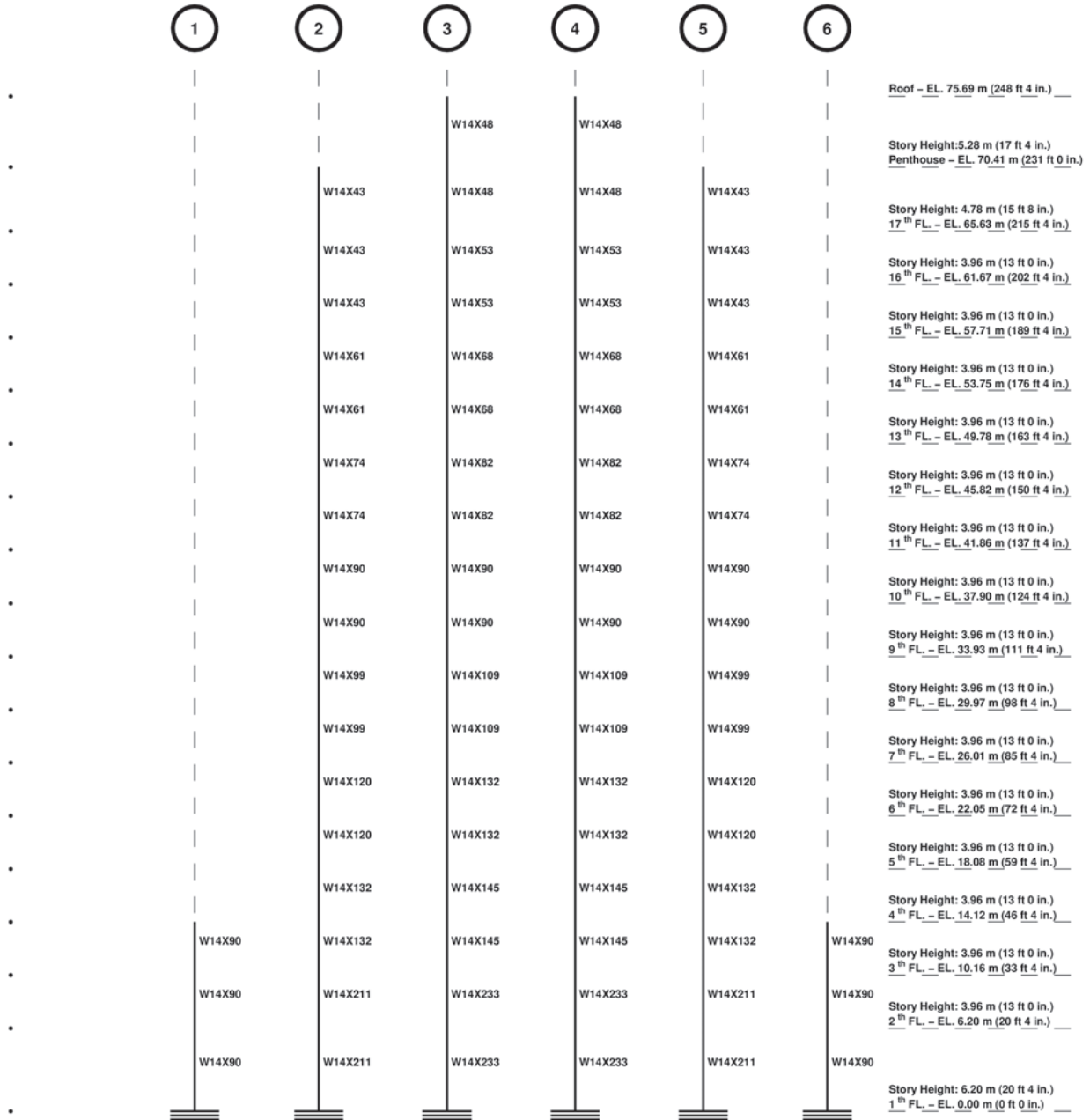


Figure F.5: East-west frame elevation along grid E (Braced frame - UBC 1994 - Site Category : S_2)

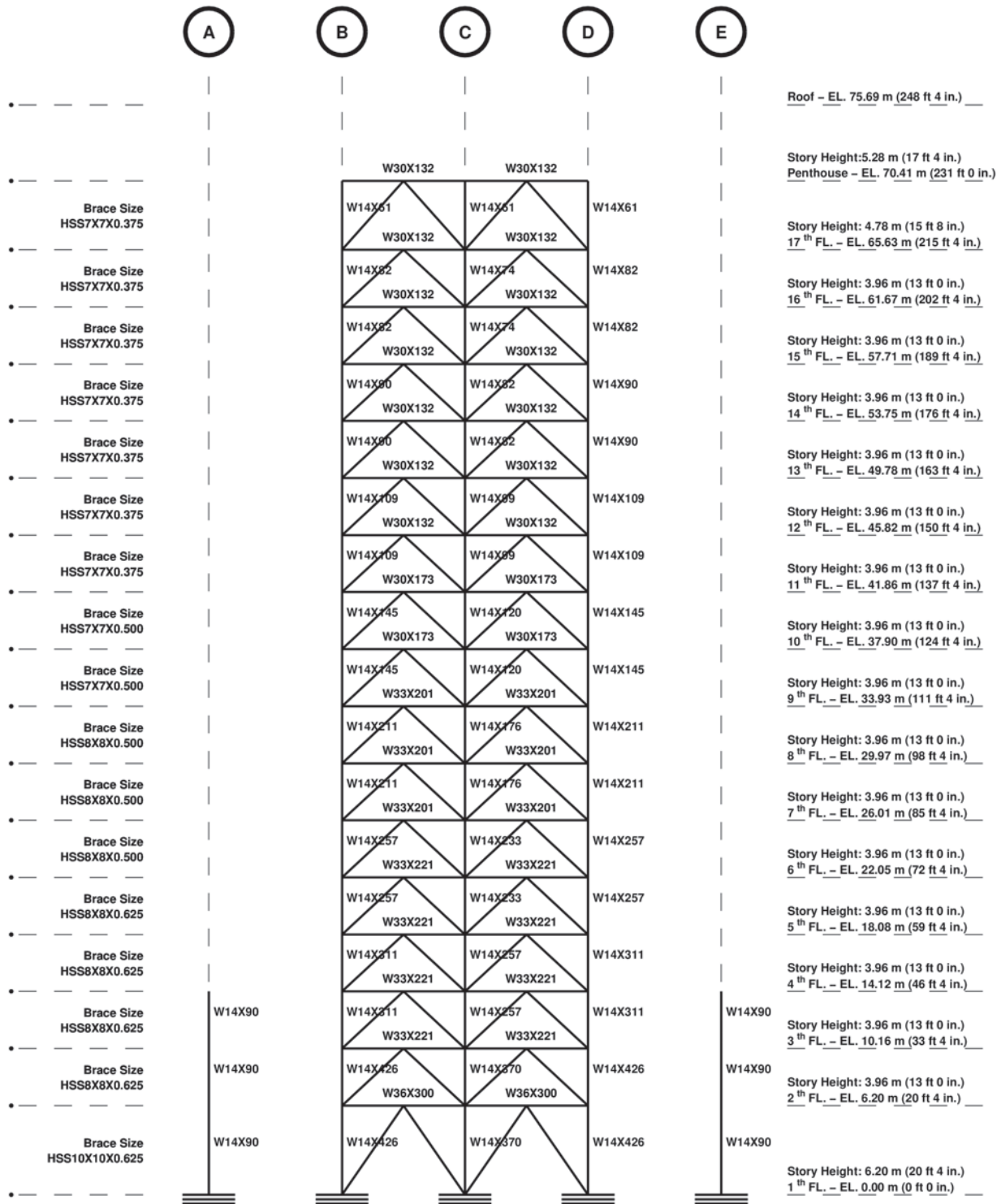


Figure F.6: North-south frame elevation along grid 1 (Braced frame - UBC 1994 - Site Category : S_2)

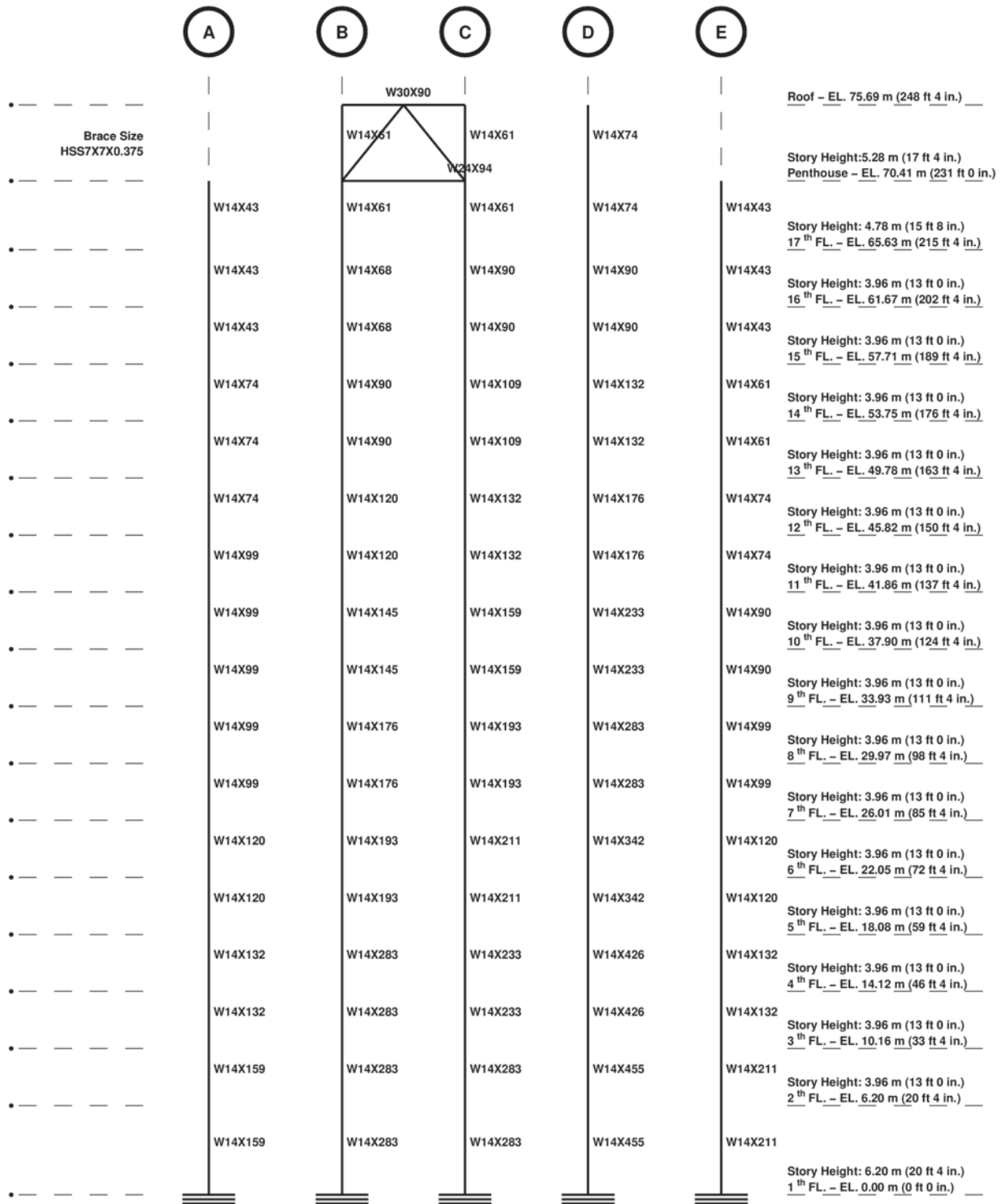


Figure F.7: North-south frame elevation along grid 2 (Braced frame - UBC 1994 - Site Category : S_2)

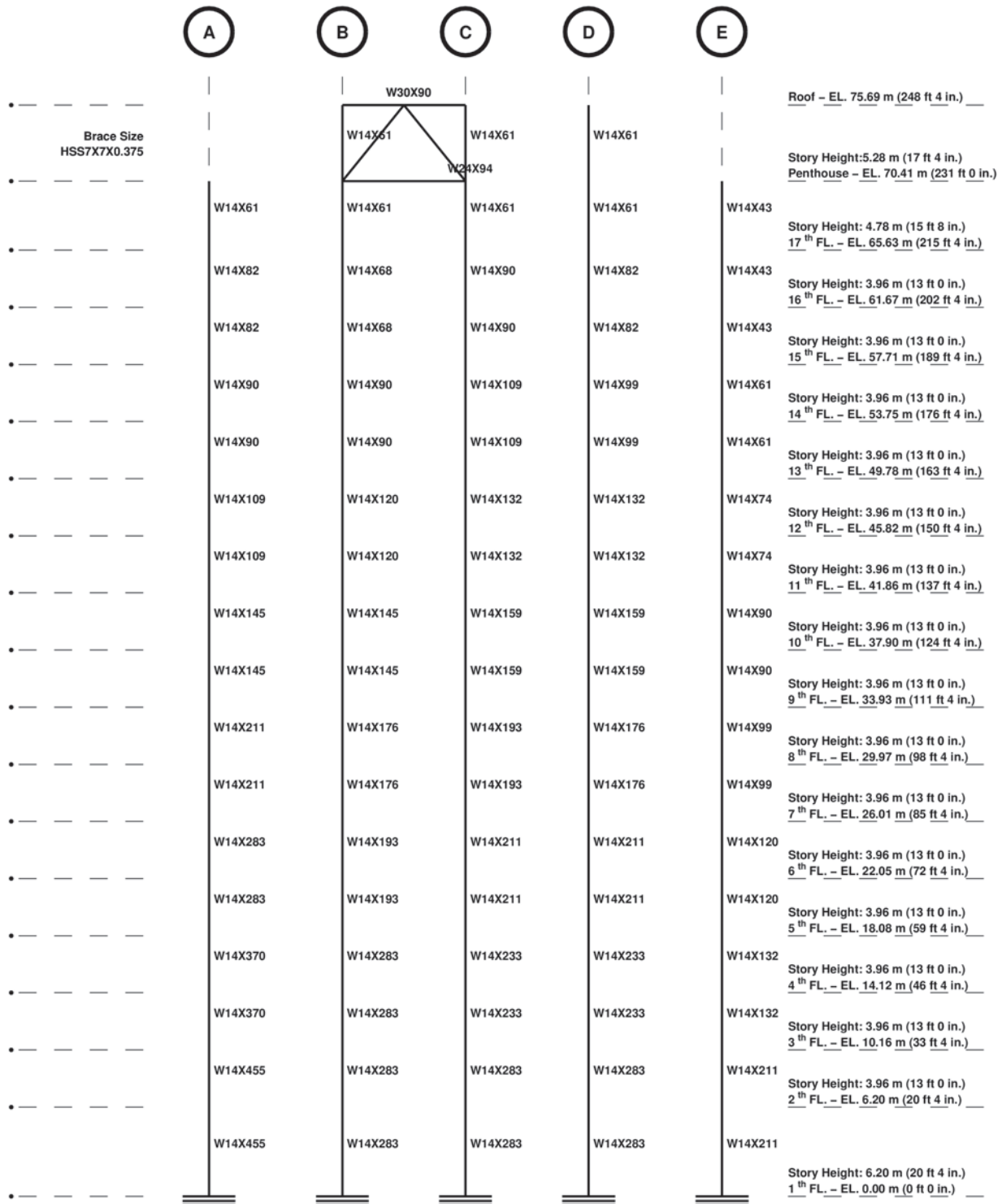


Figure F.8: North-south frame elevation along grid 5 (Braced frame - UBC 1994 - Site Category : S_2)

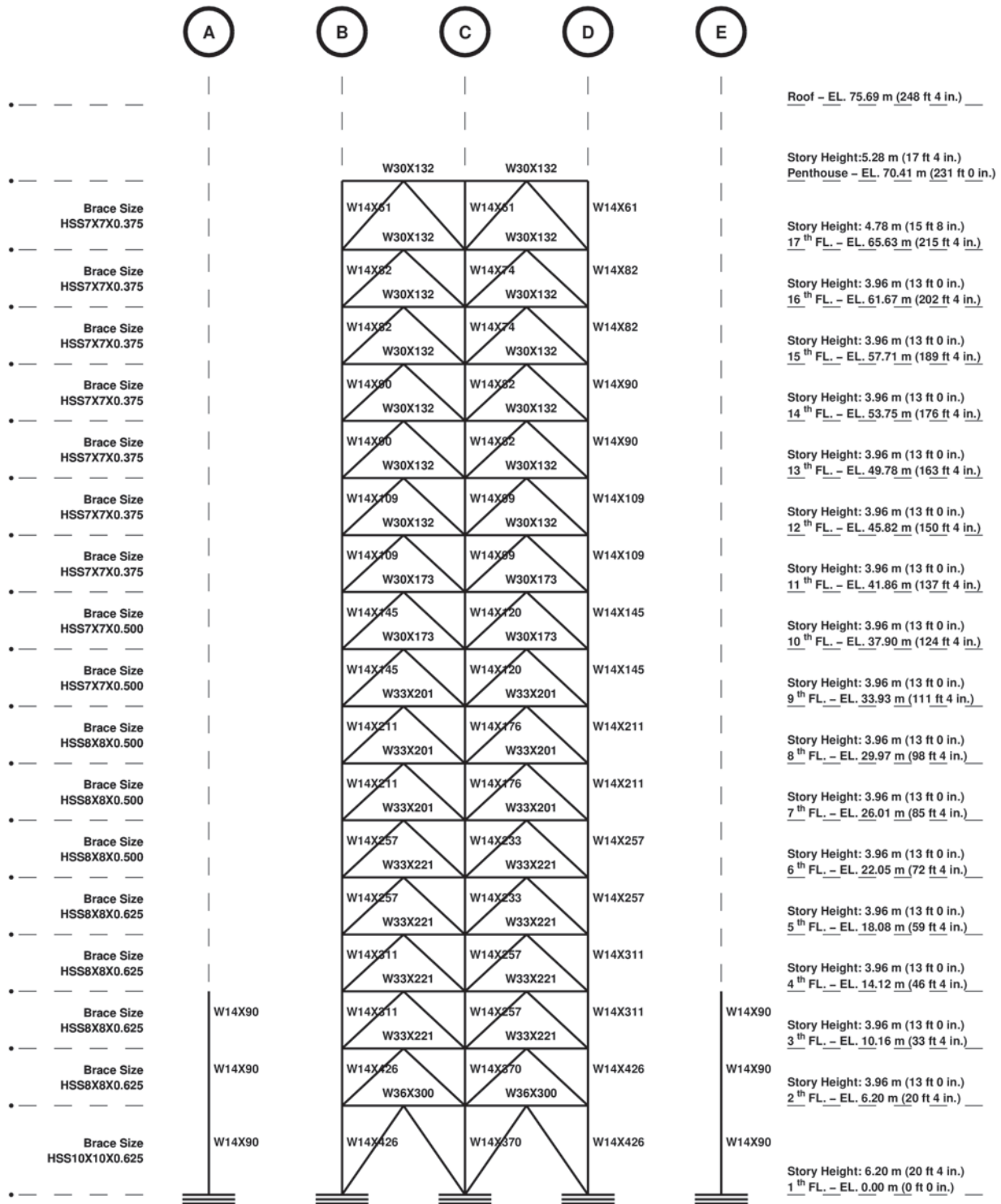


Figure F.9: North-south frame elevation along grid 6 (Braced frame - UBC 1994 - Site Category : S_2)

F.2 Braced Frame Version of Canoga Park Building

Braced Frame - UBC 1994 Building Code

S_3 Site Categories

Frame Elevations - Beam, Column, and Brace size

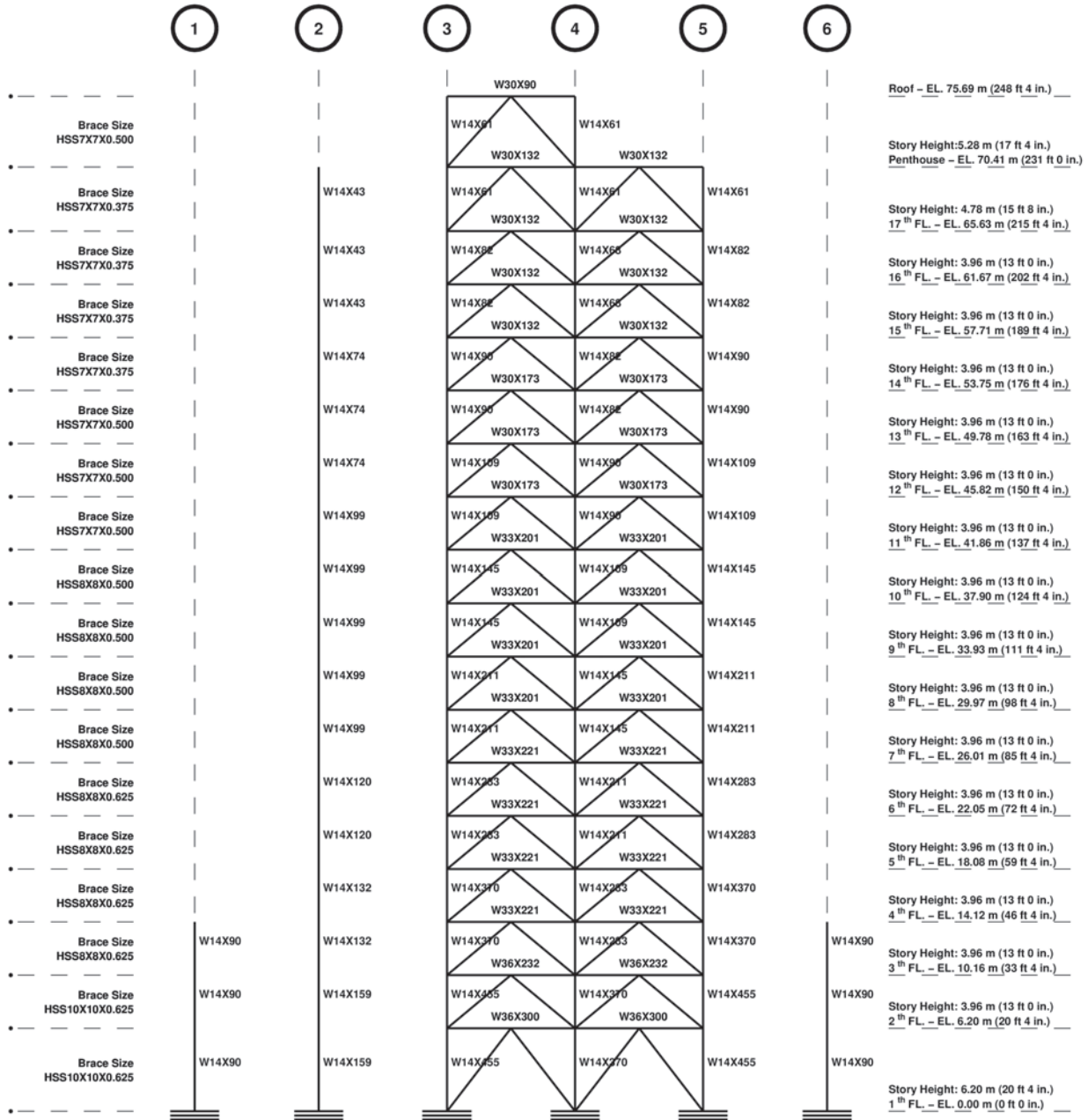


Figure F.10: East-west frame elevation along grid A (Braced frame - UBC 1994 - Site Category : S_3)

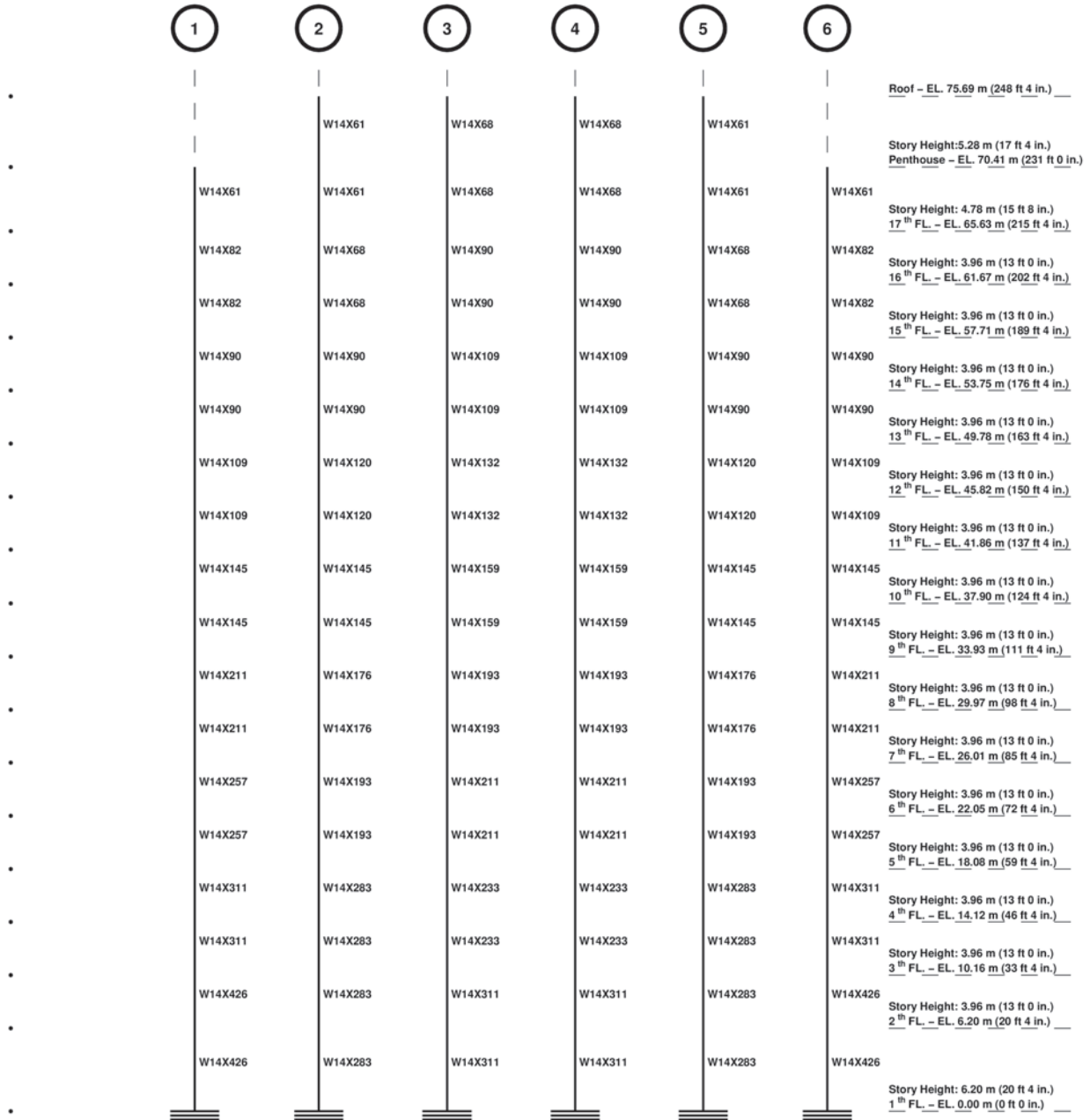


Figure F.11: East-west frame elevation along grid B (Braced frame - UBC 1994 - Site Category : S_3)

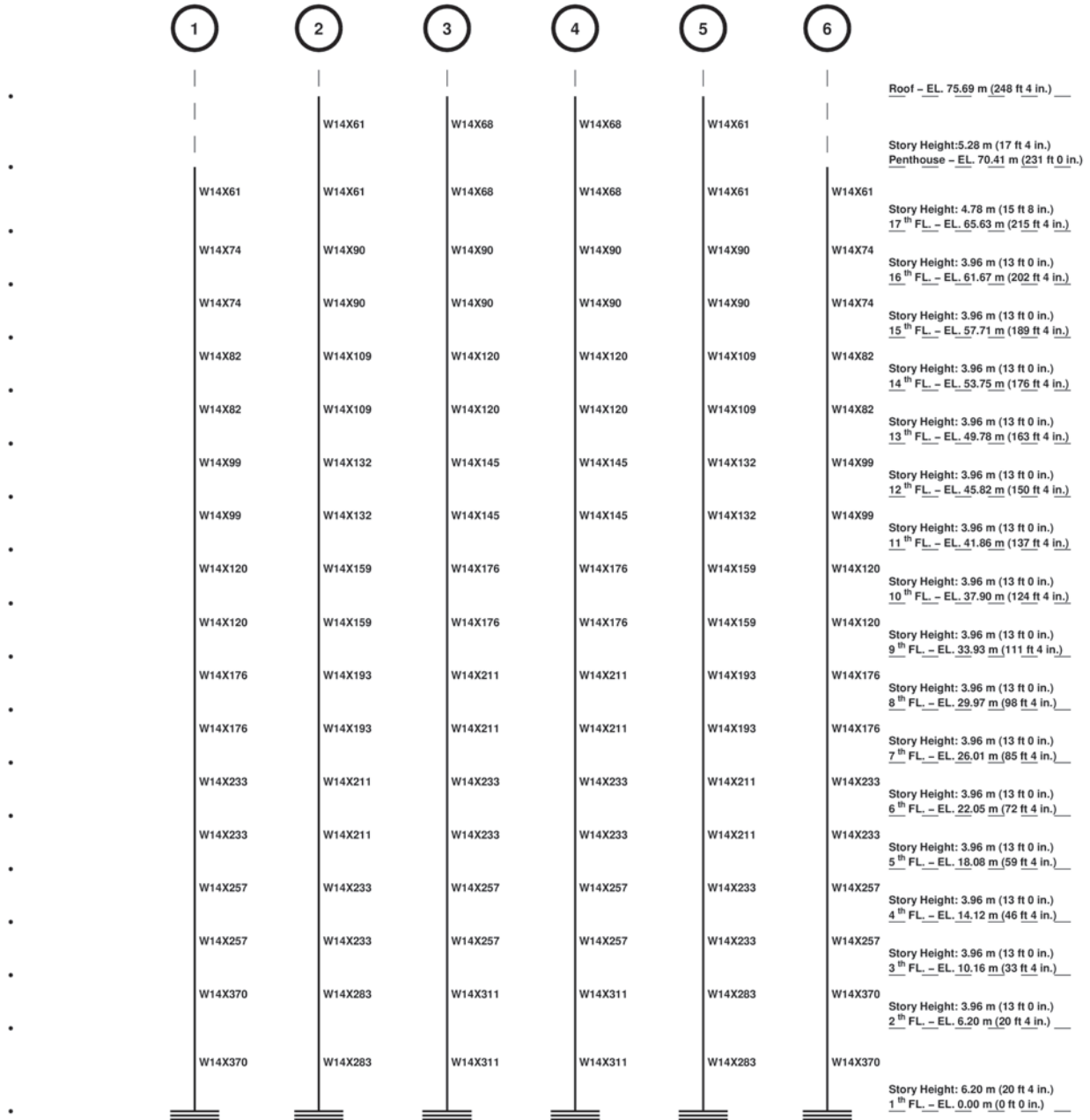


Figure F.12: East-west frame elevation along grid C (Braced frame - UBC 1994 - Site Category : S_3)

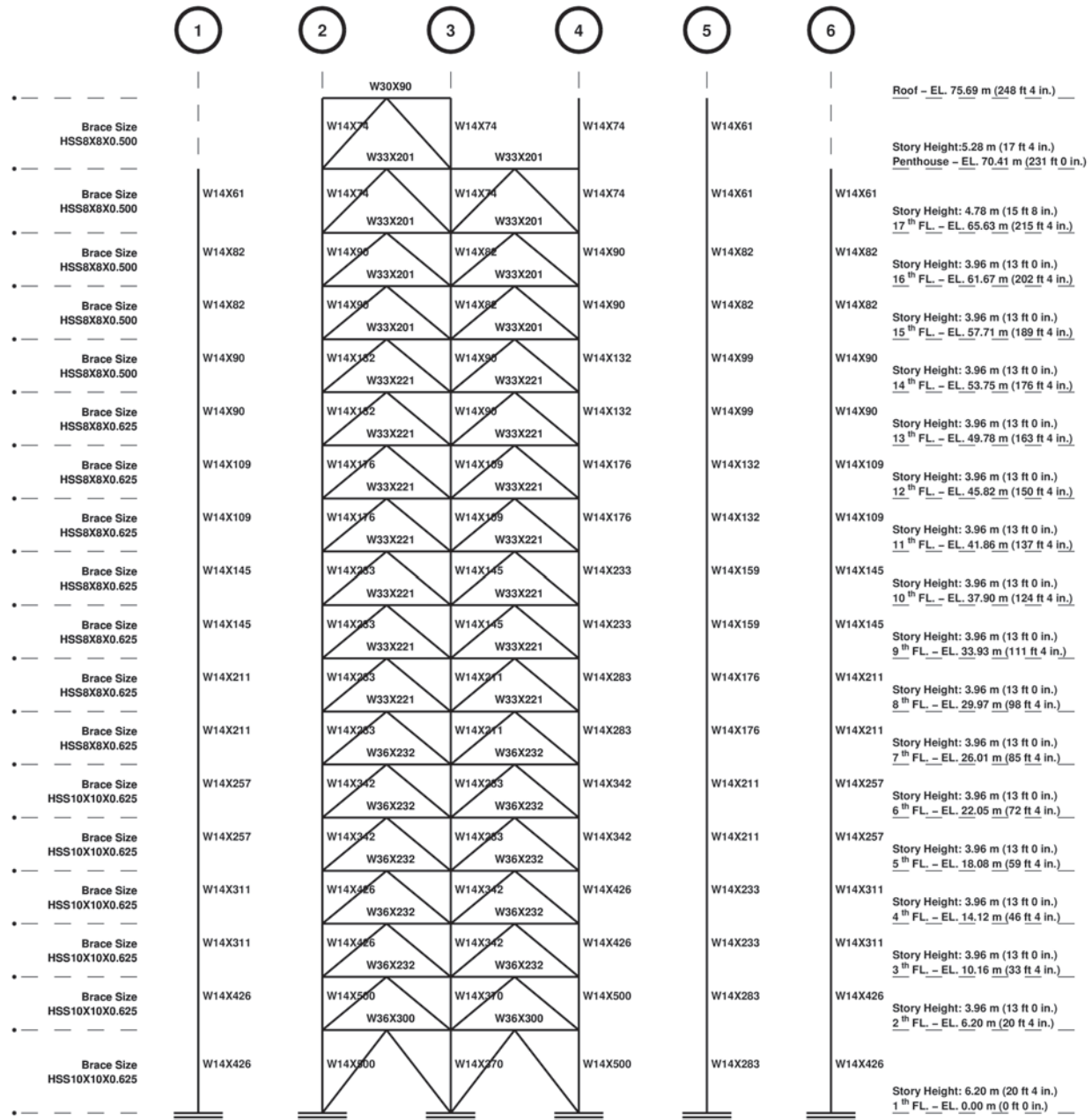


Figure F.13: East-west frame elevation along grid D (Braced frame - UBC 1994 - Site Category : S_3)

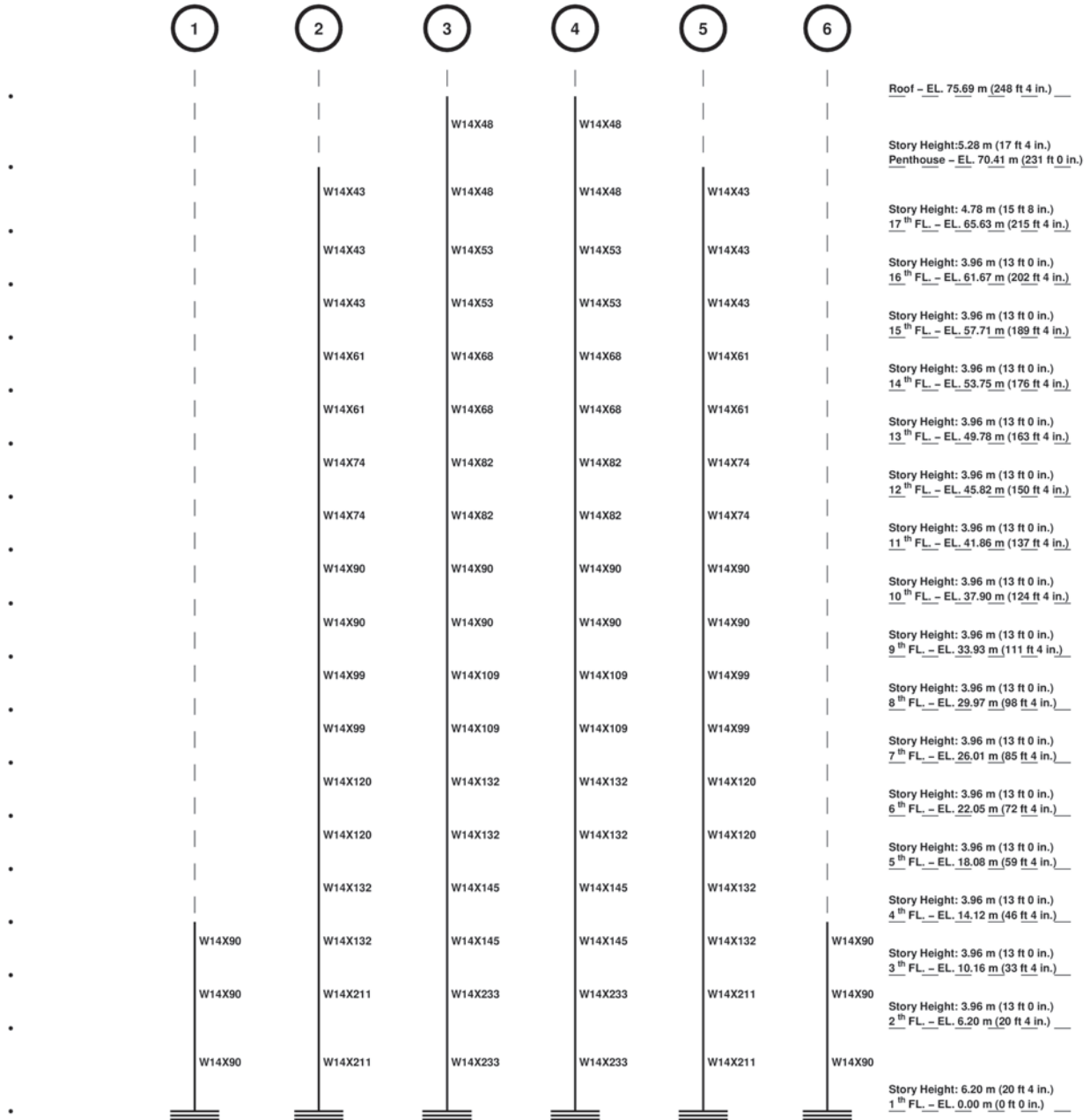


Figure F.14: East-west frame elevation along grid E (Braced frame - UBC 1994 - Site Category : S_3)

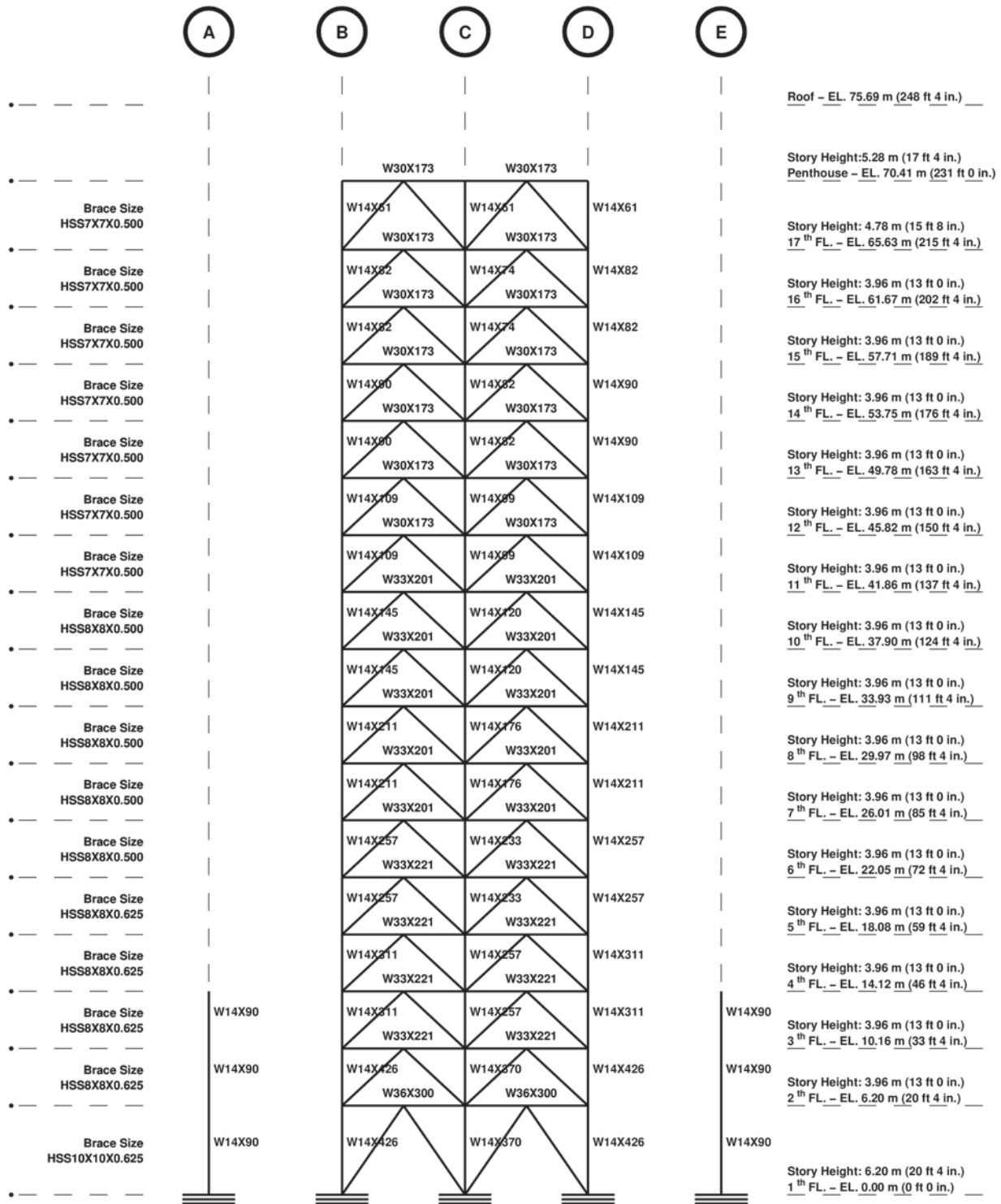


Figure F.15: North-south frame elevation along grid 1 (Braced frame - UBC 1994 - Site Category : S_3)

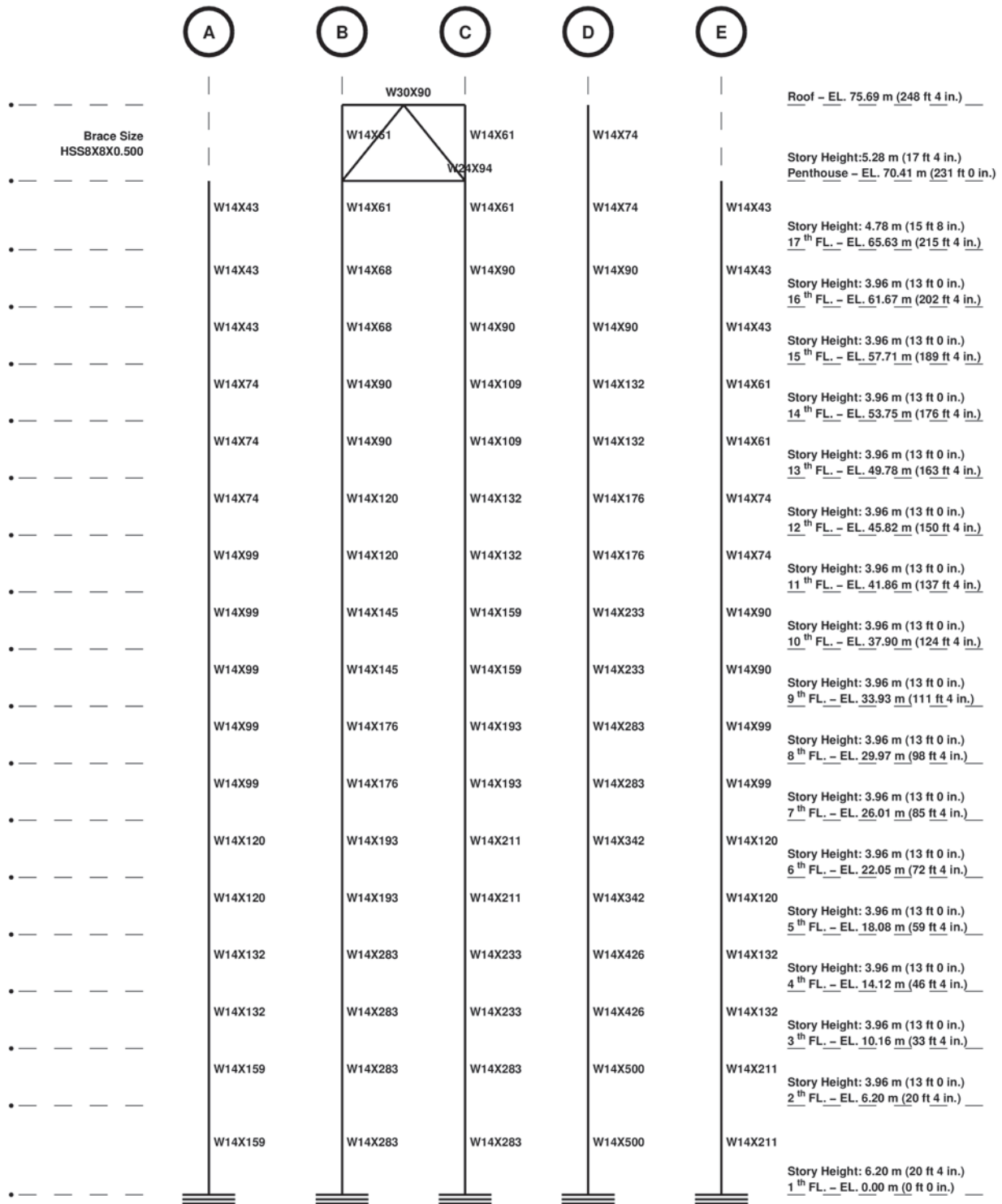


Figure F.16: North-south frame elevation along grid 2 (Braced frame - UBC 1994 - Site Category : S_3)

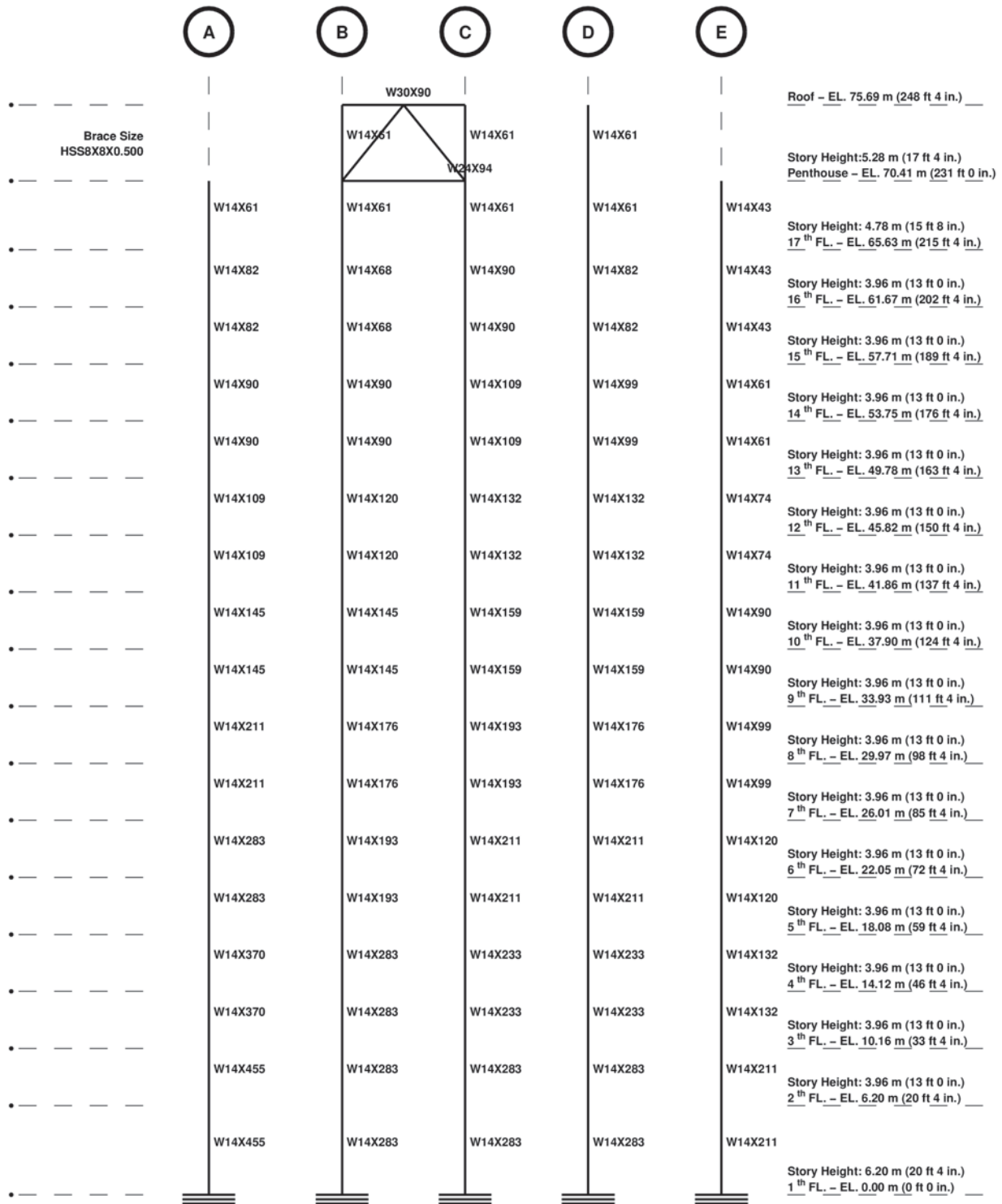


Figure F.17: North-south frame elevation along grid 5 (Braced frame - UBC 1994 - Site Category : S_3)

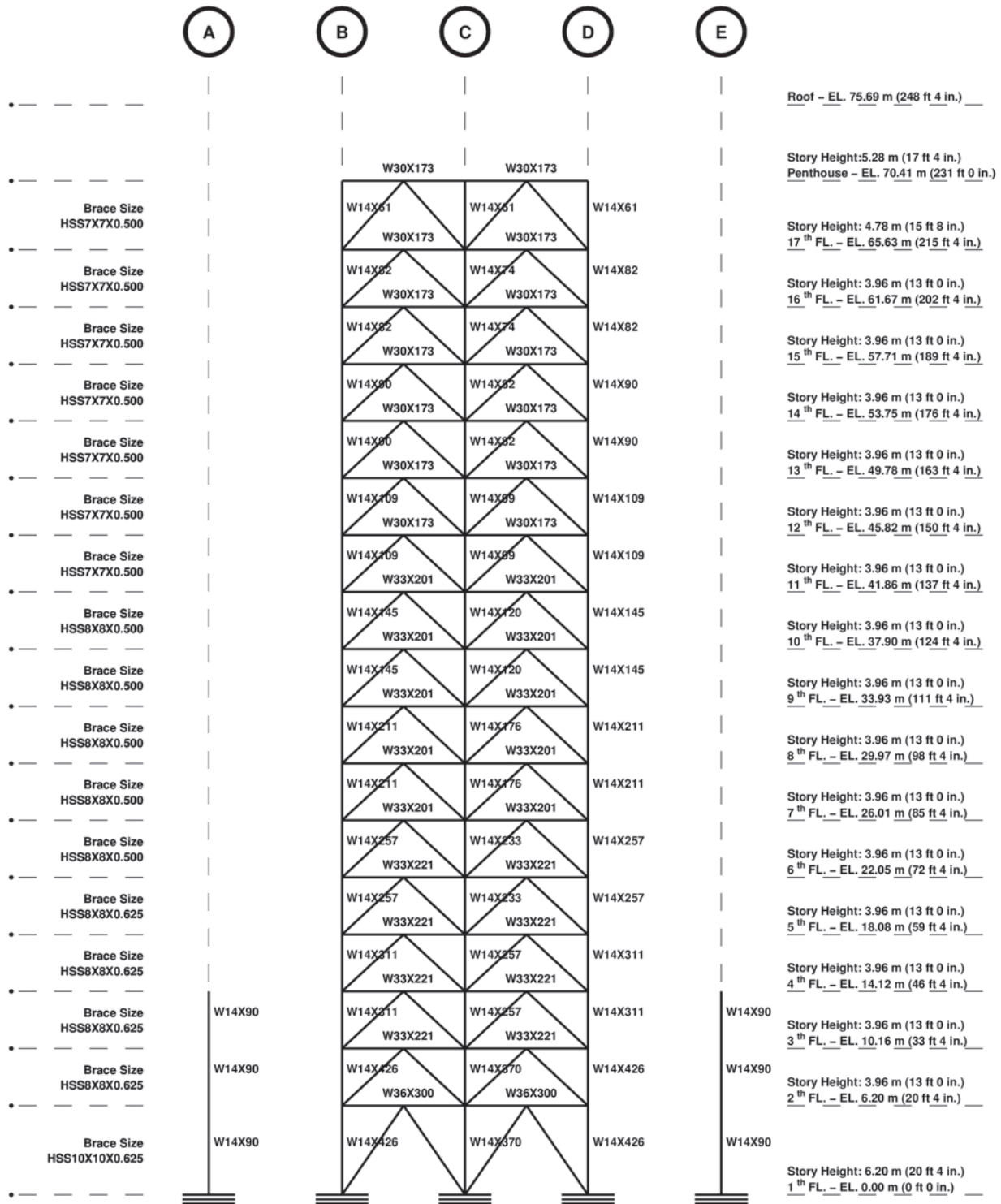


Figure F.18: North-south frame elevation along grid 6 (Braced frame - UBC 1994 - Site Category : S_3)

Appendix G

Braced Frame Version of Canoga Park Building Braced Frame - UBC 1997 Building Code

G.1 Braced Frame Version of Canoga Park Building

Braced Frame - UBC 1997 Building Code

S_B **Site Categories**

Frame Elevations - Beam, Column, and Brace size

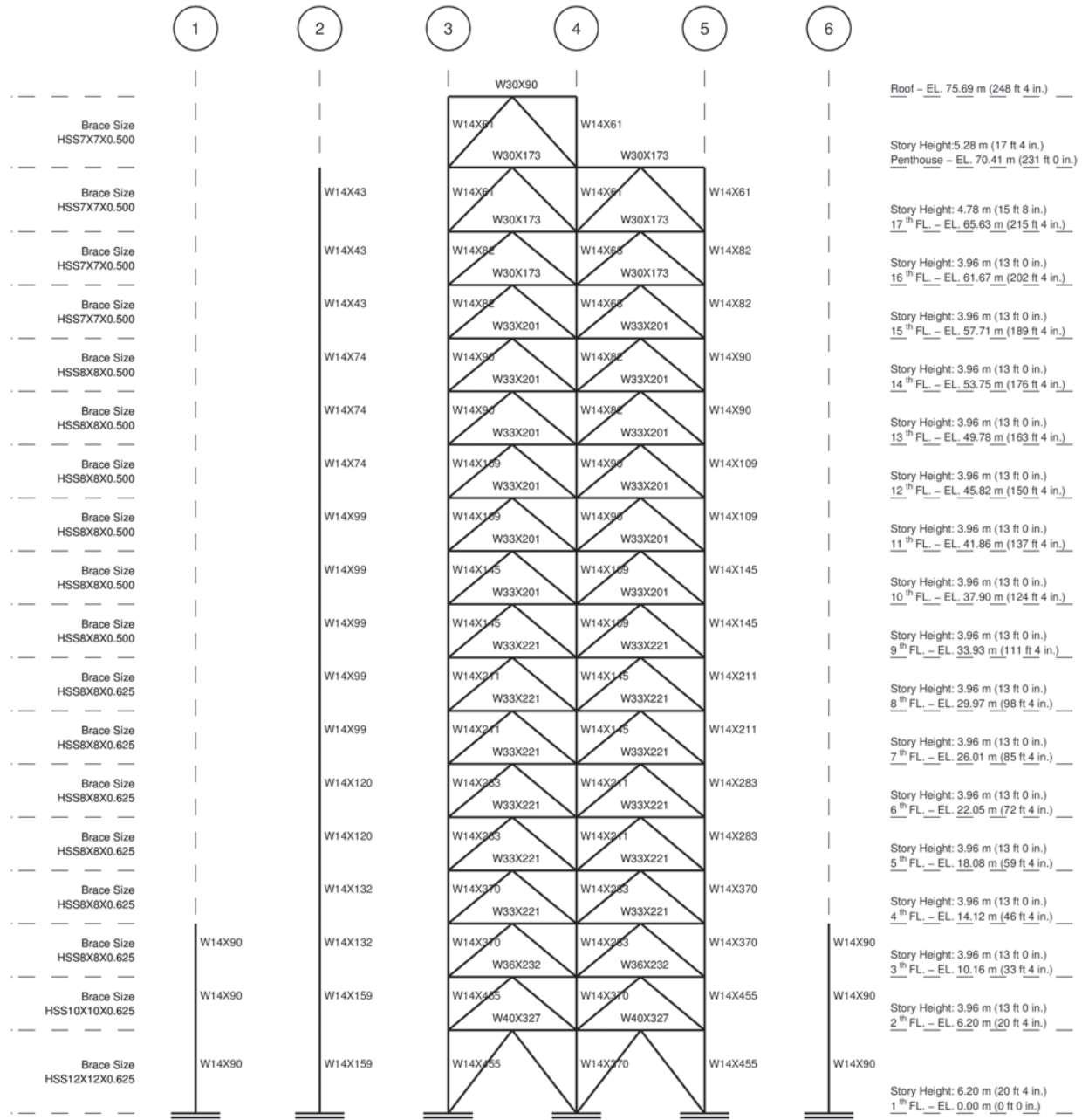


Figure G.1: East-west frame elevation along grid A (Braced frame - UBC 1997 - Site Category : S_B)

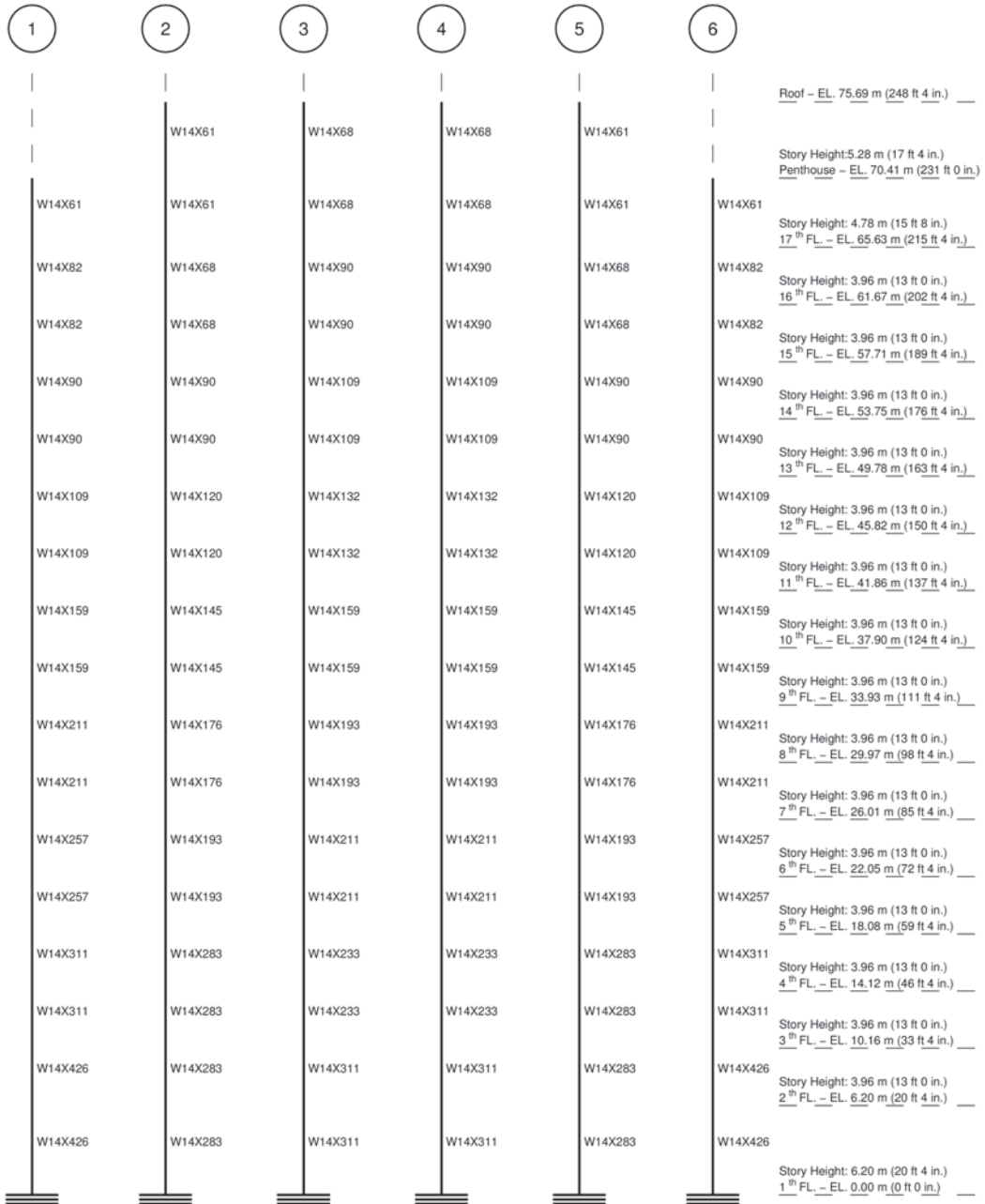


Figure G.2: East-west frame elevation along grid B (Braced frame - UBC 1997 - Site Category : S_B)

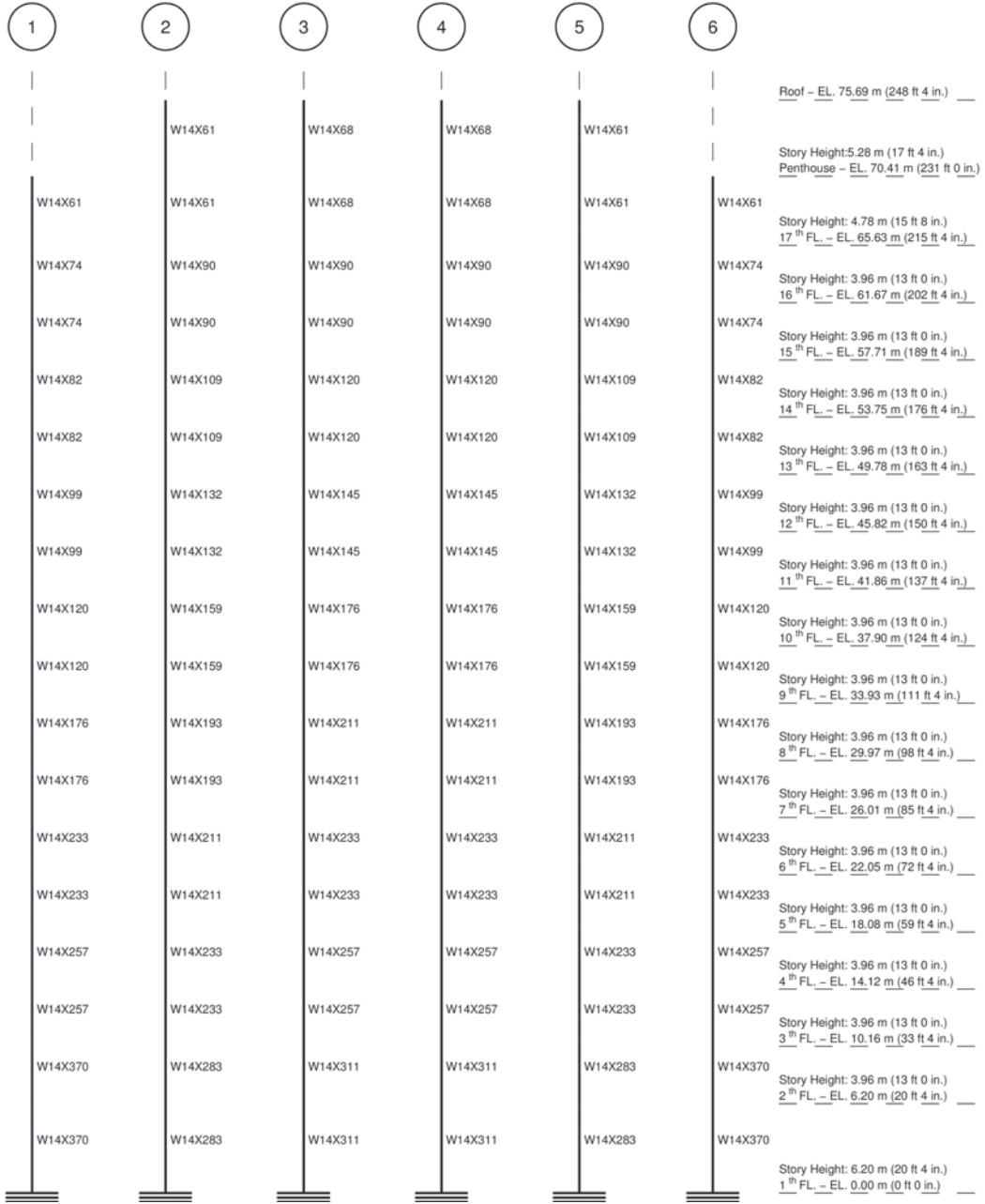


Figure G.3: East-west frame elevation along grid C (Braced frame - UBC 1997 - Site Category : S_B)

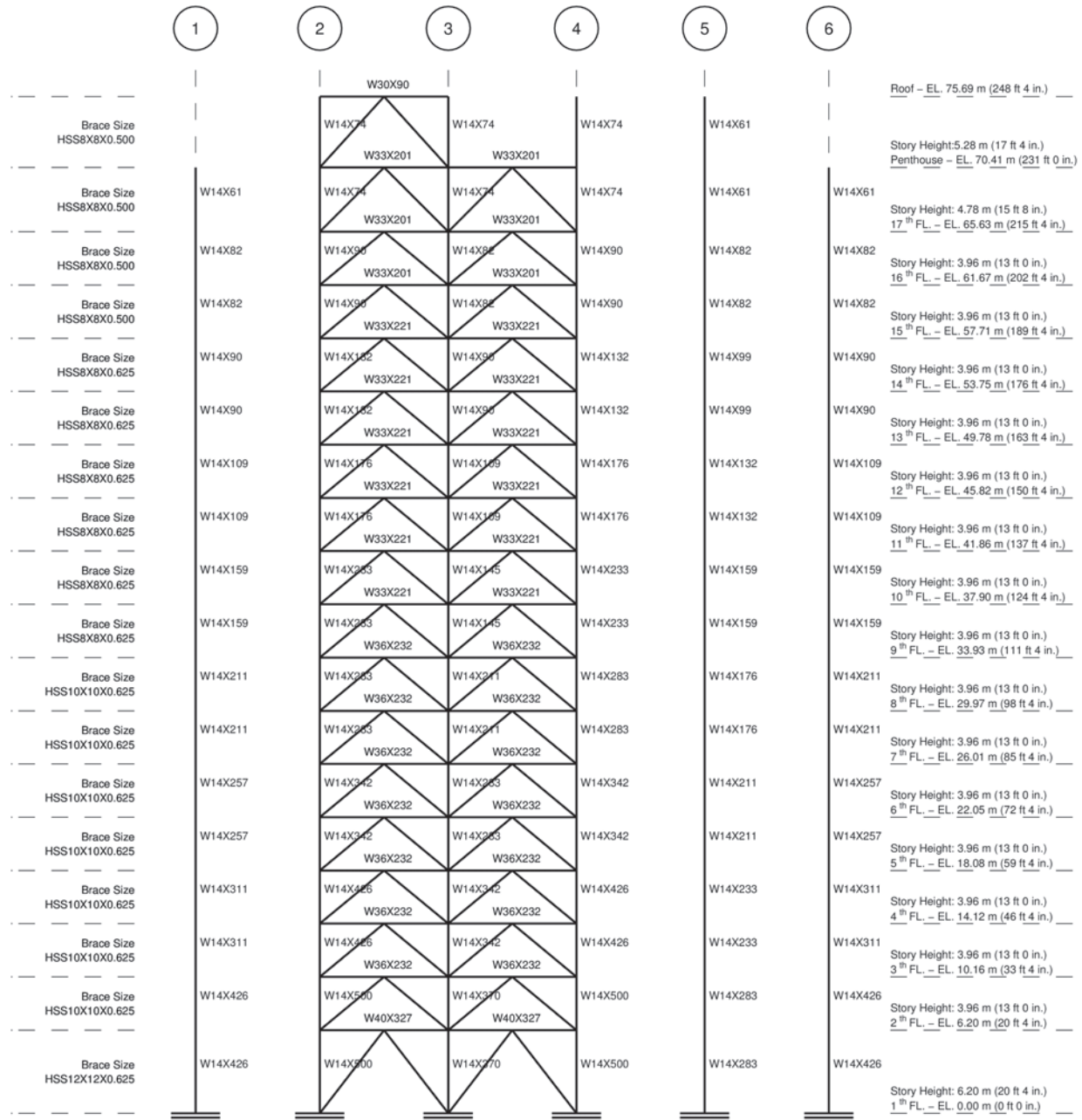


Figure G.4: East-west frame elevation along grid D (Braced frame - UBC 1997 - Site Category : S_B)

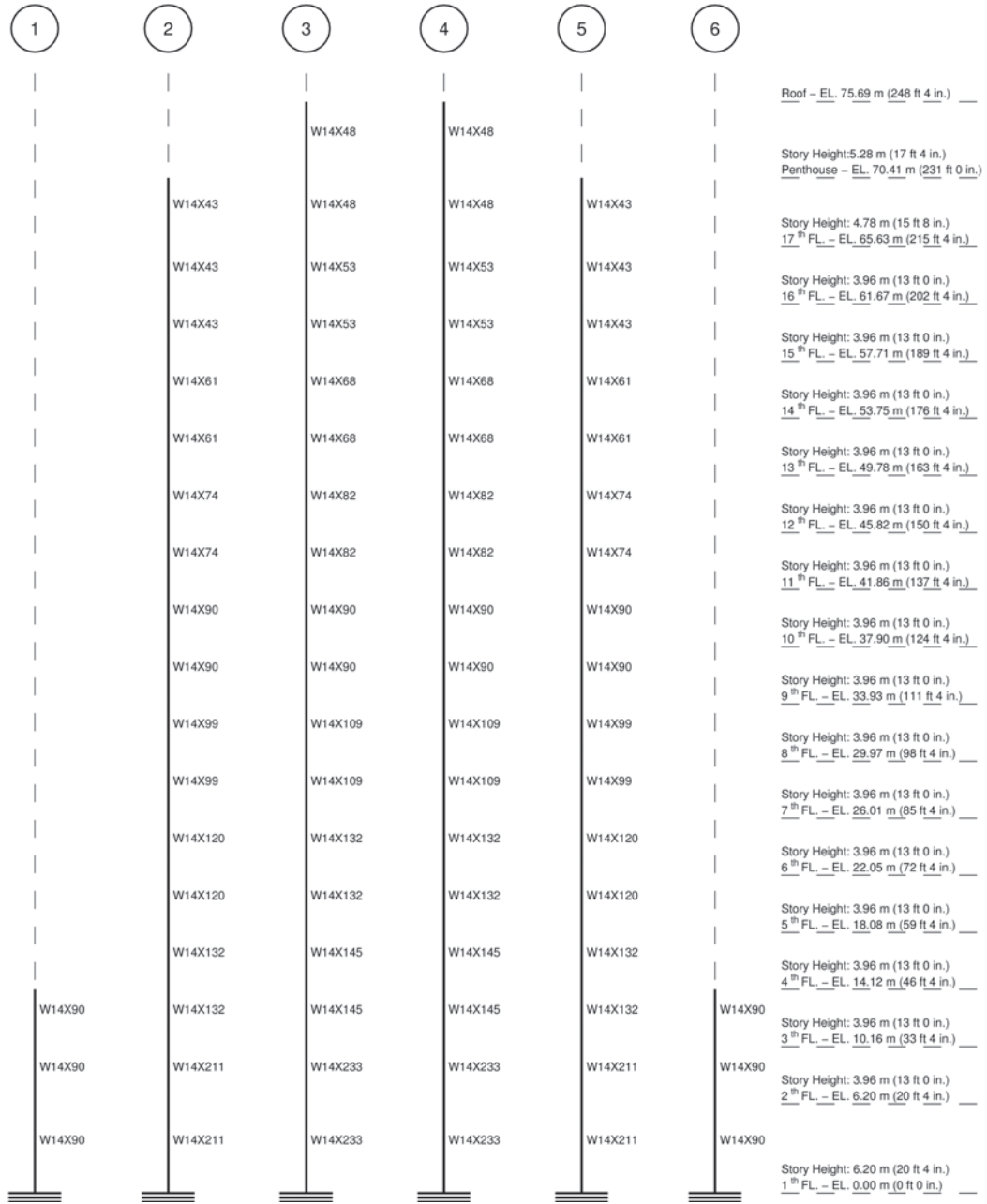


Figure G.5: East-west frame elevation along grid E (Braced frame - UBC 1997 - Site Category : S_B)

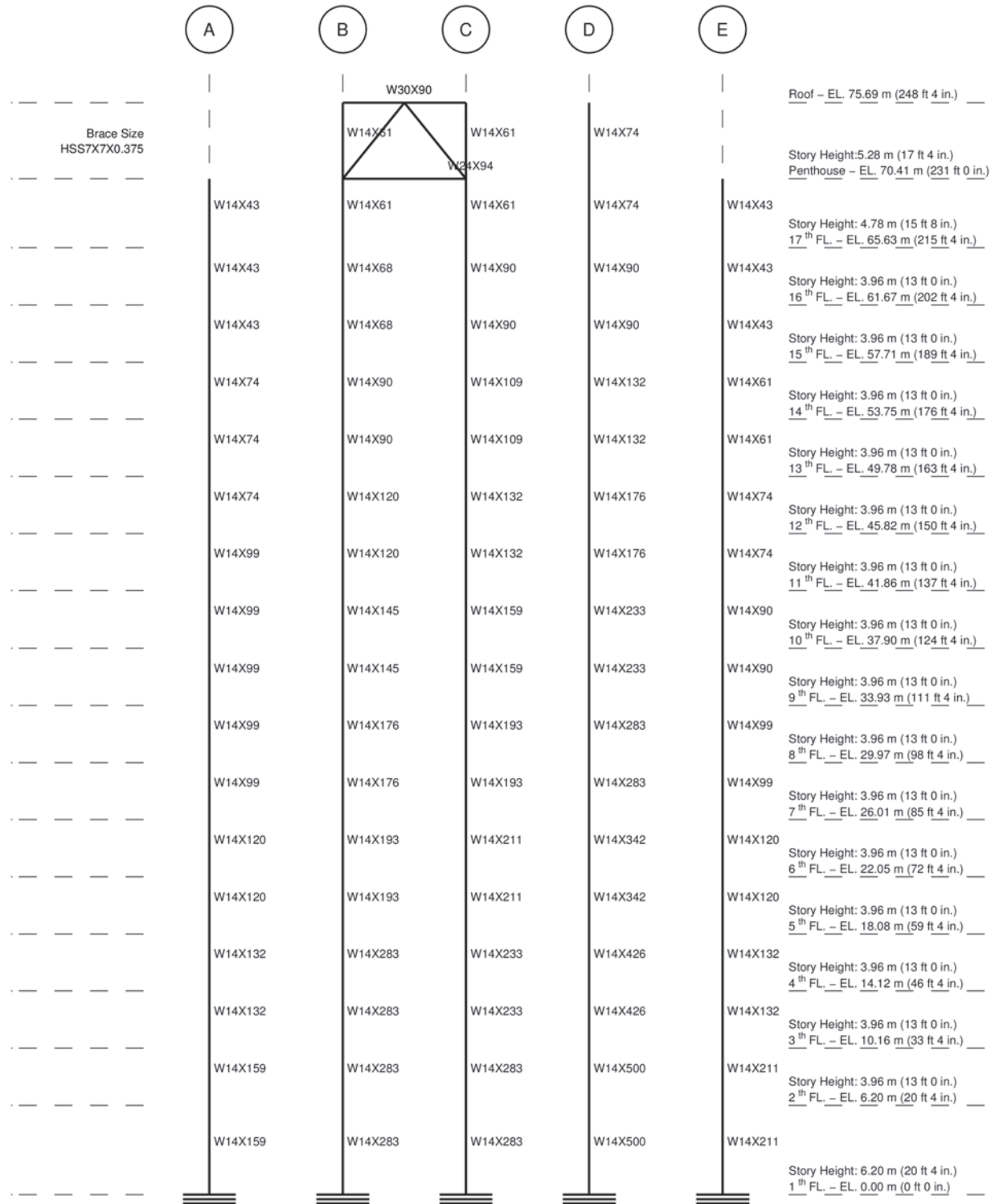


Figure G.7: North-south frame elevation along grid 2 (Braced frame - UBC 1997 - Site Category : S_B)

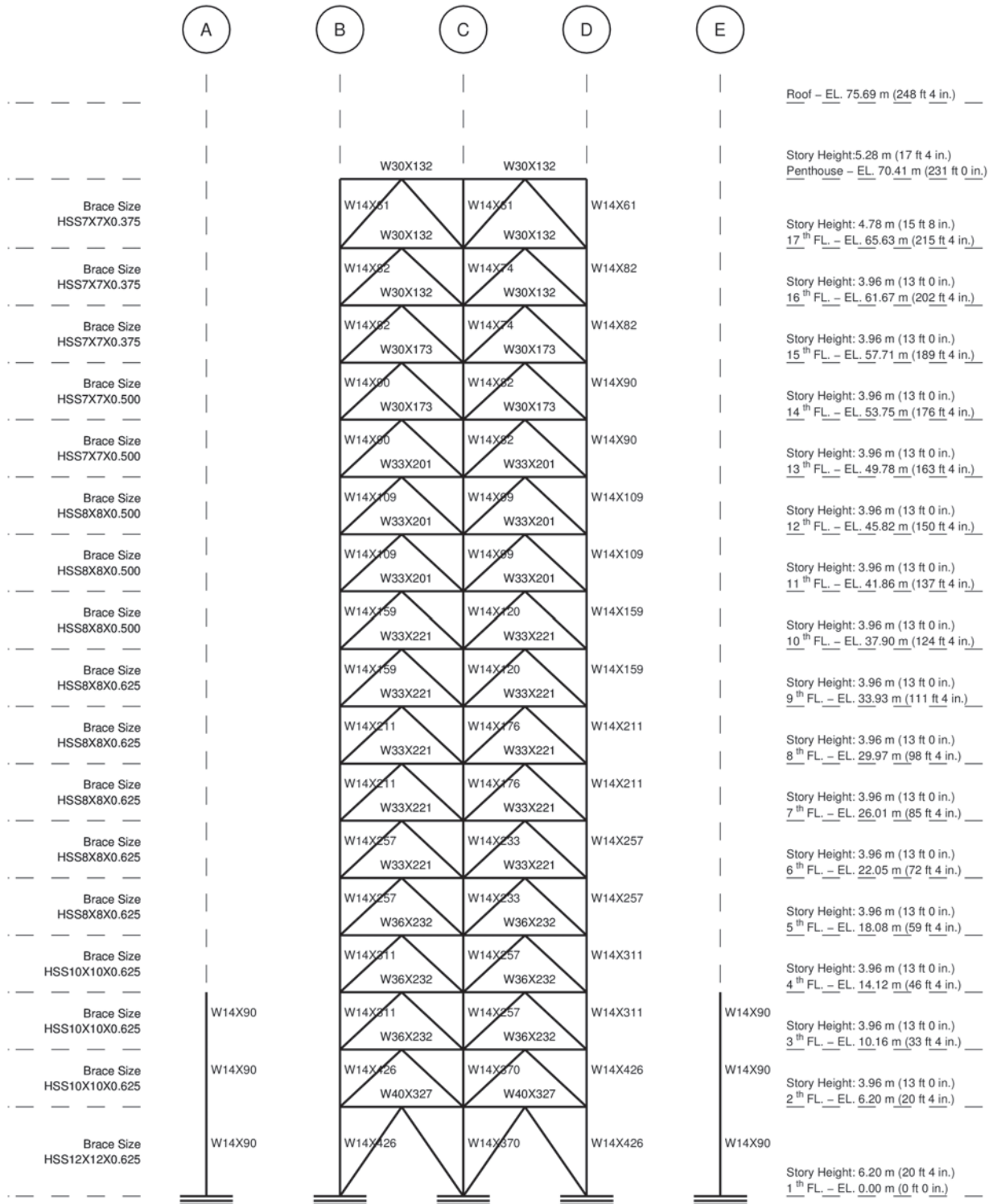


Figure G.9: North-south frame elevation along grid 6 (Braced frame - UBC 1997 - Site Category : S_B)

G.2 Braced Frame Version of Park Building

Braced Frame - UBC 1997 Building Code

S_C **Site Categories**

Frame Elevations - Beam, Column, and Brace size

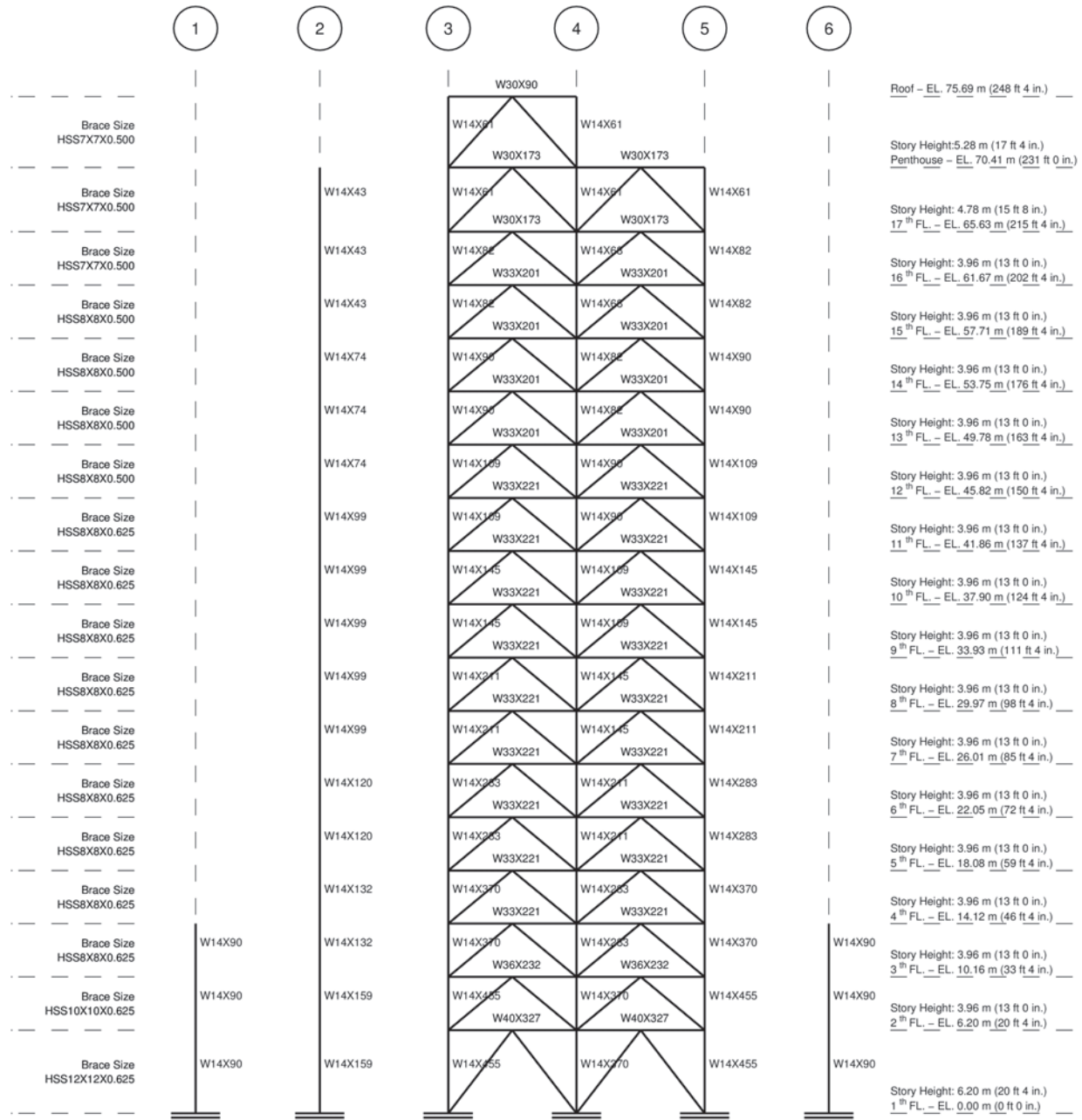


Figure G.10: East-west frame elevation along grid A (Braced frame - UBC 1997 - Site Category : S_C)

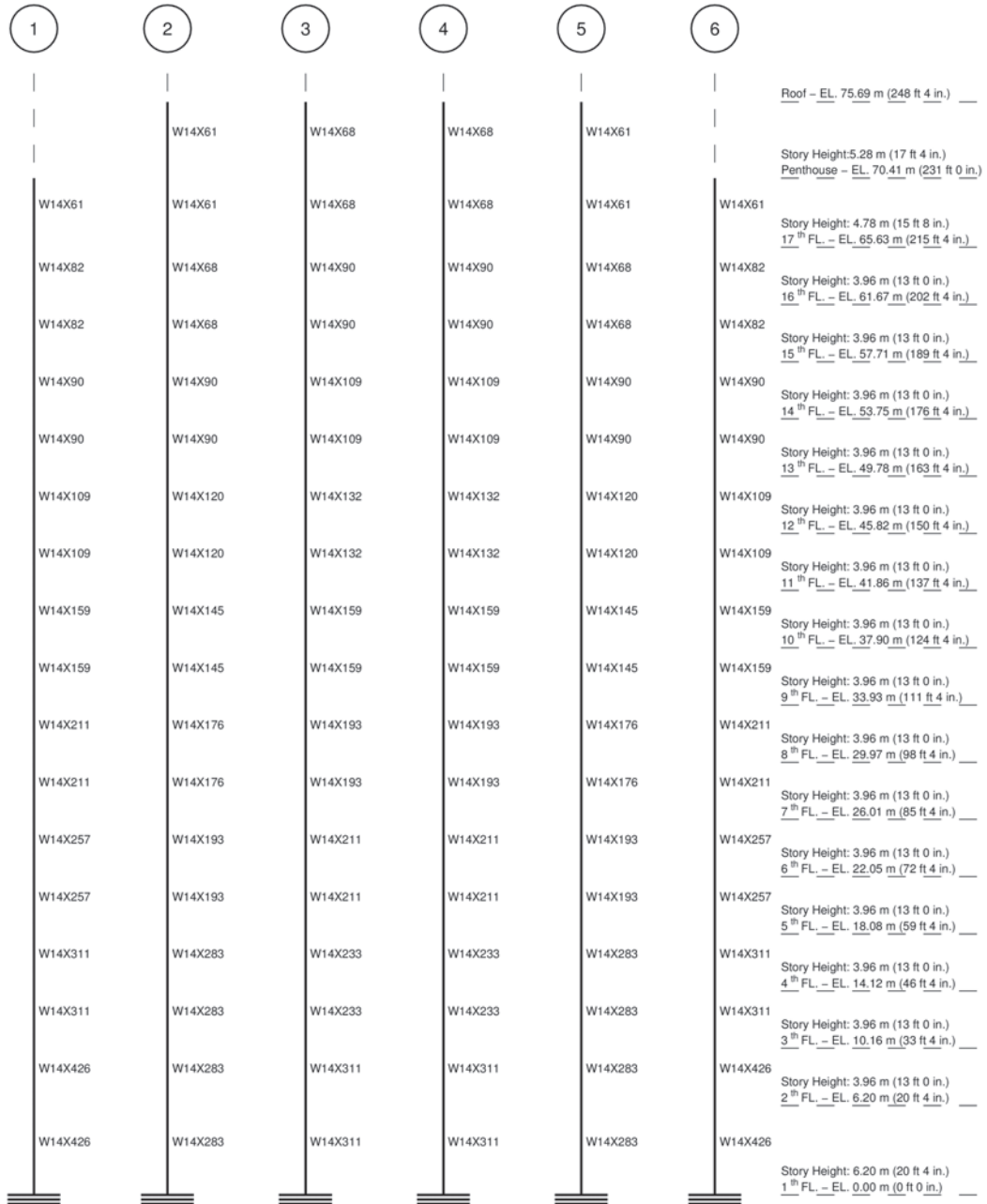


Figure G.11: East-west frame elevation along grid B (Braced frame - UBC 1997 - Site Category : S_C)

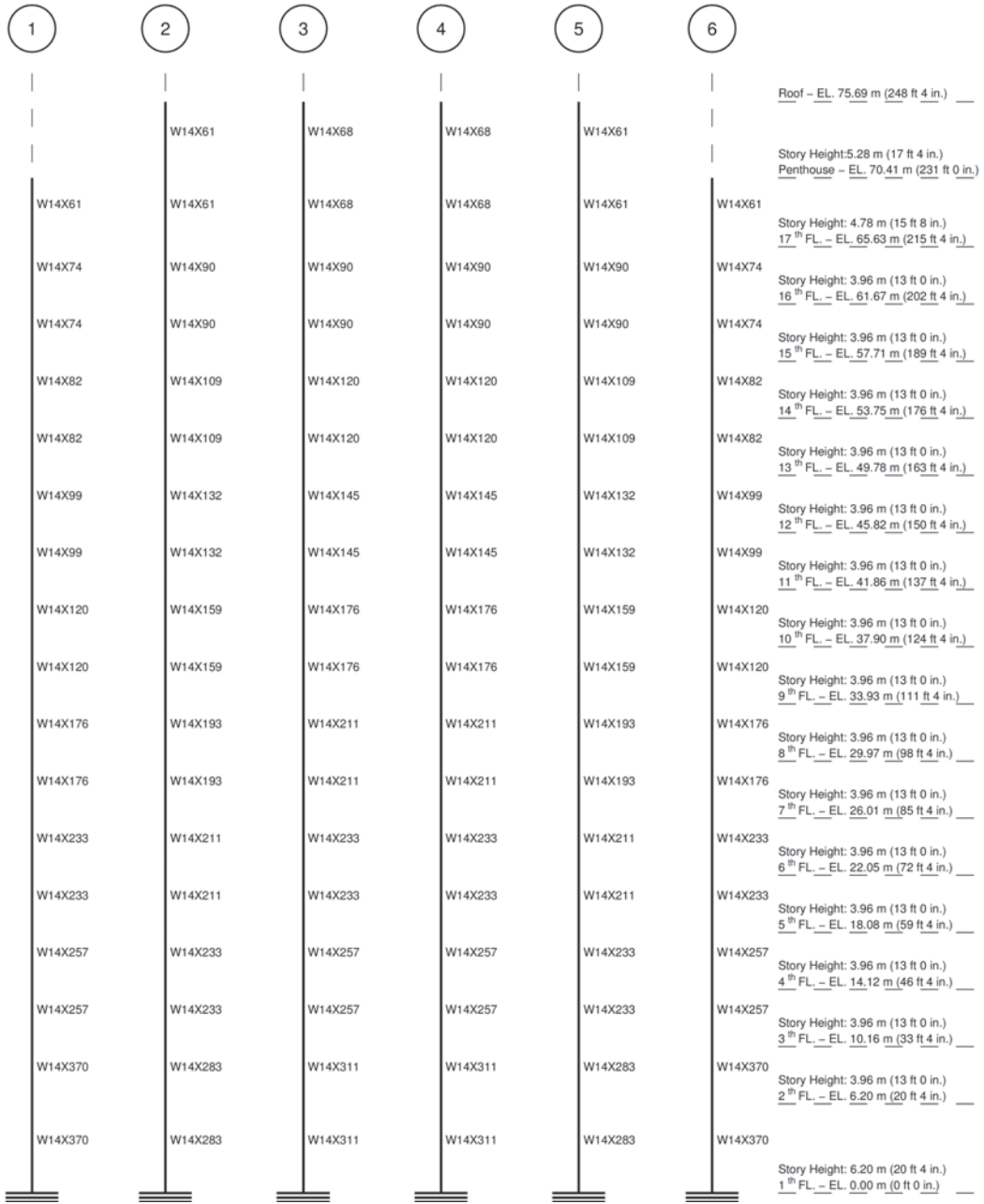


Figure G.12: East-west frame elevation along grid C (Braced frame - UBC 1997 - Site Category : S_C)

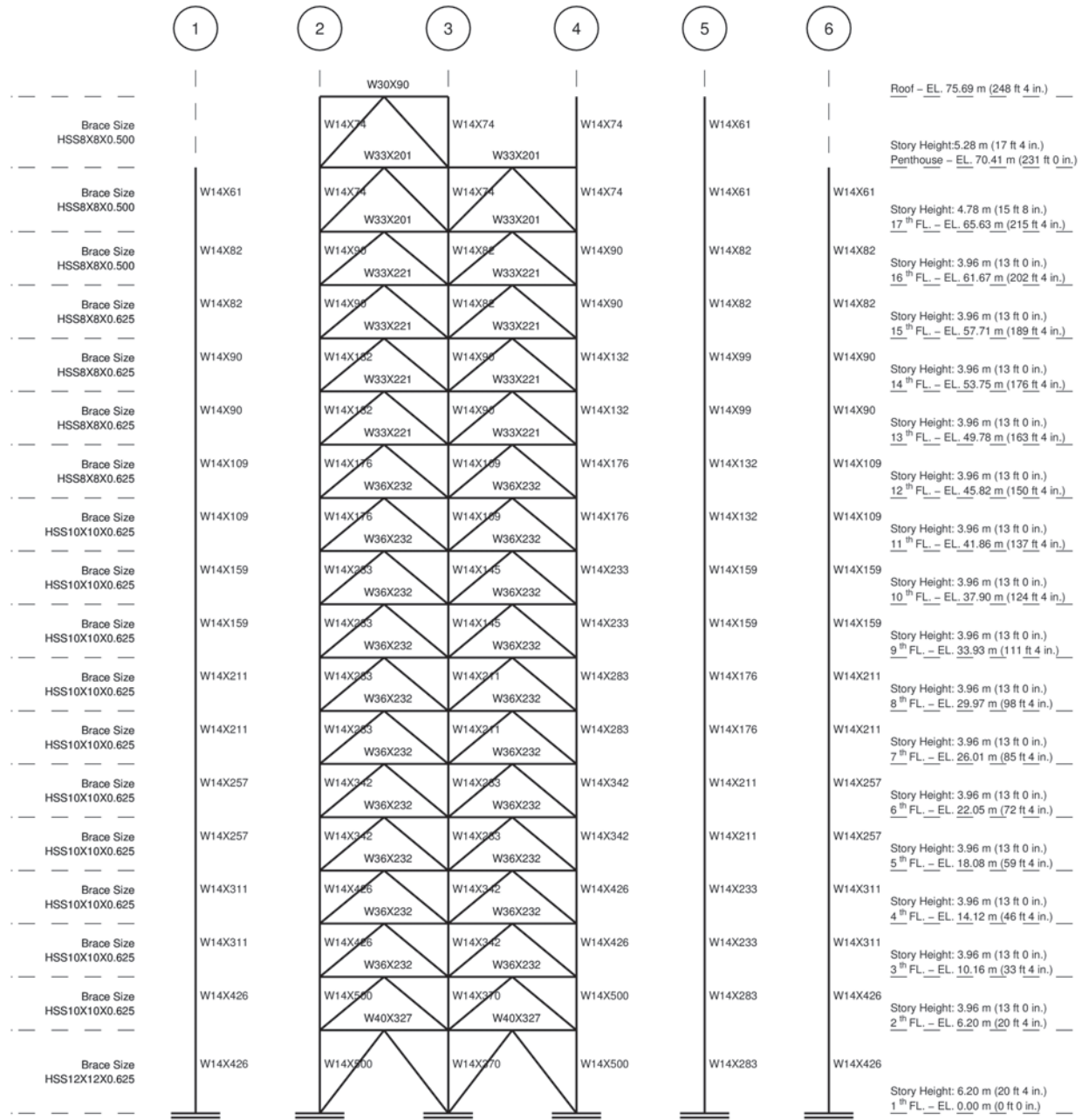


Figure G.13: East-west frame elevation along grid D (Braced frame - UBC 1997 - Site Category : S_C)

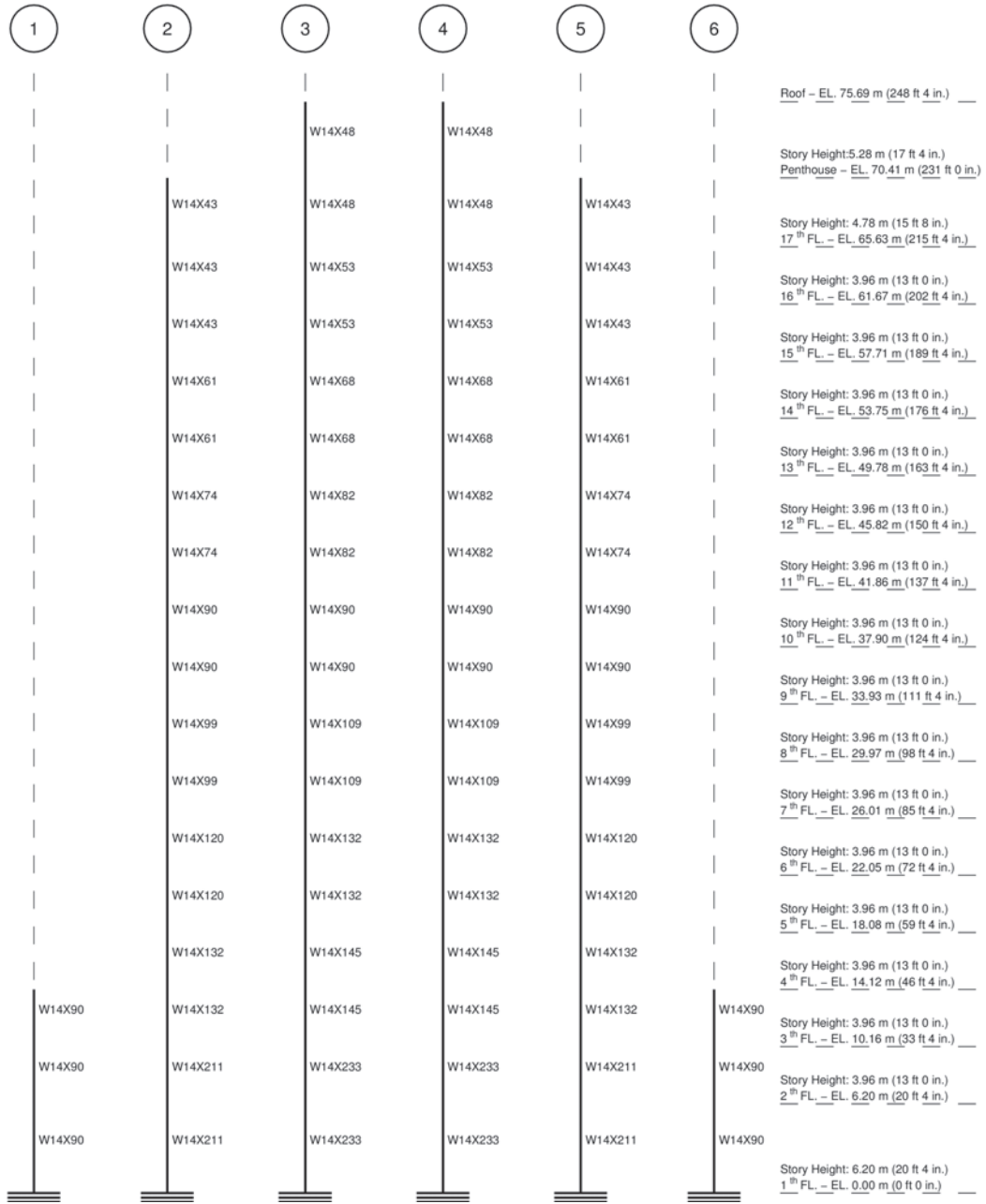


Figure G.14: East-west frame elevation along grid E (Braced frame - UBC 1997 - Site Category : S_C)

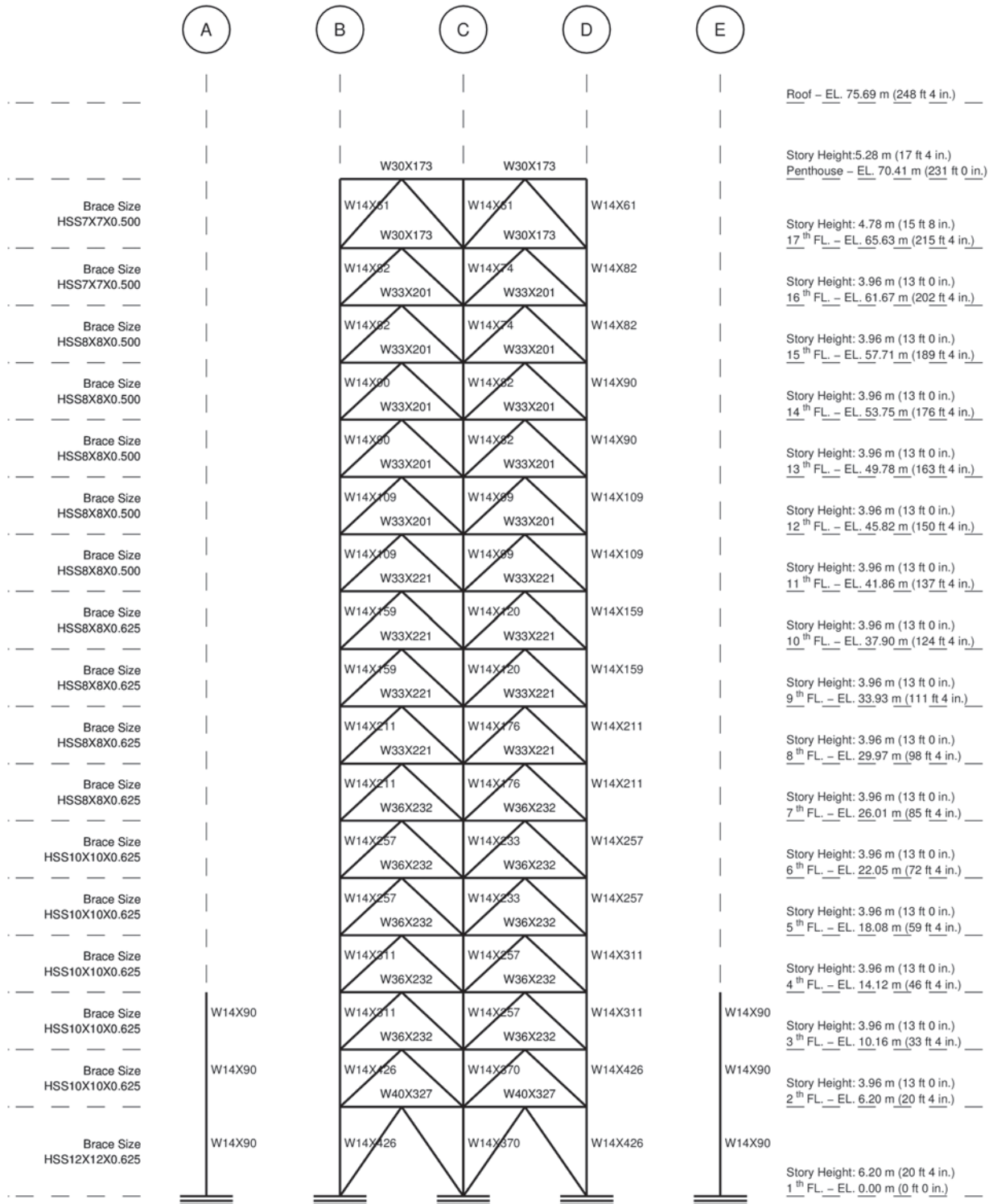


Figure G.15: North-south frame elevation along grid 1 (Braced frame - UBC 1997 - Site Category : S_C)

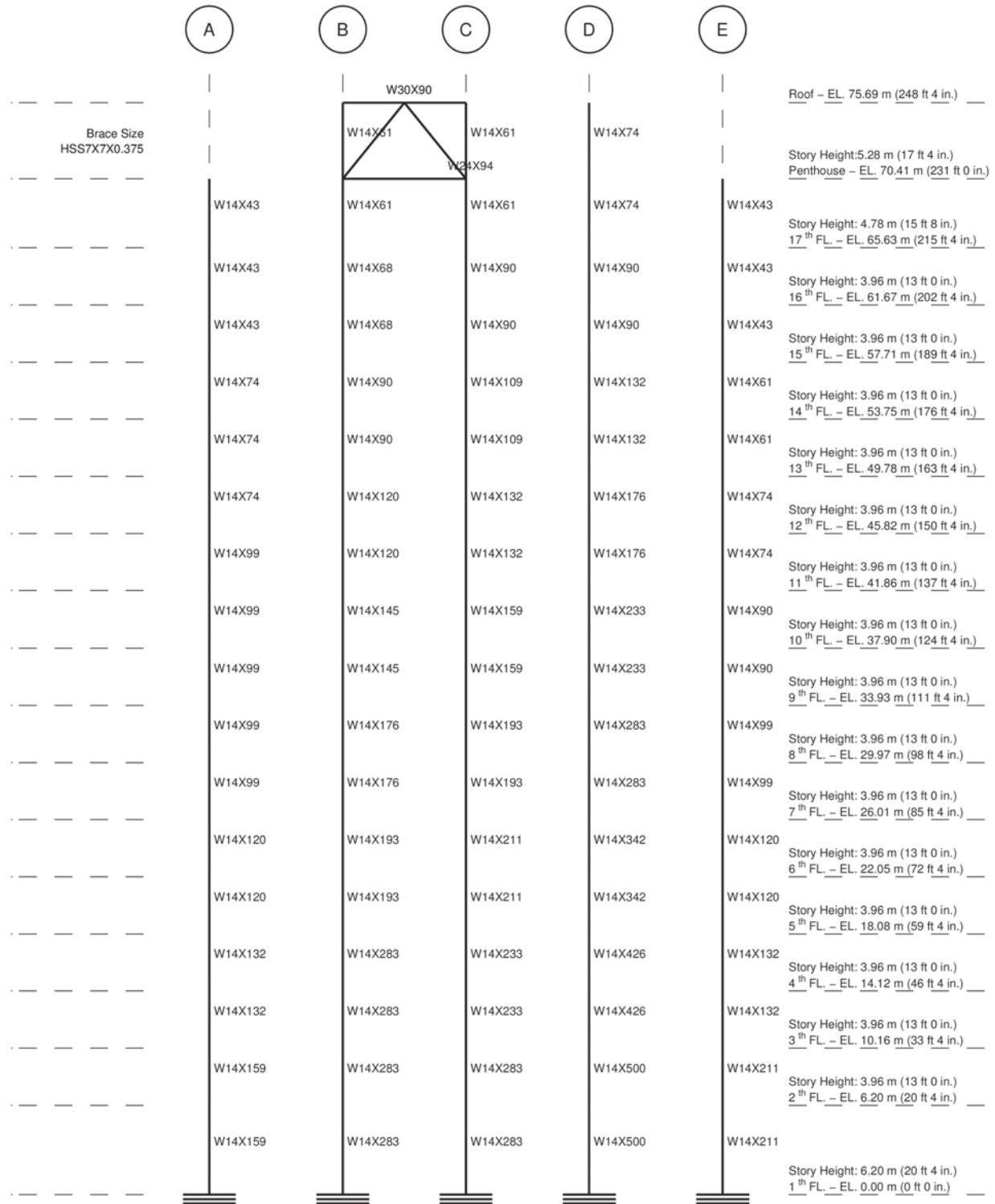


Figure G.16: North-south frame elevation along grid 2 (Braced frame - UBC 1997 - Site Category : S_C)

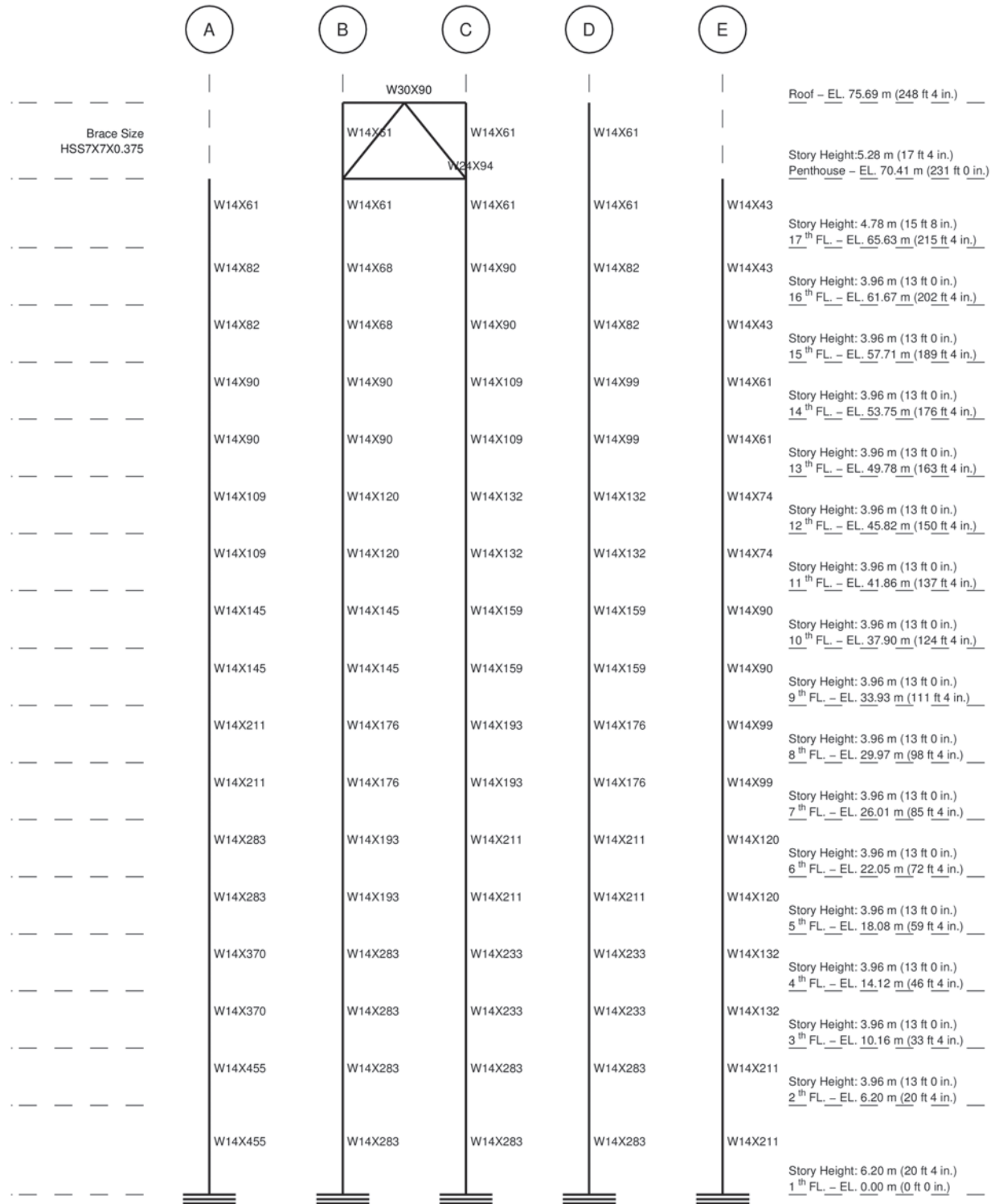


Figure G.17: North-south frame elevation along grid 5 (Braced frame - UBC 1997 - Site Category : S_C)

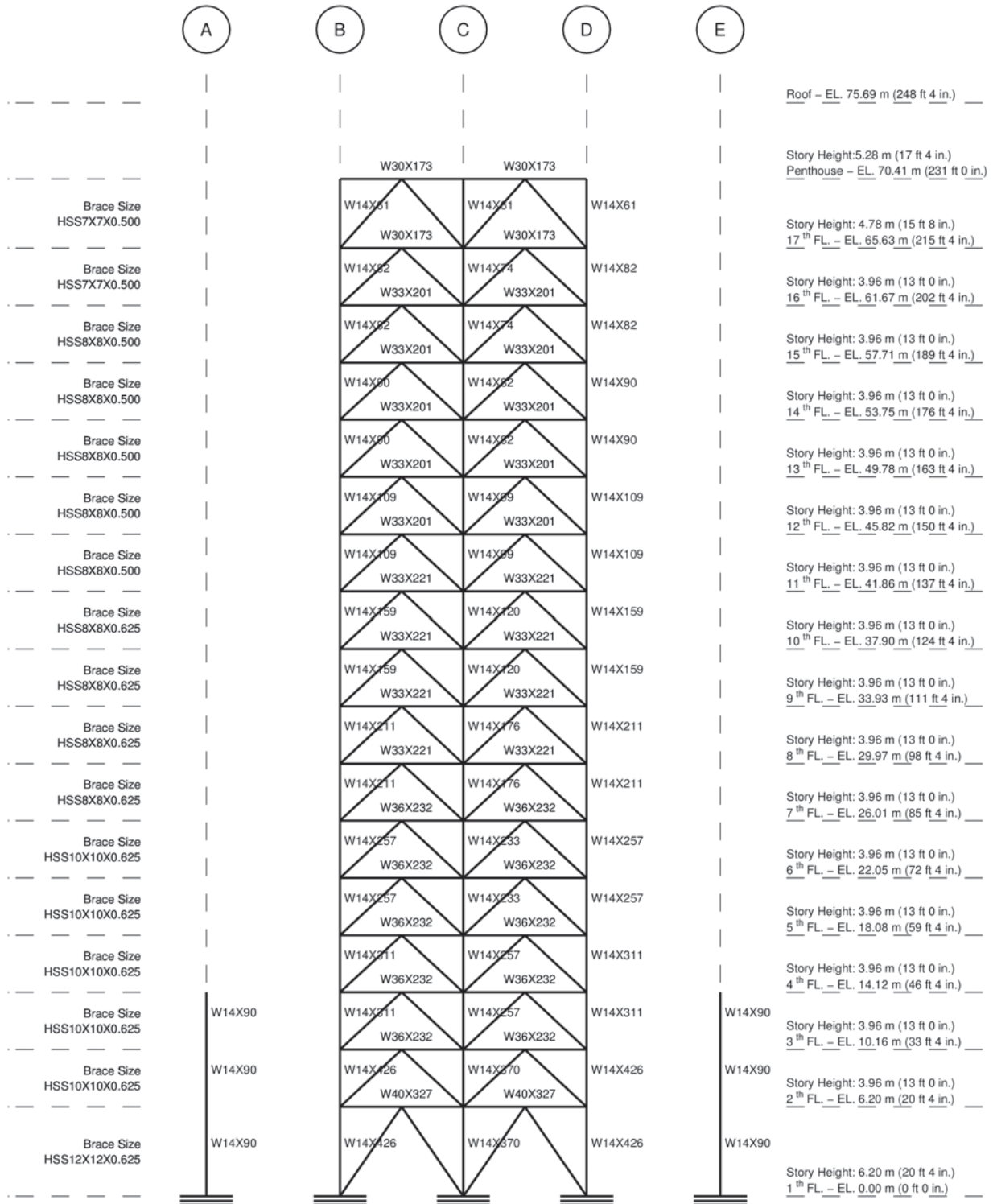


Figure G.18: North-south frame elevation along grid 6 (Braced frame - UBC 1997 - Site Category : S_C)

G.3 Braced Frame Version of Canoga Park Building

Braced Frame - UBC 1997 Building Code

S_D **Site Categories**

Frame Elevations - Beam, Column, and Brace size

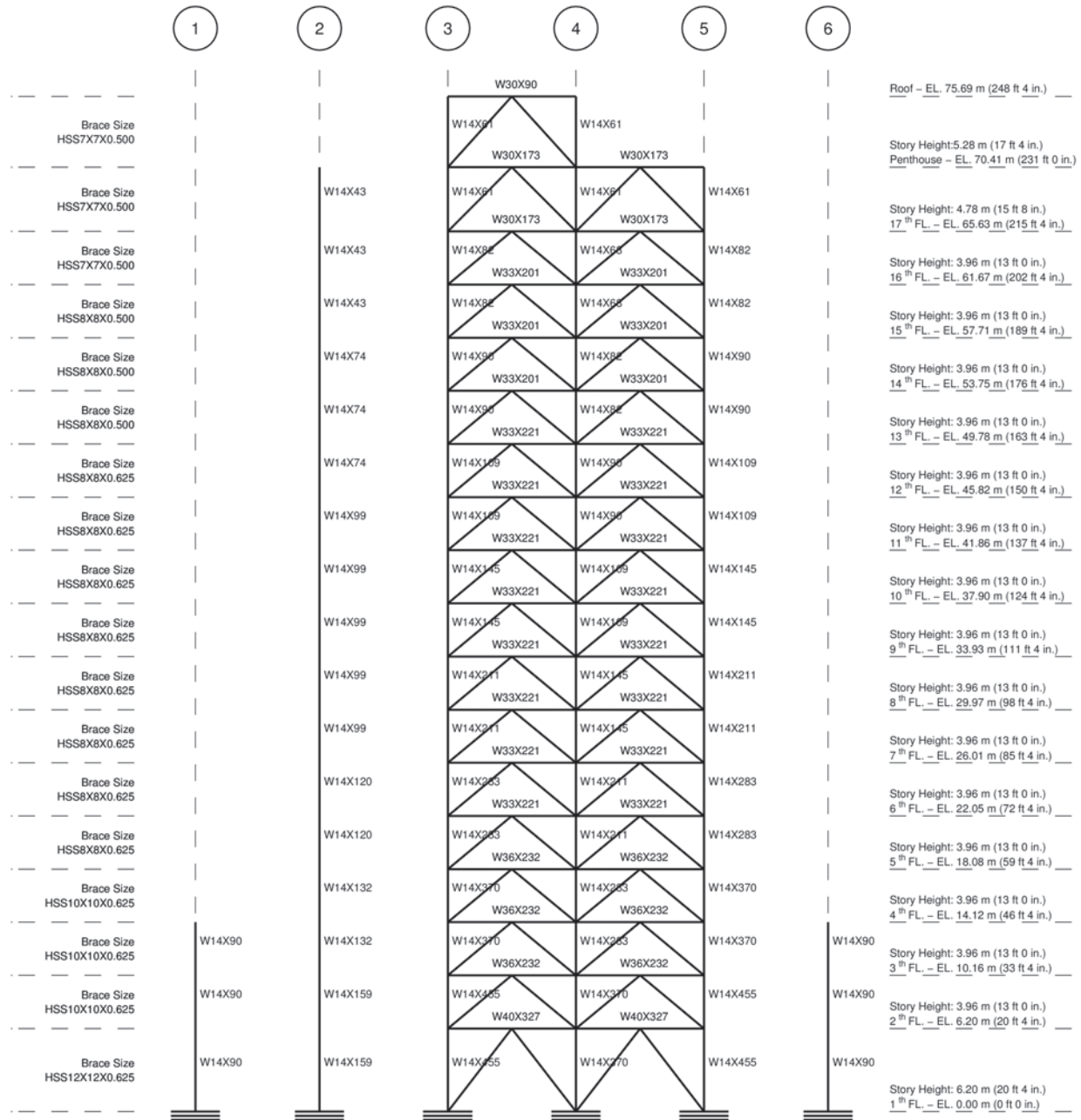


Figure G.19: East-west frame elevation along grid A (Braced frame - UBC 1997 - Site Category : S_D)

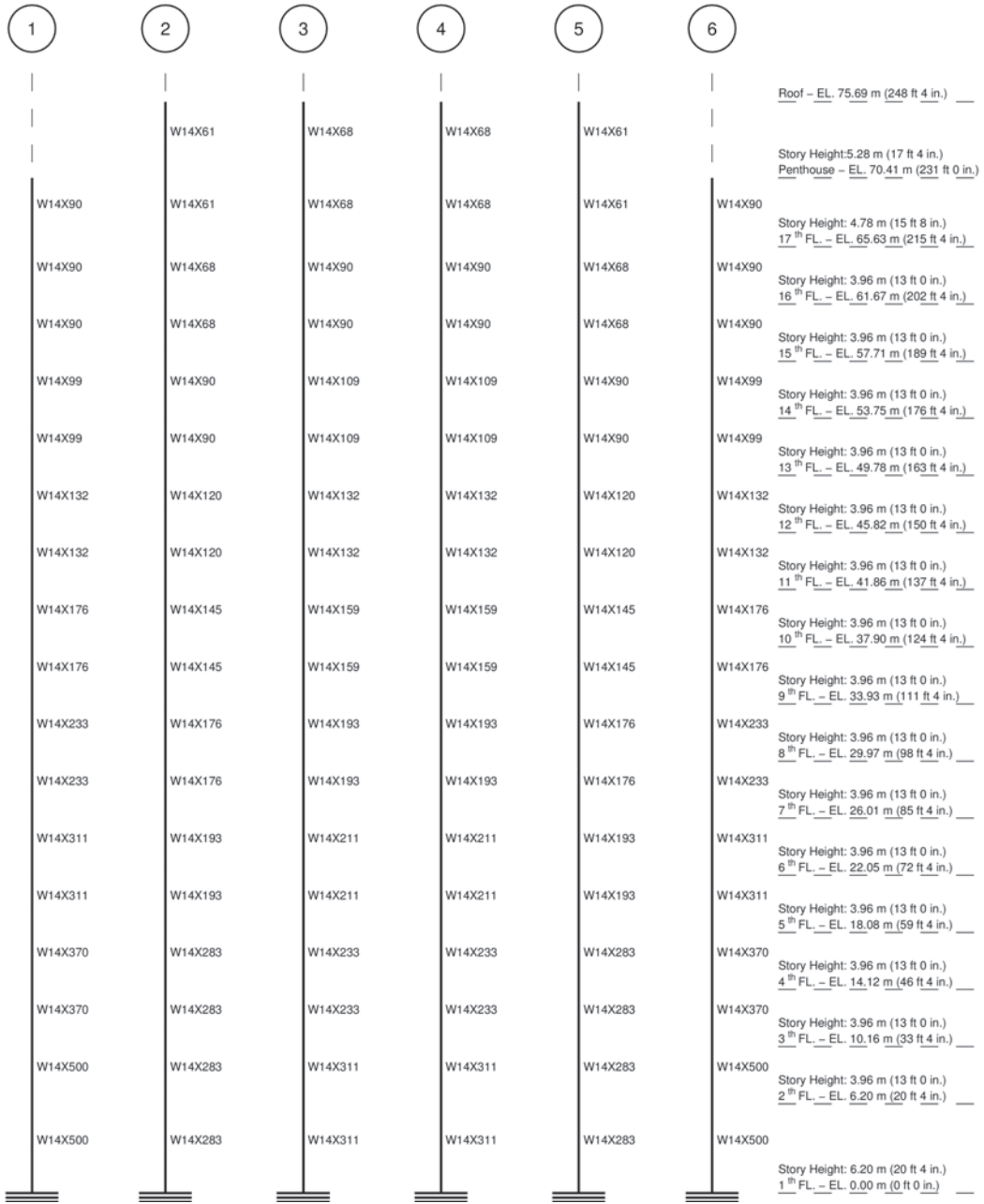


Figure G.20: East-west frame elevation along grid B (Braced frame - UBC 1997 - Site Category : S_D)

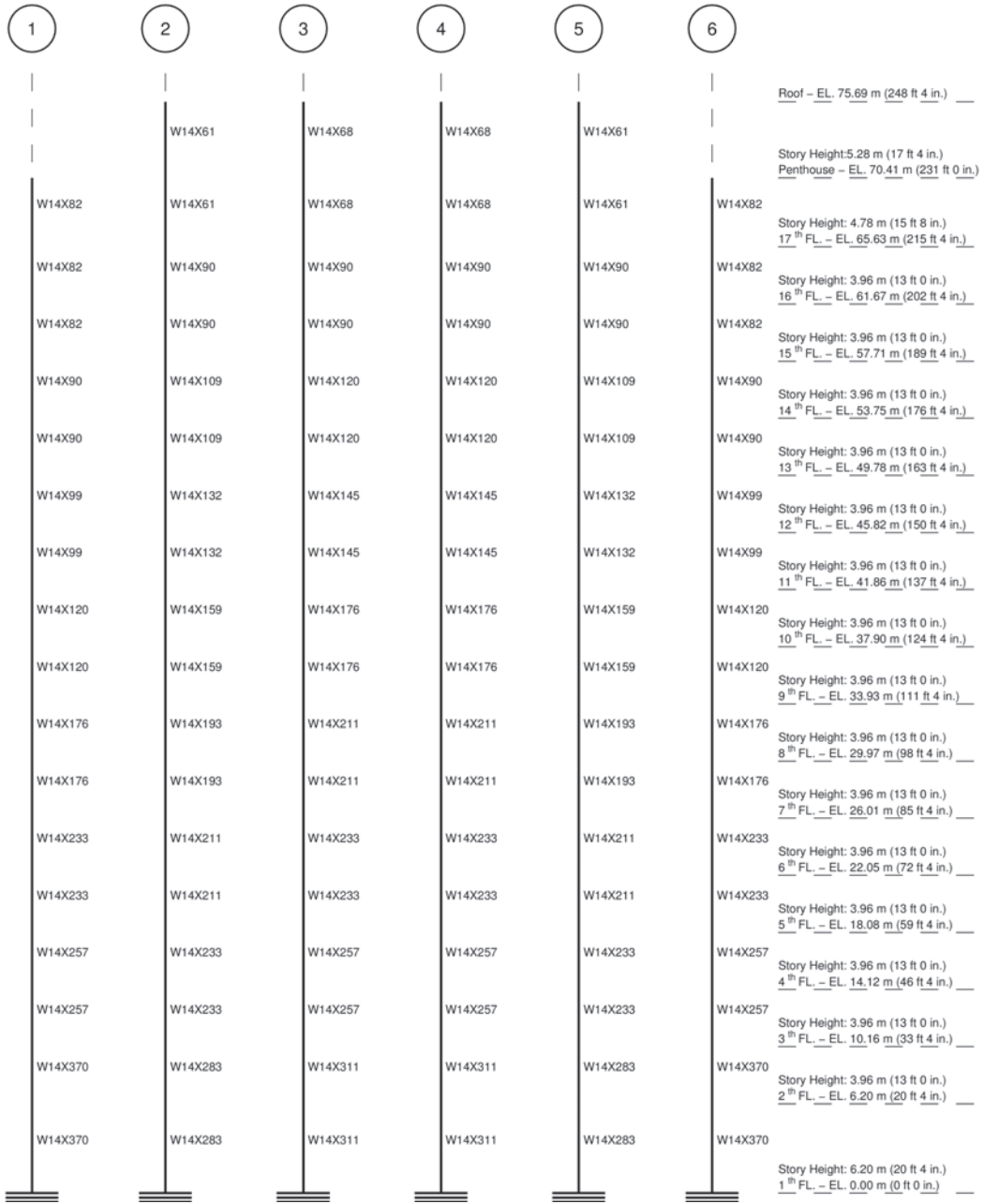


Figure G.21: East-west frame elevation along grid C (Braced frame - UBC 1997 - Site Category : S_D)

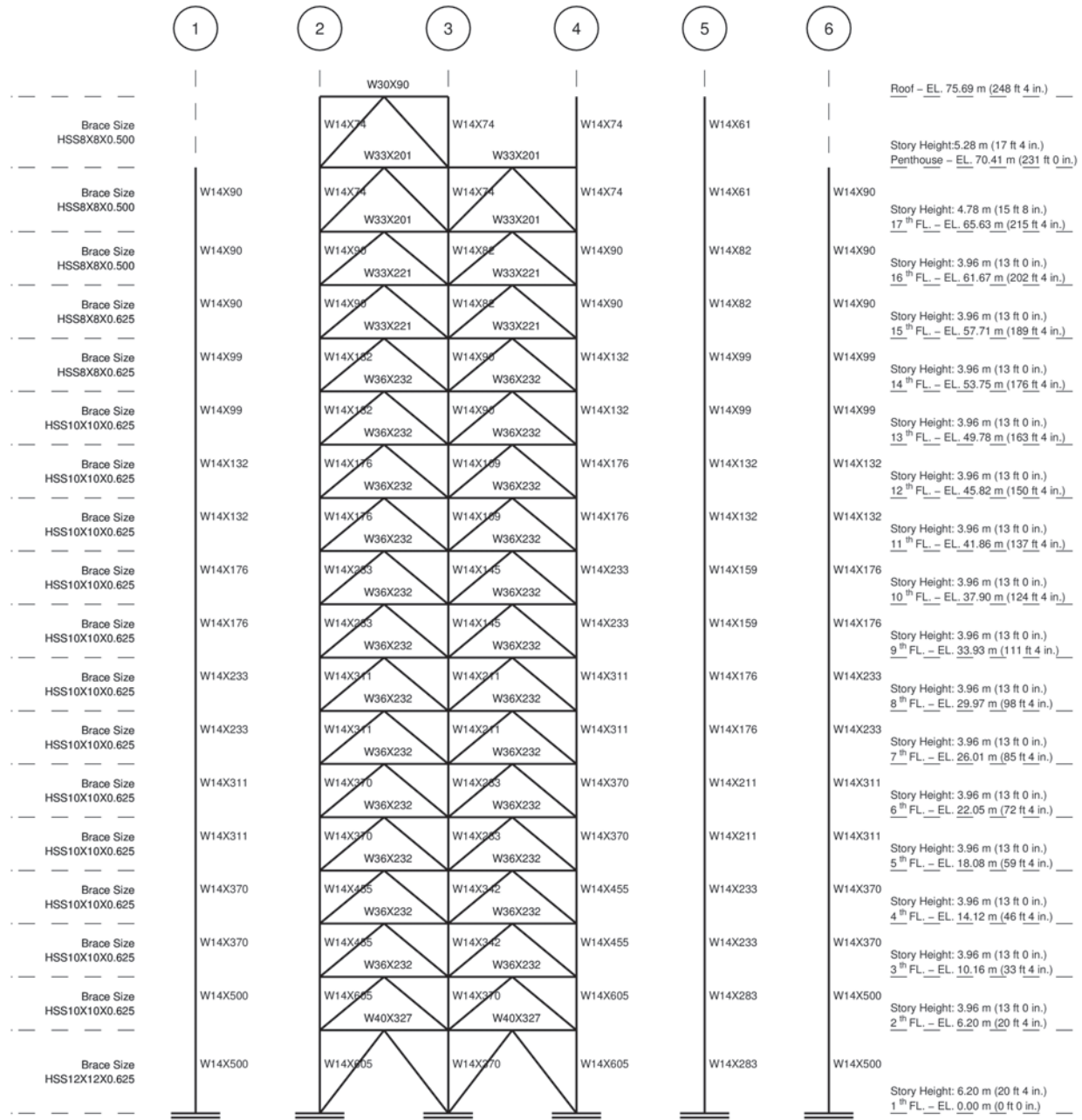


Figure G.22: East-west frame elevation along grid D (Braced frame - UBC 1997 - Site Category : S_D)

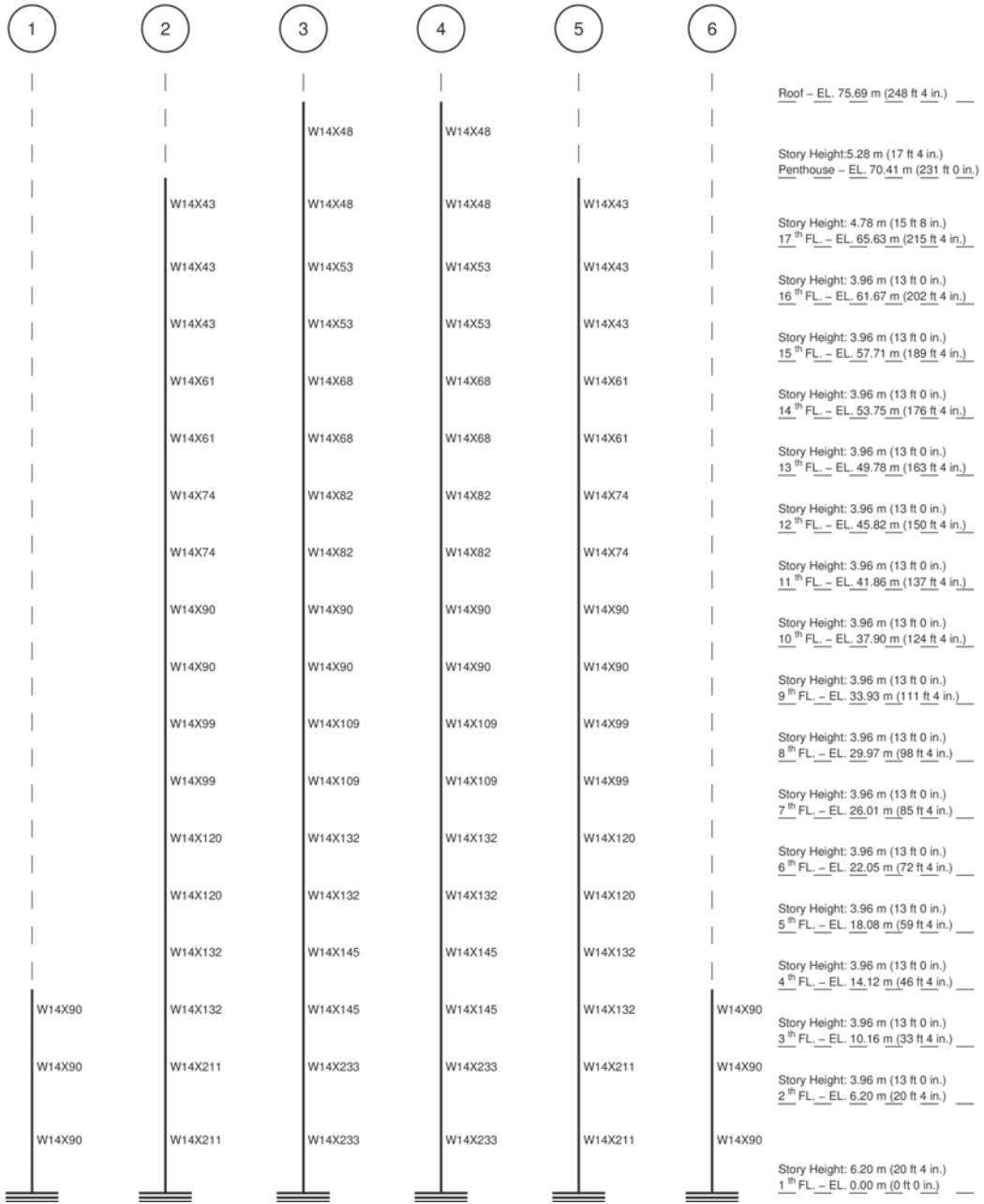


Figure G.23: East-west frame elevation along grid E (Braced frame - UBC 1997 - Site Category : S_D)

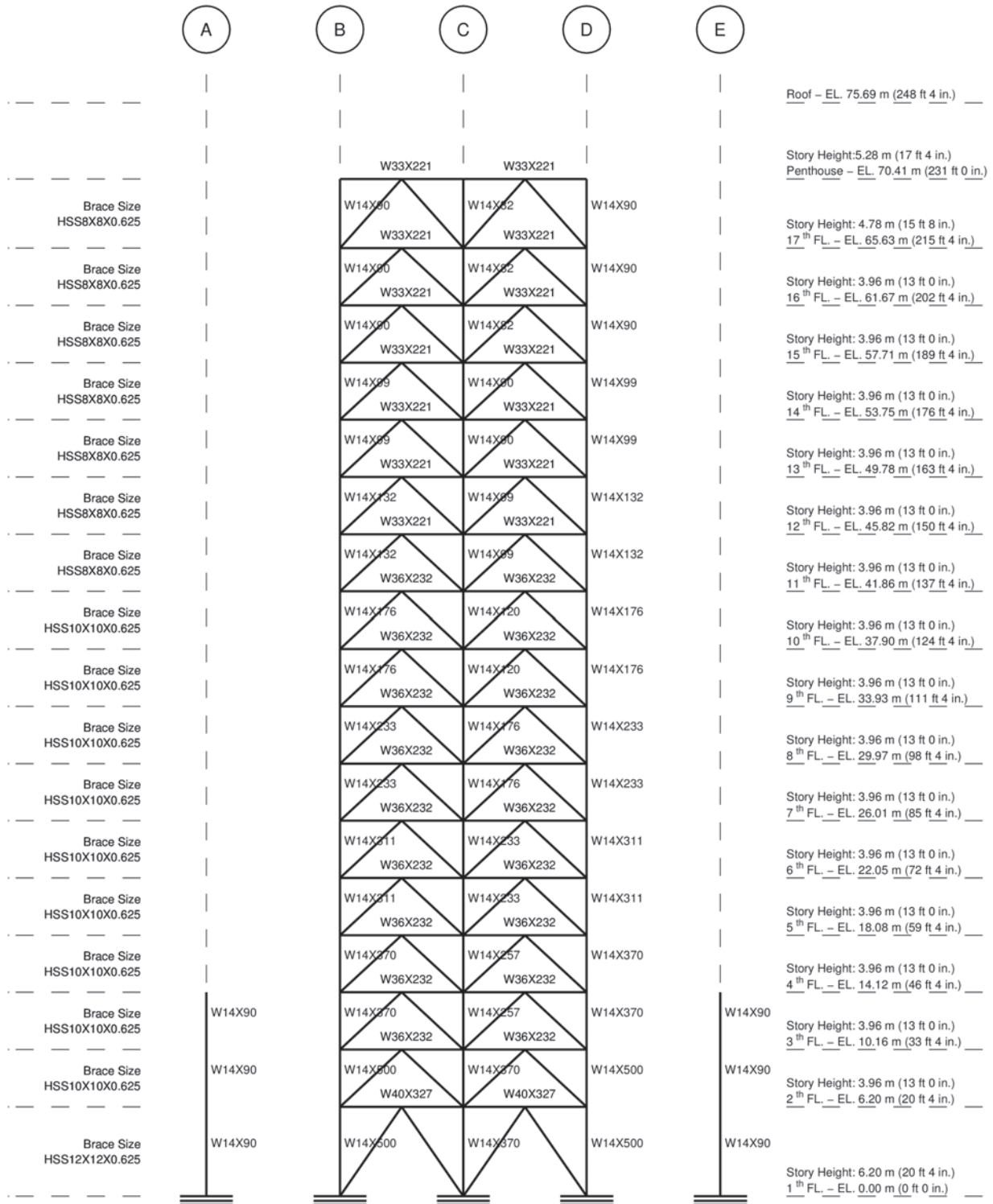


Figure G.24: North-south frame elevation along grid 1 (Braced frame - UBC 1997 - Site Category : S_D)

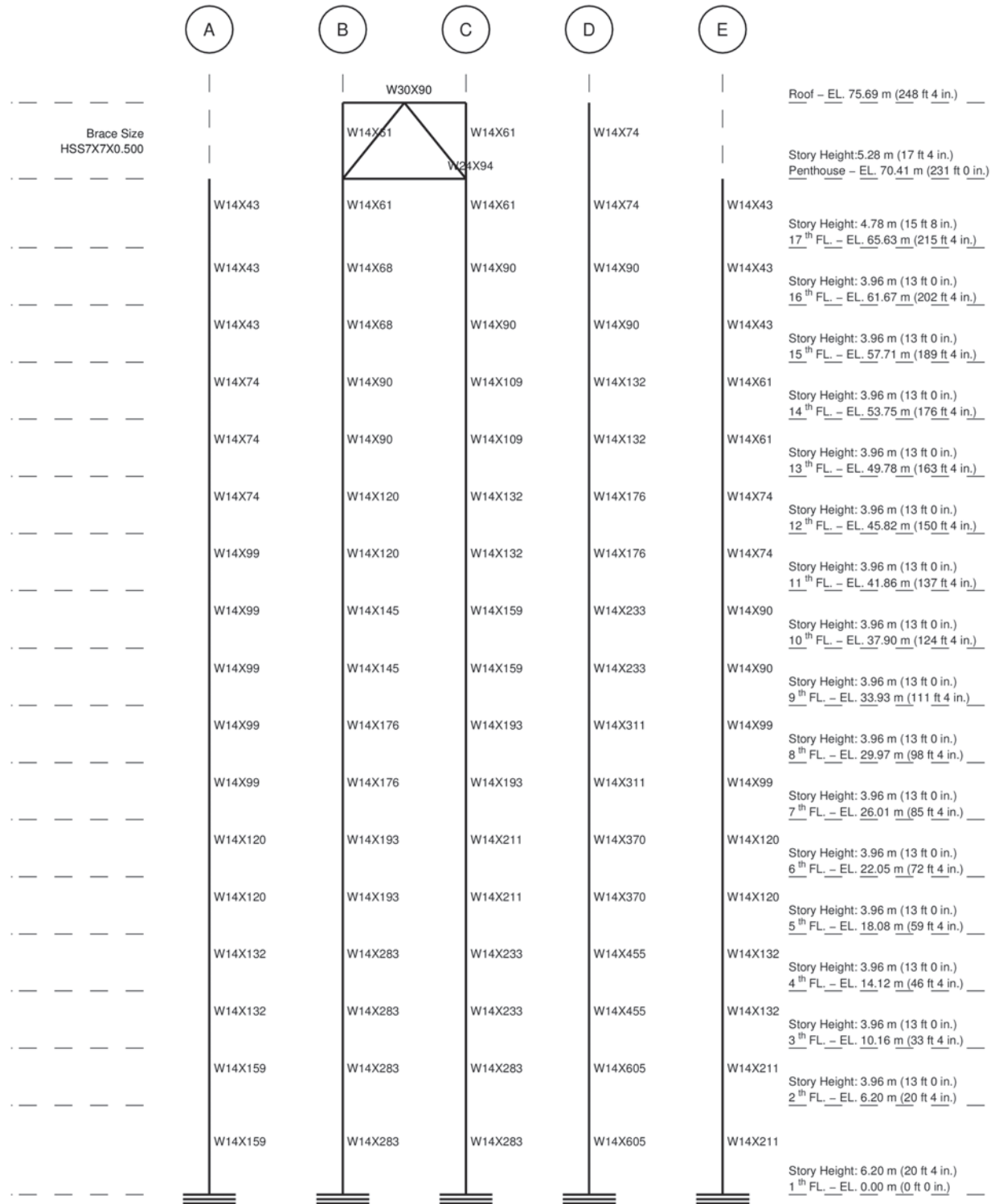


Figure G.25: North-south frame elevation along grid 2 (Braced frame - UBC 1997 - Site Category : S_D)

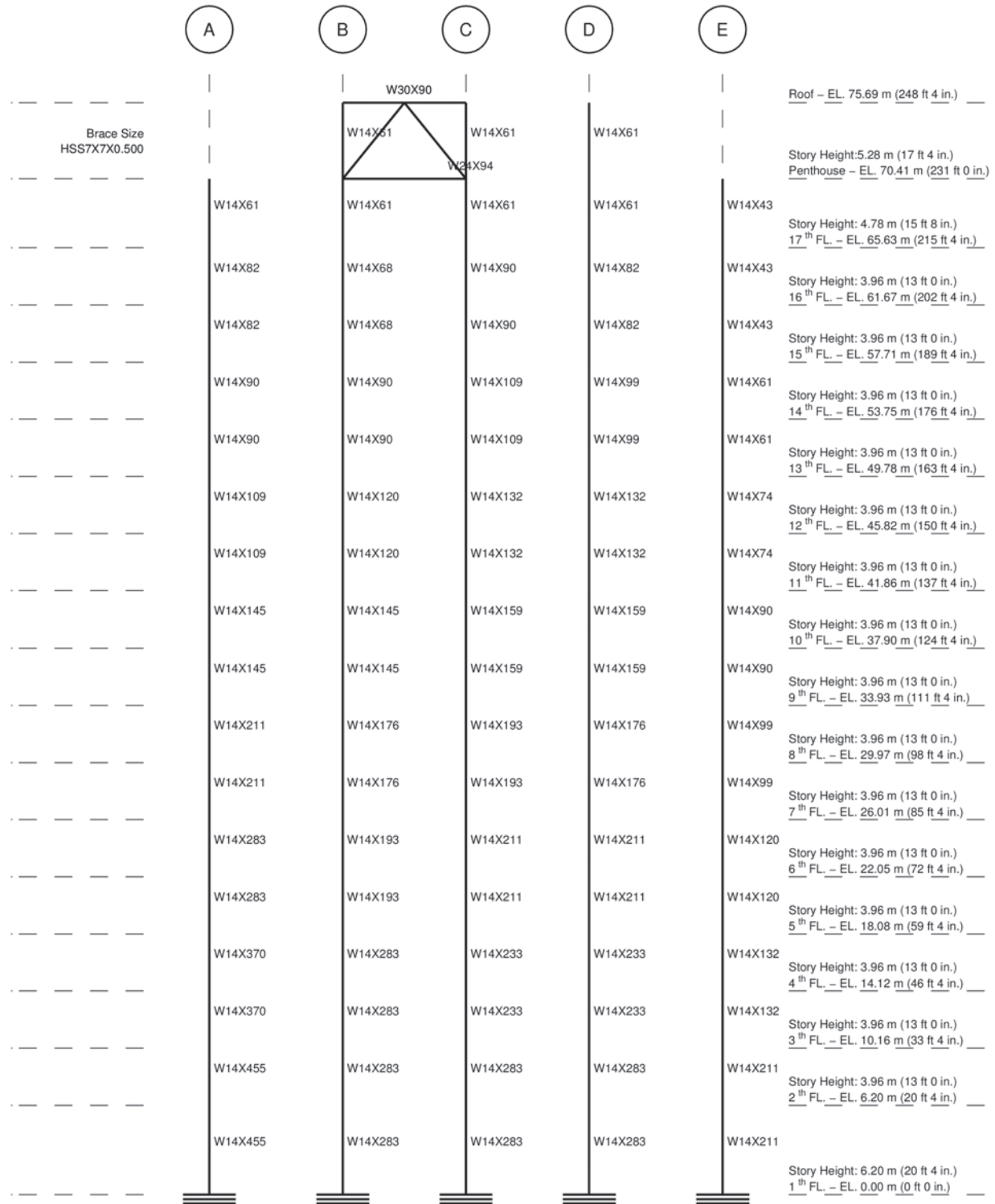


Figure G.26: North-south frame elevation along grid 5 (Braced frame - UBC 1997 - Site Category : S_D)

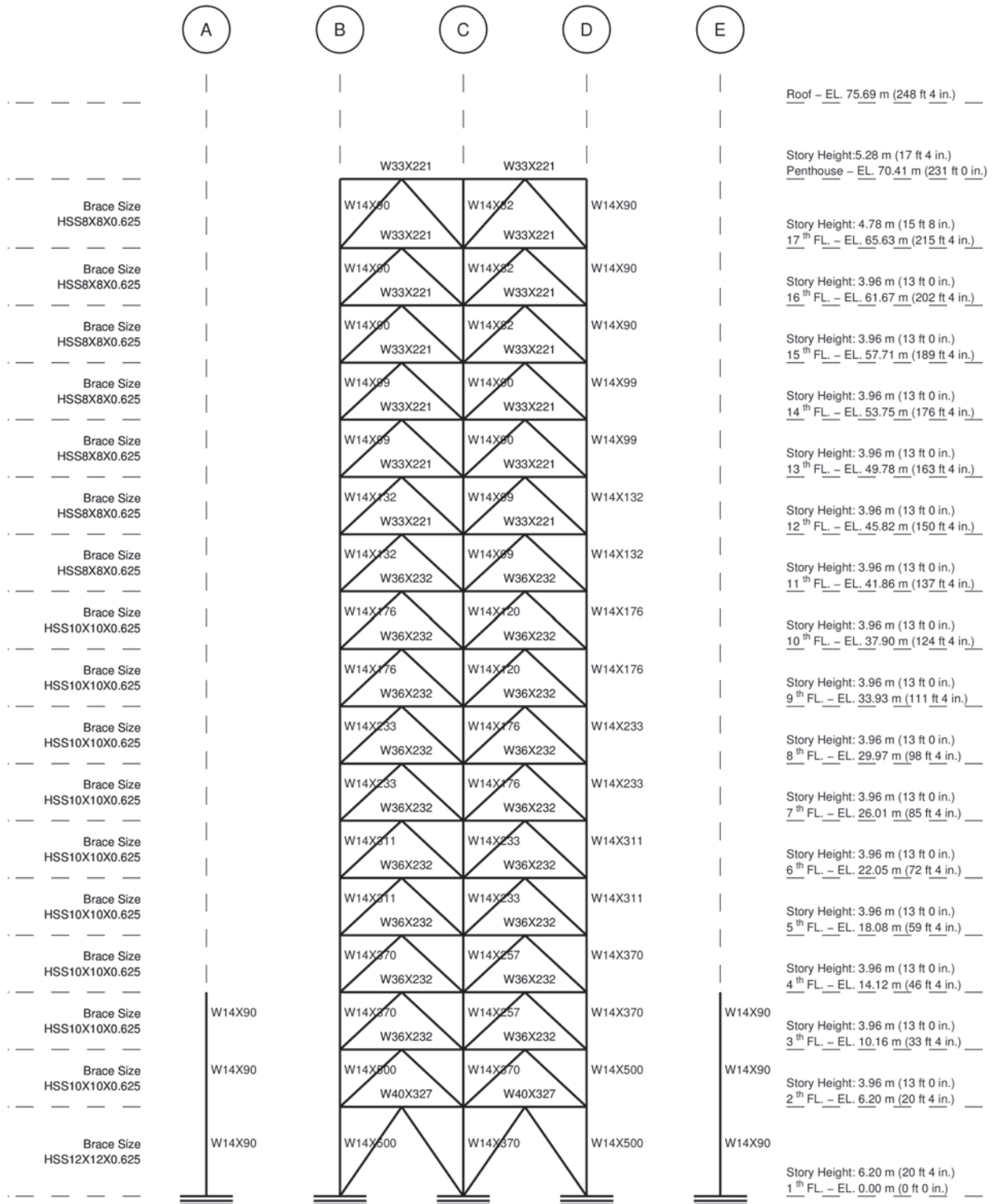


Figure G.27: North-south frame elevation along grid 6 (Braced frame - UBC 1997 - Site Category : S_D)

Appendix H

Additional Fragility Curves

H.1 Fragility Curves for 94S2, 97SB, and 97SC

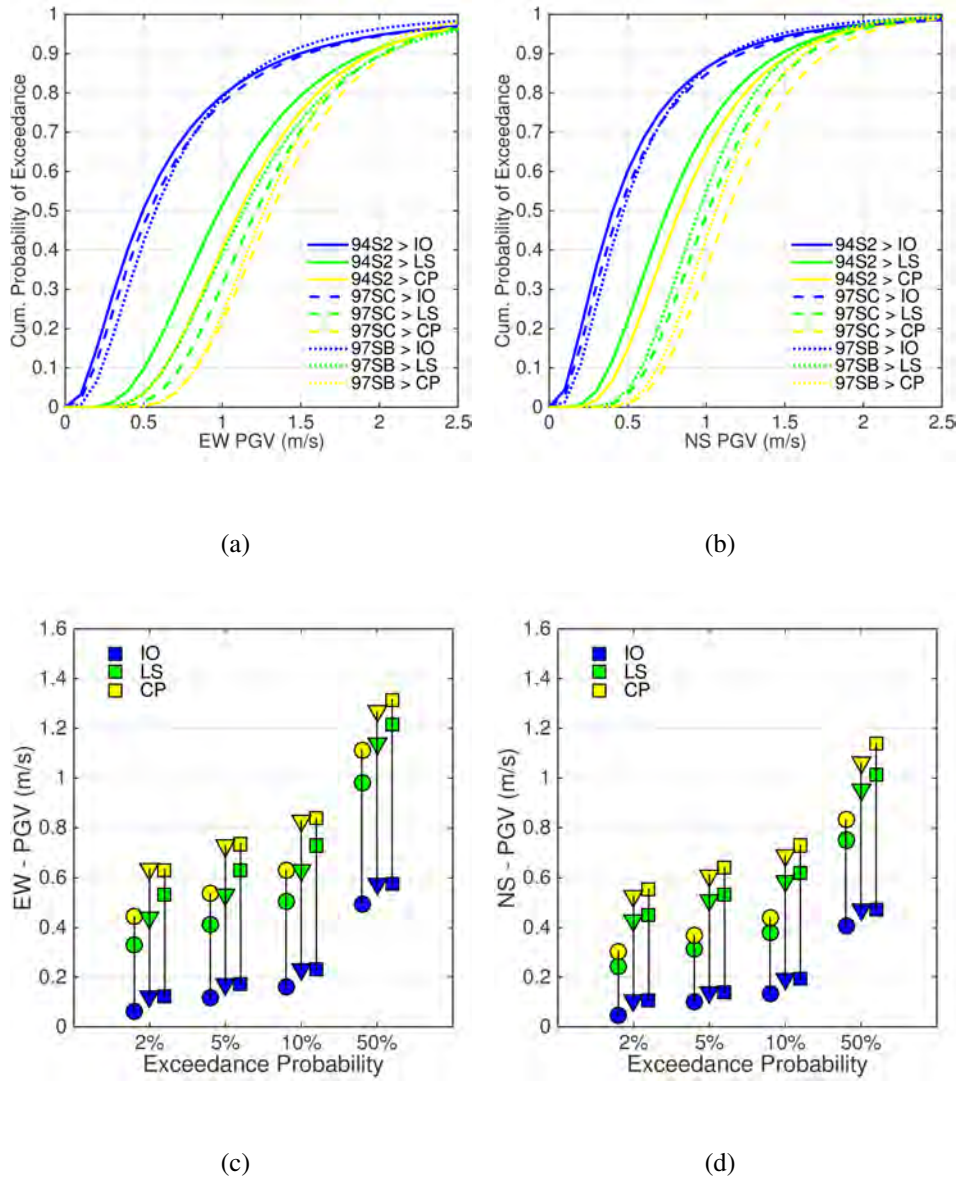
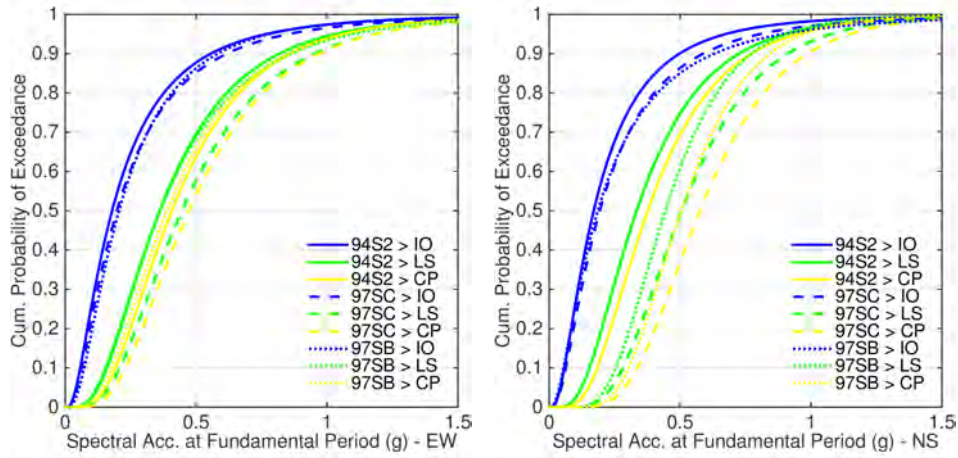
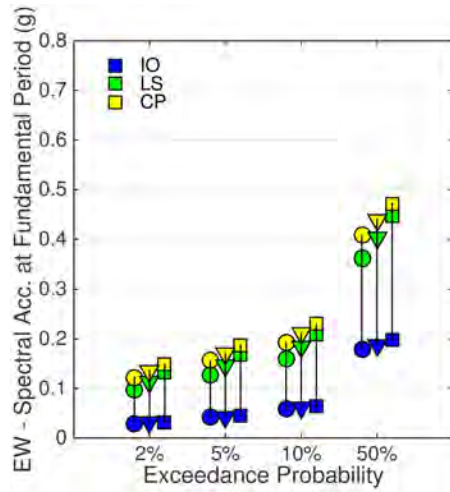


Figure H.1: Fragility curves of the probability of the peak IDR in the 94S2 (solid), the 97Sb (dotted), and the 97Sc (dashed) buildings exceeding the IO, LS, and CP performance levels as a function of the PGV in the (a) E-W and the (b) N-S directions. (c) The E-W and (d) the N-S PGV thresholds for 2%, 5%, 10%, and 50% exceedance probabilities of various performance levels in the 94S2 (circles), the 97Sb (triangle), and 97Sc (squares) designs.

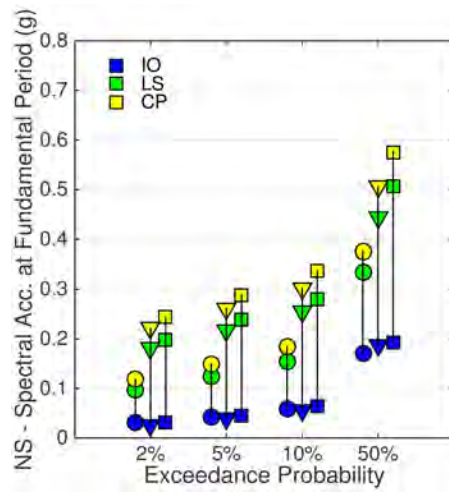


(a)

(b)



(c)



(d)

Figure H.2: Fragility curves of the probability of the peak IDR in the 94S2 (solid), the 97Sb (dotted), and the 97Sc (dashed) buildings exceeding the IO, LS, and CP performance levels as a function of the spectral acceleration at the building period in the (a) E-W and the (b) N-S directions. (c) The E-W and (d) the N-S S_a thresholds for 2%, 5%, 10%, and 50% exceedance probabilities of various performance levels in the 94S2 (circles), the 97Sb (triangle), and 97Sc (squares) designs.

Bibliography

- Abrahamson, N. and W. Silva (2008). Summary of the Abrahamson & Silva NGA Ground-Motion Relations. *Earthquake Spectra* 24(1), 67–97.
- Akcelik, V., J. Bielak, G. Biros, I. Epanomeritakis, A. Fernandez, O. Ghattas, E. J. Kim, J. Lopez, D. O'Hallaron, T. Tu, et al. (2003). High resolution forward and inverse earthquake modeling on terascale computers. In *Supercomputing, 2003 ACM/IEEE Conference*, pp. 52–52. IEEE.
- Akçiz, S. O., L. G. Ludwig, J. R. Arrowsmith, and O. Zielke (2010). Century-Long Average Time Intervals Between Earthquake Ruptures of the San Andreas fault in the Carrizo Plain, California. *Geology* 38(9), 787–790.
- Anderson, J. C. and F. C. Filippou (1995, December). Dynamic response analysis of the 17-story Canoga building. Technical Report: Analytical and Field Investigations of Buildings Affected by the Northridge Earthquake of January 17, 1994. SAC 95-04 Part 2 (revised). 12.1–12.53, SAC joint Venture, Sacramento, California.
- Anderson, J. G. and M. D. Trifunac (1978). Uniform Risk Functionals for Characterization of Strong Earthquake Ground Motion. *Bulletin of the Seismological Society of America* 68(1), 205–218.
- ATC-63 (2013). ATC-63 FEMA P-695 Quantification of Building Seismic Performance Factors by Jon A. Heintz. Slides of a talk given at LATBSCDC Annual Meeting, May 7-2010.
- Bakun, W. H. and A. G. Lindh (1985). The Parkfield, California, Earthquake Prediction Experiment.

Science 229(4714), 619–624.

- Bao, H., J. Bielak, O. Ghattas, L. F. Kallivokas, D. R. O'Hallaron, J. R. Shewchuk, and J. Xu (1998). Large-scale simulation of elastic wave propagation in heterogeneous media on parallel computers. *Computer methods in applied mechanics and engineering* 152(1), 85–102.
- Bielak, J., R. W. Graves, K. B. Olsen, R. Taborda, L. Ramírez-Guzmán, S. M. Day, G. P. Ely, D. Roten, T. H. Jordan, P. J. Maechling, et al. (2010). The shakeout earthquake scenario: Verification of three simulation sets. *Geophysical Journal International* 180(1), 375–404.
- Bjornsson, A. B. (2014). *A retrofitting framework for pre-Northridge steel moment-frame buildings*. Ph.D. thesis, California Institute of Technology.
- Björnsson, A. B. and S. Krishnan (2014). Low-Complexity Candidate for Benchmarking Collapse Prediction of Steel Braced Structures. *Journal of Structural Engineering* 140(8).
- Boore, D. M. and G. M. Atkinson (2008). Ground-Motion Prediction Equations for the Average Horizontal Component of PGA, PGV, and 5%-damped PSA at Spectral Periods Between 0.01 s and 10.0 s. *Earthquake Spectra* 24(1), 99–138.
- Bouchon, M., M. N. Toksöz, H. Karabulut, M.-P. Bouin, M. Dietrich, M. Aktar, and M. Edie (2002). Space and time evolution of rupture and faulting during the 1999 izmit (turkey) earthquake. *Bulletin of the Seismological Society of America* 92(1), 256–266.
- Brune, J. N. (1970, Jun). Tectonic stress and the spectra of seismic shear waves from earthquakes. *Journal of Geophysical Research* 75(26), 4997–5009.
- Burridge, R. and L. Knopoff (1964). Body force equivalents for seismic dislocations. *Bulletin of the Seismological Society of America* 54(6A), 1875–1888.
- Campbell, K. W. and Y. Bozorgnia (2008). NGA Ground Motion Model for the Geometric Mean Hor-

- horizontal Component of PGA, PGV, PGD and 5 % Damped Linear Elastic Response Spectra for Periods Ranging from 0.01 to 10 s. *Earthquake Spectra* 24(1), 139.
- Carlson, A. (1999). Three-dimensional Nonlinear Inelastic Analysis of Steel Moment Frame Buildings Damaged by Earthquake Excitations. *Tech. Rep. EERL 99-02, Earthquake Engineering Research Laboratory, California Institute of Technology, Pasadena, California, USA, 1999.*
- Casarotti, E., M. Stupazzini, S. J. Lee, D. Komatitsch, A. Piersanti, and J. Tromp (2008). CUBIT and seismic wave propagation based upon the spectral-element method: An advanced unstructured mesher for complex 3D geological media. In *Proceedings of the 16th International Meshing Roundtable*, pp. 579–597. Springer.
- Chi, W.-M. (1996). Inelastic analyses of a high-rise steel moment-frame building damaged in the Northridge earthquake. Master's thesis, Cornell University.
- Chiou, B.-J. and R. R. Youngs (2008). An NGA Model for the Average Horizontal Component of Peak Ground Motion and Response Spectra. *Earthquake Spectra* 24(1), 173–215.
- Cornell, C. A. (1968). Engineering Seismic Risk Analysis. *Bulletin of the Seismological Society of America* 58(5), 1583–1606.
- Custódio, S., P. Liu, and R. J. Archuleta (2005). The 2004 M_w 6.0 Parkfield, California, earthquake: Inversion of near-source ground motion using multiple data sets. *Geophysical Research Letters* 32(23), L23312.
- Ely, G., T. H. Jordan, P. Small, and P. J. Maechling (2010). A v_s^{30} derived near-surface seismic velocity model. In *Proceedings of the American Geophysical Union Fall Meeting, USA*.
- FEMA (2000). Recommended Seismic Design Criteria for New Steel Moment-Frame Buildings, prepared for the Federal Emergency Management Agency, FEMA-350, Washington, D.C.

- Field, E., G. Biasi, P. Bird, T. Dawson, K. Felzer, D. Jackson, K. Johnson, T. Jordan, C. Madden, A. Michael, K. Milner, M. Page, T. Parsons, P. Powers, B. Shaw, W. Thatcher, I. Weldon, R.J., and Y. Zeng (2013). Uniform California Earthquake Rupture Forecast, Version 3 (UCERF3) – The time-independent model: U.S. Geological Survey Open-File Report 20131165. pp. 97. California Geological Survey Special Report 228, and Southern California Earthquake Center Publication 1792, <http://pubs.usgs.gov/of/2013/1165/>.
- Field, E. H., T. E. Dawson, K. R. Felzer, A. D. Frankel, V. Gupta, T. H. Jordan, T. Parsons, M. D. Petersen, R. S. Stein, R. J. Weldon, and C. J. Wills (2009). Uniform California Earthquake Rupture Forecast, Version 2 (UCERF 2). *Bulletin of the Seismological Society of America* 99(4), 2053–2107.
- Filippou, F. C. (1995, December). Nonlinear static and dynamic analysis of a 17-story building with feap-struct. Technical Report: Analytical and Field Investigations of Buildings Affected by the Northridge Earthquake of January 17, 1994. SAC 95-04 Part 2 (revised). 11.1–11.22, SAC joint Venture, Sacramento, California.
- Frankel, A. (1995). Simulating strong motions of large earthquakes using recordings of small earthquakes: The Loma Prieta mainshock as a test case. *Bulletin of the Seismological Society of America* 85(4), 1144–1160.
- Frankel, A. (2009). A constant stress-drop model for producing broadband synthetic seismograms: Comparison with the next generation attenuation relations. *Bulletin of the Seismological Society of America* 99(2A), 664–680.
- Gan, W. (1996). Earthquake Response of Sell Braces and Braced Steel Frames. *Tech. Rep. EERL 1996-06*, Earthquake Engineering Research Laboratory, California Institute of Technology, Pasadena,

California, USA, 1996..

- Gan, W. and J. F. Hall (1998). Static and dynamic behavior of steel braces under cyclic displacement. *Journal of engineering mechanics* 124(1), 87–93.
- Graves, R. and A. Pitarka (2010). Broadband ground-motion simulation using a hybrid approach. *Bulletin of the Seismological Society of America* 100(5A), 2095.
- Graves, R. W. (1998). Three-dimensional finite-difference modeling of the San Andreas fault: Source parameterization and ground-motion levels. *Bulletin of the Seismological Society of America* 88(4), 881–897.
- Graves, R. W., B. T. Aagaard, and K. W. Hudnut (2011). The ShakeOut Earthquake Source and Ground Motion Simulations. *Earthquake Spectra* 27(2), 273–291.
- Hall, J. F. (1998). Seismic Response of Steel Frame Buildings to Near-Source Ground Motions. *Earthquake engineering & structural dynamics* 27(12), 1445–1464.
- Hall, J. F. and V. M. Challa (1995). Beam-column modeling. *Journal of engineering mechanics* 121(12), 1284–1291.
- Hall, J. F., T. H. Heaton, M. W. Halling, and D. J. Wald (1995). Near-Source Ground Motion and its Effects on Flexible Buildings. *Earthquake spectra* 11(4), 569–605.
- Hartzell, S. H. (1978, Jan). Earthquake aftershocks as Green's functions. *Geophysical Research Letters* 5(1), 1–4.
- Hartzell, S. H. and T. H. Heaton (1983). Inversion of Strong Ground Motion and Teleseismic Waveform Data for the Fault Rupture History of the 1979 Imperial Valley, California, Earthquake. *Bulletin of the Seismological Society of America* 73(6A), 1553–1583.
- Hauksson, E. (2000). Crustal structure and seismicity distribution adjacent to the Pacific and the north

- America plate boundary in southern California. *Journal of Geophysical Research* 105(B6), 13875–13.
- Heaton, T., J. Hall, D. Wall, and M. Halling (1995). Response of high-rise and base-isolated buildings to a hypothetical M_w 7.0 blind thrust earthquake. *Science* 267(5195), 206–211.
- Heaton, T. H., J. F. Hall, D. J. Wald, and M. W. Halling (1995). Response of High-Rise and Base-Isolated Buildings to a Hypothetical M_w 7.0 Blind Thrust Earthquake. *Science* 267(5195), 206–211.
- Heaton, T. H. and S. H. Hartzell (1989). Estimation of strong ground motions from hypothetical earthquakes on the Cascadia subduction zone, Pacific northwest. *Pure and Applied Geophysics* 129.
- Hudnut, K., B. Aagaard, R. Graves, L. Jones, T. Jordan, L. Star, and J. Stewart (2008). ShakeOut Earthquake Source Description, Surface Faulting and Ground Motions. *US Geol. Surv. Open File Rep 1150*, 2008.
- Irikura, K. (1983). Semi-empirical estimation of strong ground motions during large earthquakes. *Bulletin of Disaster Prevention Research Institute* 33(Part 2 - No. 198), 63–104.
- Irikura, K. (1986, May). Prediction of strong acceleration motions using empirical Green's functions. *Proceedings of the Seventh Japan Earthquake Engineering Symposium*, 151–156.
- Ji, C., D. Helmberger, and D. Wald (2002). Preliminary slip history of the 2002 denali earthquake. In *AGU Fall Meeting Abstracts*, Volume 1, pp. 1344.
- Ji, C., D. J. Wald, and D. V. Helmberger (2002a). Source description of the 1999 Hector Mine, California, earthquake, Part I: Wavelet domain inversion theory and resolution analysis. *Bulletin of the Seismological Society of America* 92(4), 1192–1202.
- Ji, C., D. J. Wald, and D. V. Helmberger (2002b). Source description of the 1999 Hector Mine, California, earthquake, Part II: Complexity of slip history. *Bulletin of the Seismological Society of*

- America* 92(4), 1208–1226.
- Jones, Lucile M and Benthien, Mark (2011). Preparing for a Big One: The Great Southern California ShakeOut. *Earthquake Spectra* 27(2), 575–595.
- Joyner, W. and D. Boore (1986). On simulating large earthquakes by Green’s-function addition of smaller earthquakes. *Earthquake Source Mechanics, American Geophysical Union Monograph* 37.
- Kellogg, L. (2011, June). Computational infrastructure for geodynamics. <http://geodynamics.org>.
- Kohler, M. D., H. Magistrale, and R. W. Clayton (2003). Mantle heterogeneities and the SCEC reference three-dimensional seismic velocity model version 3. *Bulletin of the Seismological Society of America* 93(2), 757–774.
- Komatitsch, D. (2011). Fluid-solid coupling on a cluster of GPU graphics cards for seismic wave propagation. *Comptes Rendus de l’Academie des Sciences Mecanique* 339, 125–135.
- Komatitsch, D., G. Erlebacher, D. GÖddeke, and D. Michéa (2010). High-order finite-element seismic wave propagation modeling with MPI on a large GPU cluster. *Journal of Computational Physics* 229(20), 7692–7714.
- Komatitsch, D., Q. Liu, J. Tromp, P. Süß, C. Stidham, and J. H. Shaw (2004). Simulations of ground motion in the Los Angeles basin based upon the spectral-element method. *Bulletin of the Seismological Society of America* 94(1), 187–206.
- Komatitsch, D. and J. Tromp (1999). Introduction to the spectral element method for three-dimensional seismic wave propagation. *Geophysical Journal International* 139(3), 806–822.
- Krishnan, S. (2003). FRAME3D - A Program for Three-dimensional Nonlinear Time-history Analysis of Steel Buildings: User Guide. *Technical Rep. No. EERL 2003-03*.

- Krishnan, S. (2009). *FRAME3D V2.0: A Program for the Three Dimensional Nonlinear Time-History Analysis of Steel Structures: User Guide*. California Institute of Technology.
- Krishnan, S. (2010). Modified Elastofiber Element for Steel Slender Column and Brace Modeling. *Journal of structural engineering* 136(11), 1350–1366.
- Krishnan, S. and J. F. Hall (2006a, April). Modeling Steel Frame Buildings in Three Dimensions. I: Panel Zone and Plastic Hinge Beam Elements. *Journal of Engineering Mechanics* 132(4), 345–358.
- Krishnan, S. and J. F. Hall (2006b, April). Modeling Steel Frame Buildings in Three Dimensions. II: Elastofiber Beam Element and Examples. *Journal of Engineering Mechanics* 132(4), 359–374.
- Krishnan, S., C. Ji, D. Komatitsch, and J. Tromp (2006a). Case Studies of Damage to Tall Steel Moment-Frame Buildings in Southern California during Large San Andreas Earthquakes. *Bulletin of the Seismological Society of America* 96(4A), 1523–1537.
- Krishnan, S., C. Ji, D. Komatitsch, and J. Tromp (2006b). Performance of two 18-story steel moment-frame buildings in southern California during two large simulated San Andreas earthquakes. *Earthquake Spectra* 22(4), 1035–1061.
- Krishnan, S. and M. Muto (2012). Mechanism of collapse of tall steel moment-frame buildings under earthquake excitation. *Journal of Structural Engineering* 138(11), 1361–1387.
- Lin, G., P. M. Shearer, E. Hauksson, and C. H. Thurber (2007). A three-dimensional crustal seismic velocity model for southern California from a composite event method. *Journal of Geophysical Research: Solid Earth (1978–2012)* 112(B11).
- Liu, Q., J. Polet, D. Komatitsch, and J. Tromp (2004). Spectral-element moment tensor inversions for earthquakes in southern California. *Bulletin of the Seismological Society of America* 94(5), 1748–1761.

- Magistrale, H., S. Day, R. W. Clayton, and R. Graves (2000). The SCEC southern California reference three-dimensional seismic velocity model version 2. *Bulletin of the Seismological Society of America* 90(6B), S65–S76.
- Magistrale, H., K. McLaughlin, and S. Day (1996). A geology-based 3D velocity model of the Los Angeles basin sediments. *Bulletin of the Seismological Society of America* 86(4), 1161–1166.
- Mai, P. M., W. Imperatori, and K. B. Olsen (2010). Hybrid broadband ground-motion simulations: Combining long-period deterministic synthetics with high-frequency multiple S-to-S backscattering. *Bulletin of the Seismological Society of America* 100(5A), 2124–2142.
- McGuire, R. K. (1977). Seismic Design Spectra and Mapping Procedures Using Hazard Analysis Based Directly on Oscillator Response. *Earthquake Engineering & Structural Dynamics* 5(3), 211–234.
- McGuire, R. K. (1995). Probabilistic Seismic Hazard Analysis and Design Earthquakes: Closing the Loop. *Bulletin of the Seismological Society of America* 85(5), 1275–1284.
- Mitrani-Reiser, J. (2007). *An ounce of prevention: probabilistic loss estimation for performance-based earthquake engineering*. Ph. D. thesis, California Institute of Technology.
- Mourhatch, R. and S. Krishnan (2015a). Risk Analysis Using Rupture-to-Rafters Simulations: Inferring Probabilities of Scenario Earthquakes from the Uniform California Earthquake Rupture Forecast. *Manuscript, to be submitted to Seismological Research Letters*.
- Mourhatch, R. and S. Krishnan (2015b, Under Review). Simulation of broadband ground motion by superposing high-frequency empirical green's function synthetics on low-frequency spectral-element synthetics. *Bulletin of the Seismological Society of America*.
- Muto, M. and S. Krishnan (2011). Hope for the Best, Prepare for the Worst: Response of Tall Steel Buildings to the Shakeout Scenario Earthquake. *Earthquake Spectra* 27(2), 375–398.

- Muto, M., S. Krishnan, J. Beck, and J. Mitrani-Reiser (2008). Seismic loss estimation based on end-to-end simulation. In *Proceedings of the first international symposium on life-cycle civil engineering, Varenna, Lake Como, Italy*, pp. 215–232.
- Naeim, F. (2001). *The Seismic Design Handbook, 2nd Edition*. Springer Science & Business Media.
- Olsen, K., R. Archuleta, and J. Matarese (1995). Three dimensional simulation of a magnitude 7.75 earthquake on the San Andreas fault. *Science* 270(5242), 1628–1632.
- Olsen, K., S. Day, L. Dalguer, J. Mayhew, Y. Cui, J. Zhu, V. Cruz-Atienza, D. Roten, P. Maechling, T. Jordan, et al. (2009). ShakeOut-D: Ground Motion Estimates Using an Ensemble of Large Earthquakes on the Southern San Andreas Fault with Spontaneous Rupture Propagation. *Geophysical Research Letters* 36(4).
- Paret, T. F. and K. K. Sasaki (1995, December). Analysis of a 17 story steel moment frame building damaged by the Northridge earthquake. Technical Report: Analytical and Field Investigations of Buildings Affected by the Northridge Earthquake of January 17, 1994. SAC 95-04 Part 2 (revised). 10.1–10.52, SAC joint Venture, Sacramento, California.
- Plesch, A., C. Tape, J. Graves, P. Small, G. Ely, and J. Shaw (2011). Updates for the CVM-H Including New Representations of the Offshore Santa Maria and San Bernardino Basin and a New Moho Surface. In *2011 Southern California Earthquake Center Annual Meeting, Proceedings and Abstracts, Volume 21*.
- Plesch, A., C. Tape, R. Graves, J. H. Shaw, P. Small, and G. Ely (2011). Updates for the CVM-H including new representations of the offshore Santa Maria and San Bernardino basins and a new Moho surface. In *SCEC 2011 Annual Meeting*, pp. Poster B–128. Southern California Earthquake Center.

- Porter, K. A. (2003). An Overview of PEERs Performance-Based Earthquake Engineering Methodology. In *Conference on Applications of Statistics and Probability in Civil Engineering (ICASP9)*, pp. 6–9. Civil Engineering Risk and Reliability Association (CERRA) San Francisco,, California.
- Prindle, K. and T. Tanimoto (2006). Teleseismic surface wave study for S-wave velocity structure under an array: southern California. *Geophysical Journal International* 166(2), 601–621.
- Sandia National Laboratory, U. (2011, November). CUBIT: Geometry and mesh generation toolkit. <http://cubit.sandia.gov>.
- Sieh, K. E. (1978). Prehistoric Large Earthquakes Produced by Slip on the San Andreas Fault at Palmet Creek, California. *Journal of Geophysical Research: Solid Earth (1978–2012)* 83(B8), 3907–3939.
- Siriki, H., R. Mourhatch, and S. Krishnan (2015). Limit State Probabilities of Tall Steel Moment Frame Buildings due to Large San Andreas Fault Earthquakes. *Manuscript, to be submitted to Earthquake Engineering and Structural Dynamics*.
- Somerville, P., M. Sen, and B. Cohee (1991). Simulation of strong ground motions recorded during the 1985 Michoacan, Mexico and Valparaiso, Chile earthquakes. *Bulletin of the Seismological Society of America* 81(1), 1–27.
- SRCMOD (Finite-Source Rupture Model Database). Finite-Source Rupture Model Database (Initiated by Martin Mai)-<http://equake-rc.info/SRCMOD/>.
- Stein, S. and M. Wysession (2003). *An Introduction to Seismology, Earthquake, and Earth Structure*. Malden, MA: Blackwell Publishing Ltd.
- Suss, M. P. and J. H. Shaw (2003). P-wave seismic velocity structure derived from sonic logs and industry reflection data in the Los Angeles basin. *Journal of Geophysical Research* 108(B3), Article no.

2170.

- Süss, M. P. and J. H. Shaw (2003, Mar). P wave seismic velocity structure derived from sonic logs and industry reflection data in the Los Angeles basin, California. *Journal of Geophysical Research* 108(B3), 1–18.
- Tape, C., Q. Liu, A. Maggi, and J. Tromp (2009). Adjoint tomography of the southern California crust. *Science* 325(5943), 988.
- Tape, C., Q. Liu, A. Maggi, and J. Tromp (2010). Seismic tomography of the southern California crust based on spectral element and adjoint methods. *Geophysical Journal International* 180(1), 433–462.
- Taranath, B. S. (2004). *Wind and earthquake resistant buildings: structural analysis and design*. CRC press.
- Tromp, J., D. Komattisch, and Q. Liu (2008). Spectral-element and adjoint methods in seismology. *Communications in Computational Physics* 3(1), 1–32.
- Tumarkin, A. G. and R. J. Archuleta (1994, Sep). Empirical ground motion prediction. *Annali Di Geofisica* XXXVII(6), 1691–1720.
- Uang, C.-M. and V. V. Bertero (1988). Implications of Recorded Earthquake Ground Motions on Seismic Design of Building Structures. *Report No. UCB/EERC-88/13*.
- UBC (1994). Uniform building code. In *International Conference of Building Officials, Whittier, CA*.
- UBC (1997). Uniform building code. In *International Conference of Building Officials, Whittier, CA*.
- Wald, D. J. (1996). Slip History of the 1995 Kobe, Japan, Earthquake Determined from Strong Motion, Teleseismic, and Geodetic Data. *Journal of Physics of the Earth* 44(5), 489–504.

Wald, D. J. and T. I. Allen (2007). Topographic Slope as a Proxy for Seismic Site Conditions and Amplification. *Bulletin of the Seismological Society of America* 97(5), 1379–1395.

Wald, D. J. and T. H. Heaton (1994). Spatial and Temporal Distribution of Slip for the 1992 Landers, California, Earthquake. *Bulletin of the Seismological Society of America* 84(3), 668–691.